

EXPERIMENTAL INVESTIGATIONS OF VORTEX FLOW AND ITS MODIFICATION AROUND WALL-CYLINDER JUNCTIONS

by

SUBHASH CHANDER SHARMA



DEPARTMENT OF AERONAUTICAL ENGINEERING
INDIAN INSTITUTE OF TECHNOLOGY, KANPUR

JULY, 1988

AE
1988
D
SHA
EXP

DEL/11/88/D
CHDCE
-13-5

EXPERIMENTAL INVESTIGATIONS OF VORTEX FLOW AND ITS MODIFICATION AROUND WALL-CYLINDER JUNCTIONS

A Thesis Submitted
In Partial Fulfilment of the Requirements
for the Degree of

DOCTOR OF PHILOSOPHY

by

SUBHASH CHANDER SHARMA

to the

DEPARTMENT OF AERONAUTICAL ENGINEERING
INDIAN INSTITUTE OF TECHNOLOGY, KANPUR

JULY, 1988

AE-1989-D-SHA-E

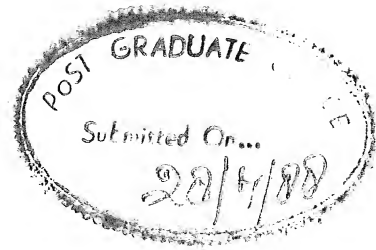
7 NOV 1989

CENTRAL LIBRARY
KALPUR

Acc. No. A106218

1h
629.1323
Sh 23e

*Dedicated
to
My Parents*



CERTIFICATE

This is to certify that the work 'EXPERIMENTAL INVESTIGATIONS OF VORTEX FLOW AND ITS MODIFICATION AROUND WALL-CYLINDER JUNCTIONS' is a record of bonafide research carried out by Subhash Chander Sharma under my supervision and guidance, and that it has not been submitted elsewhere for a degree.

A. K. Gupta

Dr. A.K. Gupta
THESIS SUPERVISOR
Professor

Department of Aeronautical Engineering
Indian Institute of Technology, Kanpur

Dated : 20-7-88

ACKNOWLEDGEMENTS

It is with a deep sense of gratitude that I wish to express my sincere thanks to Dr. A.K. Gupta for his guidance and encouragement throughout this work. He introduced me to this novel concept of HSV modification. He has been very generous in giving me time, both in the Institute and at his residence. His presence at the photographic sessions has been really inspiring and instructive. Apart from academics, he took keen interest in my well being. I have enjoyed many happy moments including the Sunday TV serials as a member of his family.

I wish to take this opportunity to express my high regards for Dr. N.L. Arora, Professor and Head of the Department of Aeronautical Engineering.

The keen interest of Professors A.C. Jain and S.C. Raisinghani in my Ph.D. Program are sincerely acknowledged.

Thanks are due to Dr. P.K. Chatterjee, Head EED and Dr. H. Hatwal of MED for sparing oscilloscope and Spectrum Analyzer respectively.

Thanks are due to the staff of Aero. Workshop for fabrication of set-up, Mr. V.C. Srivastava for handling the Camera and Mr. Ganguli for tracing work. I am thankful to

Mr. K.S. Mudappa, Technical Officer for his sincere efforts in putting my requirements in state of readiness, in time. And to my young friends JS, CSR, VK and SB for the efforts in putting this thesis in the present form.

I am thankful to Chandigarh Administration for deputing me under Q.I.P. for doctoral work. The keenness of Dr.O.S.Sahgal, the then Principal Punjab Engineering College Chandigarh and the sincere efforts of Professor V.S. Malhotra, Head, AED in this matter are gratefully acknowledged. Thanks are also due to Professors V.P. Vasandani and A.D. Kapoor of MED in this connection.

I wish to express my regards for our close relation Shri I.D. Swami IAS for what he did for me.

The intellectual company of Mr. Pradeep Kumar, my friend and former colleague at VSSC, was a tonic for academic activities during his stay in the IIT Campus.

I am deeply thankful to Professor N.G.R. Iyengar and Mrs. Leela Iyengar for providing me their residence in 'AS IT IS' condition during the summers of 1985 and 1986, enabling my family to join me. My special thanks are due to Mr. T.D. Jogpal IAS and Mrs. Kanta Jogpal.

The patience and persevearence of wife Kavita, and daughters Mani, Phanu and son Manik, in staying back in Chandigarh

throughout this period of three years has been source of strength for me. I promise not to desert them like this again in future.

S.C. SHARMA

CONTENTS

Page No.

CERTIFICATE

ACKNOWLEDGEMENT

LIST OF SYMBOLS

LIST OF FIGURES

SYNOPSIS

iv

v

xxi

CHAPTER I INTRODUCTION AND LITERATURE REVIEW

1.1	LITERATURE REVIEW	5
1.1a	<u>Secondary Flows</u>	6
1.1b	<u>Vertical Circular Cylinder Mounted on a Wall</u>	9
1.1c	<u>Leading Edge Geometry</u>	16
1.1d	<u>Local Scoure and its Protection</u>	20
1.1e	<u>Horseshoe Vortex Modification (Gupta, 1987)</u>	26
1.1f	<u>Aerodynamics of Delta Wing</u>	29
1.2	PRESENT INVESTIGATION	33

CHAPTER II EXPERIMENTAL EQUIPMENT AND INSTRUMENTATION

2.1	WIND TUNNEL	42
a.	<u>The Test Section</u>	43
2.2	WATER TABLE	44
2.3	MODELS	46
a.	<u>Pressure Model of Circular Cylinder</u>	46
b.	<u>Flow Visualization Models</u>	47
	(i) Circular Cylinders	47
	(ii) Pier Models	47
2.4	DELTA-WING-LIKE PASSIVE DEVICE	48

	<u>Page No.</u>
2.5 THE TURN TABLE	50
2.6 PROBES	52
a. <u>Shielded Pitot Tube</u>	52
b. <u>Hot Wire Probe</u>	52
c. <u>Pitot Tube</u>	52
2.7 INSTRUMENTS	53
2.8 PHOTOGRAPHIC EQUIPMENT	56
CHAPTER III EXPERIMENTAL TECHNIQUES	
3.1 FLOW VISUALIZATION	76
a. <u>Titanium Tetrachloride (TiCl₄) Technique</u>	76
b. <u>Potassium Permanganate (KMnO₄) Dye Technique</u>	80
c. <u>Surface Oil Film Technique</u>	81
3.2 PRESSURE MEASUREMENTS	82
a. <u>State Pressure Measurements</u>	83
b. <u>Total Head Measurements</u>	84
3.3 VELOCITY MEASUREMENTS	85
3.4 MEASUREMENT OF VORTEX OSCILLATIONS	87
3.5 CALIBRATION	88
a. <u>The Test Section</u>	88
b. <u>Hot Wire</u>	89
c. <u>Shielded Pitot Tube</u>	90
d. <u>Spectrum Analyzer</u>	91
CHAPTER IV THE MECHANISM OF HORSESHOE VORTEX MODIFICATION	
4.1 INTRODUCTION	103
4.2 CO-ORDINATE SYSTEM	103

4.3	RESULTS WITH CLEAN PIER MODEL	104
4.3.1	<u>Laminar Flow</u>	104
	a. Flow Visualization	104
	b. Pressure Measurements	108
4.3.2	<u>Transition to Turbulent Flow</u>	109
4.3.3	<u>Turbulent Flow</u>	109
	a. Surface Oil Film pattern	110
	b. Pressure Measurements	111
	c. Total head survey	113
4.4	THE MODIFIED HORSESHOE VORTEX	114
4.4.1	<u>Laminar Flow</u>	114
4.4.2	<u>Transition to Turbulent Flow</u>	118
4.4.3	<u>Turbulent Flow</u>	119
	a. Surface Oil Film pattern	119
	b. Pressure Measurements	120
	c. Total head survey	123
4.5	AERODYNAMICS OF DELTA-WING-LIKE PASSIVE DEVICE	124
4.6	DISCUSSION	129
4.6.1	<u>HSV around Vertical Pier Model with round nose</u>	130
4.6.2	<u>The Modified HSV</u>	133
CHAPTER V	MODIFICATION OF HORSESHOE VORTEX AROUND WALL-CIRCULAR CYLINDER JUNCTION	
5.1	INTRODUCTION	175
5.2	CO-ORDINATE SYSTEM	175
5.3	RESULTS WITH CLEAN CIRCULAR CYLINDER	175
5.3.1	<u>Laminar Flow</u>	176
	a. Flow Visualization	176
	b. Pressure Measurements	180

5.3.2	<u>Transition To Turbulent Flow</u>	180
5.3.3	<u>Turbulent Flow</u>	182
a.	Surface Oil Film Pattern	182
b.	Pressure Measurements	186
(i)	Floor Pressures around the Cylinder	186
(ii)	Surface Pressures on the Cylinder	187
c.	Total Head Survey	188
5.4	MODIFIED HORSESHOE VORTEX	189
5.4.1	<u>Laminar Flow</u>	190
5.4.2	<u>Transition to Turbulent Flow</u>	192
5.4.3	<u>Turbulent Flow</u>	192
a.	Surface Oil Film Patterns	193
b.	Pressure Measurements	193
(i)	Floor Pressures around the Cylinder	194
(ii)	Surface Pressures on the Cylinder	195
(iii)	Symmetry of Pressures	197
c.	Total Head Survey	197
5.5	DISCUSSION	199
5.5.1	<u>HSV Around Circular Cylinder</u>	199
5.5.2	<u>Aerodynamics of Delta-Wing-like Passive Device</u>	202
5.5.3	<u>The Modification of HSV</u>	203

CHAPTER VI	EFFECT OF LEADING EDGE SHAPE ON HSV AND MODIFIED HSV	
6.1	INTRODUCTION	255
6.2	CO-ORDINATE SYSTEM	255

	<u>Page No.</u>
6.3 RESULTS WITH CLEAN PIER MODELS	256
6.3.1 <u>Laminar Flow</u>	256
a. Dye Flow Visualization	256
(i) Dye Patterns around Rectangular Pier Model	257
(ii) Dye Patterns Around Streamline Nose Pier Models	257
b. $TiCl_4$ Flow Visualization	258
(i) $TiCl_4$ Flow around Rectangular Pier Model	258
(ii) $TiCl_4$ Flow around Streamline Nose Pier Models	259
c. Pressure Measurements	261
6.3.2 <u>Transition to Turbulent Flow</u>	261
6.3.3 <u>Turbulent Flow</u>	263
a. Surface Oil Film Patterns	263
(i) Surface-Flow Patterns around Rectangular Pier Model	264
(ii) Surface Flow Patterns around Streamline Nose Pier models	264
b. Pressure Distribution	266
(i) Pressure Distribution around Rectangular Pier Model	266
(ii) Pressure Distribution around Streamline Nose Pier Models	267

c.	Total Head Survey	268
(i)	Rectangular Pier Model	269
(ii)	Streamline Nose Pier Models	269
6.4	THE MODIFIED HORSESHOE VORTEX	270
6.4.1	<u>Laminar Flow</u>	271
a.	Dye Flow Visualization	271
(i)	Rectangular Pier Model	271
(ii)	Streamline Nose Pier Model	272
b.	TiCl ₄ Flow Visualization	273
(i)	Rectangular Pier Model	273
(ii)	Streamline Nose Pier Models	274
6.4.2	<u>Transition to Turbulent Flow</u>	275
6.4.3	<u>Turbulent Flow</u>	276
b.	Pressure Distributions	278
(i)	Upstream Plane of Symmetry, U	278
(ii)	Leading Edge Corner, L ₁	278
(iii)	Mid-Span, M ₁	279
(iv)	Trailing Edge Corner, T ₁	279
(v)	Downstream Plane of Symmetry, DS	279
(vi)	The Symmetry of Flow Around Pier Models	280
c.	Total Head Survey	280
(i)	Rectangular Pier Model	281
(ii)	Streamline Nose Pier Models	281

Page No.

6.5	DISCUSSION	283
6.5.1	<u>HSV Around Clean Pier Models</u>	283
6.5.2	<u>Aerodynamics of Delta-Wing-Like Passive Device</u>	285
6.5.e	<u>Modification of HSV</u>	286
CHAPTER VII	CONCLUSIONS AND FURTHER WORK	
7.1	THE HORSESHOE VORTEX IN LAMINAR FLOW	362
7.2	THE VORTEX OSCILLATIONS	363
7.3	THE HORSESHOE VORTEX IN TURBULENT FLOW	365
7.4	THE MECHANISM OF HSV MODIFICATION	366
7.5	FURTHER WORK	368
	REFERENCES	378
	APPENDIX	A

LIST OF SYMBOLS

A	Attachment
D	Diameter, pier width
Fr	Froude No
L	Height of the pier model
Re	Reynolds No
S	Separation
U_∞	Free Stream velocity
W	Width of Neek
X,Y,Z	Cartesian Co-ordinates
S	Local Co-ordinate
u'	Fluctuating velocity
\bar{u}	Mean velocity
r,	Polar Co-ordinates
α	Angle of attack
δ	Boundary Layer thickness
δ^*	Displacement thickness
ν	Kinematic viscosity

LIST OF FIGURES

	<u>Page No.</u>
Fig. 1.1 The Horseshoe Vortex	37
a. Side view	
b. A Perspective view	
Fig. 1.2 The Structure of Horseshoe Vortex (Baker, 1979)	38
Fig. 1.3 Sutton's Experiment (Baker, 1979)	39
Fig. 1.4 Typical Flow Over a Delta wing at Moderate Incidence	40
a. Vortex sheets formed on the suction side	
b. Surface flow patterns	
Fig. 1.5 Aerodynamic Characteristics of Delta wing of $AR = 1.5$	41
Fig. 2.1 30.5 x 40.5 Low Speed Low Turbulence Wind Tunnel	57
Fig. 2.2 A View of Low Speed Wind tunnel	58
Fig. 2.3 A view of the Test-section	58
Fig. 2.4 Schematic Diagram of the water table	59
Fig. 2.5 A view of the water table	60
Fig. 2.6 Pressure Model of Circular Cylinder	61
Fig. 2.7 Circular Cylinder Pressure Model	62
a. Component Details	
b. Finished stage	
Fig. 2.8 Circular Cylinder Models	63
Fig. 2.9 Sectional Details of Pier Models	64

Fig. 2.10	The Pier Models	65
Fig. 2.11	The Passive Devices	65
Fig. 2.12	Delta-Wing-like Passive Device	66
Fig. 2.13	Details of Turn Table	67
Fig. 2.14	Bottom Side of Turn Table I	67
Fig. 2.15	Pressure Model Mounted on Turn Table I	67A
Fig. 2.16	Bottom View of Turn Table Assembly in Test-Section	68
Fig. 2.17	Turn Table Cum Floor Assembly	69
Fig. 2.18	Details of Circular Plate II	70
Fig. 2.19	The Shielded Pitot tube	71
Fig. 2.20	Schematic View of Shielded Pitot tube	71
Fig. 2.21	The Hot Wire Probe	72
Fig. 2.22	The Pitot tube	72
Fig. 2.23	Close up view of Electronic Instruments	73
Fig. 2.24	24-Channel Pressure Selector Switch (Head, 1971)	73
Fig. 2.25	Functioning Details of Pressure Selector Switch (Head, 1971)	74
Fig. 2.26	3-D Precession Traverse Mechanism	75
Fig. 2.27	An Overall view of the Wind Tunnel and the Instruments	75
Fig. 3.1	Stainless Steel Pipettes with Chamferred ends and TiCl_4 container	92
Fig. 3.2	Illustration of TiCl_4 Techniques	93

		<u>Page No.</u>
Fig. 3.3	Representative Stations in Flow Field around various pier models	94
Fig. 3.4a	Velocity Profile in Laminar Boundary Layer	95
Fig. 3.4b	Velocity Distribution in Turbulent Boundary Layer	96
Fig. 3.4c	Typical Variation of Turbulence in Velocity Profiles	97
Fig. 3.5	Variation of δ^* with U and Re	98
Fig. 3.6	Calibration of Wind Tunnel Test Section	99
	a. C_p Distribution	
	b. Pressure gradient Parameter Distribution	
Fig. 3.7a	Hot Wire Calibration (E v/s U)	100
Fig. 3.7b	Hot Wire Calibration (E^2 v/s \sqrt{U})	101
Fig. 3.8	Calibration of Shielded Pitot tube	102
Fig. 3.9	Calibration of HP 3582A Spectrum Analyzer	102
Fig. 4.1	Dye Patterns around vertical Round Nose Pier Model, $L/D = 6$, $BR=10\%$, $Re = 3197$, $Fr = 0.146$	137
	a. Plan View	
	b. Top Front View	
	c. Top Rear View	
Fig. 4.2	Line Sketch of Dye Patterns from Fig. 4.1	138
Fig. 4.3	$TiCl_4$ Flow around vertical Round Nose Pier Model $L/D = 6$, $BR = 3\%$, $Re = 1400$, $D/\delta^* = 4.4$	139
	a. Perspective View	
	b. Top Front View	
	c. Top Rear View	

		<u>Page No.</u>
Fig. 4.4	Line Sketch of $TiCl_4$ Flow around the Pier Model From Fig. 4.3	140
Fig. 4.5	Pressure Distribution on upstream plane of symmetry of round Nose Pier Model, $L/D = 6$, $BR = 3\%$ $Re = 2265$, $D/\delta^* = 5.6$	141
Fig. 4.6	Spectra and Traces of Vortex Oscillations around Vertical Round Nose Pier, $L/D = 6$, $BR = 3\%$	142
Fig. 4.7	Variation of Vortex Oscillation Frequencies around Vertical Round Nose Pier, $L/D = 6$, $BR = 3\%$	143
Fig. 4.8	Surface Oil Film Patterns around Vertical Round Nose Pier $L/D = 6$, $BR = 3\%$, $Re = 7768$, $D/\delta^* = 11$ a. $t = 20$ Min. (Flow on) b. $t = 20$ Min.	144
Fig. 4.9	a. Surface Streamlines around Vertical Round Nose Pier $L/D = 6$, $BR = 3\%$, $Re = 7768$, $D/\delta^* = 11$ b. Flow Pattern inferred from surface flow visualization	145 145
Fig. 4.10	Pressure Distribution on Floor around vertical Round Nose Pier Mo Model $L/D = 6$, $BR = 3\%$ a. $Re = 8600$, $D/\delta^* = 11.5$ b. $Re = 13,000$, $D/\delta^* = 14.5$ c. Reynolds Number dependence Locations : U and DS d. Reynolds Number dependence Locations : L_1 , M_1 , T_1 e. C_p variation along the junction of Round Nose Pier Model, $L/D = 6$, $BR = 3\%$	146 147 148 149 150

		<u>Page No.</u>
Fig. 4.11	Total Head countours in the Y-Z Plane at Mid span of Round Nose Pier Model, $L/D = 6$, $BR = 3\%$	151
Fig. 4.12	A View of Round Nose Pier Model with Passive device	152
Fig. 4.13	A Sketch of Round Nose Pier Model with Passive device	153
Fig. 4.14	Dye Patterns around vertical Round Nose Pier with Passive device, $Re = 3026$, $Fr = 0.135$	154
	a. Plan View b. Top Front View c. Top Rear View	
Fig. 4.15	$TiCl_4$ Flow around vertical Round Nose Pier with Passive device	
	a. Perspective View from Rear b. Apex Vortex c. LESV d. Front Perspective View e. Top Front View f. Top Rear View g. Somersaulting of Apex Vortex at the Pier h. Close up view i. Merging of LESV and Apex Vortex at $Re = 1760$, $D/\delta^* = 4.9$	155 156 157
Fig. 4.16	Schematic of modified Vortex System	158
Fig. 4.17	Spectra and Traces of modified vortex Flow around vertical Round Nose Pier with Passive device	159
Fig. 4.18a	Variation of Modified Vortex Oscillations around vertical Round Nose Pier with Passive device	160
Fig. 4.18b	Variation of \bar{u} and u' upstream of Round Nose Pier with and without Passive device.	161

		<u>Page No.</u>
Fig. 4.19	Surface Oil Film Patterns around Vertical Round Nose Pier with Passive Device	162
	a. $t = 12$ Min. (Tunnel Running)	
	b. $t = 12$ Min.	
Fig. 4.20	Modified Surface Streamlines around Vertical Round Nose Pier	163
Fig. 4.21	Pressure Distribution Around vertical Round Nose Pier with and without Passive device	164
	a. On upstream plane of symmetry	164
	b. At Leading Edge Corner	165
	c. At Mid-span	166
	d. At Trailing Edge Corner	167
	e. On Downstream Plane of Symmetry	168
Fig. 4.22	Pressure Distribution around Vertical Round Nose Pier	
	a. At Leading Edge Corner L_1, L_2	169
	b. At Mid-span M_1, M_2	170
	c. At Trailing Edge Corner T_1, T_2	171
Fig. 4.23	Total Head Contours in Y-Z Plane at mid-span of Round Nose Pier Model with Device	172
Fig. 4.24	Schematic of Vortices below the Passive Device	173
Fig. 4.25	The Modified Vortex Flow around Vertical Pier with Round Nose	174
Fig. 5.1	A Perspective View of Dye Patterns around circular cylinder	204

Fig. 5.2	Dye Patterns Around Circular Cylinder, $L/D = 6$, $BR = 10\%$, $Re = 3197$, $Fr = 0.146$ (Flow from Left to Right)	205
	a. Plan View b. Top Front View c. Top Rear View	
Fig. 5.3	Line sketch of Dye Patterns	206
Fig. 5.4	$TiCl_4$ Flow Around Circular Cylinder Junction, $L/D = 6$, $BR = 3\%$, $Re = 1450$ $D/\delta^* = 4.5$ (Flow From Left to Right)	207
	a. Perspective View b. Top Front View c. Top Rear View d. Line Sketch of $TiCl_4$ Flow Patterns	208
Fig. 5.5	Pressure Distribution on the Upstream Plane of symmetry of Circular Cylinder in Laminar Flow, $L/D = 6$, $BR = 3\%$	209
Fig. 5.6a	Spectra and Traces of Vortex Oscillations Around Circular Cylinder, $L/D = 6$, $BR = 3\%$	210
Fig. 5.6b	Variation of Vortex Oscillations with Re , D/δ^*	211
Fig. 5.6c	Variation of \bar{u} and u' with Reynolds Number	212
Fig. 5.7	Surface Oil Film Patterns Around 50 mm Circular Cylinder	213
Fig. 5.8	Surface Oil Film Patterns Around 37.5 mm Circular Cylinder	214
Fig. 5.9	Surface Oil Film Patterns Around 25 mm Circular Cylinder	215
Fig. 5.10	Surface Oil Film Patterns Around 12.5 mm Circular Cylinder	216

Page No.

Fig. 5.11	Surface Oil Film Patterns 6 mm Circular Cylinder	217
Fig. 5.12	Surface Oil Film Patterns Around 3 mm Circular Cylinder	218
	a. Flow On b. $t = 10$ minutes	
Fig. 5.13	Surface Streamlines Around Circular Cylinder	219
	a. Four Vortex System b. Two Vortex System	
Fig. 5.14	Variation of x_s Upstream of Circular Cylinder	220
Fig. 5.15a	Pressure Distribution on the Wall upstream of symmetry of Circular Cylinder, $L/D = 6$, $BR = 3\%$	221
Fig. 5.15b	Pressure Distribution on the Wall around Circular Cylinder $L/D = 6$, $BR = 3\%$	222
Fig. 5.16a	Pressure Distribution on the Circular Cylinder Periphery $L/D = 6$, $BR = 3\%$	223
Fig. 5.16b	Pressure Distribution on Wall Circular Cylinder Junction	224
Fig. 5.17	Total Head Contours in Y-Z plane at mid-span of Circular Cylinder $L/D = 6$, $BR = 3\%$	225
Fig. 5.18a	A view of circular Cylinder with Passive Device	226
Fig. 5.18b	Circular Cylinder with Passive Device	227
Fig. 5.19	A Perspective View of Dye Patterns Around Circular Cylinder with Passive Device	228
Fig. 5.20	Dye Patterns Around Circular Cylinder with Passive Device, $Re = 3026$, $Fr = 0.135$ (Flow from Left to Right)	229
	a. Plane View b. Top Front View c. Top Rear View	

Page No.

Fig. 5.21	TiCl ₄ Flow Around Circular Cylinder with Passive Device, Re = 1450, D/δ* = 4.5	230
	a. Rear Perspective View	
	b. Front Perspective View	
	c. Top Front View	
	d. Top Rear View	
Fig. 5.22	Line Sketch of Modified Vortex Flow around Circular Cylinder	231
Fig. 5.23a	Spectra and Traces of Modified Vortex Oscillations Around Circular Cylinder L/D = 6, BR = 3%	232
Fig. 5.23b	Variation of Vortex Oscillations Frequencies around Circular Cylinder with Passive Device L/D = 6, BR = 3%	233
Fig. 5.23c	Variation of \bar{u} and u' with Reynolds Number	234
Fig. 5.24	Modified Surface Oil Film Patterns Around 25 mm Dia Circular Cylinder (t = 18 minutes), Re = 7800, D/δ* = 11	235
	a. Flow On	
	b. Flow off	
	c. Modified surface Stream lines Arounds Circular Cylinder	236
Fig. 5.25	Floor Pressure Distribution around Circular Cylinder with and without Passive Device	
	a. $\varphi = 0$	237
	b. $\varphi = 20$	238
	c. $\varphi = 45$	239
	d. $\varphi = 90$	240
	e. $\varphi = 135$	241
	f. $\varphi = 180$	242
Fig. 5.26	Surface Pressure Distribution on Circular Cylinder	
	a. $\varphi = 0$, 20	243
	b. $\varphi = 45$, 90	244

	c. $\phi = 135, 180$	245
	d. Schematics of modified flow regions on Circular Cylinder	246
Fig. 5.27	Symmetry of Floor Pressure Distribution around Circular Cylinder	
	a. $\phi = 20$	247
	b. $\phi = 45$	248
	c. $\phi = 90$	249
	d. $\phi = 135$	250
Fig. 5.28	Symmetry of Surface Pressure Distribution on Circular Cylinder	
	a. $\phi = 20, 45$	251
	b. $\phi = 90, 135$	252
Fig. 5.29	Total Head Contours in Y-Z plane at Mid Span of Circular Cylinder with device $L/D = 6.0$, $BR = 3\%$	253
Fig. 5.30	Variation of Vortex Oscillations around Circular Cylinder (Composite Plot)	254
Fig. 6.1	Dye Patterns around Rectangular Pier Model $L/D = 6$, $BR = 10\%$, $Re = 3197$, $Fr = 0.146$ (Flow from left to right)	288
	a. Plan view	
	b. Top Front view	
	c. Top Rear view	
Fig. 6.2	Dye Patterns around wedge nose Pier Model, $L/D = 6$, $BR = 10\%$, $Re = 3197$, $Fr = 0.146$, (Flow from left to right)	289
	a. Plan view	
	b. Top front view	
	c. Top rear view	
Fig. 6.3	Dye Patterns around Lenticular Pier Model, $L/D = 6$, $BR 10\%$, $Re = 3197$, $Fr = 0.146$ (Flow from left to right)	290
	a. Plan view	
	b. Top front view	
	c. Top rear view	

Page No.

Fig. 6.4	Line Sketches of Dye patterns around Pier Models	291
Fig. 6.5	TiCl ₄ FLOW around Rectangular Pier Model L/D = 6, BR = 3%, Re = 1450, D/δ* = 4.5, (Flow from left to right)	292
Fig. 6.6	TiCl ₄ Flow around wedge nose Pier Model, L/D = 6, BR = 3%, Re = 1450, D/δ* = 4.5 (Flow from left to right) a. Perspective view b. Top front view c. Top rear view	293
Fig. 6.7	TiCl ₄ Flow around Lenticular Pier Model, L/D = 6, BR = 3%, Re = 1450, D/δ* = 4.5 (Flow from left to right) a. Perspective view b. Top front view c. Top rear view	294
Fig. 6.8	Schematic sketches of TiCl ₄ flow around Pier Models	295
Fig. 6.9	Pressure distribution on upstream plane of symmetry of Blunt and Streamline nose Pier models, L/D = 6, BR = 3%	296
Fig. 6.10	Spectra and Traveses of HSV Oscillations a. Rectangular Pier Model, L/D = 6, BR = 3% b. Wedge Nose Pier Model, L/D = 6, BR = 3% c. Lenticular Pier Model, L/D = 6, BR = 3%	297 298 299
Fig. 6.11	Variation of Vortex Oscillations with Re and D/δ* a. Rectangular Pier Model L/D = 6, BR = 3% b. Streamline Nose Pier Models, L/D = 6, BR = 3%	300 301

	<u>Page No.</u>
Fig. 6.12 Variation of u and u' upstream of Pier Model $L/D = 6$, $BR = 3\%$	302
Fig. 6.13a Surface Oil Film patterns around Rectangular Pier Model $L/D = 6$, $BR = 3\%$, $Re = 7768$, $D/\delta^* = 11$	303
Fig. 6.13b Surface Oil Film pattern around Wedge Nose Pier Model $L/D = 6$, $BR = 3\%$, $Re = 7768$, $D/\delta^* = 11$	304
Fig. 6.13c Surface Oil Film pattern around Lenticular Pier Model $L/D = 6$, $BR = 3\%$, $Re = 7768$, $D/\delta^* = 11$	305
Fig. 6.14 Surface streamlines around Pier Models $L/D = 6$, $BR = 3\%$, $Re = 7768$, $D/\delta^* = 11$	306
Fig. 6.15 Surface Pressure Distribution around Pier Model $L/D = 6$, $BR = 3\%$	
a. Rectangular	307
b. Wedge Nose	308
c. Lenticular	309
d. C_p Variation along the junctions of Pier Models	310
Fig. 6.16 Total Head contours in Y-Z plane at mid span of	
a. Rectangular pier model	311
b. Wedge Nose pier model	312
c. Lenticular Pier model	313
Fig. 6.17a ^{View of} Rectangular pier model with device	314
Fig. 6.17b ^{View of} Wedge nose pier model with device	315
Fig. 6.17c ^{View of} Lenticular pier model with device	316
Fig. 6.18a Rectangular pier model with device	317
Fig. 6.18b Wedge nose pier model with device	318
Fig. 6.18c Lenticular pier model with device	319

- | | | |
|-----------|---|-----|
| Fig. 6.19 | Dye patterns around rectangular pier with passive device | 320 |
| | a. Plan view | |
| | b. Top front view | |
| | c. top rear view | |
| Fig. 6.20 | Dye patterns around Wedge Nose pier with passive device | 321 |
| | a. Plan view | |
| | b. Top front view | |
| | c. Top rear view | |
| Fig. 6.21 | Dye patterns around lenticular pier with passive device | 322 |
| | a. Plan view | |
| | b. Top front view | |
| | c. Top rear view | |
| Fig. 6.22 | TiCl ₄ Flow around rectangular pier with passive device, $L/D = 6$, $BR = 3\%$, $Re = 1450$, $D/\delta^* = 4.5$ | |
| | a. Perspective view | 323 |
| | b. Top front view | |
| | c. Close up view | |
| | d. Gross view | 324 |
| | e. LESV | |
| | f. Surface flow patterns | |
| Fig. 6.23 | TiCl ₄ flow around Wedge nose pier with passive device $L/D = 6$, $BR = 3\%$, $Re = 1450$, $D/\delta^* = 4.5$ | 325 |
| | a. Rear perspective view | |
| | b. Front perspective view | |
| | c. Top front view | |
| | d. Close up view | |
| Fig. 6.24 | TiCl ₄ Flow around lenticular pier with device $L/D = 6$, $BR = 3\%$, $Re=1450$, $D/\delta^* = 4.5$ | 326 |
| | a. Rear perspective view | |
| | b. Front perspective view | |
| | c. Top front view | |
| | d. Close up view | |

Fig. 6.25	Schematic of modified vortex flow around pier model	
	a. Rectangular pier	327
	b. Wedge Nose pier	328
	c. Lenticular pier	329
Fig. 6.26	Spectra and Traces of modified vortex flow around pier models	
	a. Rectangular	330
	b. Wedge nose	331
	c. Lenticular pier	332
Fig. 6.27a	Modified surface oil film patterns around Rectangular pier with passive device,	333
Fig. 6.27b	Modified surface oil film patterns around wedge nose pier model with passive deivce	334
Fig. 6.27c	Modified surface oil film patterns around lenticular pier model with passive device	335
Fig. 6.28a	Modified surface streamlines around Rectangular pier model	336
Fig. 6.28b	Modified surface streamlines around Wedge Nose pier model	337
Fig. 6.28c	Modified surface streamlines around Lenticular pier model	338
Fig. 6.29	Floor pressure on upstream plane of symmetry with and without device	
	a. Rectangular pier model	339
	b. Wedge nose pier model	340
	c. Lenticular pier model	341
Fig. 6.30a	Floor pressure at leading edge corner of rectangular pier with and without passive device	342
Fig. 6.30b	Floor pressure, leading edge corner of wedge nose pier with and without passive device	343

	<u>Page No.</u>
Fig. 6.31a	Floor pressure at mid span of Rectangular pier model with and without passive device 344
Fig. 6.32b	Floor pressure at mid span of Wedge nose pier model with and without device 345
Fig. 6.31c	Floor pressure at mid span of lenticular pier model with and without passive device 346
Fig. 6.32a	Floor pressure trailing edge corner of Rectangular pier with and without passive device 347
Fig. 6.32b	Floor pressure at trailing edge corner of wedge nose pier with and without passive device 348
Fig. 6.33a	Floor pressure downstream of Rectangular pier model with and without passive device 349
Fig. 6.33b	Floor pressure down stream of wedge nose pier model with and without passive device 350
Fig. 6.33c	Floor pressure downstream of Lenticular pier model with and without passive device 351
Fig. 6.34	Floor pressure symmetry around Rectangular pier with and without passive device
	a. Leading edge corner 352
	b. Mid span 353
	c. Trailing edge corner 354
Fig. 6.35	Floor pressure symmetry around wedge nose pier model with and without device
	a. Leading edge corner 355
	b. Mid span 356
	c. Trailing edge corner 357

Page No.

Fig. 6.35d	Floor pressure symmetry around lenticular pier model with and without device	358
Fig. 6.36a	Total head contours in Y-Z plane at mid span of rectangular pier model with device	359
Fig. 6.36b	Total head contours in Y-Z plane at mid span of wedge nose pier model with device	360
Fig. 6.36c	Total head contours in Y-Z plane at mid span of lenticular pier model with device	361
Fig. 7.1	Similarity of pressure distribution on the upstream plane of symmetry of the pier models	375
Fig. A1	Schematics of oil film flow over a flat wall	A1

SYNOPSIS

EXPERIMENTAL INVESTIGATIONS OF VORTEX FLOW AND
ITS MODIFICATION AROUND WALL-CYLINDER JUNCTIONS

A Thesis Submitted
In Partial Fulfilment of the Requirements
For the Degree of

DOCTOR OF PHILOSOPHY

by

SUBHASH CHANDER SHARMA

to the

DEPARTMENT OF AERONAUTICAL ENGINEERING
INDIAN INSTITUTE OF TECHNOLOGY, KANPUR

There exist several situations in the field of aerodynamics/hydraulics, where boundary layer like shear flow has to pass through a wall-cylinder junction. Some examples are : i) wing-fuselage junctions in aircraft and fin-body junctions in rockets in aerospace engineering, ii) passages in axial flow compressors and turbines in turbomachinery, iii) river bridge piers located on sand bed in civil engineering, and iv) tall buildings and structures in wind engineering.

It is a complex fluid mechanics problem as three dimensional separation of the boundary layer upstream of the junction results in the formation of a strong horseshoe vortex flow around the body. This creates peculiar engineering problems like additional drag and modified heat transfer rates in aerospace engineering, complex secondary flows in turbomachinery, local scour holes around river bridge piers

and strong buffeting currents in wind engineering. Because of the great difficulties in analysing locally separated flow problems, most of the scientific efforts in the past have been experimental and empirical in nature, and in particular have been concentrated towards determining the local maximum scour depths around river bridge piers in civil engineering. In the fifties, a few inviscid analytical investigations predicting the streamwise vorticity generated due to the turning of the vortex filaments of boundary layer shear flows have also been reported with major emphasis on the problem of secondary flows in cascade aerodynamics.

A vertical circular cylinder mounted on floor represents, perhaps, the simplest geometry of a wall-cylinder junction. This configuration has been studied quite extensively in the past in laboratory experiments. A recent detail experimental investigation carried out in low speed wind tunnels on this geometry has shown that the horseshoe vortex flow structure formed upstream of the wall-circular cylinder junction depends upon the Reynolds number, $Re = \frac{U_{\infty} D}{\nu}$, $\frac{D}{\delta^*}$, and $\frac{L}{D}$ where U_{∞} , D , L , δ^* and ν are freestream wind speed, cylinder diameter and length, displacement thickness of the approaching boundary layer and dynamic viscosity of the fluid respectively. An even number of vortices upto six were observed in the upstream plane of symmetry with increasing Re , as long as the approaching boundary layer remained laminar; and as it became turbulent,

a constant number of four vortices were identified in the range of $4,000 < Re < 90,000$ and $4 < D/S^* < 30$ for L/D of about 5. Clearly, an additional parameter for non-circular cylinders will be the leading edge geometry, whose effect has been observed in local scour investigations, but has not been studied in detail in wind tunnel experiments.

Another aspect of the problem of flow past wall-cylinder junction is the hydrodynamic modification of the horseshoe vortex flow structure with the alleviation of local scour problem as one of the objectives. Recently an aerodynamic delta-wing-like passive device has been employed to modify the horse-shoe vortex flow structure significantly as demonstrated by the flow visualization experiments. The leading edge separation vortices from the passive device appeared to modify the structure of the streamwise arms of the horseshoe vortex. Subsequent experiments in an open channel flume with the sand bed also showed reduction in local maximum scour depth around a semi-circular leading edge pier model fitted with the delta-wing-like passive device. The detail mechanism of this hydrodynamic modification of horseshoe vortex, however, remains to be investigated.

The present experimental investigation was undertaken to study the mechanism of the above mentioned hydrodynamic modification around semi-circular leading edge shaped pier,

its effect on the upstream separation and the static pressure distribution on the floor. This vortex flow modification was also investigated for circular cylinder and piers with blunt and streamlined nose shapes. The effect of the leading edge geometry of the pier on the horseshoe vortex flow structure was investigated in detail for both the laminar and turbulent boundary layers to bring it in line with the understanding obtained for the circular cylinder case. It was also found during the course of the present experiments that the oscillating behaviour of the vortex flow around the circular cylinder was not as random as reported earlier. This aspect was also investigated for pier models having other leading edge shapes, along with the modification of the oscillating behaviour brought about by the passive device for different pier models.

The experiments were conducted in low speed, low turbulence, closed jet, open circuit wind tunnel of test section size of 30.5 cm x 40.5 cm at two nominal wind speeds of 1 m/sec. and 5 m/sec corresponding to $Re \approx 1450$, $D/\delta^* \approx 4.5$ and $Re \approx 8600$, $D/\delta^* \approx 11.5$ respectively. The flow visualization tests at low speed were carried out using Titanium tetrachloride technique, and surface oil film patterns were obtained at higher wind speed. Other tests included floor pressure measurements, total head survey of the streamwise vortices, and hot wire probing of the oscillatory behaviour of the horseshoe vortex, prior to and after its modification using the passive

device. A shallow water-table of width 25 cm and depth 7.5 cm was also used for dye flow visualization studies.

The pier model of 25 mm width with semi-circular nose fitted with the above mentioned passive device was extensively used in both the wind tunnel and water table facilities. A series of circular cylinders with diameters ranging from 1 mm to 50 mm were employed for flow visualization. The Reynolds number range for $TiCl_4$ flow visualization varied from 60 to 2900, and for surface oil film patterns Re ranged from 970 to 15540. Most of the other data on circular cylinder was collected on 25 mm diameter cylinder. To study the effect of the leading edge geometry of the pier, three additional models : one with truncated flat nose (rectangular) and the other two with streamlined shapes, i.e., wedge and lenticular, were used. All these models were 25 mm in width, 100 mm in length and 150 mm in height. The geometry of the delta-wing-like passive device was the same as used in the earlier reported investigations. The base and the altitude of the delta plate being 37.5 mm and 50 mm respectively and the base height equal to 12.5 mm.

Several interesting results have been found from the present experimental investigation and these are summarised in the following :

1. The delta-wing-like passive device considerably reduces the adverse pressure gradient on the floor upstream of the semi-circular nose pier by creating a low pressure region on the

leeward side of the passive device. The large separation region upstream of the wall-cylinder junction gets reduced to a small localized separated region around the apex of the passive device. The original vortex filaments of the approaching shear flow wrap around the apex and move parallel to the spinal rib as considerably weak streamwise vortices rotating in the same sense as the original horseshoe vortex. These weak apex vortex lines appear to somersault on reaching the pier nose and come out along the sides of the pier. In addition, strong leading edge separation vortex is formed which is rotating in a direction opposite to the original horseshoe vortex. This delta wing separation vortex is the dominant streamwise vortex which interacts with the apex vortex in the side region of the pier. As the Reynolds number of the flow is slightly increased, the apex vortex seems to become part of the much stronger delta wing separation vortex in the side region of the pier. This dominant feature of the delta wing separation vortex was also revealed for the modified turbulent horseshoe vortex at $Re \approx 8300$, by means of total head contours of the streamwise vortices.

2. The horseshoe vortex structure in ring form in laminar flow ($Re \approx 1450$, $D/\delta^* \approx 4.5$), all around the circular cylinder was visualized for the first time using $TiCl_4$ fumes. Upto six vortex rings, extending downstream were observed in the laminar case. For $Re > 7700$ in approaching turbulent boundary layer, four vortices were observed in accordance with the earlier investigation. However, the vortex structure in turbulent flow

was observed to depend upon Re , as two vortex structure was observed from the surface oil film patterns. The constant total head contours obtained by traversing a shielded pitot probe in a vertical Y-Z plane normal to the free stream, at the mid-span of the cylinder also revealed four vortex structure at $Re \approx 8300$ and $D/\delta^* \approx 11.3$, thereby confirming the observations from surface oil film patterns.

3. The number of vortices around semi-circular nose shape pier in laminar flow at $Re \approx 1450$, $D/\delta^* \approx 4.5$, were observed to be six from $TiCl_4$ fumes. Under the same test conditions, the rectangular pier exhibited oscillatory behaviour of the vortex flow, and wedge nose shape and lenticular pier models exhibited four and two vortex structure of the horseshoe vortex respectively. In turbulent flow four vortex structure was observed upstream of rectangular and round nose pier and the two vortex structure for both the wedge nose and lenticular pier models from surface oil film patterns, at $Re \approx 7800$, $D/\delta^* \approx 11$. Probing of the streamwise arm of horseshoe vortex in each of these four pier models confirmed the number of vortices as observed from the surface oil film patterns. 'It is, therefore, found that the number of vortices in horseshoe vortex around a pier model is a function of the leading edge geometry.' It was further observed from $TiCl_4$ flow visualizations that the modification of horseshoe vortex by the passive device was also dependent upon the pier nose geometry as was evident from the

difference in the movement of the apex vortex and its lift up as it came out from below the passive device. The constant total head contours provided patterns of the modified vortex flow at the mid-span of each pier model, showing that the leading edge separation vortex was the larger and the stronger vortex.

4. It was observed that the oscillating behaviour of the laminar horseshoe vortex flow around circular cylinder was not as random as reported earlier. For the circular cylinder of $L/D = 6$, $BR = 3\%$ and $2200 < Re < 4400$, $6 < D/S^* < 10$, the Strouhal frequency of laminar oscillations was about 0.21. Steady higher harmonics were also observed. Semi-circular nose shape cylinder exhibited identical unsteady behaviour. There was an early onset of steady oscillations in the case of rectangular pier model whereas for the streamlined nose shaped pier models, the onset of the vortex oscillations was delayed as compared to the corresponding Reynolds number of circular cylinder. These oscillations of laminar horseshoe vortex were found to be almost absent when the passive device was mounted at the leading edge foot of the pier models. Weak oscillations, however, seemed to appear at Re close to the onset of the turbulent boundary layer on the tunnel floor.

CHAPTER 1

INTRODUCTION AND LITERATURE REVIEW

Whenever a boundary layer like incompressible shear flow moves past a cylindrical body kept vertically on a flat wall, a typical flow phenomenon is observed around its base. The presence of the body causes an adverse pressure gradient in the upstream flow. As the flow approaches the body, the adverse pressure gradient grows stronger and separation of the flow takes place upstream of this body. The separated shear layers experience downward gradient of the Bernoulli constant on the upstream facing end of the body, which makes these shear layers roll up ahead of the body. This results in the formation of a strong vortex region which wraps around the base of the body, with its two ends extending downstream as two distinct streamwise vortices, rotating opposite to each other. This vortex system is known as the horseshoe vortex (HSV) due to its shape in the plan view. A side view of this phenomenon is shown in Fig. 1.1a. These two arms of HSV interact with the periodically shed vortices in the body wake. As a vortex is shed, its low pressure pulls the opposite arm of HSV towards it, and the shed vortex itself moves downstream. In the mean time, another vortex is shed from the other side which in a similar manner pulls the opposite arm of HSV. This results in the formation of a 'neck' type region downstream of the body. A perspective view of the horseshoe vortex system is shown in Fig. 1.1b.

There exist several situations in engineering, where boundary layer like shear flow has to pass through such geometrical boundaries, conveniently called a wall-cylinder junction. Some important examples are ;

- (i) Wing-fuselage junction, wing-strut junction and fin-body junction in aerospace engineering,
- (ii) Passages in axial flow compressors and turbines in turbo-machinery,
- (iii) River bridge pier located on sand bed in civil engineering,
- (iv) Tall buildings/structures in wind engineering.

This is a complex fluid mechanics problem involving three dimensional separating boundary layer. The flow field is entirely different from the two dimensional case, and results in additional drag in case of wing fuselage junction, modified heat transfer rates at the fin body junction, complex secondary flows in cascade passages and strong buffeting currents in wind engineering. High shear stresses are developed on the surfaces beneath these vortical flows and in case of soft erodible surfaces, this results in erosion of the sand like bed material. Thus, around the river bridge piers on sand-like bed, erosion of the bed material called local scour hole takes place. This scouring process produces large ditch like formation which exposes the pier foundation rendering the bridge unsafe.

Because of the great difficulty in analysing locally separated flow, most research efforts have been experimental in this area, mainly in civil engineering, to determine the local maximum scour depths around river bridge piers. Empirical relations based on the laboratory and field data are used to predict the local maximum scour depth from the design point of view. The simple geometry of a circular cylinder has been used extensively in the systematic investigations of this phenomenon. Efforts in the case of other nose shape cylindrical piers have also been made. It has been recognised that the nose shape does affect the scour depth significantly. Local scour depth is maximum with flat nose shape, and it reduces with increasingly streamlined nose shape piers. The scour depth has been known to depend on the strength of horseshoe vortex. The protection of local scour is an important task for the field engineers. Several methods like Caisson foundation, piles placed upstream of the pier and rip rap mats are commonly employed. The rip rap method in which the scour prone region is filled with large stones, is the method most employed for this purpose.

The problem of HSV has also been studied in turbomachinery for a non-uniform shear flow through cascade passages. A complex secondary flow builds up in the process. Inviscid theories have been developed to predict the generation of the secondary vorticity and detail experiments have been carried out to understand the physical phenomenon. The horseshoe

vortex can also be viewed from the point of view of three dimensional separating boundary layers.

A recent detail experimental investigation carried out on a circular cylinder in a wind tunnel has revealed that the structure of the horseshoe vortex system formed upstream of the cylinder depends upon Reynolds number, $Re = \frac{U_{\infty} D}{\nu}$, $\frac{D}{\delta^*}$ and $\frac{L}{D}$ where U_{∞} , D , L , δ^* and ν are freestream wind speed, circular cylinder diameter, height, displacement thickness of the approaching boundary layer and kinematic viscosity of the fluid respectively. An even number of vortices upto six were observed in the upstream plane of symmetry, number of vortices increasing with increasing Re , as long as the flow remained laminar. The vortex flow exhibited oscillatory behaviour, random in nature, as the transition from laminar to turbulent flow started. As the flow became turbulent, only four vortices were identified in the range of $4000 < Re < 90,000$, and $4 < \frac{D}{\delta^*} < 30$ for $\frac{L}{D}$ of about 5. Furthermore, the locations of the separation point and the vortex upstream of the cylinder were also found to depend upon Re and $\frac{D}{\delta^*}$. It appears that an additional parameter for non-circular cylinders will be the leading edge geometry, whose effect has been observed in local scour investigations but has not been studied in detail in wind tunnel experiments.

Another interesting aspect of the problem of flow past a wall-cylinder junction is the hydrodynamic modification of the

horseshoe vortex flow, with one of the objectives to be the alleviation of the local scour problem. It has been shown recently that by mounting a delta-wing-like passive device at the leading edge foot of a vertical pier, the HSV structure can be significantly modified. This hydrodynamic modification was demonstrated by dye flow visualization experiments on a water table. Subsequent experiments in an open channel flume with sand bed have shown a significant reduction of the local maximum scour depth around a semi-circular leading edge pier model with the delta-wing-like device fitted at its leading edge foot. However, the detail mechanism of this hydrodynamic modification of HSV remained to be determined.

1.1 LITERATURE REVIEW

For the purpose of presentation and understanding, the literature relevant to the different aspects of the present problem has been reviewed under the following subsection headings;

- a) Secondary flows,
- b) Vertical circular cylinder mounted on the floor,
- c) Leading edge geometry
- d) Local scour and its protection
- e) Horseshoe vortex modification (Gupta, 1987)
- f) Aerodynamics of the delta wing.

1.1a Secondary Flows:

Whenever a non-uniform flow field undergoes turning, a new flow field comes into existence which appears quite different from the original one. The new flow field has been thought of as a combination of the original flow and a superimposed flow with a deviating direction. This superimposed flow has been termed secondary flow. This terminology was introduced by Gruschwitz (Schlichting, 1968 p. 214) and Goldstein (1938).

In one of the earliest works, Kármán and Tsien (1945) formulated an inviscid lifting line theory for a finite wing placed in a non-uniform flow. The two dimensional properties of the aerofoil section were however, required to be known a priori for the solution of the problem.

A more complex problem is that of the shear flow turning through a cascade of blades of an axial flow compressor or turbine. Here the secondary flow appearing as regions of streamwise vorticity is made up of ;

- i) a pair of two large streamwise counterrotating vortices in the outlet channel due to the turning of shear flow,
- ii) The streamwise arms of HSV formed at the junction of blade with the disc and modified by the presence of adjacent blade junction. In addition, there is the wake flow of individual blades.

Because of theoretical difficulties, most of the investigations in this area of cascade aerodynamics have been experimental.

Squire and Winter (1951) approximated non-uniform flow through a compressor blade cascade passage by a bent duct in an inviscid parallel shear flow using the theory of Kármán and Tsien (1945) for small deflections. The secondary vorticity

ξ in the bent duct was calculated to be a 'product of the velocity gradient $\frac{\partial u}{\partial z}$, of the approaching stream and twice the angle of deflection ϵ' ,

$$\xi = - 2 \epsilon \frac{\partial u}{\partial z} \quad \dots \quad \dots \quad (1.1)$$

The flow field was computed by introducing a stream function for the secondary flow, and adding it to the stream function of the undisturbed parallel shear stream. A good agreement was obtained with their experimental results on ducts turning up to 90° .

Hansen et. al. (1953) conducted a detail flow visualization study on compressor blade cascades in non-uniform flow in a cascade tunnel. The physical flow phenomenon within the blade cascade passage was clarified with detail smoke flow pictures and surface oil flow patterns. It was shown that the two large counterrotating vortices were formed within the cascade passage and not at the outlet as was hitherto understood. The interaction of the streamwise arm of HSV formed at the blade leading edge with the flow on the adjacent blade junction

was shown in detail by the smoke flow pictures. It was also shown from this experimental study that the flow within a cascade passage and an equivalent bent duct differed in the leading edge region.

Hawthorne (1954) presented an inviscid, small perturbation theory for calculating secondary flow about an isolated strut placed in a non-uniform flow along its span. The dependence of the generated secondary flow on the leading edge shape of the strut was established in an analytical work, probably for the first time and shall be discussed in a subsequent subsection of the chapter. The mechanism of generation of the streamwise vorticity was visualized by considering a 'vortex tube initially upstream of the strut and at right angle to the flow. As it travelled downstream, the end near the body got left behind and the vortex tube stretched until it was nearly parallel to the flow. As it stretched, its cross-sectional area decreased and by Helmholtz's theorem the vorticity increased'. It was shown that the streamwise vorticity persisted far downstream as well, and the energy therein was shown to vary as the fourth power of the thickness of the strut.

Preston (1954) obtained the same results as those of Squire and Winter (1951) and Hawthorne (1954), but with a simpler approach by considering the turning of the vortex filaments and making use of Kelvin's theorem. It was also

shown in the process that the secondary vorticity in the streamwise arm of HSV was equal to but opposite in sense of rotation of the 'trailing vorticity arising from the change of circulation about the cascade elements in the spanwise z-direction', for sudden and constant turning of the non-uniform shear stream.

Armstrong (1957) conducted an experimental study of the compressor blade cascades placed in a non-uniform flow in a wind tunnel by making total head surveys in the plane of the cascade trailing edge and in another plane further downstream. A complete picture of the complex secondary flow comprising of 'a pair of vortices rotating near each trailing edge and a pair of vortices within the blade passages having sense of rotation opposite to that of the trailing wake vortices' was observed from the total head contours.

Hawthorne (1967) surveyed in detail the progress made in the inviscid analysis of the secondary flows. It was remarked that many problems having complex secondary flows could not be successfully analyzed using inviscid theories.

1.1b Vertical Circular Cylinder Mounted on a Wall:

Because of the geometric simplicity of the circular cylinder, this model appears to have been investigated more extensively than other geometric shapes. In aerodynamics, uniform flow past a circular cylinder is a classical problem

both in the theoretical and experimental sense. For the same reason flow past a wall-circular cylinder junction has been investigated more extensively through experiments.

Hornung and Joubert (1963) conducted an experimental study of three dimensional turbulent boundary layers by turning the approaching flow with a 56 cm diameter cylinder mounted vertically on a flat plate in a wind tunnel at $Re \approx 6 \times 10^6$, based on its distance from the leading edge of the plate. Static pressures on the plate were measured from half to about two diameters upstream of the cylinder and constant pressure contours were compared with the potential flow theory. The region directly upstream of the cylinder with adverse pressure gradient was observed with smoke flow at low Reynolds number, to be a 'backflow region where the outer streamlines doubled up on themselves resulting in a standing vortex, wrapped around the base of the cylinder'. This standing vortex was shown in smoke pictures at an unspecified 'low Reynolds number'.

Bělik (1973) carried out an experimental investigation of secondary flow due to wall mounted circular cylinder at Re varying from 0.36 to 2.2×10^5 , based on diameter. The surface flow patterns showed the primary separation line and the course of the horseshoe vortex core. Other vortices of low intensity and of opposite sense of rotation were found to exist close to the wall, but were not readily traceable. Static

pressures measured in the upstream plane of symmetry showed a dip in the pressure plot at about $0.23D$ upstream of the cylinder. This dip was identified with the location of the horseshoe vortex core and was found to be in 'good agreement' with the surface flow patterns. Furthermore, it was also shown from the dimensional analysis that the position of the primary separation line upstream of the cylinder depended uniquely upon Reynolds number based on the boundary layer thickness δ , both for laminar and turbulent flows.

Okamoto and Yagita (1973) conducted an experimental study on circular cylinder mounted in a wind tunnel test section mainly to investigate the wind loads for the structural design of tall cylindrical installations e.g., telegraph poles and chimneys etc. Measurements of static pressure on a vertical generator with z/D upto 7 were made all around the cylinder, in the Reynolds number range $1.33 \times 10^4 < Re < 1.5 \times 10^5$. The separation line upstream of the cylinder was found to move further upstream with decreasing L/D as observed by means of surface flow patterns in turbulent flow and dye tests at $Re \approx 550$ in a water tank.

Baker (1979) carried out a detail wind tunnel study on HSV around vertical circular cylinder when approaching boundary layer was laminar. Detail static pressure measurements and smoke flow visualizations with motion picture photography were made on its upstream plane of symmetry. It was shown

from dimensional analysis that the primary separation line and the primary horseshoe vortex location are function of similarity parameters Re and $\frac{D}{\delta^*}$ for $\frac{L}{D} > 5$. Furthermore, it was observed from detail flow visualization that two, four or six vortices (Fig. 1.2) appeared in the HSV system with increasing Re and $\frac{D}{\delta^*}$, as long as the flow remained laminar. A smoke picture of six vortices upstream of a stubby cylinder, given in the frontis-piece of Thwaites (1960) and shown by Baker in Fig. 1, as Sutton's experiment is reproduced in Fig. 1.3. Pressure measurements on the upstream plane of symmetry showed that the minima in the pressure plots represented primary HSV locations and the absence of minima at higher Re , implied oscillatory HSV system. These minima moved further upstream with increase in Re and decrease in $\frac{D}{\delta^*}$. The skin friction coefficient below the primary horseshoe vortex was found to be five times that of the free stream at $Re=2610$, $D/\delta^*=14.8$ and the velocity profiles within the horseshoe vortex region at the above flow condition were found to be almost invariable in the dimensionless velocity profiles. It was reported that a steady vortex system existed for $Re < 5,000$ and unsteady vortex system existed for $5000 < Re < 16,000$, before the approaching flow became turbulent. Furthermore, it was also reported that the unsteady oscillations of the vortex system around circular cylinder of $L/D = 4.8$ for $4000 < Re < 14,000$ and $10 < D/\delta^* < 60$, were random in character. The frequency spectra showed that

at any one speed setting, one of the four possible patterns could be observed. These patterns were as follows

- i) Steady trace with no oscillation ;
- ii) A low frequency oscillation at $St = 0.26$;
- iii) A higher frequency oscillation at $St = 0.40$ or even more at higher Re ; and
- iv) An irregular turbulent trace.

These trends were thought to be characteristic of the transition phenomenon of horseshoe vortex.

Baker (1980) reported a similar investigation of HSV around vertical circular cylinder when approaching boundary layer flow was turbulent. Pressure measurements were made on the upstream plane of symmetry. From the surface oil flow patterns around circular cylinder, four vortex structure was observed in the range of $4000 < Re < 90,000$ and $4 < \frac{D}{S^*} < 30$. It was found from the pressure plots that the position of 'minima' i.e., the location of the primary horseshoe vortex was almost invariant with Re , while those of the primary separation and primary horseshoe vortex were observed to depend upon Reynolds number, Re_{S^*} (based on S^*), and $\frac{D}{S^*}$.

Gupta (1984) conducted a wind tunnel study of the horseshoe vortex in turbulent flow around a vertical circular cylinder at $Re \approx 6 \times 10^4$ and $\frac{S}{D}$ varying from 0.47 to 2.2 (S , based on $\frac{u}{U_\infty} \approx 0.99$), with the objective of estimating initial vortex

strength prior to the onset of the scouring process. Detail pressure measurements on a vertical generator with z/D upto 4.8, all around the cylinder and on the floor were plotted in the form of constant pressure contours.

Muzzamil (1985) carried out experimental investigations of open channel flow past a circular cylinder mounted on rigid bed and on mobile bed, in the range $2 \times 10^4 < Re < 4.5 \times 10^4$ and $0.23 < Fr \leq 0.55$, and suggested a method to predict the strength of H&V from the pressure distribution on the rigid bed in the separated flow region, and also obtained surface flow impressions under these laboratory conditions by using paint to find out the HSV structure. Muzzamil and Gangadharaiiah (1987) reported close agreement of the results from open channel flow (Muzzamil, 1985) with wind tunnel results on the same circular cylinder (Gupta, 1984) and obtained a relationship between the vorticity parameter and the strength of the vortex. These results were found to be independent of the free surface effect.

The information from the literature on the vortex flow around a wall-circular cylinder junction reviewed in this section is summarised in Table 1.1.

TABLE 1.1

Year	Author	Cylinder Re	$\frac{L}{D}$	$\frac{D}{\delta^*}$	BR	Boundary Layer
1963	Hornung and Joubert	6.5×10^5	-	-	-	Turbulent
1973	Belik	3.6×10^4 to 2.2×10^5	1.67-5	-	-	Turbulent
1973	Okamoto and Yagita	1.33×10^4 to 1.5×10^5	1-12.5	-	3.75%	Turbulent
1979	Baker	2×10^3 to 1.6×10^4	0.5-4.8	21.7 to 65.8	5.3 to 6.2%	Laminar
1980	Baker	4×10^3 to 9×10^4	3-12.2	4 to 30	2.1 to 8.5%	Turbulent
1984	Gupta	6×10^4	6	-	12.5%	Turbulent
1987	Muzzamil and Gangadharaiiah	4×10^4	6	-	12.5%	Turbulent

It appears from the preceding review that the details of vortex structure and pressure measurements are available on the upstream plane of symmetry. However, the flow phenomenon around a body at one plane cannot be studied in isolation of other regions of the flow. The flow around the cylinder and in its wake remains to be studied to form a complete picture of the horseshoe vortex around a circular cylinder base. Detail pressures need to be measured to find the number of vortices in turbulent flow at lower Reynolds number. Furthermore, it would be interesting to verify the random character of vortex oscillations by an independent investigation. Probing of the streamwise arm of HSV could also be useful for a complete picture of the horseshoe vortex flow.

1.1c Leading Edge Geometry :

It appears that the effect of leading edge geometry on HSV structure has not been investigated in detail in the wind tunnel investigations. However, it has been recognised that the leading edge geometry plays an important role in determining the strength of HSV. The leading edge shapes can be classified as

- i) Blunt edge,
- ii) Round edge,
- iii) Streamlined edge.

It has also been found that in general weaker horseshoe vortex structures develop on the cylinders with streamlined and pointed leading edges as compared to cylinders with blunt or rounded leading edges.

Hansen et.al. (1953) conducted smoke flow visualization through a compressor blade cascade and an identical cascade of thin arc like bent duct. It was noticed that 'for the same geometric parameters of cascade and duct, the main flow streamline patterns were quite similar away from the leading edge region'.

Hawthorne (1954) showed theoretically using the inviscid theory that the secondary vorticity induced by the blunt leading edge shape struts was infinite and it was much less with sharp edge nose shape struts. A bicuspid profile gave minimum induced vorticity. The experimental results performed on a shallow water channel with sand bed showed that pier with elliptic leading edge profile had a scour depth of about ten times that produced due to a bicuspid nose profile. However, at a nominal incidence of about 5° , the percentage increase of depth in case of bicuspid nose profile was higher than that for elliptic nose profile. It was argued that the phenomenon of scour around river bridge piers on sand bed could be attributed to secondary flows.

Armstrong (1957) conducted smoke flow visualisation around single airfoil mounted on the tunnel floor and observed a 'nose

vortex' around the leading edge. As the leading edge radius was reduced, the 'nose vortex' moved closer to the leading edge. When the leading edge was made sharp, the 'nose vortex' could not be distinguished with the scale of the experiment. The effect of the angle of incidence was only mentioned without providing any details.

It has been recognised that scour depth at the pier nose would be greater in case of blunt nose pier compared to sharp nose piers. Breusers et.al. (1977) have reported that Laursen and Toch observed the effect of pier shape at standard test conditions and observed relative scour depth of 0.91 for elliptic and lenticular profiles, with this ratio being 1.0 for round nose pier. These were the average values as the scour depth varied with time due to passage of dunes, Verziliotes (quoted from Breusers et.al., 1977) observed the scour depth at the round nose pier to be about 57% of that at square nose pier while for bevel nose and lenticular pier, it was 61% and 45% respectively.

Tison (1961) showed that the scour around bridge piers was mainly caused by the streamline curvature. His results with different shape piers were as follows.

<u>Pier shape</u>	<u>Scour depth ratio</u>
Rectangular	1.00
Simple rounding	0.72
Triangular	0.61
Aerodynamic	0.54
Lens shape	0.48

Laursen (1960) defined the shape coefficient as the ratio of scour depth due to a particular shape to that of a rectangular shape and reported the following values for different nose shapes

<u>Pier shape</u>	<u>Shape coefficient</u>
Rectangular	1.00
Semi-circular	0.90
Elliptic 2:1	0.80
3:1	0.75
Lenticular 2:1	0.80
3:1	0.70

An excellent review of the effect of pier shape on scour depth is given by Breusers et.al. (1977).

Most information available on the effect of leading edge geometry on HSV is from the scour depth point of view. The vortex flow structure has not been investigated around piers of leading edge shape other than circular cylinder. It remains to be seen how the variation in the vortex structure takes place for blunt nose, round nose, wedge nose and lenticular pier model for the same upstream flow conditions.

1.1.d Local Scour and its Protection:

The problem of local scour around a river bridge pier on a sedimentary bed is as old as the first river bridge pier, and perhaps it was Leonardo da Vinci who first drew the vortex lines ahead of the pier junction. Local scour has received considerable attention of hydraulic engineers in recent times. In general local scour around a river bridge pier is defined as sudden decrease of the sedimentary bed level near the pier. This decrease is known to be caused due to the erosion of the sedimentary bed by the vortex dominated flow near the pier junction, which results from the concentration of the transverse vorticity of the approaching stream at the pier. These concentrated vortex filaments roll up ahead of the pier to form a solid body like rotating flow, which wraps around the pier, and is known as the horse-shoe vortex. This horseshoe vortex has been studied extensively and is well documented. This flow structure has been shown by pictures and sketches by Thwaites (1960), Taylor (1967), Shen, Schneider and Karaki (1969), Bělik (1973) and Baker (1979, 1980).

The investigation of various aspects in the area of local scour may be classified for the convenience of the brief literature review as,

- i) prediction of maximum scour depth based on empirical relations obtained from the correlations of laboratory and field

data, ii) physical mechanism of the process of scour, the formation of vortices and the resulting secondary flows, iii) methods of local scour protection.

These three aspects are described in the following.

(i) Maximum Local Scour Depth :

One of the earliest empirical relations proposed for the estimation of maximum scour depth is known as Lacey regime depth,

$$d_{\text{Lacey}} = 0.473 \left(\frac{Q}{f} \right)^{1/3} \quad (\text{metres})$$

where d_{Lacey} is the depth measured from the water surface,

Q = discharge in m^3/sec , f = silt factor = $1.76 D^{1/2}$,

D = median grain size in mm. For design purposes, generally

a value of $2 d_{\text{Lacey}}$ is used, therefore

$$d_o + d_s = 0.95 \left(\frac{Q}{f} \right)^{1/3}$$

where d_o and d_s are water depth and scour depth respectively.

This formula does not account for the pier shape and the upstream flow conditions. Laursen (1960) considered the pier nose geometry, its angle of attack with the upstream, and upstream flow depth. Design charts and curves were proposed for the prediction of maximum scour depth. These charts and curves have been discussed at length in ASCE proceedings of year 1960. An empirical relation has been proposed by Arunachalam (1965).

$$\frac{d_s}{b} = \frac{dr}{b} \left[1.95 \left(\frac{dr}{b} \right)^{1/6} - 1 \right],$$

where dr = regime depth and b = pier width. This relation takes care of b and for $\frac{dr}{b} \approx 1$, the result approximated to $ds + dr \approx 1.95 dr$ and was shown as a compromising effort between the two schools of thought. Tison (1961) clearly demonstrated the importance of the pier nose geometry from laboratory tests on pier models having, rectangular, simple rounding of the blunt face, triangular, aerodynamic and lens shape nose profiles. The maximum scour depth was observed with flat nose, which decreased in the same order, giving minimum scour depth with lens shape or biconvex profile. Shen, Schneider and Karaki (1969) considered pier nose geometry as an important parameter and showed that it could be classified as blunt nose or streamlined nose shape.

There does not appear a unified approach to predict the maximum scour depth by considering important physical parameters of the bridge pier the grain size of the sediment and the approaching flow characteristics as about twenty odd formulas are available in literature. In recent comparative studies of these relations, Jain (1981), and Jain and Modi (1986) conclude that Laursen and Toch relation appears to be the best.

(ii) Physical Mechanism of Local Scour :

The physical mechanism of the formation of HSV and the resulting secondary flows have been described earlier. Shen, Schneider and Karaki (1969) have defined two types of scours : clear water scour, when the movement of the sediment takes place

near the bridge pier only, and scour with continuous sediment motion, when the whole river bed is in motion. The dependence of the vortex flow structure was described as a function of pier nose shape, which could consist of any, none or all of the basic systems, e.g., the horseshoe vortex system, wake vortex system, and the trailing vortex system. The vorticity generated in HSV is due to the freestream (as described earlier) and that of the wake-vortex system is created at the pier by the rolling up of the unstable shear layers generated at the pier surface in the process of the separation from the pier side walls. The trailing vortex system, like that in case of a finite lifting wing, may occur in the case of completely submerged piers.

It was shown from smoke flow pictures (Breusers et.al., 1977) that HSV dominated the flow structure in case of piers with blunt nose, causing large scour depth at the pier nose, whereas HSV system was weaker for sharp nose piers and strong wake-vortex system dominated the flow structure causing large scour holes downstream.

Melville (1975) found that the strength of HSV increased as the scour hole was enlarged, and along with the sinking of HSV, additional fluid attained downward component of velocity at the pier nose, Melville and Raudkivi (1977) measured the turbulence intensities and the shear stresses on a fixed bed model of local scour zone. It was observed that one or more

vortices might exist depending upon the bed condition and Re , but it was the primary horseshoe vortex which was found to be the main cause of the local scour depth. The core diameter of the vortex was found to be about $0.5D$ at the beginning of the scour and it was found to further enlarge as HSV sank in the developing scour zone. Baker (1980a) observed from dye flow that the same amount of fluid enters the vortex system in a scour hole or on a fixed bed, demonstrating thereby that the strength of HSV remained the same throughout the process of scour.

Shen, Schneider and Karaki (1969), Baker (1980a), Qadar (1981), Gangadharaiah, Muzzamil and Subramanya (1985), Muzzamil and Gangadharaiah (1987) have attempted to estimate the strength of HSV using different approaches.

(iii) Local Scour Protection :

The local scour exposes the bridge pier foundation to the flow and reduces the effective depth of the foundation. These two factors render the bridge unsafe. Much deeper foundations may be laid as a factor of safety but Breusers, Nicolett and Shen (1977) have stressed that the cost factor has to be linked with the safety measures. Thus deeper foundations alongwith the founding of the pier on a large dimension Caisson is a relatively expensive method.

The scouring process is dependent upon the type of the sediment (i.e. its fineness or coarseness) of the bed, pier nose shape and the approaching flow characteristics. It may thus be possible to put the scouring process under some check by controlling anyone or a combination of these factors.

The most commonly employed method of preventing local scour is associated with the sediment characteristics around the pier and is known as 'rip-rap mat'. Light particles are easily erodible. Posey (1974) has described the original method of Englis in the year 1893, 'this involved excavation of the bed sediment around the pier and filling it with rip rap, broken rock or stones too large to be removed by the current', and make it flush with the surface bed. Breusers, Nicolett and Shen (1977) provide empirical relations to determine the size of the boulders for the rip rap mat, extending horizontally up to twice the pier width from the pier surface. Randkivi and Ettema (1985) investigated the nature of local scour around piers with armoured bed.

The pier nose shape has been shown to affect the formation of the horseshoe vortex (Shen, Schneider and Karaki, 1969). The horseshoe vortex gets weaker with pointed or streamlined nose shapes, thus the maximum scour depth at the leading edge for streamlined nose piers is lesser than in the case of a blunt nose shape (in which case the horseshoe vortex

is quite strong). Bridge pier - sand bed junctions may also be modified as done by Breusers (1972), by employing a flexible skirt around the models of the offshore drilling platform. A horizontal co-axial flat plate of three times the diameter of the circular pier and embedded slightly below the bed was found to be effective in reducing the local scour under the laboratory conditions. Such methods give good results so long as the water level remains sufficiently above the 'skirt', once it goes below, the formation of horseshoe vortex may take place below the skirt itself.

Tison (1961) modified the upstream flow characteristics of the approaching stream, by placing small diameter piles ahead of the pier in an arrow pattern. The action of the piles is believed to produce low velocity modified flow. It reduced scouring around the pier. However, the local scour around the piles would be there because of the formation of the horseshoe vortices. It was cautioned that if the upstream piles were placed beyond a 'certain' distance, it may not be effective at all.

1.1e Horseshoe Vortex Modification (Gupta, 1987)

It would appear from the above that a modification or suppression of the horseshoe vortex, which is the prime cause of the phenomenon of local scour would be a step towards the alleviation of this problem. Gupta (1987) recently reported

a dye flow visualization study in which aerodynamic concepts were employed to invent a delta-wing-like plate mounted at the leading edge foot of a round nose vertical pier placed on a water table, which appeared to modify the horseshoe vortex significantly. It was believed from the dye patterns that the action of the passive device was as follows :

(i) The passive device looking like an upramp to the approaching flow acted like a barrier to the roll up of the transverse vortices into HSV at the pier junction, instead the approaching transverse vortices were believed to wrap around the apex of the passive device, and moved beneath the device towards the pier nose.

(ii) The passive device which was essentially a delta wing at negative angle of attack, produced a pair of counter rotating leading edge separation vortices, in the streamwise direction. The attitude of the device made the sense of rotation of these vortices to be opposite to that of HSV around the pier junction. These leading edge vortices were believed to be stronger than the residue vortex from the apex coming out from below the device. Thus it would be possible to counteract the action of original HSV. It was also believed that a change in direction of rotation of the trailing arms of HSV would also modify the wake-vortex system. It was concluded that this device would be useful in solving the classical problem of scour around river bridge piers quite favourably.

Recent experiments of Gupta and Gangadharaiiah (to be reported) performed with the same pier model and the passive device of Gupta (1987) on a mobile bed in an open channel flume showed a reduction of the scour depth upto 67%. Two types of sediments, i.e., Ganges sand ($d_{50} = 0.16$ mm) and the Yamuna sand ($d_{50} = 0.8$ mm) were used for the bed. The coarser one from Yamuna showed better results. The extent of the scour affected zone was quite reduced when the passive device was used in high Fr. conditions of the laboratory tests.

Ngheini (1988) carried out similar experiments in the open channel flume, and varied the geometrical parameters of the passive device and observed reduction of local scour around a pier model with a modified passive device made up of two triangular plates, one at the negative angle of attack and the other flush with the bed.

The action of the delta-wing-like passive device to modify the flow around wall-vertical pier junction is thus known only from dye flow visualization and scour reduction studies on the sand bed. The mechanism of this vortex modification has not yet been determined. The action of the flow structure beneath the device in modifying the pressure distribution on the pier leading edge and the floor is not known quantitatively. The action of leading edge separation vortex on the residual weak HSV remains to be determined. For complete understanding of the hydrodynamic modification of HSV, detail pressure measurements around the pier junction, below the device, on the upper

surface of the device and on the leading edge of the pier model need to be made. Detail flow visualization studies are also needed to clarify this interesting hydrodynamic phenomenon.

1.1f Aerodynamics of Delta Wing :

The aerodynamics of thin, low aspect ratio, delta wing with sharp leading edges is of primary interest for the high speed flight, and its aerodynamic characteristics differ significantly from those of high aspect ratio, straight wings with more thickness ratio used for subsonic flight. The production of lift on a straight wing at low speed can be explained with the help of lifting line inviscid theory of Lancaster and Prandtl (Anderson, 1984), which assumes the turning of the bound vortex at the wing tips by 90° , resulting in trailing vortices formed due to the pressure difference on the lower and upper surface of the wing. As the leading edge of a wing is swept backwards, there occurs a reduction of lift. With substantial increase of the sweep back and reduction of aspect ratio, the wing appears like a slender triangular plate in plan-form and is called delta wing. With the sharp leading edges and at moderate to high angles of attack, the boundary layer from the pressure side flows towards the suction side around the leading edge, resulting in the formation of free shear layers after the separation at the leading edges. These shear layers curve upwards and

and inboard, rolling up into a solid body rotation like high vorticity core. The vortex thus formed, moves in the streamwise direction like a spiral vortex. A spanwise flow occurs on the suction side after the reattachment and the fluid passes below the main vortex towards the leading edge and separates again, termed secondary separation. This results in a pressure distribution with peaks towards the leading edges. The size and strength of these spiral vortex sheets increase with increasing incidence. These are the dominant leading edge separation vortices from the suction side of a delta wing and are shown in Fig. 1.4. At negative angles of attack the sense of coiling of the shear layers would be opposite to that due to HSV around a wall-pier junction. The delta wing has non-linear lifting characteristics, as part of the lift force is due to the leading edge separation vortex. A successful theoretical method for prediction of aerodynamic characteristics of delta wing was developed by Polhamus (1966), based on the suction analogy. The theory of delta wing aerodynamics is well understood and is described in details by Küchemann (1978). However, the leading edge vortex flow structure shall be described below in brief.

Harvey (1958) determined the physical nature of the flow on the suction side of a slender delta wing from smoke flow visualization and total head surveys over the delta wing at one

chord wise station. The formation of leading edge vortex was clarified as the formation of shear layers due to the combination of the separated flow from the pressure side at the sharp leading edge with the flow at the suction side and the roll up of these shear layers. The rolling of these shear layers was identified as spiralling regions of total head and were observed to complete one revolution before disappearing into the vortex core. A secondary separation region was observed from total head contours. The axial velocity of the vortex core was observed from the smoke flow to be higher than the freestream. It was also found that by increasing the delta incidence, the strength of the leading edge vortex core increased, the two vortex cores moved closer to each other and away from the delta wing surface.

Elle (1958) performed water tunnel and wind tunnel experiments at low speed on sharp edge delta wings and found that the vortex cores moved closer to the centre line with smaller apex angles. Good agreement with the theory of Brown and Michael (1955) was obtained for the inclination of the vortex core centerline to the wing surface.

Earnshaw (1961) conducted a detail investigation of the structure of leading edge vortex above a sharp edge delta wing at about 15° and found that conical flow existed within the vortex core. Within the viscous sub-core region the circumferential velocity was of the order of freestream wind speed

while the streamwise velocity was about 2.3 times the free-stream wind speed. The size of the viscous sub-core and vortex core was found to be approximately 5% and 30% of the local semi-span respectively.

Lawford (1964) obtained detail surface oil film patterns over a series of delta wings with varying sweep for different delta incidences with an objective of the study of boundary layer flow. Conical flow was indicated at moderate incidences. Primary attachment, secondary separation and secondary attachment lines were clearly seen from the surface flow patterns at moderate incidence.

Polhamus (1966) presented a concept for the calculation of vortex lift of sharp edge delta wings, based on a suction analogy. 'The analogy assumes that with reattached flow, the normal force on the upper surface required to maintain the flow about the vortex is the same as the leading edge suction force required to maintain the flow about the leading edge in the potential flow case'. The total lift was shown as the sum of the vortex lift calculated from the suction analogy and the potential lift. The Polhamus method provided good agreement with the experimental results and is very much in use for predicting delta wing lift forces.

Hummel (1978) carried out an experimental investigation of the flow field of a delta wing of $AR=1$ at incidence of 20.5°

by surface flow patterns, detail total head, static head and dynamic head surveys at and downstream of the delta wing trailing edge. It was found that a trailing edge vortex with an opposite sense of rotation to the leading edge vortex comes into existence at about 70% of the semi-span and moves downstream in a helical path around the leading edge vortex.

The aerodynamic characteristics of an isolated delta wing of $AR=1.5$ (same as that of the delta plate of the passive device) are shown in Fig. 1.5. However, the operating conditions of the passive device are different from that of the delta wing which is believed to affect the flow phenomenon. Extensive flow visualization of this phenomenon should be of interest to clarify the flow below the passive device. Total head survey at one representative station downstream of the trailing edge of the passive device with a shielded pitot probe are likely to provide a complete picture of the flow as it comes out from beneath the passive device.

1.2 PRESENT INVESTIGATION

The foregoing brief literature review highlights the multifacet nature of the problem of wall-body junction flows. The interest in the problem started with the hydrodynamic modification of the horseshoe vortex at the wall-body junction as reported earlier by Gupta (1987) as a means of local scour

protection for river bridge piers. However, the scope of the present experimental investigation expanded to include many other fundamental aspects of the problem like the effect of pier nose shape on the HSV flow structure and the onset of HSV oscillations in the case of circular cylinder-floor junction.

In particular, following were the objectives of the present experiment.

1. To determine the mechanism of HSV modification around a semi-circular nose shape cylinder with the delta-wing-like passive device mounted at its leading edge foot, along with its effect on the upstream separation of flow and the static pressure distribution on the floor around the pier junction.
2. To make detail measurements of pressures on the flow and the periphery of circular cylinder, to find out the details of HSV structure at $Re < 4000$, from surface oil film and probe the streamwise arm of HSV by total head survey for a clear picture of vortex structure, and a fresh look into the vortex oscillations, to make use of recent and simple technique of $TiCl_4$ fumes to visualize the HSV flow around the cylinder junction and the effect of the passive device in modifying the flow field around the circular cylinder.
3. To investigate the effect of the leading edge geometry of the pier on the horseshoe vortex structure both for laminar and turbulent flows, and the modification of vortex flow brought about by the passive device.

The contents of this thesis are divided into seven chapters.

- Chapter II provides details of the apparatus and instruments used for the present experiments.
- Chapter III describes the details of the experimental techniques developed and employed during the course of these experiments.
- Chapter IV describes the mechanism of the HSV modification around a vertical pier with round nose with the passive device mounted at its leading edge foot, the configuration originally employed by Gupta (1987). The HSV around the pier model is also described.
- Chapter V presents the use of $TiCl_4$ fumes in independent verification of the findings of vortex structure by Baker (1979), alongwith detail pressure measurements all around on the floor and the periphery of circular cylinder, a new insight into the oscillations of HSV. The vortex structure of HSV in turbulent flow from constant total head contours and finally the results of modified HSV with the use of the passive device, are presented.
- Chapter VI provides the results of the HSV structure around blunt and streamline nose shape piers, and brings

out the effect of leading edge geometry on the structure and the modification of HSV.

Chapter VII summarises the various conclusions and suggestions for further research are made.

Relevant figures are grouped at the end of each chapter.

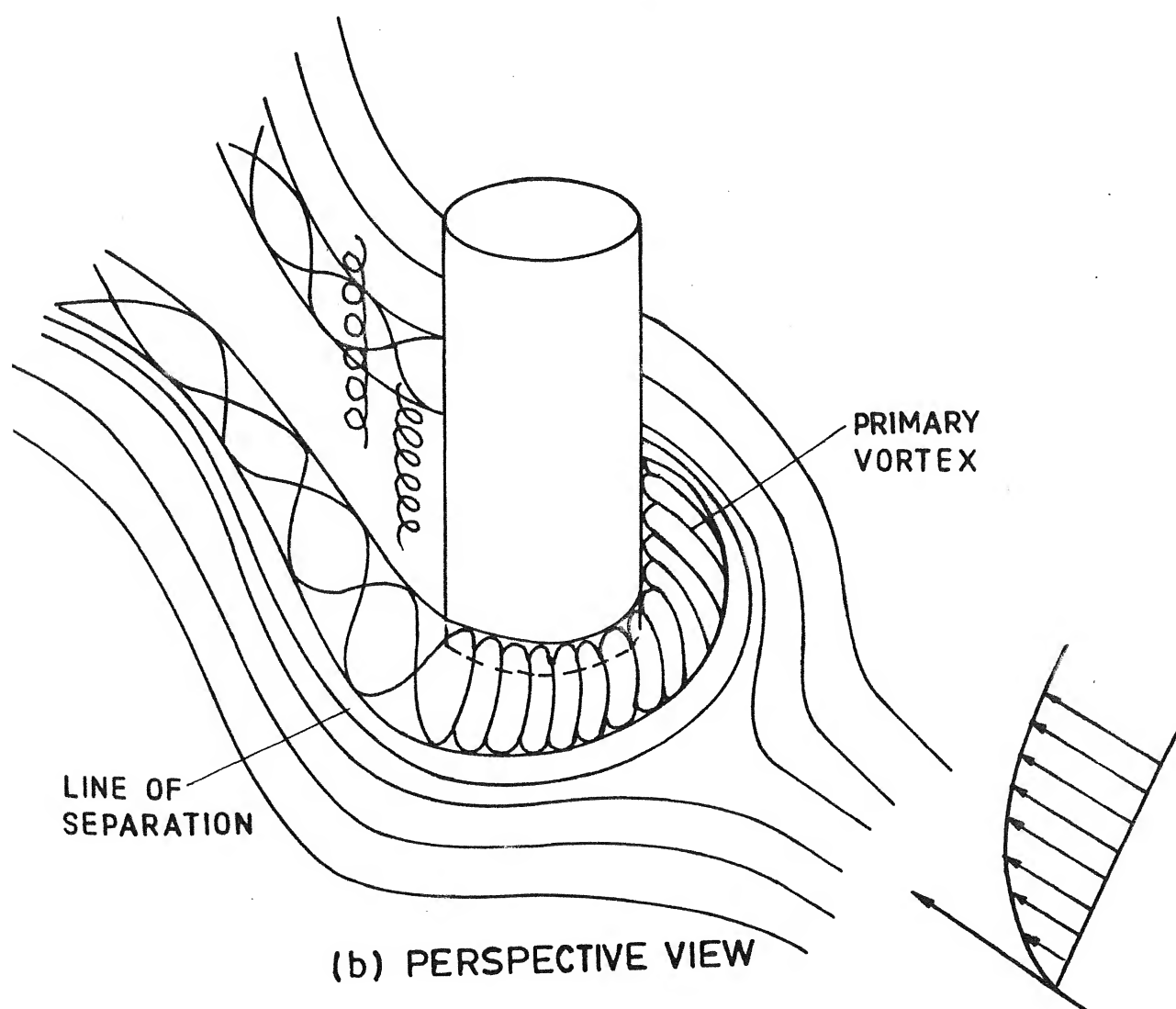
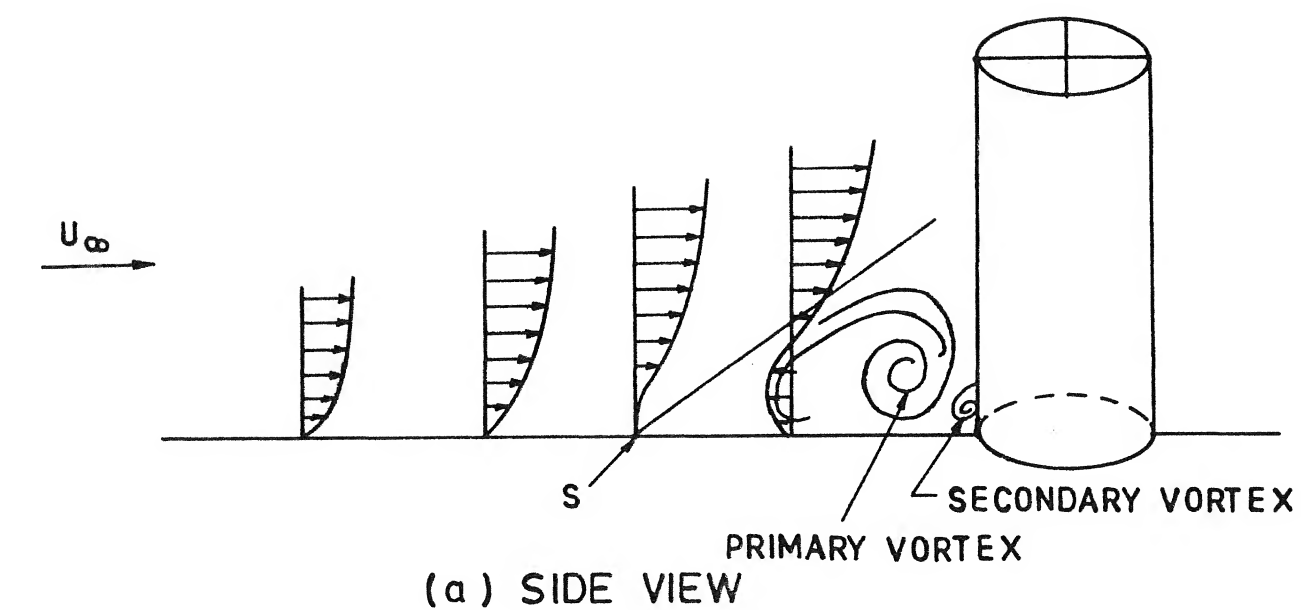
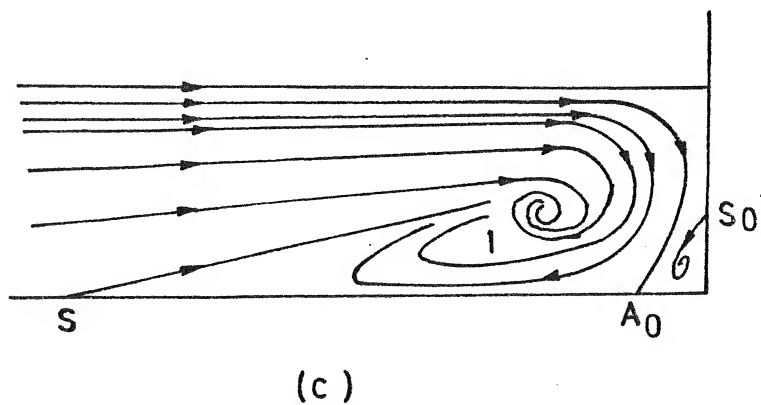
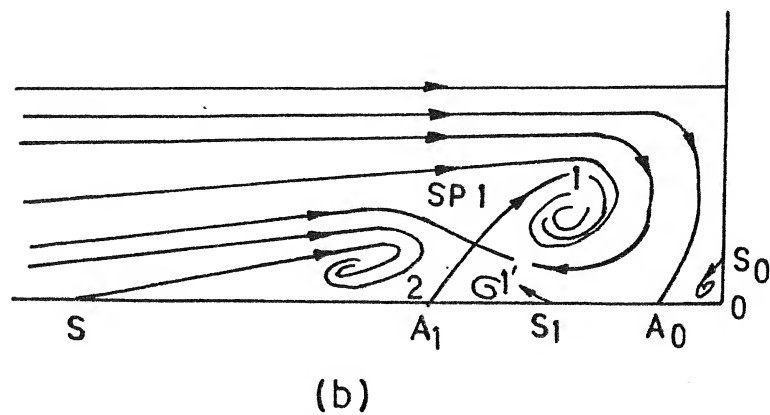
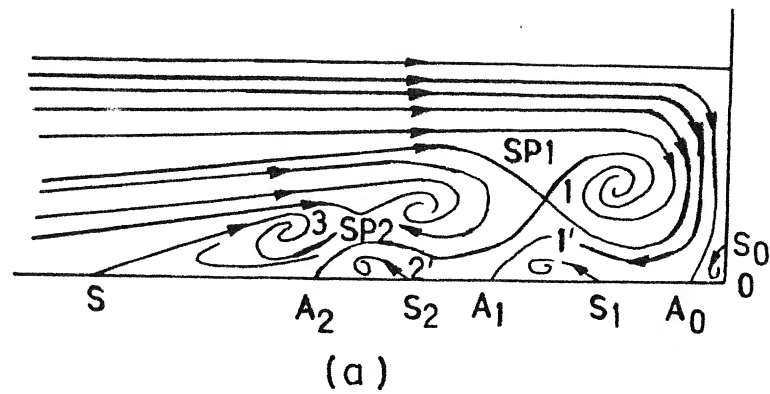


FIG. 1.1 THE HORSESHOE VORTEX



STREAMLINE PATTERNS :- (a) Six vortex ,
 (b) Four vortex , (c) Two vortex system .
 S : Separation line , A : Attachment line ,
 SP: Stagnation point .

FIG. 1.2 HORSESHOE VORTEX STRUCTURE (Baker, 1979)

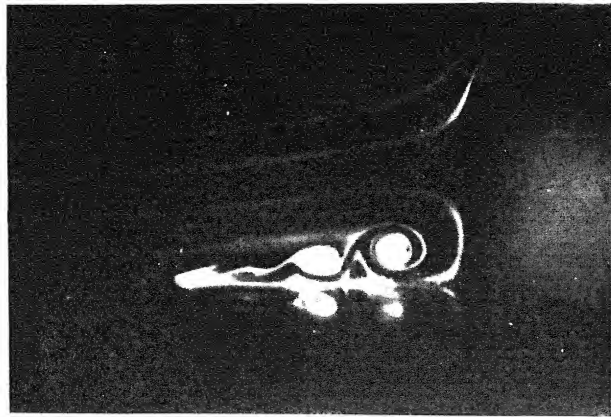
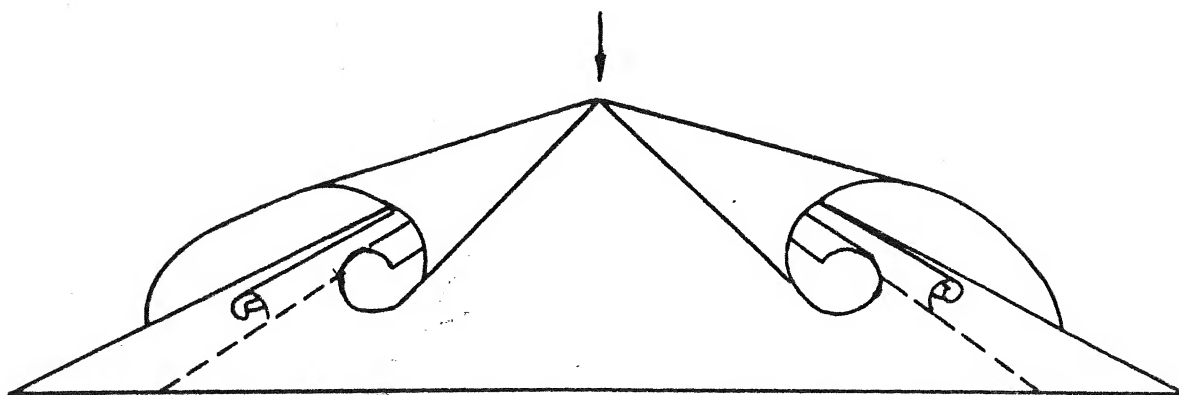
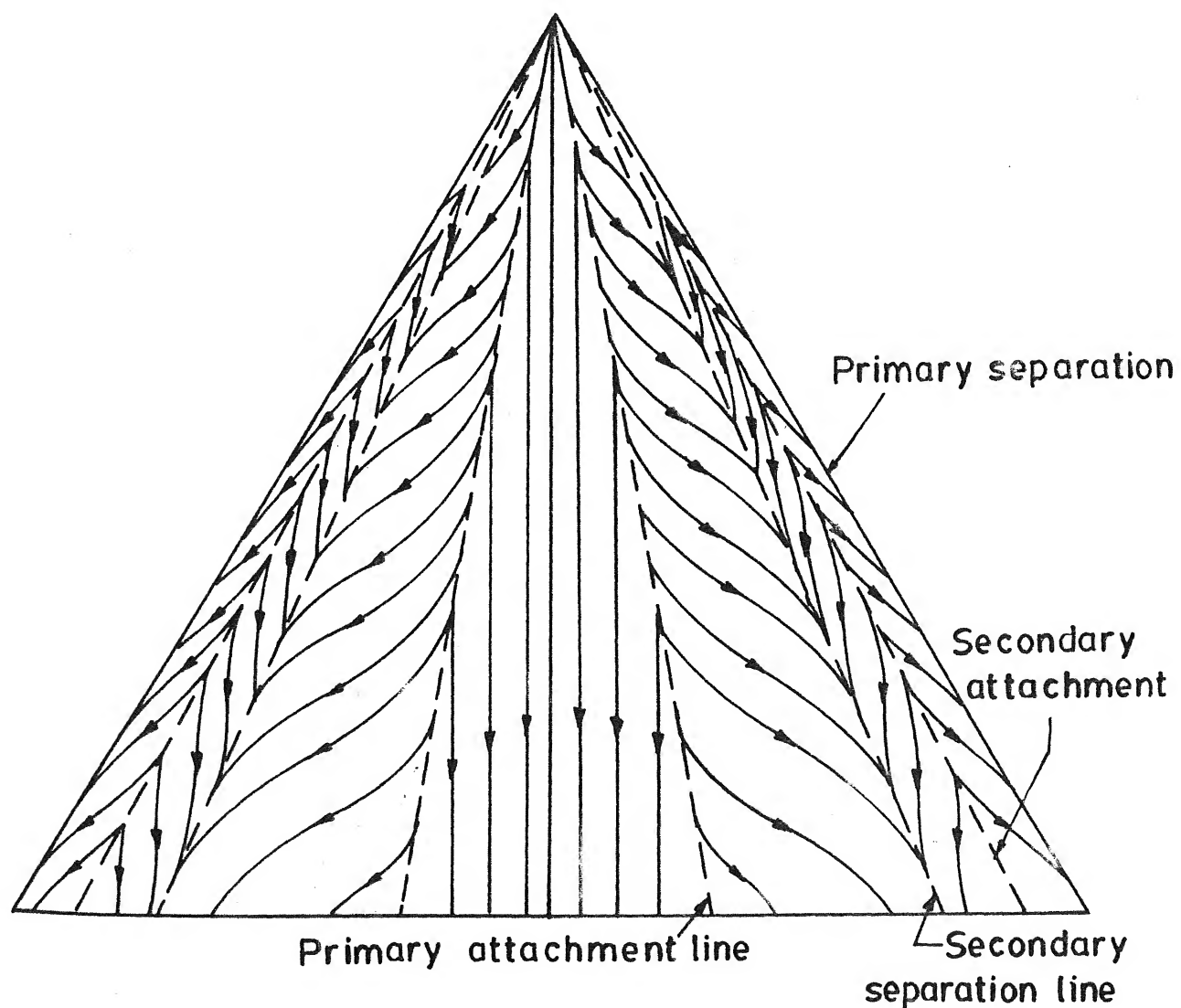


Fig. 1.3 SUTTON'S EXPERIMENT (BAKER, 1979)



(a) Vortex sheets formed on the suction side



(b) Surface flow pattern

FIG. 1-4 TYPICAL FLOW OVER A DELTA WING AT MODERATE INCIDENCE

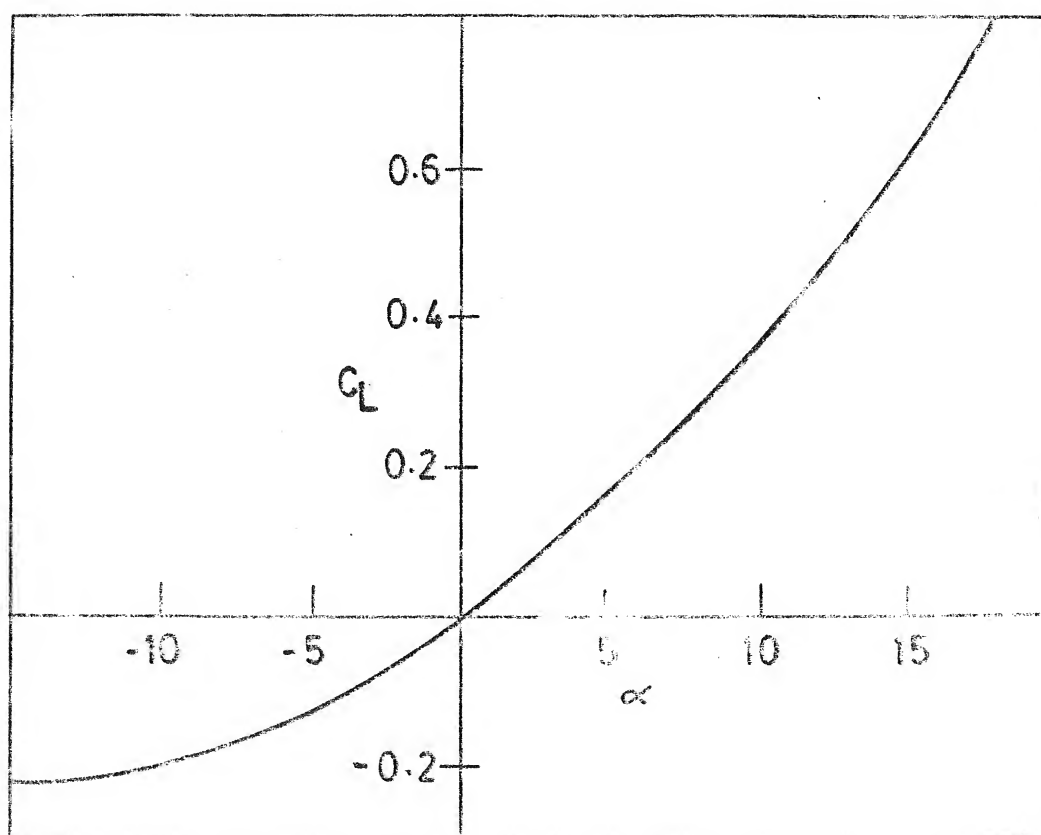


FIG. 1.5 . AERODYNAMIC CHARACTERISTICS OF DELTA WING , AR = 1.5 (Polhemus , 1966)

CHAPTER II

EXPERIMENTAL EQUIPMENT AND INSTRUMENTATION

2.1 WIND TUNNEL

Most of the experimental investigations were carried out in the low speed, low turbulence, suction type, closed jet, open circuit wind tunnel of the Aerodynamics Laboratory. This tunnel is housed in a spacious hall (20 m x 20 m) of the laboratory along with other wind tunnels. The size of the test section of the wind tunnel is 30.5 cm height x 40.5 cm width x 101.6 cm long. The maximum wind speed in the clear test section is about 10 m/sec.

The tunnel has a contraction ratio of 9 obtained by means of two 2-D contractions arranged in tandem. The settling chamber has a 2.5 cm square, metal honey-comb at its entrance. There are six wire mesh screens located at appropriate intervals in between the honeycomb and the end of the first 2-D contraction cone. An air filter made of bolting cloth is also stretched across the tunnel inlet before the honeycomb to minimise the entry of dust into the test section. The diffuser section following the test section is circular in cross-section and is achieved by the gradual divergence of the rectangular test section. The fan housing is located at the end of the diffuser. An axial flow fan coupled to a 2 HP ducted DC variable speed motor having stabilized power supply provides a maximum wind speed of about 10 m/sec. with a turbulence intensity of about 0.5%. The motor

assembly rests on a 6 cm thick thermocol mat and is isolated from the main tunnel structure by means of an endless cycle tube rubber strap joining the fan duct to the diffuser outlet. The object of this rubber strap is to keep the test section free from vibrations transmitted from the fan motor assembly. A schematic view of the tunnel drawn to scale and a photograph are shown in Figs. 2.1 and 2.2 respectively. This tunnel was earlier used by Gupta (1973), Sullerey (1974) and Sinha (1978) for their dissertation work, and has undergone several overhauls of both the tunnel structure and the motor-fan assembly.

a. The Test Section

The top of the rectangular test section measuring 40.5 cm x 101.6 cm is covered with a 12 mm thick perspex sheet. Two such cover plates were employed ; one with central longitudinal slot of width 10 mm x 900 mm long and the other with a slot of width 100 mm x 900 mm long. For each cover plate, special T plugs of appropriate sizes were fitted into the slot to prevent any leakage of air.

The far side of this test section measuring 30.5 cm x 101.6 cm is a 6 mm thick aluminium plate painted matt black for good photographic contrast. It has a series of 1 mm dia. pressure tappings located at the tunnel mid-height and spaced 50 mm apart along the test section length.

The bottom plate is made of a 6 mm thick perspex sheet. Titanium tetrachloride flow visualization experiments were conducted with this sheet as the tunnel floor. A 2.5 cm square grid in red was marked on this plate which was light brown in color, whereas the grid was changed into white when the plate was painted matt black, for good photographic contrast in each of the two cases. For oil flow visualization, a 6 mm thick glass sheet was employed as the bottom plate for the test section. A black sheet with 2.5 cm square grid marked in white was pasted below this glass plate for photography sessions. For the pressure measurements on the floor in the presence of the vertically mounted models, a separate floor assembly with a turn-table like arrangement was mounted flush with the bottom plate of the test section. This will be described in greater detail in a subsequent section of this chapter.

The front of the test-section is made of a glass door hinged at the top edge, spanning the entire length of the test section. This door is locked in place by means of two shutter type hooks. During the present experiments, whenever the door was closed, it was also sealed all along its periphery by scotch tape. Fig. 2.3 shows a perspective view of the test section.

2.2 WATER TABLE

The dye flow visualization experiments were conducted on the water table of Aerodynamics Laboratory. A sketch of this apparatus and a picture are shown in Figs. 2.4 and 2.5 respectively.

The apparatus is a recirculating type, open, shallow water channel in which a centrifugal pump connected to the outlet from the water drainage tank at the end of the open channel delivers the water through a rotameter to the inlet section of the water table, by means of a T-type arrangement of 37 mm diameter pipes. The two entry water reservoirs have a depth of about 40 cm and are fitted with wire mesh screens. Water from these reservoirs rises up through a rising curved bottom to provide a depth of about 7 cm in the settling region of the water table. The 94 cm wide settling region is fitted with two fine brass screens of mesh size 130 per square inch to reduce the turbulence level of the flow. The contraction reduces the 94 cm width of the settling region gently to 25 cm at the inlet of the test-section in a length of 112 cm. The test section is 25 cm wide, 7.5 cm in depth and 32 cm in length and is fabricated out of 2.5 cm thick perspex sheet. It is followed by the diffuser section with the section width increasing gradually from 25 cm to 40 cm over a length of 60 cm. At the exit of the diffuser, an adjustable vertical flap is mounted to control the water level in the test-section. The discharged water is collected in a 45 cm x 90 cm metallic drainage tank with a depth of 75 cm. The outlet at the bottom of the tank is connected to an inverted T-joint ; one end of which is connected to the centrifugal pump and the other end is fitted with a gate valve, which drains the water outside. When the gate valve is closed, the water circulates

through the pump. The whole assembly is mounted on slotted channels and angle-iron frames, with castor wheels for mobility. This facility had been used earlier by Gupta (1987) for his flow visualization experiments.

2.3 MODELS

Basically two types of models mostly made out of seasoned wood have been employed in the present investigations. These are : circular cylinders of different diameters and pier models of constant width with different leading edge shapes. Their details are mentioned in the following subsections.

a. Pressure Model of Circular Cylinder

A pressure model of 25 mm diameter, 3 mm wall thickness and 150 mm long, hollow circular cylinder was fabricated out of brass. Details of this model are shown in Fig. 2.6. Along one vertical generator and one vertical end of the cylinder, fifteen holes each of 1 mm diameter were drilled, first ten holes from the end were at an interval of 2.5 mm each and the last five were at an interval of 5 mm each. Stainless steel hypodermic tubings of 1 mm outer diameter and of appropriate lengths were embedded through the inner wall of the cylinder and were taken out through the inner cylinder. These tubes were made flush with the outer surface of the cylinder. Views of this model during fabrication and finished stages are shown in Fig. 2.7 a and b.

b. Flow Visualization Models

(i) Circular cylinders

A number of circular cylinder models were fabricated out of aluminium and brass rods as detailed in Table 2.1 and are shown in Fig. 2.8. In addition two stainless steel tubes of 1 mm and 3 mm diameter spanning the test section vertically were also used as cylinders.

TABLE 2.1
CIRCULAR CYLINDERS

Sl.No.	Diameter, D mm	Height, L mm	L/D	B R %	Material
1	50	150	3	6.1	Aluminium
2	37.5	150	4	4.56	"
3	25	150	6	3.04	Brass
4	12.5	150	12	1.52	"
5	12.5	80	6.4	0.81	"
6	6.00	80	13.3	0.39	"
7	6.00	55	9.2	0.27	"

(ii) Pier Models

Four pier models with leading edge shapes, rectangular, semi-circular, wedge and lenticular in plan view were fabricated out of seasoned teak wood. All these symmetrical models were

15 cm in height, 10 cm (8 cm in case of semi-circular nose pier) in streamwise direction and 2.5 cm in maximum lateral dimension. The sectional shapes of these models drawn to scale are shown in Fig. 2.9.

These models were dope sprayed for protection against water when used for dye flow visualization experiments. Each of these models along with 2.5 cm circular cylinder were provided with a vertical slit of 1 mm width, 15 mm height and 5 mm in depth in their respective leading edge foot regions, in their planes of symmetry for holding the delta-wing-like passive device. For the flow visualization experiments with $TiCl_4$ these models were painted matt black in the region of interest upto half of their heights for getting good photo contrast. A picture of these models is shown in Fig. 2.10.

2.4 DELTA-WING-LIKE PASSIVE DEVICE

The geometry of the passive device used for hydrodynamic modification of the horseshoe vortex consisted of a thin delta-wing-like plate in plan view. A spinal rib of thickness 1 mm was attached along the line of symmetry of this plate. The spinal rib had a height of 12 mm at the delta base and tapered down to almost zero height at the delta vertex. The dimensions of this device were originally proposed by Gupta (1987) and has been termed 'standard passive device' for comparison with other variants.

A total of five such similar passive devices were fabricated out of 1 mm thick perspex sheet to observe the effect of minor variations of the 'standard passive device' on the characteristics of the hydrodynamic modification of the horseshoe vortex. Details of these devices are shown in Table 2.2 and a pictorial view of these variants and the 'standard passive device' is shown in Fig. 2.11, and details of the 'standard passive device' are given in Fig. 2.12.

TABLE 2.2
DELTA-WING-LIKE PASSIVE DEVICES

Sl.No.	length mm	base mm	height mm	spinal rib yes/no	L.E.shar- pened yes/no
1*	50	37.5	12.5	yes	no
2	50	37.5	12.5	no	no
3	50	37.5	12.5	yes	yes
4	50	37.5	12.5	no	yes
5	50	25.0	12.5	yes	no

* The Sl. No. 1 is termed the 'standard passive device'.

In order to fit the delta-wing-like passive device to the pier's leading edge foot, the spinal rib of the passive device was extended beyond the delta base by an amount of about 5 mm. The extended portion of the spinal rib was push fitted into the slit provided at the foot of the pier as described earlier.

2.5 THE TURN TABLE

To measure static pressures on the floor around the pier junction, a 2.5 cm thick perspex turn table of outer diameter equal to 30.8 cm was fabricated. This turn table fitted snugly into a circular cavity of 30.8 cm nominal diameter cut into the test-section floor perspex plate of 40.5 cm x 101.6 cm size. The centre of the turn table was located at a downstream distance of 60 cm from the beginning of the test section. The turn table had a total of 96 static pressure holes each of 1 mm diameter distributed equally along four radial lines in a 'cross' pattern with a central hole of 12.5 mm diameter for seating the circular cylinder pressure model. Thus each of the four radial lines had 24 static pressure taps. First sixteen taps (moving radially outwards from a radius of 6.25 mm) were spaced 2.5 mm apart, followed by the last eight holes each spaced at an interval of 10 mm. Thus a total distance of 12 cm was covered by a set of 24 holes on one radial line. Stainless steel hypodermic tubings of 1 mm diameter and of appropriate lengths were embedded in these holes from below and were made flush with the turn table

floor surface. Details of this turn table are shown in Fig. 2.13 and its pictorial views are provided in Figs. 2.14 to 2.16 during fabrication and finished stages.

This turn table rested on a base plate, which was screwed to the floor and the angle iron supports forming the test-section frame from below. Two 6 mm wide circular arc slots in the opposite quadrants were milled in the base plate, through which moved the guide bolts, one in each arc slot from the turn table. This enabled to achieve the desired angular rotation of the radial lines of pressure tapplings with respect to the free stream direction. After tightening the nuts from below, on the guide bolts, the turn table attained a flush position with the tunnel floor. The whole assembly can be seen from below the test-section in Fig. 2.16 and the details of this turn table-cum-floor assembly are shown in Fig. 2.17.

In order to measure the pressure distribution on the windward side of the passive device, another circular plate of the same dimensions as for the turn table was fabricated separately. In this case the spinal rib of the delta-wing-like passive device was cast in situ with stainless steel hypodermic tubes of 1 mm diameter to provide static pressure tapplings on the upper surface of the device. These details of the second circular plate are shown in Fig. 2.18.

2.6 PROBES

a. Shielded Pitot Tube

A shielded pitot tube (Fig. 2.19) was fabricated out of stainless steel tubing. The outer diameter was 2 mm and a 0.75 mm diameter inner tube was set concentric with the outer one as shown in Fig. 2.20a. This probe was used to obtain the total head contours in one vertical Y-Z plane passing through the mid-streamwise station of the piers or the circular cylinder.

b. Hot Wire Probe

Wollaston process platinum wire of 0.0003" diameter with a cold resistance of 1220 ohms per foot was used as a sensor for a hot wire u-probe. The distance between the prongs was 1 mm. This resulted in an aspect ratio of about 133. A picture of this hot wire probe is given in Fig. 2.21.

c. Pitot Tube

A 0.75 mm diameter stainless steel hypodermic tube was used to obtain velocity profiles on the floor of the clean tunnel, and is shown in Fig. 2.22.

A standard pitot-static tube of 3 mm OD was used to monitor the dynamic head of the flow during the test runs.

2.7 INSTRUMENTS

Fig. 2.23 shows a close-up view of the electronic instruments used in the present experiments. Following are the particulars of these instruments.

(i) A Barocel Type 1014 Electronic Manometer with analog output was employed for the measurements of pressures in conjunction with a Barocel pressure cell with range upto 10 psi. For measurements at wind speeds below 2m/sec, the lowest range of 0.001 with a least count of 0.0001 was used.

(ii) A Datametrics Type 1018 Electronic Manometer with digital read out was employed for pressure measurements in conjunction with a Barocel pressure sensor with range up to 10" of H_2O . For measurements at wind speeds above 2 m/sec, 1" of H_2O range was selected with a least count of 0.0001.

(iii) A DISA 55M Constant Temperature Anemometer set consisting of the modular units, 55 MO5 main unit, 55M 10 CTA Bridge, 55 D30 Digital Voltmeter and 55 D35 RMS meter, was used for the measurements of velocity profiles and spectra.

(iv) A Kikusui Digital Storage Oscilloscope Model DSS 6521 with dual trace and a range of DC to 20 MHz was used to monitor the signals from Hot Wire Anemometer.

(v) A Dual Channel, HP 3582-A, Spectrum Analyzer having a range of DC-25 KHz, was used extensively for the spectrum analysis in conjunction with the Constant Temperature Anemometer. This

spectrum analyzer is based on the calculation of the discrete Fourier Transform having the highly efficient FFT Algorithm. Two digitally stored display traces alongwith fourlines of alphanumeric data provided complete results on the CRT section. It was operated in the 'Single Channel Amplitude Spectrum Measurement' mode by using channel B and channel sensitivity of 0 dBV FS, by selecting appropriate frequency span.

(vi) A UNITEC 1 MHz Sine/Square Audio Generator OW14 was employed for the calibration of the HP 3582-A Spectrum Analyzer using Sine Wave form. Frequency range from 10 Hz to 1 MHz could be selected in five ranges with an accuracy of $\pm 3\% \pm 1$ Hz and drift less than 0.2% after initial warm up. Total harmonic distortion was less than 0.5%. Continuous control through four steps of 20 dB and accuracy of $\pm 0.2\%$ provided zero to full output of 10 V RMS at each step.

All these instruments were operated through a stabilized power supply from Type EMS-8 AC Automatic Voltage Stabilizer with a sensitivity of $\pm 0.50\%$.

Following mechanical instruments were also used in the present experiments.

(vii) A manual pressure selector switch (Head, 1971) was employed as a scanner in conjunction with Electronic Manometers

as the sensing units. Up to twentyfour pressure channels could be scanned in the multiplexing mode. Fig. 2.24a shows a perspective view and Fig. 2.25 provides the functioning details of this selector switch.

In the preliminary experiments a Single Scanivalve System SSS-48C with a 1.00 psi transducer was tried for recording static pressures in the flow field. This was not very successful at velocities below 2 m/sec and consequent low pressures below 0.0004 psi.

(viii) A traversing mechanism designed and fabricated by Prasad (1975) having three translational degrees of freedom was used for traversing the hot wire probe and the shielded pitot tube. Two mechanical counters with provision for digital display were fitted to read the displacements. The resolutions in x (longitudinal), y (span-wise) and z (vertical) were 0.125 mm, 0.05 mm and 0.05 mm respectively. To minimize the backlash in the traverses, displacements in x, y and z directions were increased or decreased monotonically. Fig. 2.26 shows a perspective view of this traverse mechanism.

A vertical micro-traverse mechanism was used to hold the pitot-static tube at the desired vertical location near the entrance to the test section to monitor the free stream velocity and the static pressure.

2.8 PHOTOGRAPHIC EQUIPMENT

One Asahi Pentax K 1000 SLR camera with lens f 1:2 was employed for still photography during flow visualization tests and for photographically recording the spectrum from the spectrum analyser and hot wire traces from the storage oscilloscope.

During all the flow visualization shots, the test section was flood lit with one Flectalux 1000 W Sungun and two 500 W studio lights.

Kodacolor Gold 100 films were used for flow visualization shots and ORWO B&W films for the spectrum and oscilloscope traces.

An overall view of the instruments positioned near the wind tunnel is shown in Fig. 2.27.

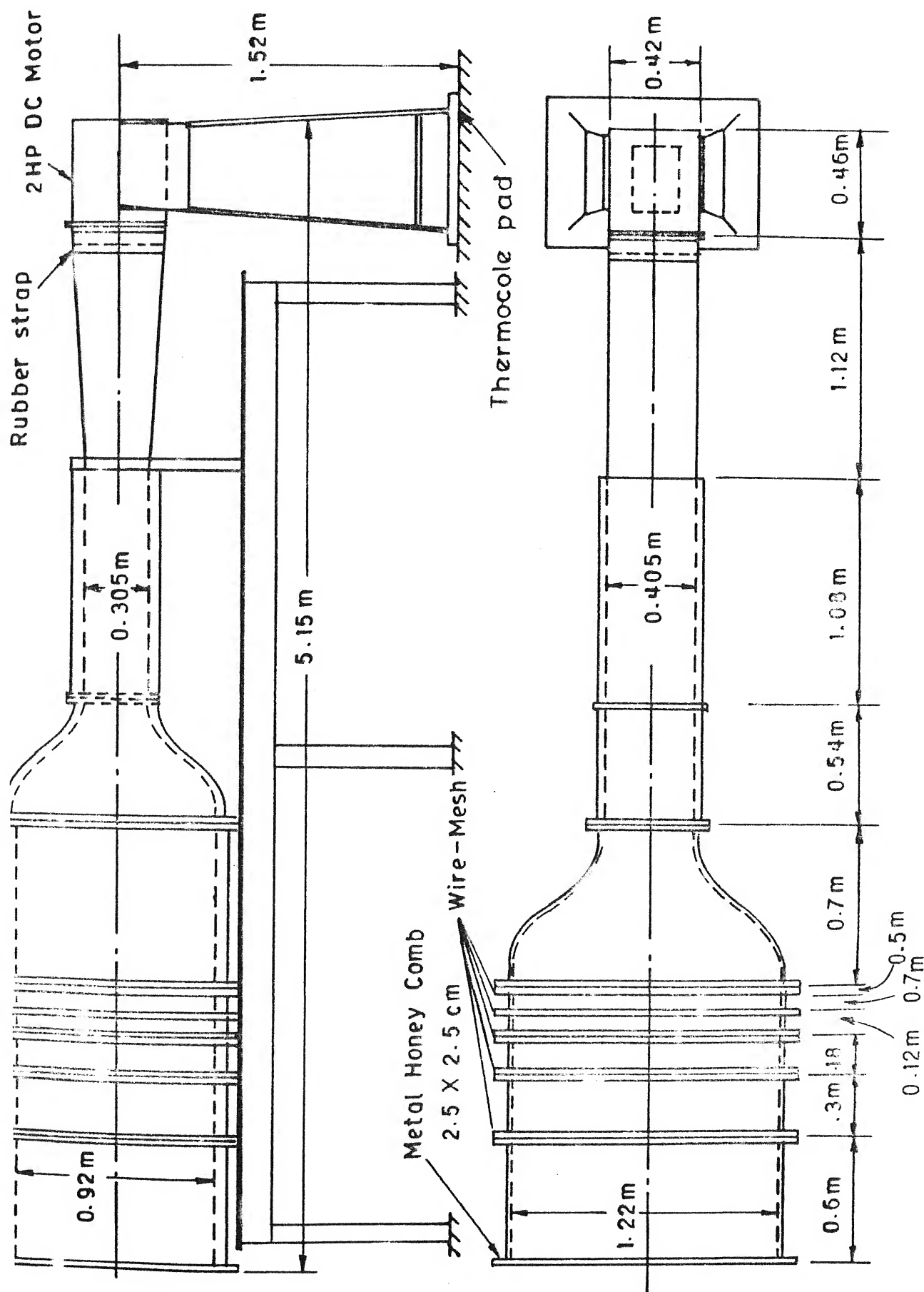


FIG 2.1 30.5 x 40.5 cm LOW SPEED LOW TURBULENCE WIND TUNNEL

Fig. 2.2 A VIEW OF LOW SPEED WIND TUNNEL

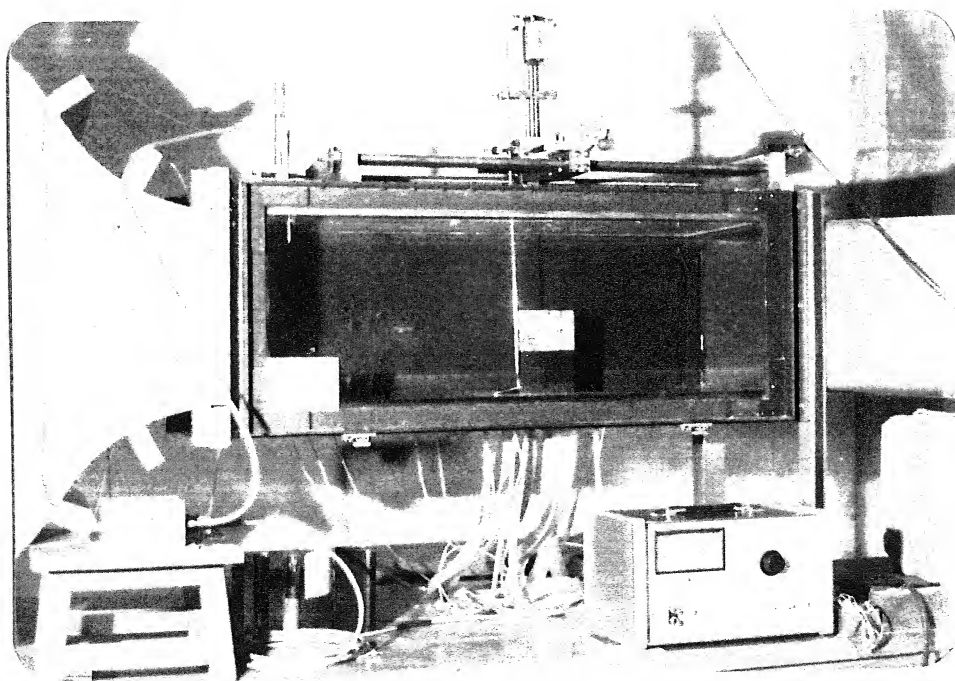


Fig. 2.3 A VIEW OF THE TEST SECTION

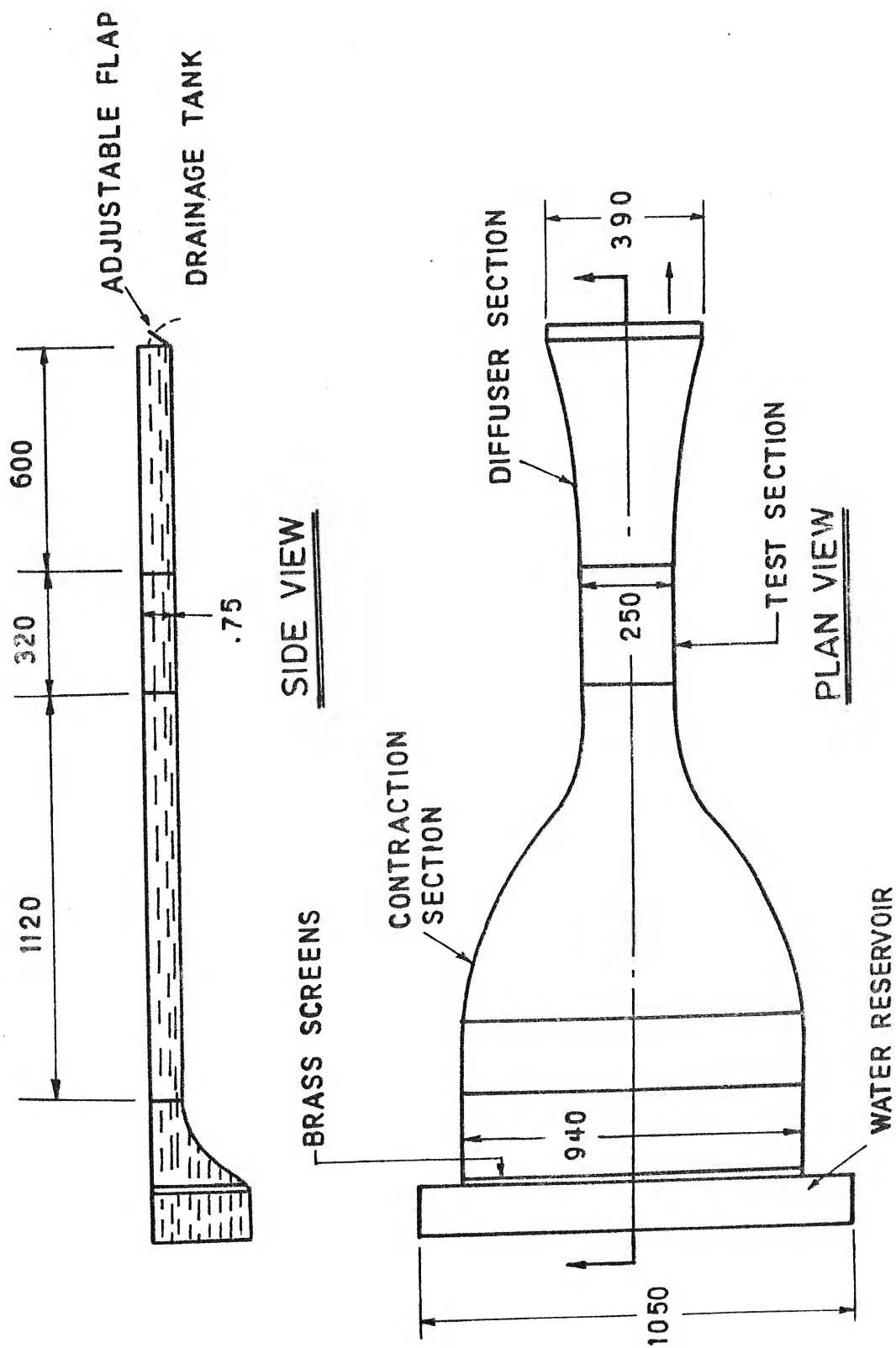


FIG. 2.4 SCHEMATIC DIAGRAM OF THE WATER TABLE

Fig. 2.5 A VIEW OF THE WATER TABLE

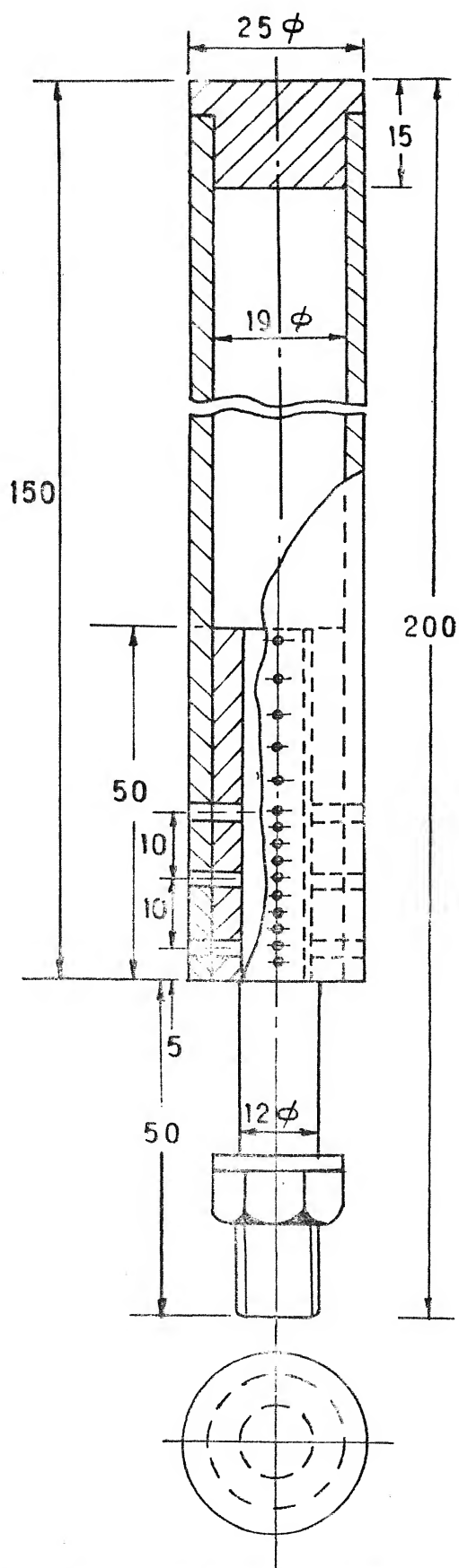
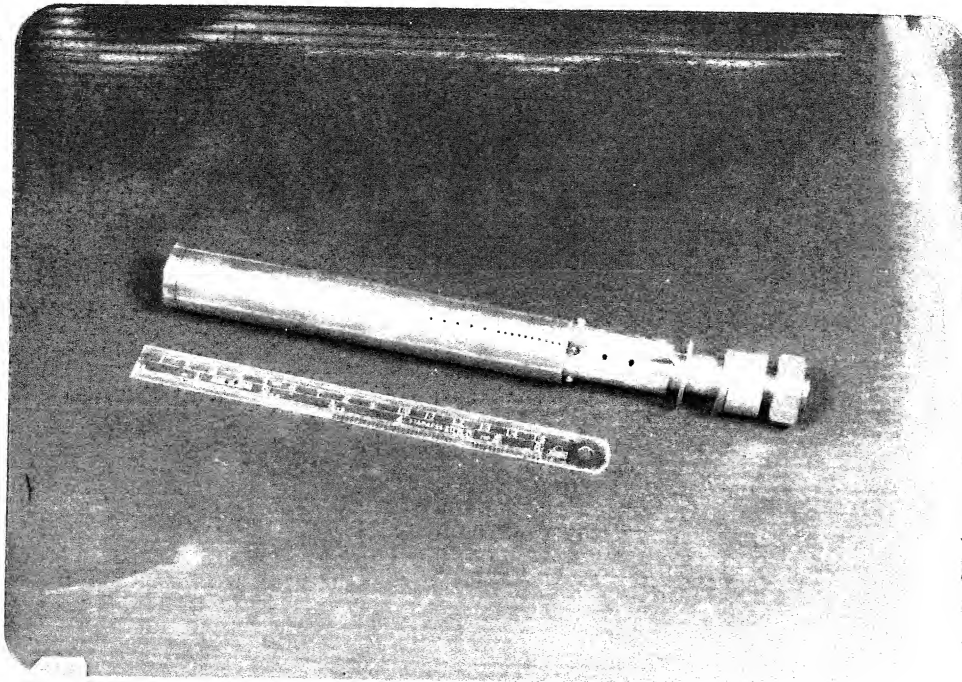
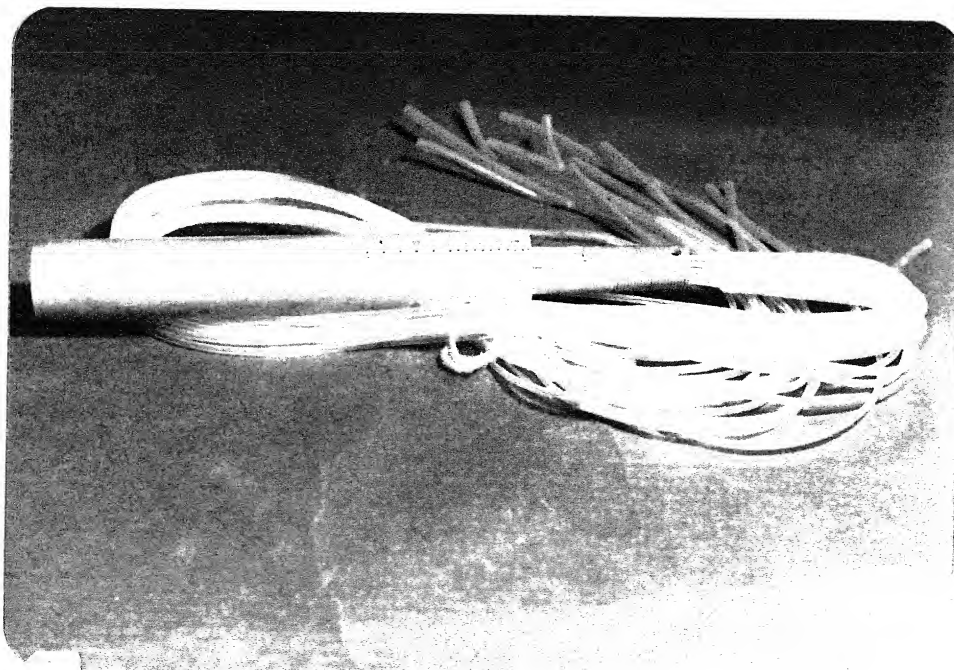


FIG. 2.6 PRESSURE MODEL OF CIRCULAR CYLINDER



a. COMPONENT DETAILS



b. FINISHED STAGE

Fig. 2.7 CIRCULAR CYLINDER PRESSURE MODEL

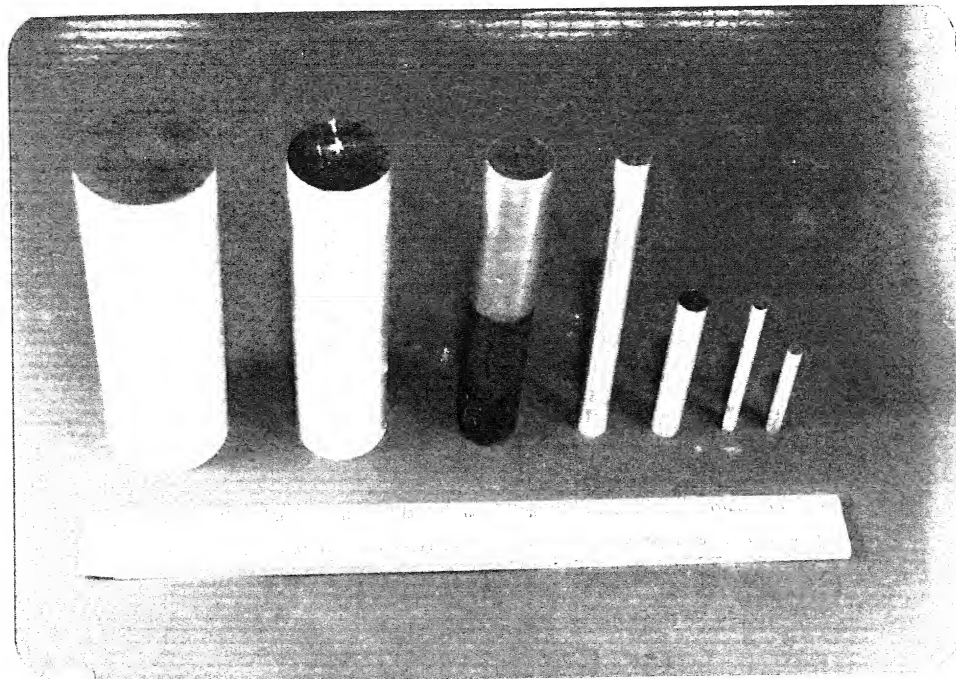


Fig. 2.8 CIRCULAR CYLINDER MODELS

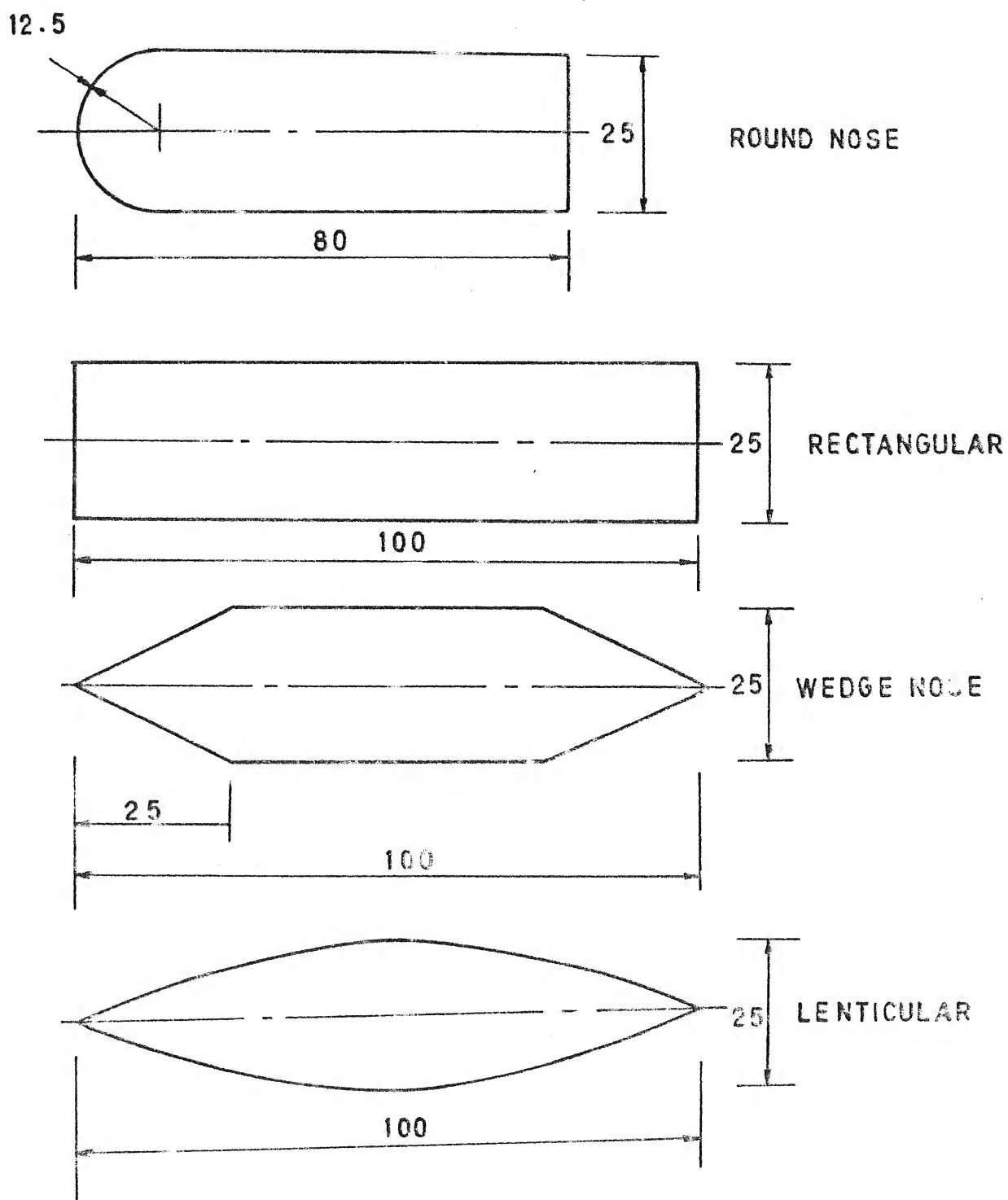


FIG. 2.9 SECTIONAL DETAILS OF PIER MODELS

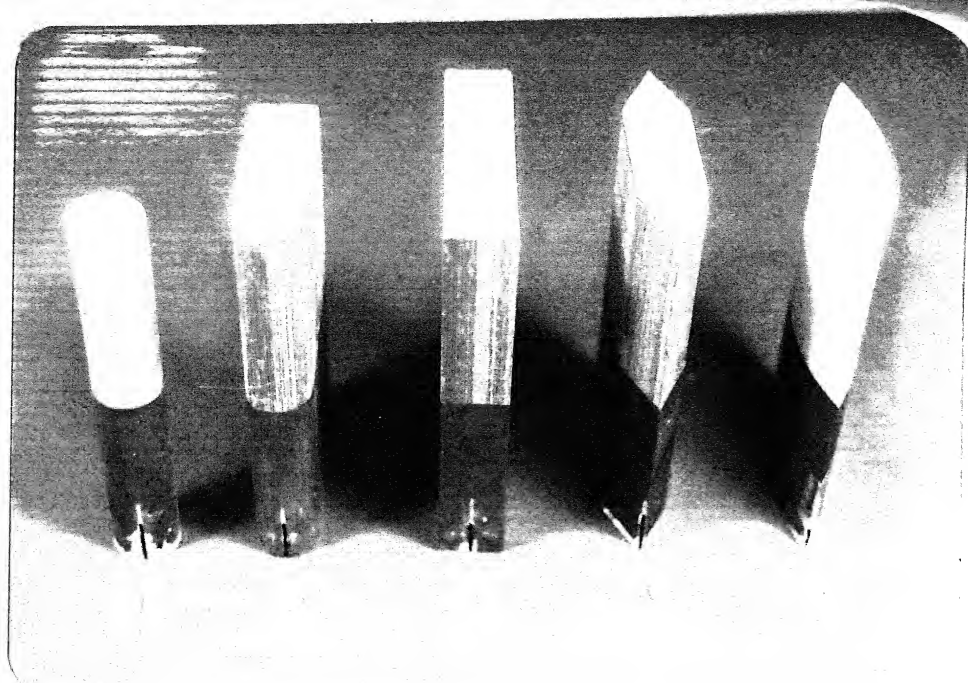


Fig. 2.10 THE PIER MODELS

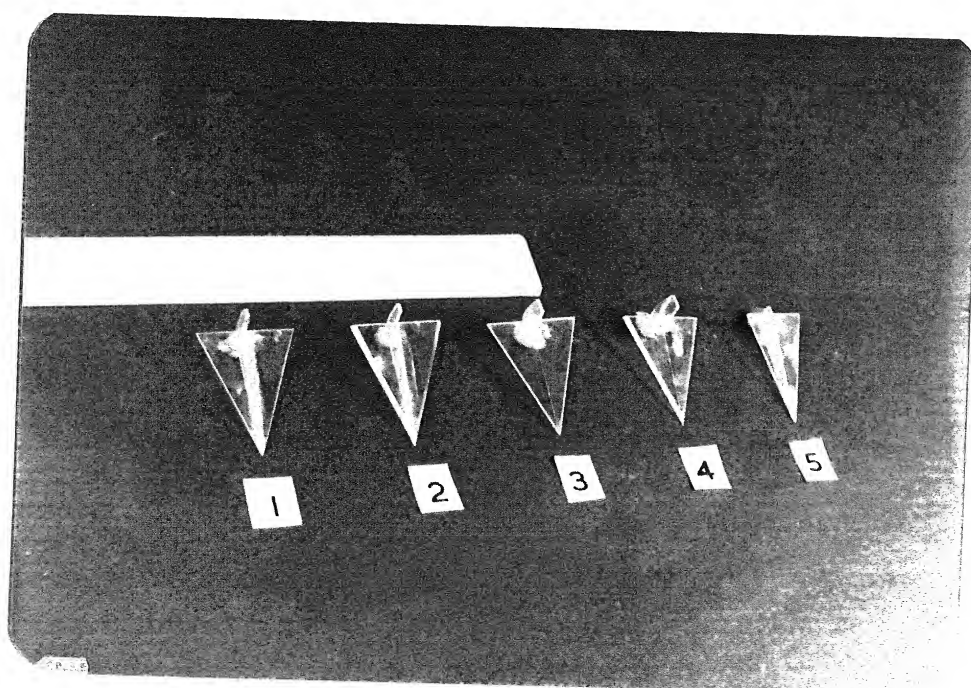
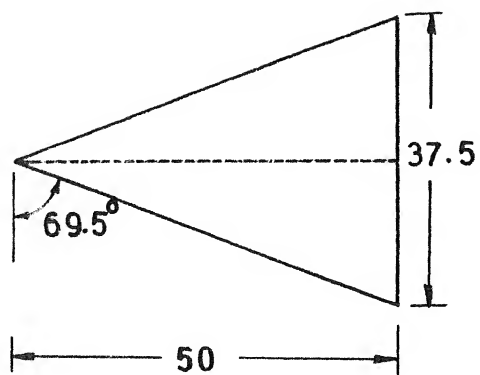
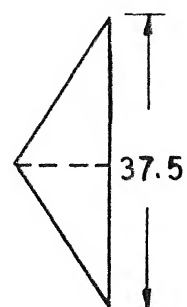


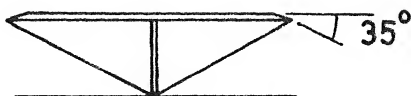
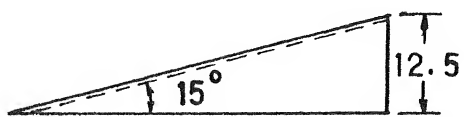
Fig. 2.11 THE PASSIVE DEVICES



PLAN VIEW



FRONT VIEW

Details of sharp leading edge
at 2 and 4 (Table 2.2)

SIDE VIEW



PERSPECTIVE VIEW

FIG. 2.12 DELTA-WING-LIKE PASSIVE DEVICE

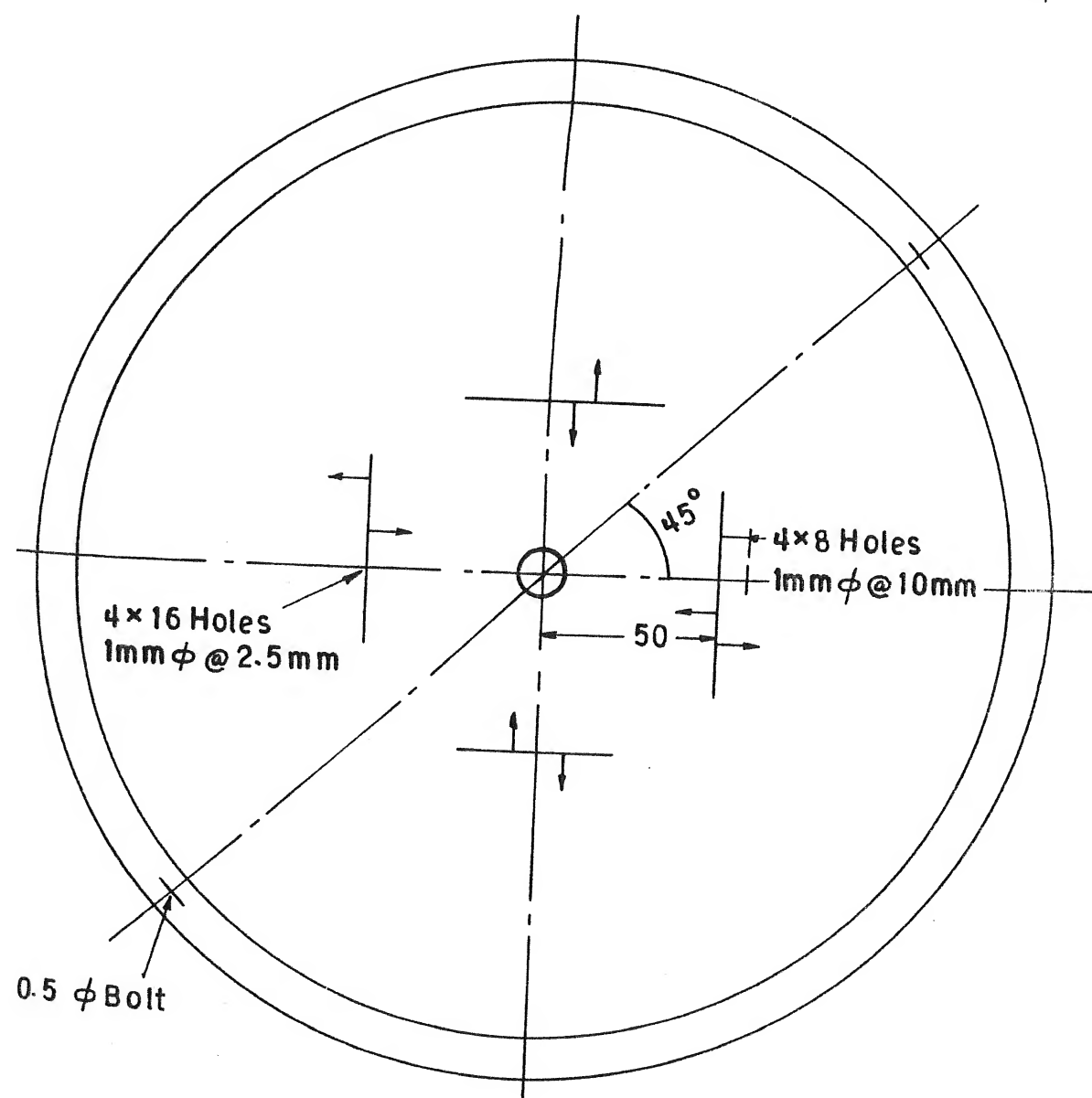
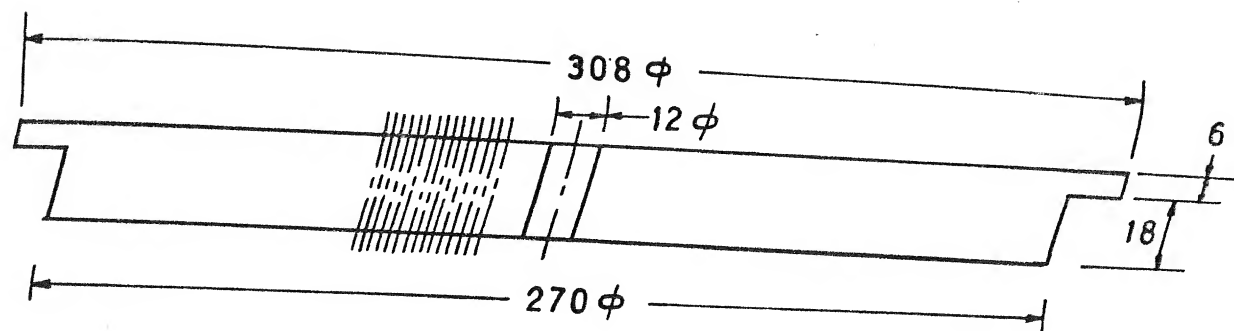


FIG. 2.13 DETAILS OF TURN TABLE

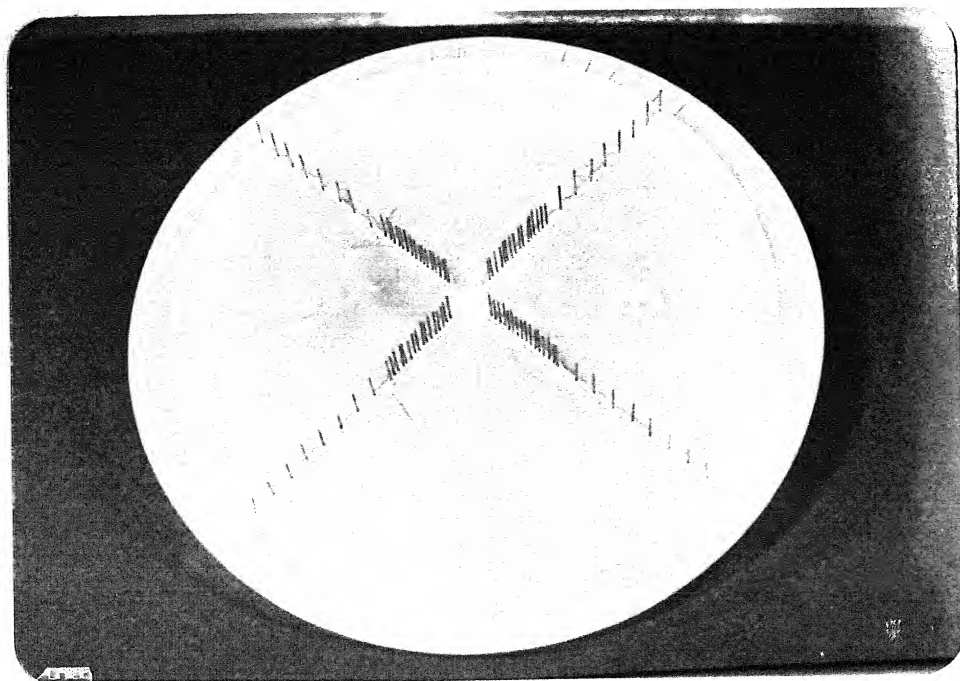


Fig. 2.14 BOTTOM SIDE OF TURN TABLE I

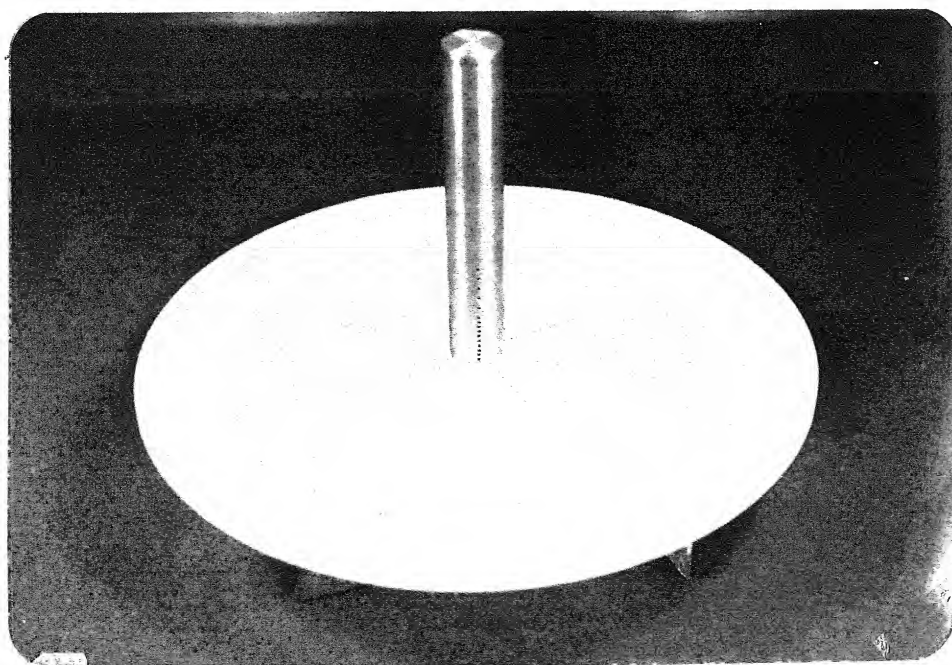


Fig. 2.15 PRESSURE MODEL MOUNTED ON TURN TABLE I

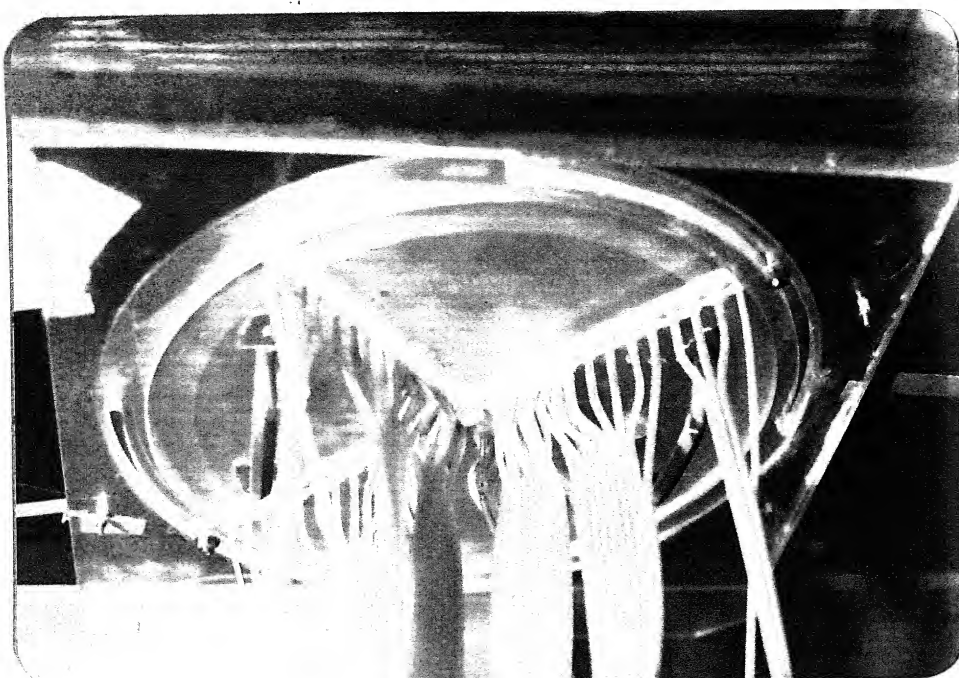


Fig. 2.16 BOTTOM VIEW OF TURN TABLE ASSEMBLY IN
TEST SECTION

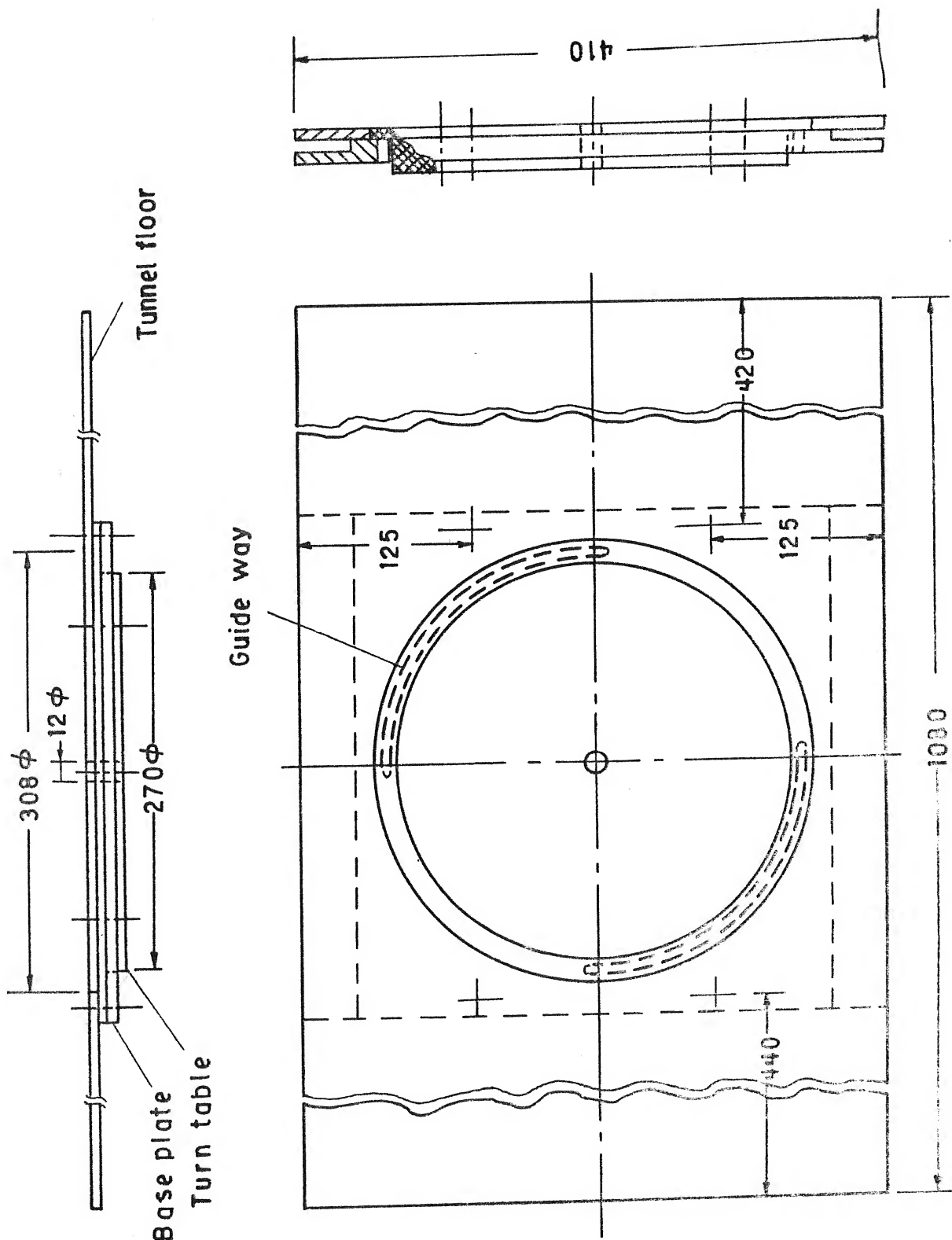


FIG. 2.17 TURN TABLE CUM FLOOR ASSEMBLY

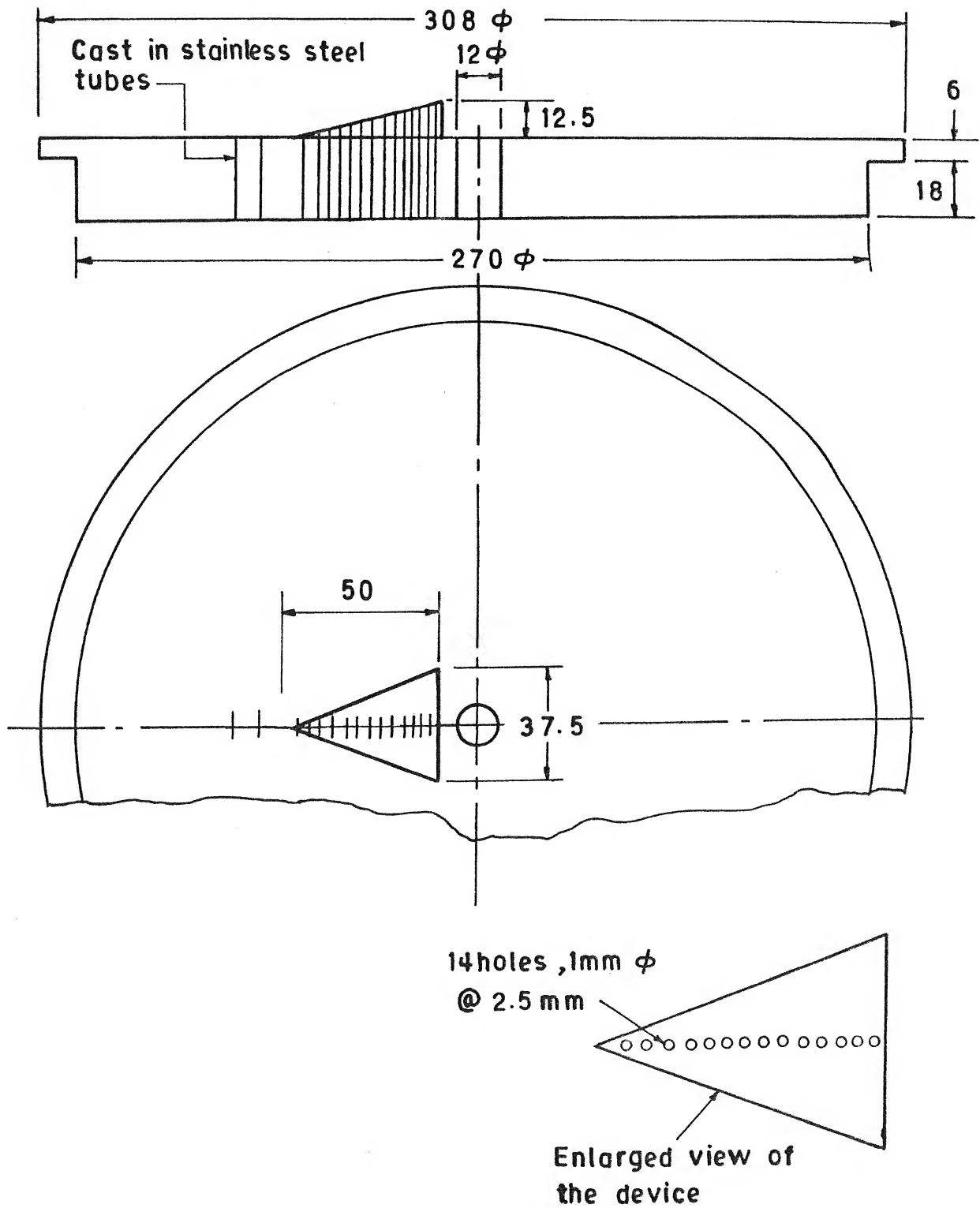


FIG. 2.18 DETAILS OF CIRCULAR PLATE II

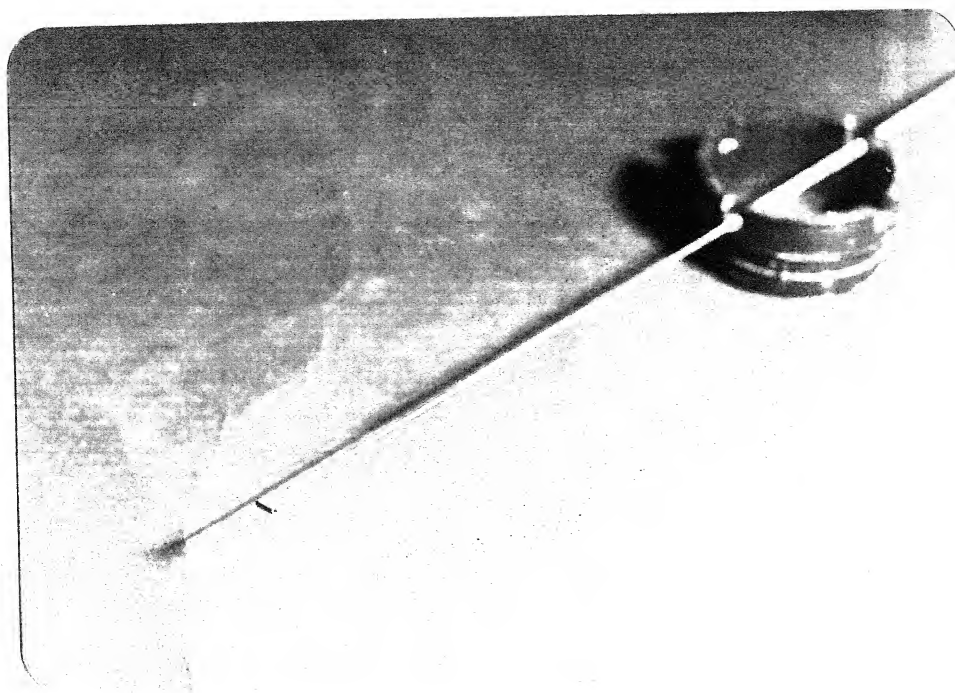


Fig. 2.19 THE SHIELDED PITOT TUBE

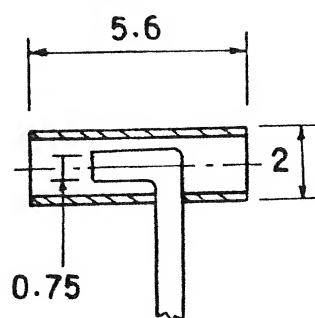


FIG. 2.20 SCHEMATIC VIEW OF SHIELDED PITOT TUBE

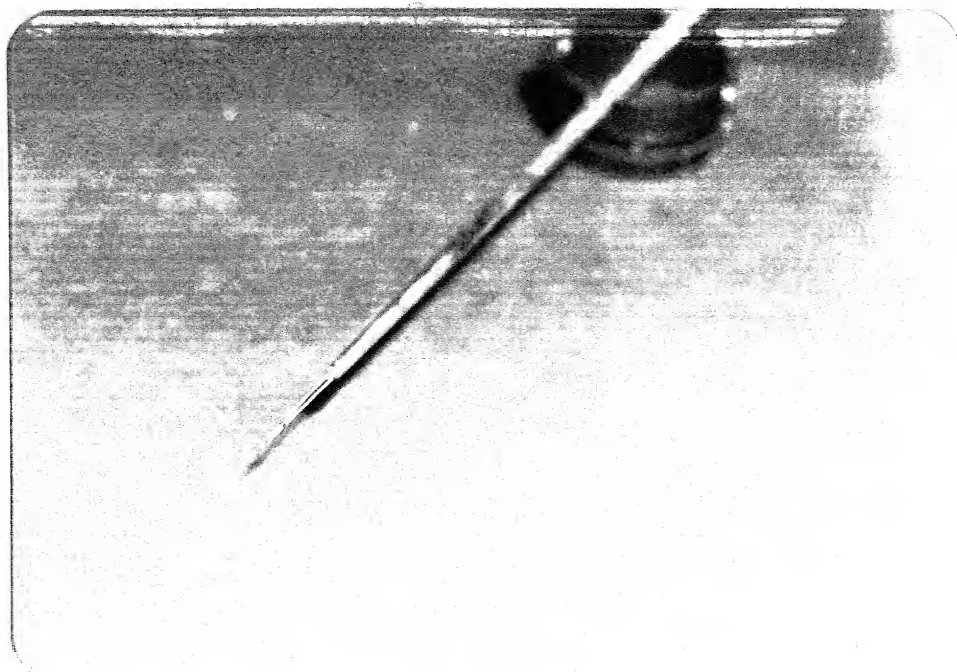


Fig. 2.21 THE HOT WIRE PROBE

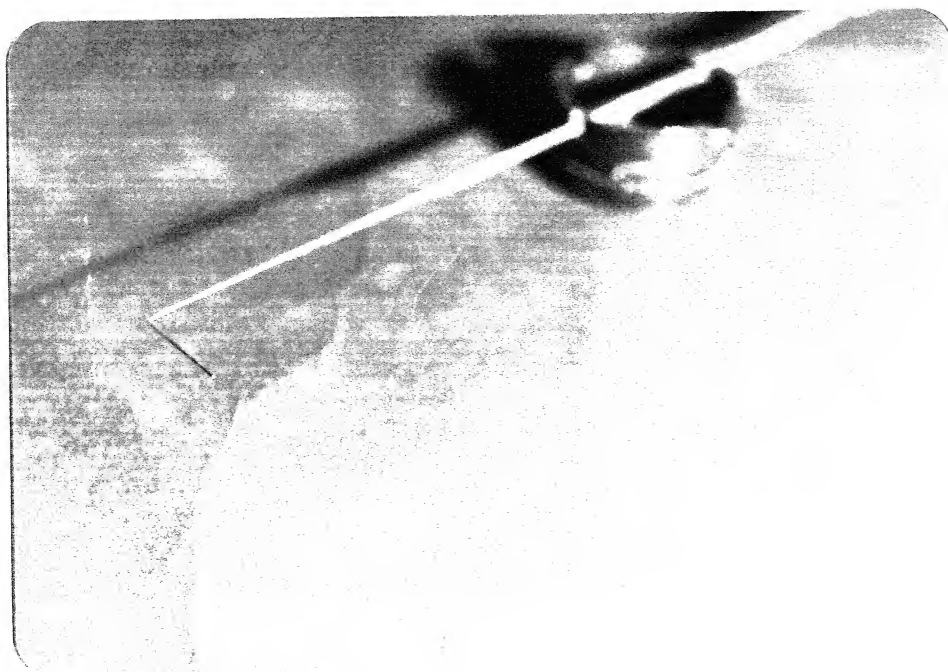


Fig. 2.22 THE PITOT TUBE

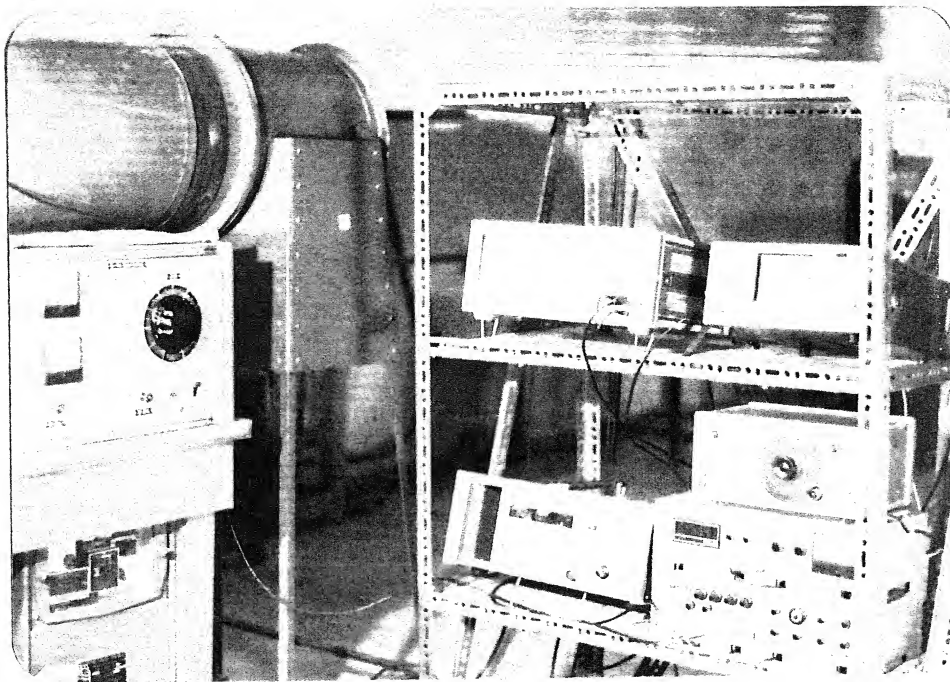


Fig. 2.23 CLOSE UP VIEW OF ELECTRONIC INSTRUMENTS

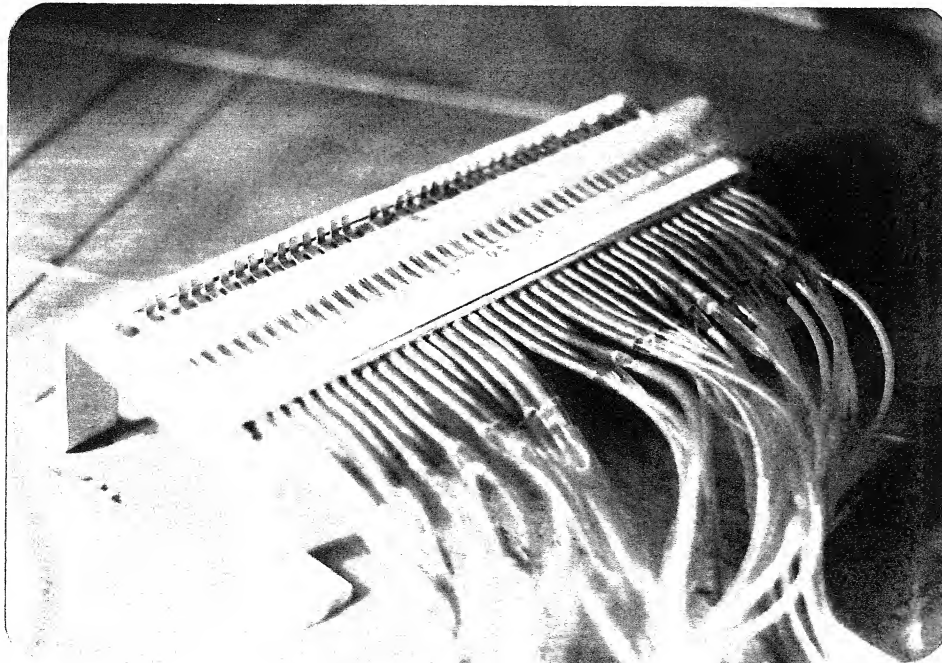


Fig. 2.24 24-CHANNEL PRESSURE SELECTOR SWITCH
(HEAD, 1971)

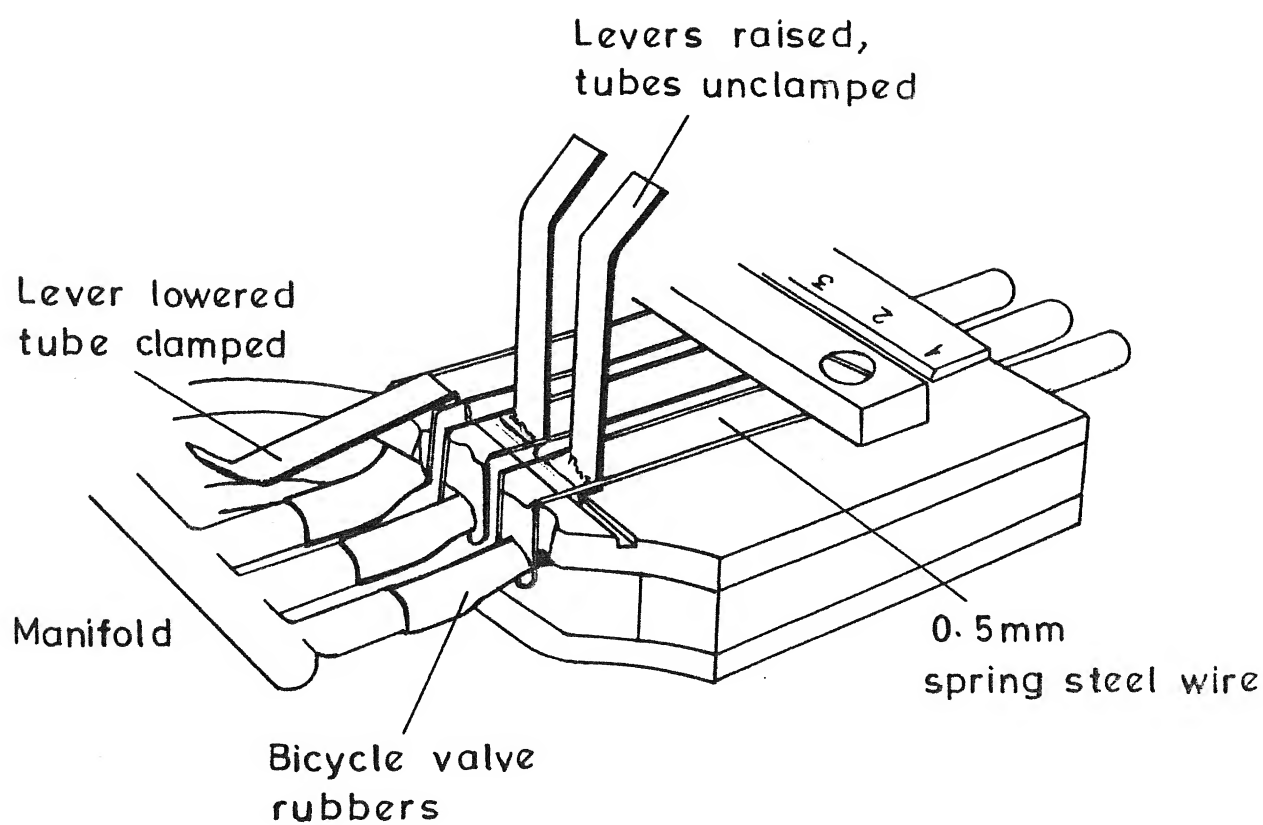


FIG. 2.25 FUNCTIONING DETAILS OF PRESSURE
SELECTOR SWITCH (Head, 1971)

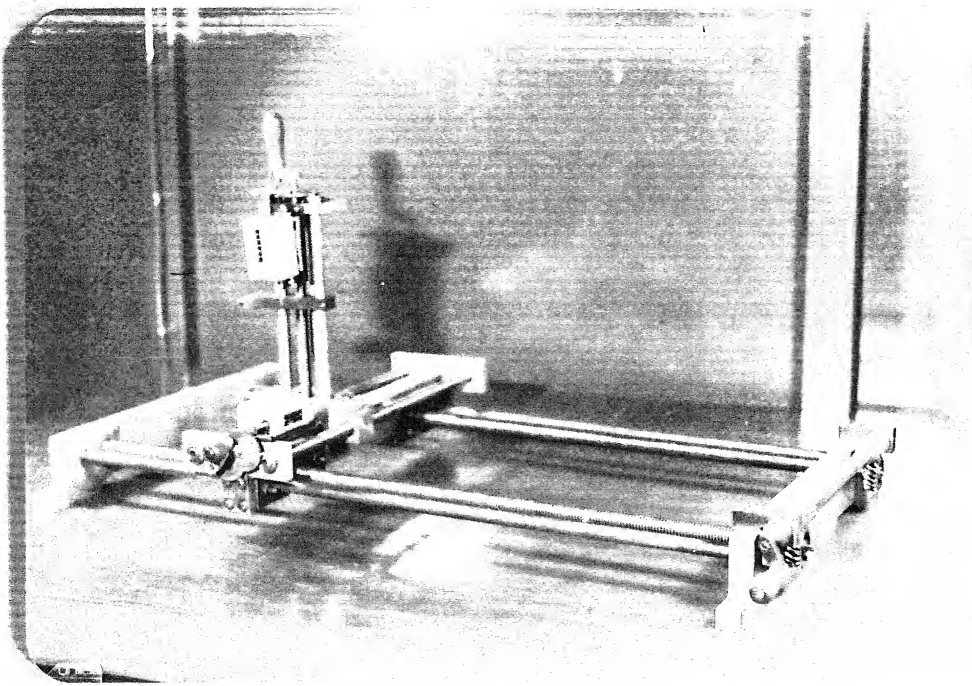


Fig. 2.26 3-D PRECESSION TRAVERSE MECHANISM

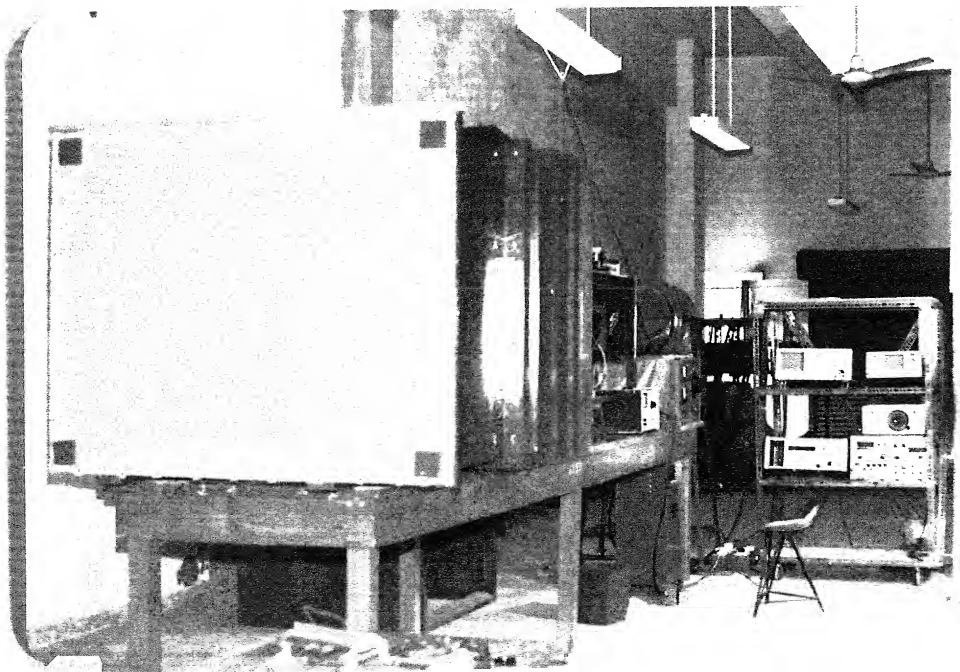


Fig. 2.27 AN OVERALL VIEW OF THE WIND TUNNEL AND THE INSTRUMENTS

CHAPTER III

EXPERIMENTAL TECHNIQUES

3.1 FLOW VISUALIZATION

The visualization of flow is a powerful technique in experimental aerodynamics/fluid mechanics to observe and understand a complex flow phenomenon. It provides an overall picture of the flow field under observation which is largely qualitative in nature. In some cases, however, it is also possible to quantify the observations if the phenomenon under investigation is reasonably well understood.

In the present experimental investigation, flow field has been studied both in the laminar and turbulent flow regimes. In laminar flow regime, two flow visualization techniques, namely Titanium Tetrachloride (TiCl_4) in wind tunnel and Potassium Permanganate (KMnO_4) dye in water table were employed. In turbulent flow regime, the surface flow patterns were obtained using oil film technique. These techniques are described in the following subsections.

a. Titanium Tetrachloride (TiCl_4) Technique

The first well documented account of the use of TiCl_4 for flow visualization has been given by Freymuth et.al. (1985). TiCl_4 is a light yellow liquid with a pungent acid smell. As it comes in contact with moisture from air, it develops dense white fumes according to the relation.



Operationally the liquid TiCl_4 is allowed to spread on the surface over which the flow visualization is desired by applying it with a stainless steel or a brass pipette, Freymuth (1985a) has pointed out that "the amount of TiCl_4 , location and procedure of its introduction, the lighting technique, viewing angle, close up area, photographic technique, the wind tunnel and the surface conditions of the body influence the final photographic results". And furthermore, more than several runs may have to be made to achieve the desired repetitive results. Freymuth et.al. (1985 b, 1985 c, 1986, 1986 a) and Finaish et.al. (1986) used TiCl_4 technique extensively for the visualization of starting and accelerating flows along with motion picture photography providing complete details of the physical phenomenon of starting vortex over wings, formation of tip vortices, vortex formation and shedding over circular cylinder, and separation over forward facing steps, fence and spoilers.

Thus, the TiCl_4 technique of flow visualization appeared quite promising for the present vortex flow studies at the wall-cylinder junctions. The quantity of TiCl_4 and the technique of applying it over the body depended upon the objectives of the experiment. One has to evolve a compatible combination of the quantity of TiCl_4 and location of its application to obtain optimum results as mentioned in the following. It may also be

pointed out that this is the first time that the Titanium tetrachloride flow visualization technique has been successfully employed in the aerodynamics laboratory of IIT Kanpur and perhaps in the country as well.

There were three distinct manners in which the liquid TiCl_4 was applied to the models mounted on the tunnel floor.

I. To visualize the general behaviour of the flow around the wall-cylinder junction and its neighbourhood for the cylinder/pier, both without and with the delta-wing-like passive device, TiCl_4 filled in a stainless steel pipette with chamfered delivery end (Fig. 3.1) was applied through a small opening in the top of the test section, on to the plane of symmetry of the model at its mid-height, by gently opening the thumb covered top end of the pipette. At the same time the delivery end of the pipette was moved along the model down to its leading edge foot and upstream on the floor in the plane of symmetry of the model, upto a distance of about three times the characteristic lateral dimension of the model.

When the delta-wing-like passive device was mounted at the leading edge foot of the pier model, the pipette end applied the TiCl_4 liquid on the model's leading edge down to the passive device's upper surface, towards its apex and then in the upstream direction on the floor.

II. To visualize the pair of leading edge separation vortices formed at the lower surface of the delta-wing-like passive device and their motion in the presence of the side wall of the pier, liquid TiCl_4 was applied over the upper surface of the passive device by placing the delivery end of the pipette at the junction of the passive device with the pier leading edge and moving the pipette end over the centreline of the upper surface short of its apex. This technique enabled to 'capture' the leading edge separation vortex alone by means of TiCl_4 fumes. It was found that a slight amount of TiCl_4 in the apex region caused dense white fumes to be drawn on to the lower side of the device which interacted with the leading edge vortex coming out from under the passive device.

III. To visualize the modification of the original horseshoe vortex at the apex of the delta-wing-like passive device, and its subsequent behaviour under the passive device as it comes out from below the passive device at pier leading edge region and moves parallel to the pier's side walls, a small amount of TiCl_4 was applied by the pipette on the wind tunnel floor slightly upstream of the apex of the passive device. This technique enabled to 'capture' the attenuated horseshoe vortex around the apex of the passive device. Fig. 3.2 illustrates these three techniques.

These three methods of applying TiCl_4 were used extensively to clarify the mechanism of the hydrodynamic modification of the

vortex flows around wall-cylinder junctions. TiCl_4 when dried up on the wind tunnel floor, left a patchy, extremely thin, white sticky deposit over the surface where it was applied. This was cleaned with soap and water before a fresh application of TiCl_4 was made for further photography. The still photography employed two studio lights illuminating the test section from front, and a sun gun mainly positioned from above to eliminate the shadows as much as possible and to highlight the region of interest. The camera was positioned either on the top or in the front of the test section for both the perspective and straight view shots.

b. Potassium Permanganate (KMnO_4) Dye Technique

This simple technique of flow visualization in water provides quicker results with reasonable steadiness. Fine particles of KMnO_4 were uniformly sprinkled at a station slightly upstream of the test-section of the water table, with the model placed in the middle of the test section. KMnO_4 colored the water in the region close to the surface. As the position of the model was approached, the colored water formed a distinct separated region/pattern characteristic of the shape of the model around its vicinity. The colorless portion could thus be distinguished as the separated region around the model due to the horseshoe vortex flow structure. The test section was flood lit with the

81.

studio lights placed on either side of it, and a sun gun was used to highlight the region of interest as in case of $TiCl_4$ shots in wind tunnel, The position of the camera was kept fixed above the test section, while the model position was shifted slightly to take shots of the top front, top rear and top plan views for a complete view of the flow field around the model. A 2.5 cm x 2.5 cm grid pasted below the test section made interpretation of the separated region around the body easier.

The same procedure was repeated with the delta-wing-like passive device attached to the models.

c. Surface Oil Film Technique

For turbulent regime of the flow, surface flow patterns were obtained by employing oil film technique. Bělik (1973) and Baker (1980) used a suspension of Titanium dioxide (TiO_2) in liquid paraffin for obtaining flow patterns around a circular cylinder mounted on a flat plate. Langston and Boyle (1982) reported a 'novel technique of surface flow visualization', wherein the difficulties due to excessive deposits of TiO_2 experienced by Bělik and Baker were claimed to have been eliminated.

The surface oil film flow visualization results depend on several factors like, the particle size, specific gravity and concentration of the suspension apart from the viscosity of oil, duration of the test run and the wind speed. A detail

discussion of these factors is given in Appendix A. For the present investigations, the freestream wind speed was about 5 m/sec. Several combinations of powder and liquid, like TiO_2 in liquid paraffin, talcum powder in liquid paraffin, and aluminium paint in kerosene were tried before the talcum powder suspension in light sewing machine oil was observed to give good results.

A mixture of 37.5 gm. of talcum powder in 500 cc of commercially available 'Singer' sewing machine oil was prepared. A uniform coat of the mixture was laid on the test section glass floor by means of a 10 cm broad painting brush. The model was placed on the centreline of the floor. Within minutes of starting the tunnel, patterns of the flow around the body were formed. For photography the test section illumination was set in the same manner as for TiCl_4 shots. Static shots were taken from above the test section with top glass plate, model in position and tunnel running, at different time intervals. Shots were also taken after stopping the tunnel and removing the model. The 2.5 cm x 2.5 cm grid from below made interpretation of pictures easier.

3.2 PRESSURE MEASUREMENTS

Detail static pressures were measured by electronic manometer on the floor around different pier models and on the periphery of 25 mm diameter cylinder. For plotting the total head contours

in Y-Z plane a shielded pitot-tube was traversed to measure the total pressures.

a. Static Pressure Measurements

Electronic Manometers, Type 1014 (analog) in laminar flow and Type 1018 (digital) in turbulent flow were employed as the pressure monitors alongwith a twentyfour channel pressure selector switch designed by Head (1971) as the scanning unit to measure static pressures on the floor. Static pressures were measured at the angular positions of 0 , $\pm 20^\circ$, $\pm 45^\circ$, $\pm 90^\circ$, $\pm 135^\circ$ and 180° in case of circular cylinder, both on the floor and the surface of the cylinder by rotating the turn table to the desired location. In case of other pier models, five representative floor stations (three in case of lenticular pier model), were selected for pressure measurements in a direction locally normal to the pier at that point. These representative stations are shown for all the models in Fig. 3.3. The model position was shifted such that the fixed pressure taps in the lateral or longitudinal plane were aligned with the desired stations. Markings on the models were made for this purpose. Each time the model position was shifted it was ensured with precise measurements, that its longitudinal axis was aligned with the line of symmetry on the floor and therefore with the mean flow direction. A standard pitot-static tube was held in a microtraverse mechanism mounted on the top plate close to the test section entrance, to monitor the free stream dynamic

head. This pitot-static tube was lowered to monitor the dynamic head and retracted up immediately thereafter.

The same procedure was repeated when the passive device was fitted into the vertical notch of the pier models. In the case of pressure measurements on the upstream plane of symmetry, the spinal rib of the passive device would cover first sixteen radial taps on the floor. To overcome this situation, the turn table was yawed by about 3° , so that these pressure tapings were clear of the spinal rib. It was not expected to cause any significant effect on the inferences drawn from the comparison of the respective data. In all such measurements, one row of the tapings was used at a time, while others were blocked by scotch tape.

The static pressure from the tapping on the rear wall, close to the entrance of the test section was used as the reference pressure for all floor pressure measurements, and was connected to the pressure sensor. Thus the electronic manometer directly provided the pressure difference $p-p_{\infty}$, for each tapping. If q be the dynamic pressure measured with the standard pitot-static tube, then the pressure coefficient

$$C_p = \frac{p-p_{\infty}}{q}$$

b. Total Head Measurements

A shielded pitot-tube was traversed to measure total head of flow in the Y-Z plane of all the pier models at their mid-

span locations. This probe was held in the 3-D precision traverse mechanism, mounted on top of the test section with the perspex top plate II in position. The streamwise location of the centre of the models was maintained at the centre of the turn table. The longitudinal axis of the model and the midline of the tunnel floor were aligned. The probe was set parallel to the side wall of the model. The zeroes of Y and Z counters were set with the probe just touching the side wall, and just above the floor respectively. The traverses were made in equal steps of 1.25 mm in both the Y and Z directions. The appropriate distances thus covered were about 30 mm and 20 mm in Y and Z directions respectively.

The free stream dynamic pressure q was recorded in the same manner as described in 3.2a. The difference between the total head P , and p_{∞} , was directly read from Type 1018 manometer. Then the total head parameter H was calculated as

$$H = \frac{P - p_{\infty}}{q}$$

During these traverses all the static pressure tapings on the floor were blocked by scotch tape.

3.3 VELOCITY MEASUREMENTS

The velocity profiles at the location of the model in its absence were measured with Constant Temperature Hot Wire Anemometer (CTA) as well as with a miniature pitot tube.

The hot wire u -probe was inserted from the top of the test section. Its long stem was held in the 3-D precision mechanism mounted on the top of the test section. Only z direction traverses were made. The probe was kept normal to the flow direction. The 'z-zero' of the probe location was determined when the hot wire just touched the floor (i.e., when the hot wire prongs and their image appeared to touch each other). The over heat ratio was kept 1.5. The output from CTA bridge was given to the digital voltmeter and the r.m.s. meter and was also monitored on a storage oscilloscope. Traverses were made from about 2.5 cm above the floor to 'z-zero'. The intervals between data points were finer near the wall than those in the outer region.

The pitot-tube was made to touch the floor and traversed up in the z -direction. The static pressure was taken from the side wall tapping close to the tip of the pitot tube. The pressures were monitored by Type 1014 and 1018 manometers in laminar and turbulent regimes respectively. These velocity profiles were measured at the same station by changing the fan speed in steps through the rheostat dial control of the wind tunnel. These profiles at different velocities, but at one location were plotted in non-dimensional form according to Blasius plot (Schlichting 1968, p. 127) for laminar regime and for turbulent regime according to the method of Clauser (1956) and Coles (1956), and are shown in Figs. 3.4 alongwith

the variation of turbulent quantity within these profiles.

Fig. 3.5 shows the variation of δ^* v/s U_∞ , and $\frac{D}{\delta^*}$ and $\frac{\delta}{\delta^*}$ v/s $\frac{U_\infty D}{\nu}$, the solid line in the latter plot was taken from Schlichting (1968).

3.4 MEASUREMENT OF VORTEX OSCILLATIONS

The oscillatory behaviour of horseshoe vortex was investigated in the test section of the wind tunnel. The location of the model position was kept the same as in the case of total head measurements.

The hot wire u-probe inserted from the top wall was held in the 3-D traverse mechanism, mounted on the test section top, with the perspex plate I in position. This probe was kept normal to the flow direction. It's vertical distance was kept 1 mm above the floor and 3 mm upstream of the leading edge of the pier model in the plane of symmetry. This location was determined when a clear, distortion free signal was monitored on the storage oscilloscope. This location of the hot wire was maintained throughout this part of the investigations. With the passive device in position, the vertical location of the probe above the windward surface of the delta wing plate was maintained at 1 mm, and 3 mm upstream of the model in the plane of symmetry. The cold resistance of the hot wire probe was 4.87 ohms and was changed to a hot resistance according to an overheat of 1.5. The out-put from CTA bridge was connected to the digital voltmeter and r.m.s. meter, for d.c. volts and fluctuating signals respectively. The output from CTA bridge

was also taken through a T connector ; one connected to the spectrum analyzer and the other to the storage oscilloscope, for monitoring the signals.

For still shots of the frequency spectrum, NON-REPETITIVE mode was employed by using ARM control in conjunction with the REPETITIVE button to define 'Single Shot Trigger Mode'. In REPETITIVE mode, new block of data was collected by the FFT analyzer when the previous set of data was processed and displayed on the CRT section. The traces of signals were stored in the oscilloscope by pressing the appropriate control buttons. Single channel was used in both of these instruments. For still shots of the spectra and the hot wire traces, the two appropriate button controls in these two instruments were pressed almost simultaneously for consistency of the results. The CRT section of the spectrum analyzer provided complete details of the traces thus stored with the use of the MARKER section, which were recorded along with other relevant data.

3.5 CALIBRATION

a. The Test Section

The static pressures from the rear side wallappings were recorded with the help of the electronic manometers. The reference pressure p_{∞} and the free stream dynamic pressure q were recorded as for the pressure measurements. Thus $p-p_{\infty}$ was

directly read, where p was the static pressure from certain tapping, then the pressure coefficient was obtained as

$$C_p = \frac{p - p_\infty}{q}$$

This C_p variation was plotted along the test section length. Static pressures from the pressure tapings aligned with the longitudinal axis, from the turn table were also recorded. However, the pressure variations were also plotted in the form of a non-dimensional pressure gradient parameter defined by Kline et.al. (1967). The plots of these variations are shown in Fig. 3.6.

b. Hot Wire

A standard pitot-static tube and the hot wire u-probe were kept 5 cm on either side of the plane of symmetry of the test section at its mid-height. The dynamic pressure, bridge d.c. volts and r.m.s. millivolts were recorded. Bradshaw (1971) has suggested that a plot of tunnel speed v/s bridge d.c. volts would also provide good calibration curve. One such plot for low velocities is shown in Fig. 3.7a. A plot of $E^2 v/s \sqrt{U}$ is given in Fig. 3.7 b. The bridge d.c. volts and r.m.s. millivolts, thus recorded were converted to mean velocity and turbulence intensities respectively using these curves and with zero wind hot wire voltage, to normalize the calibration between different runs.

c. Shielded Pitot Tube

The shielded pitot-tube was calibrated in the wind tunnel. It was inserted from top and held in the micro-traverse mechanism in such a way that its vertical location was not changed, but it could be yawed to desired angle. The angular displacements were read with the help of a fine pointer attached to the support of the probe, and a 360° protractor, held on the top plate. When aligned with the tunnel axis at the mid-height, this probe gave the same reading as that from the pitot tube.

This shielded pitot tube was initially yawed in step of 5° , and when it started showing smaller values the interval was reduced to 2.5° . This was repeated for rotations in opposite direction as well. However, the yaw angle was not exceeded beyond $\pm 45^{\circ}$. No calibrations were made in the pitch up or pitch down positions as it was assumed that the same accuracy would be achieved in pitching as well, for the reason that the inner and outer tubes were concentric.

This calibration curve is shown in Fig. 3.8. The earliest shielded pitot tube known as Kiel tube (Rae and Pope 1984, p. 106) was insensitive to yaw upto 40° . A simple shielded pitot tube (Ower and Pankhurst 1977, p. 49) was insensitive to 45° misalignment, but was difficult to manufacture'. The use of a 5-tube, pre-calibrated yaw meter might have been an

alternative choice, but the limitations due to the proximity of the pier wall, prohibited its use.

d. Spectrum Analyzer

A standard sine/square function generator was employed to calibrate HP 3582-A Spectrum Analyzer using sine wave form. The output from the function generator was taken through a T connector to the input of the spectrum analyzer and the r.m.s. meter. The channel sensitivity was kept 0 dBV FS. It was observed that the CRT section of the spectrum analyzer displayed the generated frequency. The amplitude dBV values from CRT section were plotted against r.m.s. mV as shown in Fig. 3.9. This calibration curve was used for converting the amplitude dBV to r.m.s. volts.

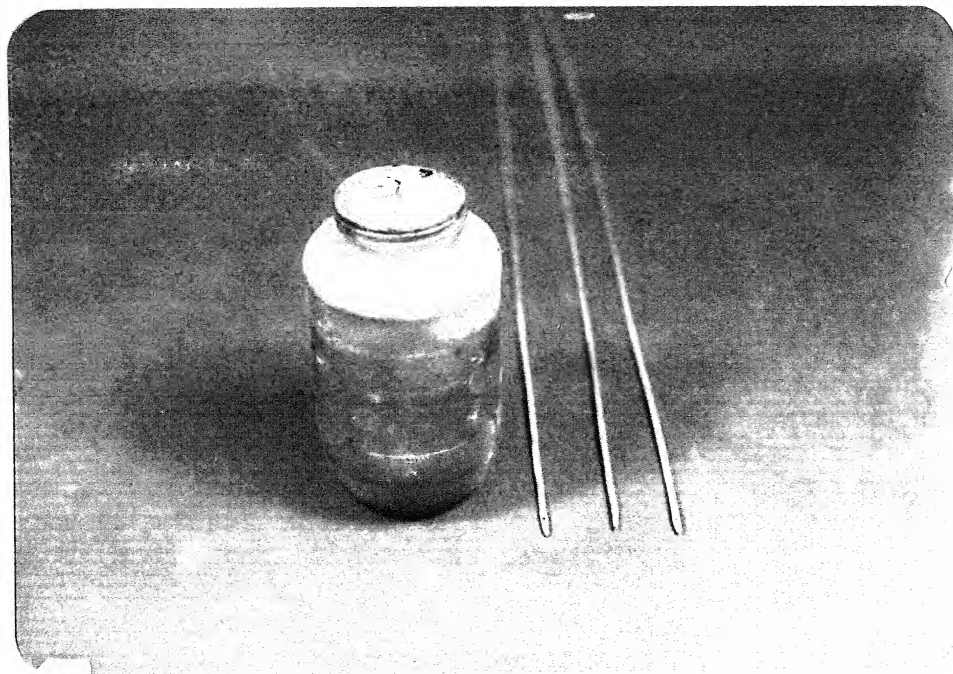
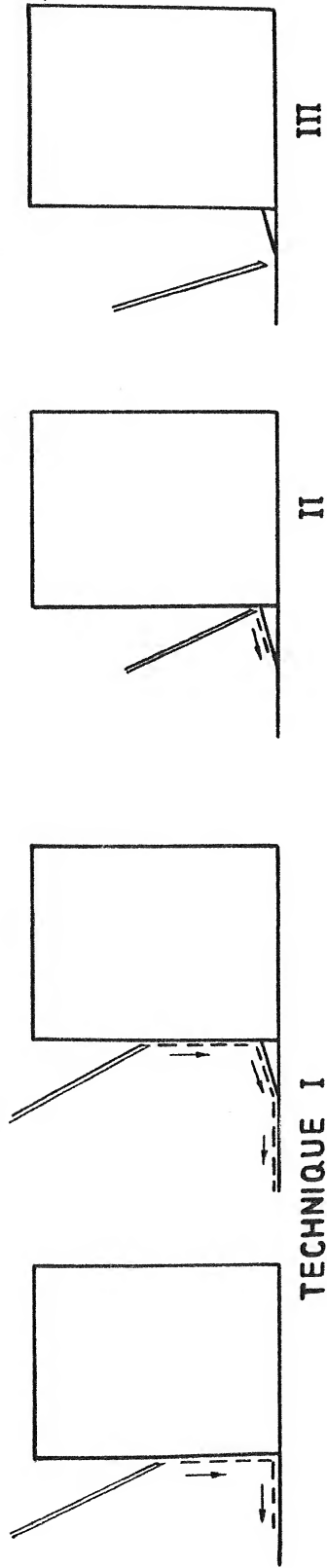
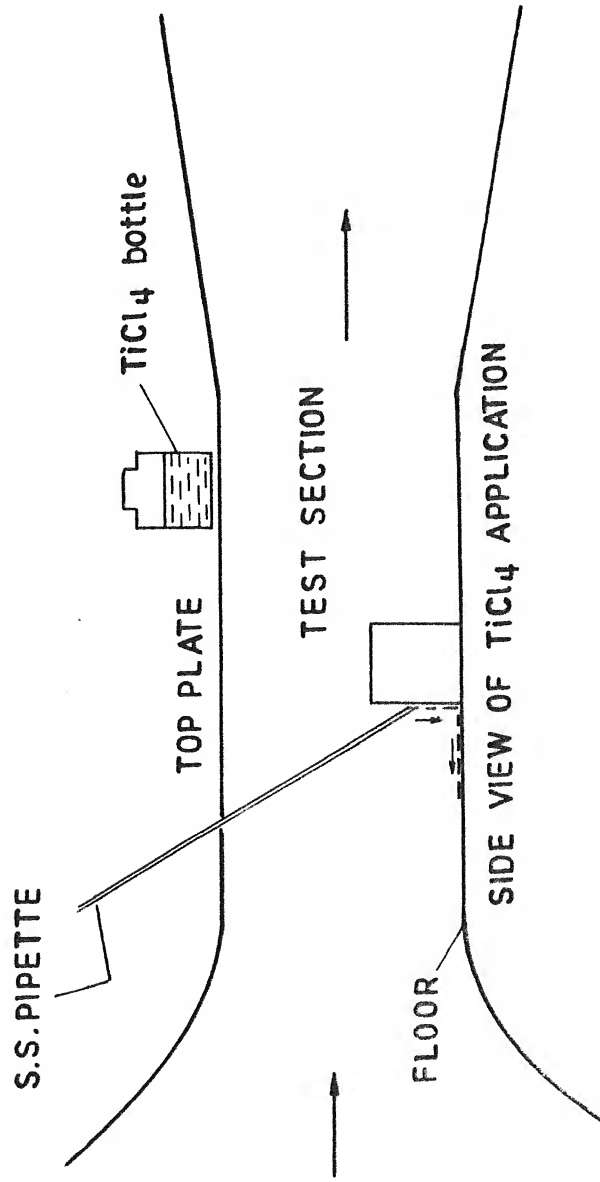


Fig. 3.1 STAINLESS STEEL PIPETTES WITH CHAMFERRED
ENDS AND TiCl_4 CONTAINER

Pier model



TECHNIQUE I



-----Path of the Pipette
end releasing TiCl_4

FIG.3.2 ILLUSTRATION OF TiCl_4 TECHNIQUES

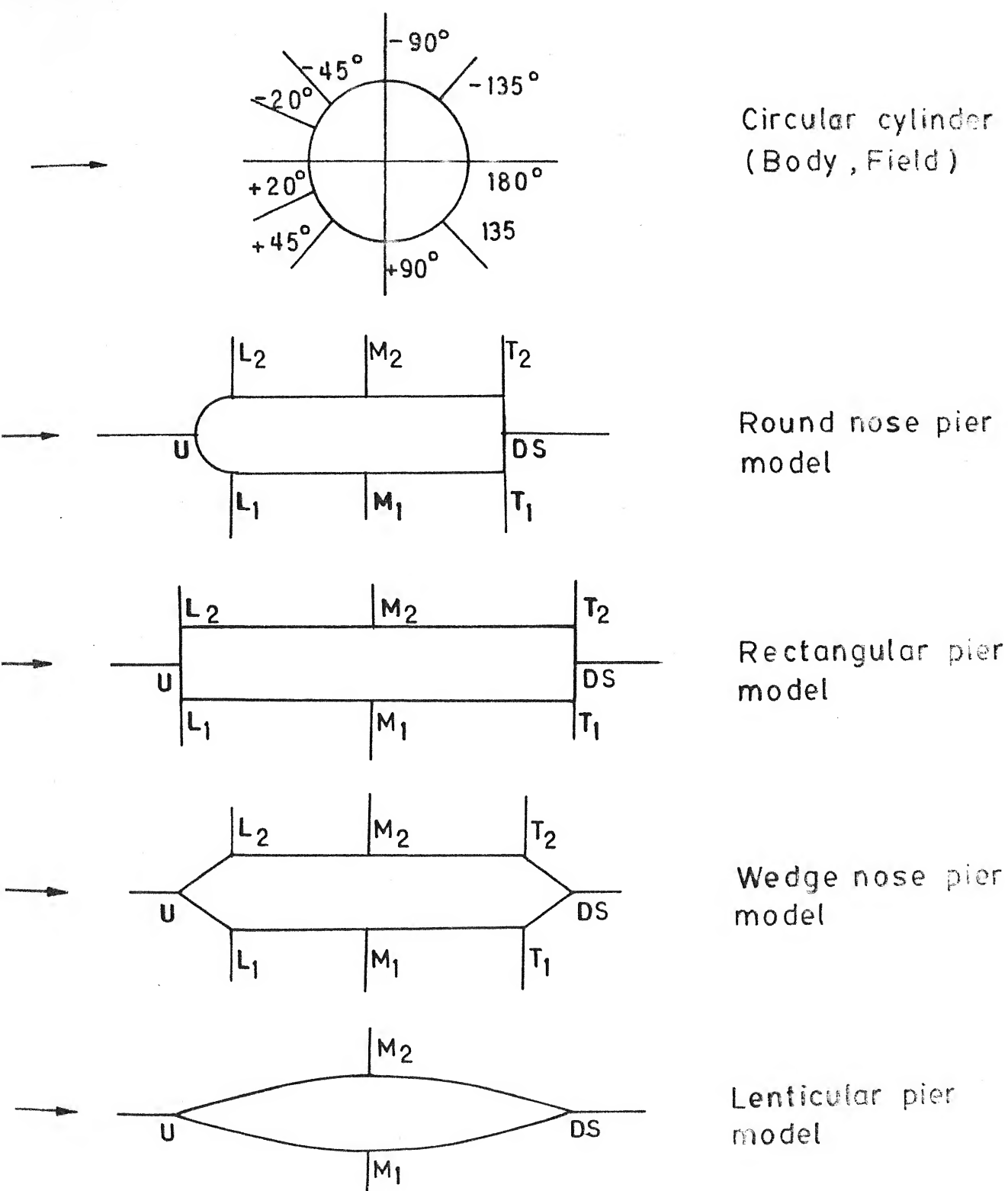


FIG. 3.3 REPRESENTATIVE STATIONS IN FLOW FIELD AROUND VARIOUS PIER MODELS

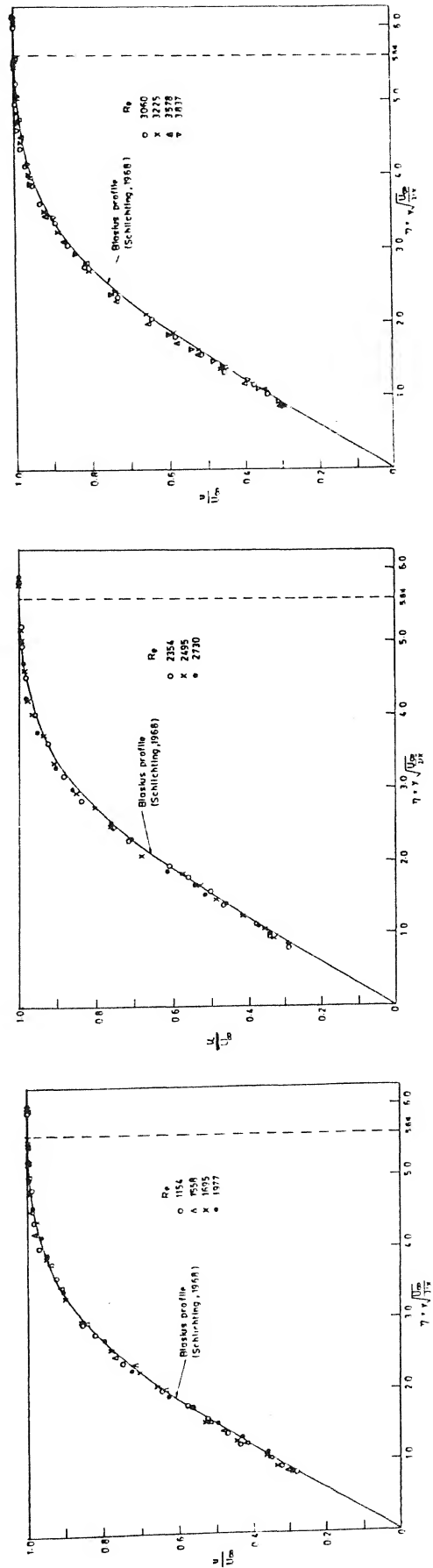


FIG. 3.4a VELOCITY PROFILE IN LAMINAR BOUNDARY LAYER

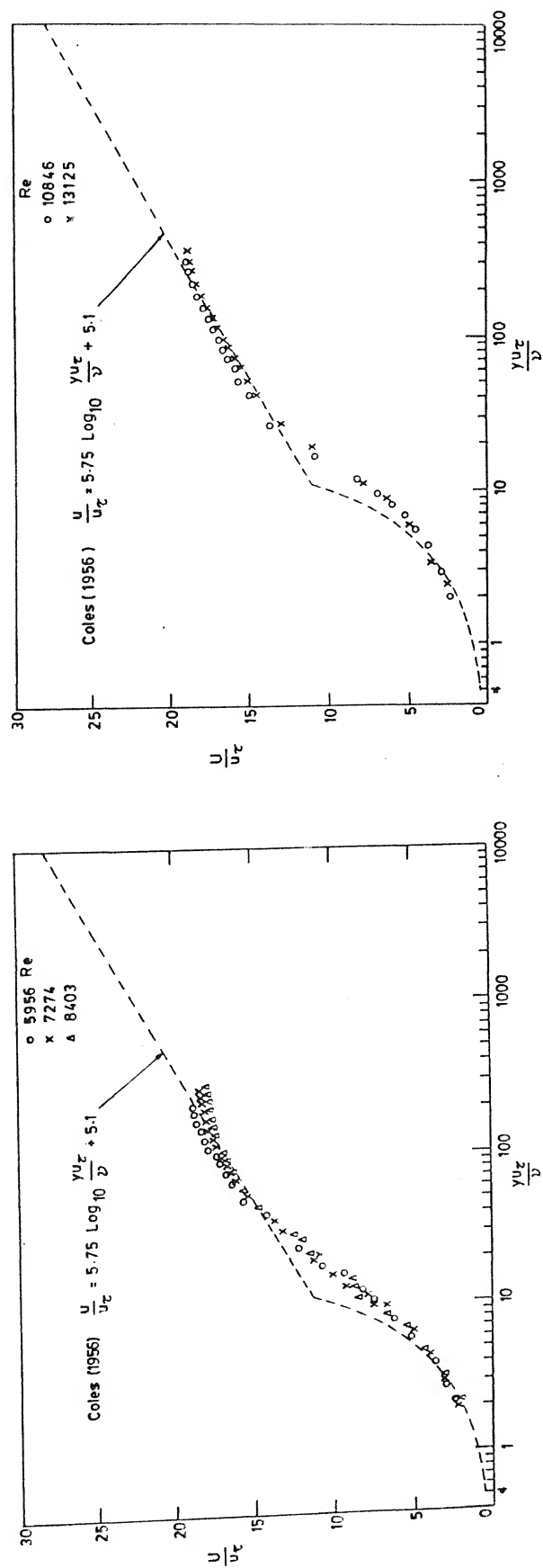


FIG. 3.4 b VELOCITY DISTRIBUTION IN TURBULENT BOUNDARY LAYER

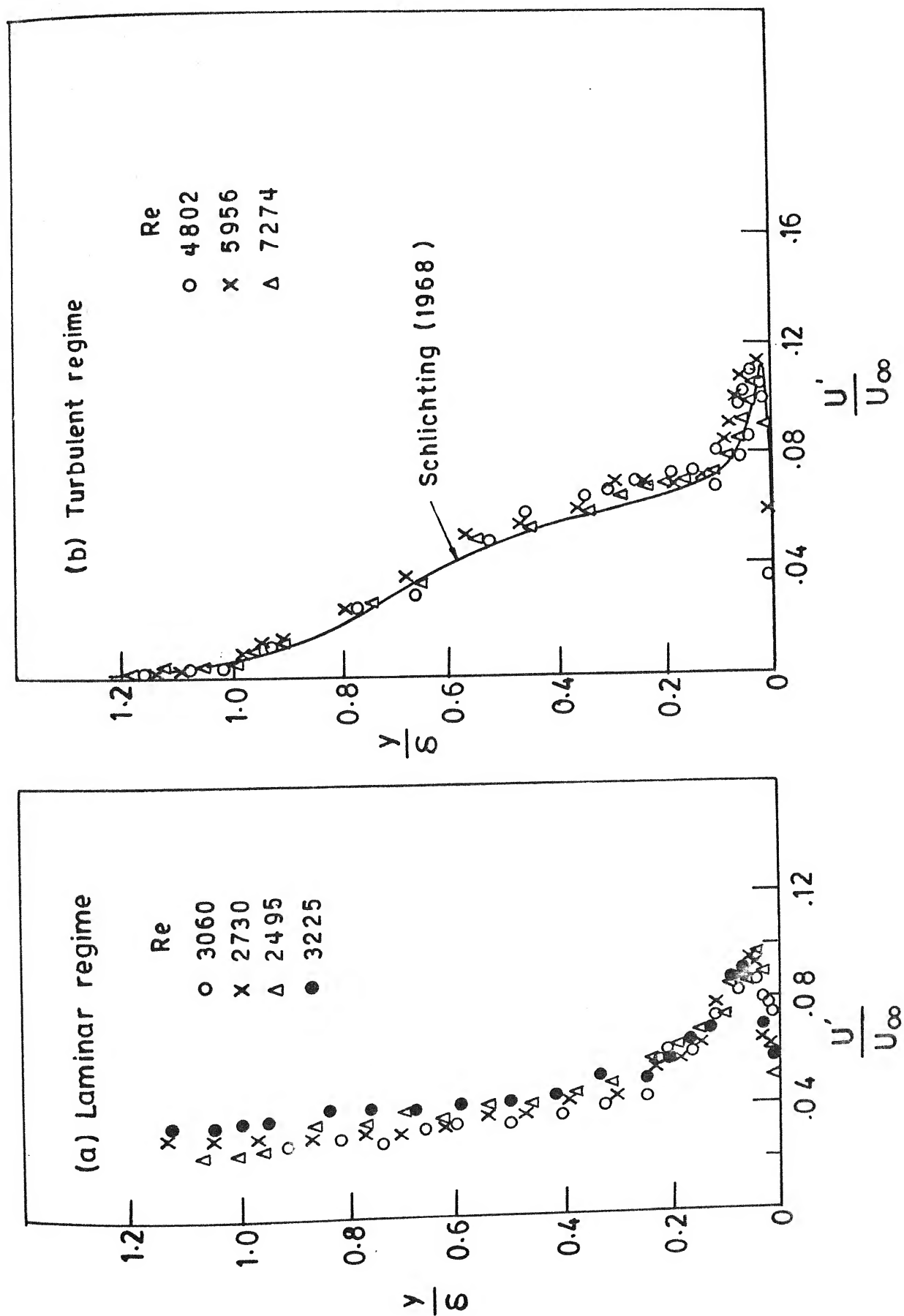
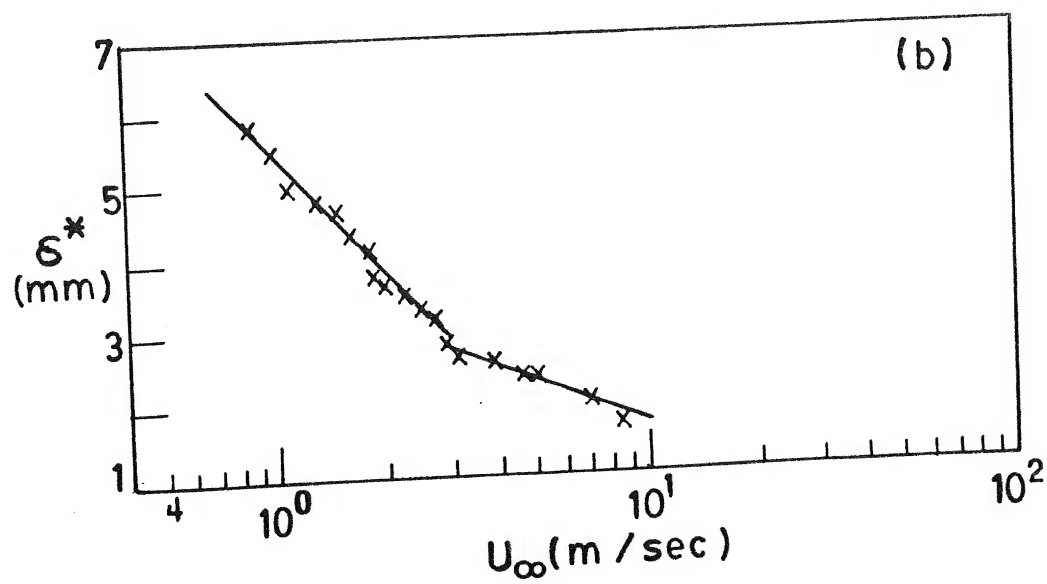
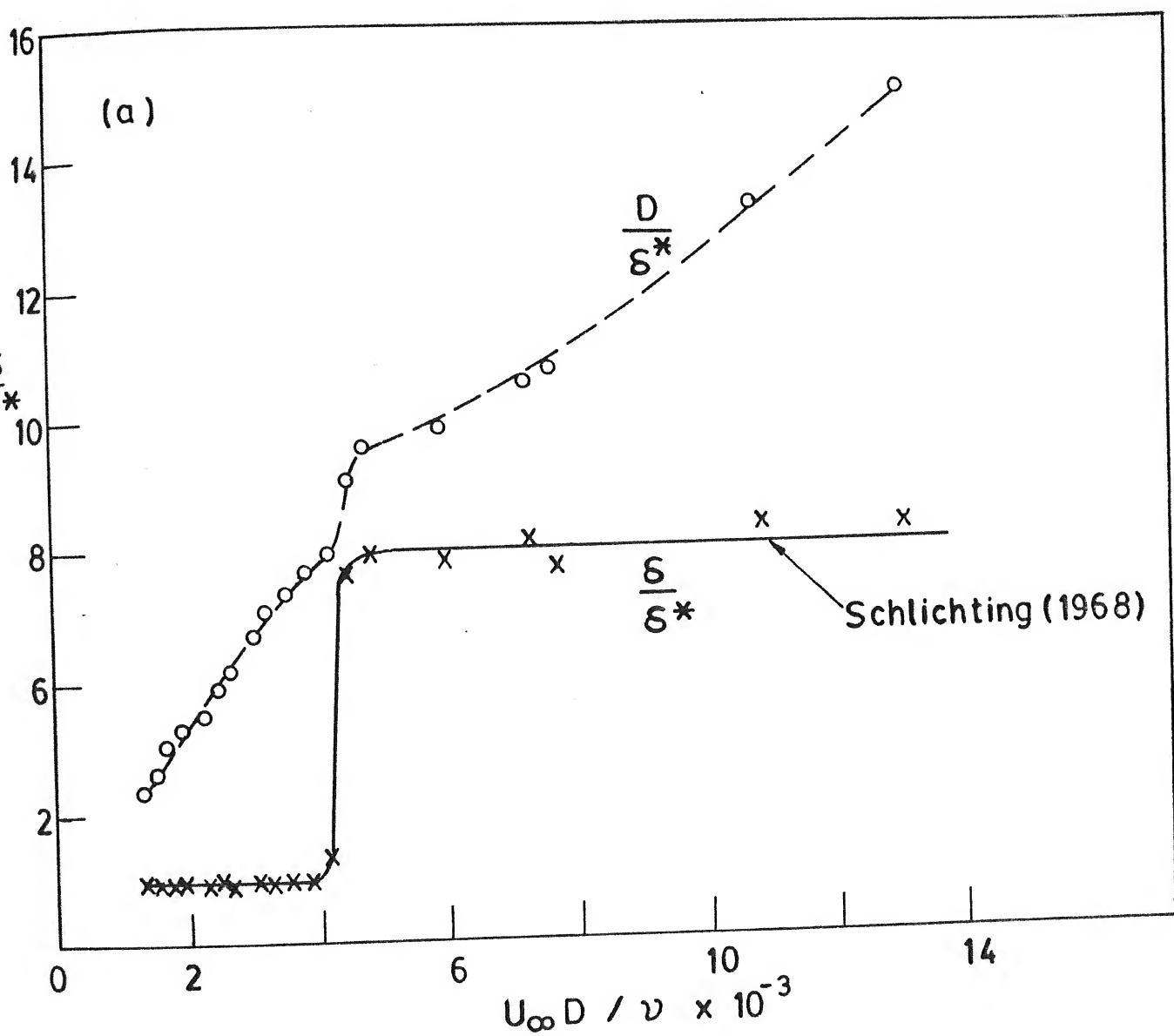
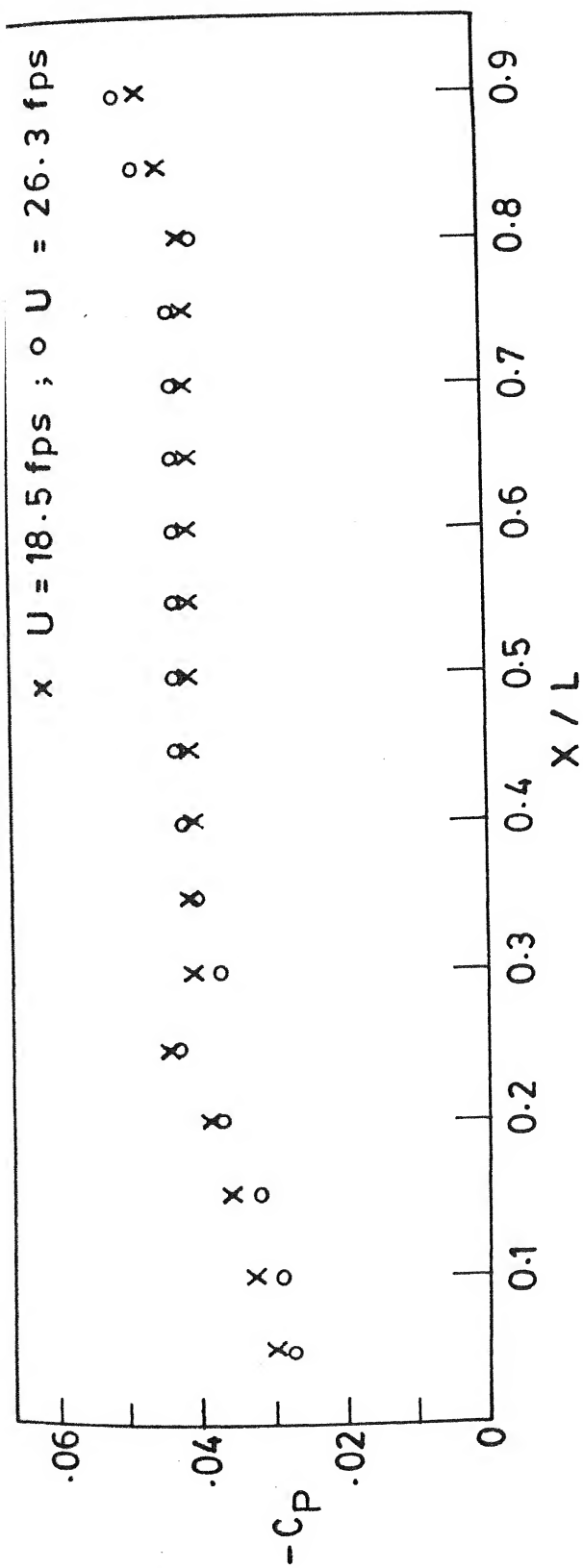
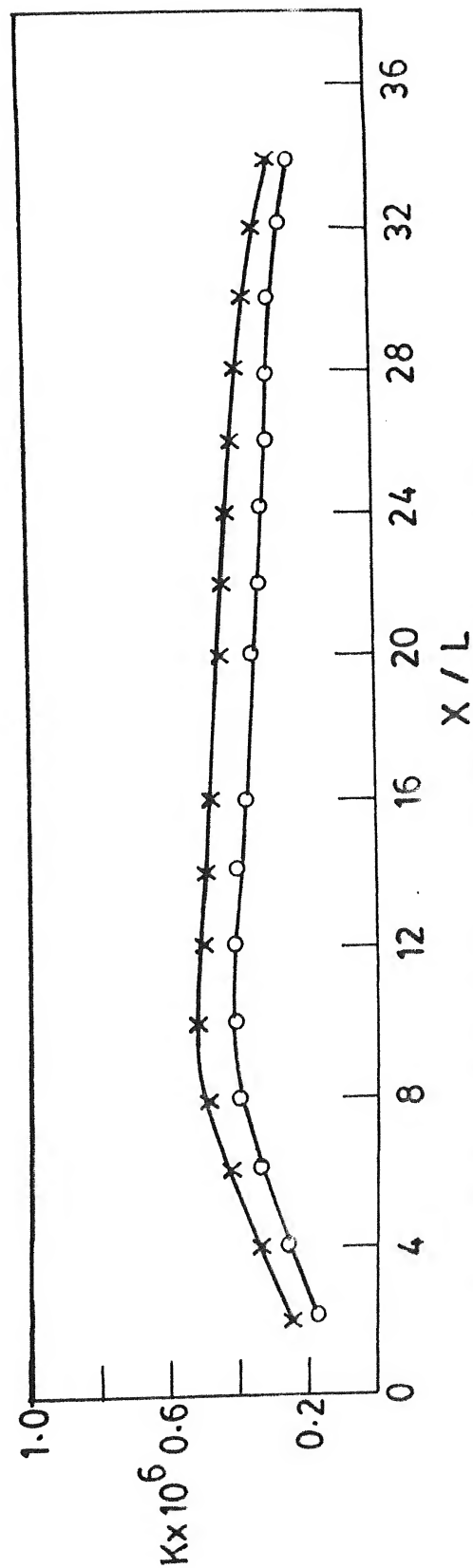


FIG. 3.4 c TYPICAL VARIATION OF TURBULENCE IN VELOCITY PROFILES



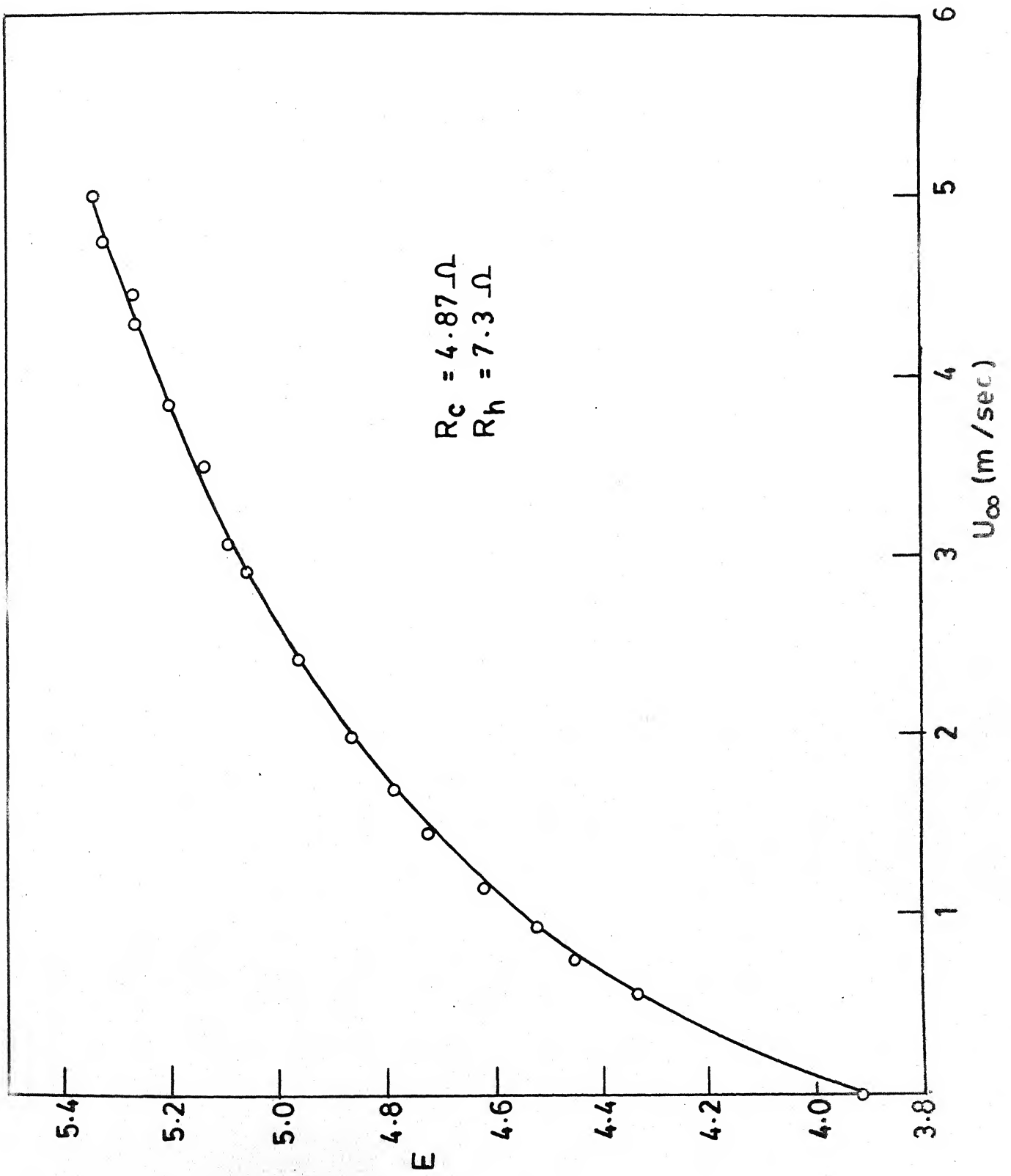


(a) C_p Distribution



(b) Pressure gradient parameter distribution

FIG. 3.6 CALIBRATION OF WIND TUNNEL TEST SECTION

FIG. 3.7a HOT WIRE CALIBRATION (E v/s U_∞)

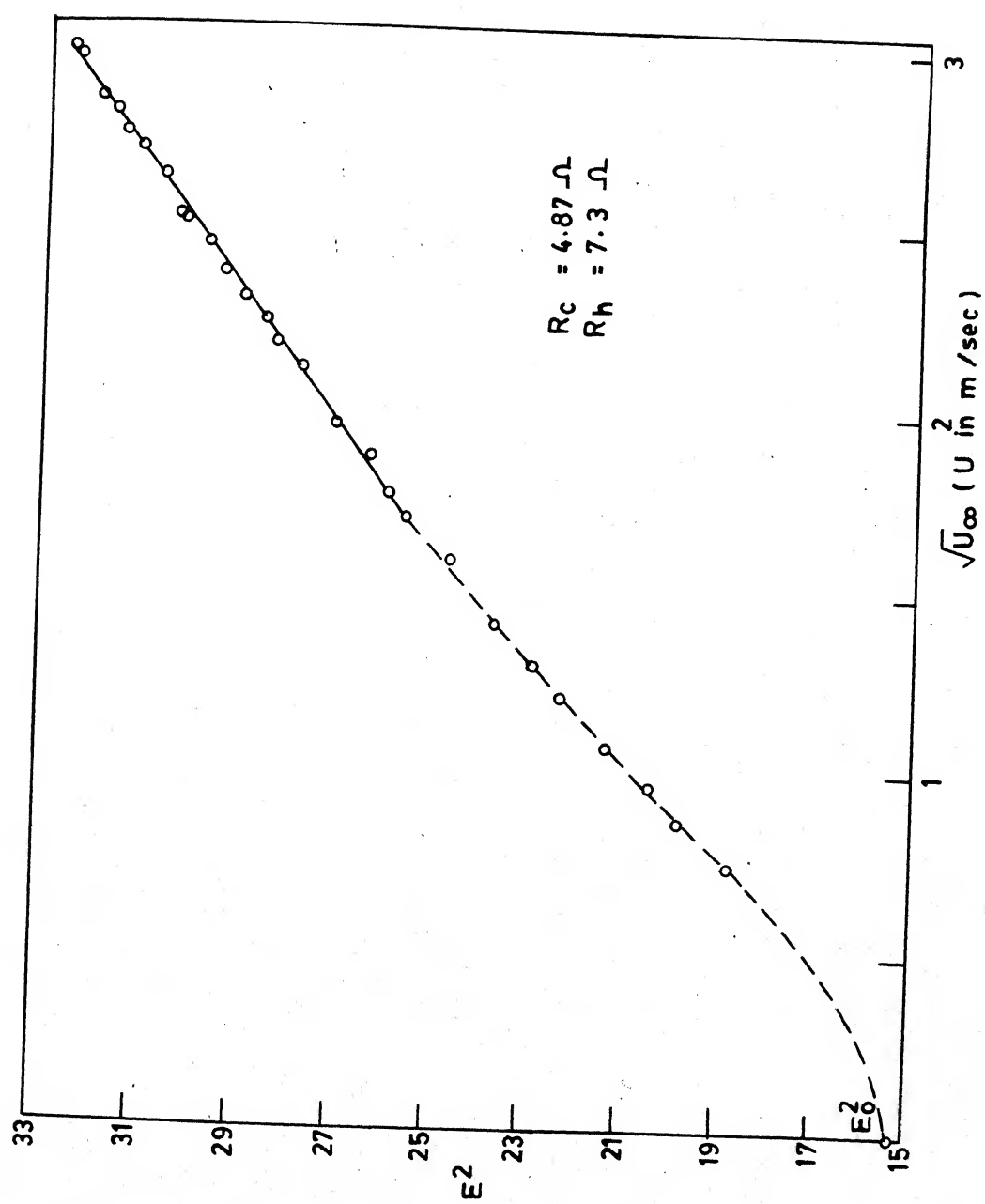


FIG. 3.7b HOT WIRE CALIBRATION (E^2 v/s $\sqrt{U_\infty}$)

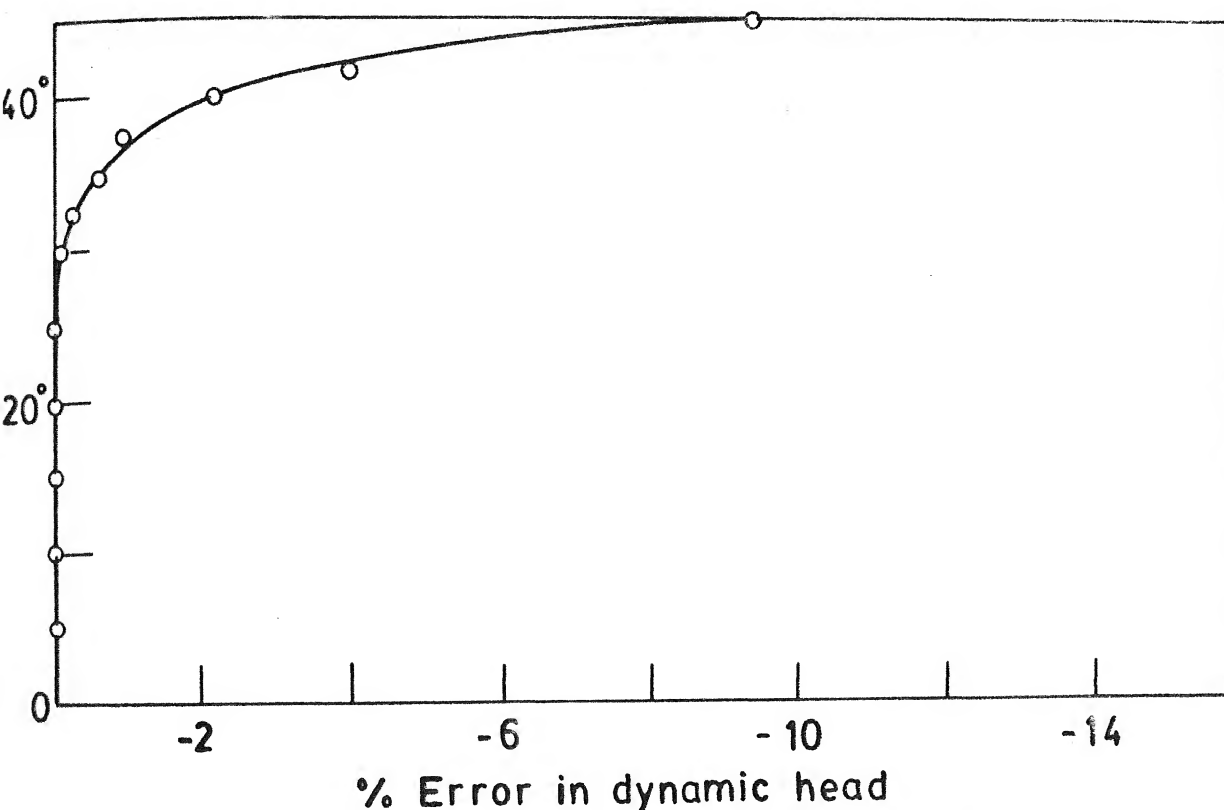


FIG. 3.8 CALIBRATION OF SHIELDED PITOT TUBE ($U_{\infty} \approx 5.5 \text{ m/sec}$)

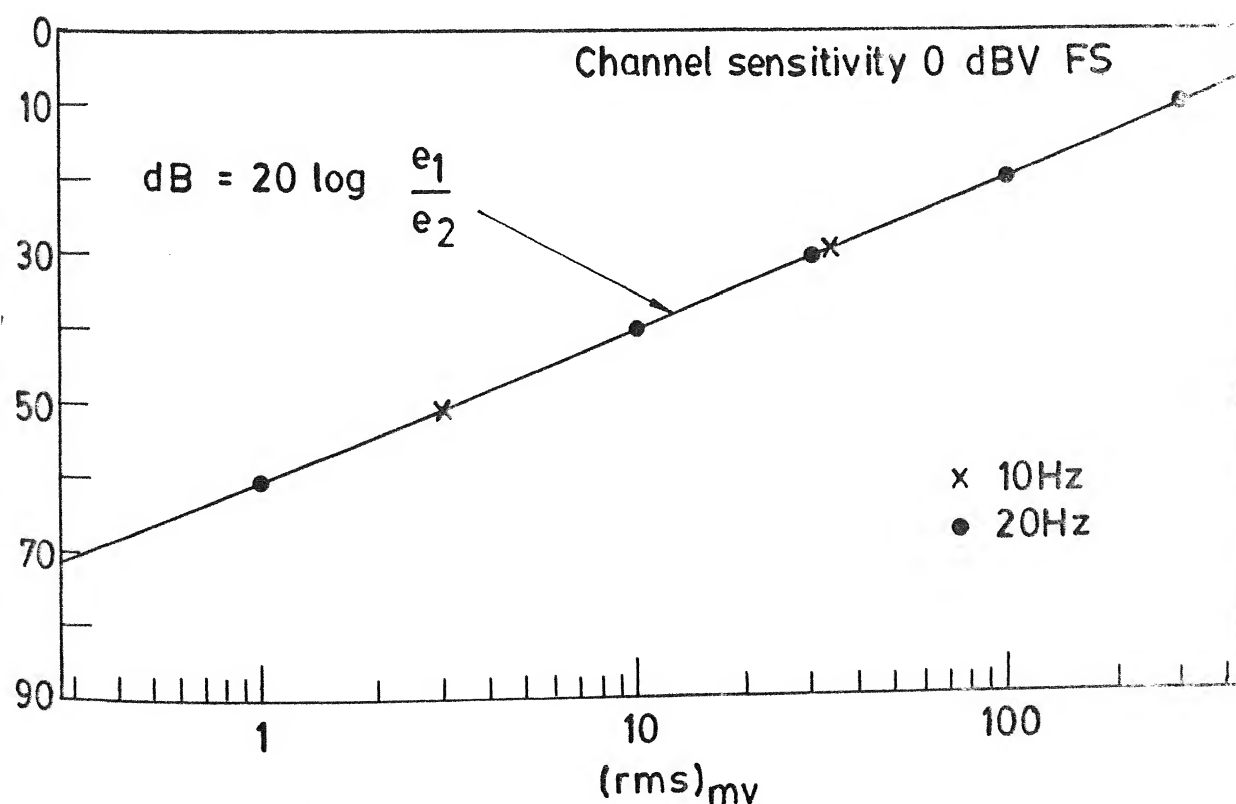


FIG. 3.9 CALIBRATION OF HP 3582 A SPECTRUM ANALYZER

THE MECHANISM OF HORSESHOE VORTEX MODIFICATION

4.1 INTRODUCTION

The hydrodynamic modification of the horseshoe vortex (HSV) around the junction of a vertical pier with round nose, by mounting a delta-wing-like passive device at the pier's leading edge foot, demonstrated earlier with dye flow visualization on a water table by Gupta (1987) will be explained in this chapter. This will be done by means of extensive flow visualization studies using finely powdered potassium permanganate (KMnO_4) on a water table, titanium tetrachloride (TiCl_4) fumes and surface oil film patterns in the low speed, low turbulence wind tunnel. Detail pressure measurements on the wind tunnel floor around the pier model junction and total head survey in the Y-Z plane at the mid-span of the pier model with and without the passive device will also be presented to demonstrate the effect of HSV modification. For these experiments, the geometry of the pier model and the passive device was kept identical to that used by Gupta (1987). The results with the clean pier model are described first followed by those with the model fitted with the passive device emphasizing the aerodynamic aspect of the delta-wing-like passive device. The mechanism of HSV modification is described in the discussion part of this chapter.

4.2 CO-ORDINATE SYSTEM

A right hand Cartesian co-ordinate system with origin at the centre of the leading edge circle of the round nose

THE MECHANISM OF HORSESHOE VORTEX MODIFICATION

4.1 INTRODUCTION

The hydrodynamic modification of the horseshoe vortex (HSV) around the junction of a vertical pier with round nose, by mounting a delta-wing-like passive device at the pier's leading edge foot, demonstrated earlier with dye flow visualization on a water table by Gupta (1987) will be explained in this chapter. This will be done by means of extensive flow visualization studies using finely powdered potassium permanganate (KMnO_4) on a water table, titanium tetrachloride (TiCl_4) fumes and surface oil film patterns in the low speed, low turbulence wind tunnel. Detail pressure measurements on the wind tunnel floor around the pier model junction and total head survey in the Y-Z plane at the mid-span of the pier model with and without the passive device will also be presented to demonstrate the effect of HSV modification. For these experiments, the geometry of the pier model and the passive device was kept identical to that used by Gupta (1987). The results with the clean pier model are described first followed by those with the model fitted with the passive device emphasizing the aerodynamic aspect of the delta-wing-like passive device. The mechanism of HSV modification is described in the discussion part of this chapter.

4.2 CO-ORDINATE SYSTEM

A right hand Cartesian co-ordinate system with origin at the centre of the leading edge circle of the round nose

pier model is used. However, when presenting pressures around the pier model, a local co-ordinate 's' with origin at the pier wall junction with floor and in the direction locally normal to the pier at that station is used for convenience.

4.3 RESULTS WITH CLEAN PIER MODEL

The results with the clean pier model are presented in the following order of the flow approaching the pier model :
(i) laminar flow, (ii) transition to turbulent flow, and
(iii) fully turbulent flow.

For the present results, the model size was fixed and the Reynolds no. in a facility was increased by increasing the flow speed.

4.3.1 Laminar Flow :

The HSV around the pier model in approaching laminar flow was investigated by flow visualization using KMnO_4 on a water table, TiCl_4 fumes and pressure measurements on the upstream plane of symmetry of the pier model in the low speed, low turbulence wind tunnel. The overall range of Reynolds no. covered was $1400 < \text{Re} < 3200$ in the laminar regime.

a. Flow Visualization

The experiments on water table were conducted at a nominal water-speed of 10 cm/sec. corresponding to $\text{Re}=3197$ based on the 2.5 cm of the model width and $\text{Fr}=0.146$ based on the water depth

With the help of the top front and rear views, a line sketch of the plan view is shown in fig. 4.4. Referring to Sutton's experiment of smoke flow visualization of vortices ahead of a stubby cylinder from the frontis-piece in Thwaites (1960), Baker (1979) and shown in fig. 1.3, it is possible to interpret the TiCl_4 fume pictures in terms of the number of vortices. The key to Sutton's and Baker's pictures is the following : For the flow from left to right, an even number of vortices appear depending upon the Reynolds number. Each pair of vortices consists of a clockwise rotating primary vortex and an anti-clockwise rotating secondary vortex attached to the floor.

Thus for the present TiCl_4 flow visualization technique, the pictures in fig. 4.3 show presence of the secondary vortices where dense white fumes of TiCl_4 are accumulated and the primary vortices where there is depletion of these white fumes. A smoke ring, therefore, indicates a floor attached secondary vortex. Two smoke rings bounded by depleted regions of smoke can be identified upstream of the pier nose. The third smoke ring is like a thread of smoke located at the junction of the pier nose and the floor. Thus the pictures in fig. 4.3 show a six vortex ring HSV flow structure.

It may be noted from fig. 4.3 that the three primary vortices are formed above the floor and therefore, could not be captured by the thick white fumes of TiCl_4 applied on the floor, ahead of the pier. However, a signature was left by

each of these primary vortices immediately after the application of liquid TiCl_4 , and the one from primary vortex 1 lasting longer than the other two. The two secondary vortices formed due to the generation of surface vorticity (Mason and Morton, 1987) were effectively captured by the thick white fumes.

Top plan views in figs. 4.3 b and c further show modulation of the different vortices, as they move around the round nose pier model. While the two secondary vortices seem to become thinner, they also appear to lift up away from the floor (fig. 4.3a). On the other hand, the primary vortex farthest from the nose, appears to bend around the trailing edge junction most to form a neck region.

The complex wake-vortex interaction behind the blunt trailing edge can be observed in fig. 4.3a and appears similar to that observed in the dye flow in fig. 4.1. Thick white fumes immediately behind the blunt trailing edge in fig. 4.3a correspond to the accumulation of red dye at the trailing edge in fig. 4.1c and the neck formation due to the interaction of the vertical vortices behind the trailing edge and the stream-wise vortices of HSV is observed in fig. 4.3c. This is perhaps the first time that a complete picture of multi-ring HSV around a pier model with round nose alongwith its wake-vortex system has been presented using TiCl_4 visualization at low speed in a wind tunnel.

b. Pressure Measurements

Pressures were measured on the upstream plane of symmetry of the pier model at a nominal wind speed of 1.5 m/sec, corresponding to $Re = 2265$, $D/\delta^* = 5.6$, and blockage ratio of 3%. (The electronic manometers did not show meaningful pressures at other measuring stations in the flow field with the available sensors because of lower pressures). Fig. 4.5 presents the pressure distribution, showing three weak pressure dips, at $0.9D$, $1.1D$ and $1.5D$ upstream of the centre of the round nose of the pier model. Bělik (1973) and Baker (1979, 1980) identified such local minimum pressure region as the location of the core of primary vortex of HSV. It is also observed earlier from $TiCl_4$ visualization of HSV around this pier model, that the number of vortices is six for $Re = 1400$, before the oscillations of HSV appear at increased wind speed. Three weak pressure regions on the upstream plane of symmetry in fig. 4.5, therefore, may be identified with the core locations of three primary vortices. For the sake of comparison, Baker's (1979) data on circular cylinder at $Re=2050$, $D/\delta^*=21.7$ and $BR=5.3\%$ is also shown on this plot. However D/L in Baker's case was 2.0, compared to a value of 0.16 in the present case. The present data on the round nose pier, however, appears in qualitative agreement with the similar data for a circular cylinder from Baker (1979).

4.3.2 Transition to Turbulent Flow

The oscillations of HSV around the junction of pier model were recorded by inserting a 'u' sensitive hot wire probe, which was kept 1 mm above the floor and 3 mm upstream of the pier model surface in its plane of symmetry, in conjunction with a constant temperature anemometer, storage oscilloscope and spectrum analyzer having FFT processor.

The pictures of spectra and the hot wire traces with increasing wind speed are presented in fig. 4.6. First appearance of steady HSV oscillations (at 10 Hz) is around $Re=2392$ and $D/\delta^*=5.9$. Steady, distinct and discrete vortex oscillation frequencies with higher harmonics are observed with gradual increase in wind speed, till the appearance of mixed frequencies at $Re \approx 4200$. The transition to turbulent flow starts at $Re \approx 4,000$ (fig. 3.5a).

The variation of Strouhal frequency St with Re and D/δ^* in fig. 4.7 shows that there exists a value of $St \approx 0.22$ with higher harmonics in the range $2400 < Re < 4500$ and $5 < D/\delta^* < 10$. Beyond this range mixed frequencies alongwith intermittent bursts of turbulence started appearing leading to fully turbulent flow.

4.3.3 Turbulent Flow

The horseshoe vortex around the junction of round nose pier model in approaching turbulent flow was investigated from surface oil flow around it, detail pressure measurements all around on the floor and total head surveys in the Y-Z plane at the mid-span of the pier model.

a. Surface Oil Film Pattern :

Fig. 4.8 shows the surface oil film patterns obtained around the pier model at a nominal wind speed of 5 m/sec., corresponding to $Re = 7768$ and $D/\delta^* = 11$. The shot 'a' was taken after twenty minutes of tunnel run and the shot 'b' was taken subsequently, immediately after stopping the tunnel fan and removing the pier model. A sketch of these oil film patterns from the picture is also shown in fig. 4.9.

Two distinct regions of oil film pattern can be identified upstream of the pier model leading edge; an inner semi-circle like region and the outer region with two nearly clear arc like patches and distinguished by a distinct line, identified as the primary separation line S , which was found nearly concentric with the semi-circular leading edge, located at a radius of about $1.2D$ from the centre of the leading edge circle of the pier model. The space downstream of this separation line is the region occupied by HSV. Two nearly concentric regions around the pier leading edge in the region of HSV are identified; one narrow ring like region around the leading edge semi-circle, and the other at about $0.69D$ from the centre. Referring to the turbulent horseshoe vortex structure from Baker (1980), the narrow clear ring around the pier is identified as due to the secondary vortex O , similar to the one around the pier as observed from $TiCl_4$ pictures in fig. 4.3 a and b, and the outer boundary of the second concentric region as the secondary separation line S_1 , where an accumulation of the

powder mixture should indicate the secondary vortex, which is not distinguished from the scale of the experiment. The saddle point of primary separation, though not distinguishable clearly, should lie on the distinct, concentric primary separation line S. The nodal point of attachment between these two separation points (Hunt et.al., 1978) is not clear in this picture. Thus it appears that it is a four vortex structure of HSV around pier model with round nose. This vortex structure extends to about $0.5D$ from the pier wall at the leading edge corner and appears slightly less further downstream all along the pier wall, Bělik (1973) obtained surface flow patterns at wind speed ranging from 30 to 55 m/sec, about a 40 mm cylinder and observed a strong vortex upstream of the cylinder, using TiO_2 in liquid paraffin. Baker (1980), however, identified four vortex structure of HSV around circular cylinder in the range $4,000 < Re < 90,000$.

b. Pressure Measurements :

Detail pressures around the pier model with round nose, measured at $Re \approx 8600$, $D/\delta^* \approx 11.6$ at five representative stations U, L1, M1, T1 and DS as shown in fig. 3.3 are presented in fig. 4.10a.

The pressure plot on the upstream plane of symmetry shows a weak dip in the pressure at about $0.4D$ upstream of the pier model, which may be identified with the location of the core

of HSV as was suggested by Bělik (1973) and Baker (1979,1980) for the circular cylinder case. The adverse pressure field induced by the pier is observed to appear at about $3.5D$ upstream from the pier surface and builds up rapidly near the pier in the region less than $1.5D$.

At the pier leading edge corner L_1 , a low pressure peak of $C_p = -0.8$ is observed as the flow turns around the pier nose and the region extends to about $0.5D$ from the pier wall. Low pressure regions are also observed at the mid-span M_1 and the pier trailing edge corner T_1 . The junction pressure at L_1 is relatively lower at $C_p = -0.8$ than that at M_1 and T_1 at about $C_p = -0.35$. The magnitude of pressures at stations M_1 and T_1 , to be almost equal. The higher suction pressure appears at L_1 indicates stronger bending vortex in the leading edge region. Beyond $0.5D$, away from the wall, the pressures tend to approach constant values.

A low pressure region with a base pressure of $C_p = -0.36$ upto about $1D$ behind the blunt trailing edge is shown by the pressure plot on the downstream plane of symmetry. Beyond this region, pressure recovery is indicated by the variation in C_p .

Pressure measurements repeated at $Re \approx 13,000$, $D/\delta^* \approx 14.5$ are presented in fig. 4.10b. Fig. 4.10c plotted from the above two plots, shows C_p variations at U, and DS, locations. A good agreement appears between the corresponding C_p 's at both these Reynolds numbers which shows Reynolds similarity in turbulent flow on the upstream plane of symmetry. The solid line shows Baker's (1980) data on circular cylinder for the sake of comparison,

which is in good agreement with the C_p 's for round nose pier. At the downstream location, however, the lower pressure region behind the blunt trailing edge appears to have decreased at higher Re . A good agreement between the C_p 's at the two Re , appears at the locations L_1 , M_1 and T_1 in fig. 4.10d. The trend of C_p variation at the pier base is shown in fig. 4.10e.

c. Total Head Survey

The streamwise arm of HSV around the junction of the vertical pier with round nose was probed for the vortex structure through constant total head contours, plotted by traversing a shielded Pitot tube (fig. 2.20) in a grid measuring 30 x 15 mm, at 300 points in a vertical plane normal to the free stream at the mid-span of the pier model. These contours are presented in fig. 4.11, as viewed from the downstream end. The interpretation of these contours for the number of vortices (secondary flows) and their sense of rotation is worked out from similar plots of Armstrong (1957), Harvey and Perry (1971) and constant velocity plot in fig. 21.10 of Schlichting (1968), which indicate that a lift up/depression of constant total head contours for one or more values suggests upward/downward movement of the secondary flow.

Four vortices are observed from fig. 4.11 as follows :

- (i) a counter clockwise vortex at the pier side wall (this is the secondary vortex O, formed on the upstream face of the

pier, which follows the geometry of the pier at the junction with floor). The constant total head contours further indicate that this vortex appears lifted upwards,

(ii) a large clockwise rotating vortex, located between $0.1D$ and $0.5D$ from the pier wall, identified as primary vortex 1,

(iii) a counter clock-wise rotating vortex, which is the secondary vortex 1', on the floor surface, located between $0.5D$ and $0.7D$ from the pier wall,

(iv) a smaller clockwise rotating vortex, which is the primary vortex 2, located about $0.7D$ from the wall.

Such constant total head contours for the vortex structure in the streamwise arm of HSV around a vertical pier model with round nose are presented for the first time.

4.4 THE MODIFIED HORSESHOE VORTEX

Fig. 4.12 shows a picture of the round nose pier model with the passive device mounted at its leading edge foot, and the three orthogonal views are provided in fig. 4.13. The results of the modified HSV around the pier model with passive device are presented in this article in the same order of flow conditions upstream of the pier as in the preceding section 4.3.

4.4.1 Laminar Flow

The dye flow patterns obtained at nominal waterspeed of 10 cm/sec corresponding to $Re = 3026$ and $Fr=0.135$ around the

pier model with the passive device are shown in figs. 4.14 a,b,c showing top, top front and top rear views. A comparison of these pictures with the corresponding dye shots with clean pier in figs. 4.1 a,b and c, shows that the white region identified as HSV flow in the clean pier case is significantly modified by the passive device by bringing the colored fluid around the pier model.

The small ablong like whitish region around the apex of the passive device can be identified with the three dimensional separation of the laminar boundary layer flow approaching the apex-floor junction, and subsequent roll up of the transverse approaching vortex filaments which wrap around the apex floor junction. Two dark red streaklines observed to progress downstream along the spinal rib of the device are identified as the streamwise arms (apex vortices) of the attenuated horseshoe vortex (AHSV) formed at the apex of the passive device in fig. 4.14 b.

Two distinct red streak^klines in relatively light colored water identified as the region of spirals of the leading edge separation vortices (LESV) are observed below the leading edge region of the transparent passive device in figs. 4.14 a and b. Furthermore it is also observed in these pictures that the light colored region closes on to the round nose of the pier model and moves downstream along the side wall, bringing the colored water towards the pier along the floor due to the sense of rotation of LESV.

The wake vortex interaction behind the pier model with passive device, in fig. 4.14c is also observed to be modified as compared with fig. 4.1c. The colored fluid from near the surface in fig. 4.14c appears to move upwards and this effect is observed in the farwake as well.

Fig. 4.15 shows a perspective view (from rear) of TiCl_4 fumes around the pier model with passive device, wherein the overall phenomenon of the HSV modification is observed at $\text{Re} = 1430$, $D/\delta^* = 4.4$. The liquid TiCl_4 was applied by technique I (described in chapter III). A comparison with fig. 4.3a shows a significant modification of the vortex flow. The multicellular structure of HSV visible in clean pier case appears to be replaced by two distinct vortices emerging from below the passive device and progressing downstream along the side wall of the pier model. The wake-vortex modification in throwing up of the two vertical vortices behind the blunt trailing edge by LESV is also observed in fig. 4.15a.

The vortex lifted upwards in fig. 4.15a is the streamwise arm of AHSV formed at the apex-floor junction and wrapped around it. It progresses downstream along the spinal rib and comes out from beneath the passive device along the leading edge of the pier model. This vortex named apex vortex was captured as an isolated vortex by the application of liquid TiCl_4 with technique III (chapter III) and is shown in fig. 4.15b. The sense of rotation of this vortex will be same as that of HSV around clean pier.

The vortex moving parallel to the floor (fig. 4.15a) and the pier side wall, is LESV from the passive device. This vortex with counter clockwise sense of rotation (as viewed from rear) and opposite to the rotation of apex vortex was captured as an isolated vortex by the application of liquid TiCl_4 with technique II (chapter III) and is shown in fig. 4.15c. This LESV appears to be stronger than the apex vortex.

Figs. 4.15d and e present the front perspective and top views respectively, of the vortices coming out from beneath the device, showing the close proximity of the LESV to the pier side wall. The apex vortex is observed to get lifted up as in fig. 4.15a and b. Fig. 4.15 f shows the wake-vortex interaction, showing significant modification brought about by the passive device apparently by LESV (Gupta, 1987) as compared with the clean pier case in fig. 4.3c, in the corresponding view.

Fig. 4.15 g and h provide close up views of the dominant vortices as they come out of the passive device-pier nose junction. The apex vortex is observed to lift up and somersault at the pier nose (fig. 4.15g) and hits the floor after its exit from the confined region. The formation of LESV and its progress downstream within the device and along the pier side wall is clearly visible. The apex vortex after hitting the floor is observed to be lifted up by LESV. In a simple manner, this behaviour of the apex vortex at the pier could be visualized as

lifting and spiralling of a coiled rope. It was also observed that at slightly higher wind speed, corresponding to $Re=1760$, $D/\delta^*=4.9$, the apex vortex appeared to merge with the leading edge separation vortex as shown in fig. 4.15 i.

This phenomenon showing apex vortex, LESV and their interaction at the passive device-pier nose junction and the pier side wall has been sketched in fig. 4.16, which shows the side and plan views of the modified vortex flow around the pier model with the passive device. The dotted line shows the region of lift up, and somersaulting of the apex vortex, which is believed to be under the adverse pressure built up in this region due to the pier leading edge.

4.4.2 Transition to Turbulent Flow

The oscillations of the modified vortex flow around the pier model with device were recorded with a 'u' sensitive hot wire probe inserted from top and kept 1 mm above the upper surface of the passive device and 3 mm upstream of the pier in its plane of symmetry, using the same procedure as in the previous section 4.3.2.

The pictures of spectra and traces of the hot wire signal are shown with increasing wind speed in fig. 4.17. The vortex oscillations on the upper surface get changed altogether, apparently due to the accelerating flow. Low frequency, low amplitude oscillations are observed in the range $2000 < Re < 4500$ and $5 < D/\delta^* < 9$,

beyond which the flow became turbulent.

Fig. 4.18a presents variation of St with Re and D/δ^* . The Strouhal frequency appears to be confined to below 0.05 in the above range of Re . The local mean velocity ratio \bar{u}/U_∞ which was less than 0.1 in clean pier case, was found to vary from about 0.2 to 0.28, prior to the onset of turbulence. The local turbulence level decreased from the clean pier case to just about 0.2%.

4.3 Turbulent Flow

The modified vortex flow around the pier model with the passive device was investigated from surface oil film patterns, detail pressure measurements on the floor and total head survey in Y-Z plane at the mid-span of the pier model.

a. Surface Oil Film Patterns

Figs. 4.19 a and b show the surface oil film pattern obtained around the pier model with the passive device at a nominal wind speed of about 5 m/sec, corresponding to $Re=7768$, $D/\delta^*=11$. The picture 'a' was taken after twelve minutes of tunnel run time and the picture 'b' was taken immediately after stopping the tunnel and removing the pier model.

The surface flow patterns below the passive device appear to be formed due to the streamwise arm of AHSV formed at the apex-floor junction, and LESV in their respective pairs about the spinal rib. A small clear patch just upstream of the apex

of the passive device, observed to extend about $1D$ downstream along the spinal rib and distinguished from the adjoining clear region by a distinct bordering line, is identified as due to the formation of AHSV. The deposit of powder suspension along the spinal rib appears to be due to a counter rotating surface vortex formed at the junction of the spinal rib with floor. The other region of deposit below the leading edge of the passive device appears to be due to a pair of counter rotating surface vortices generated below LESV and the apex vortex. Harvey and Perry (1971) reported the generation of counterrotating surface vortex due to an isolated trailing vortex from a wing, travelling close to the ground. The dark red streaklines below the leading edge region of the passive device in figs. 4.14 a and b, are identified as the surface vortices formed below the LESV and the apex vortex. A clear region indicating high surface shear stresses is observed around the device, which extends around the nose of the pier. The surface streamlines indicate the flow towards the pier and resulting in accumulation of the powder mixture all along its side walls due to the sense of rotation of LESV. The modification of wake-vortex interaction is also observed from surface flow patterns. These surface flow patterns are sketched in detail in fig. 4.20.

b. Pressure Measurements

Pressure measurements were made at five representative stations, around the pier model with the passive device at nominal

wind speeds of 5.5 m/sec. and 8.5 m/sec. corresponding to $Re \approx 8500$, $D/\delta^* \approx 11.4$ and $Re \approx 13,000$, $D/\delta^* \approx 14.5$ respectively. Pressure plots are presented at these locations in the left half of the flow field. The symmetry of the pressures around the pier model with and without the passive device is presented separately.

Fig. 4.21 a shows the pressure distribution on the upstream plane of symmetry of the pier model with the passive device at $Re \approx 8600$, $\frac{D}{\delta^*} \approx 11.5$ and $Re = 12700$, $\frac{D}{\delta^*} \approx 14.3$. The pressure variations with the clean pier at $Re = 8538$, $\frac{D}{\delta^*} = 11.3$ and $Re \approx 12,900$, $\frac{D}{\delta^*} \approx 14.5$ are also presented for direct reference. The surface pressures below the device have been modified significantly. There appears 80% and 67% reduction in the pressure gradient $1.5D$ upstream of the pier at $Re=8600$ and $12,700$ respectively. The respective reductions in C_p at the pier foot were 82% and 70% respectively. Tests were repeated with a passive device with leading edges sharpened to 35° , at $Re = 8290$ and $\frac{D}{\delta^*} = 11.3$, 90% reduction in the pressure gradient at $1.5D$ upstream of the pier and 89% reduction in the C_p at leading edge foot was measured thereby giving an improvement of about 10% over the mostly ^{used} truncated edge passive device. The difference between the floor and the upper surface pressure of the device can also be observed, which is the net pressure difference created by the presence of the passive device. It is important to note that for pressure measurements on the upstream

plane of symmetry below the device the turn table was yawed by about 3° such that the pressure taps were clear of the spinal rib. The lower pressure on the surface below the passive device is due to weak vortices present there.

Fig. 4.21 b shows pressure variations on the floor around the pier model with and without the device at the leading edge corner L1, at $Re \approx 8400$, $D/\delta^* \approx 11.3$ and $Re \approx 13,000$, $D/\delta^* \approx 14.5$. A pressure recovery of about 23% is indicated at the pier side wall, which appears to be reduced to about 11% up to about $0.8D$ in a direction normal to the pier wall. Beyond $0.8D$, pressures tend to remain the same with and without the device. A good agreement is observed between the pressures at these two Reynolds numbers.

The variations of the pressure at the locations M_1 and T_1 with and without the device at $Re \approx 8400$, and $12,800$ and $D/\delta^* \approx 11.3$, 14.5 respectively are shown in figs. 4.21c and d. Both the plots at each of the two Reynolds numbers appear to give almost identical results. This seems plausible because the streamwise arm of HSV in clean pier case has been replaced by a LESV moving above the pier-wall junction, when the device is mounted.

It is observed from the pressure measurements on the downstream plane of symmetry of the pier model with and without the device in fig. 4.21e, that a further pressure reduction of

about 11-15% occurs with the device. This appears to be a consequence of the modified wake-vortex interaction, as the leading edge separation vortex is believed to be a stronger vortex. A quicker pressure recovery appears in this case as compared with the clean pier case.

The pressure plots in figs. 4.22 a, b and c show the pressure measurements on both the sides of the pier model with and without the passive device at the locations, leading edge corner at $Re \approx 8400$, $D/\delta^* \approx 11.4$, mid-span at $Re \approx 8400$, $D/\delta^* \approx 11.4$ and the trailing edge corner at $Re \approx 8500$, $D/\delta^* \approx 11.5$ respectively. In each case good agreement between the corresponding pressure fields on either side of the pier model was observed. This symmetry of flow was also observed at higher Reynolds number.

c. Total Head Survey

The streamwise arm of the modified HSV around the pier model with the passive device was probed for its vortex flow structure. Total head contours plotted from traversing a shielded pitot-probe in a grid of 30x22 mm at 450 points, in the Y-Z plane at the mid-span of the pier model with the passive device, at $Re \approx 8300$, $D/\delta^* \approx 11.3$ are presented in fig. 4.23 as viewed from the downstream end. The number of vortices and their sense of rotation were worked out as in 4.3.3.c, and are described as follows.

- (i) a large counter clockwise LESV from the passive device
- (ii) a small counter clockwise vortex on the floor at the pier-floor junction
- (iii) a small clockwise vortex above the vortex (ii), the constant total head contours indicating that this vortex (apex vortex) appears to be lifted upwards along the pier side wall.
- (iv) a large clockwise vortex away from the region of influence of LESV.

There also appears a vertically downward flow region at $z/D \approx 0.6$ near the wall. The apex vortex appears to get lifted up, as was observed in the laminar flow with $TiCl_4$ fumes. The formation of small counter clockwise vortex on the floor at the pier side wall is believed to be due to an interaction of LESV with the pier wall, which causes the surface flow towards the pier. It becomes clear from this constant total head plot that the size and strength of LESV are more than that of the apex vortex.

A complete picture of the streamwise arm of the modified HSV around the junction of a vertical pier with the passive device is presented for the first time.

4.5 AERODYNAMICS OF DELTA-WING-LIKE PASSIVE DEVICE

Some salient features of the flow phenomenon due to the passive device mounted on the leading edge foot of the round

nose pier model as observed from the experiments are described in this article as follows.

1. It is known (Gupta, 1987) that the passive device behaves as a slender delta wing with a sweep of 69.5° , at a negative angle of attack of about 15° , with the additional feature of the central spinal rib in contact with the wind tunnel floor. The leading edge separation vortices from an isolated delta wing as viewed from downstream are shown in fig. 1.4. The close contact of the spinal rib with floor makes the slender delta plate of the passive device to operate under strong ground effect, the net effect of which is similar to that on a conventional wing (Houghton and Carruthers, 1982) at positive angle of attack, resulting in a decrease of downwash at the trailing edge causing a net increase in the lift force. At negative angle of attack, the sense of rotation of the trailing vortices is reversed, the ground effect would therefore, decrease the net upwash; this means an increase in the downward normal force on the passive device.

2. The device operates in the boundary layer like shear flow of the approaching stream. The flow on the leeward side of the passive device consists of

- (i) an attenuated HSV formed at the apex-floor junction, resulting from the partial roll up of the transverse vortex filaments and their subsequent wrapping around the apex (Gupta, 1987)

The stream wise arms of this attenuated HSV, named apex vortices move downstream on either side of the spinal rib.

(ii) a pair of counter rotating leading edge separation vortices formed by the separation of the accelerating upper surface boundary layer at the leading edges. LESV appears to be stronger than the apex vortex from the modified structure of the vortex flow at the pier side wall in section 4.4.2c. A new accelerating boundary layer flow is believed to start on the upper surface of the passive device, where remaining stretched transverse vortex rolls over the upramp formed by the delta plate junction with the vertical pier.

3. Following phenomenon were observed from the dye flow below the transparent passive device.

A distinct reverse flow region, close to the central spinal rib was observed from the traces of the dye flow moving upstream towards the apex, and uptowards the the delta plate along the spinal rib appearing to form a transverse vortical flow in the counter clockwise direction, in the left half of the device as viewed from the downstream end. This region was found to extend continuously away from the spinal rib as it progressed towards the leading edge of the pier model (i.e. the trailing edge of the passive device).

Furthermore, it was observed from the dye flow below the passive device that the two LESV appeared to sway away from their original path at about $0.5D$ upstream of the pier and tended to

close on to the pier after coming out from beneath the device as shown in fig. 4.14 b.

It can be inferred from above that the two main vortices below the device experience adverse pressure gradients in transverse and streamwise directions, due to the central spinal rib and the pier respectively. It is further believed that the severity of the adverse pressure gradient would depend upon the nose geometry of the pier model.

4. Two distinct regions of the accumulation of powder mixture (figs. 4.19) below the passive device are observed ; along the spinal rib and below the leading edge, the latter appears from about 10 upstream of the pier. These two regions appear to be due to the surface vorticity at the spinal rib and the floor respectively as a consequence of apex vortex and LESV.

5. A three dimensional separation of the accelerating boundary layer was observed about $0.5D$ upstream of the pier, on the upper surface by sprinkling finely powdered $KMnO_4$ on the passive device, during the dye flow visualization experiments.

An overall picture of the vortex flow below the passive device can be framed at this stage. The gap between the delta plate of the passive device and the floor downstream of its apex is very narrow. It permits just the wrapped up vortex at the apex to get in below the device upto a certain distance

downstream of the apex. This distance appears to be about $0.5D$ at $Re=3026$, $Fr=0.135$ in fig. 4.14b and $1D$ at $Re=7768$, $D/\delta^*=11$ in fig. 4.19b. A schematic of the flow below the device at this distance is given in fig. 4.24. A small vortex counter rotating to the apex vortex due to the generation of the surface vorticity (Mason and Morton, 1987) is believed to exist at each of the two junctions the spinal rib makes with the delta plate and the floor. The latter one is evident from the deposit of suspension in fig. 4.19b.

The formation of LESV appears to start just downstream of the apex region. A schematic of the flow at a typical station downstream is shown in fig. 4.24. The separating boundary layer from the upper surface of the delta plate coils up at the lower surface giving rise to LESV and a small counterrotating secondary vortex near the leading edge like that shown in fig. 1.4. The reattached flow is believed to separate under the adverse pressure gradient in the transverse direction due to the spinal rib and forms a counter rotating vortex, This vortex has the same sense of rotation as that of the apex vortex; therefore, their co-existence is not possible (Freymuth, 1985a) and results in a single counter-rotating vortex progressing along the spinal rib. Under the combined flow field of LESV and the apex vortex, following surface vortices are generated below the device ;

- (i) two counter rotating vortices, one each at the two junctions, the spinal rib makes with the delta plate and the floor.

- (ii) a pair of counter rotating surface vortices below LESV and the apex vortex, evident from a ridge like deposit of the suspension in surface flow patterns in ~~fig.~~ 4.19b.

The position of LESV depends upon the freestream velocity and the angle at which the delta plate is incident to it (Kuechemann, 1978).

4.6 DISCUSSION

The earlier experimental investigations of Bělik (1973) and Baker (1979, 1980) on the horseshoe vortex around circular cylinder were confined to probings on the upstream plane. It is well known from aerodynamics that flow around a cylindrical body cannot be studied in isolation from that in the region of trailing edge, and it may depend upon the shape of the trailing edge, for example the sharp trailing edge is required for satisfying Kutta condition in lifting flows requiring finite velocity at trailing edge (Anderson, 1984). This situation may arise in case of a river bridge pier incident to the flow at non-zero angles. It therefore appears that in general the flow phenomenon upstream of the bridge pier like cylindrical bodies cannot be isolated from that about its side walls and the trailing edge. This calls for a complete investigation of HSV around the cylindrical body under consideration, meaning thereby, a simultaneous probing of the vortex structure in the

streamwise arms, and the flow phenomenon at the trailing edge apart from the usual investigations of the flow field upstream of the body.

4.6.1 HSV around Vertical Pier Model with Round Nose

In this chapter an overall experimental study of HSV around a vertical round nose pier junction with ground has been described by extensive flow visualization from dye flow patterns, which provide an overall picture of the gross region of HSV, and from $TiCl_4$ flow visualization which provides detail flow structure within the HSV, shown in figs. 4.1 and 4.3 respectively. Six floor vortex rings were identified in fig. 4.3b and the primary separation line was found to be concentric with the semi-circular leading edge of the pier for $-75^\circ < \varphi < 75^\circ$. Pressure measurements at $Re = 22\ 65$, $D/\delta^* = 5.6$, provided three marginally low pressure minima at $0.4D$, $0.6D$, and $1D$ upstream of the pier model surface and were indicative (Baker, 1979) of the presence of three primary vortices on the upstream plane of symmetry.

The formation of the secondary vortex O , on the upstream face of the round nose pier is due to the vertically downward gradient of the Bernaulli constant of the approaching boundary layer like shear flow, normal to the upstream face of the pier model. This vortex can be visualized as a forced vortex attached to the upstream face of the pier model due to the pressure gradient. As the flow progresses downstream along the pier (i.e.,

accelerates around the curvature of the round nose pier), the intensity of the downward gradient of the Bernoulli constant reduces due to corresponding reduction of the normal component of the pressure force. This reduction of pressure force is explained by Mason and Morton (1987) as a consequence of the approximate local invariance of the pressure head as the flow accelerates round the sides of an obstacle. This downward pressure gradient on the pier becomes zero as the pier side wall becomes aligned with the free stream direction and the secondary vortex O now becomes a free vortex, and gets detached from the surface of the pier model at this station. The suction pressure immediately above this station is quite close to that in the two dimensional case, which should be higher and therefore annihilates this free vortex. This vortex was observed as rising and curling up of TiCl_4 fumes maintaining its vortical flow before getting completely smeared along the pier side wall. This phenomenon observed from extensive TiCl_4 visualization experiments in the course of the present work, is visible as a faint white patch of TiCl_4 fumes on the pier wall in fig. 4.3a.

Steady Strouhal frequencies of $St \approx 0.22$ with higher harmonics for vortex oscillation were observed with the increase in Re in the range of $2400 < Re < 4500$. Transition of the approaching free stream occurs at about $Re = 4200$ and the approaching boundary layer becomes turbulent at $Re = 5000$ (Fig. 3.5a). It therefore appears that the onset of intermittency

during the vortex oscillations appears to be associated with the transition of the approaching laminar boundary layer.

The surface oil flow patterns (fig. 4.8) show the HSV region extending about $0.7D$ around the pier leading edge. It further seems that the streamwise arms of HSV, also extend to about $0.7D$ almost parallel to the pier side wall. A four vortex structure of HSV is identified on the upstream of the pier model. The two clear arc like patches upstream of the separation line and located almost symmetrically about the pier nose can be explained as follows. The vortical flow around the pier nose, downstream of the separation line is believed to act as a locally larger cylinder on the surface, which causes more acceleration of the turbulent flow turning around this cylinder resulting in higher surface shear stresses on the floor upstream of the separation line. The pressure plot in figs. 4.10 show the extent of the vortical region around the pier model from the steep pressure gradient at the leading edge corner region extending to about $0.6D$ from the pier wall, the variation of C_p beyond this point appears nominal. Similar trend, but with reduced pressure gradient is observed at other two spanwise stations M_1 and T_1 . The constant total head contours in fig. 4.11 at the mid-span location in the Y-Z plane provide a picture of the structure of the streamwise arm of HSV, showing four vortices, along with their sense of rotation. A complete picture of laminar and turbulent HSV around a vertical round nose pier model with round nose has been presented for the first time.

4.6.2 The Modified HSV

The delta-wing-like passive device mounted at the leading edge foot of the round nose pier model modifies the HSV flow structure in the following manner.

1. Concentration of the transverse vortex filaments of the approaching shear flow at the upstream face of the cylinder is prevented.
2. A significant reduction in the surface pressures and the pressure gradient below the passive device.
3. An interaction of LESV and the apex vortex in modifying the streamwise arm of HSV, and interaction of the pair of LESV and the vertical vortices behind the blunt trailing edge of the pier model, in significantly modifying the wake-vortex interaction.

These are discussed in some more detail in the following paragraphs.

The apex-floor junction of the passive device acts as a barrier in allowing only a part of the transverse vorticity of approaching boundary layer like shear flow to be rolled up, rest of it passes over the upramp formed by the upper surface of the delta-wing-like passive device where an accelerating boundary layer formation takes place. The roll up of vorticity at the apex floor junction results in the formation of an attenuated HSV at the apex. The vorticity of the AHSV (Apex vortex) is believed to be significantly lesser than that of the HSV formed

at the junction of clean pier model with floor. The formation of AHSV (Apex vortex or Attenuated HSV) was observed from flow visualization in figs. 4.14a and b, 4.15 b and 4.19.

The streamwise arms of AHSV, thus formed (named apex vortices) progress downstream along the spinal rib, and can be observed clearly from the $TiCl_4$ pictures presented in this chapter. In case of an isolated delta wing the formation of LESV takes place at the apex itself, while it was shown from flow visualization in figs. 4.14 and 4.19 that LESV from the leading edge of the passive device starts forming $0.5D$ to $1D$ downstream of the apex, having an opposite sense of rotation to that of the apex vortex, which is of the same sense of rotation as the original HSV at the junction of the clean pier model. The presence of both of these vortices causes significant reduction of surface pressures below the device as observed in the pressure plots of fig. 4.21a.

The constant total head contours in fig. 4.23 indicate that the strength of LESV from the passive device is greater than that of the apex vortex. The apex vortex lifts and undergoes somersaulting at the pier-device junction, like the lifting and coiling of a rope, before hitting the floor as it comes out from beneath the device in figs. 4.15 g and h. The stronger LESV lifts up this apex vortex and the movement of these two vortices is shown in figs. 4.15. This interaction of the two dominant

vortices produced by the device in the modification process, causes the surface flow towards the pier side wall as observed from the dye pictures in figs. 4.14.

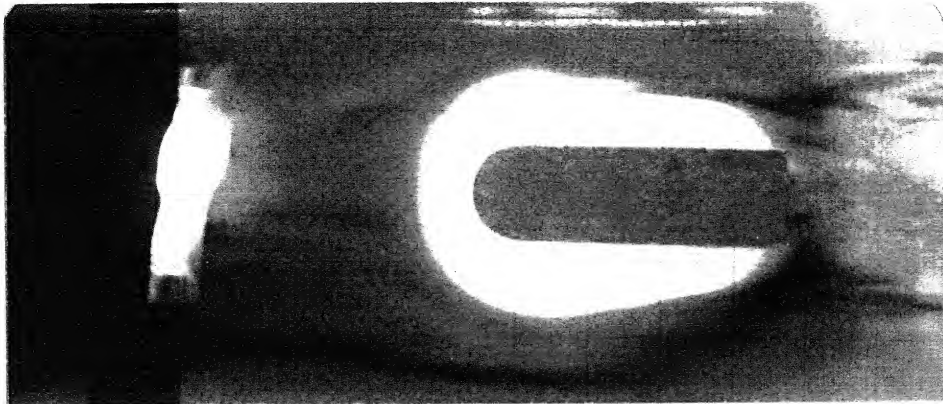
The two vertical vortices formed behind the trailing edge of the device are pushed up by the counter rotating pair of LESV, observed in $TiCl_4$ picture in fig. 4.15 a. The 'neck' region behind the blunt trailing edge is reduced.

The oscillatory behaviour of HSV modified by the presence of the device, shows very low Strouhal frequency, indicating that the HSV oscillations are effectively suppressed by the passive device till the approaching flow itself becomes turbulent, and turbulent signals ~~were~~ observed.

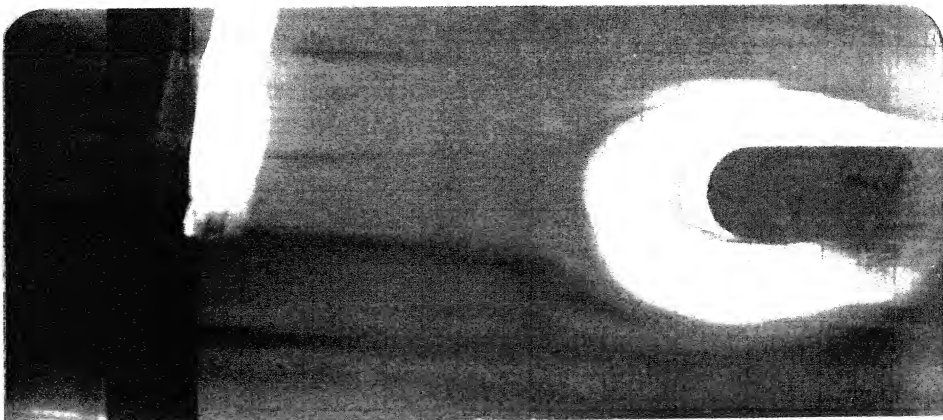
The outlines of the modified vortex flow around the junction of a vertical round nose pier with the passive device attached to its leading edge foot~~are~~ sketched in fig. 4.25.

(to be reported)

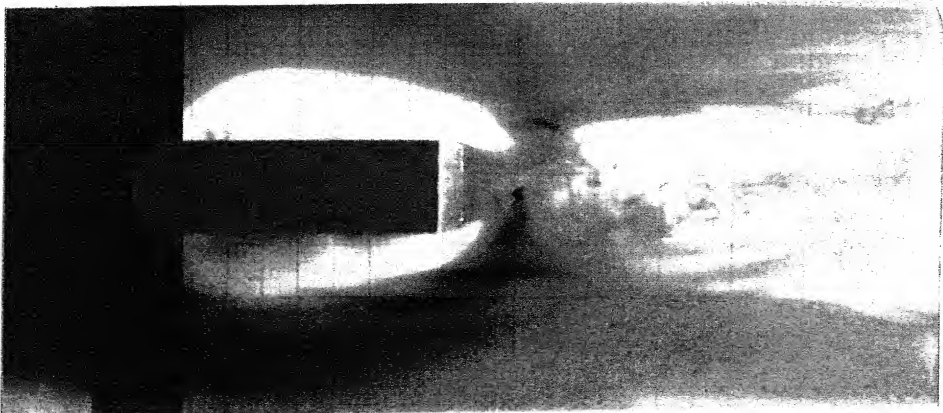
Gupta and Gangadharaiyah/ observed significant reduction in the local scour depth and its extent around the leading edge of the pier model of the same geometry in an open channel flume, with sand bed (the region of lift up and somersaulting by the apex vortex) and deposits of sand along the pier side wall and behind the blunt trailing edge.



a.
PLAN VIEW



b.
TOP FRONT VIEW



c.
TOP REAR VIEW

Fig. 4.1 DYE PATTERNS AROUND VERTICAL ROUND NOSE
PIER MODEL $L/D=6$, $BR = 10\%$, $Re = 3147$,
 $Fr = 0.146$ (FLOW FROM LEFT TO RIGHT)

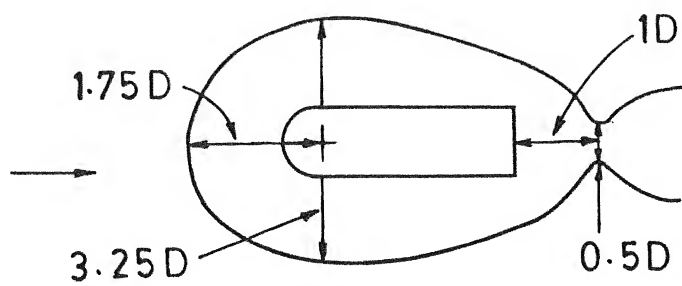
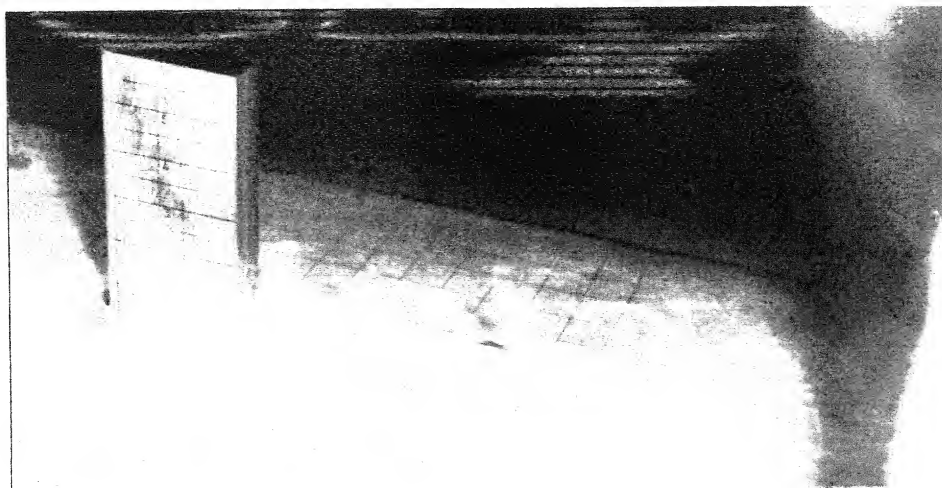
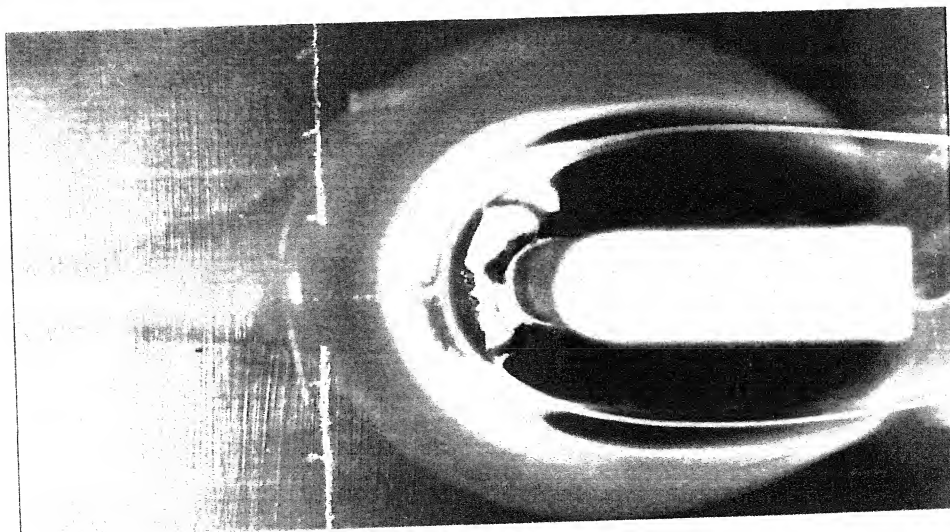


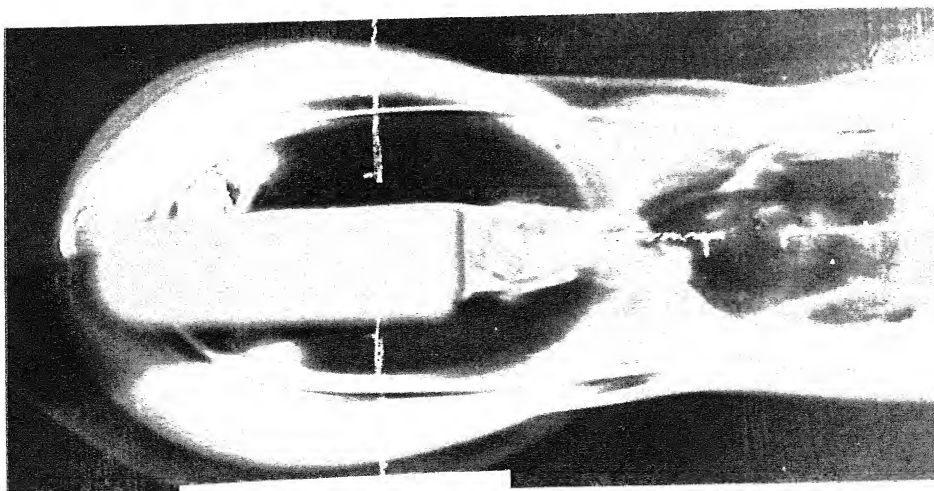
FIG. 4.2 LINE SKETCH OF DYE PATTERNS
(from fig. 4.1)



a.
PERSPECTIVE VIEW



b.
TOP FRONT VIEW



c.
TOP REAR VIEW

Fig. 4.3 TiCl_4 FLOW AROUND VERTICAL ROUND NOSE
PIER MODEL, $L/D = 6$, $BR = 3\%$, $Re = 1400$,
 $D/\delta^* = 4.4$ (FLOW FROM LEFT TO RIGHT)

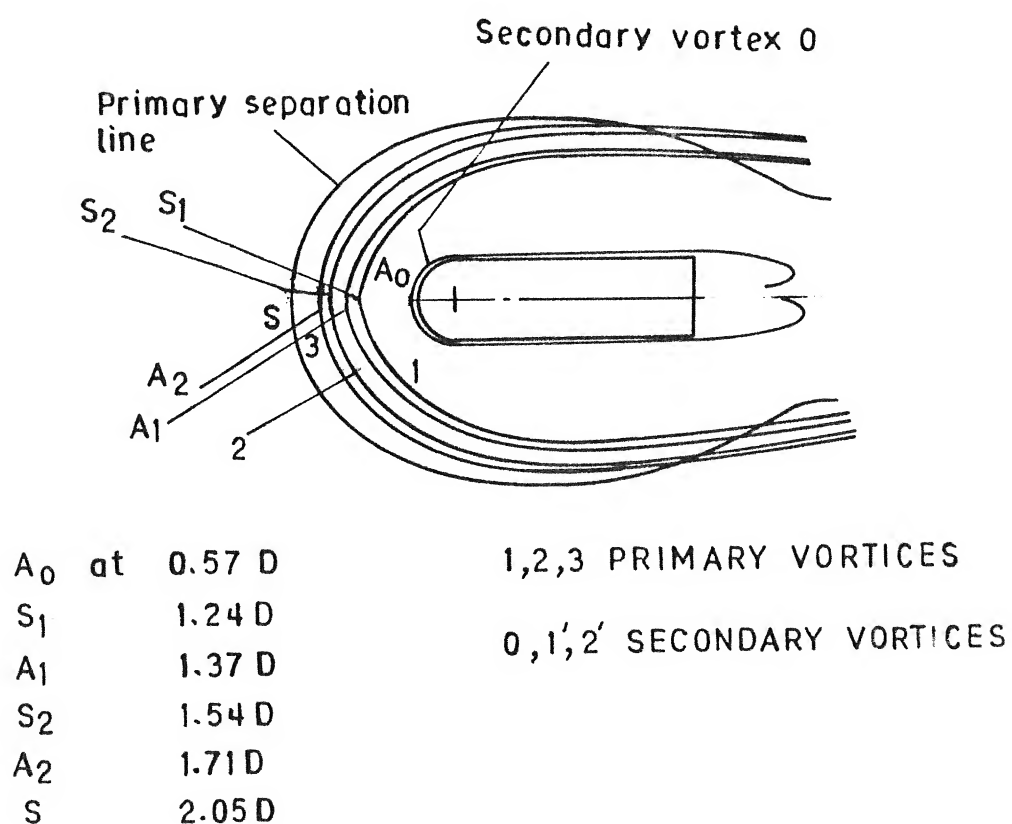


FIG. 4.4 LINE SKETCH OF $TiCl_4$ FLOW AROUND THE PIER MODEL (From fig. 4.3)

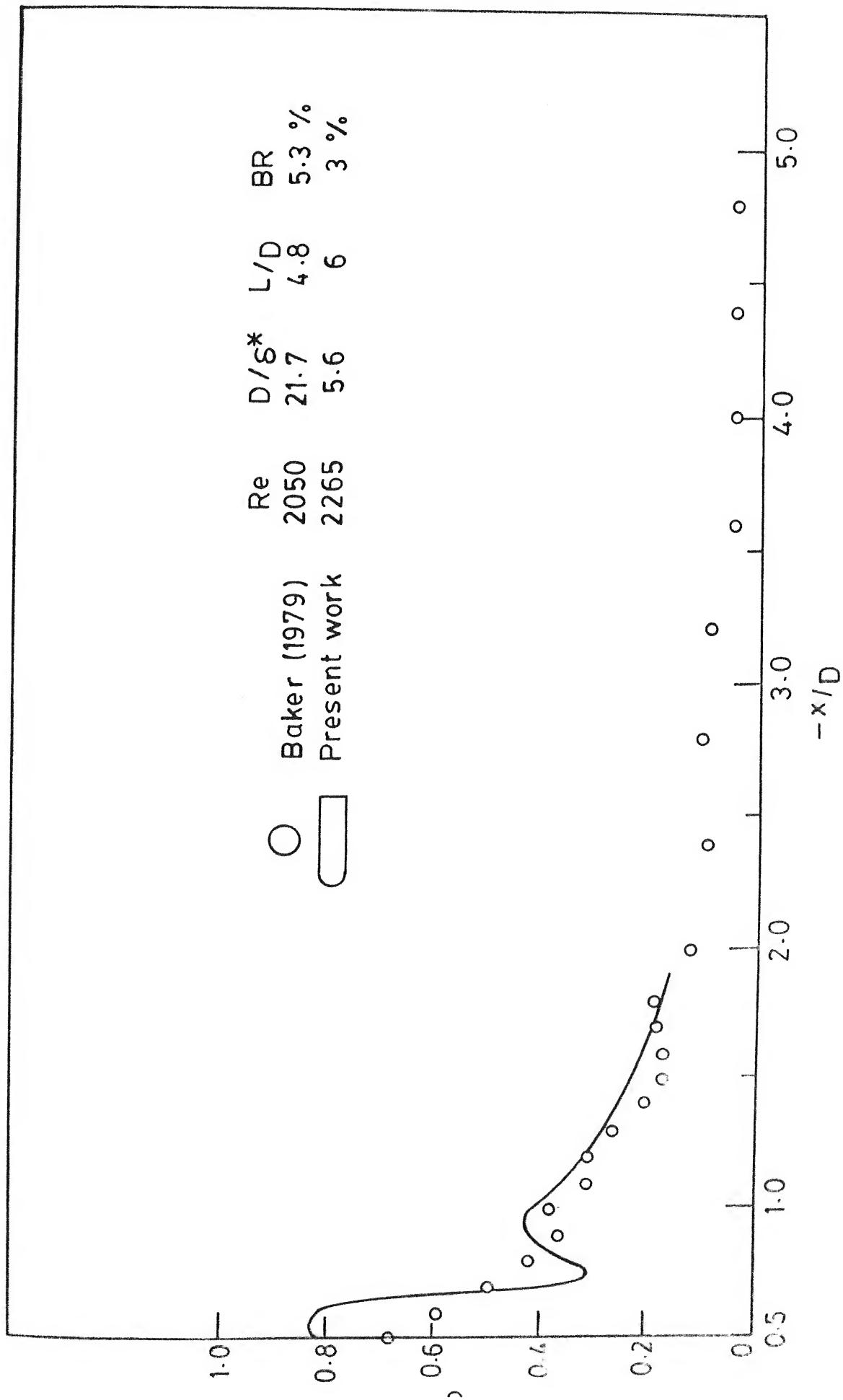


FIG. 4.5 PRESSURE DISTRIBUTION ON UPSTREAM PLANE OF SYMMETRY OF ROUND NOSE PIER MODEL

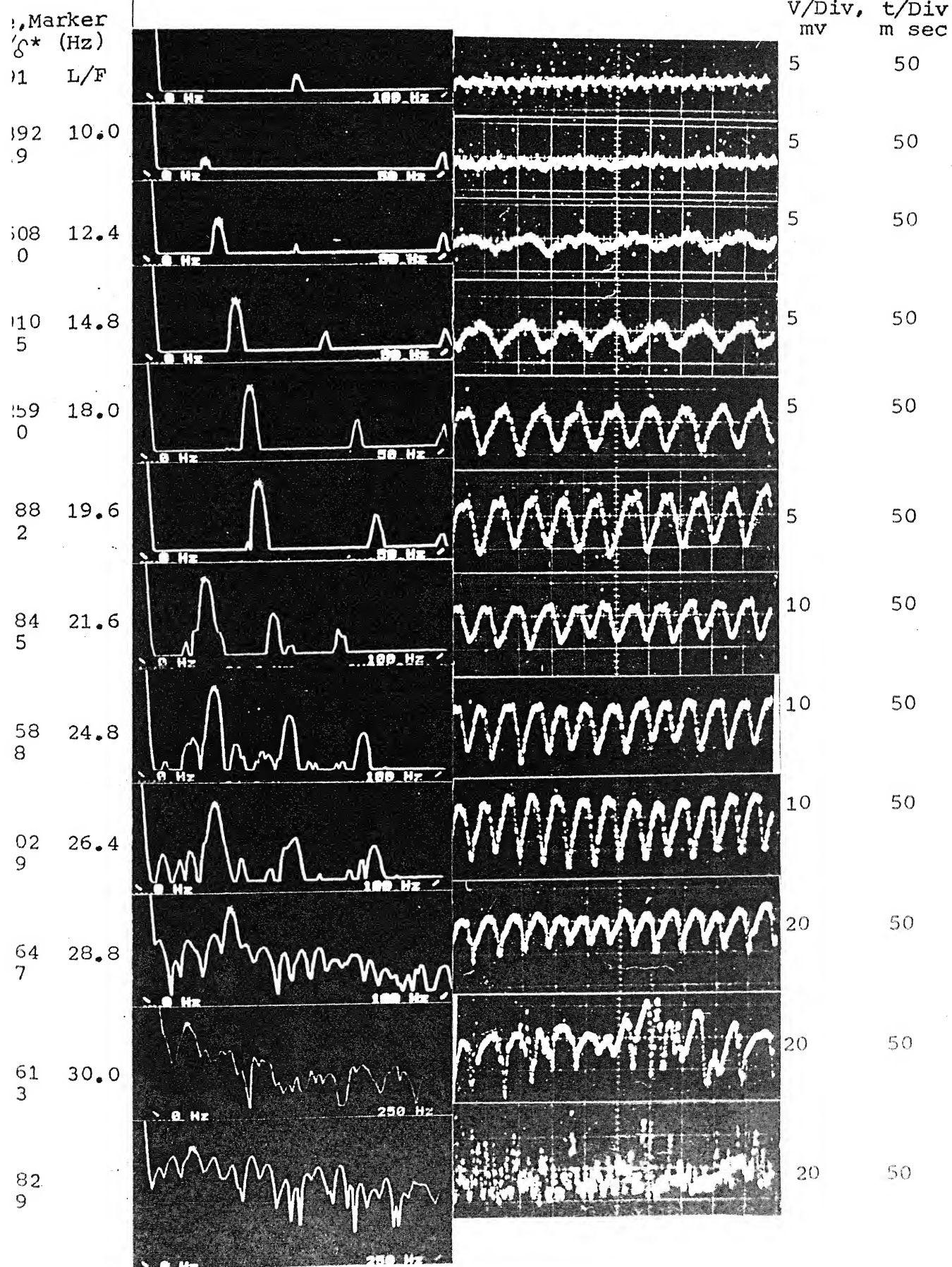
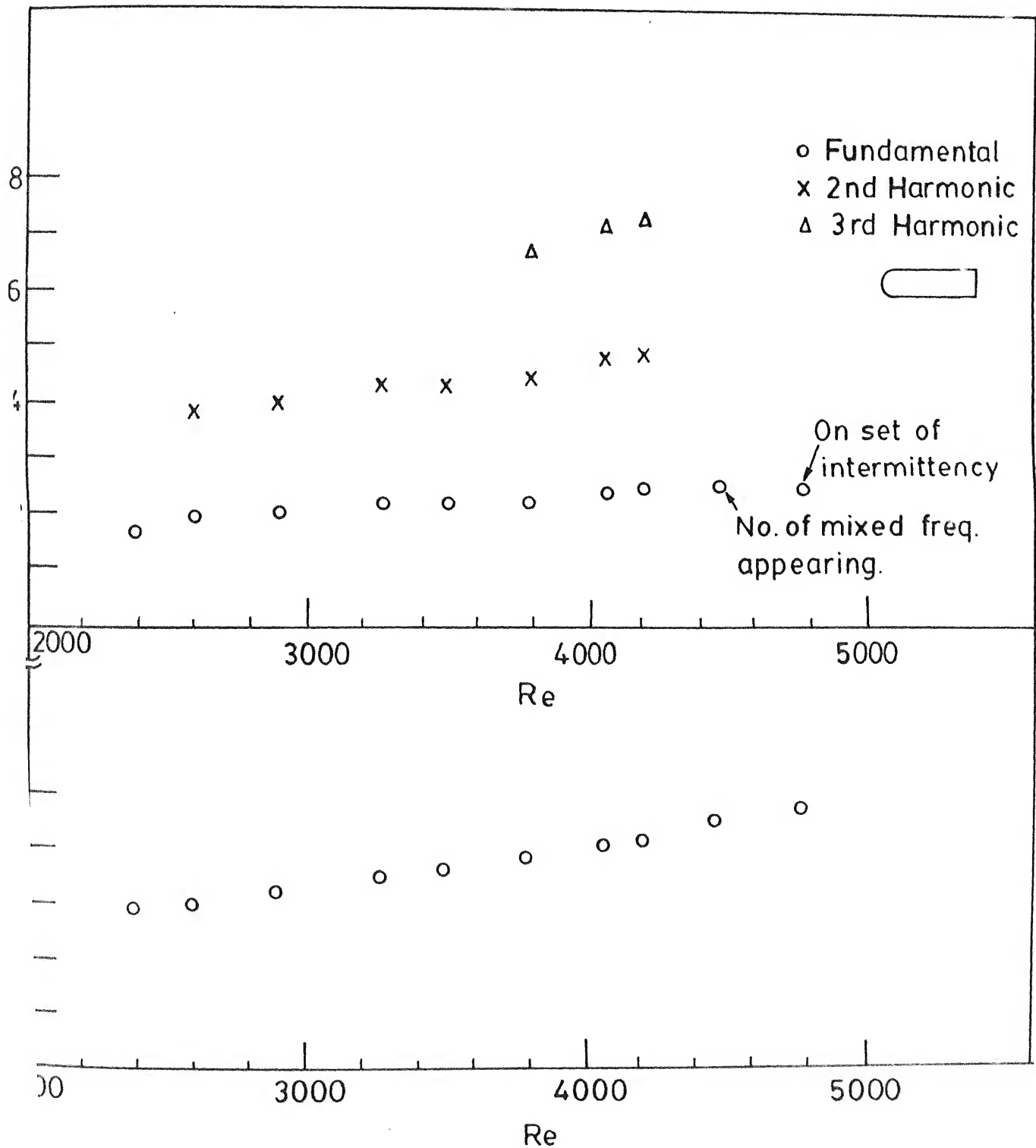


Fig. 4.6 SPECTRA AND TRACES OF VORTEX OSCILLATIONS
AROUND VERTICAL ROUND NOSE PIER MODEL



4.7 VARIATION OF VORTEX OSCILLATION FREQUENCIES AROUND VERTICAL ROUND NOSE PIER. $L/D = 6$, $BR = 3\%$

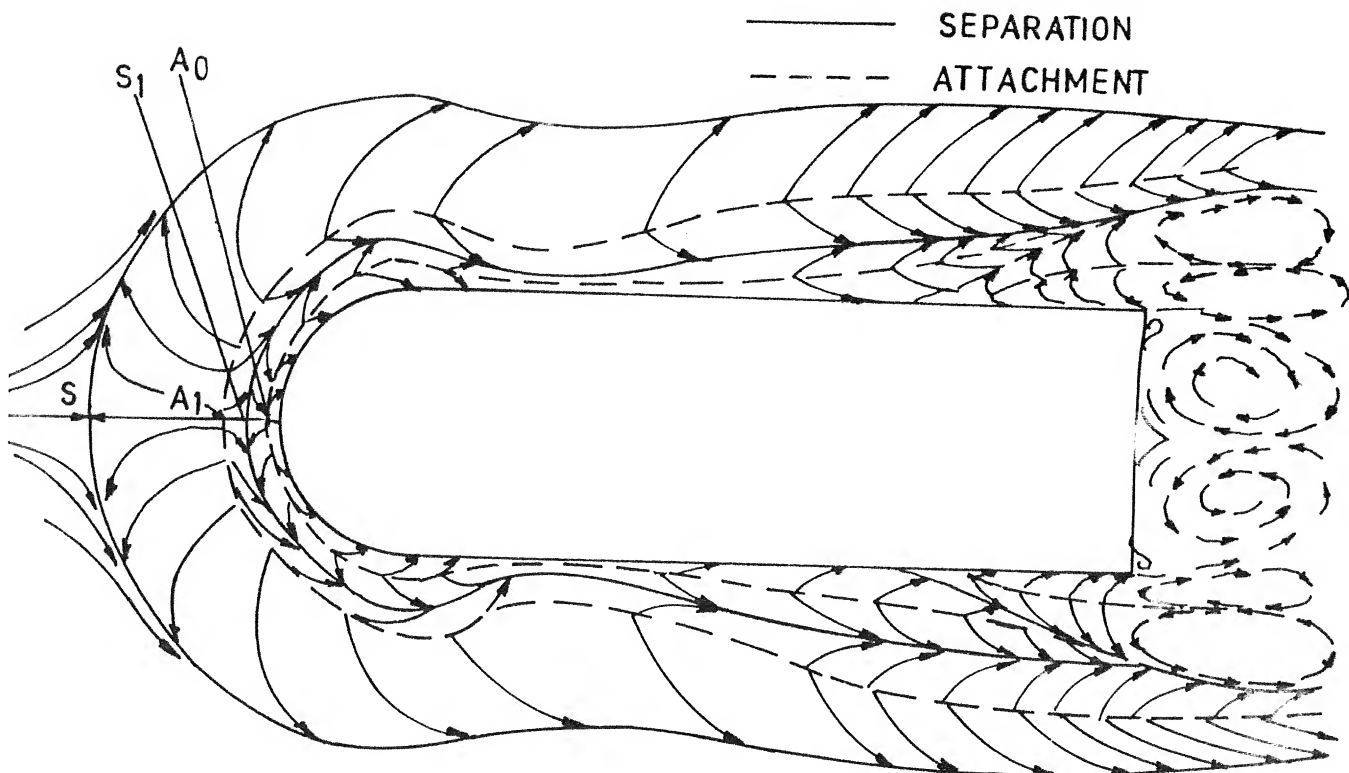


FIG. 4.9 (a) SURFACE STREAMLINES AROUND VERTICAL ROUND NOSE PIER $L/D = 6$, $BR = 3\%$, $Re = 7768$, $D/\delta^* = 11$

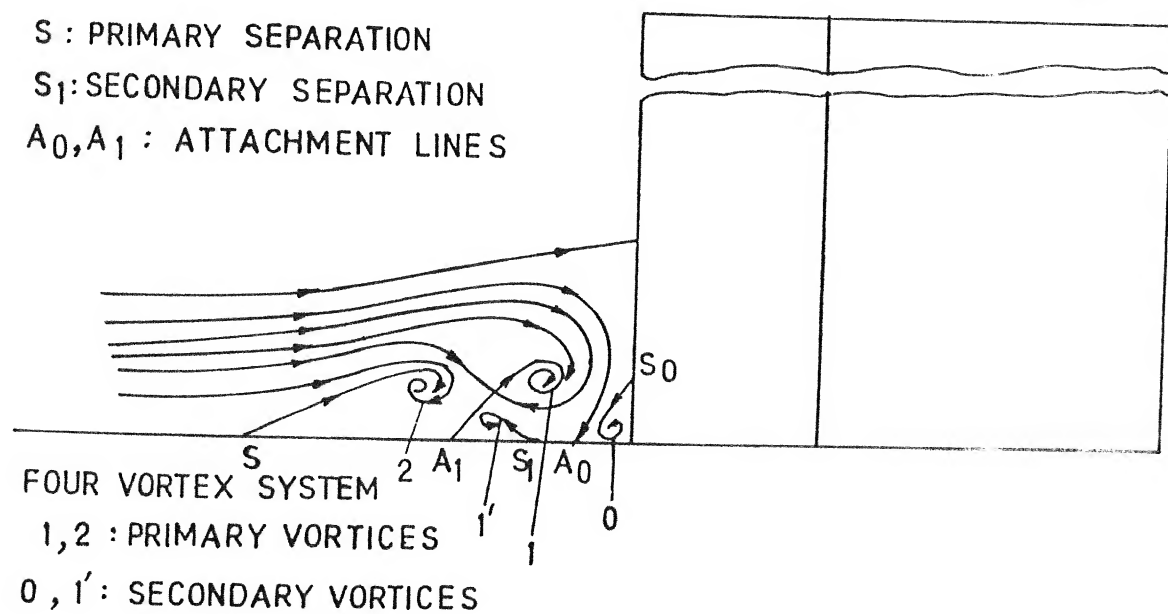


FIG. 4.9 (b) FLOW PATTERN INFERRED FROM SURFACE FLOW VISUALIZATION

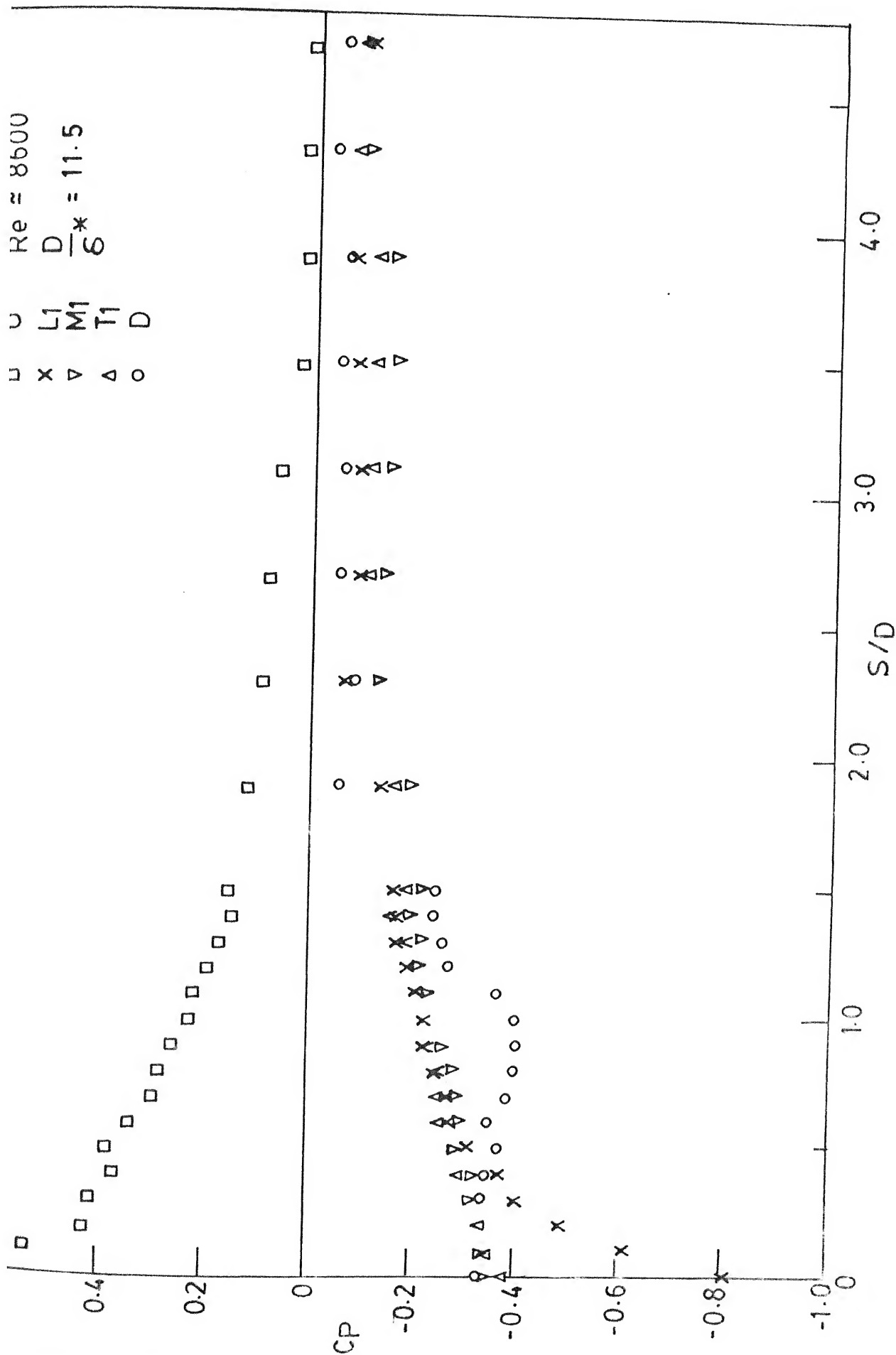


FIG. 4.10a PRESSURE DISTRIBUTION ON FLOOR AROUND VERTICAL ROUND NOSE
 MODEL $L/D = 6$, $BR = 3\%$

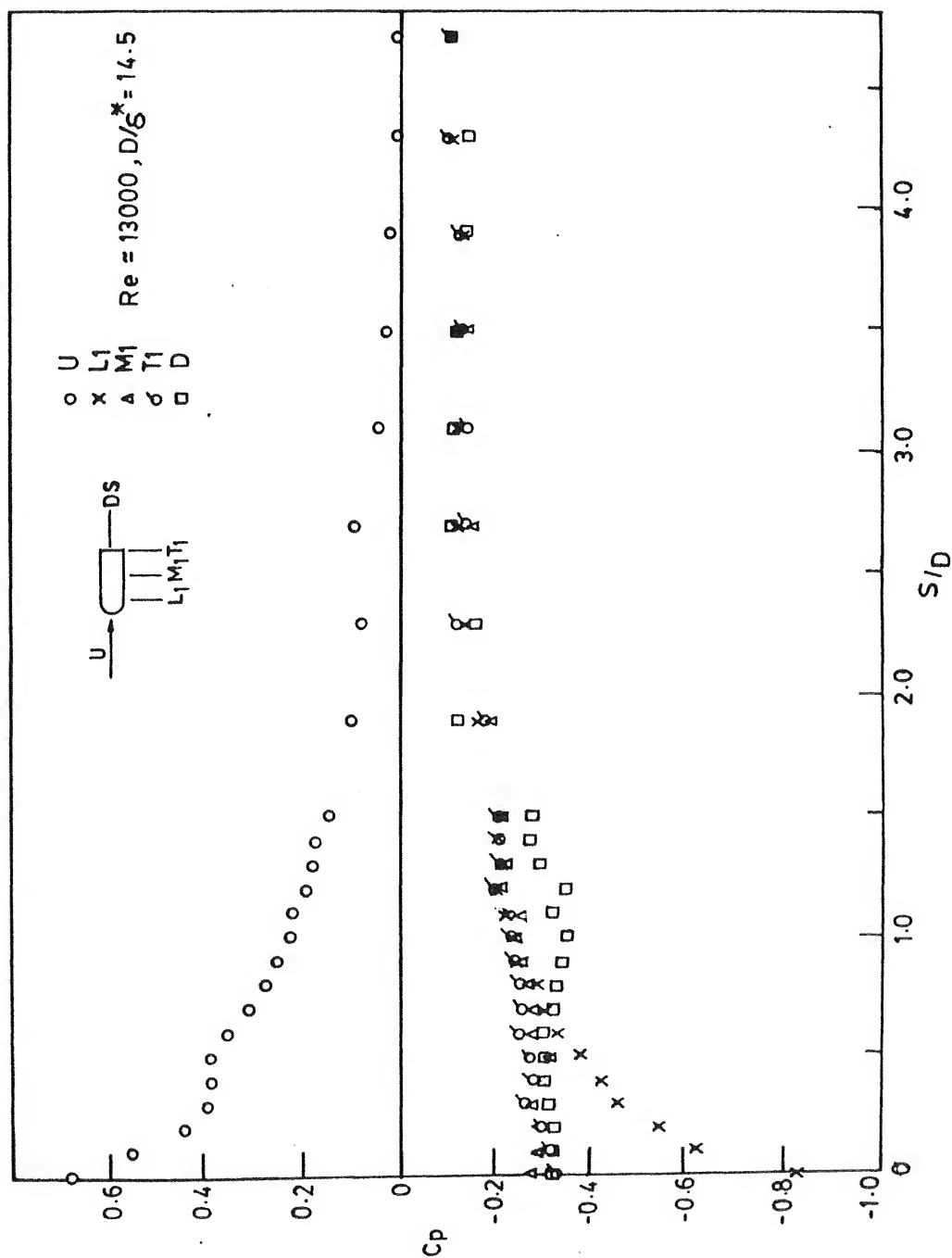


FIG. 4.10b PRESSURE DISTRIBUTION ON FLOOR AROUND VERTICAL ROUND NOSE
MODEL $L/D = 6$, $BR = 3\%$.

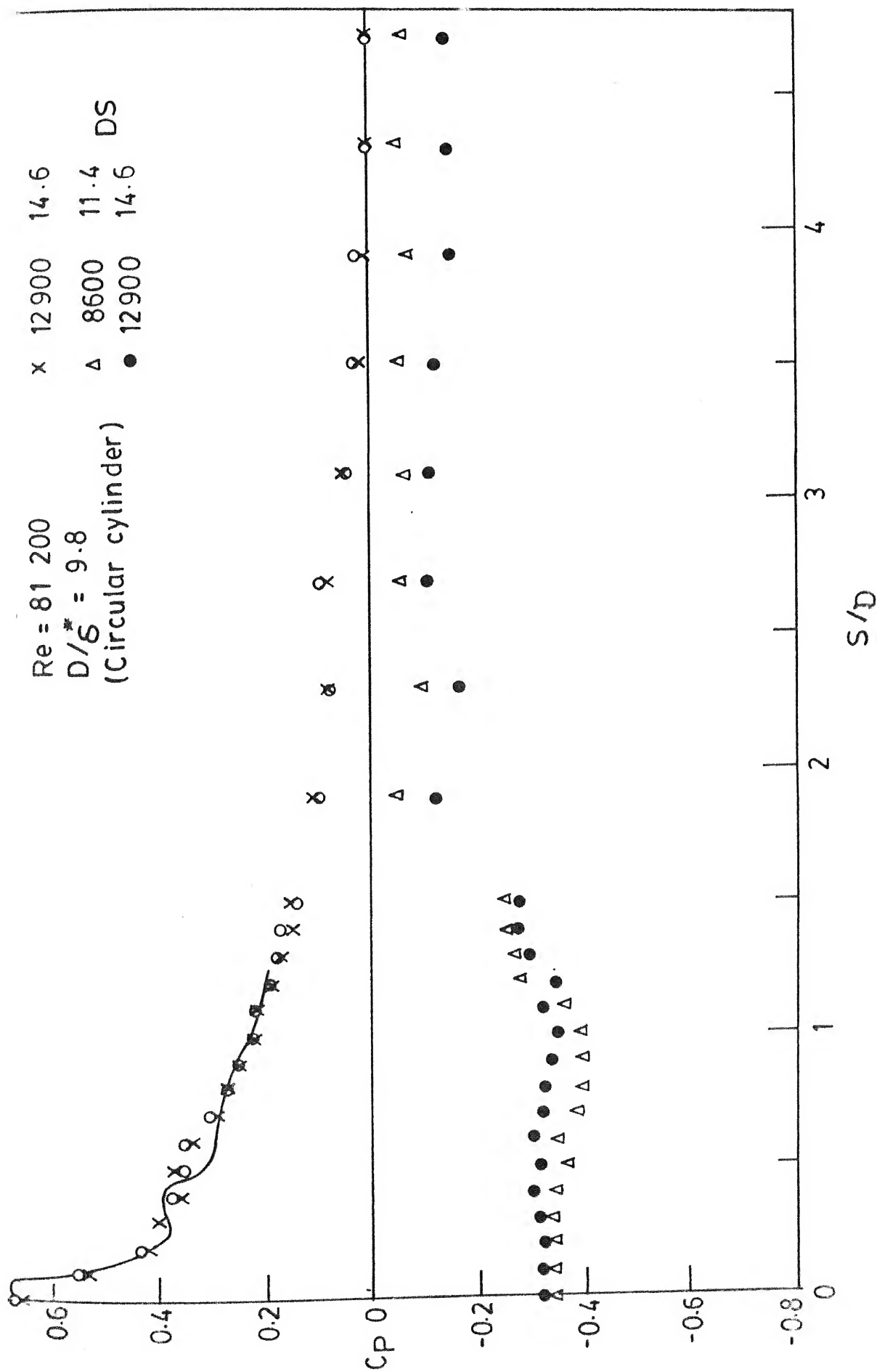


FIG. 4.10c PRESSURE DISTRIBUTION ON FLOOR AROUND VERTICAL ROUND NOSE PIER
 MODEL - $L/D = 6$, $BR = 3\%$, Re number dependence locations U and DS

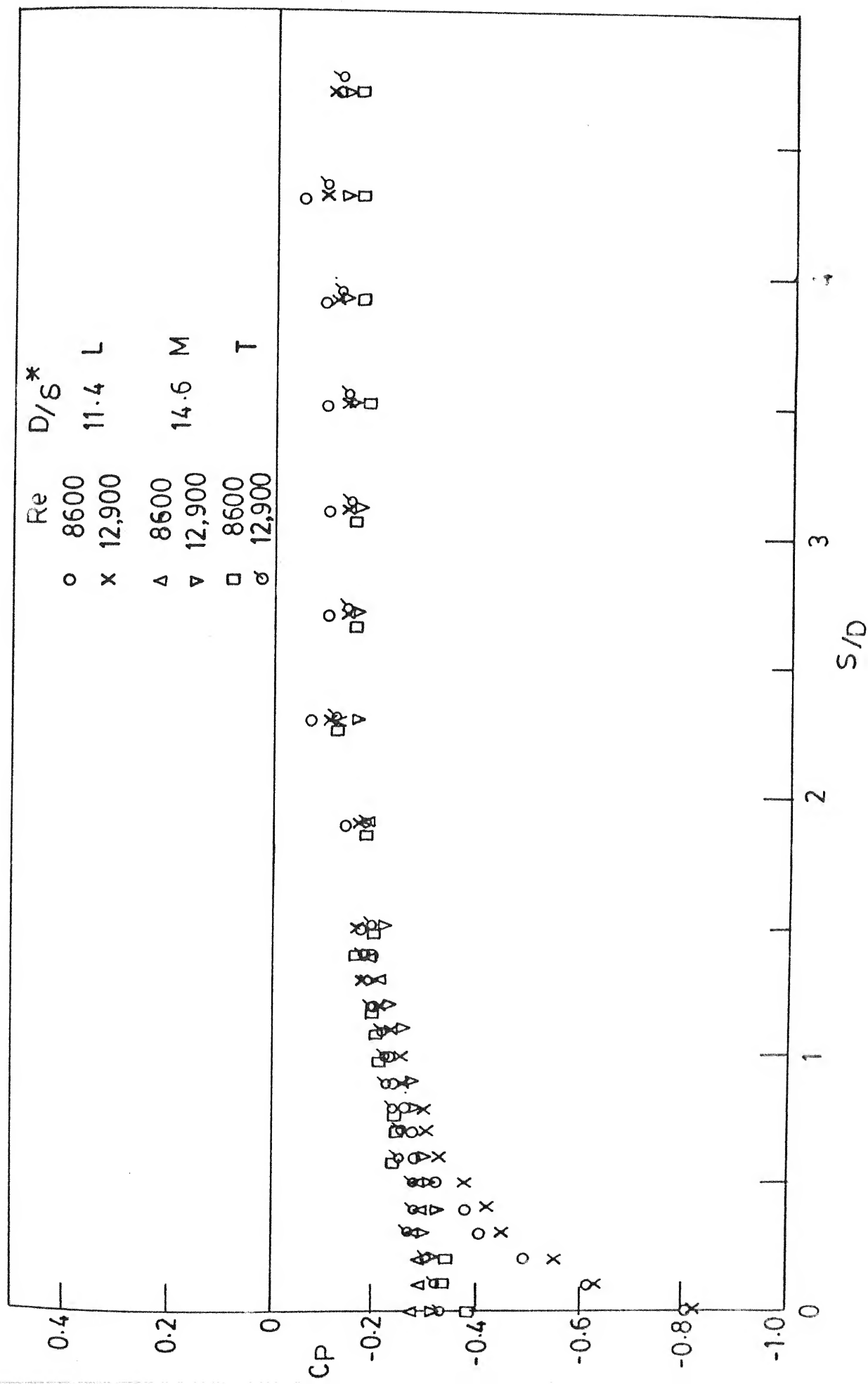


FIG. 4.10d PRESSURE DISTRIBUTION ON FLOOR AROUND VERTICAL ROUND NOSE PIER
 MODEL . L/D = 6 , BR = 3 % , Re. number dependence, locations L₁, M₁, T₁

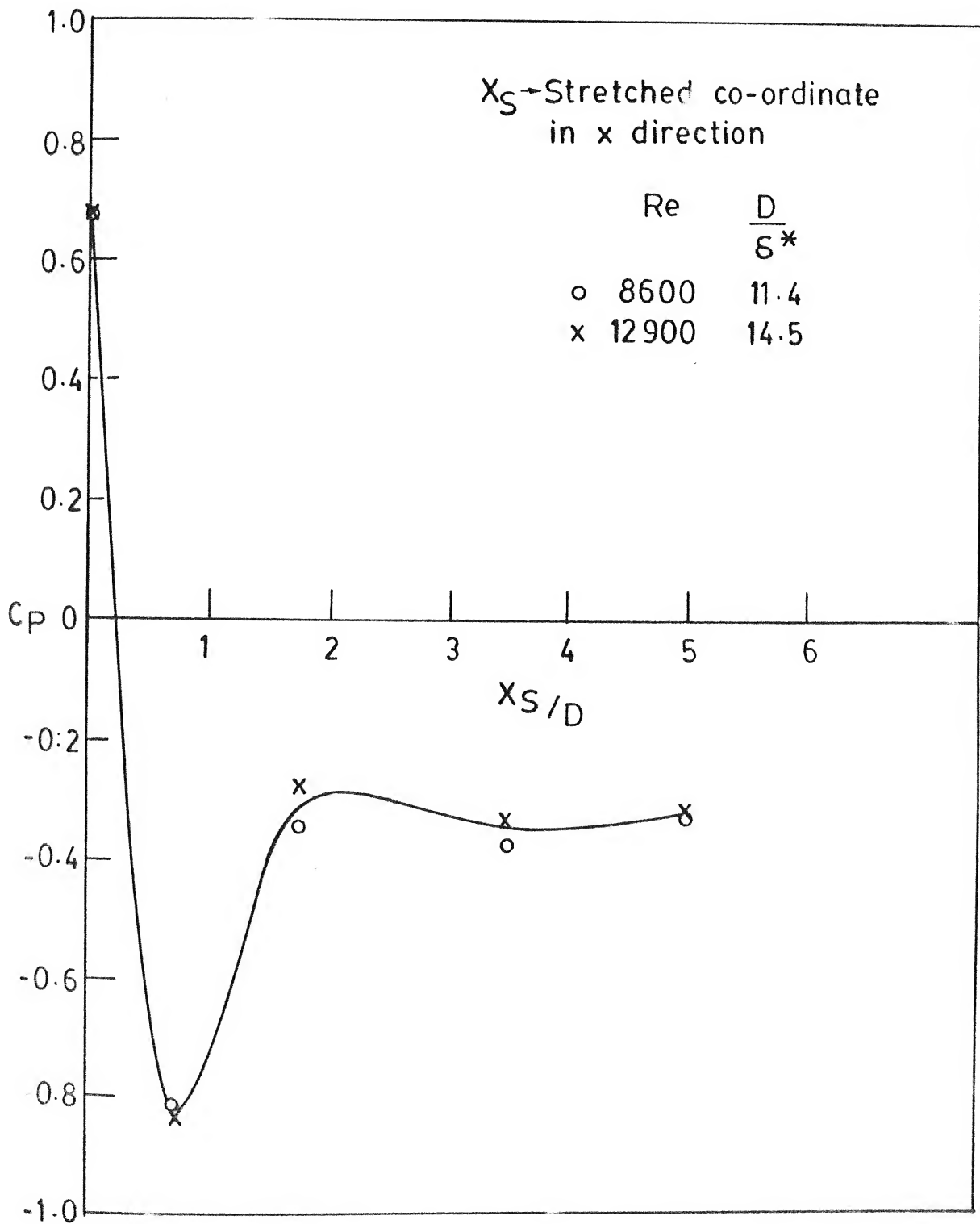


FIG. 4.10e. C_P VARIATION ALONG THE JUNCTION OF
ROUND NOSE PIER MODEL $L/D = 6$, $BR = 3\%$.

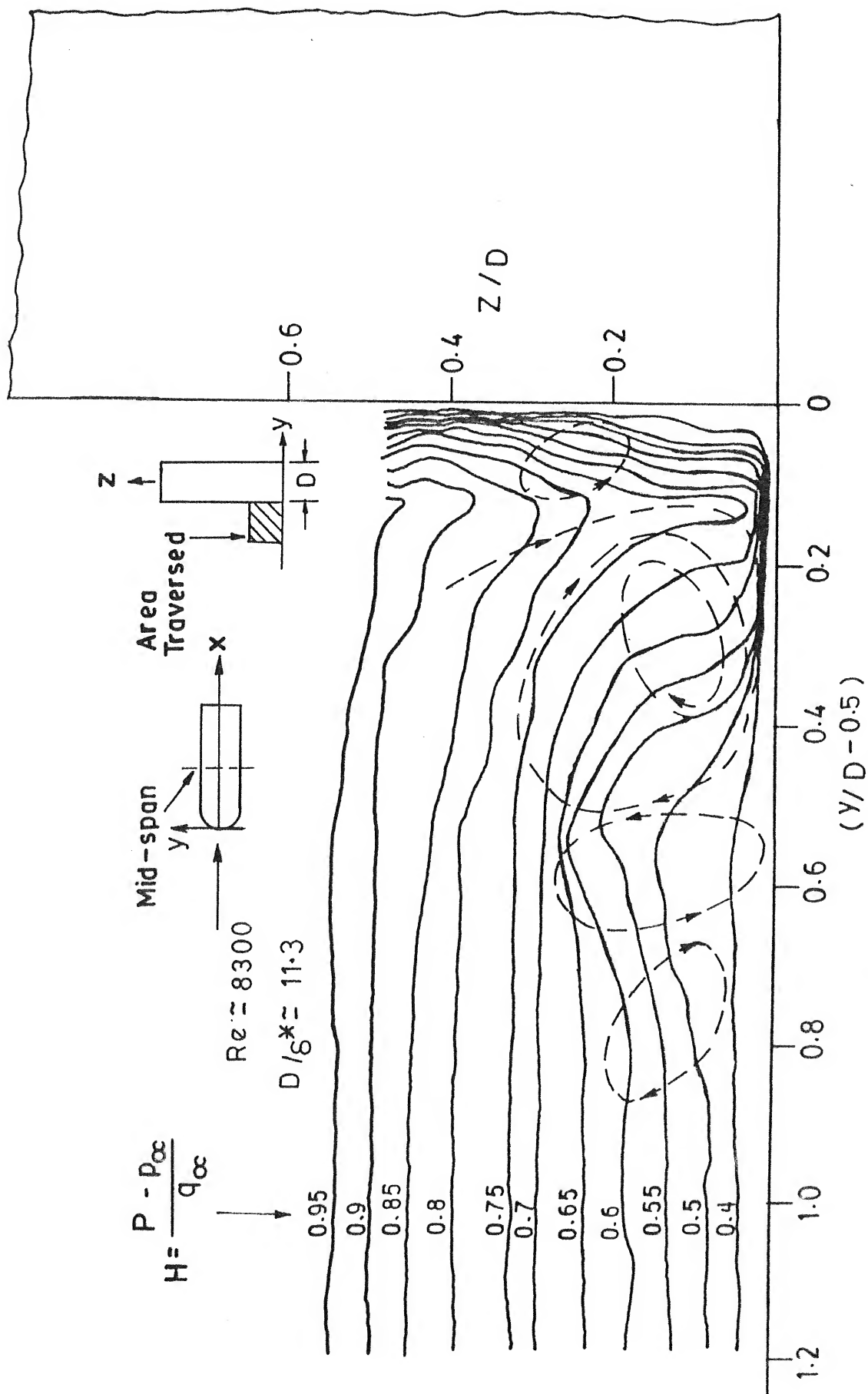


FIG 4.11 TOTAL HEAD CONTOURS IN THE $y-z$ PLANE AT MID-SPAN OF ROUND NOSED PIER MODEL. $L/D = 6$, $BR = 3\%$

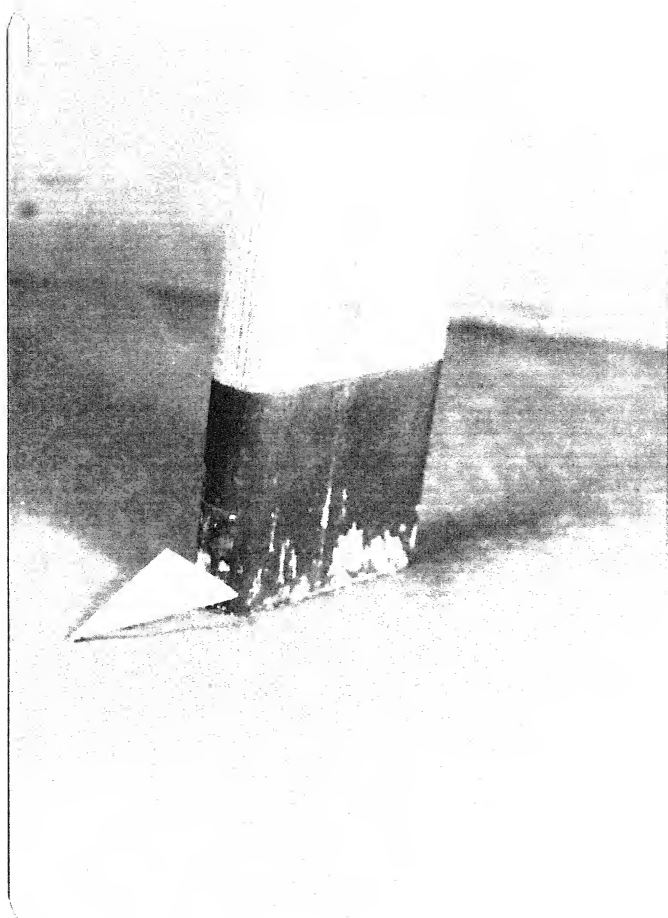


Fig.4.12 A VIEW OF ROUND NOSE PIER MODEL WITH
PASSIVE DEVICE

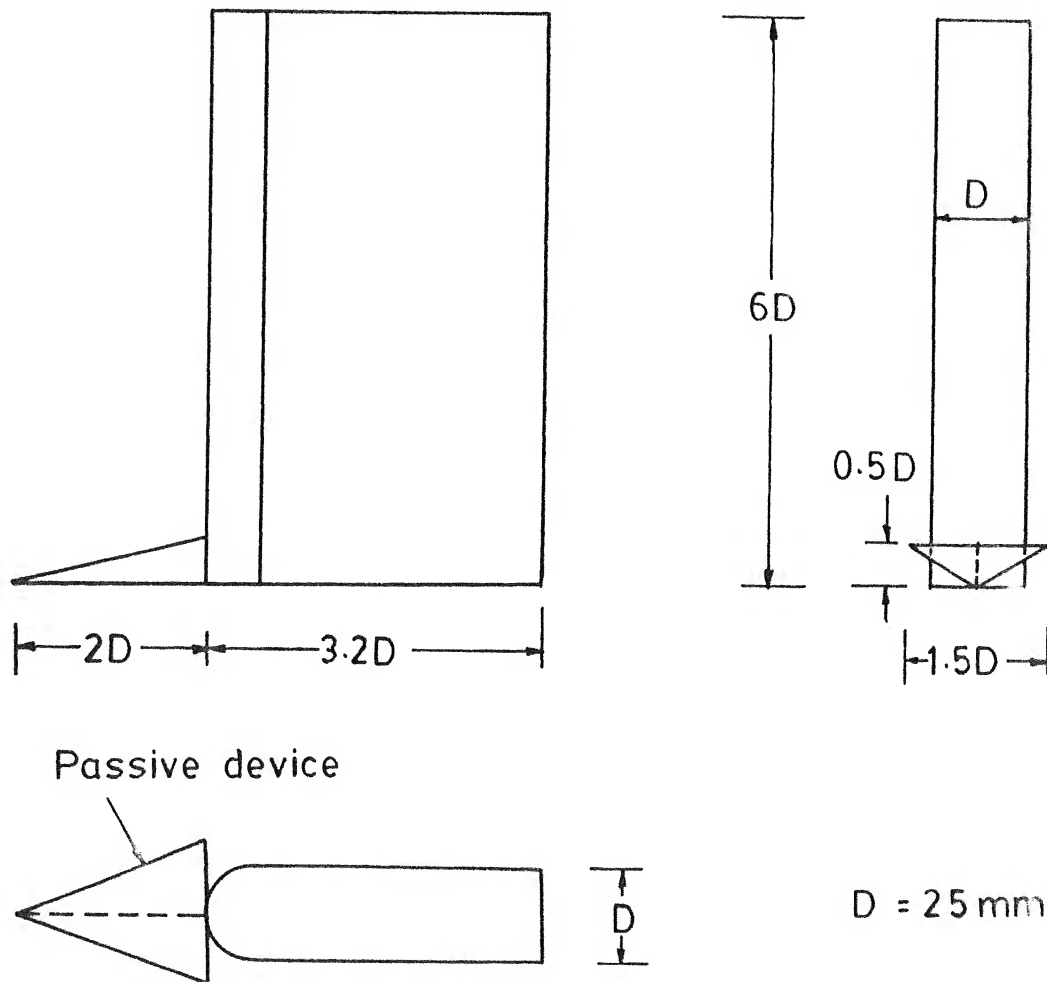
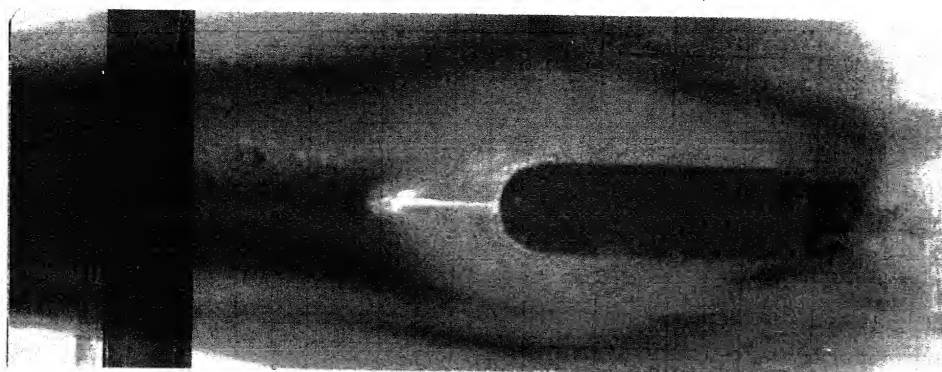
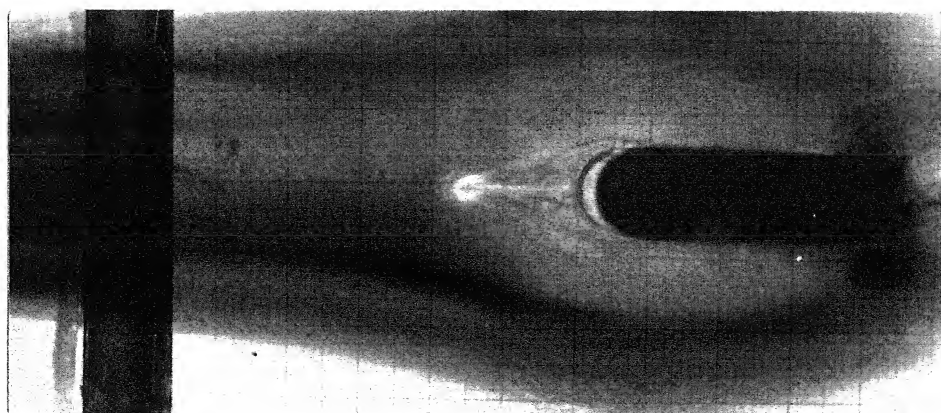


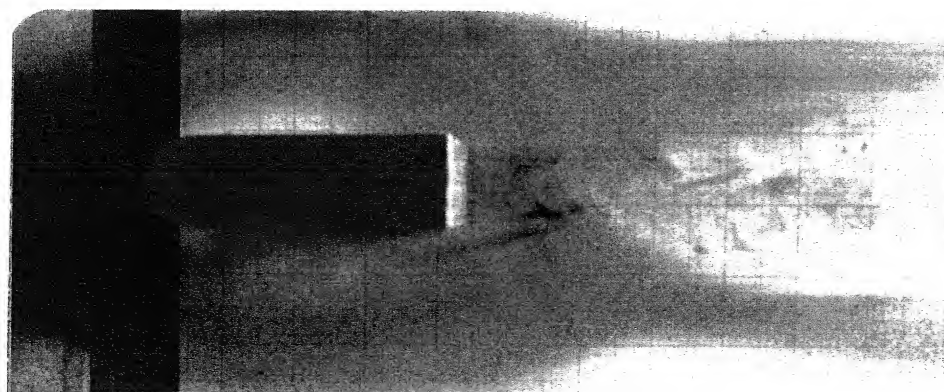
FIG. 4.13 A SKETCH OF ROUND NOSE PIER MODEL WITH PASSIVE DEVICE



a. PLAN VIEW

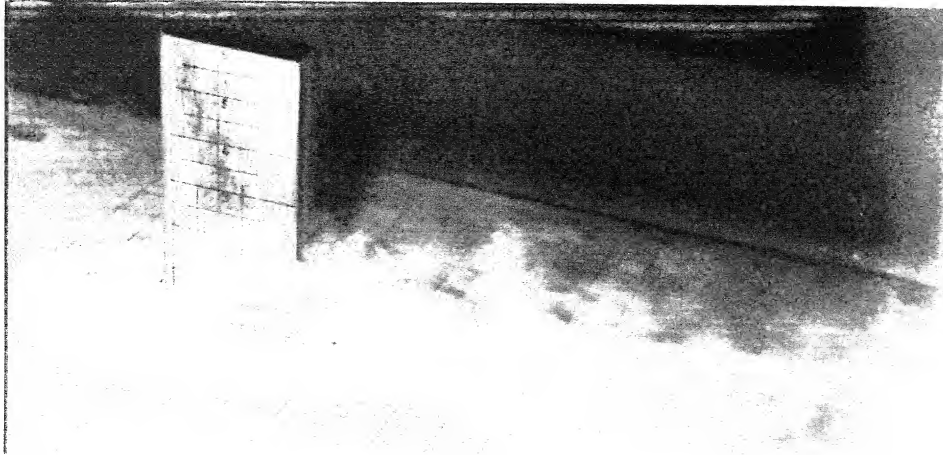


b. TOP FRONT VIEW

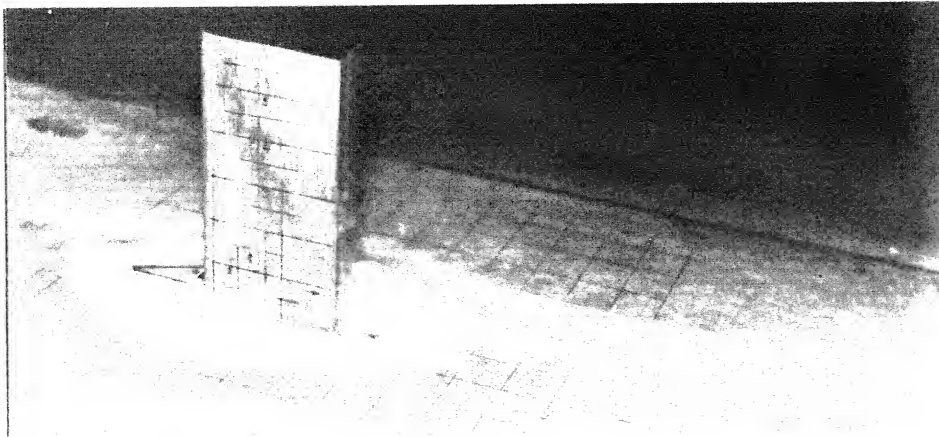


c. TOP REAR VIEW

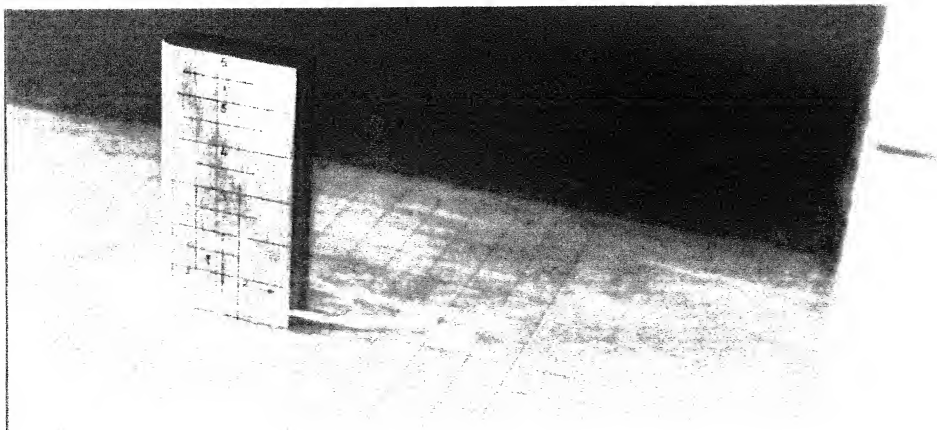
Fig. 4.14 DYE PATTERNS AROUND VERTICAL ROUND NOSE
PIER WITH PASSIVE DEVICE $L/D = 6$, $BR = 10\%$,
 $Re = 3026$, $Fr = 0.135$ (FLOW FROM LEFT TO
RIGHT)



a. GROSS PHENOMENON

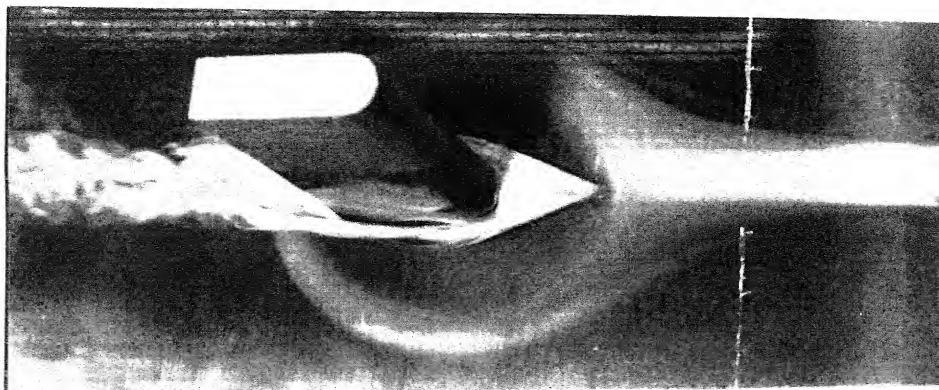


b. APEX VORTEX

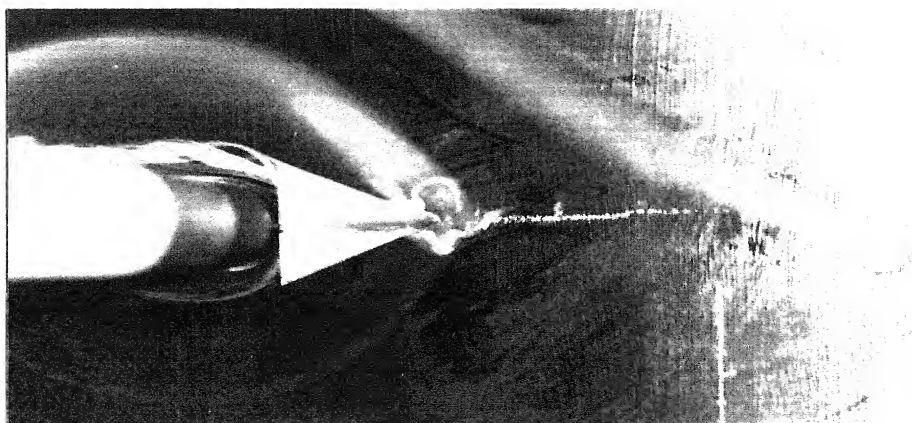


c. LESV

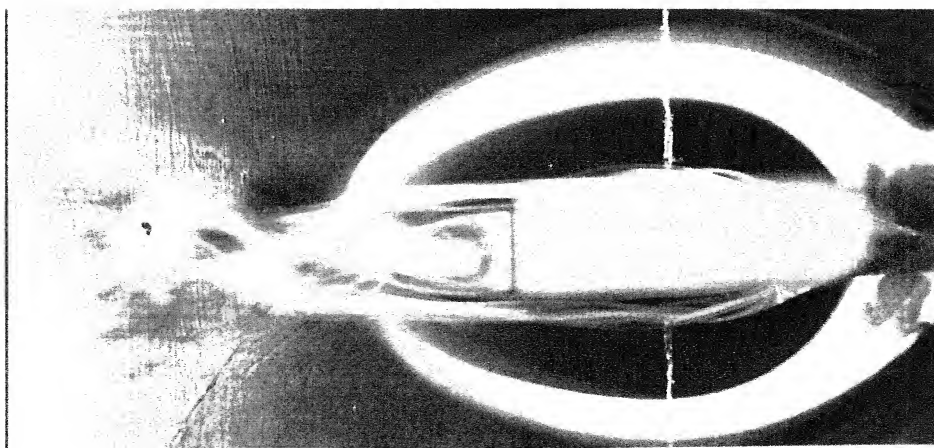
Fig. 4.15 TiCl_4 FLOW AROUND VERTICAL ROUND NOSE PIER
WITH PASSIVE DEVICE $L/D = 6$, $BR = 3\%$, $Re = 1400$,
 $D/\delta^* = 4.5$



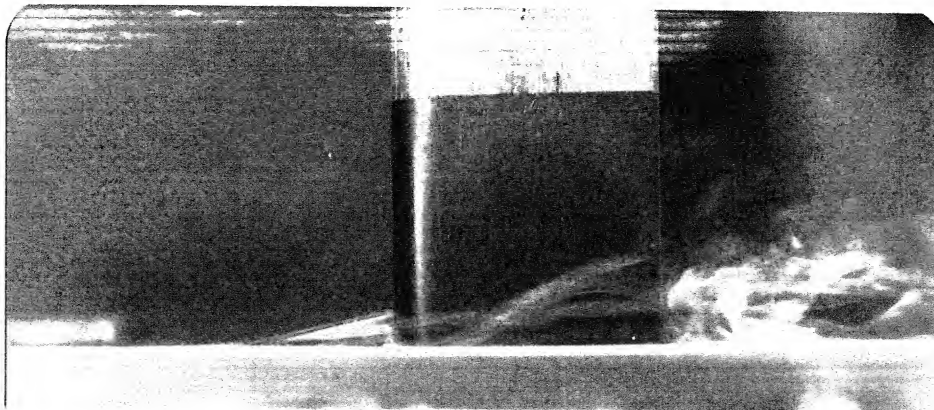
d. FRONT PERSPECTIVE VIEW



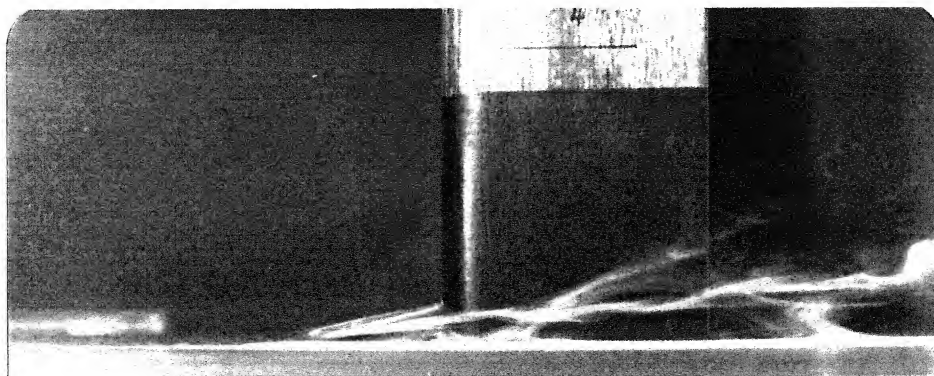
e. TOP FRONT VIEW



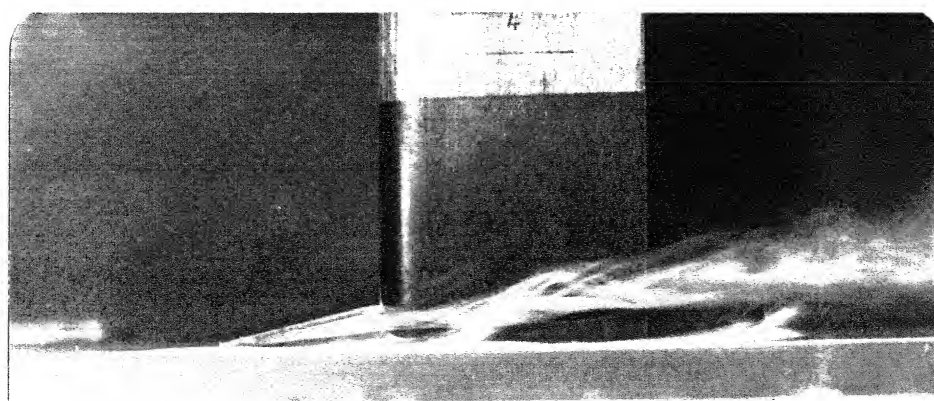
f. TOP REAR VIEW



g. SOMERSAULTING OF APEX VORTEX AT
PIER NOSE



h. CLOSE UP VIEW



i. MERGING OF LESV AND APEX VORTEX AT
 $Re = 1760$, $D/\lambda^* = 4.9$

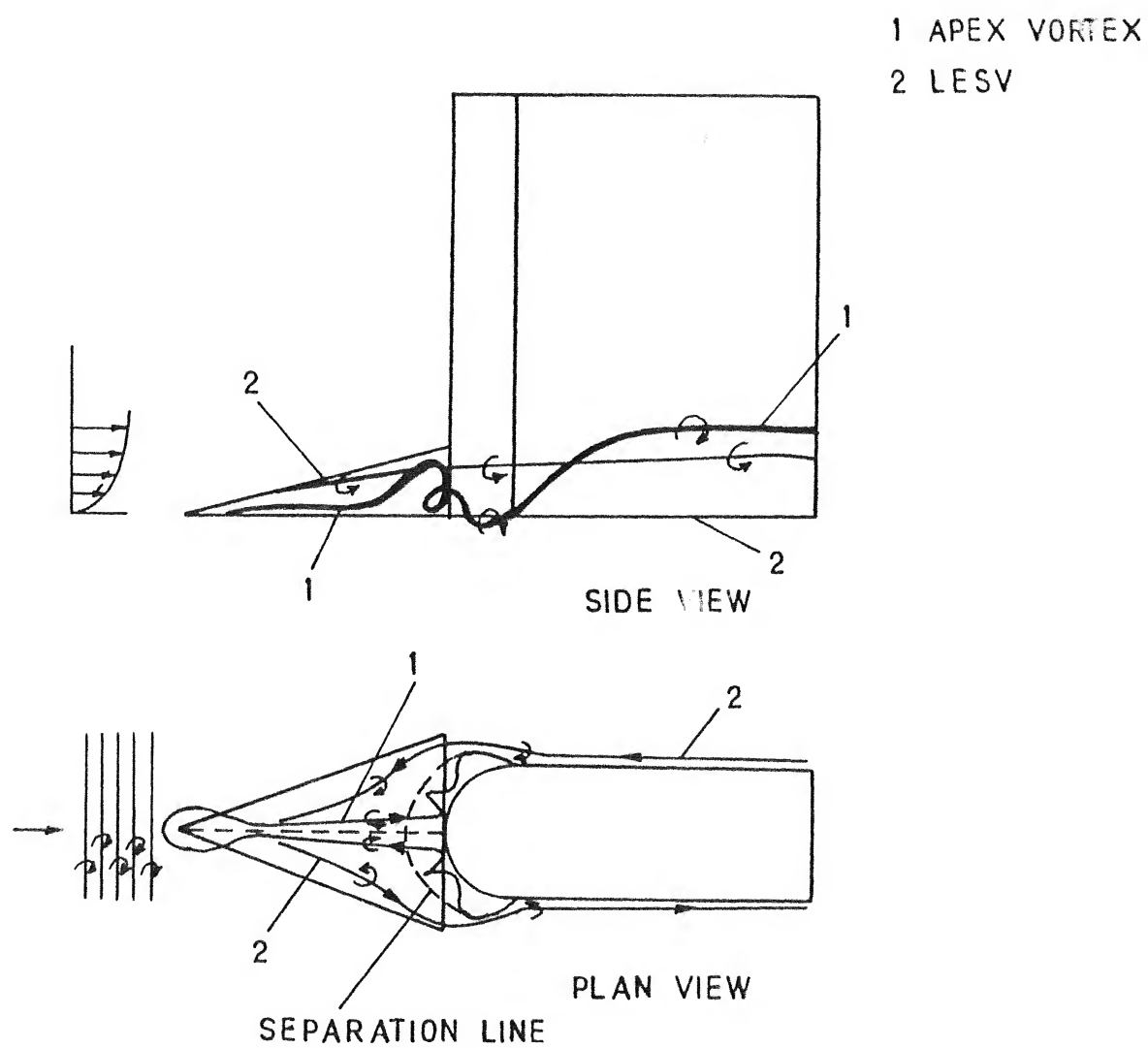


FIG. 4.16 SCHEMATIC VIEW OF MODIFIED VORTEX SYSTEM

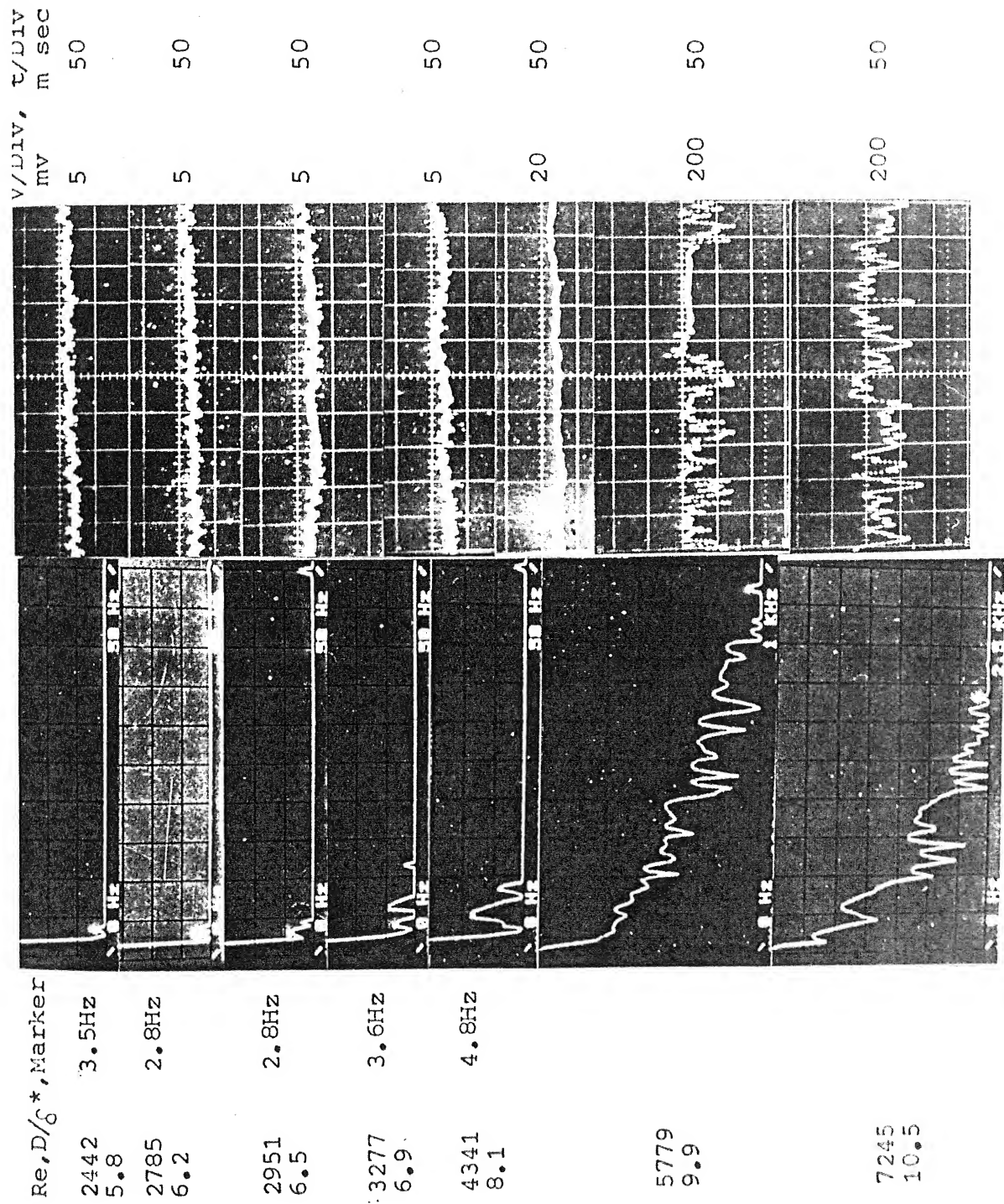


Fig. 4.17 SPECTRA AND TRACES OF MODIFIED VORTEX FLOW
 AROUND VERTICAL ROUND NOSE PIER MODEL $L/D = 6$,
 $ER = 3\%$

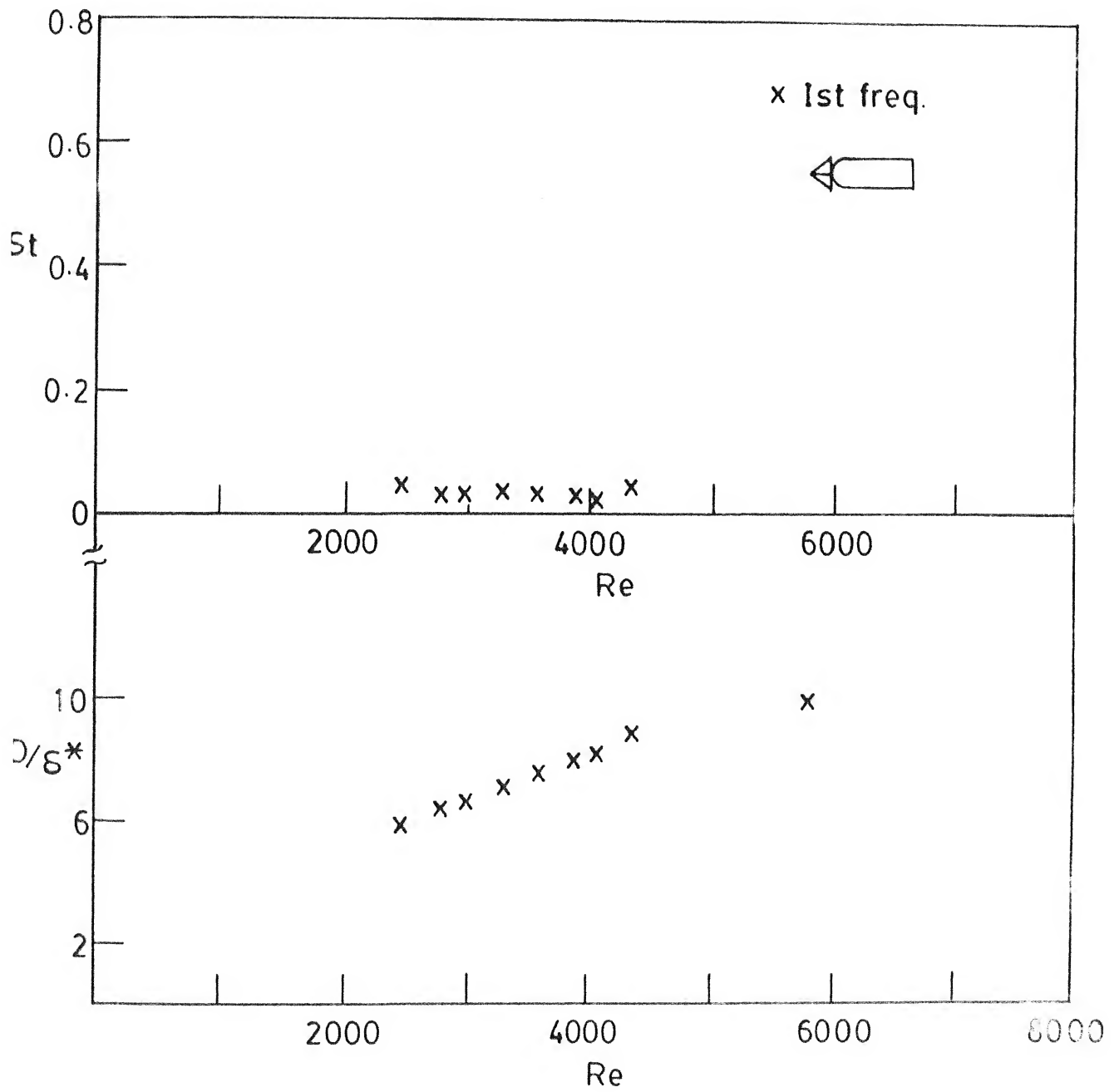
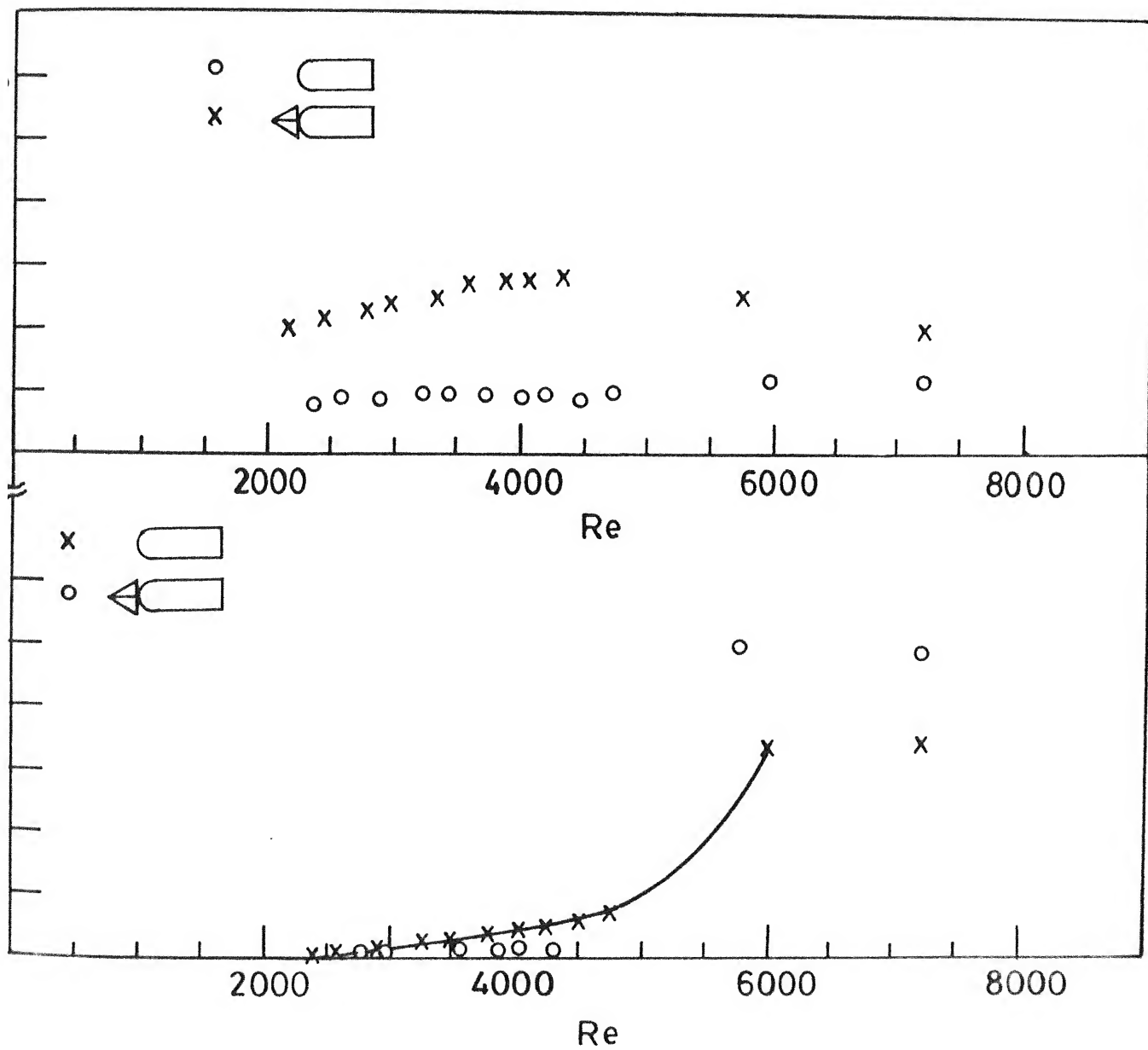
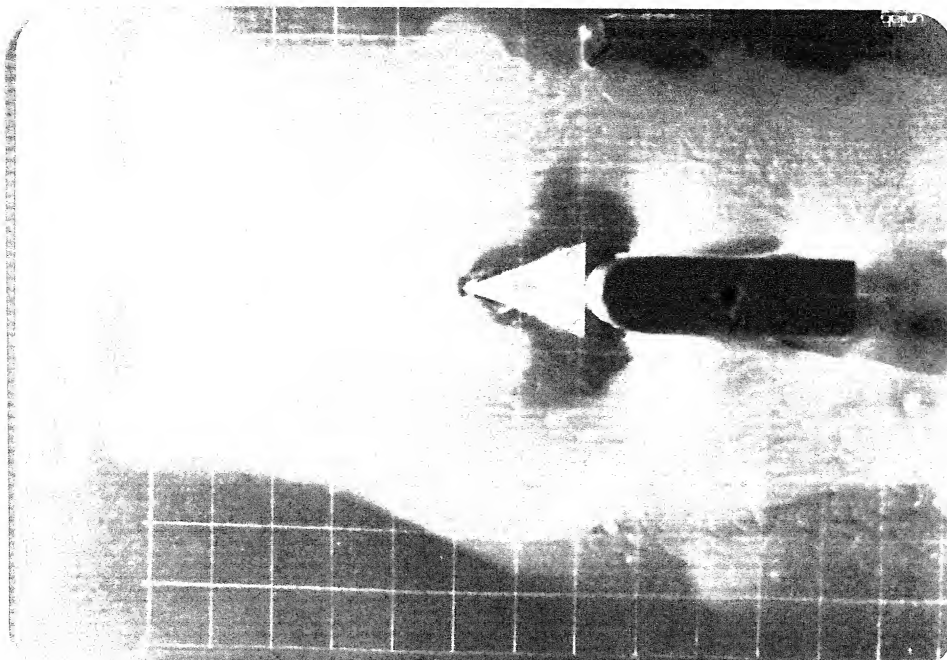


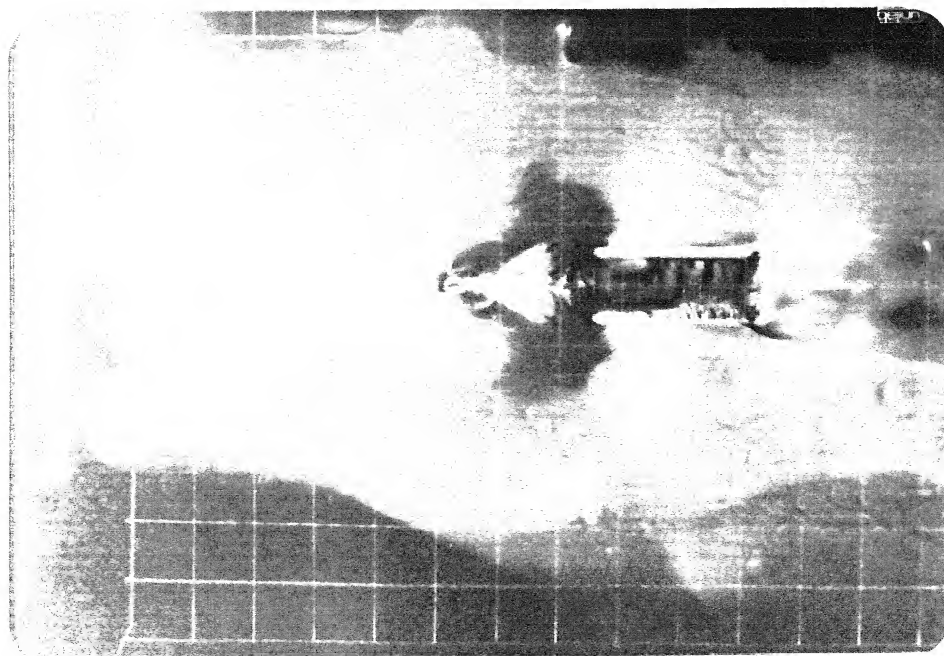
FIG.4.18a VARIATION OF MODIFIED VORTEX OSCILLATIONS AROUND VERTICAL ROUND NOSE PIER WITH PASSIVE DEVICE



.18 b VARIATION OF \bar{u} AND u' UPSTREAM OF ROUND NOSE PIER WITH AND WITHOUT PASSIVE DEVICE



$t = 12 \text{ Min. (FLOW ON)}$



$t = 12 \text{ Min.}$

Fig. 4.19 MODIFIED SURFACE OIL FILM PATTERNS AROUND VERTICAL ROUND NOSE PIER WITH PASSIVE DEVICE, $L/D = 6$, $BR = 3\%$, $Re = 7768$, $D/\ast = 11$ (FLOW FROM LEFT TO RIGHT)

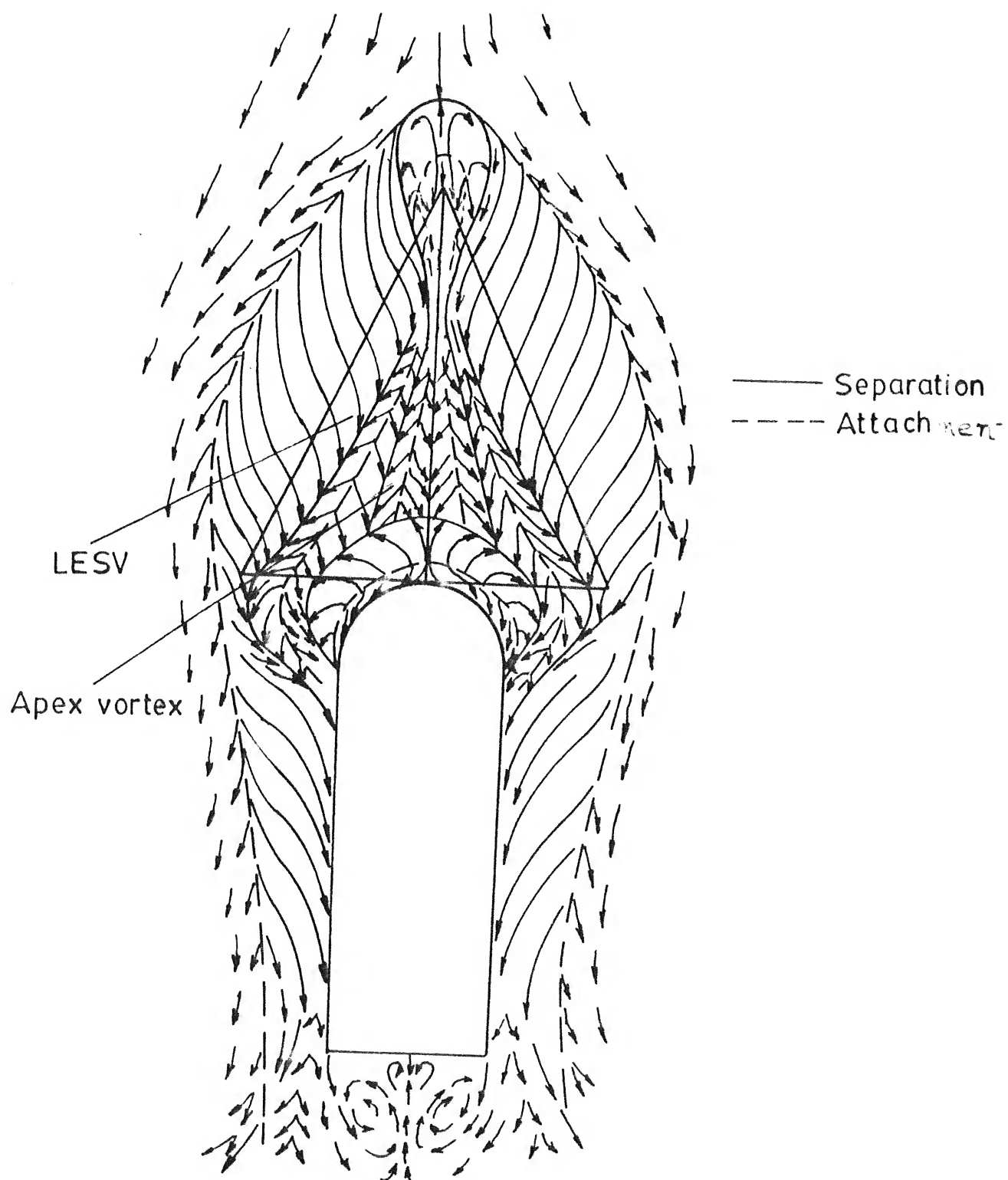


FIG. 4.20 MODIFIED SURFACE STREAMLINES AROUND
VERTICAL ROUND NOSE PIER $L/D=6$, $BR=3\%$

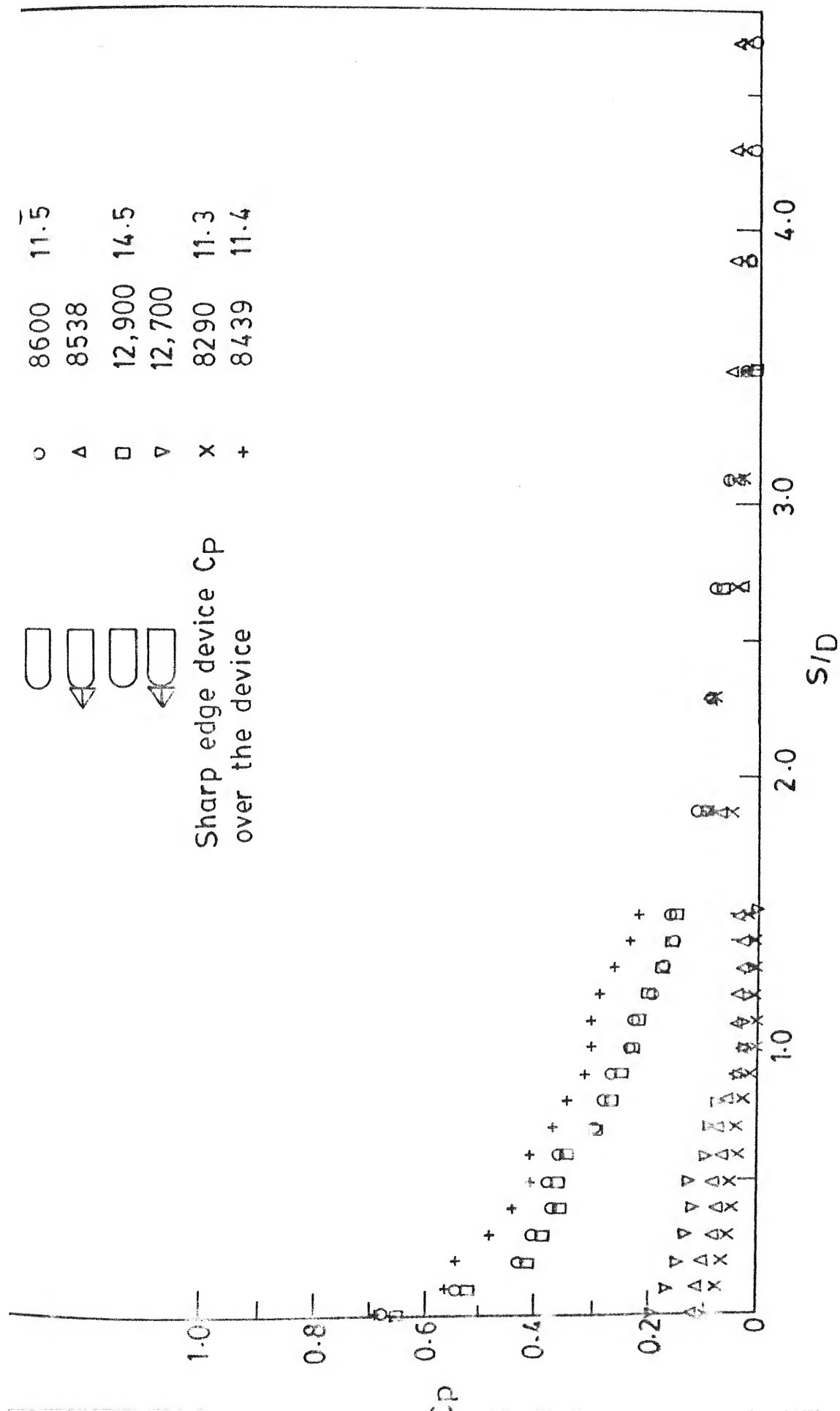


FIG. 4.21a PRESSURE DISTRIBUTION AROUND VERTICAL ROUND NOSE PIER WITH AND WITHOUT PASSIVE DEVICE ON UPSTREAM PLANE OF SYMMETRY

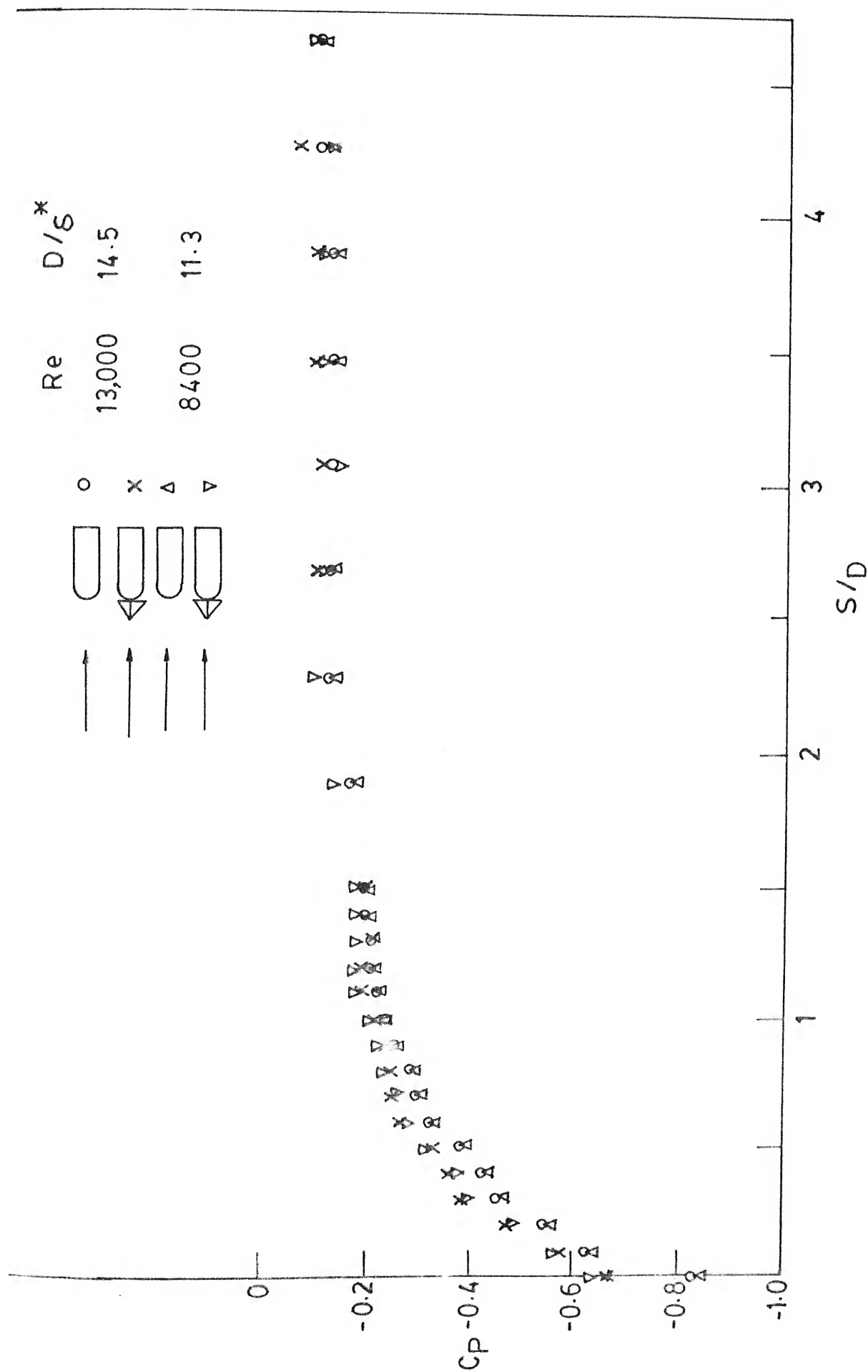


FIG. 4-21 b PRESSURE DISTRIBUTION AROUND VERTICAL ROUND NOSE PIER WITH AND WITHOUT PASSIVE DEVICE AT LEADING EDGE CORNER

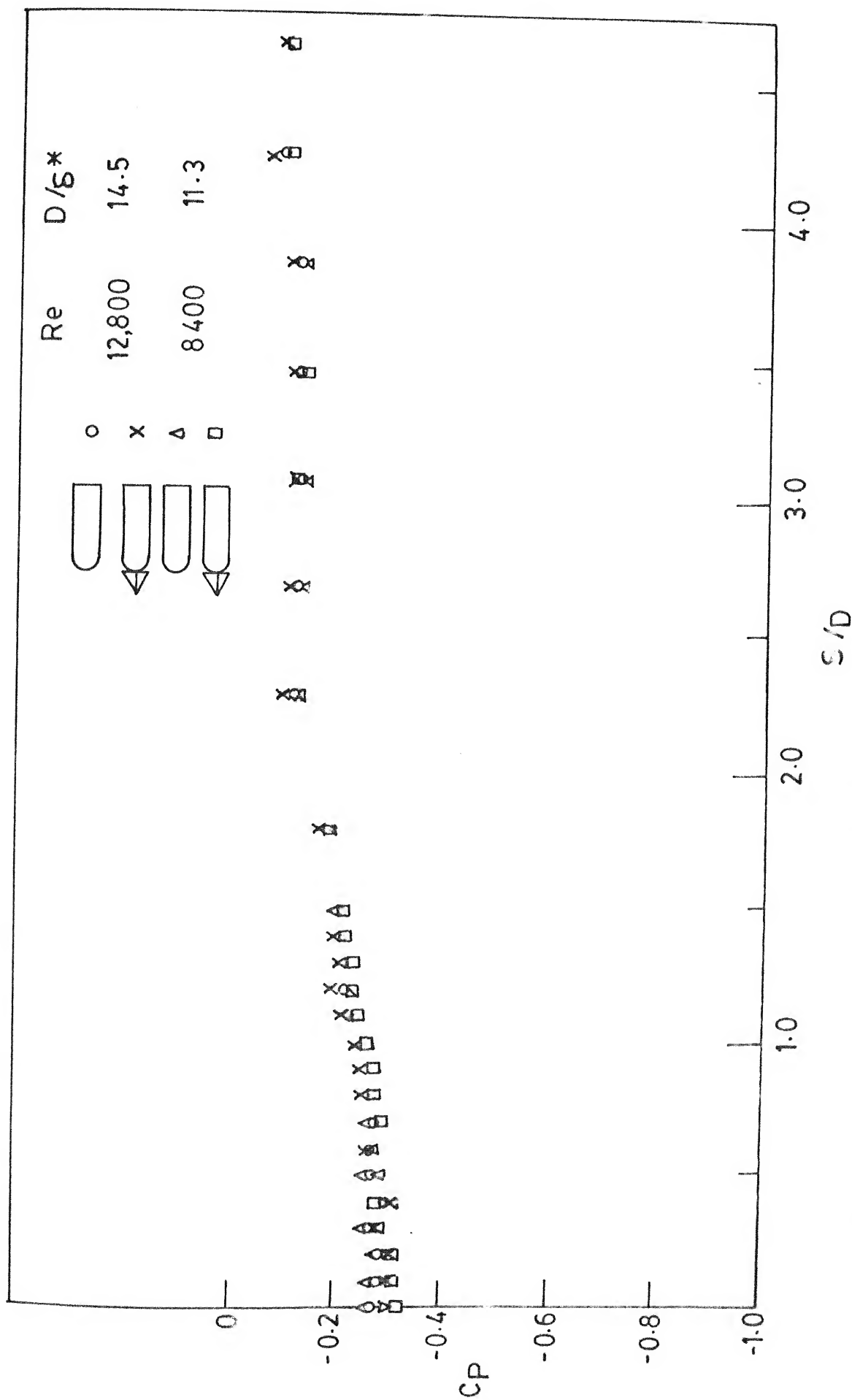


FIG. 4.21c PRESSURE DISTRIBUTION AROUND VERTICAL ROUND NOSE PIER WITH AND WITHOUT PASSIVE DEVICE AT MID-SPAN

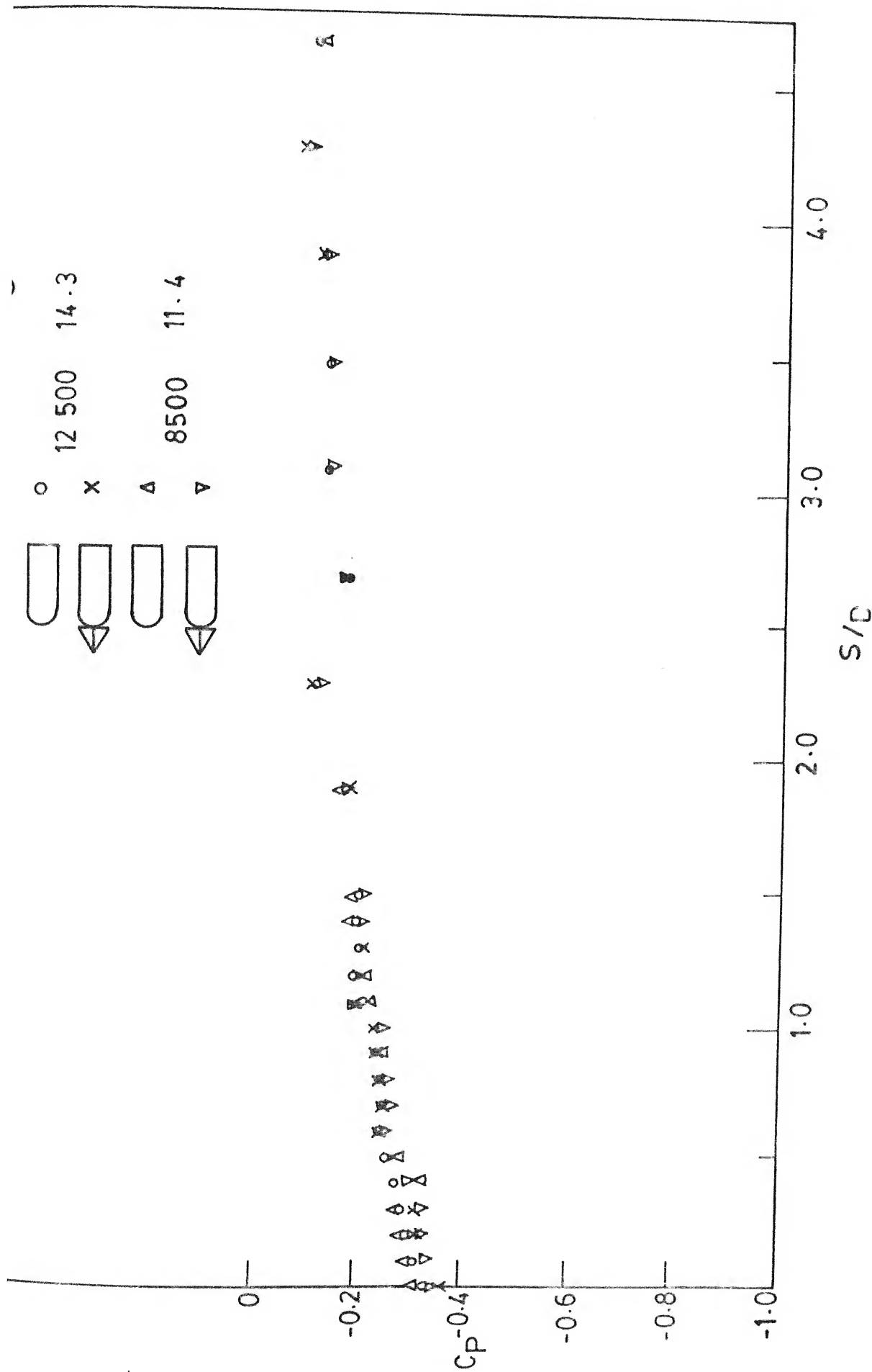


FIG. 4-21d PRESSURE DISTRIBUTION AROUND VERTICAL ROUND NOSE PIER WITH AND WITHOUT PASSIVE DEVICE AT TRAILING EDGE CORNER

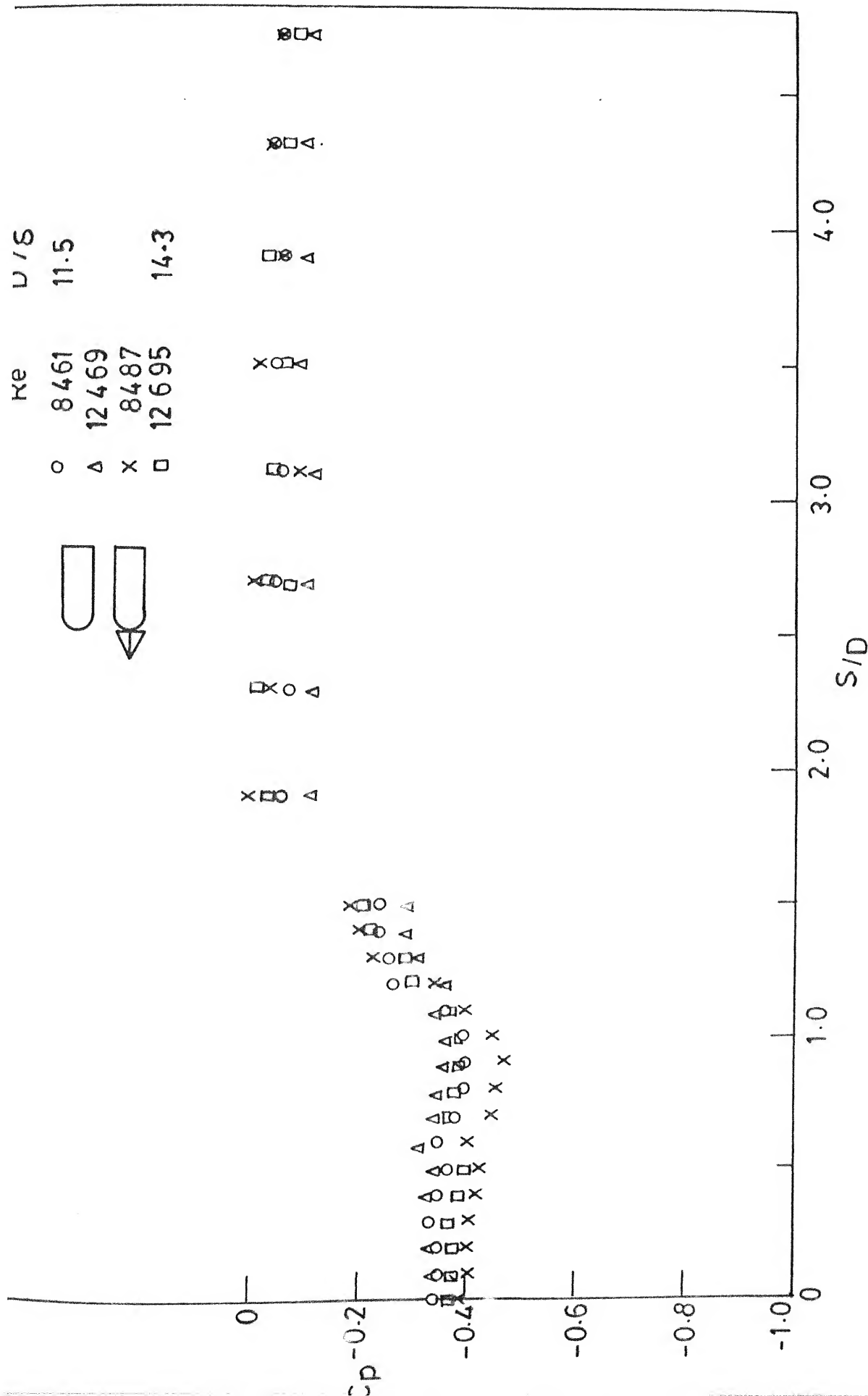


FIG 4-21 e PRESSURE DISTRIBUTION AROUND VERTICAL ROUND NOSE PIER WITH AND WITHOUT PASSIVE DEVICE ON DOWNSTREAM PLANE OF SYMMETRY

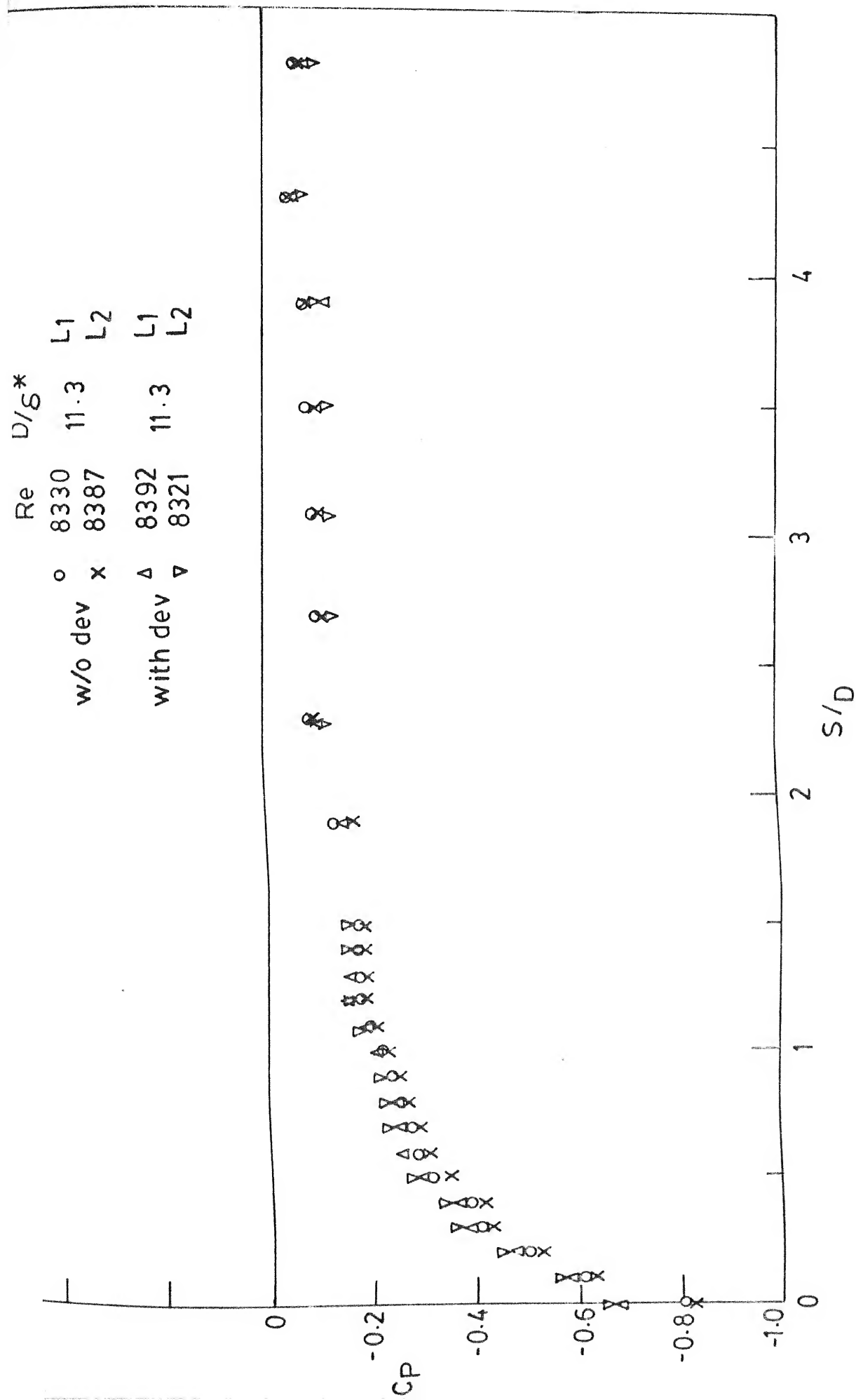


FIG. 4.22a PRESSURE DISTRIBUTION AROUND VERTICAL ROUND NOSE PIER AT LEADING
EDGE CORNER L1, L2

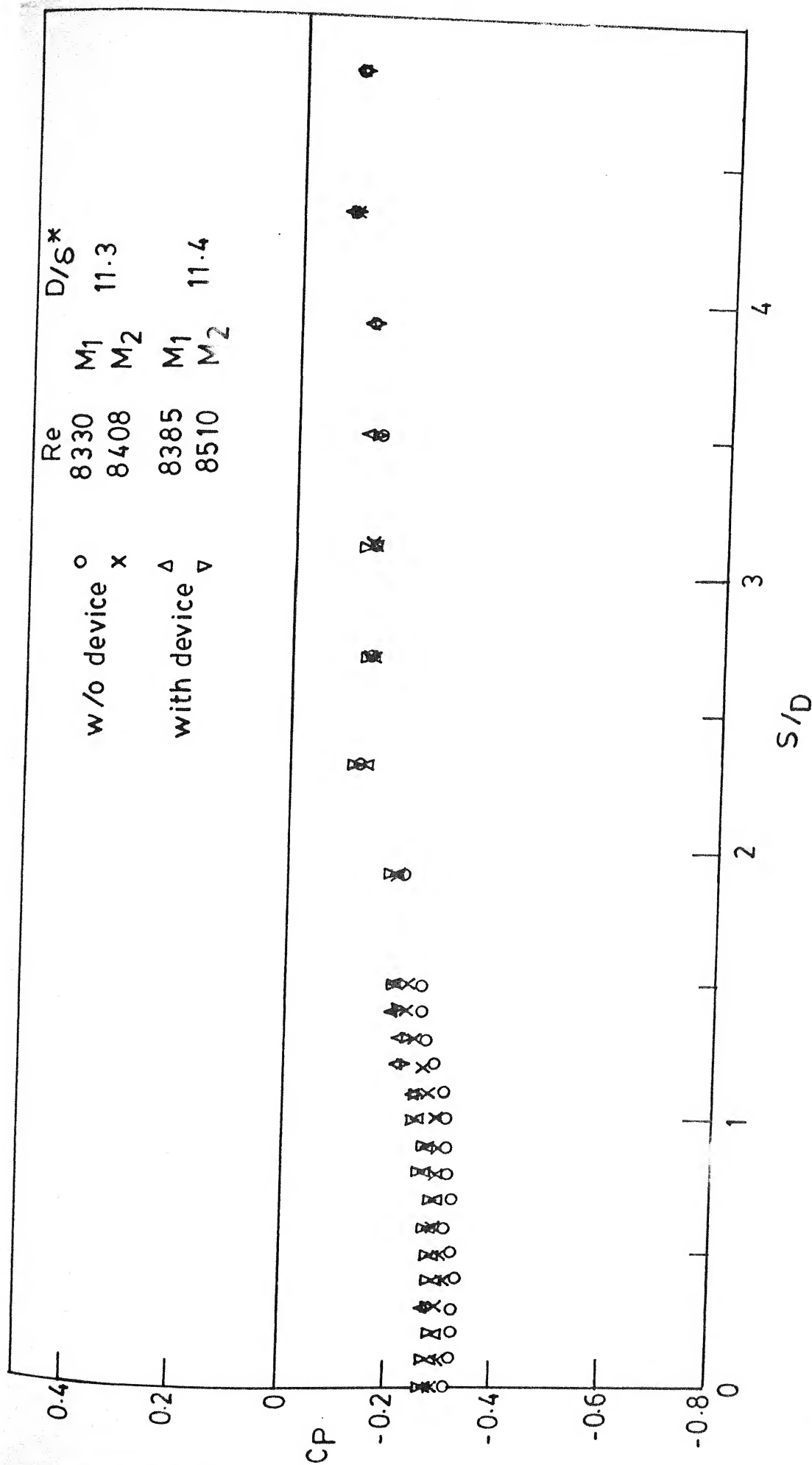


FIG. 4-22b PRESSURE DISTRIBUTION AROUND VERTICAL ROUND NOSE PIER AT MID-SPAN
 M_1, M_2

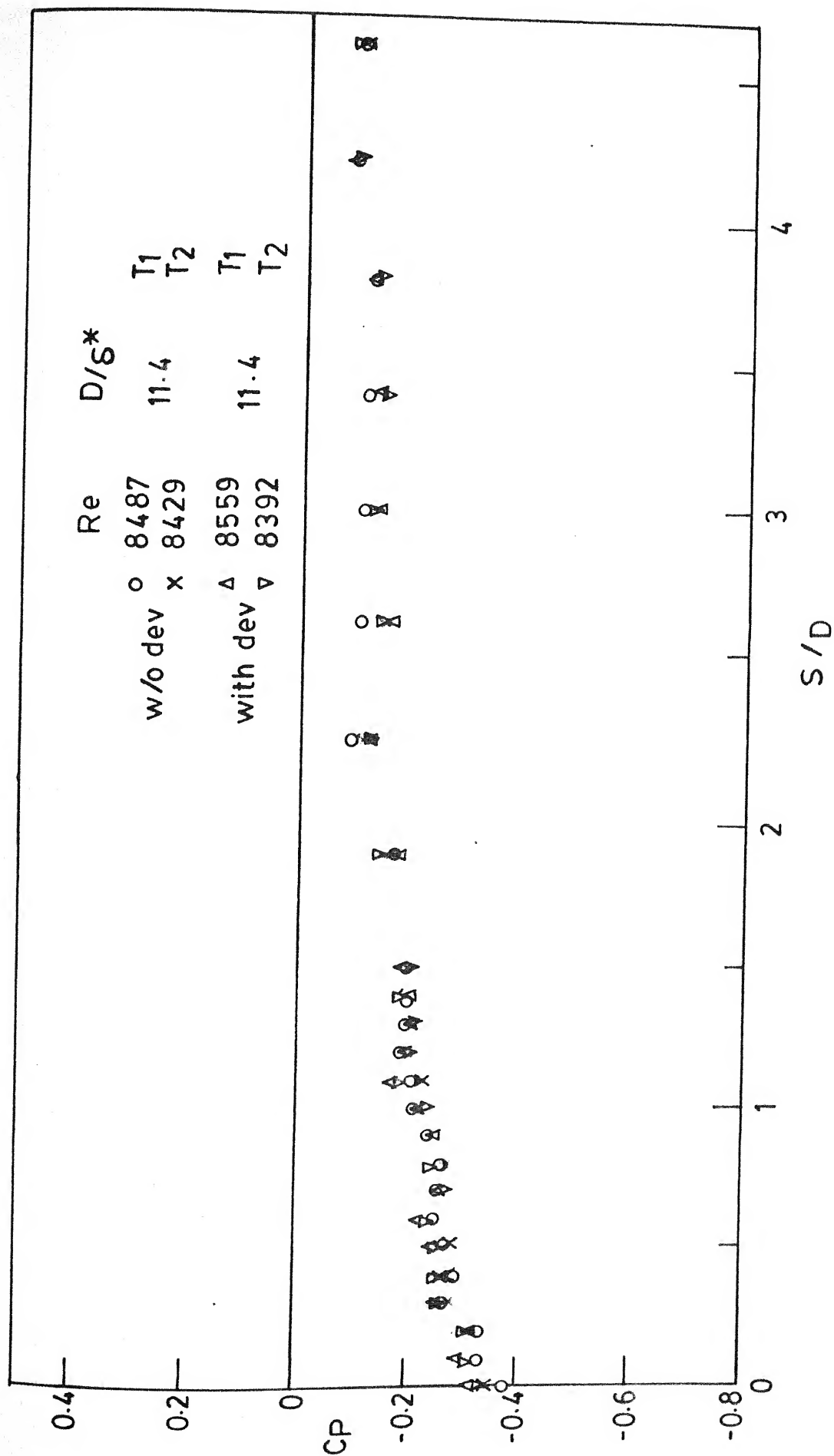
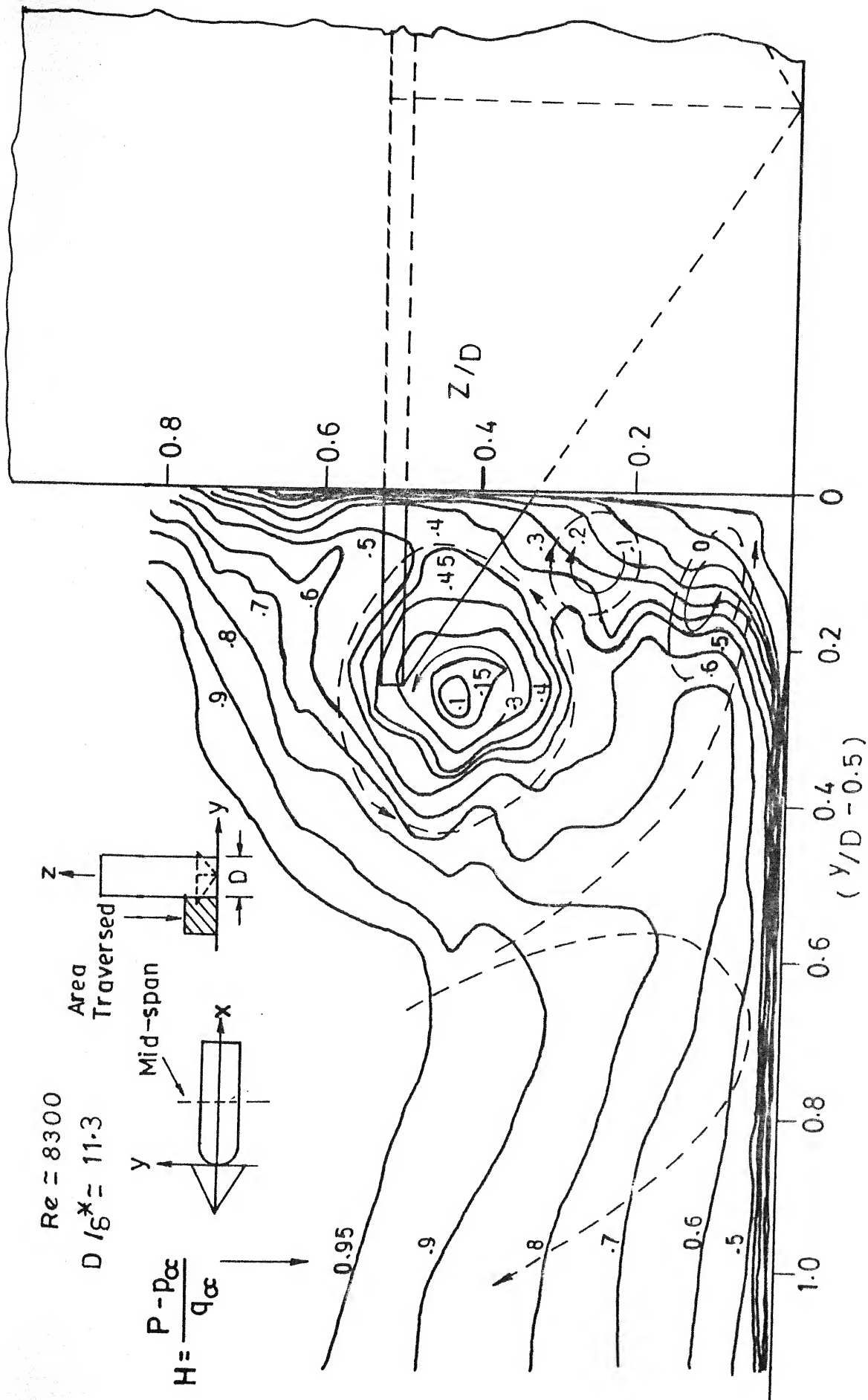


FIG. 4-22c PRESSURE DISTRIBUTION AROUND VERTICAL ROUND NOSE PIER AT TRAILING
EDGE CORNER T₁, T₂



4-23 TOTAL HEAD CONTOURS IN y - z PLANE AT MID-SPAN OF ROUND NOSED PIER MODEL WITH DEVICE

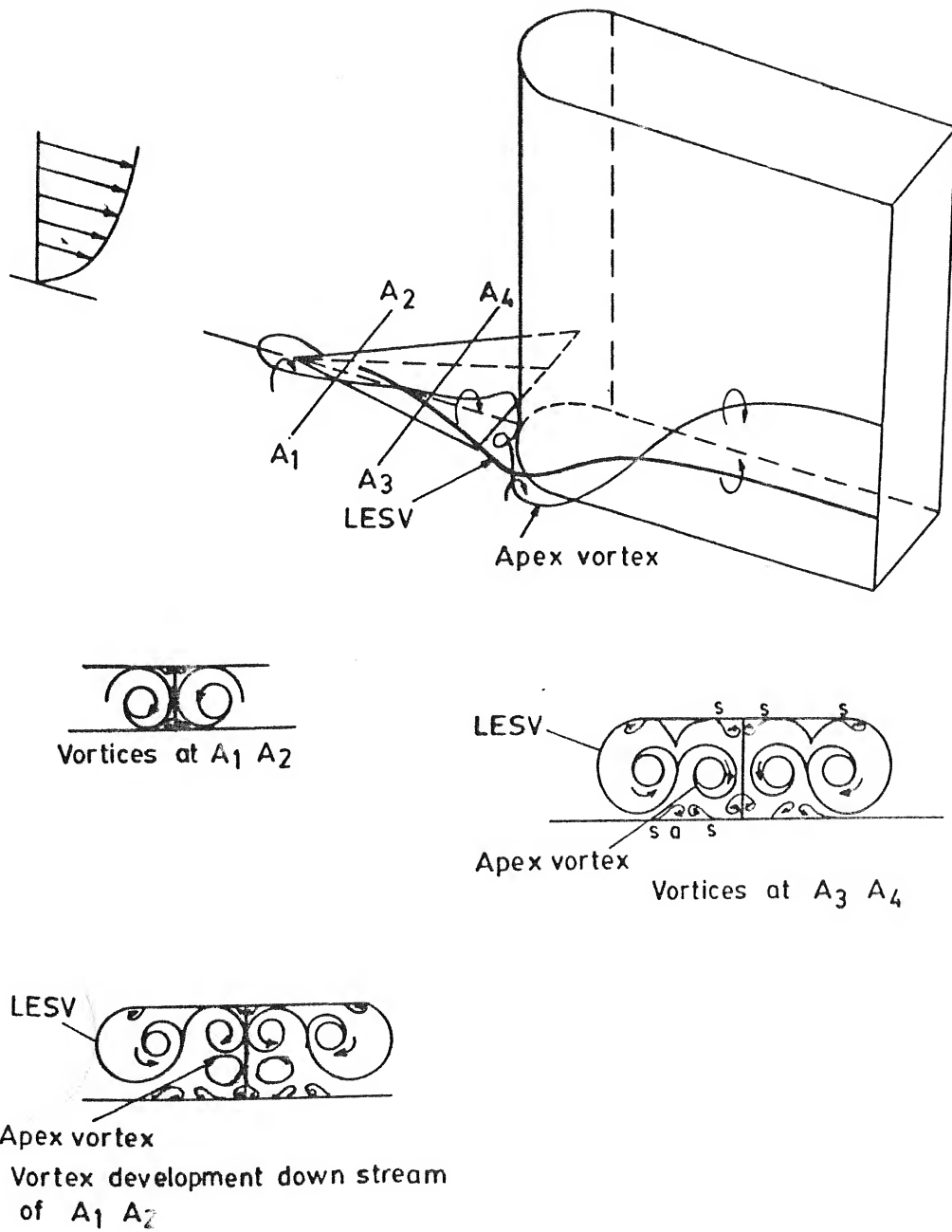
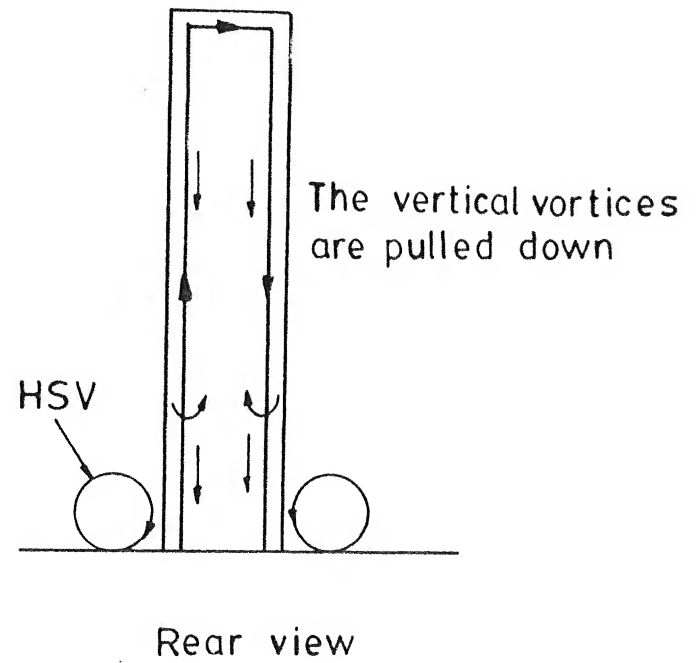
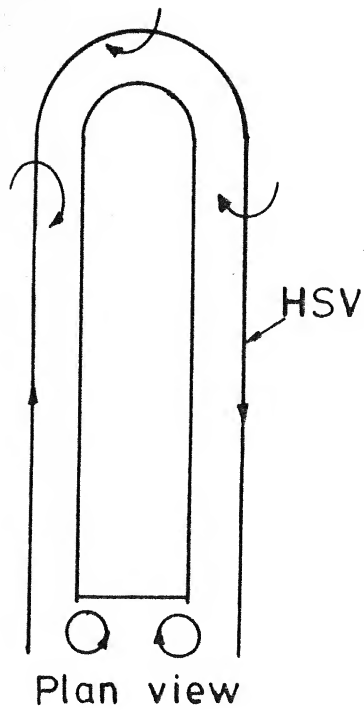
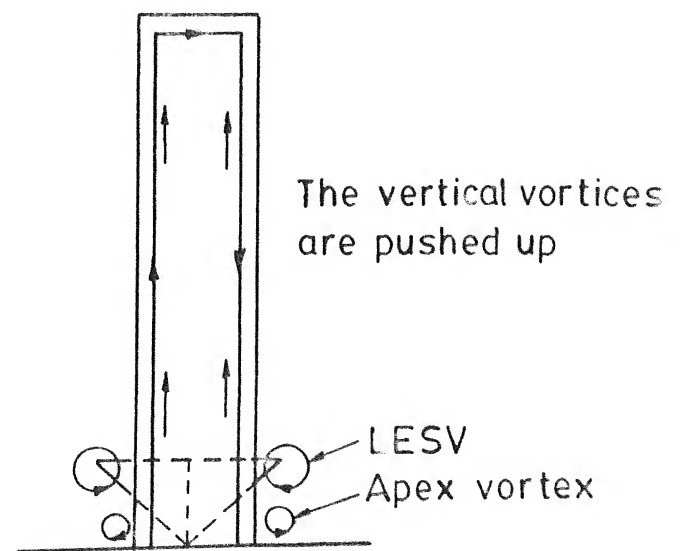
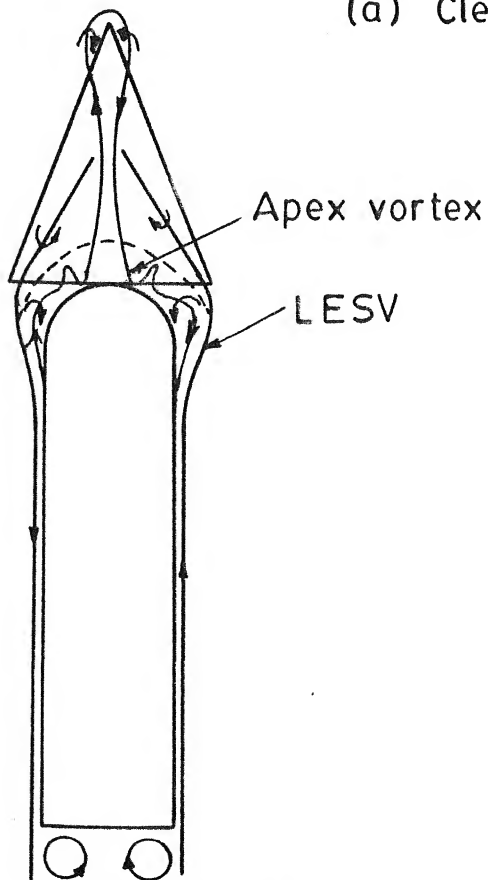


FIG. 4-24 SCHEMATIC OF VORTICES BELOW THE PASSIVE DEVICE



(a) Clean pier



(b) Modification with passive device

FIG.4.25 THE MODIFIED VORTEX FLOW AROUND VERTICAL PIER WITH ROUND NOSE

CHAPTER V

MODIFICATION OF HORSESHOE VORTEX AROUND WALL-CIRCULAR
CYLINDER JUNCTION

5.1 INTRODUCTION

The mechanism of hydrodynamic modification of horseshoe vortex (HSV) around a vertical pier with round nose, mounted on a flat wall, and the delta-wing-like passive device attached to its leading edge foot was explained in chapter IV. The modification of HSV around circular cylinder with the passive device fitted into its leading edge foot will be described in this chapter, by making use of the techniques and procedures employed in the previous chapter. The results with the clean cylinder are described first, followed by the modified results when the passive device was made use of and the discussion.

5.2 CO-ORDINATE SYSTEM

A right hand Cartesian co-ordinate system (X,Y,Z) with positive X taken on the downstream direction and the polar co-ordinate system (r,ϕ) with origin at the centre of the circle are used.

5.3 RESULTS WITH CLEAN CIRCULAR CYLINDER

The results on the clean circular cylinder are described in the following order of the flow approaching the circular cylinder : (i) laminar flow, (ii) transition to turbulent flow, and (iii) fully turbulent flow.

For the present results, the Reynolds number was increased/decreased by changing both the circular cylinder size and the flow speed.

5.3.1 Laminar Flow

The HSV around circular cylinder in approaching laminar flow was investigated by the visualization of flow with powdered KMnO_4 on a water table and TiCl_4 fumes in low speed, low turbulence wind tunnel and pressure measurements on the upstream plane of symmetry of the circular cylinder. The overall range of Reynolds number covered was $60 < \text{Re} < 3200$

a. Flow Visualization

The picture in Fig. 5.1 shows a perspective view of the dye flow around the junction of 25 mm diameter circular cylinder kept vertically in the test section of the water table. The dye flow experiments were conducted at a nominal water speed of 10 cm/sec, corresponding to $\text{Re} = 3197$, based on the 2.5 cm diameter of the cylinder and $\text{Fr} = 0.146$, based on the water depth of about 5 cm. The dye patterns obtained are shown in plan, top front and top rear views in the pictures of fig. 5.2 a, b and c respectively. The camera shutter time was 1/125 sec. Fig. 5.3 shows a composite outline of the flow, drawn from the three views of the dye pattern, showing the various salient dimensions in terms of the cylinder diameter, D . The region in between the solid line and the circular cylinder, (fig. 5.3), appearing white in figs. 5.2 a and b can be identified as the

local scour affected region around the circular cylinder and the red dye as the sand like sedimentary bed around a circular cylinder shape river bridge pier. The wake-vortex interaction is observed in fig. 5.2c, highlighting the formation of 'neck' like region, about $2D$ downstream of cylinder, due to the bending of the two streamwise arms of HSV, under the alternate pulling action of the two vertical vortices formed at the rear of the circular cylinder, causing a low pressure region in the near wake region of the cylinder, termed as vacuum cleaner action by Breusers et.al. (1977).

Figs. 5.4 a,b and c show pictures of $TiCl_4$ fumes around 25 mm diameter cylinder in perspective, top front and top rear views, at a nominal wind speed of 95 cm/sec. corresponding to $Re \approx 1450$ and $D/\delta^* \approx 4.5$. The liquid $TiCl_4$ was applied by Technique I described in chapter III. A line sketch of the plan view is shown in fig. 5.4d, drawn from the shots b and c. Two dominant rings of the accumulation of $TiCl_4$ fumes are observed in figs. 5.4 a and b which are identified as the two secondary vortices around the circular cylinder. A thread like region is also observed around the base of the cylinder in fig. 5.4a. Referring to Sutton's experiment in the frontispiece of Thwaites (1960), Baker (1979), reproduced in fig. 1.3 and as described in section 4.3.1 a of chapter IV, a six vortex system of HSV around circular cylinder is identified in fig 5.4. The present test conditions i.e., $Re \approx 1450$ and $D/\delta^* \approx 4.5$,

however, show a borderline case between two and four vortex system from fig. 6 of Baker (1979), for a circular cylinder of $\frac{L}{D} = 0.5$ and blockage ratio of 6.2%.

The bending of the streamwise arms of HSV is observed from the white impressions of the surface flow and the streamwise ends of the dense, white rings of the accumulation of TiCl_4 fumes (secondary vortices), in figs. 5.4 a,b and c. These secondary vortices were observed to get lifted up in the near wake region. Fig. 5.4c shows the low pressure region, from the TiCl_4 fumes in the near wake of the circular cylinder.

TiCl_4 flow visualization of HSV around circular cylinders of other diameters was also carried out under the same wind speed, and the model location. The results of this visual study are shown in Table 5.1. This is perhaps the first time that a picture of the multicellular HSV all around the circular cylinder in laminar flow has been presented from TiCl_4 flow visualization technique in a wind tunnel. It also verifies the multivortex structure of HSV presented by Baker (1979) with the independent technique of TiCl_4 flow visualization.

Table 5.1

179.

Structure of HSV around Circular Cylinder
junction in Laminar Flow

Sl. No.	Diameter (mm)	$\frac{L}{D}$	$Re = \frac{U_{\infty} D}{\nu}$	$\frac{D}{\delta^*}$	Vortex structure
1	50	6	2900	9	Oscillatory
2	37.5	6	2175	6.75	6 vortices
3	25	6	1450	4.5	6 vortices
4	12.5	6.4	725	2.25	4 vortices
5	6	9.2	363	1.13	4 vortices
6	3	∞	182	0.56	2 vortices
7	1	∞	60	0.19	2 vortices

b. Pressure Measurements

Fig. 5.5 shows the pressure distribution on the upstream plane of symmetry of the pressure model of circular cylinder at $Re=2200$, $D/\delta^*=5.5$. Three weak pressure dips at $0.9D$, $1.1D$ and $1.5D$ upstream of the centre of the cylinder are observed. Bělik (1973) and Baker (1979, 1980) identified such local dips of pressure associated with the core of primary horseshoe vortex. $TiCl_4$ flow visualization of HSV around 25 mm dia circular cylinder shows six vortex structure at $Re \approx 1450$ (figs. 5.4), before the oscillations of HSV appeared at increased wind speed. Three lower pressure regions, therefore, may be identified with the core locations of three primary vortices. Baker's (1979) data at $Re = 2050$, $D/\delta^* = 21.7$ (this was the lowest D/δ^* reported) is shown on the same plot and appears in good qualitative agreement. However, Baker's (1979) data shows one strong pressure dip at about $0.7D$ from the centre of cylinder.

5.3.2 Transition to Turbulent Flow

The oscillatory behaviour of HSV was probed by a 'u' sensitive hot wire inserted from the top of the wind tunnel test section maintaining the same location of the hot wire probe from the floor and surface of the circular cylinder, and in the same manner as in the case of round nose pier in section 4.3.2.

The pictures of spectra and traces of hot wire signals of HSV oscillations with increasing wind speed are presented in fig. 5.6a. Steady oscillations of HSV with a frequency of 11.2 Hz appear around $Re = 2440$ and $D/\delta^* = 6$. Steady, distinct and discrete frequencies of HSV oscillation alongwith higher harmonics are observed as the wind speed is gradually increased, till the onset of mixed frequencies at $Re \approx 4200$, $D/\delta^* \approx 7.5$, beyond which it tends to become turbulent flow. Highly random behaviour of HSV oscillations was reported by Baker (1979) from wind tunnel experiments. The range of Strouhal frequency observed was $0.26 < St < 0.40$, with $St \approx 0.6$ at higher Re . A detail discussion is given in 5.5.1.

The variation of Strouhal frequency, St with Re and D/δ^* in fig. 5.6b shows $St \approx 0.2$ with higher harmonics in the range $2200 < Re < 4400$ and $6 < D/\delta^* < 10$. The local mean velocity \bar{u} is observed to be about 0.10 of U_∞ and u' increases from about zero to 0.015 of U_∞ in the above range of Re and D/δ^* in fig. 5.6c. Beyond this range a number of mixed frequencies with intermittent bursts of turbulence started appearing, and appears to be associated with the transition in the free stream from fig. 3.5a. The local mean velocity \bar{u} becomes steady at about 0.11 of U_∞ upto $Re \approx 7500$ and u' rises to about 0.07 U_∞ at $Re \approx 6,000$. It may be observed from figs. 4.6 and 4.7 that the oscillatory behaviour of HSV around the vertical pier with round nose appears similar to that around circular cylinder.

ring like patterns and the outer region consisting of two nearly clear arc like patches. These two regions are distinguished by the outer boundary of the inner region, identified as the primary separation line S , located at a radius of about $1.2D$ from the centre of the circle. The region downstream of this separation line is the space occupied by the HSV and is interpreted from Baker (1980) as follows : the narrow clear region around the circle is identified as due to the secondary vortex O , similar to the one observed around the cylinder in $TiCl_4$ flow visualization in figs. 5.4a and b, and the powder-oil accumulation in between the separation line S and the vortex O is identified as the secondary vortex on the surface, and its downstream edge as the secondary separation line S_1 . The saddle point of primary separation, though not clearly visible, should lie on the primary separation line S . The nodal point of attachment between these two saddle points S and S_1 (Hunt et.al., 1978) is not distinguishable in this picture. The streamwise arm of the HSV at mid-span of the cylinder shows a continuation of the thread like ring from the upstream side, and showing a clear region in between this line and the cylinder, and three other regions of varying density of the suspension mixture. It, therefore, shows that there is a four vortex system around 50 mm dia. cylinder at $Re = 15536$, $D/\delta^* = 22$. Furthermore, it may be observed from figs. 5.8 and 5.9, that for 37.5 mm and 25 mm diameter cylinders, at $Re = 11652$, $D/\delta^* = 16.5$ and $Re = 7768$, $D/\delta^* = 11$ respectively,

the surface oil film patterns appear similar to that around 50 mm diameter cylinder. It can, therefore, be inferred from above that the four vortex system of HSV exists around these two circular cylinders as well.

Figs. 5.10 a and b show the pictures of surface oil film pattern around 12.5 mm circular cylinder, at $Re = 3884$ and $D/S^* = 5.5$, taken after 10 minutes of tunnel run. The primary separation line S , is identified in the similar manner as for the 50 mm diameter cylinder, and in between this line and the cylinder, there appears a thread like narrow ring encircling the 12.5 mm dia cylinder in shot 'a', which referring to fig. 1.2, is identified as vortex O and it is inferred that it is a two vortex structure. It may also be observed that the overall characteristics of this flow pattern appear different from the four vortex patterns. The surface flow patterns in figs. 5.11 and 5.12, around circular cylinders of diameter 6 and 3 mm respectively appear, similar to around 12.5 mm diameter cylinder. It is, therefore, inferred from above that for Reynolds number below 4000, it is two vortex system of HSV around circular cylinder. Figs. 5.12 a and b show line sketches of the four and two vortex structures.

These observations are summarised in Table 5.2, which also includes x_s and x_{s_1} , the distances from cylinder's centre to the separation line S and S_1 , on the upstream plane of symmetry and w the maximum lateral width of the surface pattern. The variations of x_s/D and w/D are plotted in fig. 5.14.

Table 5.2

185.

Summary of results from Surface Flow Patterns

Sr.No.	Cylinder dia mm.	$Re = \frac{U_{\infty} D}{\nu}$	$\frac{D}{\delta^*}$	No. of vorti- ces	$\frac{x_s}{D}$	$\frac{x_{s1}}{D}$	$\frac{w}{D}$
1	50	15,536	22	4	1.19	0.67	2.52
2	37.5	11,652	16.5	4	1.26	0.69	2.78
3	25	7,768	11	4	1.33	0.67	3.07
4	12.5	3,884	5.5	2	1.64	-	3.0
5	6	1,942	2.75	2	1.74	-	4.0
6	3	971	1.38	2	1.54	-	3.68

which shows that x_s/D increases with Re upto $Re \approx 2,000$ and decreases rapidly upto $Re \approx 8,000$, beyond which the decrease in x_s/D appears to be almost asymptotic. The variation of w/D appears to follow the similar trend and $\frac{x_{s1}}{D}$ appears to remain constant for this Re No. range.

b. Pressure Measurements

(i) Floor Pressures Around the Cylinder

Detail pressures on the floor around the pressure model of circular cylinder were measured at $Re \approx 8600$, $D/\delta^* \approx 11.6$, and $Re \approx 13,000$, $D/\delta^* \approx 14.5$ at the angular positions (fig. 3.3) $\phi=0^\circ$, $\pm 20^\circ$, $\pm 45^\circ$, $\pm 90^\circ$, $\pm 135^\circ$ and 180° . The pressure distribution on the upstream plane of symmetry of the circular cylinder is presented in fig. 5.15a. The adverse pressure gradient begins to appear at about $4D$ upstream of the centre of the cylinder and builds up rapidly within about $2D$ close to the cylinder. A weak dip in the pressure is observed at about $0.9D$ upstream and is identified as the core location of the primary vortex from Bělik (1973) and Baker (1980), whose data are also plotted for the sake of comparison. The details of complete test conditions of Bělik are not available. It was pointed out by Baker (1987) that the horseshoe vortices were found sensitive to L/δ^* and blockage ratio. A difference in the core location is therefore, due to different experimental

setup. A good qualitative agreement, however, appears between these pressure plots and the present work.

It is observed from the floor pressures all around the cylinder at $Re \approx 8600$, $D/\delta^* \approx 11.5$ and $Re \approx 13,000$ and $D/\delta^* \approx 14.5$ in fig. 5.15b, that the lower pressure region, associated with the location of primary vortex, appears to widen as the HSV turns around the cylinder, and the core location of primary vortex appears to move towards the circular cylinder. At $\phi = 20^\circ$ and 45° , it shifts to $0.8D$ and $0.7D$ respectively. At $\phi \geq 90^\circ$, the pressure dips are not distinguishable. A nearly constant region of lower pressure was found to exist at $\phi = 180^\circ$ up to about $1D$ downstream of the centre, beyond which the tendency of pressure recovery appeared.

(ii) Surface Pressures on the cylinder

The pressure distribution on the periphery of the circular cylinder upto $\frac{z}{D} = 2$, at the same test conditions and the angular locations, where floor pressures were measured, is shown in fig. 5.16a. A vertically downward and favourable pressure gradient of about 0.5 is measured on the cylinder at $\phi = 0$, from z/D of about 0.6 to 0.1 and near the floor, a slight positive gradient exists, which appears to indicate the presence of the secondary vortex. As the HSV starts turning along the periphery of the cylinder, the downward gradient appears to change in magnitude and

sign progressively as is evident from the pressure plots at $\phi=20^\circ$ and 45° , where the downward gradient along the vertical generator appears to decrease both in the extent and the magnitude and the upward flow region tends to increase accordingly. Furthermore, it can be observed from the pressure plots at $\phi \geq 90^\circ$, that no vertical pressure gradient is evident on the circular cylinder at these angular locations. Fig. 5.16b presents the pressure plot on the wall-cylinder junction, showing higher suction pressures on the surface of the cylinder, beyond the region of secondary flows.

c. Total Head Survey

The streamwise arm of HSV around the 25 mm dia circular cylinder was probed for its vortex structure through the traverses of shielded Pitot-tube in a grid of 300 points, measuring 30×15 mm, at $\phi=90^\circ$ in the Y-Z plane as viewed from the downstream end in fig. 5.17. The number of vortices and their sense of rotation are interpreted in the same manner as in 4.3.3c for the round nose pier.

Four vortices are observed from fig. 5.17 as follows :

- (i) a faint appearance of a small counter clockwise vortex at the cylinder, identified as the secondary vortex O,

- (ii) a large clockwise rotating vortex, identified as the primary vortex 1, located between $0.1D$ and $0.4D$ from the surface of the cylinder,
- (iii) a counter clockwise rotating vortex, identified as the secondary vortex 1, on the floor, located at about $0.5D$ from the cylinder,
- (iv) The fourth vortex, clockwise in rotation is not prominent in appearance from these total head contours, but the continuity of the velocity gradient demands that there should be a clockwise vortex close to the vortex (iii), identified as the primary vortex 2.

A complete picture of the structure of the streamwise arm of HSV around circular cylinder has been presented from constant total head contours for the first time.

5.4 THE MODIFIED HORSE SHOE VORTEX

Fig. 5.18a shows a picture of 25 mm diameter circular cylinder with the passive device fitted into its leading edge foot, and its three orthogonal views are shown in fig. 5.18b. The results of modified HSV around the circular cylinder with passive device are presented in this article in the same order of flow conditions approaching the cylinder as in the preceding section 5.3.

5.4.1 Laminar Flow

The picture in fig. 5.19 presents a perspective view of the circular cylinder with passive device, kept in the test section of water table. It's comparison with the corresponding view (fig. 5.1) of clean cylinder shows that the white region around the cylinder is altered by the passive device in bringing the red color region around the junction of the cylinder.

The dye patterns around the circular cylinder with the passive device at $Re = 3026$ based on 25 mm diameter of the cylinder and $Fr = 0.135$ based on 5 cm depth of water, at nominal water speed of 10 cm/sec. are shown in plan, top front and top rear views in figs. 5.20 a, b and c respectively. A comparison with the corresponding pictures with clean pier (figs. 5.2a, b and c) shows a significant modification of the vortex flow brought about by the passive device. The small oblong region around the apex of the passive device and two red streaklines progressing downstream along the central spinal rib are identified as the attenuated horseshoe vortex formed at the apex-floor junction, and its streamwise arms in figs. 5.20 a and b. Furthermore, two distinct red streaklines in relatively light colored water appear to be due to the spiralling region of LESV below the leading edges. The passive device modifies the wake-vortex interaction significantly as evident from the upward movement of the colored water behind the cylinder, through the

action of LESV (fig.5.19), and its effect is observed in the far wake as well, as shown in fig. 5.20c, where an overall change of flow pattern is observed, as in the case of round nose pier with device in chapter IV.

The picture in fig. 5.21 a provides a perspective view (from rear) of TiCl_4 fumes around the circular cylinder with passive device, showing the overall phenomenon at $\text{Re} = 1430$, $D/\delta^* = 4.5$. The liquid TiCl_4 was applied by technique I (chapter III). Two vortices coming out of the passive device are observed in place of the six vortex system HSV without the passive device in fig. 5.4a. The upper vortex behind the cylinder (fig.5.21a) is identified as the apex vortex (streamwise arm of AHSV), formed at the apex-floor junction in fig. 5.21b which shows a top perspective view of the same phenomenon. The innermost streaklines are identified as the apex vortices. The outer vortex identified as LESV modifies the wake-vortex interaction, shown by the 'neck' of $1D$ width located at about $3D$ downstream. Top front view in fig. 5.21c shows the proximity of LESV to the surface of the cylinder. The action of LESV in reducing the 'neck' region is shown clearly by the bringing in of the dense fumes of TiCl_4 from the outer flow field and throwing them upwards by both the arms of LESV, in the rear top view in fig. 5.21d. A line sketch of the modified vortex structure around circular cylinder is shown in fig. 5.22.

5.4.2 Transition to Turbulent Flow

The oscillations of the modified vortex flow around the circular cylinder with passive device were recorded using the same procedure as in section 4.4.2 by maintaining the identical location of the 'u' sensitive hot wire probe on the upper surface of the passive device.

The pictures of spectra and traces of the hot wire are shown with increasing wind speed in fig. 5.23a. The oscillations of the vortex flow on the upper surface of the passive device are changed, apparently due to the accelerating flow. Low frequency, low amplitude oscillations can be observed in the range $2000 < Re < 4400$ and $5 < D/\delta^* < 10$. Fig. 5.23b shows that these low frequency oscillations correspond to a value of $St \approx 0.05$ in the above range of Re and D/δ^* . However, an increase in the local mean velocity ratio $\frac{\bar{u}}{U_\infty}$ from about 0.10 (clean cylinder) to a linear variation from 0.18 to 0.24, in the range $2000 < Re < 4200$, is observed in fig. 5.23c. The local turbulence $\frac{u'}{U_\infty}$ is below 0.05 in this range. Beyond $Re \approx 4200$, a jump in the turbulence to about 10% at $Re \approx 6,000$ is shown, which is apparently due to the flow having become turbulent at $Re \approx 5000$ (fig. 3.5a).

5.4.3 Turbulent Flow

The modified vortex flow around the junction of circular cylinder with passive device attached to its leading edge foot was investigated from surface oil film patterns, detail pressure

measurements on the floor and the periphery of the cylinder, and total head survey in the Y-Z plane at its mid-span.

a. Surface Oil Film Patterns

Figs. 5.24a and b show surface oil film pattern around 25 mm dia circular with the passive device, at a nominal wind speed of about 5 m/sec., corresponding to $Re = 7800$, $D/\delta^* = 11$. Shots 'a' and 'b' were taken as in section 4.3.3a. The surface flow patterns below the device appear similar to that around the pier model of round nose with the passive device in section 4.4.3. The oblong looking line around the apex of the passive device is identified with the formation of AHSV and the accumulations of powder-oil mixture below the passive device along the spinal rib and in the region below the leading edge, indicate the surface generated vorticity due to the apex vortex and LESV, as in case of round nose pier with device in figs. 4.8a and b. The almost clean region around the cylinder appears to be due to LESV in bringing the fluid towards the cylinder, as indicated by the surface streamlines. This region extends about $2D$ downstream of the cylinder. These surface flow patterns are sketched in fig. 5.24c.

b. Pressure Measurements

Detail pressures were measured on the floor and periphery of the pressure model of the cylinder with the passive device

mounted at its leading edge foot, at $Re \approx 8500$, $D/\delta^* \approx 11.4$ and $Re \approx 12,800$, $D/\delta^* \approx 14.3$ corresponding to nominal wind speeds of 5.7 m/sec. and 8.5 m/sec. respectively, at the angular locations $\phi=0^\circ$, $+20^\circ$, $+45^\circ$, $+90^\circ$, $+135^\circ$ and 180° along with corresponding pressures on clean cylinder. The symmetry of flow about the circular cylinder is also presented.

(1) Floor Pressures around the Cylinder

Fig. 5.25a shows pressure distribution on the upstream plane of symmetry of the circular cylinder at $Re = 8377$, $D/\delta^* = 11.2$ and $Re = 12560$, $D/\delta^* = 14.3$ respectively. The surface pressures below the passive device are modified significantly. A reduction of 79% and 75% in the pressure gradient at $Re \approx 8400$ and $Re \approx 12,600$ respectively, below the passive device (2D upstream of the centre). The corresponding reductions in C_p at the foot of the cylinder are 77% and 73% respectively. The pressure variations over the upper surface of the device are also plotted. The difference of pressure between the upper surface and the floor shows the pressure jump across the passive device, which causes the formation of leading edge separation vortices.

Fig. 5.25b presents reduction of 66% and 50% in the floor pressure gradient at $r \approx 2D$, and C_p at the foot of the cylinder, at $\phi=+20^\circ$. Fig. 5.25c shows that there appears a tendency of favourable pressure gradient towards the cylinder at $r \approx 2D$, at $\phi = +45^\circ$, the pressure at the foot of the cylinder appears

to remain unaltered.

Fig. 5.25d shows that there appears an improvement of about 50% in the favourable pressure gradient at $r \approx 0.9D$, at $\phi = +90^\circ$ and 25% reduction in C_p at the foot of the cylinder is observed.

Fig. 5.25e shows a tendency of favourable pressure gradient at $r \approx 2D$, at $\phi = 135^\circ$ and a reduction of about 33% in C_p at the foot.

Fig. 5.25f shows a marginal reduction in the pressures upto $r \approx 1.5D$, the pressure recovery, thereafter, appears to be faster at $\phi = 180^\circ$.

(ii) Surface Pressures on the Cylinder

Pressure measurements on the periphery of the cylinder with the passive device were made along the vertical generator at the angular locations of floor pressure measurements. Fig. 5.26a presents these pressure variations at $\phi=0^\circ$ and $+20^\circ$, both with and without the passive device. The downward pressure gradient on the cylinder face at $\phi = 0^\circ$ shows a discontinuity at the trailing edge of the passive device. The reduction in C_p at $z/D=0.5$, and the flow are about 68% and 78% respectively within the device, and the reduction of pressure gradient appears to be 35%. The pressure variations at $\phi=+20^\circ$ shows the various flow regions on the vertical cylinder as follows.

- (i) an upward flow from $z/D \approx 0.8$ onwards
- (ii) a downward flow from $z/D \approx 0.8$ to $z/D \approx 0.5$
- (iii) an upward flow from $z/D \approx 0.3$ to $z/D \approx 0.5$
- (iv) a downward flow from $z/D \approx 0.3$ to $z/D \approx 0.1$
- (v) a weak upward flow from the floor region

This typical pressure variation on the cylinder surface at $\phi = 20^\circ$ within the height of the device, appears due to the somersaulting of the apex vortex at the cylinder face. The downward flow at (ii) appears to be due to the downstream movement of HSV like flow from the junction of upper surface trailing edge of the device with the cylinder.

Fig. 5.26b shows the pressure variations on the cylinder surface at $\phi = +45^\circ$ and $+90^\circ$ with and without the passive device. The various flow regions at $\phi = +45^\circ$ are as follows.

- (i) a downward flow upto $z/D \approx 0.7$
- (ii) an upward flow from $z/D \approx 0.4$
- (iii) a downward flow from $z/D \approx 0.4$ to $z/D \approx 0.2$
- (iv) an upward flow from the floor region

It may be mentioned that the apex vortex has come out from beneath the passive device at this angular location of the cylinder and is believed to be in the process of lift up under the action of LESV, and this typical variations of pressure appear due to this interaction of apex vortex and LESV, at the cylinder. The pressure plot at $\phi = +90^\circ$ shows only two distinct flow regions, i.e.,

- (i) a downward flow from $z/D \approx 0.6$ to $z/D \approx 0.2$
- (ii) an upward flow from the floor region

It may be noted from the above plots that, in $\phi = +90^\circ$, a comparatively stronger upward flow is observed. This shows that the lift up process of apex vortex gets completed at $\phi \approx 90^\circ$.

Fig. 5.26c shows the pressure variations along the cylinder height with and without the passive device at $\phi = +135^\circ$ and $\phi = +180^\circ$. Both of these plots indicate upward flow along the cylinder, being more pronounced at $\phi = 180^\circ$. The observations from the pressure variation on the cylinder with the passive device are summarized in the line sketches in fig. 5.26d.

(iii) Symmetry of Pressures

Figs. 5.27 a-d show the floor pressure measurements around the circular cylinder with and without the device at $\phi = \pm 20^\circ$, $\pm 45^\circ$, $\pm 90^\circ$ and $\pm 135^\circ$ respectively at $Re \approx 8600$, $D/\delta^* \approx 11.5$. The corresponding modified pressures are also plotted. The flow symmetry around the circular cylinder is observed from these plots. Figs. 5.28a and b show the symmetry of flow on the periphery of the cylinder with and without the passive device.

c. Total Head Survey

The streamwise arm of the modified vortex flow around 25 mm diameter cylinder was probed by plotting constant total head contours from the traverses of a shielded pitot tube in a grid of

30x22 mm at 450 points, in the Y-Z plane at the mid-span, at $Re \approx 8300$, $D/\delta^* \approx 11.3$, Fig. 5.29 presents these contours as viewed from the downstream end. The number of vortices and their sense of rotation were interpreted in the same manner as in 4.3.3.c for the round nose pier as follows :

- (i) a large counter clockwise leading edge separation vortex from the passive device,
- (ii) a small counter clockwise vortex on the floor close to the cylinder,
- (iii) a small clockwise vortex (apex vortex) at the cylinder
- (iv) a large clockwise vortex away from the region of influence of LESV.

In addition a vertically downward flow region at $z/D \approx 0.5$ (also in fig. 5.26c, $\phi=90^\circ$) is observed. The small counter clockwise vortex close to the cylinder junction is believed to form due to an interaction of LESV with the cylinder and the apex vortex. This plot makes it clear that the size and strength of LESV are more than the apex vortex.

A complete picture of the streamwise arm of the modified vortex flow around circular cylinder junction with floor, and the passive device attached to its leading edge foot, is presented.

5.5 DISCUSSION

The earlier experimental investigations of HSV around the junction of circular cylinder with floor, carried out in wind tunnel by smoke flow visualization, surface oil flow patterns and pressure measurements by Bělik (1973) and Baker (1979, 1980) were restricted to the upstream plane of symmetry of the cylinder. It has been discussed in chapter IV, that it is essential to investigate the streamwise arm of HSV along with a study of the flow phenomenon at the trailing edge, apart from the flow field in the upstream plane of the body. An experimental investigation of HSV around the junction of circular cylinder with floor, and its modification using the passive device (Gupta, 1987) has been described from detail flow visualization and pressure measurements in this chapter.

5.5.1 HSV Around Circular Cylinder

The water-dye flow visualization provided complete picture of the gross region of HSV around the circular cylinder junction with floor and the detail structure of this vortex flow was provided by TiCl_4 fumes in a low speed wind tunnel in figs. 5.1, 5.2 and 5.4 respectively. The use of the dense white fumes of TiCl_4 (Freymuth et.al., 1985) for visualization of complete HSV in figs. 5.4, at $\text{Re} \cong 1450$, $D/\delta^* \cong 4.5$, in a simple manner with ordinary photographic techniques, indicating six vortex structure is an independent verification of Baker's (1979) results. The

nature and number of vortices observed with different cylinders at the nominal wind speed of 95 cm/sec are presented in Table 5.2. The pressure distribution on the upstream plane of symmetry of circular cylinder (fig. 5.5) at $Re = 2200$, $D/\delta^* = 5.5$, $L/D = 6$, $L/\delta^* = 33$, $BR = 3\%$ shows three pressure dips, and Baker's (1979) data, at $Re = 2050$, $D/\delta^* = 21.7$, $L/D = 4.8$, $L/\delta^* = 104$, $BR = 5.3\%$ shows one pressure dip. Baker (1987) has pointed out that horse-shoe vortices were sensitive to L/δ^* and blockage ratio.

The oscillatory behaviour of HSV around circular cylinder appeared similar to that around the pier model with round nose, and was not found random as reported by Baker (1979), who found 'one of the following four different wave forms, at different times under the same test conditions, i.e., (i) steady trace with no oscillation, (ii) a low frequency oscillation, (iii) a high frequency oscillation and (iv) an irregular turbulent trace'. In the present work steady, distinct and discrete fundamental frequencies of $St \approx 0.2$, alongwith higher harmonics were observed in the range $2200 < Re < 4400$, and $5 < D/\delta^* < 10$ from a u-probe hot wire, as shown in figs. 5.6 a-c. A composite plot of fig. 5.6b and Baker's results is presented in fig. 5.30. This calls for a careful look at the oscillatory behaviour of HSV and the following points in Baker's data (1979) are highlighted to this end.

- (1) the 'u'-probe hot wire for measurement of vortex oscillations was inserted into the test section through a hole beneath the HSV system.

- (ii) the smoke flow visualization with the probe in this position did not affect the flow.
- (iii) Fig. 10 a shows pressure distribution on the upstream plane of symmetry of the cylinder in laminar flow at $Re=4790$, $D/\delta^* = 33.8$ with a pressure minima at about $0.8D$ from the centre of the cylinder.
- (iv) Fig. 13 shows HSV spectra ($x/D = -0.82$, $y/D = 0.063$, $z/D = 0$) at $Re=4720$, $D/\delta^* = 33.8$, and $Re=4780$, $D/\delta^* = 34.2$, showing two different peaks of St , at 0.26 and 0.36 respectively.

It was, however, not clear, as to why a laminar horseshoe vortex should present an oscillatory behaviour at nearly identical test conditions. It is conjectured at this stage, that the randomness of vortex oscillations might have been due to some inadvertent leakage of air from outside to the HSV through the hole for inserting the hot wire probe. This aspect was examined in some detail. A 0.5 mm dia. hole was drilled slightly upstream of the cylinder. $TiCl_4$ flow visualization at $Re \approx 1400$, $D/\delta^* \approx 4.4$ showed an oscillatory character. When the hole was plugged from below the six vortex system re-appeared. This was repeated a number of times, providing the same observation. It was therefore, inferred that the highly random oscillatory behaviour of HSV reported by Baker (1979) might have been caused by some leakage of air into the horseshoe vortex flow.

The number of vortices in HSV, in turbulent flow inferred from surface flow patterns (figs. 5.7-5.12) showed that the vortex structure depends upon Reynolds number. Four vortices were observed in the range $7700 < Re < 16,000$ in agreement with Baker (1980), and two vortex structure was observed at $Re < 4,000$. However, Langston and Boyle (1982) obtained two vortex structure from their 'novel technique of dot in' matrix and wintergreen oil', around 16 cm diameter cylinder, at $Re = 2.46 \times 10^5$ and $D/\delta^* = 42.1$, $BR = 8.74\%$ ($\frac{L}{D} = \infty$, $\frac{L}{\delta_*} = \infty$). It was also pointed out by them that 'detail pressure measurements need to be carried out to verify this result'.

Detail pressure measurements on the floor around the cylinder provide location of the core of the primary horseshoe vortex, but do not give consistent clue to the exact number of vortices. This was provided by the constant total head contours, which clearly showed four vortex structure of HSV at $Re \approx 8300$, $D/\delta^* \approx 11.3$ in the streamwise arm of HSV around the circular cylinder in fig. 5.17.

5.5.2 Aerodynamics of Delta-Wing-Like Passive Device

It was observed from the present work that the phenomenon associated with the movement of the streamwise arm of AHSV, i.e. the apex vortex, and its exit from the passive device were similar to that described in Chapter IV. This identical behaviour below the device appears to be due to the same leading edge shape of the round nose pier and the circular cylinder.

5.5.3 The Modification of HSV

The delta-wing-like passive device attached to the leading edge foot of the circular cylinder modifies the HSV flow structure in the same way as described in section 4.5, with the additional observation of pressure variation on the periphery of the cylinder.

The passive device causes significant reduction of the downward pressure gradient, and the C_p , on the upstream face of the cylinder within the device i.e. $z/D=0.5$. This portion of the cylinder is isolated from the rest, by the altitude of the device. A sharp discontinuity of pressure, resulting in 35% reduction in the pressure gradient was measured in this part of the cylinder. The pressure variations on clean cylinder were presented. In modified vortex flow, the somersaulting and lift of the apex vortex were observed through the pressure variations along the surface of the cylinder.

The wake-vortex system gets modified in the similar manner as in Chapter IV, by the action of LESV in pushing upwards, the two vertical vortices at the rear of the cylinder. The pressure distributions on the cylinder at $\phi=180^\circ$ (fig. 5.26c) supplement the flow visualization results.

The vortex oscillations on the upper surface of the passive device get suppressed due to the accelerating flow.

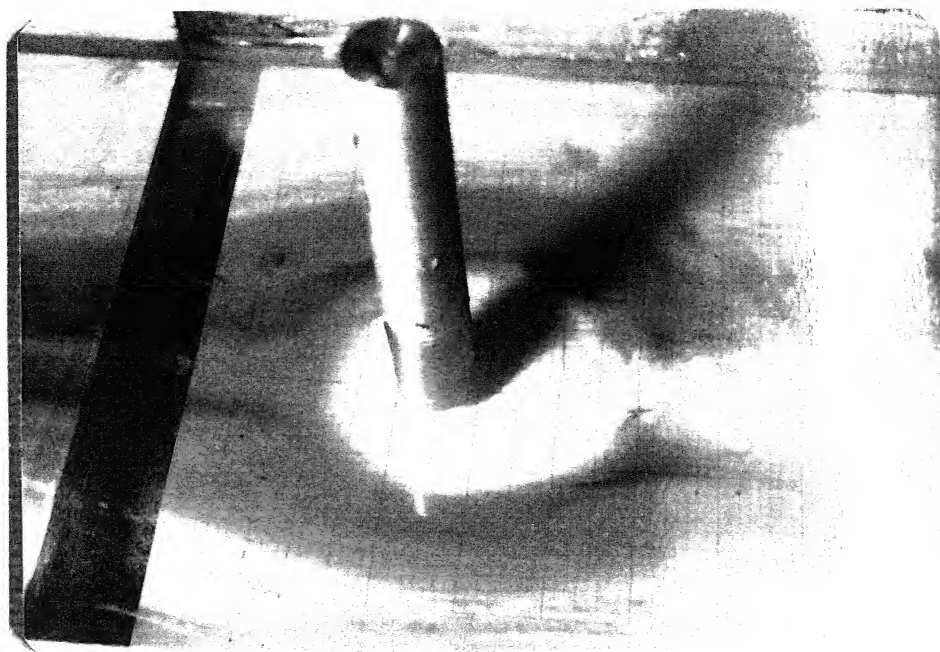
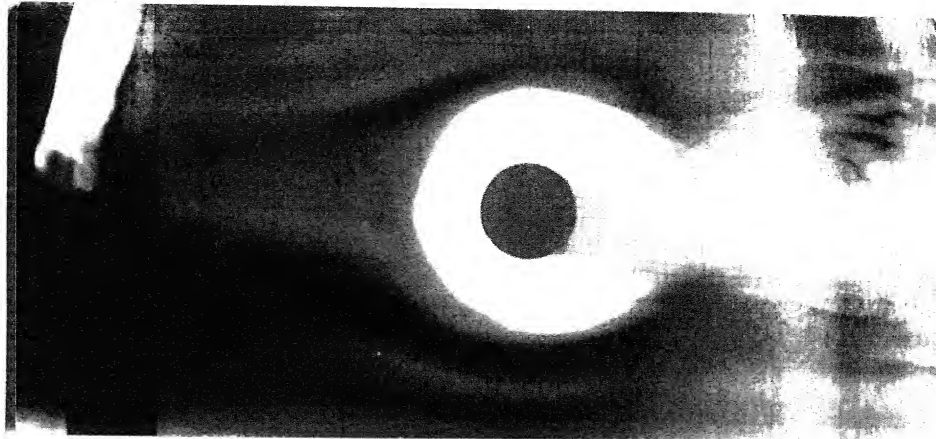
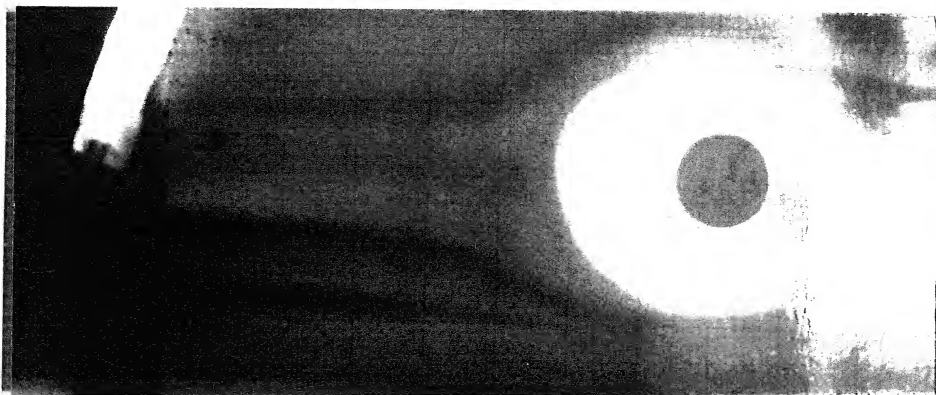


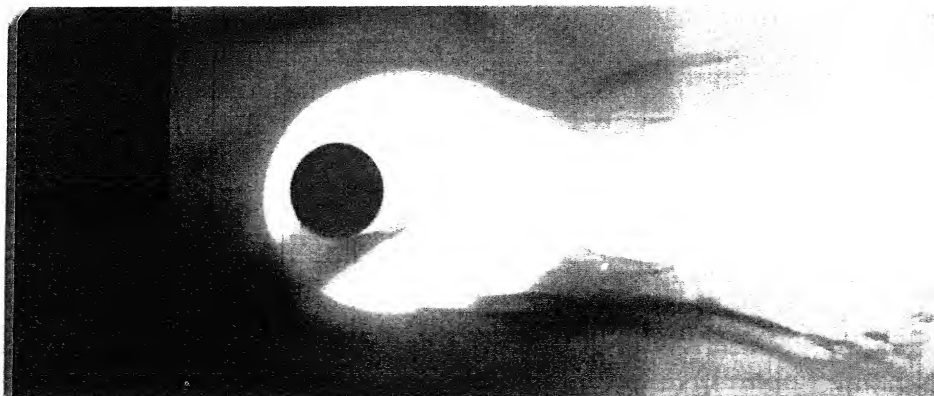
Fig. 5.1 A PERSPECTIVE VIEW OF DYE PATTERNS AROUND CIRCULAR CYLINDER



a. PLAN VIEW



b. TOP FRONT VIEW



c. TOP REAR VIEW

Fig. 5.2 DYE PATTERNS AROUND CIRCULAR CYLINDER, $L/D=6$, $BR=10\%$, $Re=3197$, $Fr=0.146$ (FLOW FROM LEFT TO RIGHT)

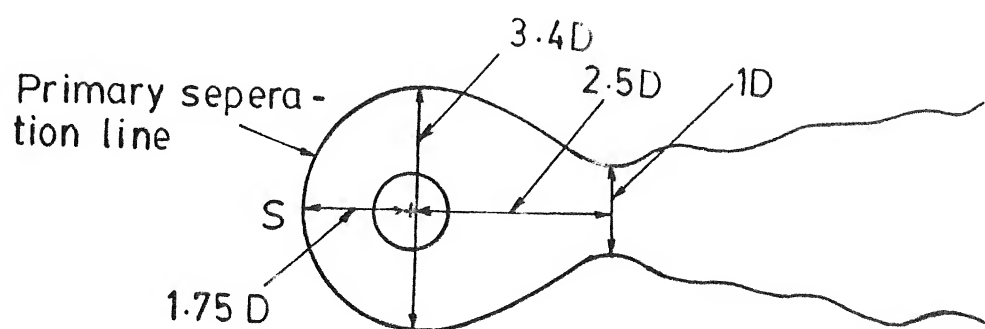
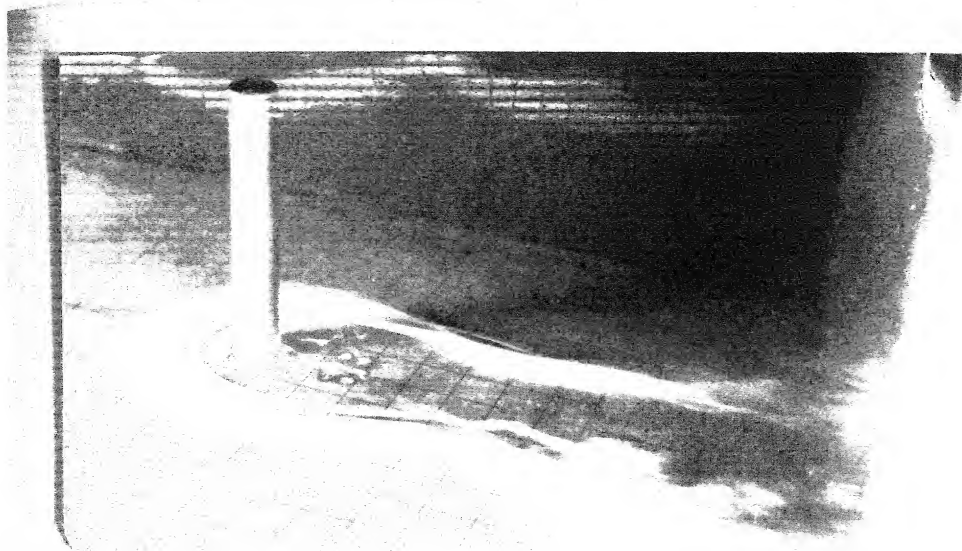
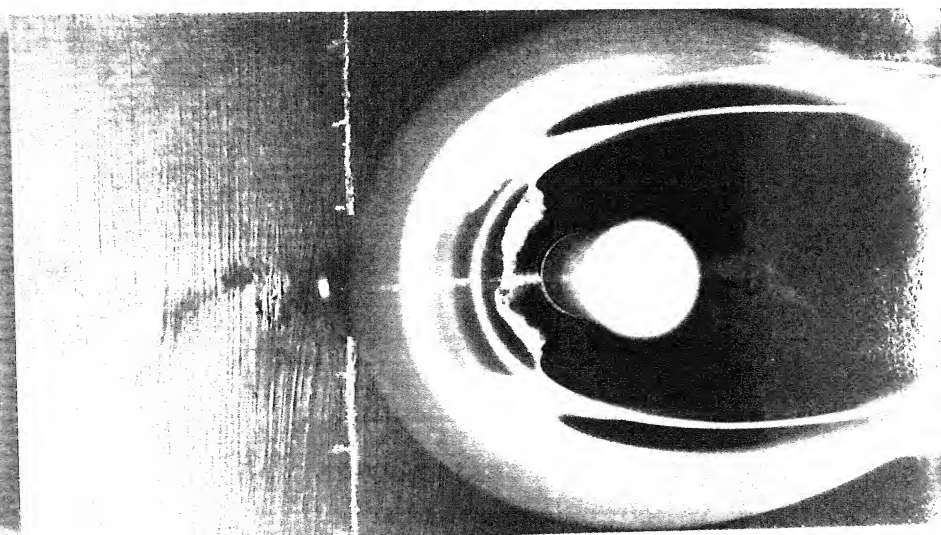


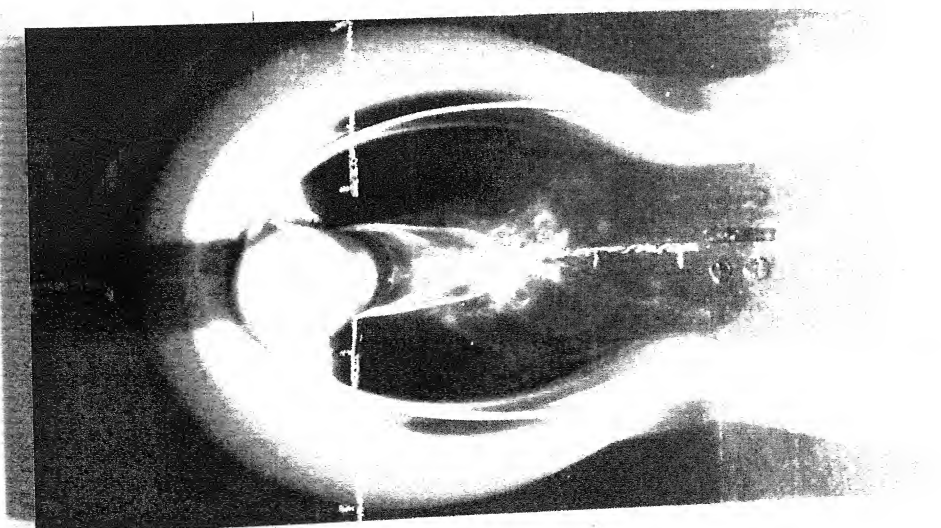
FIG. 5.3 LINE SKETCH OF DYE PATTERNS
 $Re = 3197$, $Fr = 0.146$, $L/D = 6$, $BR = 10\%$



a. PERSPECTIVE VIEW

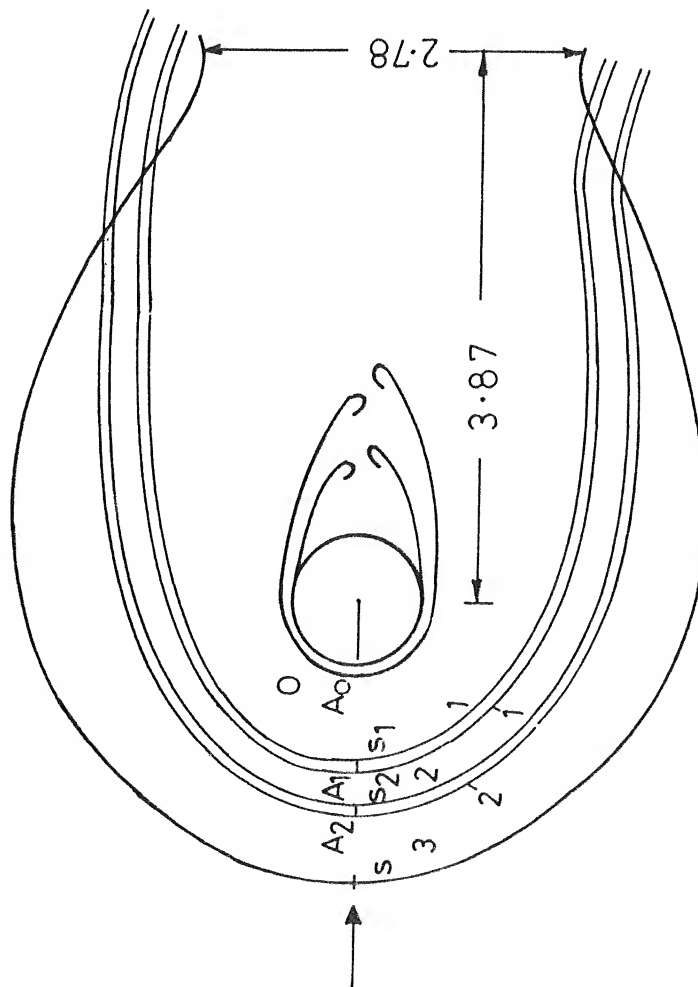


b. TOP FRONT VIEW



c. TOP REAR VIEW

Fig. 5.4 $TiCl_4$ FLOW AROUND CIRCULAR CYLINDER
JUNCTION, $L/D=6$, $BR=3\%$, $Re=1450$, $D/\delta^* = 4.5$



A ₀	at	0.59D
s ₁	at	1.18D
A ₁	"	1.28D
s ₂	"	1.5D
A ₂	"	1.63D
s	"	2.1D

Six vortex system

FIG. 5.4 d LINE SKETCH OF TiCl_4 FLOW AROUND CIRCULAR CYLINDER $L/D=6$, $BR=3\%$, $Re \approx 1450$, $D/\delta^* \approx 4.5$

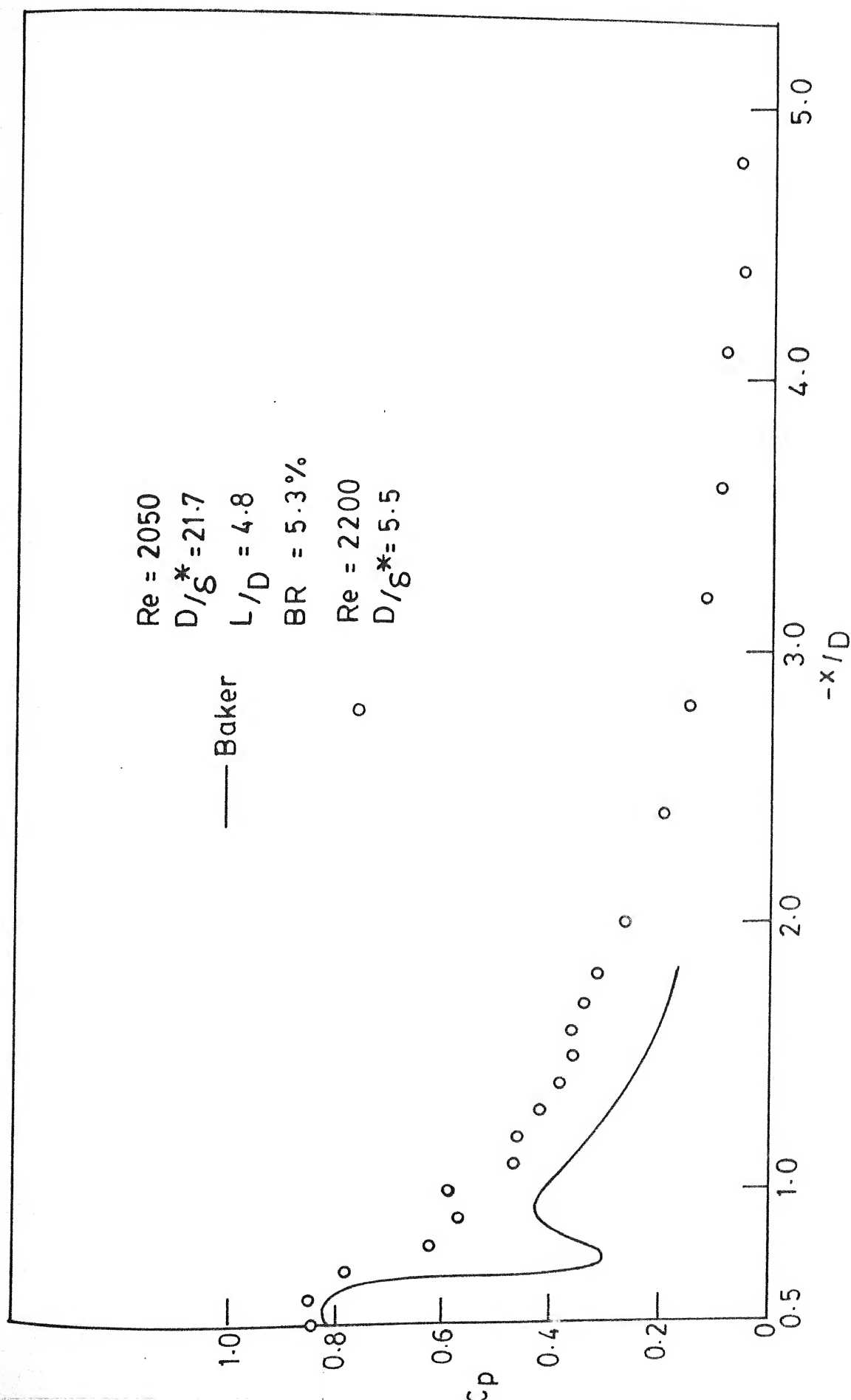


FIG.5.5 PRESSURE DISTRIBUTION ON THE UPSTREAM PLANE OF SYMMETRY OF CIRCULAR CYLINDER IN LAMINAR FLOW. $L/D = 6$, $BR = 3\%$.

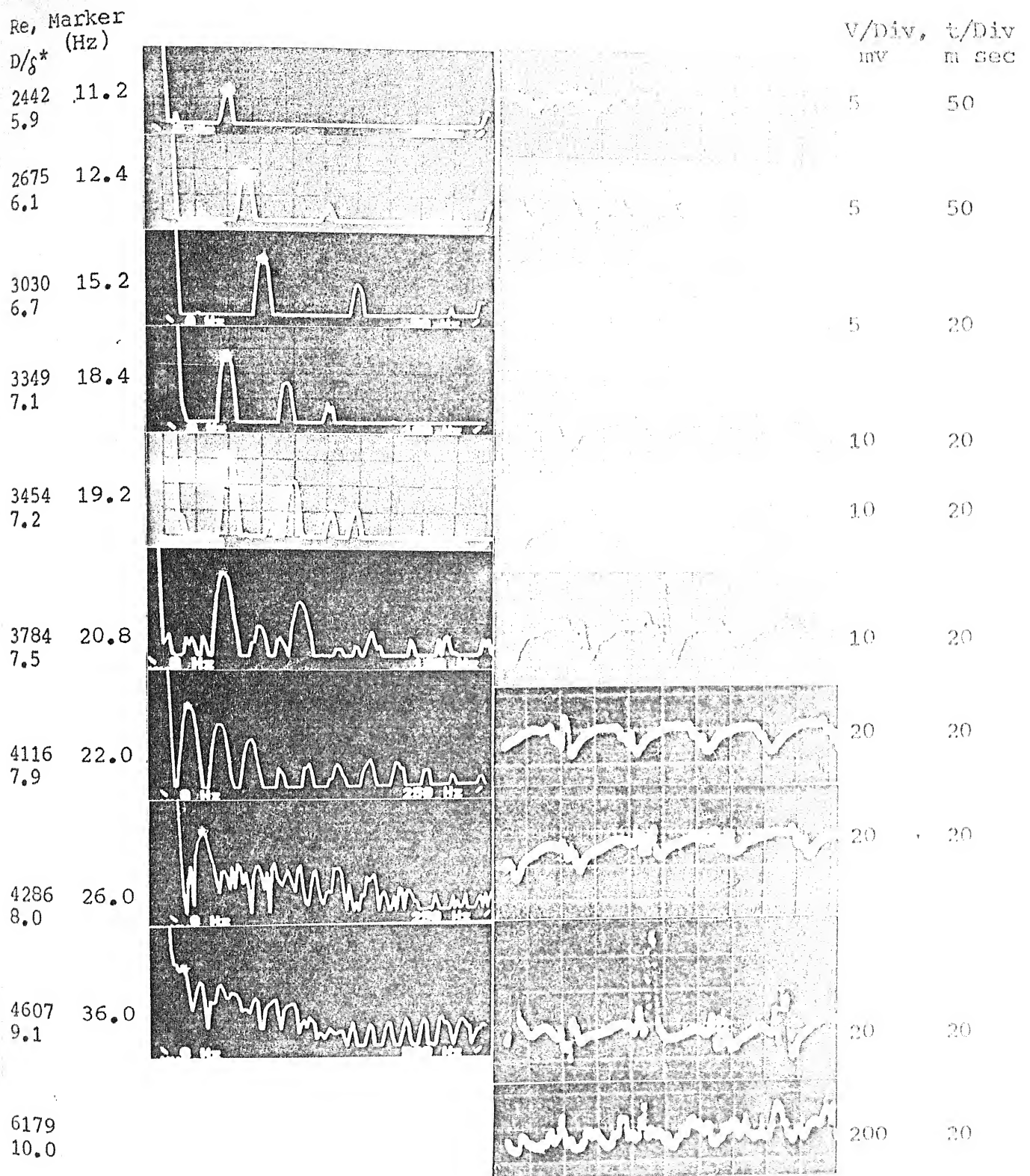
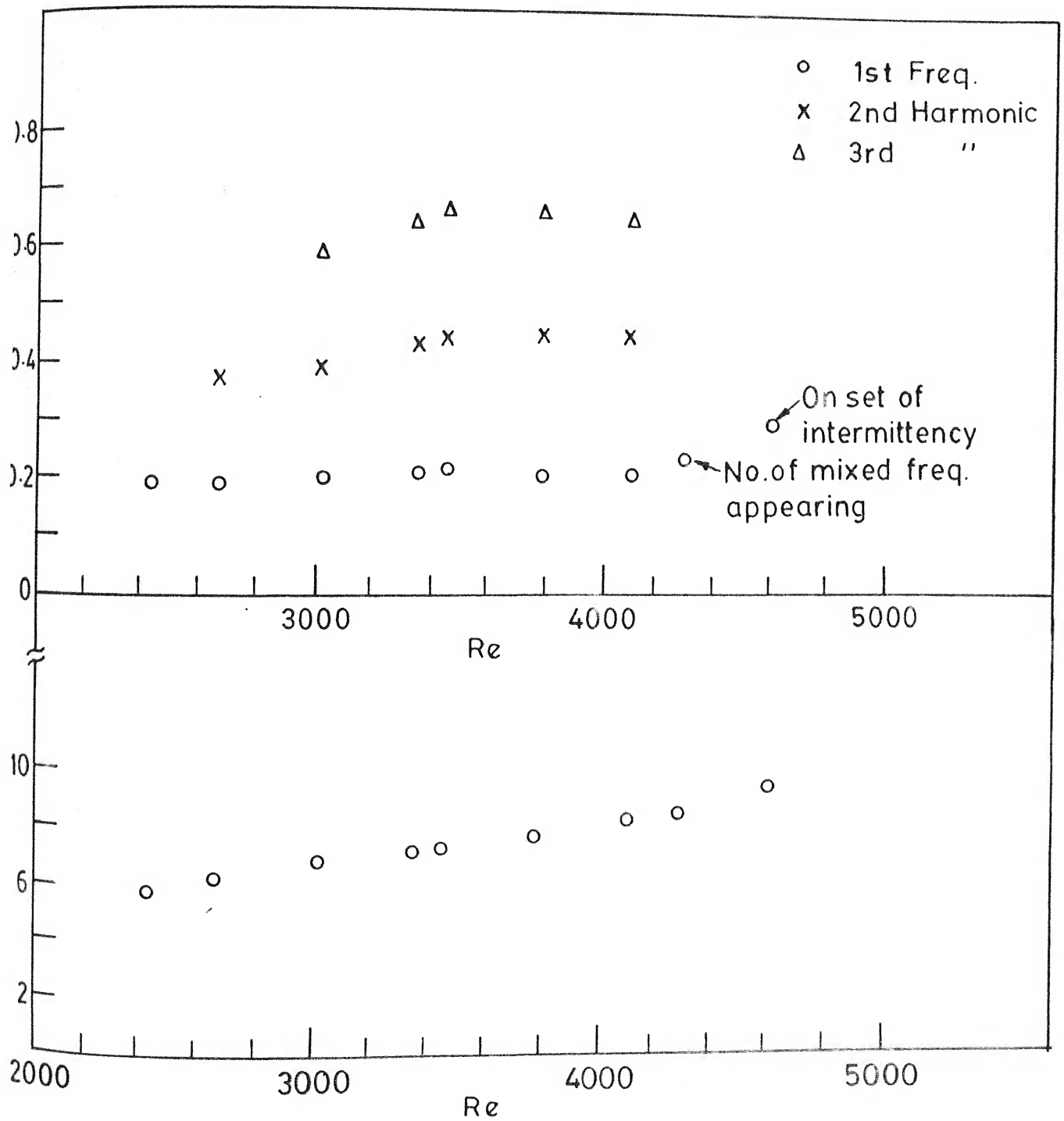


Fig. 5.6a SPECTRA AND TRACES OF VORTEX OSCILLATIONS
AROUND CIRCULAR CYLINDER, $L/D=6$, $BR=3\%$



5.6b VARIATION OF VORTEX OSCILLATION FREQUENCIES AROUND CIRCULAR CYLINDER. $L/D=6$, $BR=3\%$

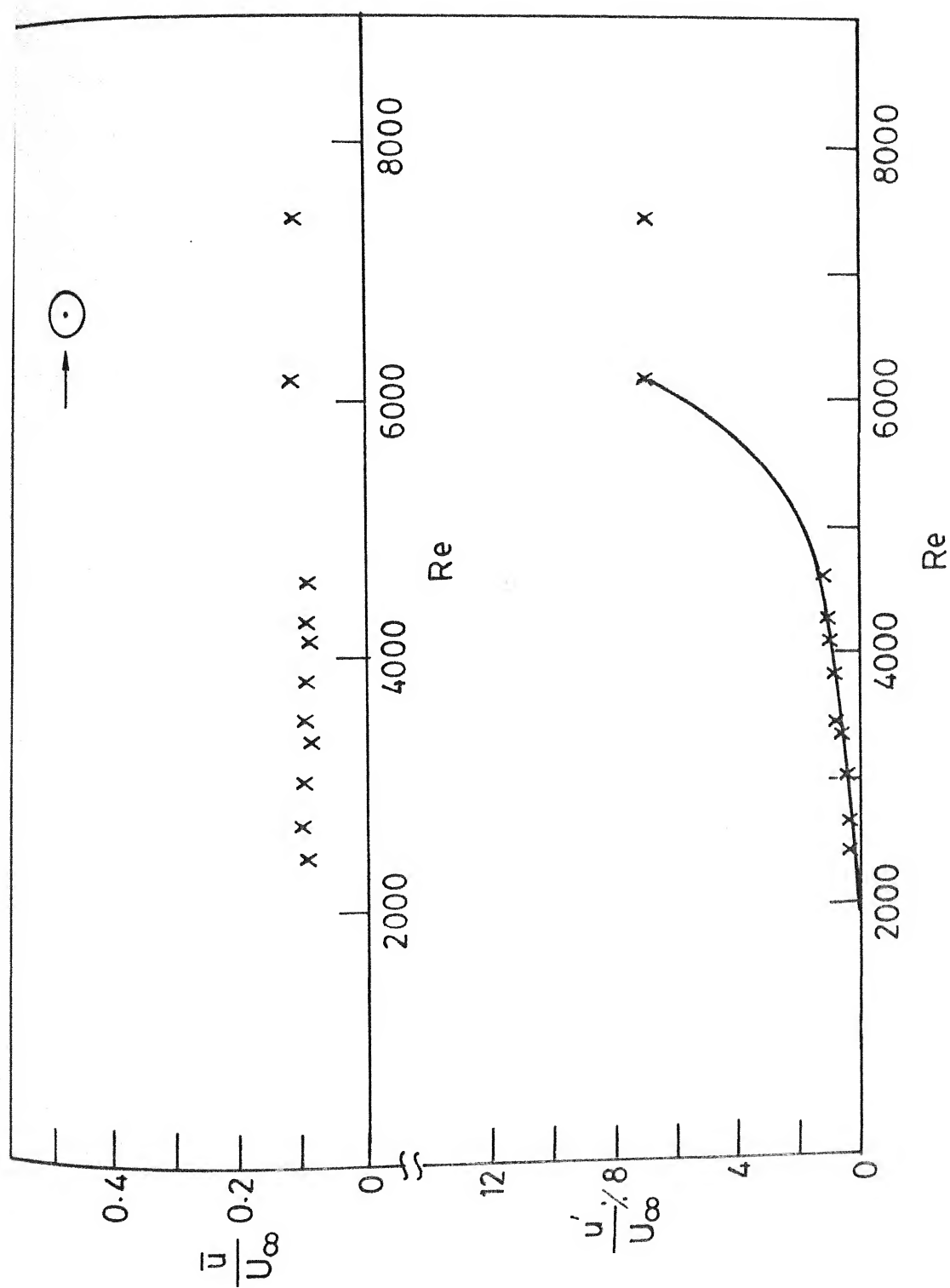
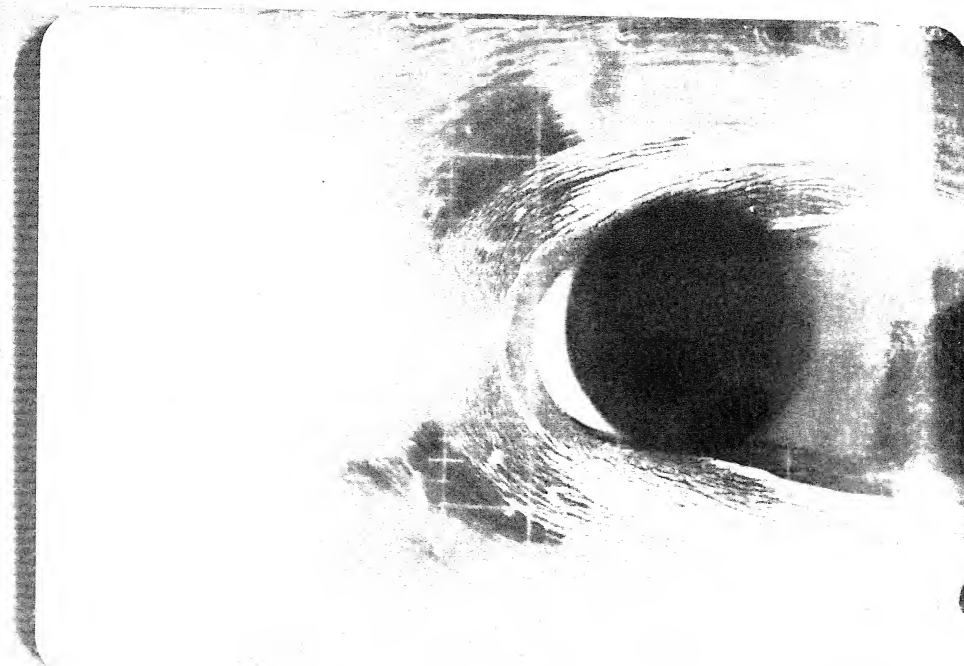
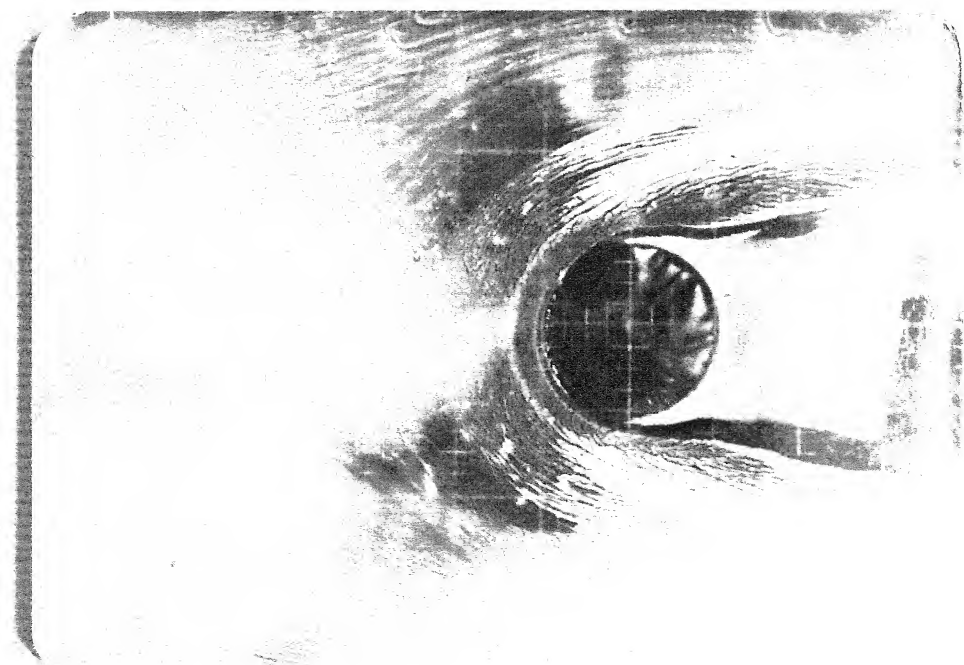


FIG. 5.6c VARIATION \bar{u} AND u' UPSTREAM OF CIRCULAR CYLINDER
 $L/D = 6$, $BR = 3\%$

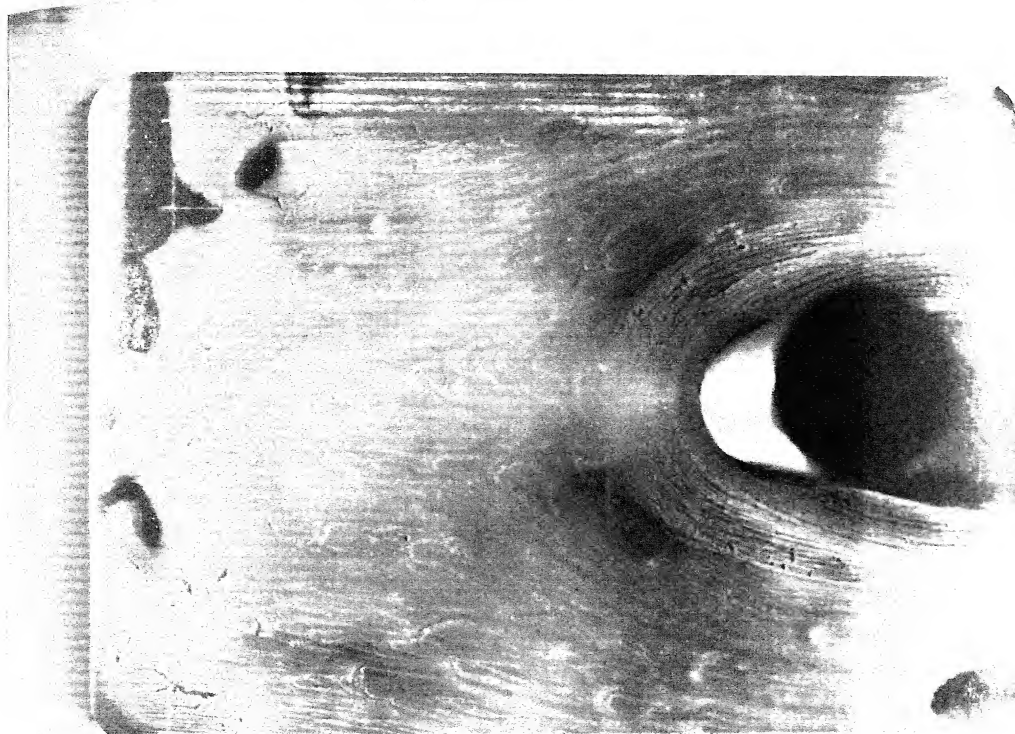


a. $t=20$ Min. (FLOW ON)

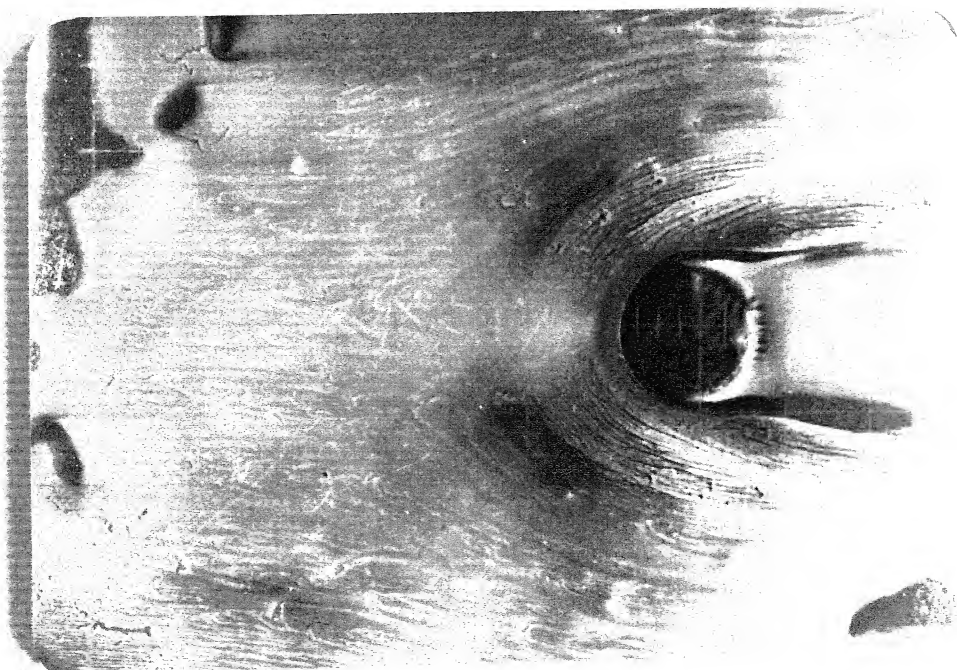


b. $t = 20$ Min.

Fig. 5.7 SURFACE OIL FILM PATTERNS AROUND 50 mm
CIRCULAR CYLINDER, $L/D=3$, $BR=6.2\%$,
 $Re=15536$, $D/\delta^* = 22$



a. $t=20$ Min. (FLOW ON)

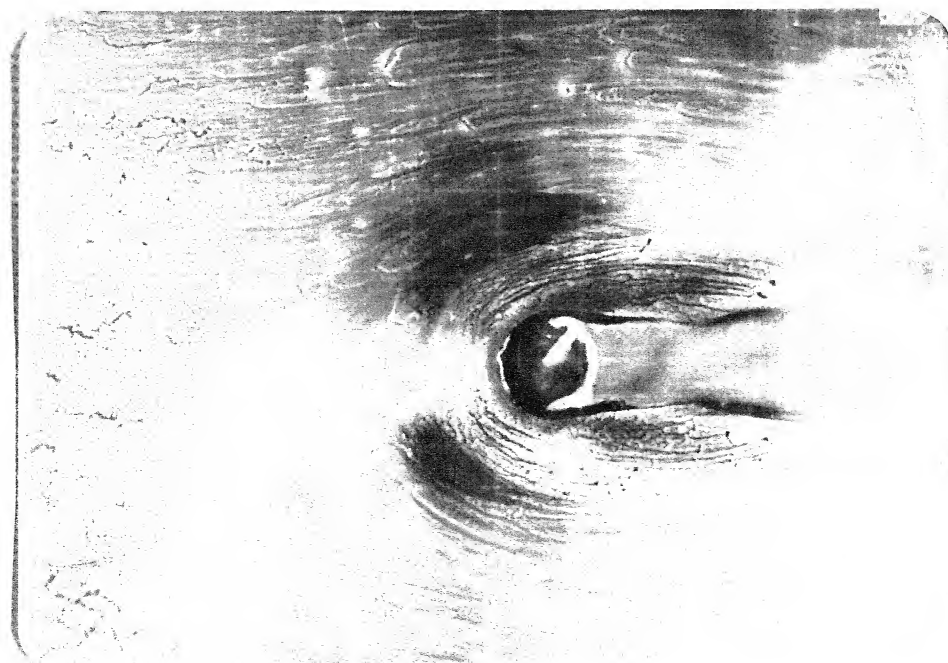


b. $t=20$ Min.

Fig. 5.8 SURFACE OIL FILM PATTERNS AROUND 37.5 mm CIRCULAR CYLINDER, $L/D=4$, $BR=4.56$, $Re=11,652$, $D/\delta^* = 16.5$ (FLOW FROM LEFT TO RIGHT)

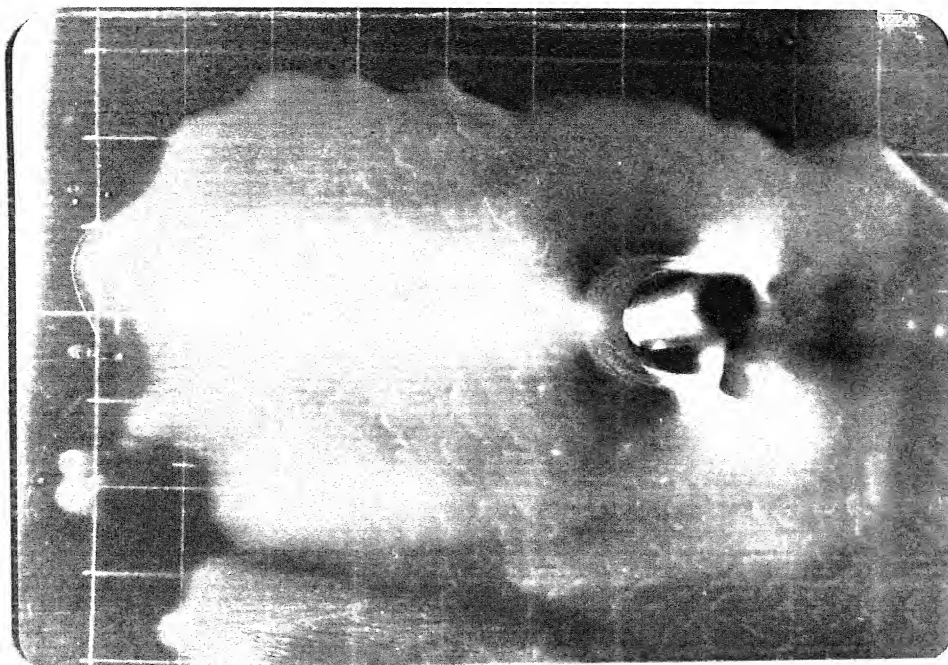


a. $t = 25$ Min. (FLOW ON)

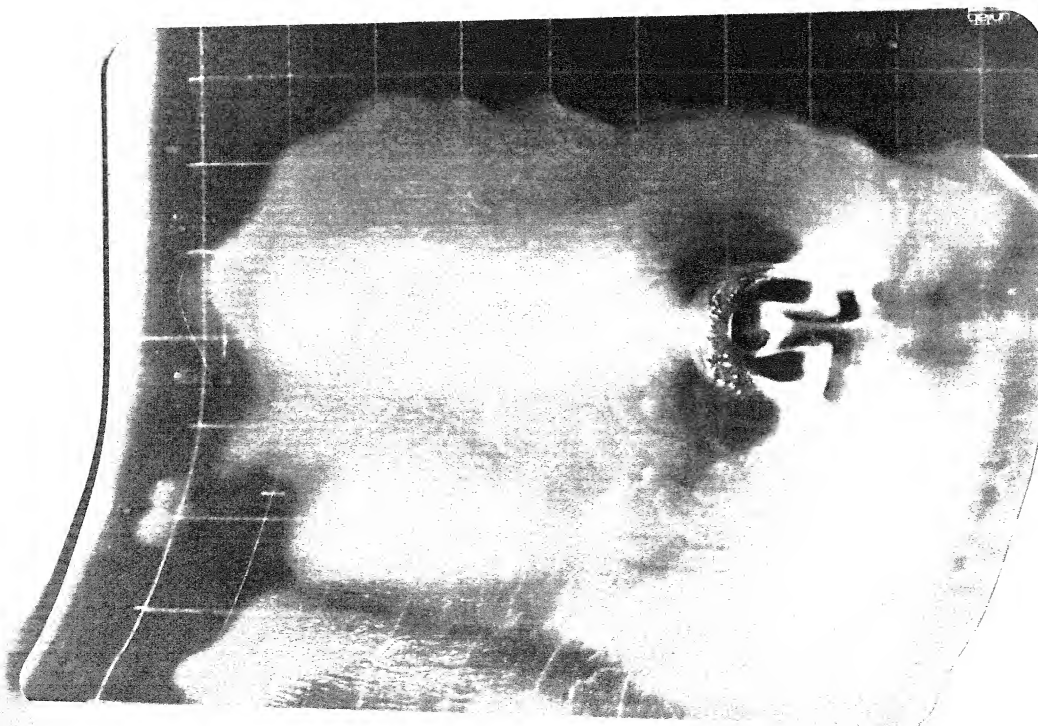


b. $t = 25$ Min.

Fig. 5.9 SURFACE OIL FILM PATTERNS AROUND 25 mm CIRCULAR CYLINDER $L/D = 6$, $BR = 3\%$, $Re = 7768$, $D/\delta^* = 11$ (FLOW FROM LEFT TO RIGHT)

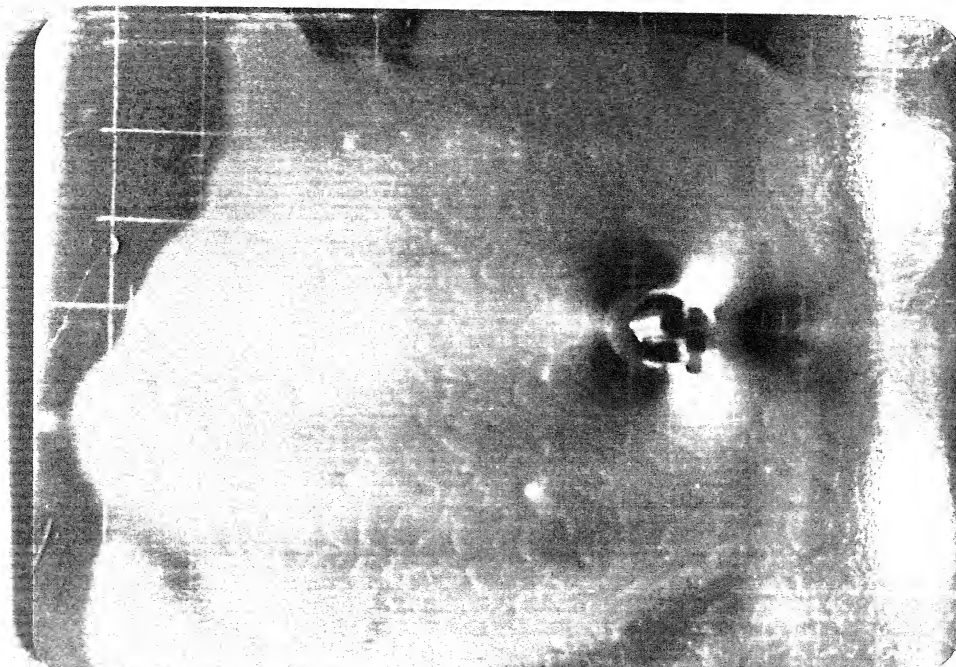


a. $t = 10$ Min. (FLOW ON)

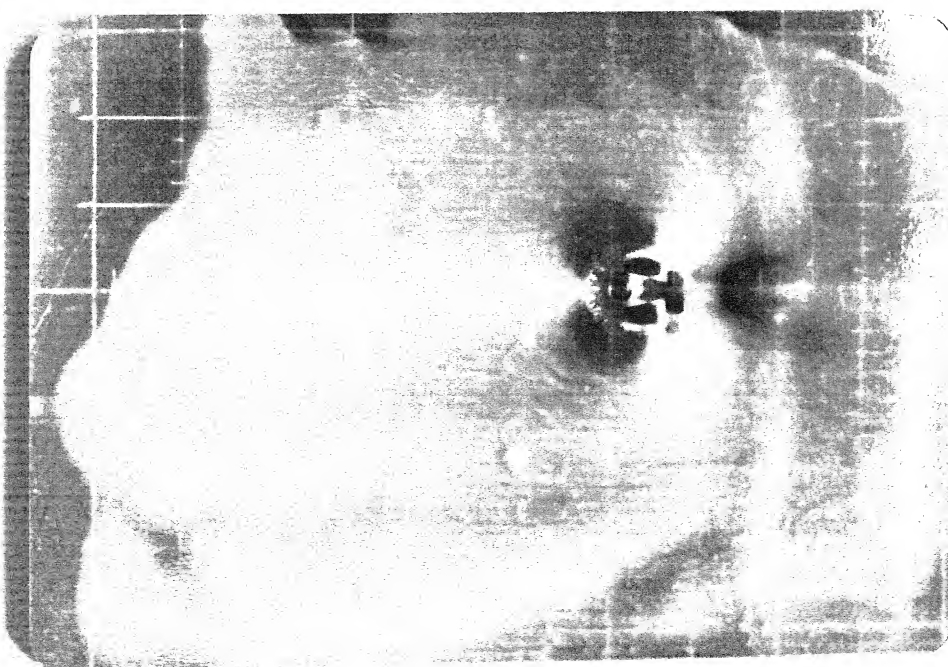


b. $t = 10$ Min.

- 5.10 SURFACE OIL FILM PATTERNS AROUND 12.5 mm
CIRCULAR CYLINDER $L/D = 64$, $BR = 0.80\%$,
 $Re = 3884$, $D/\delta^* = 5.5$ (FLOW FROM LEFT TO
RIGHT)

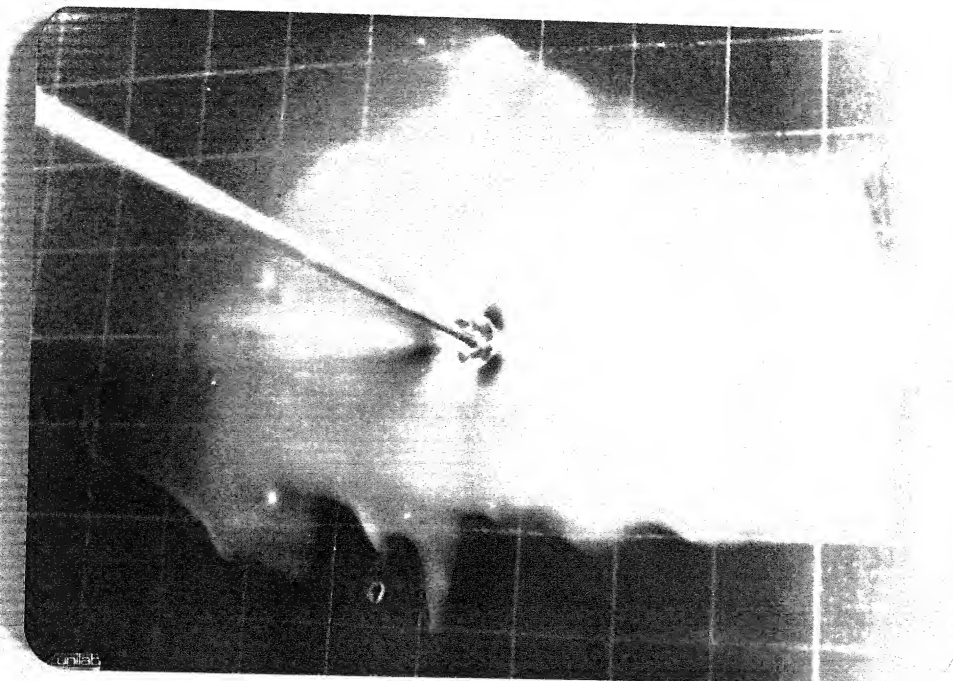


$t = 15 \text{ Min. (FLOW ON)}$

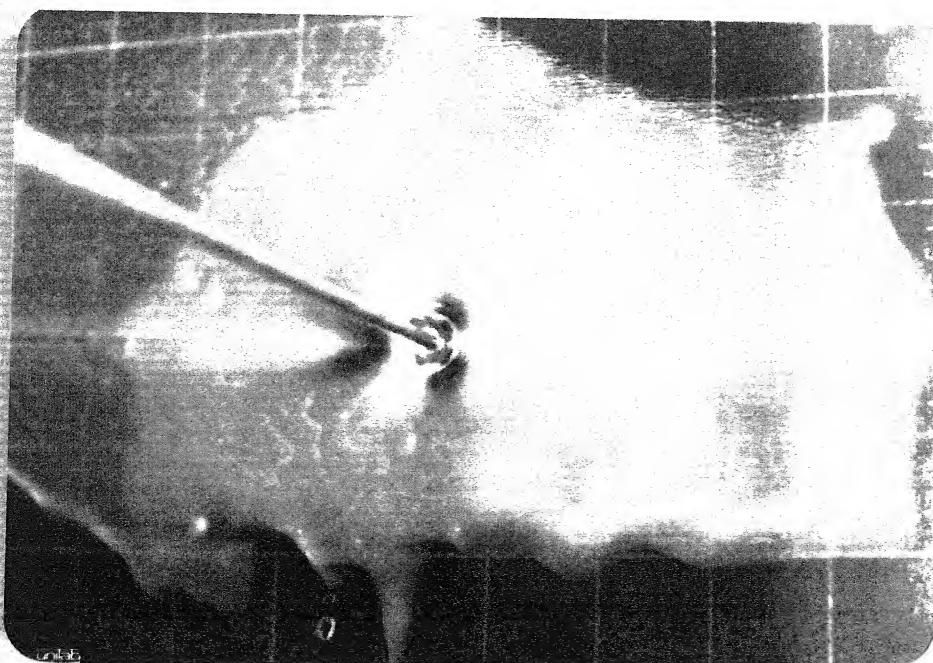


$t = 15 \text{ Min.}$

Fig. 5.11 SURFACE OIL FILM PATTERNS AROUND 6 mm
CIRCULAR CYLINDER $L/D = 9.2$, $BR = 0.28\%$,
 $Re = 1942$, $D/\delta^* = 2.75$ (FLOW FROM LEFT TO
RIGHT)

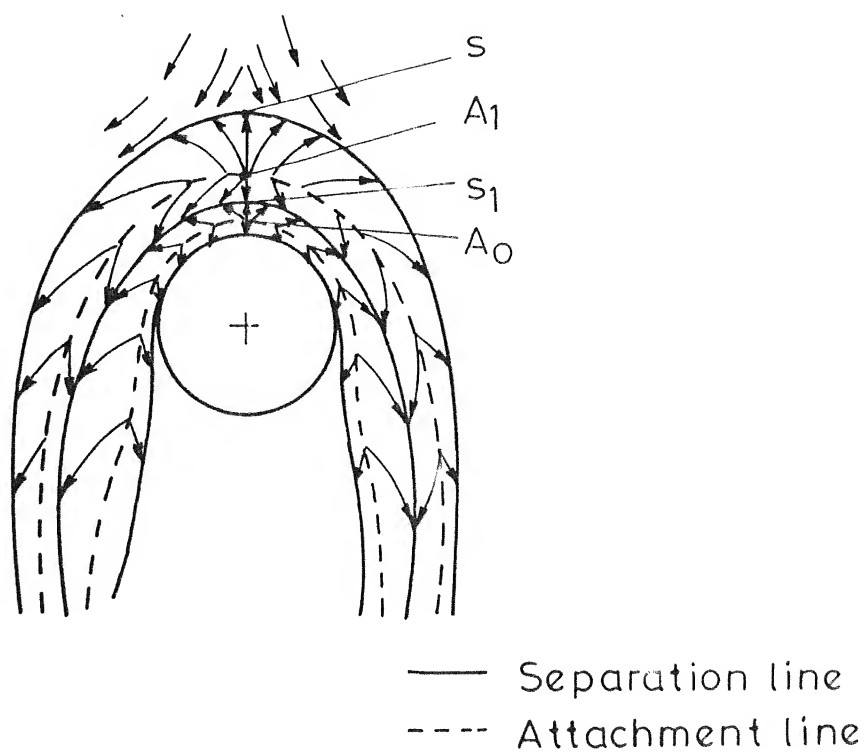


a. $t = 8$ Min. (FLOW ON)

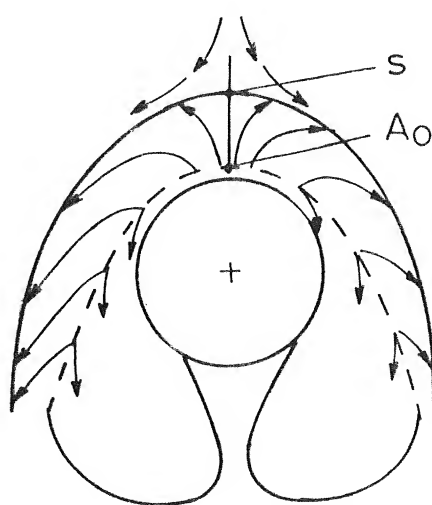


b. $t = 12$ Min. (FLOW ON)

Fig. 5.12 SURFACE OIL FILM PATTERN AROUND 3 mm
CIRCULAR CYLINDER $Re = 60$, $D/\delta^* = 1.38$
(FLOW FROM RIGHT TO LEFT)



(a) Four vortex system



(b) Two vortex system

FIG. 5.13 SURFACE STREAM LINES AROUND
 CIRCULAR CYLINDER

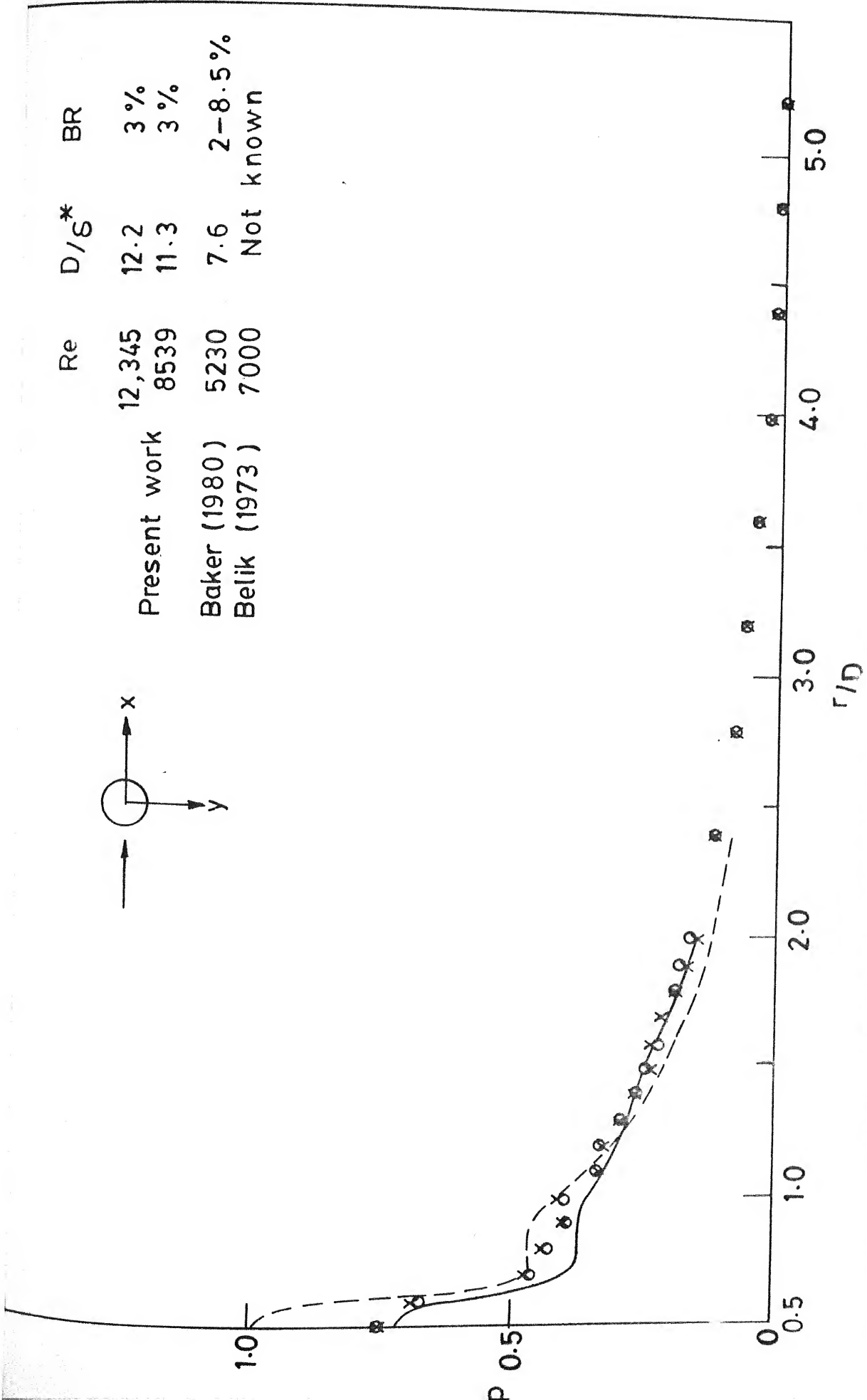


FIG. 5-15a PRESSURE DISTRIBUTION ON THE WALL IN THE UPSTREAM PLANE OF SYMMETRY OF CIRCULAR CYLINDER

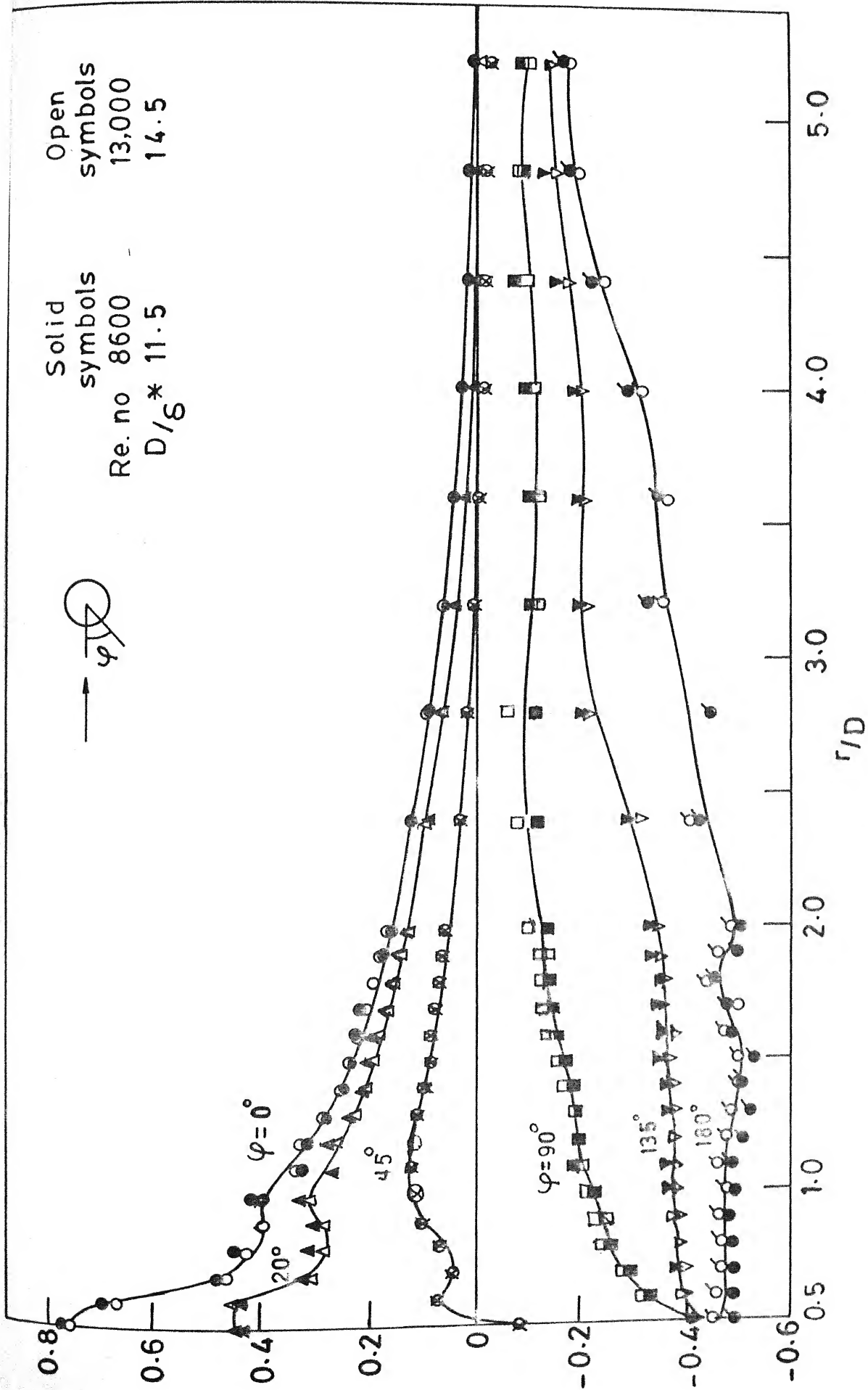


FIG 5.15b PRESSURE DISTRIBUTION ON THE WALL AROUND CIRCULAR CYLINDER

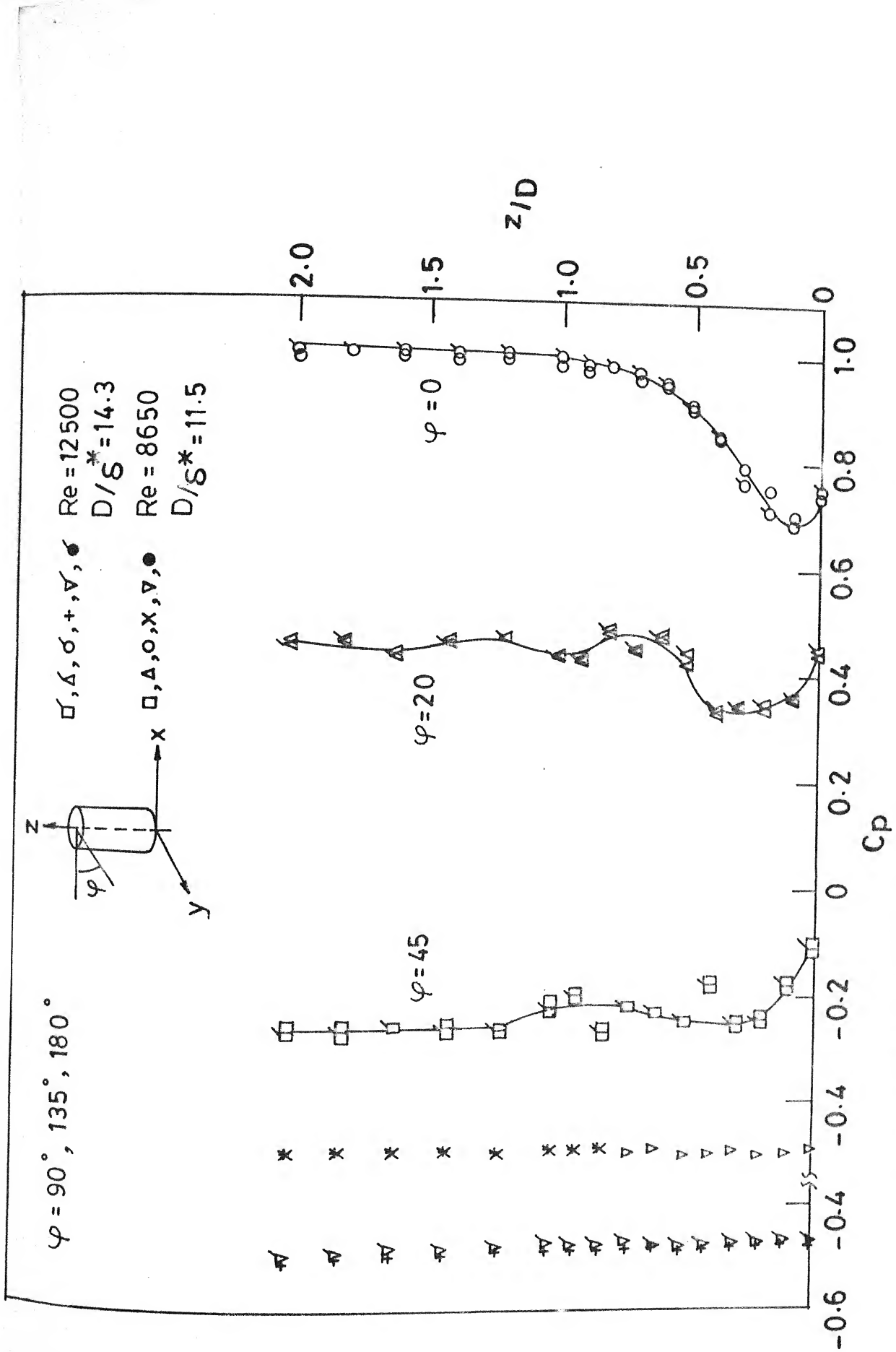


FIG. 5.16a PRESSURE DISTRIBUTION ON CIRCULAR CYLINDER SURFACE MOUNTED ON A FLAT WALL $L/D = 6$, $BR = 3\%$

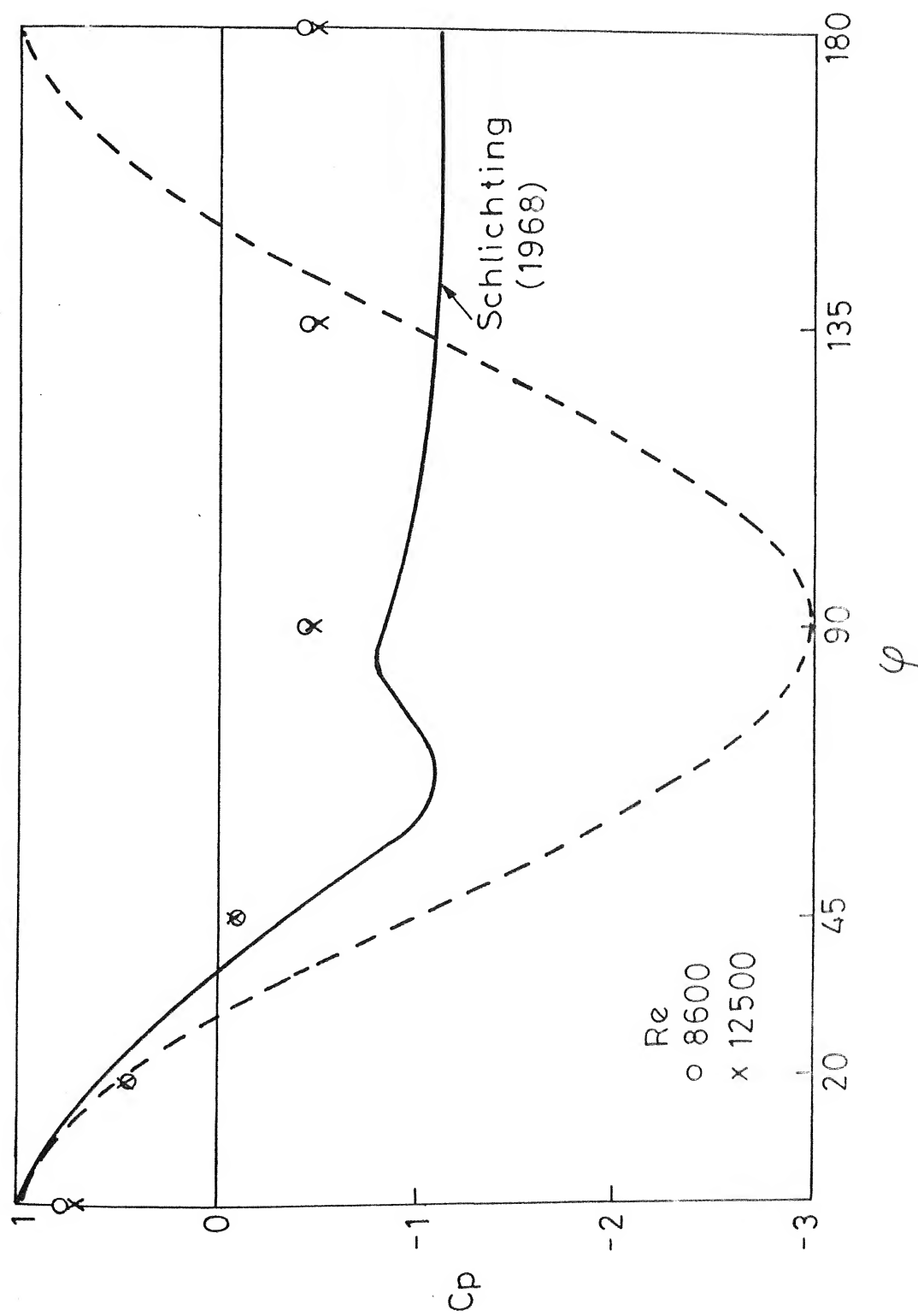
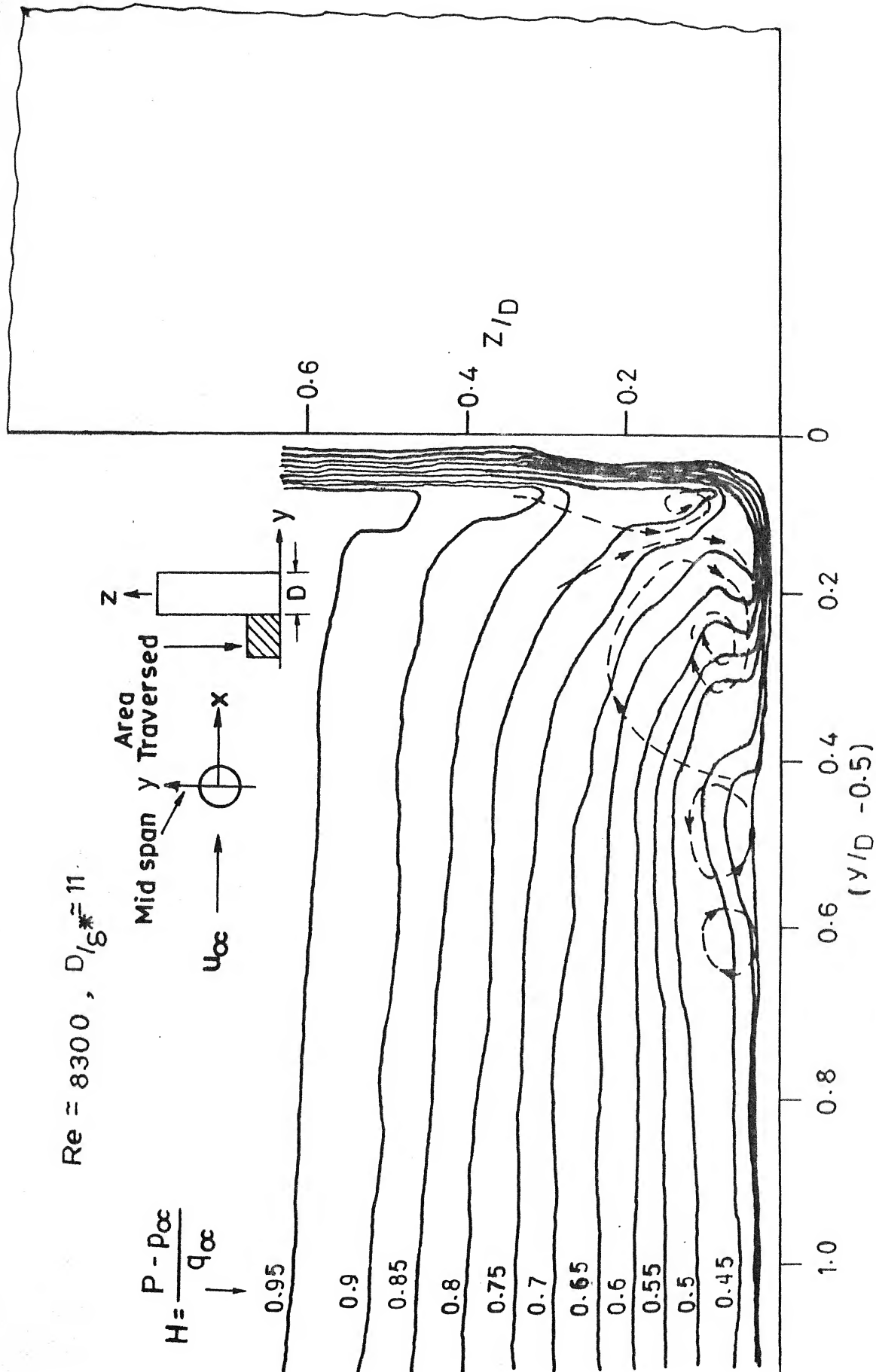


FIG. 5.16 b PRESSURE DISTRIBUTION ON WALL-CYLINDER JUNCTION

$Re = 8300$, $D/\delta^* \approx 11$



.5.17 TOTAL HEAD CONTOURS IN y - z PLANE AT MID SPAN OF CIRCULAR CYLINDER. $L/D = 6$, $BR = 3\%$

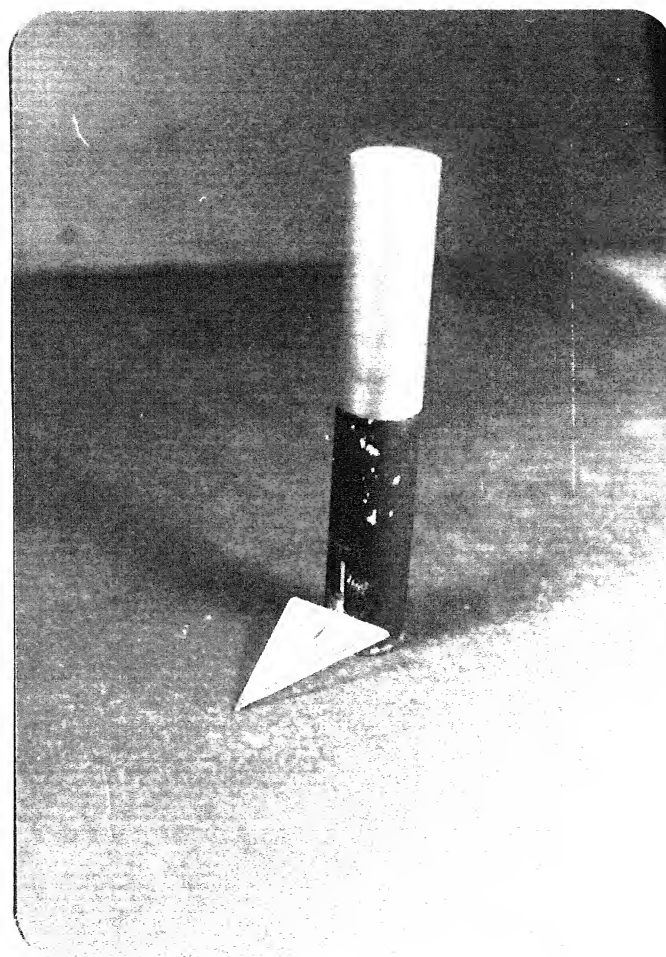
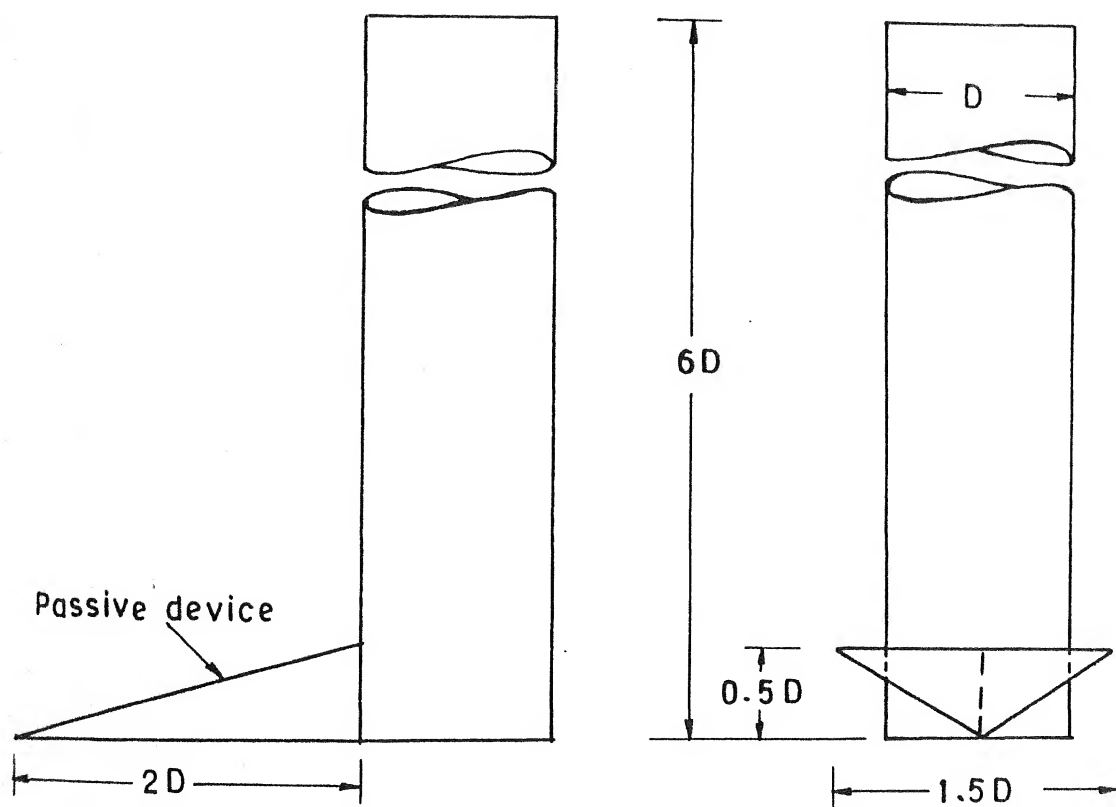


Fig. 5.18a A VIEW OF 25 mm CIRCULAR CYLINDER WITH
PASSIVE DEVICE



$$D = 25 \text{ mm}$$

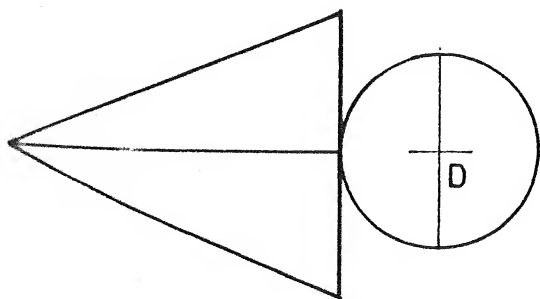


FIG. 5.18b CIRCULAR CYLINDER WITH PASSIVE DEVICE

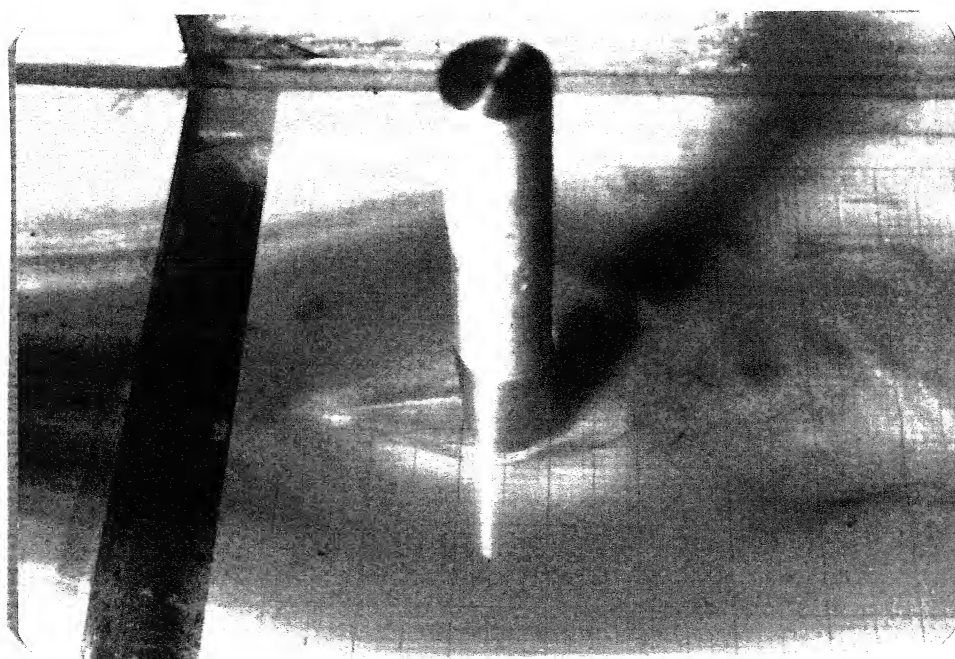
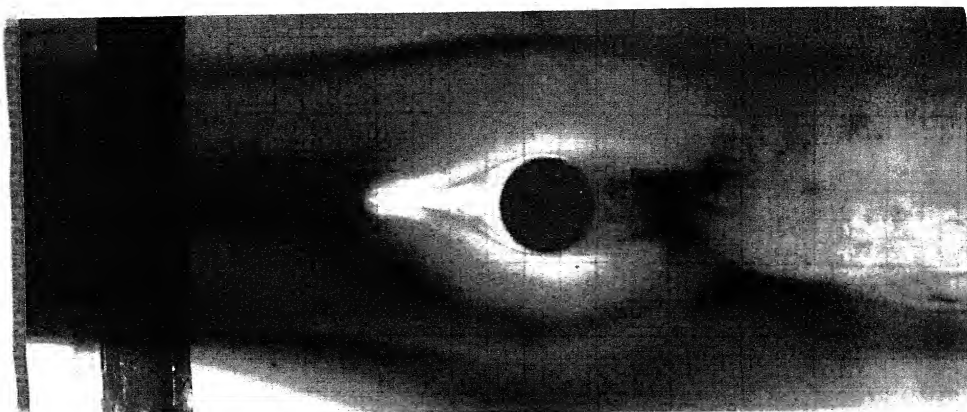
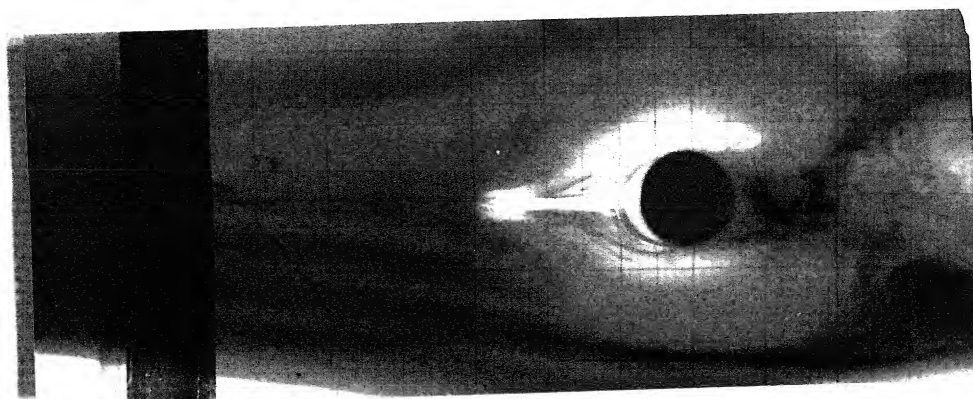


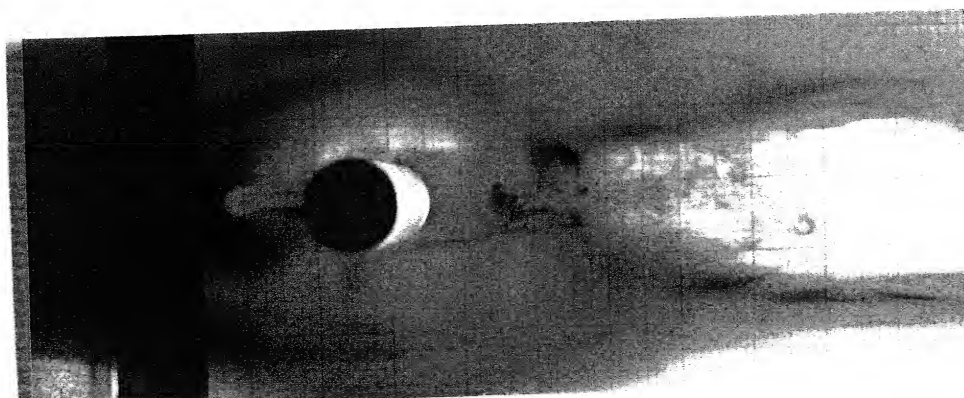
Fig. 5.19 A PERSPECTIVE VIEW OF DYE PATTERNS AROUND
CIRCULAR CYLINDER WITH PASSIVE DEVICE,
 $L/D = 6$, $BR = 10\%$, $Re = 3026$, $Fr = 0.135$



a. PLAN VIEW



b. TOP FRONT VIEW



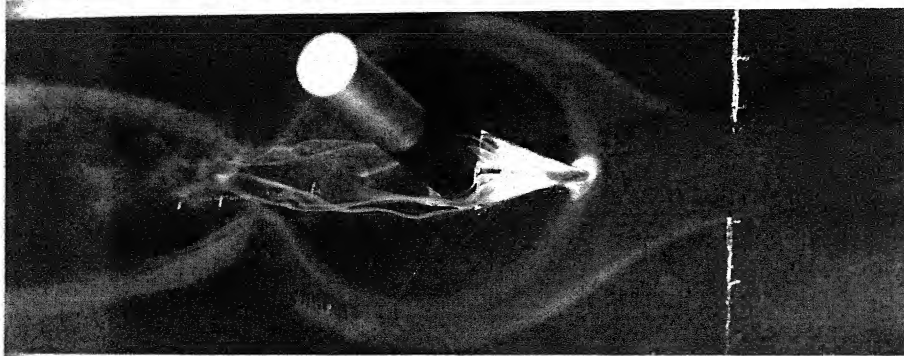
c. TOP REAR VIEW

Fig. 5.20 DYE PATTERNS AROUND CIRCULAR CYLINDER WITH PASSIVE DEVICE, $Re = 3026$, $Fr = 0.135$ (FLOW FROM LEFT TO RIGHT)



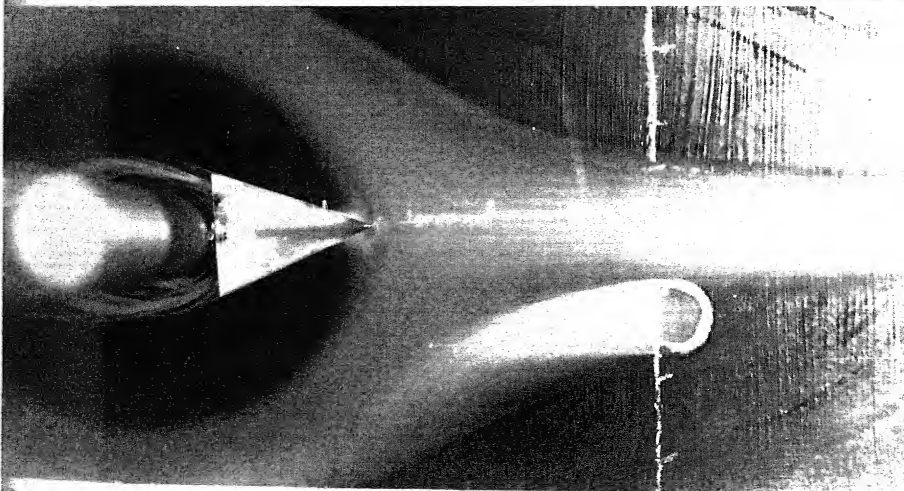
a. REAR

PERSPECTIVE VIEW

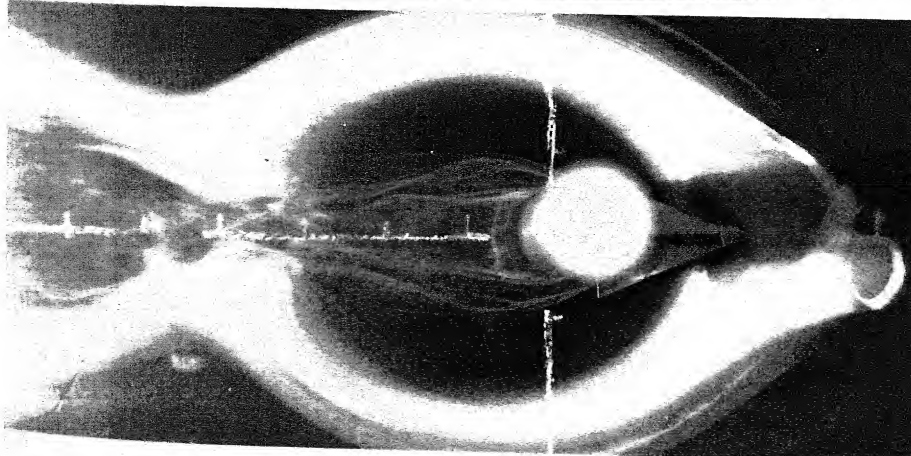


b. FRONT

PERSPECTIVE VIEW



c. TOP FRONT VIEW



d. TOP REAR VIEW

Fig. 5.21 TiCl_4 FLOW AROUND CIRCULAR CYLINDER WITH PASSIVE DEVICE $Re = 1450$, $D/\delta^* = 4.5$ FLOW FROM LEFT TO RIGHT IN (a) AND RIGHT TO LEFT IN b,c,d

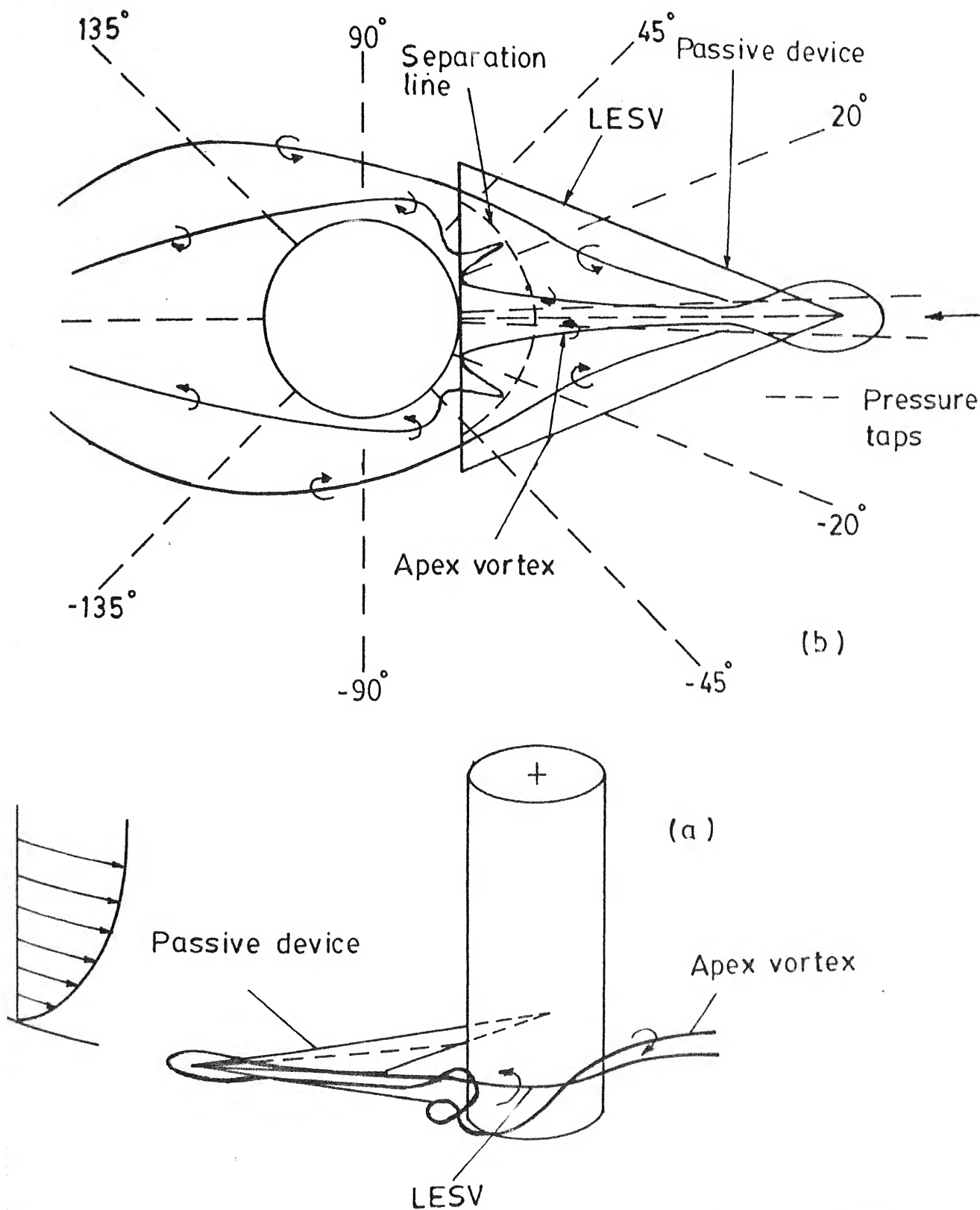


FIG 5.22 SCHEMATICS OF MODIFIED VORTEX FLOW AROUND CIRCULAR CYLINDER WITH PASSIVE DEVICE

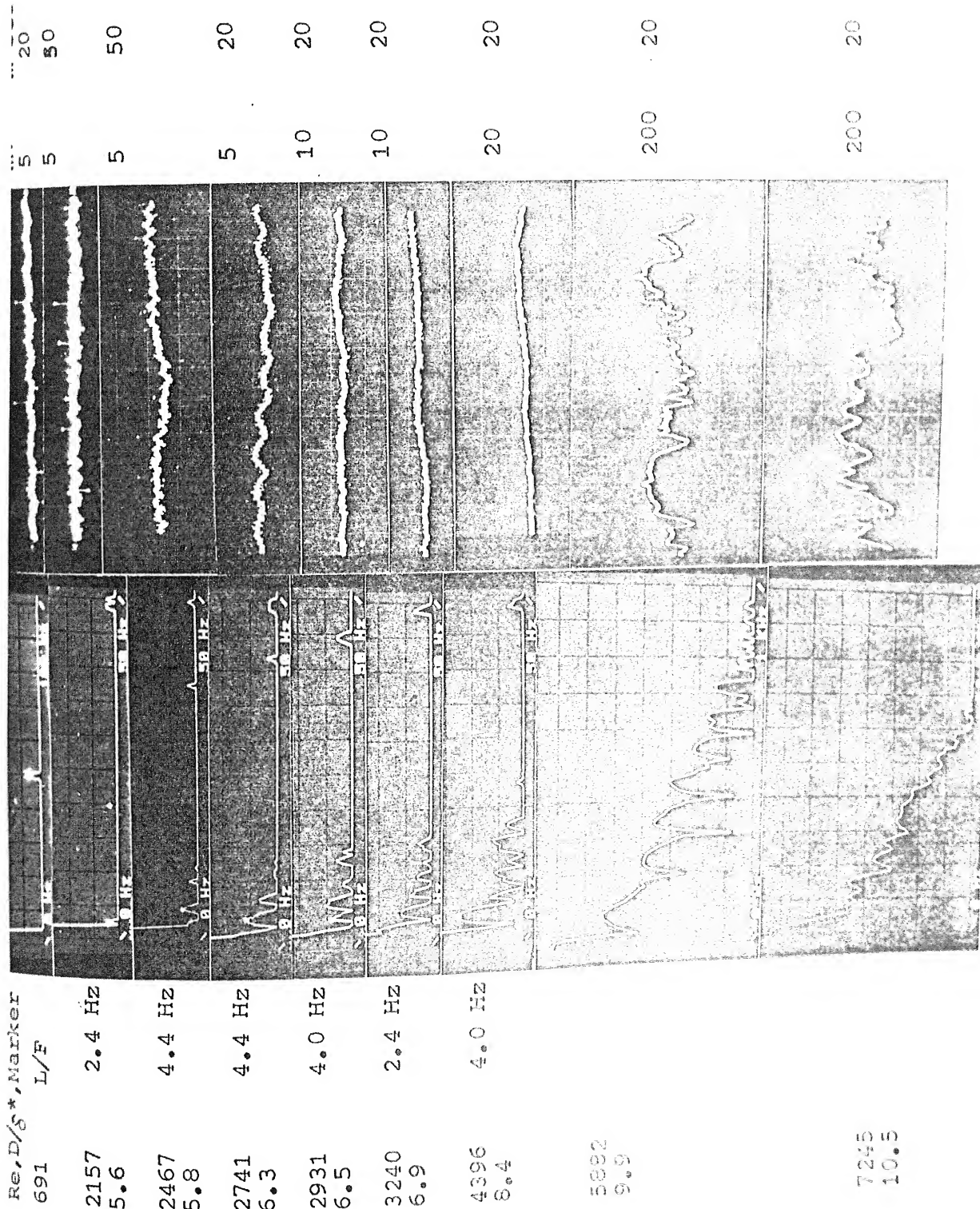


Fig. 5.23a SPECTRA AND TRACES OF MODIFIED VORTEX
OSCILLATIONS AROUND CIRCULAR CYLINDER WITH
PASSIVE DEVICE, $L/D = 6$, $Re = 3\%$

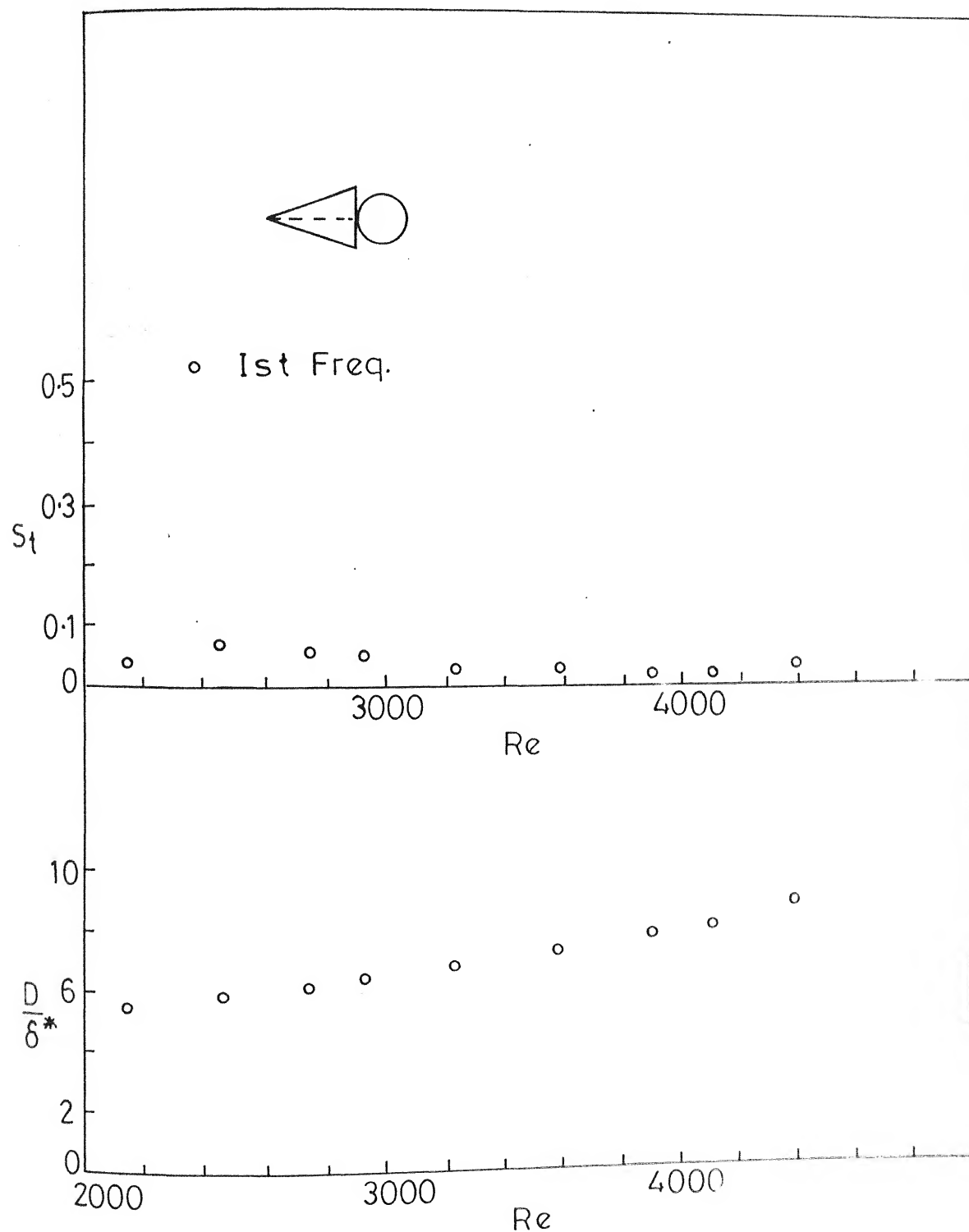
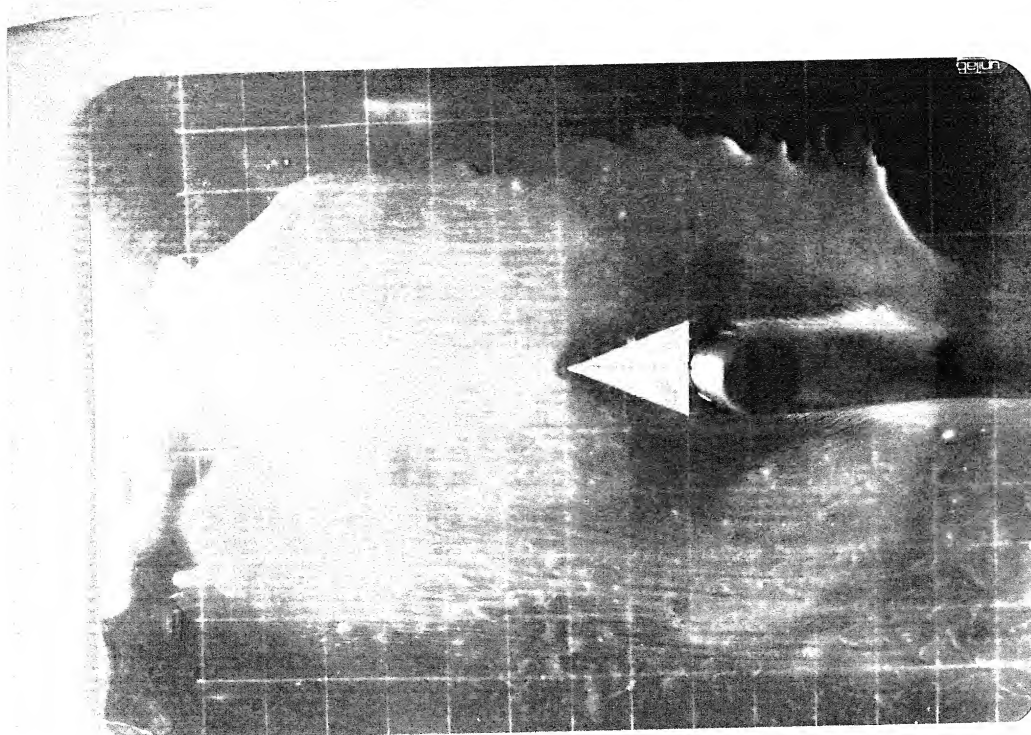


FIG. 5.23 b VARIATION OF VORTEX OSCILLATION FREQUENCIES AROUND CIRCULAR CYLINDER WITH PRESSURE DEVICE $L/D=6$, $BR=3\%$



a. $t = 18 \text{ Min}$ (FLOW ON)

b. $t = 18 \text{ Min}$

Fig. 5.24 MODIFIED SURFACE OIL FILM PATTERNS AROUND
25 mm CIRCULAR CYLINDER, $L/D = 6$, $BR = 3\%$
 $Re = 7800$, $D/\delta^* = 11$

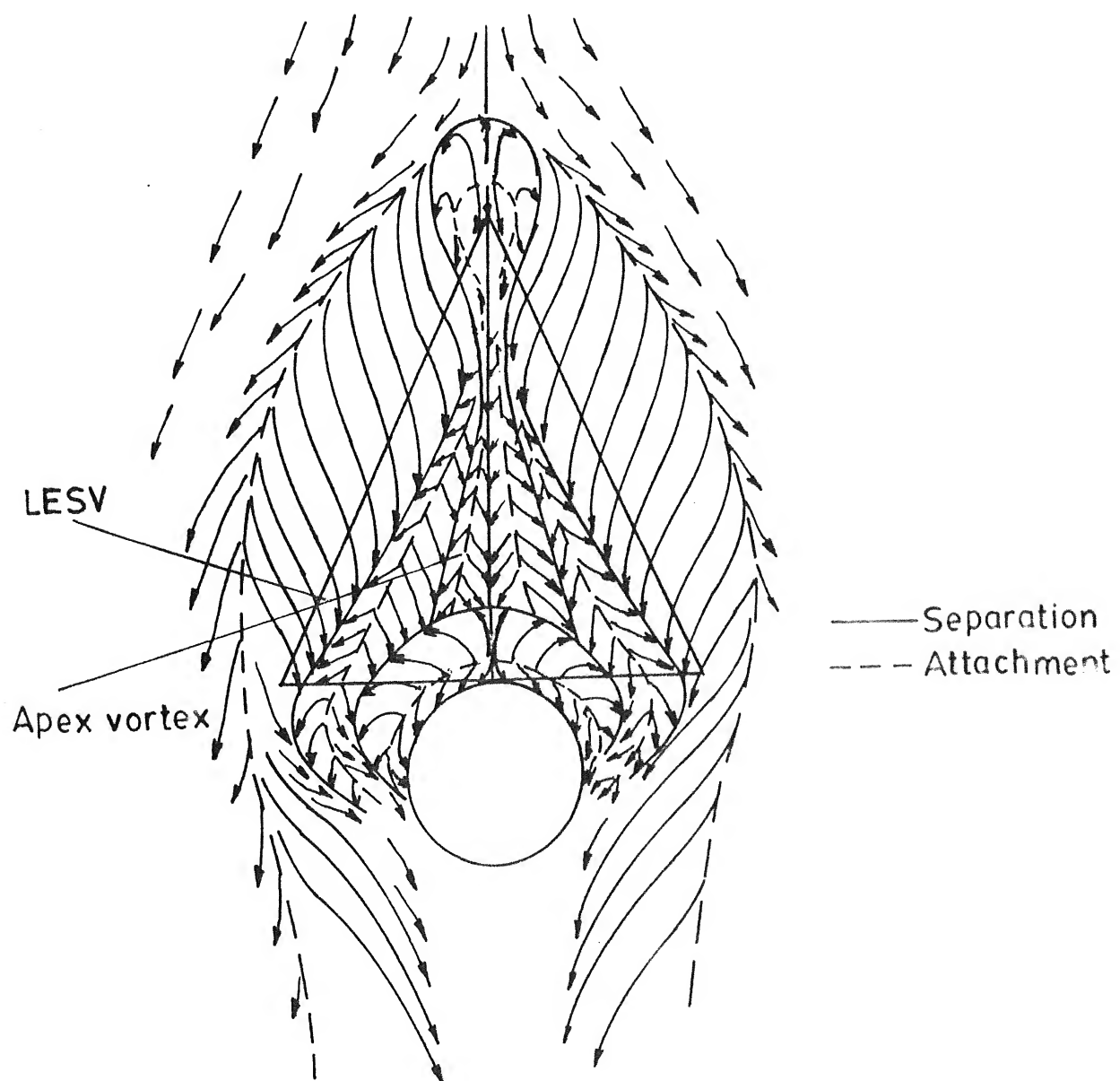


FIG. 5.24 c MODIFIED SURFACE STREAMLINES
AROUND CIRCULAR CYLINDER

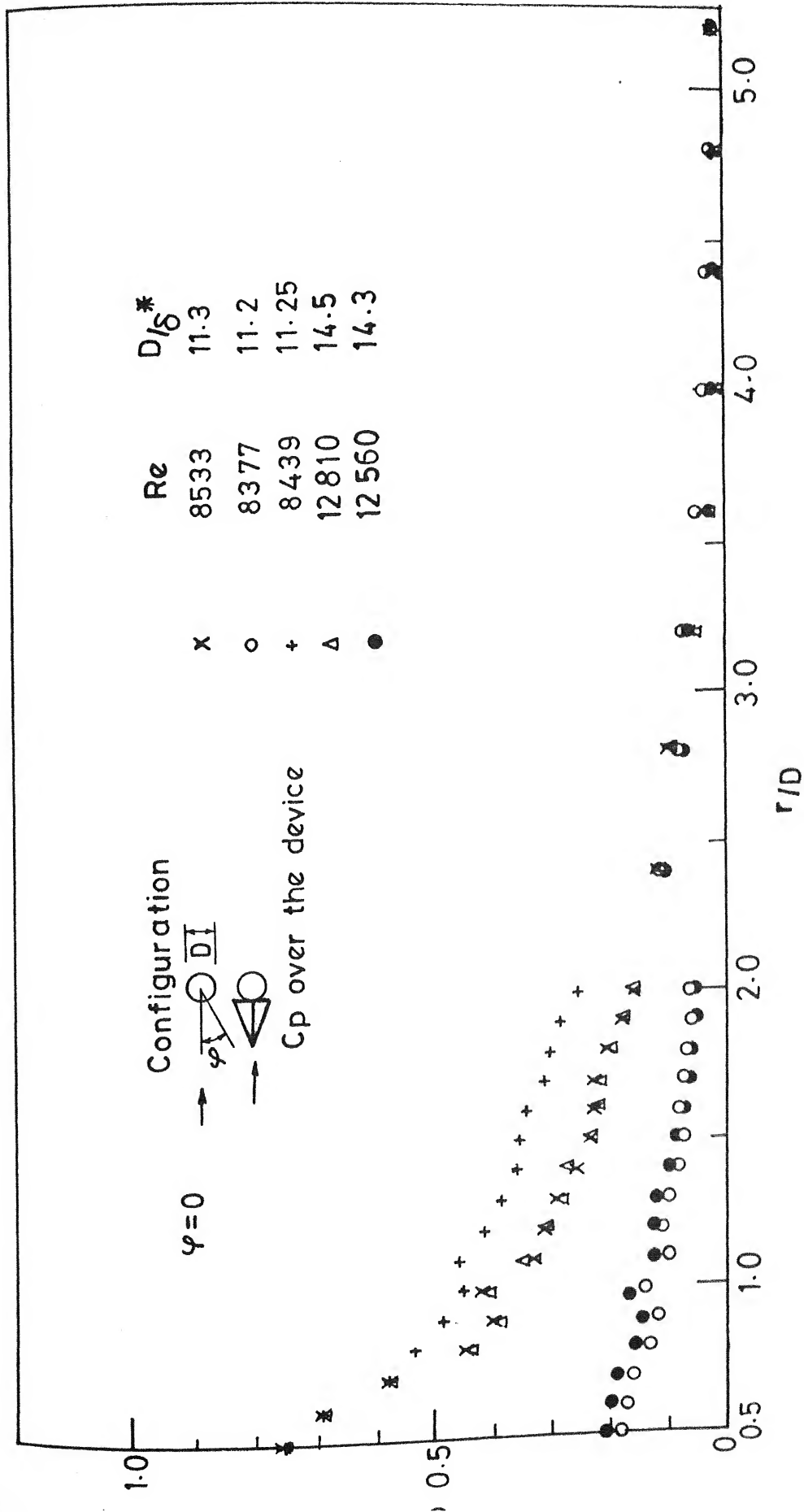
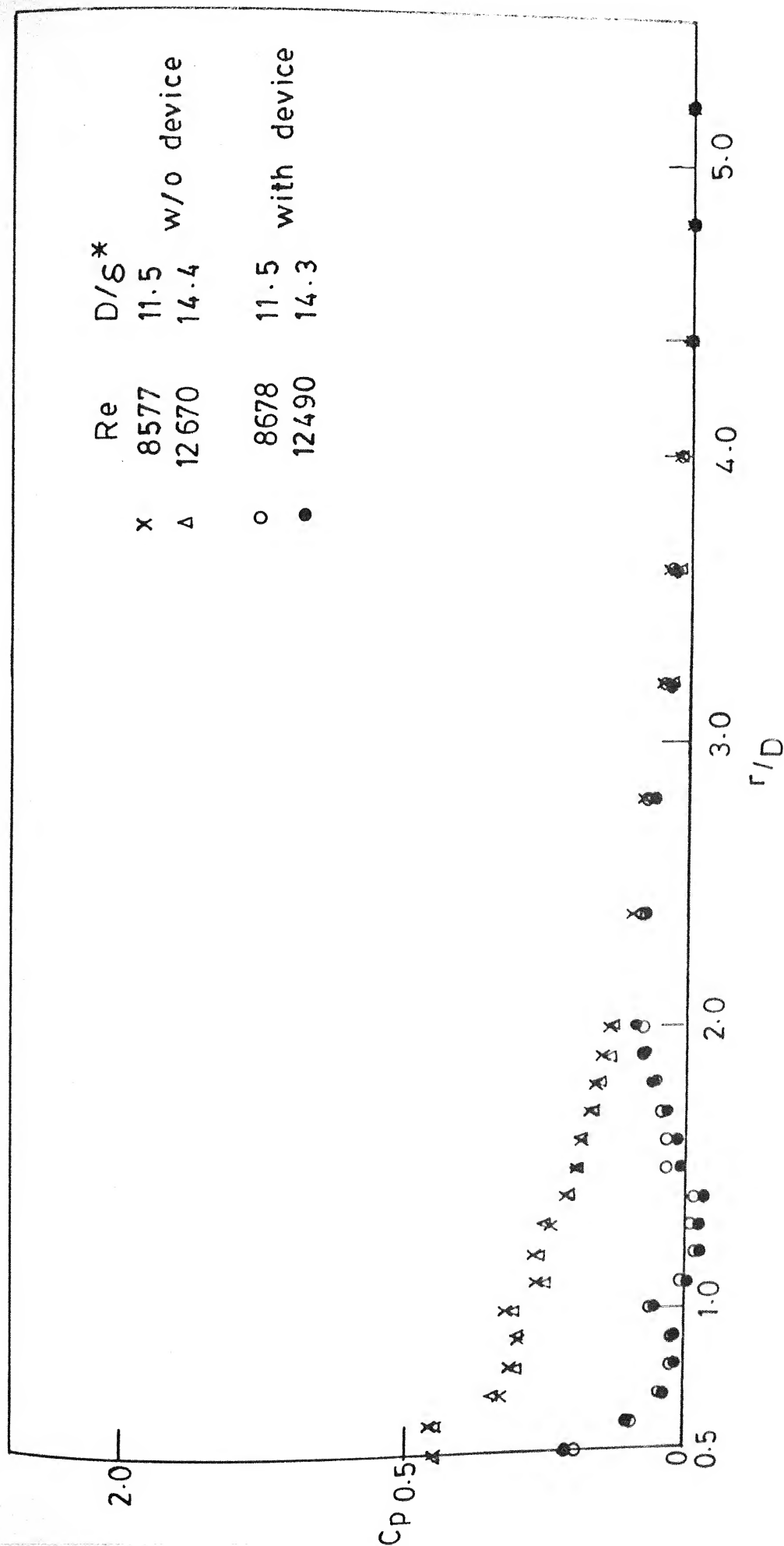
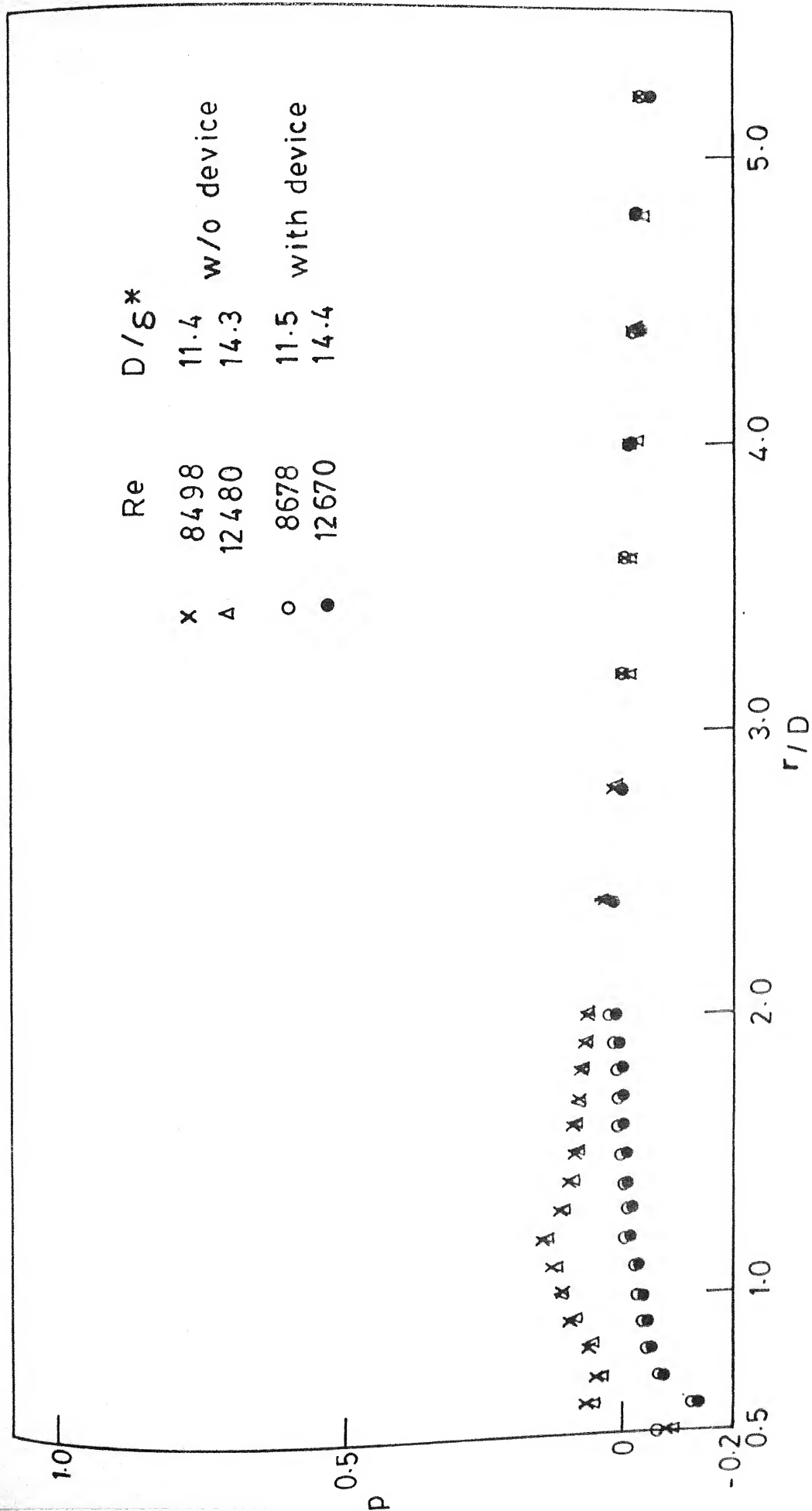


FIG. 5.25 a FLOOR PRESSURE AROUND CIRCULAR CYLINDER WITH AND WITHOUT PASSIVE DEVICE $\varphi = 0$

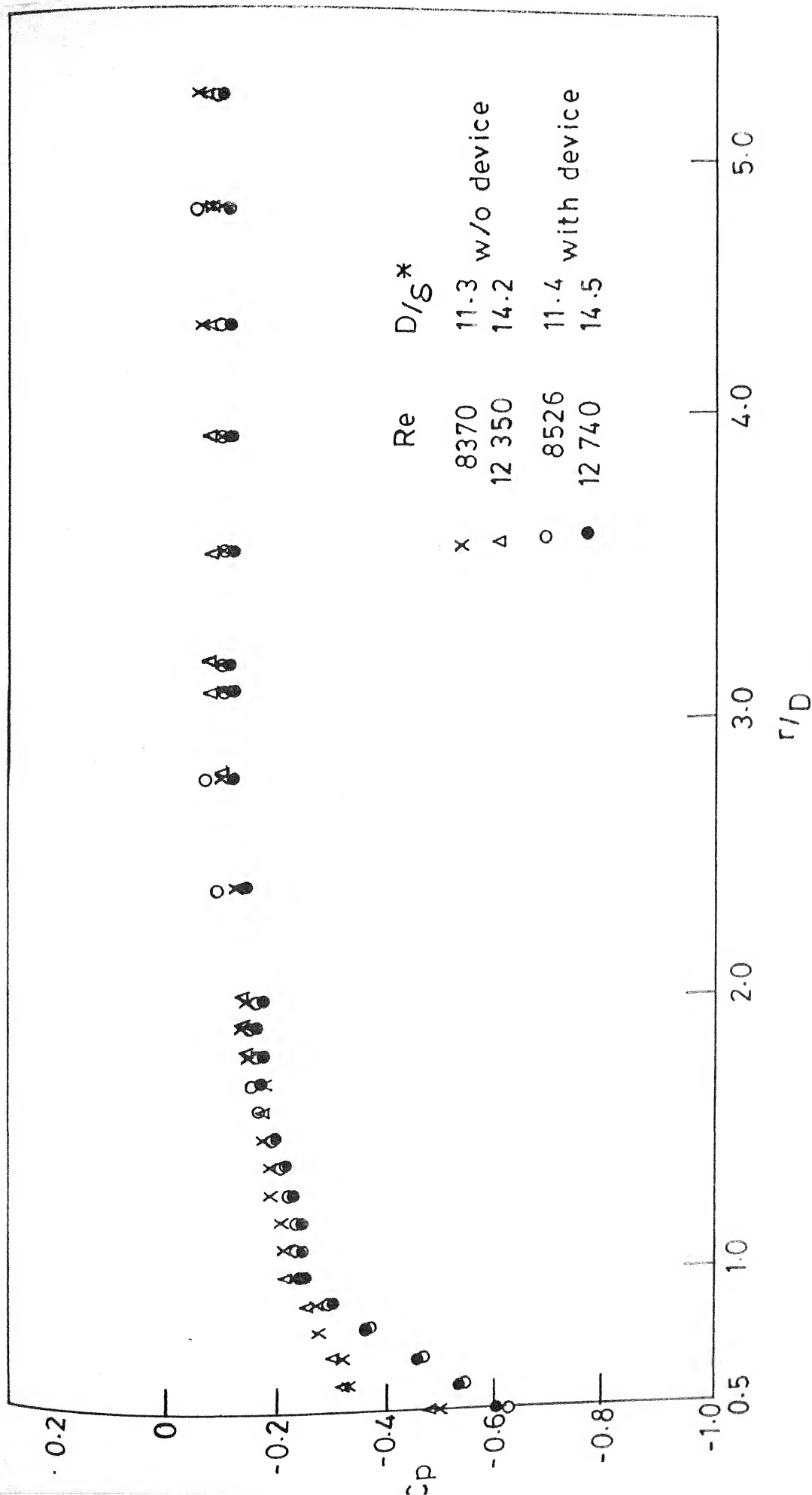


(b) $\varphi = 20^\circ$

FIG. 5.25 Contd.

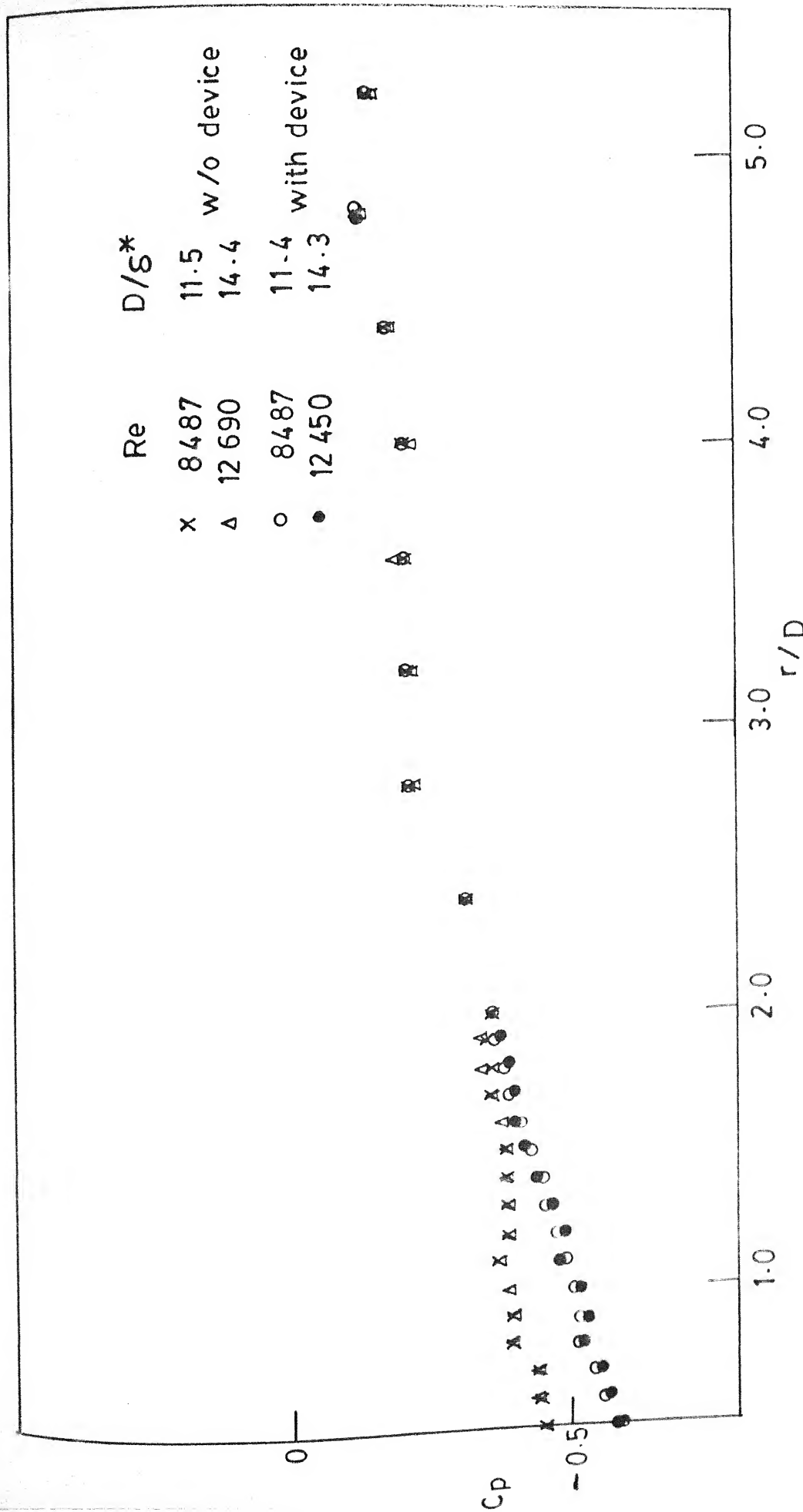


(c) $\varphi = 45^\circ$
FIG. 5.25 Contd.



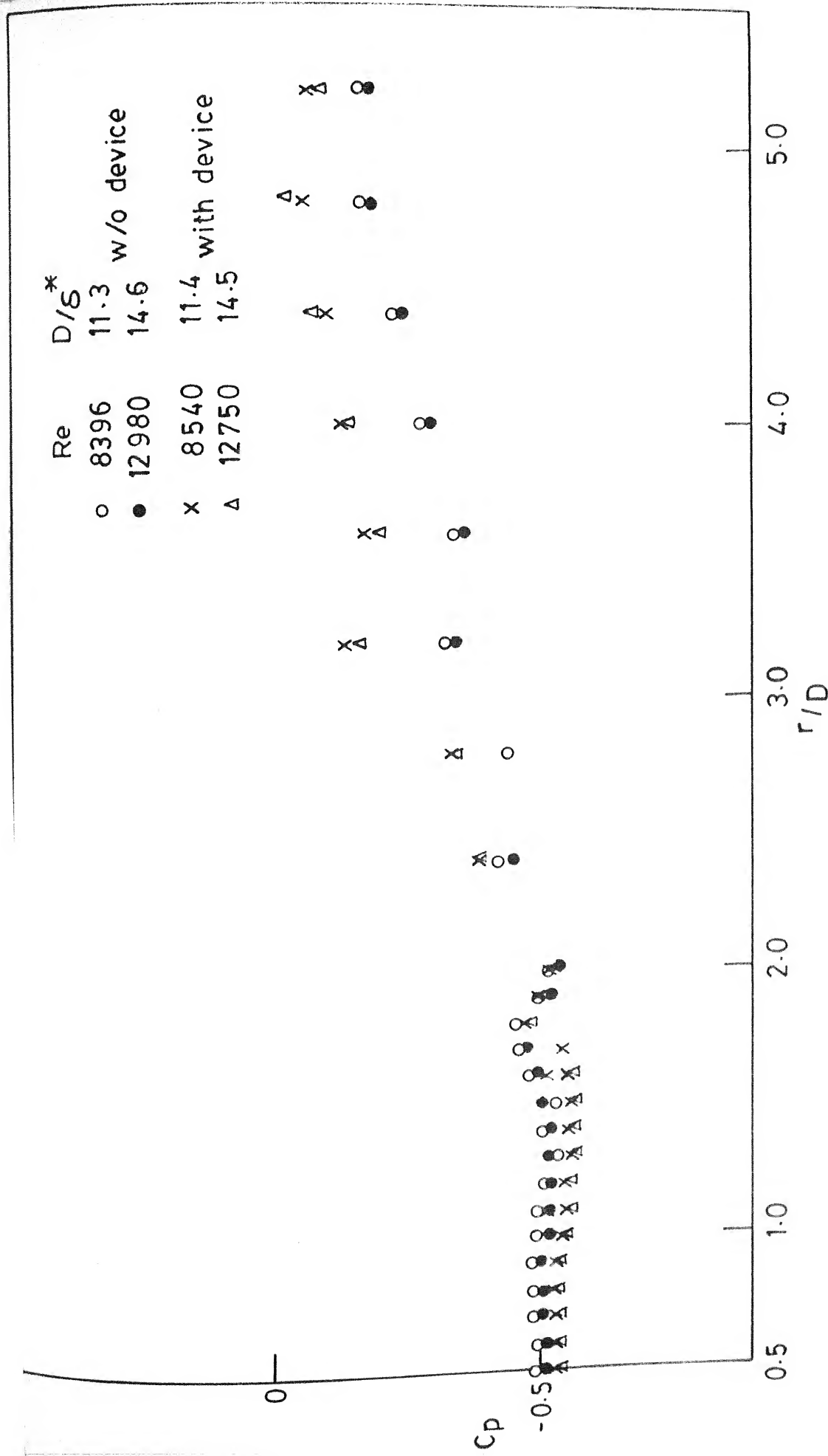
(d) $\varphi = 90^\circ$

FIG. 5-25 Contd.



(e) $\varphi = 135^\circ$

FIG. 5-25 Contd.



(f) $\varphi = 180^\circ$

FIG. 5.25 Contd.

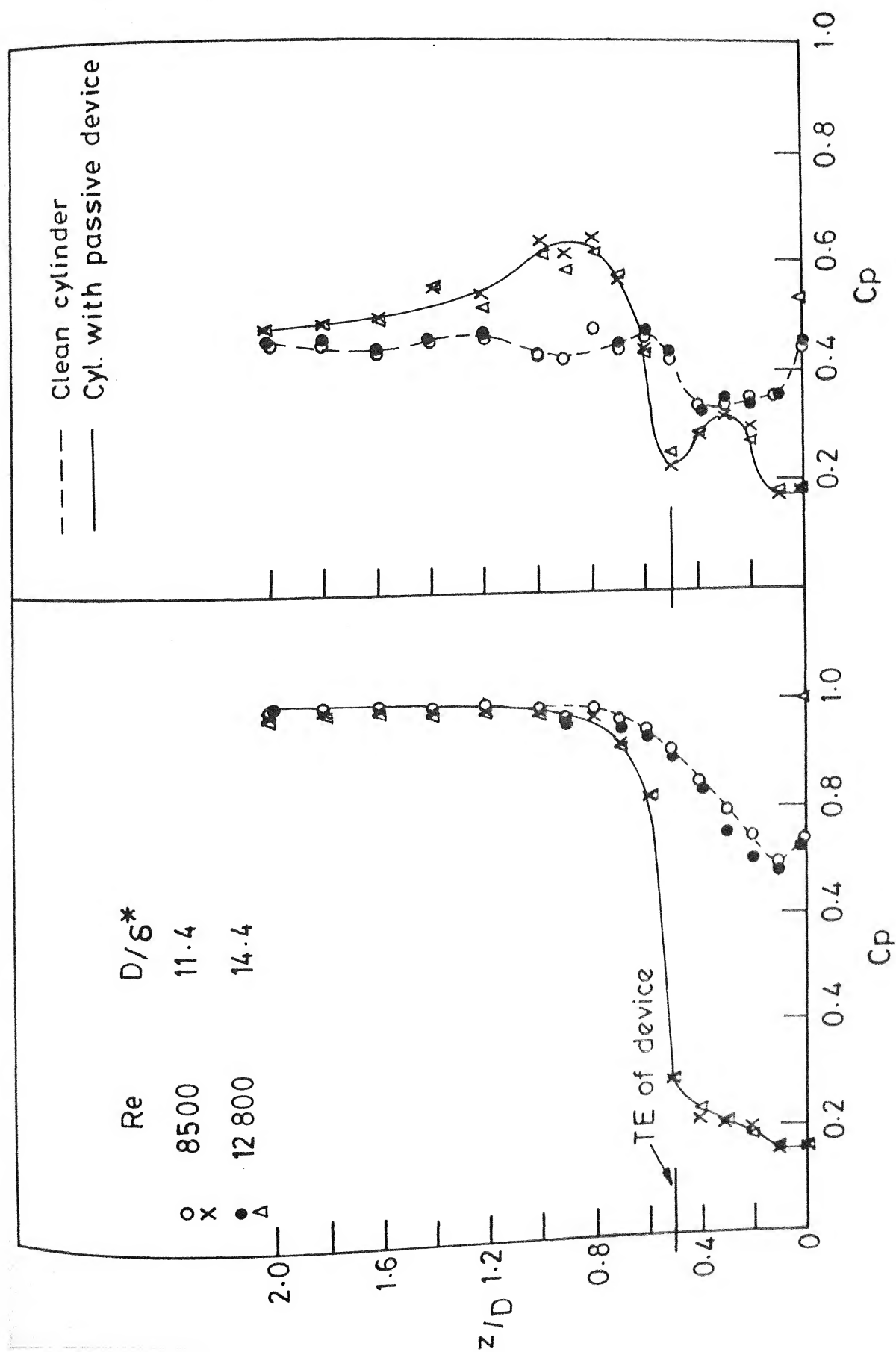
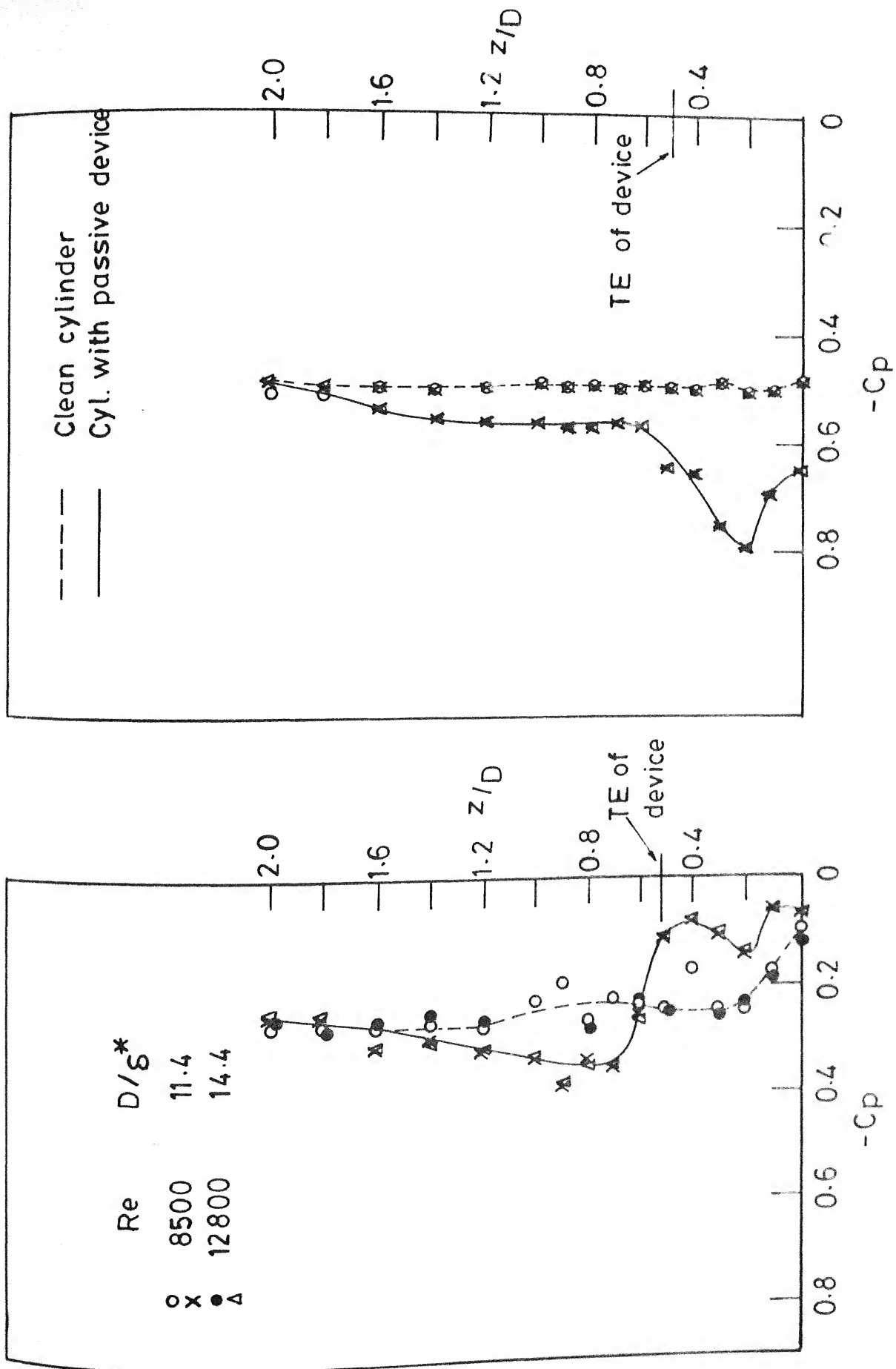
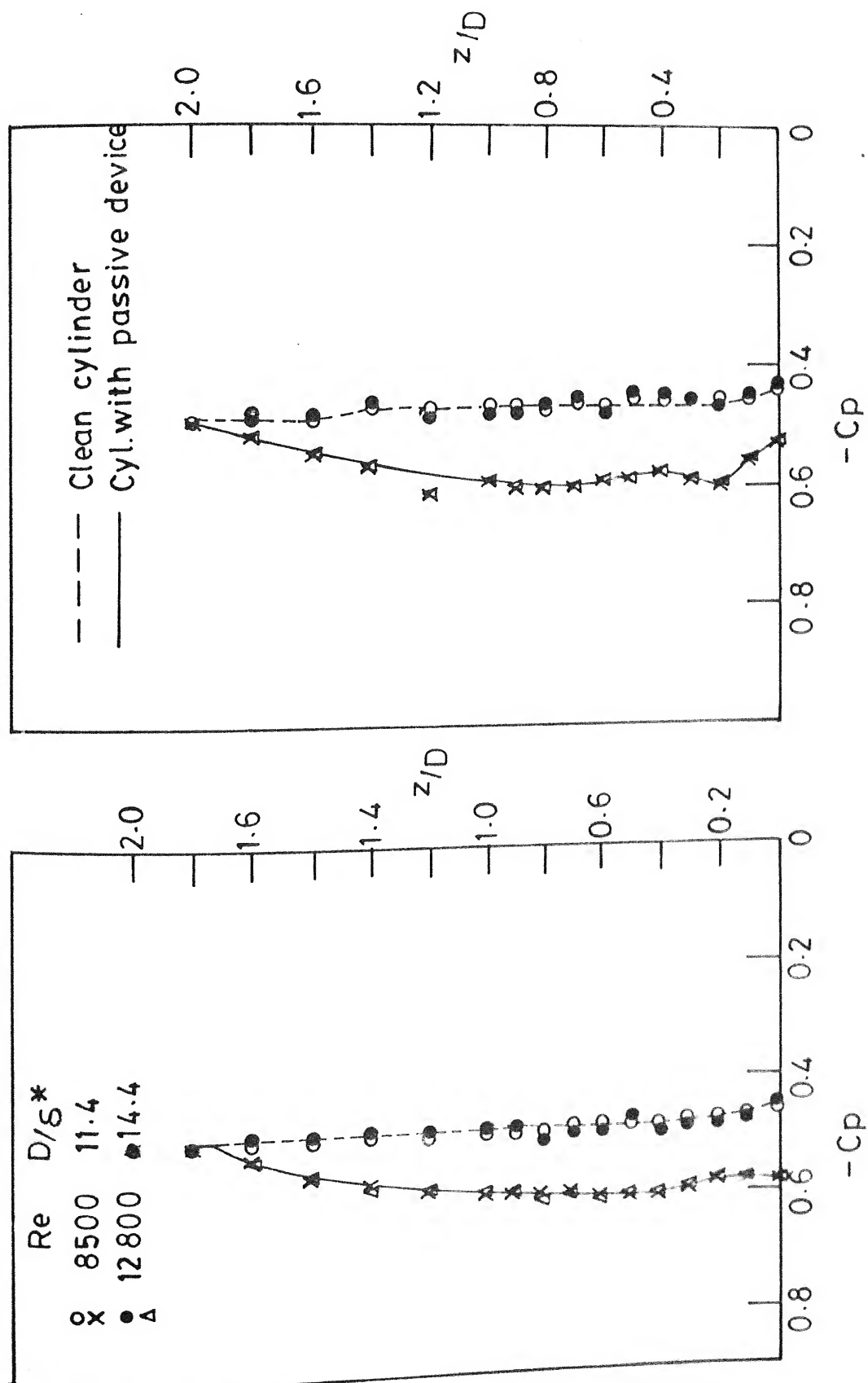


FIG. 5. 26 a SURFACE PRESSURES ON CIRCULAR CYLINDER WITH AND WITHOUT PASSIVE DEVICE $\varphi = 0$, $\varphi = 20^\circ$



(b) $\varphi = 45^\circ, \varphi = 90^\circ$
FIG. 5.26 Contd.



(c) $\varphi = 135^\circ$, $\varphi = 180^\circ$

FIG. 5.26 Contd.

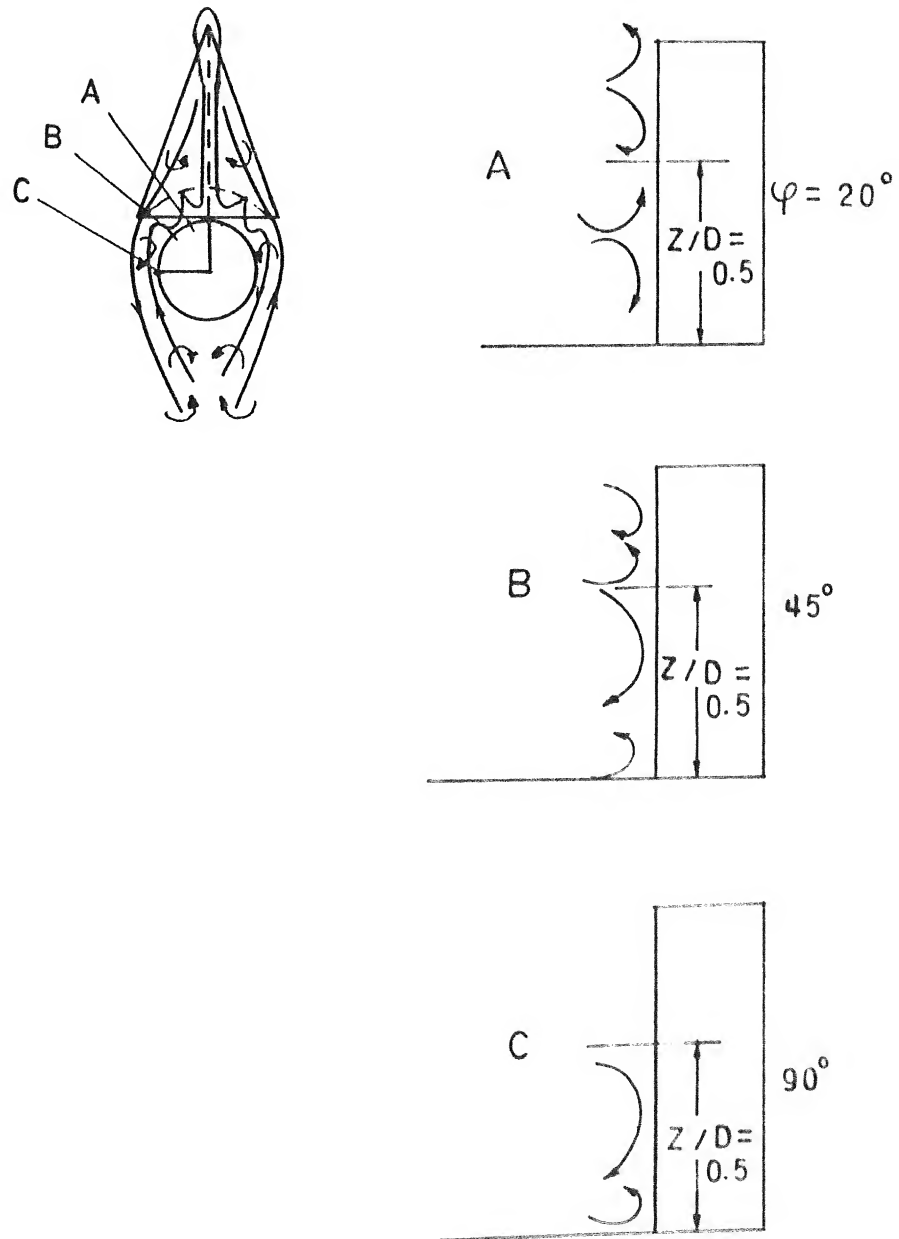
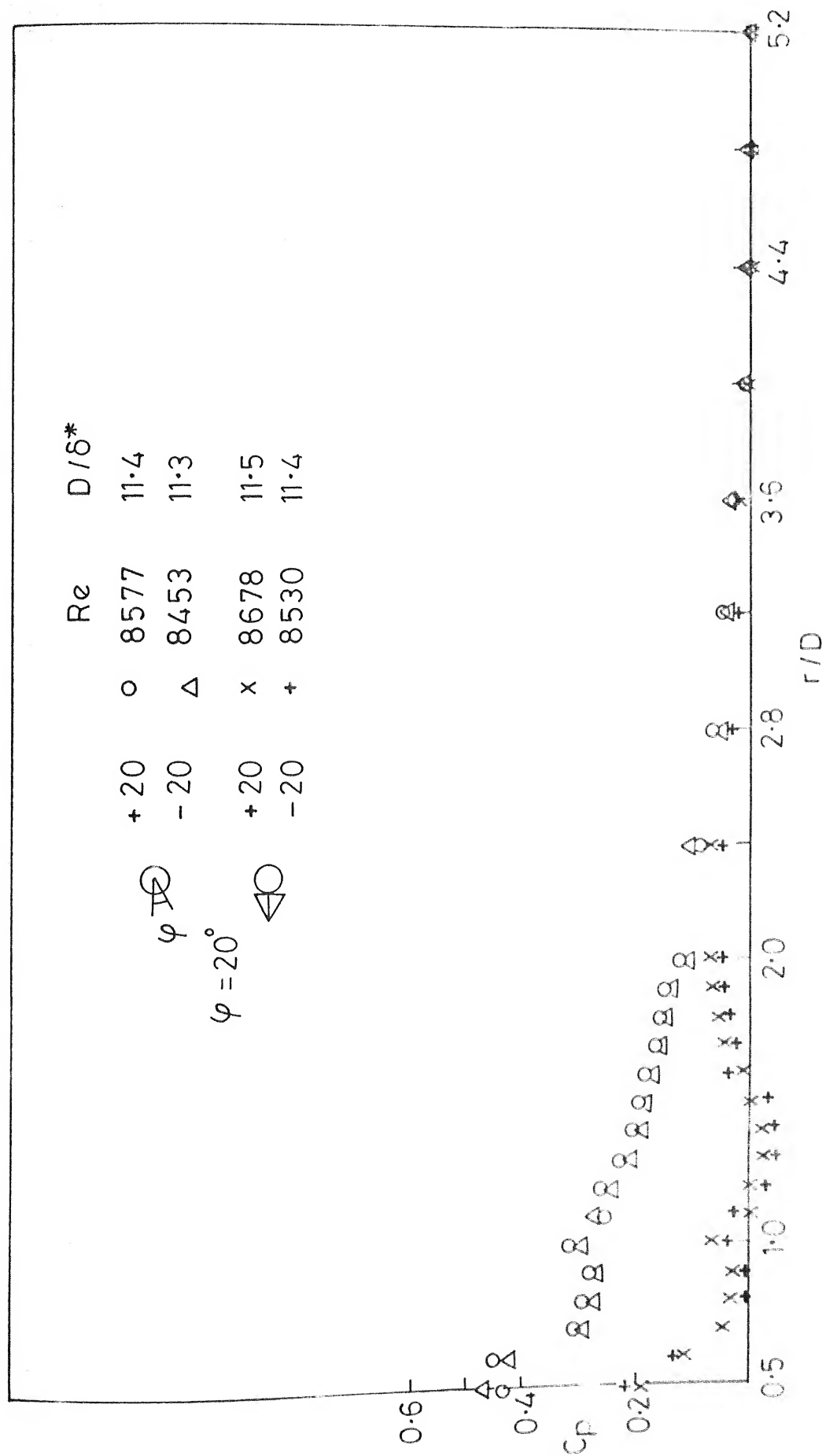
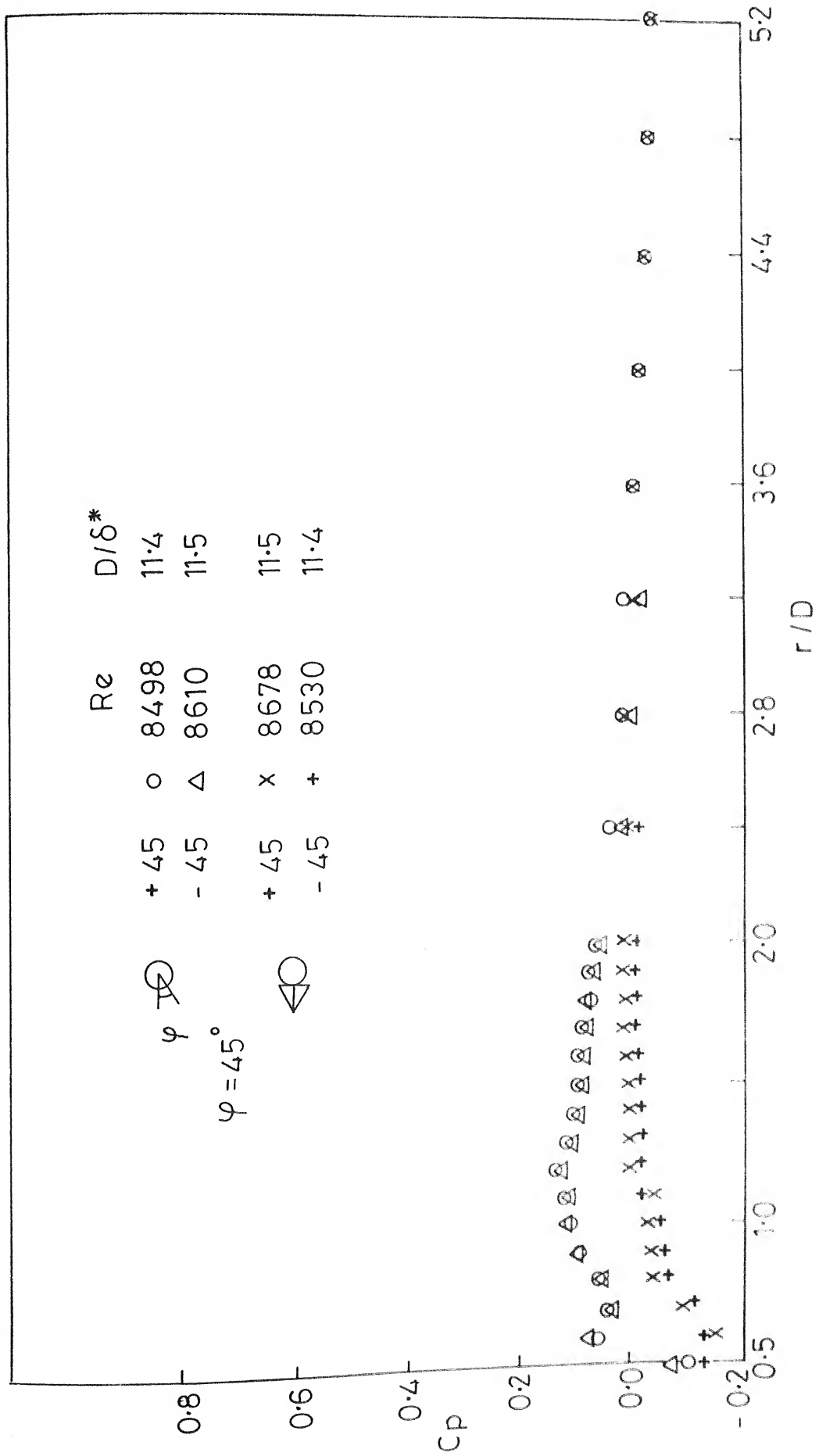


FIG. 5. 26 d SCHEMATICS OF MODIFIED FLOW REGIONS ON CIRCULAR CYLINDER



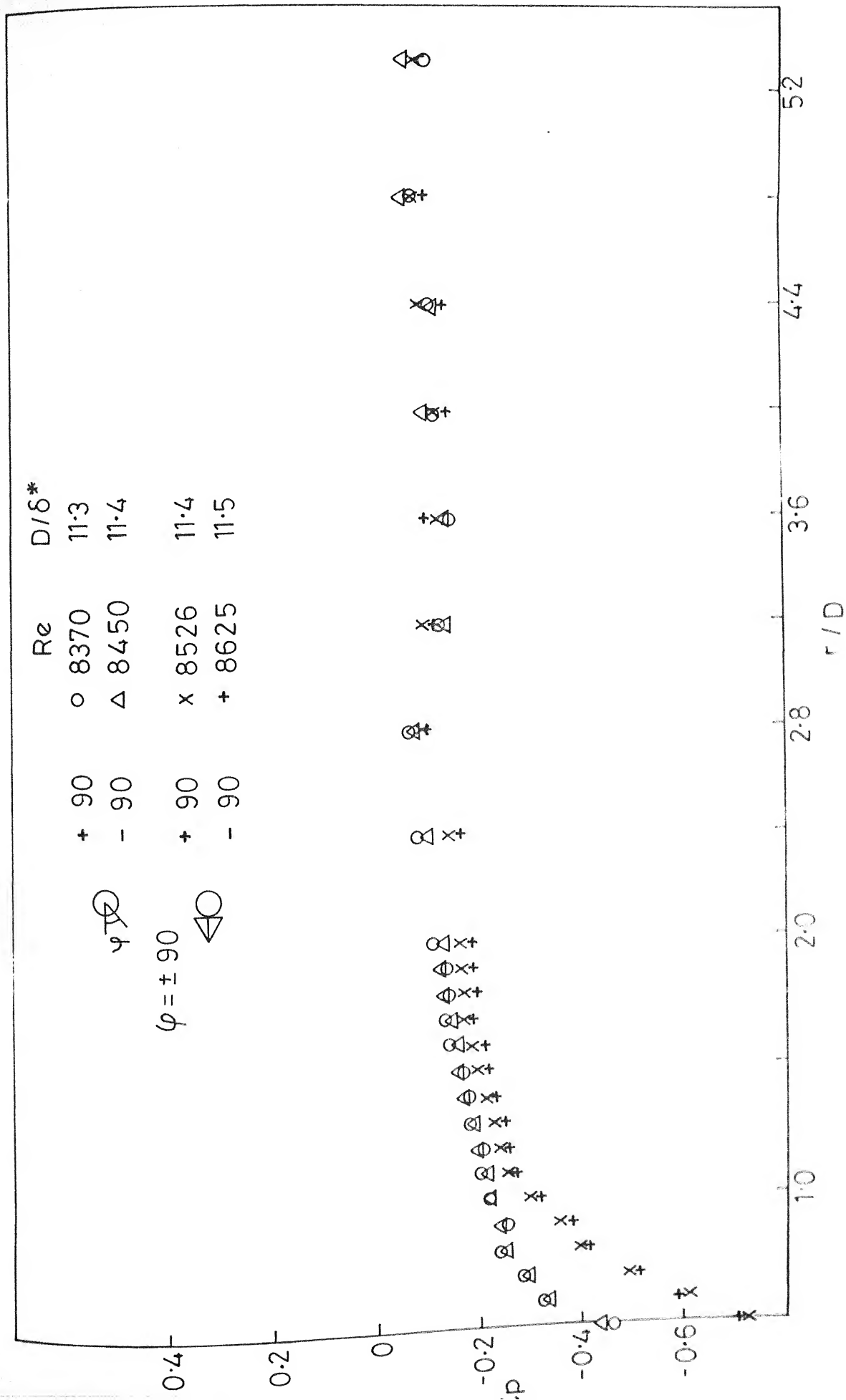
a. $\varphi = 20^\circ$

FIG.5-27 SYMMETRY OF FLOOR PRESSURE DISTRIBUTION AROUND CIRCULAR



b. $\varphi = 45^\circ$

FIG. 5.27 (CONT'D.)



c. $\phi = 90^\circ$

FIG. 5.27 (CONT'D.)

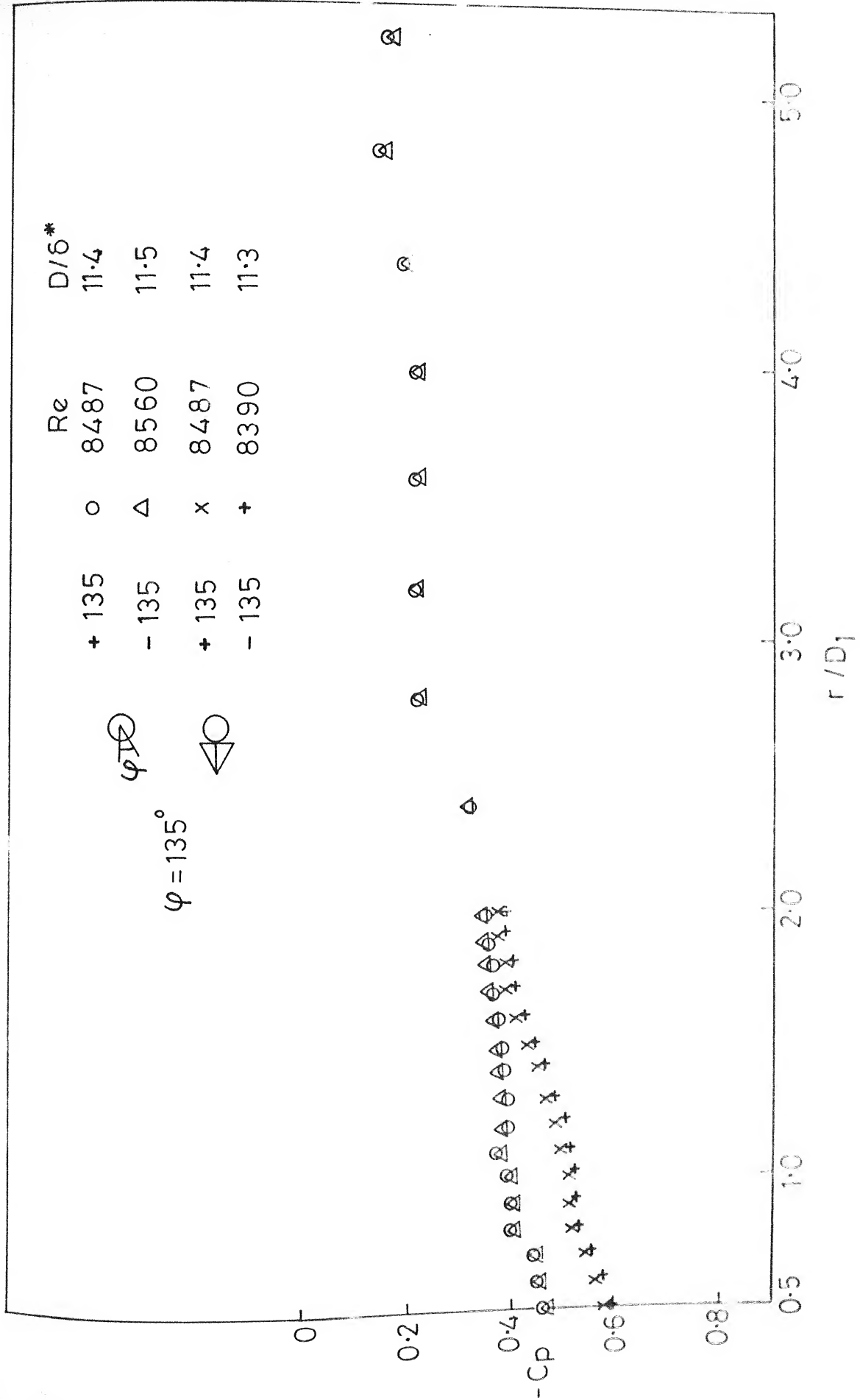
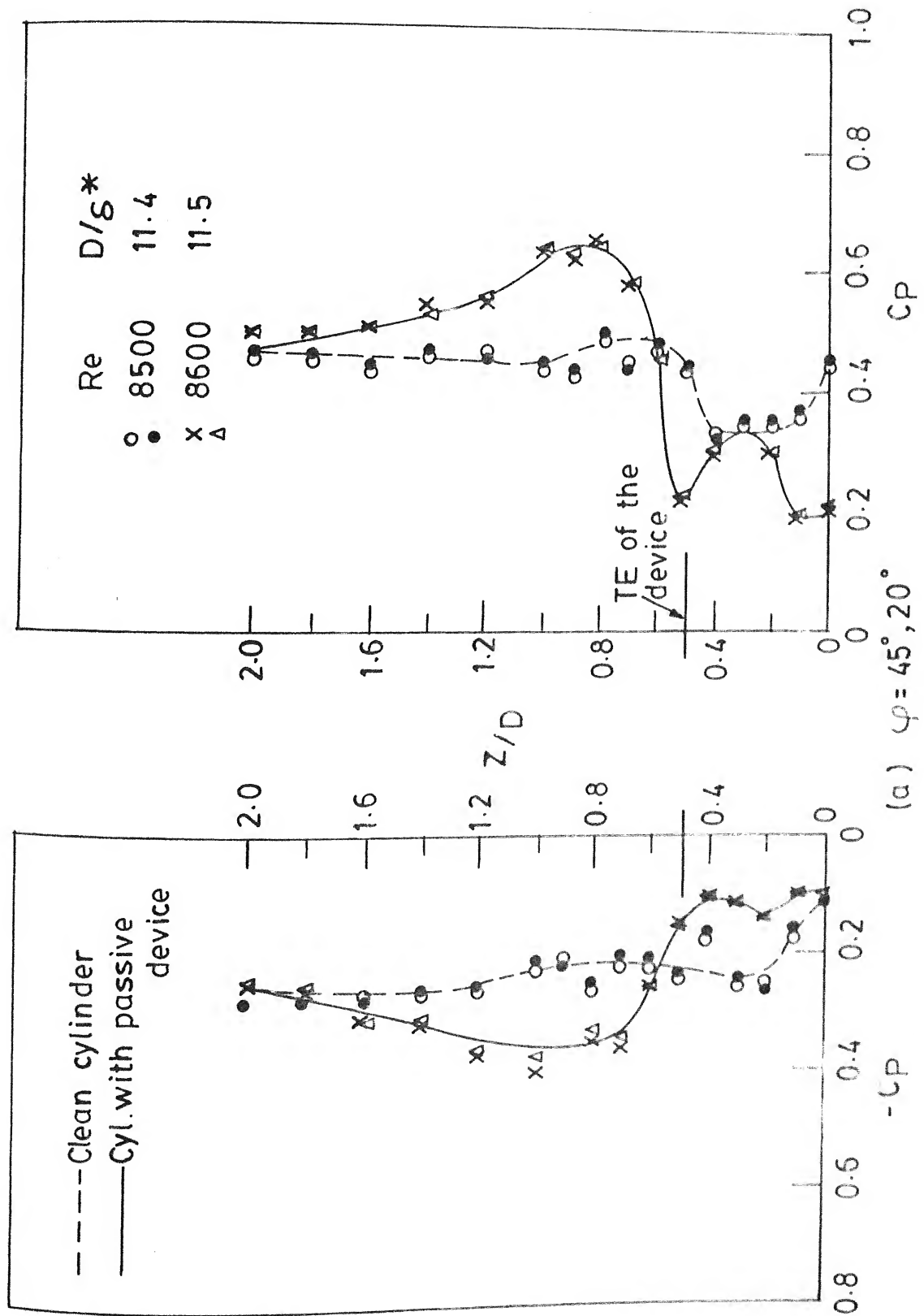


FIG. 5.27 (CONT'D.)



(a) $\varphi = 45^\circ, 20^\circ$

FIG. 5.28 SYMMETRY OF SURFACE PRESSURES ON CIRCULAR CYLINDER

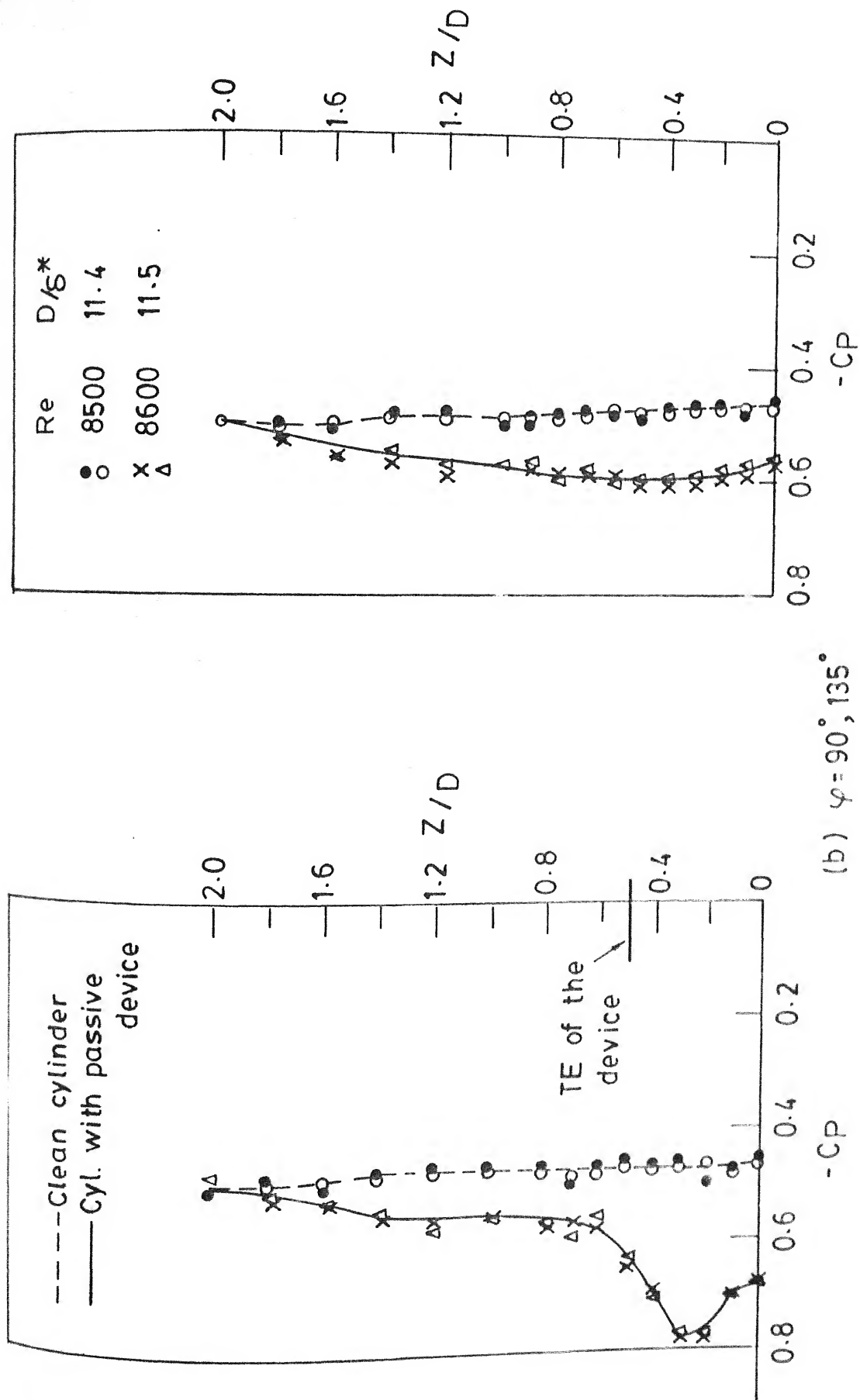
(b) $\varphi = 90^\circ, 135^\circ$

FIG. 5.28 Contd.

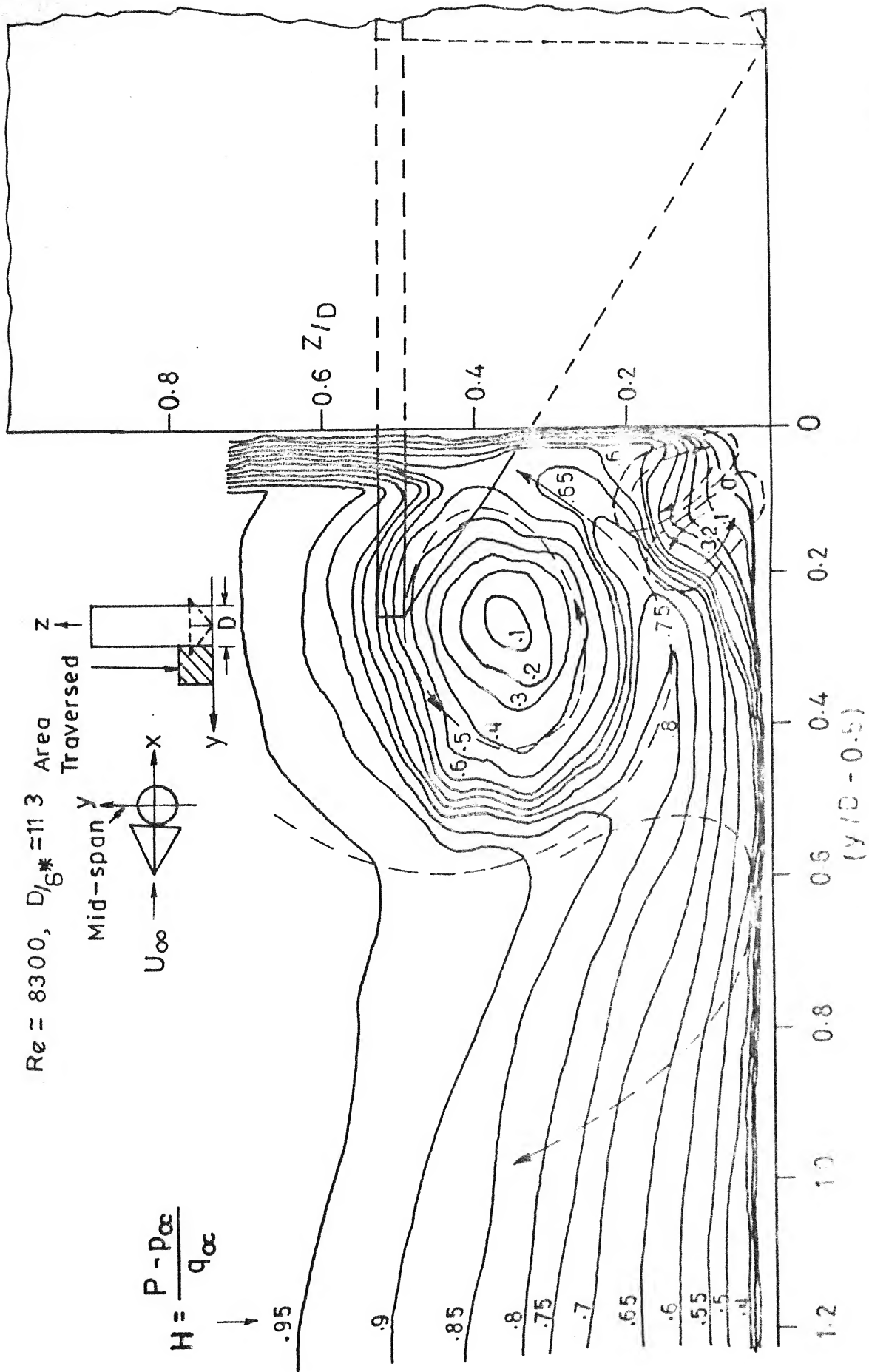


FIG. 5.29 TOTAL HEAD CONTOURS IN y - z PLANE AT MID SPAN OF CIRCULAR CYLINDER
 WITH DEVICE $L/D = 6.0$, $B.R = 3\%$

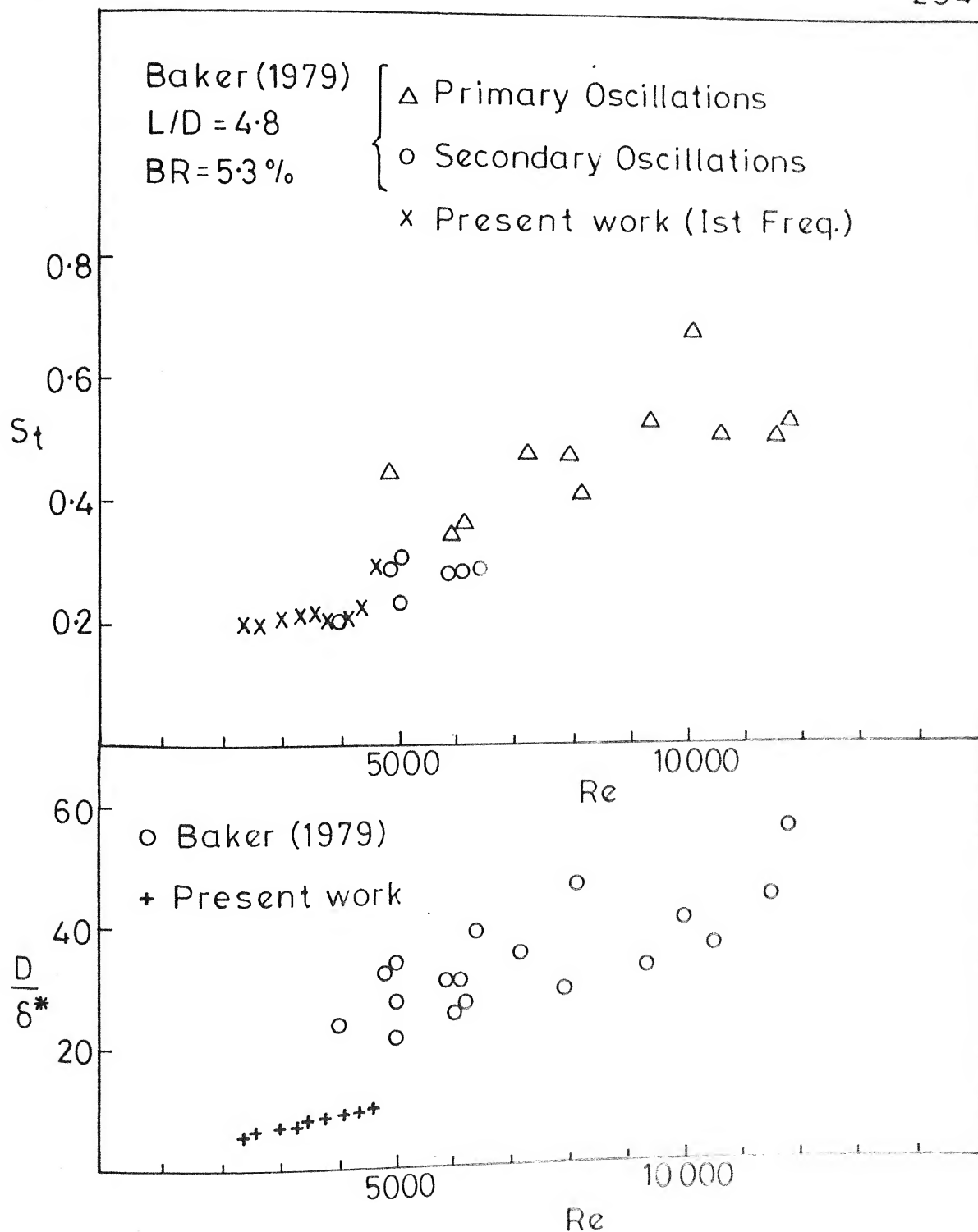


FIG. 5.30 VARIATION OF VORTEX OSCILLATIONS AROUND CIRCULAR CYLINDER (COMPOSITE PLOT)

CHAPTER VI

EFFECT OF LEADING EDGE SHAPE ON HSV AND THE MODIFIED HSV

6.1 INTRODUCTION

It was observed in Chapters IV and V that the horseshoe vortex around the junctions of round nose pier model and circular cylinder with floor, and its modification with the passive device appeared similar due to the identical leading edge shape in the two cases. The effect of leading edge shape of the pier model on the structure of HSV, and on the modified HSV due to the passive device will be established in this chapter, by using the same procedure and techniques as in the preceding chapters. The pier models with blunt and streamlined nose shapes were used. The model with truncated face, i.e., rectangular pier model is the extreme case and laboratory measurements of local scour depths at its leading edge have been reported and are used as reference data, while the streamlined leading edge shapes cause minimum local scour depth at the nose (Breusers et.al., 1977). A total of three pier models used for describing this effect, were;

(i) rectangular pier model, (ii) wedge nose model and (iii) lenticular pier model. The results of HSV around clean pier models are described first, followed by the HSV modification and the discussions.

6.2 COORDINATE SYSTEM

A right hand Cartesian co-ordinate system X, Y, Z with origin at the pier leading edge and positive X in the downstream direction in the plane of symmetry was used. However, when presenting

pressures around the pier models, a local co-ordinate 's' was used with origin at the pier-floor junction, locally normal to the pier wall for convenience.

6.3 RESULTS WITH CLEAN PIER MODELS

The results with rectangular and streamline nose pier models are described in the following order of flow approach to their leading edges : (i) laminar flow, (ii) transition to turbulent flow, and (iii) fully turbulent flow. The Reynolds number was changed by changing the flow speed in a facility.

6.3.1 Laminar Flow

The HSV around rectangular, wedge nose and lenticular pier models was investigated by flow visualization using KMnO_4 on a water table, TiCl_4 fumes, and pressure measurements on the upstream plane of symmetry of pier models in the low speed, low turbulence wind tunnel. The overall range of Reynolds number covered was $1400 < \text{Re} < 3200$ in the laminar regime.

a. Dye Flow Visualization

The dye patterns around these pier models were obtained in the test section of the water table at a nominal waterspeed of 10 cm/sec., corresponding to $\text{Re} = 3197$, based on 2.5 cm of the maximum lateral dimension of each of the models, and $\text{Fr} = 0.146$ based on the nominal water depth of 5 cm. These dye patterns were photographed in plan, top front and top rear views

with camera shutter time of $1/125$ sec. to provide maximum details of the flow phenomenon.

(i) Dye Patterns Around Rectangular Pier Model

Figs. 6.1 a and b show the plan and top front views of the dye patterns. The white region around the pier model is identified as the separated flow region. The wake-vortex interaction is observed in fig. 6.1c, as the 'neck region', located about $2D$ downstream of the trailing edge and is about $2D$ in width.

(ii) Dye Patterns Around Streamline Nose Pier Models

Fig. 6.2 a and b provide the plan and top front views of dye patterns around wedge nose pier, where the whitish regions are identified as separated flow regions respectively. Fig. 6.2c shows the wake-vortex interaction. The 'neck-region' appears to be reduced in this case.

The dye patterns around lenticular pier model appear in figs. 6.3a, b and c similar to those around wedge nose pier model. In both of these streamlined pier models, a recirculatory flow region at the rear of the model is observed. This phenomenon appears to be due to the separation of flow at the side walls of the pier models.

Line sketches of these dye patterns drawn from figs. 6.1, 6.2 and 6.3 are shown in figs. 6.4 a, b and c respectively. The

maximum width of the separated flow region around rectangular pier appears to be 1.5 times of that around the circular cylinder, the separation line is located at 1.2 times of that around circular cylinder. The respective dimensions around streamline nose pier models get reduced over those for circular cylinder.

b. TiCl_4 Flow Visualization

The visualization of HSV around these three pier models by the dense white fumes of TiCl_4 was carried out at the nominal wind speed of 95 cm/sec, corresponding to $\text{Re} \approx 1450$ and $D/S^* \approx 4.5$. The application of TiCl_4 was made using technique I as described in chapter III.

(i) TiCl_4 Flow Around Rectangular Pier Model

Fig. 6.5 a shows a rear perspective view of the vortex flow around rectangular pier model, with rings clearly visible in the dense white fumes upstream of the pier. It is an oscillating HSV. The camera shutter time for this shot was 1/60 sec. The accumulation of TiCl_4 as two surface rings identified as two secondary vortices make it an oscillating 6 vortex structure around the pier model. The top front view in fig. 6.5b (Camera shutter time 1/125 sec) shows the impressions left by these rings. An upward curling of white fumes at the pier side wall near the leading edge junction can be

L/D, and BR being same as in case of earlier models), whereas a rectangular pier exhibited oscillatory behaviour of a 6 vortex structure. An upward rising region of white fumes is visible at the pier wall in fig. 6.6a. The picture in 6.6 c shows the wake-vortex interaction and the recirculatory region by the white fumes as observed from the water-dye picture in fig.6.2c.

Fig. 6.7 a shows a clear region around the lenticular pier model in the rear perspective view. Fig. 6.7b shows a distinguishable saddle point of separation at 1D upstream of the sharp nose. A two vortex structure of HSV is identified at these test conditions around lenticular pier model from fig. 1.2. The wake-vortex interaction in fig. 6.7c shows the 'neck region' located at 2D, about 1D in width. The recirculatory region of flow is evident from white streaks at the rear of the model similar to that observed in water dye patterns (fig. 6.3c).

It is interesting to note that wedge nose pier and lenticular pier models show four and two vortex systems respectively at the same test conditions. The $TiCl_4$ flow patterns from figs. 6.5, 6.6 and 6.7 are sketched in fig. 6.8, which shows the maximum width of the separated flow region across the pier to be 1.5 times of that across the circular cylinder, it is approximately of the same size for the wedge nose pier and about 30% lesser in the lenticular pier case. The width of the neck region is maximum behind the rectangular pier case.

c. Pressure Measurements

Pressures measured on the upstream plane of rectangular, wedge nose and lenticular pier models, at a nominal wind speed of about 1.5 m/sec, corresponding to $Re \approx 2250$, $D/\delta^* \approx 5.5$ are plotted in fig. 6.9. The C_p curve for rectangular pier model appears similar to that shown in fig. 11a of Baker(1979) for $Re = 15,300$ and $15,710$ for oscillating HSV around circular cylinder, thereby indicating oscillatory HSV around rectangular pier model. The oscillating HSV rectangular pier was observed from $TiCl_4$ flow visualization at $Re \approx 1450$. The pressure distributions for wedge nose and lenticular pier model show one clear pressure dip each at about $0.4D$ upstream of the pier leading edge.

The pressure distributions upstream of the round nose pier and circular cylinder, alongwith Baker's (1979) data at $Re \approx 2050$, $D/\delta^* = 21.7$, $L/D = 4.8$ and $BR = 5.3\%$ are also presented for the sake of comparison. The trends of C_p variations in the present work appear similar, with changing magnitudes.

6.3.2 Transition to Turbulent Flow

The oscillations of HSV around these three pier models were measured by inserting a 'u'-sensitive hot wire probe from the top plate by maintaining its location, and using the same procedure as in 4.3.2.

Fig. 6.10 a presents the spectra and traces of vortex oscillations around rectangular pier models. An early onset of steady oscillations at $Re \approx 1400$, $D/\delta^* \approx 4.4$ is observed. Higher, steady, distinct and discrete harmonics appear as the wind speed is increased. No. of mixed frequencies start appearing at $Re \approx 3300$, beyond which the intermittency and bursts of turbulence were observed. The free stream transition starts at $Re \approx 4000$ (fig. 3.5a).

Fig. 6.10 b shows the spectra and traces of vortex oscillations around the wedge nose pier model with increasing wind speed. The onset of HSV oscillations is delayed to $Re \approx 3200$. The amplitudes and frequencies of oscillations are lower than those in the rectangular pier case. Mixed frequencies of low amplitude begin to appear at $Re \approx 4200$, $D/\delta^* \approx 7.9$, beyond which intermittent bursts of turbulence lead to turbulent signals. The oscillatory behaviour of HSV around lenticular pier model as shown in fig. 6.10 c appears similar to that around wedge nose pier model.

A comparison of the HSV oscillations around these three pier models with that around the round nose pier and circular cylinder reveals that there is an early onset of oscillations around the rectangular pier and the oscillations are delayed in case of the streamlined nose models, which shows that the onset of the oscillatory behaviour of HSV depends upon the pier leading edge shape.

Fig. 6.11 a and b show the variation of the Strouhal frequency with Re and D/δ^* for rectangular and streamline nose pier models respectively. A steady increase of the fundamental Strouhal frequency observed in the rectangular pier case is not found for the streamline nose pier models. Corresponding St values are lower for streamline nose shapes compared to the rectangular nose case. Fig. 6.11 b shows that the local mean velocity ratio $\frac{u'}{U_\infty}$ remains about 0.07 for rectangular pier and, it steadily increases from about 0.15 to 0.25 in the streamlined nose pier models. The local turbulence $\frac{u'}{U_\infty}$ remains below .01, and rises suddenly beyond $Re \approx 4500$ in these cases. The approaching boundary layer becomes turbulent at $Re \approx 5,000$ (fig. 3.5a).

6.3.3 Turbulent Flow

The horseshoe vortex in approaching turbulent flow around the junctions of each of the three pier models was investigated from surface oil film patterns, detail pressure measurements at the representative stations (fig. 3.3) and total head survey in the Y-Z plane at the mid-span of each of the pier models.

a. Surface Oil Film Patterns

The surface oil film patterns around rectangular, wedge nose and lenticular pier models were obtained at a nominal wind speed of 5 m/sec corresponding to $Re \approx 7800$, $D/\delta^* \approx 11$. The shots (i) and (ii) in each of the figs. 6.13a, b and c were taken respectively with the tunnel running and immediately after stopping the tunnel.

(i) Surface Flow Patterns Around Rectangular Pier Model

The pictures in fig. 6.13a show the surface oil film patterns around the rectangular pier model, which appear similar to those around the round nose pier and circular cylinders of $D \geq 25$ mm in sections 4.3.3.a and 5.3.3.a respectively. Thus four vortex system is identified as follows referring to Baker (1980). The narrow clear region parallel to and around the leading edge is due to the secondary vortex O. The first ring like accumulation of the powder-oil mixture at $0.38D$ from the leading edge is identified as a surface vortex i.e., the secondary vortex 1'. The circular looking distinct region extends to about $1.25D$ from the leading edge and its outer boundary is identified as the primary separation line S, though the saddle point is not clear. The nodal point of attachment between the two separation points (Hunt et.al., 1978) is not distinguishable. The secondary vortex O, appears to become a part of the separated region appearing black, extending from the leading edge to the side walls. The circular looking region of HSV is observed to extend upto about $1D$ from the pier wall up to about $1D$ downstream of the leading edge. The complex wake-vortex interaction is observed at the trailing edge region.

(ii) Surface Flow Patterns Around Streamline Nose Pier Models

The pictures in fig. 6.13b show the surface oil film patterns around the wedge nose pier model, which appear different from the

surface patterns around rectangular and round nose pier models, and circular cylinders of $D \geq 25$ mm. A narrow, clear and slightly curved region at the wedge nose is identified as the secondary vortex O formed on the wedge shape leading edge. Two semi-circular looking clear zones identified as the regions of separation from the wedge corner, forming vertical vortices appearing to behave as solid surfaces are observed at the leading edge corner. The secondary vortex O, appears to become a part of this separated flow region. It may be mentioned that an asymmetry of flow about this type of pier, due to some misalignment may cause the extent and the strength of such separation bubble to increase on the leeward side, increasing the local scour depths on that side of streamlined nose piers (Breusers et.al.,1977). A distinct oblong boundary line around the wedge nose, $0.3D$ from the leading edge and about $0.5D$ from the leading edge corner is identified as the primary separation line S. This is a two vortex system of HSV as inferred from these surface flow patterns. There is a complex wake-vortex interaction at the trailing edge, and separation region at the wedge corners can be observed.

Figs. 6.13a (i) and (ii) show that the surface flow pattern around lenticular pier are similar to that around the wedge nose pier model. Since there is no sharp corner in the profile of the model, the bubble formation is absent. At a misalignment this pier model may cause a strong bubble at the leading edge on the leeward side causing deeper scour holes. The primary separation line, $0.4D$

upstream of the sharp leading edge, extends about $0.5D$ from the wall at the mid-span, with one primary *vortex* and a *secondary* vortex O on the biconvex leading edge of the pier.

It is observed from these surface flow patterns that at $Re \approx 7800$, $D/\delta^* \approx 11$, the HSV around rectangular pier model contains four vortices, and around the wedge and lenticular pier models, it is two vortex structure. Thus it is found that the structure of HSV around different pier models is dependent on their leading edge shapes. Surface streamlines and the flow patterns inferred from figs. 6.13a,b and c are sketched in figs. 6.14 a,b and c respectively.

b. Pressure Distribution

Surface pressures at the representative stations around each of the pier models were measured at nominal wind speeds of 5.7 m/sec. and 8.5 m/sec. corresponding to $Re \approx 8600$, $D/\delta^* \approx 11.5$, and $Re \approx 12,800$, $D/\delta^* \approx 14.3$.

(i) Pressure Distribution Around Rectangular Pier Model

Fig. 6.15 a presents floor pressures around the rectangular pier model. A pressure dip on the upstream plane of symmetry at about $0.4D$ upstream of the flat face of the pier is identified as the core location of primary horse shoe vortex (Belik, 1973 and Baker 1979, 1980). The adverse pressure build up begins more than $4.5D$ upstream and it becomes rapid within $1.5D$, where a

pressure gradient of about 0.42 was measured. A high suction region with $C_p \approx -0.9$ exists at the leading edge corner and extends upto about 0.2D from the wall, apparently due to the separated flow from the sharp corner. The extent of HSV appears to be 0.5D farther away from this region. A pressure recovery is indicated at locations M_1 and T_1 . Lower pressures due to wake-vortex interaction, of $C_p \approx -0.5$ are observed within 1.5D from the blunt trailing edge on the downstream plane of symmetry with a pressure recovery indicated in the farwake.

(ii) Pressure Distribution Around Streamline Nose Pier Models

Fig. 6.15b presents floor pressures around the wedge nose pier model. A pressure dip at about 0.4D upstream of the pier leading edge is identified as the core location of the primary horseshoe vortex. The adverse pressure starts appearing at about 2.5D upstream of the pier leading edge. A floor pressure gradient of about 0.21 was measured at 1.5D, where rapid build up pressure was observed, this is half of that due to the rectangular pier. The extent of HSV appears to be 0.7D from the wall at location L_1 from the pressure distribution. The pressure recoveries at locations M_1 and T_1 are observed. The lower pressure region extends to about 1.5D downstream, at DS, with pressure recovery in the farwake.

Fig. 6.15c shows the floor pressures around the lenticular pier model with one pressure dip at about 0.3D on the upstream

horseshoe vortex. The pressure gradient at $1.5D$ upstream of the sharp leading edge appears to be the same as in case of wedge nose pier model. The region of HSV is observed to exist upto about $0.6D$ from the pier side wall at location M_1 . The near wake region is observed upto about $1.5D$ from the downstream end of the pier.

Fig. 6.15d present the trend of the variation of C_p at the base of these three pier models. Higher suction peaks at the leading edge corner of rectangular and wedge nose pier are observed. It may be noted that the turning of the vortex just started at the location L_1 , while it was in the process of completion in the wedge nose case. Lower pressures are observed after the midspan in case of lenticular pier model.

c. Total Head Survey

The streamwise arm of HSV around each of these pier models was probed for the vortex structure at their respective mid-spans in the similar manner as in section 4.3.3c, at a nominal wind speed of 5.5 m/sec. corresponding to $Re \approx 8300$ at $D/\delta^* \approx 11.3$. The pressure plots are presented as viewed from the downstream end in figs. 6.16a,b and c. The no. of vortices and their sense of rotations were determined using the interpretation given earlier in Chapter IV.

(i) Rectangular Pier Model

Four vortex structure of HSV is observed from fig. 6.16 a as follows :

1. a low pressure zone at the pier wall extending upto about $0.5D$ is observed and it is indicated by the direction of the turning of the contours of constant total head within this zone near the floor that the secondary vortex O, formed on the flat leading edge gets sucked up, in the process of negotiating the sharp leading edge corner, by the recirculatory zone of separated flow along the direction indicated.
2. a large clock-wise vortex, identified as the primary vortex 1, existing between $0.6D$ and $1D$ from the pier wall,
3. a counter clockwise vortex identified as the secondary vortex $1'$, located at about $1.1D$ from the wall, and
4. a clockwise vortex, identified as primary vortex 2 located close to the secondary vortex $1'$.

The four vortex structure of HSV was observed earlier around the round nose pier and the circular cylinder at the identical test conditions in chapters IV and V. The four vortex structure of HSV from constant total head contours supplements the observations of four vortex structure from surface oil flow patterns in fig. 6.13a.

(ii) Streamline Nose Pier Models

Two vortex structure of HSV is observed from fig. 6.16 b as follows :

1. a small looking counter clockwise vortex appearing to be slightly above the floor, identified as the secondary vortex 0,
2. a clockwise vortex located at about $0.2D$ from the wall, identified as the primary vortex 1.

This vortex structure appears significantly different from those observed earlier i.e., around the round nose pier, circular cylinder and the rectangular pier models.

Fig. 6.16c presents the two vortex structure of HSV around the lenticular pier model, showing the secondary vortex 0 and primary vortex 1, similar to that around the wedge nose pier.

It is established from above that the structure of HSV, around a pier model in turbulent flow depends upon its leading edge shape. For round and blunt nose piers, where stronger HSV formation takes place, four vortices are observed while with pointed and streamlined leading edges, two vortex structure is found to exist, under the same test conditions, L/D and BR respectively.

6.4 THE MODIFIED HORSESHOE VORTEX

Pictures in figs. 6.17 a, b and c present a view each of the rectangular, wedge nose and lenticular pier models respectively with the passive device mounted at the leading edge foot, and three orthogonal views are shown in figs. 6.18 a, b and c respectively. The results of modified vortex flow around these

pier models are presented in the same order of approaching flow conditions as in the section 6.3.

6.4.1 Laminar Flow

The modified vortex flow around the junctions of each of these pier models with the passive device was investigated by flow visualization using KMnO_4 in the water table and TiCl_4 fumes in a low speed, low turbulence wind tunnel.

a. Dye Flow Visualization

The experiments were conducted at a nominal water speed of 10 cm/sec, corresponding to $\text{Re} = 3026$ and $\text{Fr} = 0.135$. The pictures of dye patterns are presented in plan, top front and top rear views with camera shutter time of 1/125 sec, to provide maximum details of the flow phenomenon.

(i) Modified Dye Patterns Around Rectangular Pier Model

Figs. 6.19 a and b show the plan and top front views of the modified vortex flow around the rectangular pier model. It is observed from the corresponding views with clean pier model in figs. 6.1 a and b that a significant modification of the flow is caused by the passive device by bringing colored water towards the pier walls. The formation of AHSV and LESV are indicated by the white looking region around the apex of the device, which extends below the device. The region around the pier upto about 1D from the leading edge is believed to be caused by an interaction of the apex vortex, LESV and the separated flow

from the leading edge corner. It is believed that LESV and the apex vortex are 'pushed' away from the pier leading edge due to the presence of the flat leading edge. The whitish looking region appears to be due to LESV. A light colored region can be observed along the pier wall also. The modification of wake-vortex interaction in fig. 6.19c is observed from reduction in the neck size.

(ii) Modified Dye Patterns Around Streamline Nose Pier Models

Figs. 6.20 a and b show the modified dye flow around wedge nose pier model, which show the colored flow replacing the white region around the clean pier in figs. 6.2 a and b. This modification of the flow is brought about by LESV from the passive device. It is interesting to note that the movement of the apex vortex (streamwise arm of AHSV, formed at the apex floor junction and shown as oblong region) and LESV are observed to be almost parallel to the wedge face of the pier, unlike that in the case of round nose pier and circular cylinder. The wake-vortex interaction in this case (fig. 6.20 c) shows a reduction in the recirculatory region at the trailing edge and the pushing up of the vertical vortices is observed in the far wake.

The modified horseshoe vortex around the lenticular pier shown in figs. 6.21 a, b and c appears almost similar to that around the wedge nose pier model.

It may be observed from the modification of the vortex flow around these three pier models that, the exit of the apex vortex and LESV from beneath the passive device and their downstream progress about the pier leading edge depend upon the shape of the leading edge of the pier.

b. TiCl_4 Flow Visualization

The visualization of HSV around each of the pier models by TiCl_4 fumes was conducted at the nominal wind speed of 95 cm/sec. The liquid TiCl_4 was applied with technique I (Chapter III).

(i) TiCl_4 Flow Around Rectangular Pier Model

The picture in Fig. 6.22a shows a front perspective view of TiCl_4 fumes around the rectangular pier model with passive device. Two vortices are observed to emerge from beneath the passive device and are lifted up at the pier wall. Fig. 6.22 b shows a top front view of this phenomenon. A closer look at these shots shows the LESV below the transparent device. The formation of AHSV by the white region at the apex of the device is observed. The close up view of these vortices in fig. 6.22c shows the lifting up phenomenon, after their exit from the device. The lifting and somersaulting of apex vortex below the passive device is also observed, along with its lift up by LESV at the pier wall.

Fig. 6.22 d provides an overall view of the phenomenon from rear. The surface flow is significantly modified as compared with the clean pier in fig. 6.5. The 'neck size' behind the pier model has been reduced and the upward rising TiCl_4 fumes show this modification of the wake-vortex interaction brought about by LESV. The LESV was captured as an isolated vortex appearing to get sucked up by the separated flow region along the pier wall, by applying TiCl_4 with technique II (Chapter III) in fig. 6.22 e. The modified surface flow patterns in laminar flow are shown in fig. 6.22 f. A significant modification of the oscillating HSV around clean pier, is observed when the device is attached to its leading edge foot.

It was observed from Chapters IV and V, that the apex vortex got lifted and somersaulted at the pier nose below the device before coming out from the side. The same feature of the apex vortex at the pier nose is also observed in rectangular pier, in addition the apex vortex and LESV get sucked into the separated flow zone at the pier wall.

(ii) TiCl_4 Flow Around Streamline Nose Pier Models

Fig. 6.23 a shows a perspective view of the modified vortex flow (from rear) around wedge nose pier model. The apex vortex and LESV are observed to move almost parallel to the floor and the pier wall. The lower pressure region behind the pier, and throwing up of the vertical vortices by LESV in modifying the

wake-vortex interaction are also observed. Fig. 6.23 b shows this phenomenon from front. The apex vortex and LESV are observed to move along the wedge face, which is also shown in fig. 6.23 c. A close up view of the parallel movement of these vortices along the pier wall is observed in fig. 6.23d. The modified vortex flow phenomenon around the lenticular pier in figs. 6.24 a-d appears similar to that around the wedge nose pier observed in the corresponding views in figs. 6.23 a-d.

It may be observed that the vortex movements below the device, and after their exit from the confined region in case of streamline nose piers appeared simpler than that in the rectangular pier case. It is, therefore, inferred from above that the modification of HSV around a pier model by a passive device is dependent on the pier leading edge shape.

The schematic line sketches showing the modified vortex system around each of these pier models are shown in figs. 6.25 a, b and c.

6.4.2 Transition to Turbulent Flow

The oscillations of the vortex flow over the upper surface of the passive device upstream of each of these pier models were measured by a 'u'-sensitive hot wire, inserted from the top plate in the same manner as in the sections 4.4.2 and 5.4.2.

The modified vortex oscillations appear to be suppressed in these cases. The first appearance of oscillation around the pier model is indicated at $Re \approx 4350$, $D/S^* \approx 8.3$, beyond which turbulent signals were observed in fig. 6.26a. Low frequency, low amplitude signals were observed in fig. 6.26 b and c, in case of streamline nose pier models. The fundamental Strouhal frequency of these signals was less than 0.05 in these modified vortex flows.

6.4.3 Turbulent Flow

The modified HSV around the junctions of the rectangular, wedge nose and lenticular pier models with passive device was investigated from surface oil flow patterns, floor pressures at representative stations around the pier models and total head surveys in the Y-Z plane at their respective mid-spans.

a. Surface Oil Film Patterns

The surface flow patterns around these three models with the passive device were obtained at the nominal wind speed of 5 m/sec, corresponding to $Re \approx 7800$ and $D/S^* \approx 11$. The shots (i) and (ii) were taken as in section 4.4.3a.

(i) Modified Surface Flow Patterns around Rectangular Pier Model

Figs. 6.27 a show the surface flow patterns around the rectangular pier model with device, after a tunnel time of fifteen minutes. The formation of AHSV and the surface vortices below the passive device due to apex vortex and LESV are observed by the accumulation of the powder-oil mixture. The LESV was

found to come out of the passive device at about 45° with respect to the flat leading edge. The overall flow phenomenon below the device, appears similar to that observed from the corresponding pictures with round nose pier and the circular cylinder. The lifting of the apex vortex and LESV is also indicated within about $1.5D$ downstream of the leading edge. A comparison with the surface flow around clean pier in fig. 6.13a shows significant modification of flow around the pier walls by the absence of the separated flow region. Flow is observed to be directed towards the pier wall by LESV. The wake-vortex system modification is also observed.

(ii) Modified Surface Flow Patterns around Streamline Nose Pier Models

Fig. 6.27 a and b show the modified surface flow patterns around wedge nose and lenticular pier models respectively after a tunnel time of fifteen minutes. A misalignment of about 4° appears in the lenticular model case. However, the nature of inference drawn does not seem to alter due to this reason.

Both the apex vortex and LESV appear to come out of the device almost along the leading edge faces of these models, as observed from the surface vortex flow below the device in each case. The flow is directed towards the piers by LESV.

The vortex flow phenomenon below the device is observed to depend upon the leading edge of the pier, which is a measure of the physical constraints on the flow at the pier device

junction. The surface streamlines resulting from figs. 6.27 a,b and c are sketched in figs. 6.28 a,b and c.

b. Pressure Distributions

The modified floor pressures were measured around these three pier models with the passive device, at the representative stations, at nominal wind speeds of 5.7 m/sec and 8.5 m/sec, corresponding to $Re \approx 8000$, $\frac{U}{\delta_*} \approx 11.4$ and $Re \approx 12,800$, $\frac{D}{\delta_*} \approx 14.3$ and are presented with the corresponding pressures in clean pier case. The symmetry of floor pressures with and without the device, around each pier model is presented separately.

(i) Upstream Plane of Symmetry , U

A reduction in pressure gradient of about 87% was measured on the upstream plane of symmetry of rectangular pier model (fig. 6.29a), whereas it was about 75% and 70% in case of wedge nose and lenticular pier models in figs. 6.29 b and 6.29 c respectively. Pressures on the upper surface of the device in each of these plots are also shown, which indicate the pressure jump across the device, causing the formation of LESV.

(ii) Leading Edge Corner, L_1

The presence of low pressure region upto about $0.2D$ from the wall and another pressure dip identified with the region of HSV extending upto about $1D$ is observed at the location L_1 of rectangular pier in fig. 6.30a, and a low pressure region upto about $0.4D$ is observed at L_1 identified with the region of HSV

in case of wedge nose pier in fig. 6.30 b. The passive device causes a favourable pressure gradient in making the fluid move towards the wall region.

(iii) Mid-Span, M_1

A pressure recovery of about 30% appears to be caused by the device in the case of rectangular pier model in fig. 6.31 a, and that . at ut 15%, in wedge nose pier is measured in fig. 6.31 b. The leading edge region of lenticular pier model extends to its mid-span. Floor pressures at the location, M_1 appear to be reduced by 25-30% as the flow around the pier model is accelerating upto mid-span in fig. 6.31 c.

(iv) Trailing Edge Corner, T_1

The modified pressures appear to be slightly built up at this location in rectangular pier (fig. 6.32a) and a reduction in pressure by about 35%, upto about 0.5D from the wall is observed in case of wedge nose pier model.

(v) Downstream Plane of Symmetry

The floor pressures downstream of the blunt trailing edge of rectangular pier model appear to remain the same as in case of clean pier at lower Re. and nominal reductions over those in clean pier at higher Re are observed in fig. 6.33a. The pressure data behind the wedge nose pier model (fig. 6.33b) shows almost similar variation as that behind the lenticular pier case (fig. 6.33 c). Pressures appear to be lower by about 10-15% in the near wake region. These variations in the

pressures on the downstream plane are caused by the modified wake-vortex interaction behind the pier models.

It is observed that the floor pressures provide reliable and consistent data on the upstream plane of symmetry of the pier models, both with and without the passive device, whereas at other locations the local acceleration effects due to the profile shape interferes with the pressures and the presence of either the original HSV or the vortices from the modified HSV is not easily differentiated from surface pressures alone.

(vi) The Symmetry of Flow Around Pier Models

The floor pressure distributions on either side of each of these pier models, at the representative stations, with and without the passive device are plotted in figs. 6.34 a,b,c and figs. 6.35 a,b,c and d respectively. A good agreement of the data on the respective locations across the models can be observed.

c. Total Head Survey

Total head contours were plotted by traversing a shielded pitot tube in a grid of 30x22 mm at 490 points in the Y-Z plane at the mid-span of each pier model. The no. of vortices and their sense of rotations were interpreted as in 4.3.3c. These plots are presented in figs. 6.36 a,b and c as viewed from the downstream end.

(i) Rectangular Pier Model

The region to the right of the constant total head line, $H=0$ is identified as part of the recirculating region of the separation zone at the pier wall from the sharp leading edge corner. The group of closed contours at the tip of the passive device is identified as LESV. The annihilation of LESV by the low pressure separation bubble is observed by the direction of movement of the constant head contours indicating counter clockwise rotation of flow. This phenomenon was also observed from $TiCl_4$ flow visualization in laminar flow in fig. 6.22 e. The annihilation of the apex vortex is not observed, as it was shown in the close up view in fig. 6.22c, that it got sucked up near the leading edge. A counter clockwise vortex appears at the pier wall which brings the surface flow towards the pier. There is a clockwise vortex on the floor away from the region of influence of LESV.

(ii) Streamline Nose Pier Models

Fig. 6.36 b presents constant total head contours at the midspan of wedge nose pier model with device and following vortical regions are identified,

1. a large counterclock-wise vortex at $z/D \approx 0.4$, below the tip of the device, identified as LESV,
2. a small counter clock-wise vortex on the floor-wall junction, appeared to form as a consequence of the interaction of LESV with the apex vortex at the wall,

3. a small clockwise vortex at the wall, above the vortex at 2; this is identified as the apex vortex, and
4. a large clockwise vortex at about $1.2D$ away from the wall.

In addition a downward flow region along the wall from $z/D \approx 0.5$ to $z/D \approx 0.2$ is also observed.

Fig. 6.36 c shows the constant total head contours at the mid-span of lenticular pier model with device. The four vortical regions and a downward flow region in this figure are found identical to that observed in fig. 6.36 b.

It is observed from the total head contours and the vortical regions interpreted therefrom, that the streamwise arm of HSV gets modified significantly by the passive device. Instead of four vortex or two vortex structure in clean pier cases, the modified vortex structure comprises mainly of LESV and the apex vortex. The rectangular pier model presents an interesting phenomenon, wherein, both the apex vortex and LESV are sucked into the separation bubble at the pier wall. In the case of streamline nose pier models, the apex vortex appears moving downstream, above the floor. The surface flow is brought towards the pier model by LESV. The size and strength of LESV appear more than that of the apex vortex in all the pier models.

The modified flow structure at the side of rectangular, wedge nose and lenticular pier models has been presented for the first time.

6.5 DISCUSSION

The structure of HSV around the junctions of pier models having blunt and streamline leading edges was investigated to bring out the effect of leading edge geometry in causing a change in the vortex structure. This aspect was also studied when the passive device modified the vortex flow around these pier models.

6.5.1 HSV Around Clean Pier Models

It can be observed from the dye patterns around rectangular, wedge nose and lenticular pier models in figs. 6.1, 6.2 and 6.3 that each of these dye patterns is characteristic of the pier leading edge shape. The details of vortex structure, provided by $TiCl_4$ flow (figs. 6.5, 6.6 and 6.7) show that at $Re \approx 1450$, $D/\delta^* \approx 4.5$, the rectangular pier model shows oscillatory vortex flow, wedge nose pier shows four vortices and the lenticular pier model presents two vortex structure. In addition the rectangular pier shows a region of curling up flow at the wall-floor junction, which appears due to the annihilation of the secondary vortex O , formed on the flat leading edge, as it negotiates the sharp leading edge corner. A similar phenomenon was also observed in case of wedge nose pier model. This variation in behaviour and structure of HSV around pier models appears due to change in their leading edge shapes.

The onset of oscillations of HSV (figs. 6.10 a,b and c) around rectangular pier started at $Re \approx 1400$, $D/\delta^* \approx 4.5$, and in streamline nose pier at $Re \approx 3200$, $D/\delta^* \approx 6.9$. The early and delayed onset of these oscillations around rectangular and streamline nose pier models respectively is due to change in leading edge geometry of the pier model or the lateral distribution of the cross-sectional area of these models, which determines the extent and severity of the Bernaulli gradient on the pier nose in the shear flow region, which determines the strength of the secondary vortex O.

Another important physical parameter of the pier geometry is the angle which the leading edge region makes with the parallel walls of the pier model. A 90° turn is a severe condition, enforcing a strong separated region downstream of the corner. The wedge nose makes a 26.5° turn. The strength of secondary vortex on a flat face would be more than that on a wedge face. It, therefore, appears to be a coupled action of the leading edge vortex strength and the turning angle, which would determine the early or delayed onset of the oscillatory behaviour of HSV around pier models with different leading edge shapes.

The effect of leading edge geometry appears in the difference of the vortex structure around these pier models in turbulent flow. The surface oil film patterns at $Re \approx 7800$, $D/\delta^* \approx 11$, and constant total head contours at $Re \approx 8300$, $D/\delta^* \approx 11.3$ give consistent results in showing

- (i) four vortex structure of HSV around rectangular pier model, and
- (ii) two vortex structure of HSV around streamline nose pier models.

The extent of separated flow region can be observed at the leading edge corners of these pier models in figs. 6.13 a, b and c respectively indicative of the leading edge-angle of turn combination of each pier model. The maximum scour depths observed at the sides of streamline piers (Tison, 1961) may be due to such flow separations at the pier side walls.

6.5.2 Aerodynamics of Delta-Wing-Like Passive Device

It was observed in Chapter V that the flow phenomenon associated with the passive device mounted at the leading edge foot of a round nose pier and circular cylinder respectively, appeared to be identical due to the same leading edge shape, which means that the physical constraints of the solid boundaries to the vortex flow, below the passive device were identical.

The constraints appear to be the severest with flat face leading edge of rectangular pier model. It was observed from dye flow (figs. 6.19a, b), $TiCl_4$ flow visualization (fig. 6.22 a,b), and surface flow patterns (fig. 6.13a) that the apex vortex and LESV appeared to move farther away from the spinal rib while approaching the trailing edge of the device. This

was apparently caused by pressure gradient due to the pier below the device. The extent of the recirculatory region, below the device appeared to increase in the lateral direction. The typical behaviour of apex vortex at the pier-device junction was identical to that in case of round nose pier model and circular cylinder in Chapters IV and V respectively.

These constraints appeared relaxed with the streamline nose pier models. The apex vortex moved closer to the spinal rib and along the wedge nose and lenticular pier models, indicating reduced lateral extent of the recirculatory region at the spinal rib. The LESV was found to move closer to the spinal rib and appeared to follow the wedge nose and the lenticular pier models in figs. 6.20 a,b and 6.21 a,b respectively. A similar behaviour of the apex vortex and LESV was observed from surface flow patterns in figs. 6.13 b and 6.13 c respectively.

This brings out the effect of the leading edge geometry in the course of movement of the apex vortex and LESV at the junction of the passive device with the pier leading edge.

6.5.3 Modification of HSV

The HSV modification process around these pier models by the passive device, remains identical to that around the round nose pier and circular cylinder as described in the preceding chapters, except for the changes brought about by the

leading edge shape, which affects the downstream movement of the apex vortex and LESV along the pier wall.

Both, the apex vortex and LESV were annihilated into the separation bubble at the rectangular pier wall in figs. 6.22 a-e by TiCl_4 fumes, and also indicated by the surface oil film patterns in fig. 6.27 a. The visualization of modified flow around streamline nose pier models in figs. 6.20, 6.21 and 6.23, 6.24 from dye and TiCl_4 flow respectively, show the smooth exit of apex vortex and LESV from beneath the device.

The constant total head contours in figs. 6.36 a,b and c supplement these visual observations. The pressure measurements are presented in figs. 6.29 to 6.33.

The effect of leading edge geometry of the piers on the structure and oscillatory behaviour of HSV around their junctions with floor has been brought out from extensive flow visualization, pressure measurements and constant total head contours for the first time. Furthermore, the effect of leading edge geometry of the pier in the modifying HSV around the pier models by the passive device has also been described for the first time.

CHAPTER VII

CONCLUSIONS AND FURTHER WORK

The conclusions of the present investigations of HSV and its modification around the junction of different nose shape pier models as described in chapters IV, V and VI are presented in this chapter along with suggestions for further research in this area.

7.1 THE HORSESHOE VORTEX IN LAMINAR FLOW

The titanium tetrachloride (TiCl_4) technique (Freymuth et.al., 1985) was adopted for the visualization of HSV around the junction of circular cylinder. By the application of liquid TiCl_4 on the upstream floor, at $\text{Re} \approx 1450$, $D/\delta^* \approx 4.5$, six vortices in ring form were observed, around the cylinder, extending further downstream, showing a 'neck' formation in the surface flow due to wake wake-vortex interaction, thereby showing complete structure of HSV for the first time from TiCl_4 fumes. The observations from TiCl_4 flow around different diameter cylinders, at the same wind speed and δ^* were presented in Table 5.1.

Baker (1979) visualized multivortex structure of HSV around circular cylinder only on the upstream plane of symmetry from smoke flow. The number of vortices at $\text{Re} \approx 1450$, $D/\delta^* \approx 4.5$ appeared to lie on the borderline between two and four vortices from fig. 6 of Baker (1979) for a circular cylinder of $D/L=2$

and $BR=6.2\%$ and these values are 0.16 and 3% respectively in the present work. This shows strong dependence of the vortex structure on D/L and BR . The ^lmultivortex structure of HSV observed by Baker (1979) was verified using an independent flow visualization technique in which dense white fumes of $TiCl_4$ persist over longer duration.

The HSV structure around pier models having blunt, round and streamline nose shapes was investigated from $TiCl_4$ flow visualization and water-dye techniques to bring out the effect of leading edge shape on the vortex structure and the extent of the region occupied by the HSV around these pier models. It can be observed from Tables 7.1 a and b that the line of primary separation lies farthest on the upstream of the rectangular pier model and is closest to the leading edge of the lenticular pier. The HSV showed oscillatory six vortex structure around the rectangular shape and it was a two vortex structure around the lenticular pier, at the same test conditions, and the only change in the pier models was the leading edge shape. This showed that the vortex structure in HSV in the laminar regime depended upon the pier leading edge shape.

7.2 THE VORTEX OSCILLATIONS

The oscillations of HSV around circular cylinder in figs. 5.6 a and b were found to be steady at $St \approx 0.2$, in the range $2400 < Re < 4400$ and $5 < D/\delta^+ < 10$, unlike the highly

random oscillatory behaviour reported by Baker (1979) and it was discussed in chapter V that a leakage of air from outside into the HSV might be one of the reasons for such oscillations.

The vortex oscillations around the vertical round nose pier (fig. 4.6) were similar to that around the circular cylinder and appeared in better order due to the streamwise span of the pier model. The vortex oscillations were almost similar in case of rectangular pier, and weak oscillations were recorded around streamline nose pier models. The onset of oscillations in round nose pier and circular cylinder was at $Re \approx 2400$, $D/\delta^* \approx 6.0$. An early onset of the oscillatory behaviour around the rectangular pier was observed, while it was delayed in case of streamline nose pier models (Table 7.2). It was shown in Chapter VI that the early or delayed onset of vortex oscillations depended on the shape of the leading edge and the turning angle at the leading edge corner.

It may further be argued from above that the cause of the onset of oscillations of HSV around a pier model, appears to be a combined action of the following,

- (i) the leading edge shape, which determines the strength of secondary vortex O, due to the Bernaulli gradient,
- (ii) the turning angle at the leading edge corner, which would determine the extent and vorticity of the separated flow region, and
- (iii) the turbulence level of the free stream approaching the pier.

7.3 THE HORSESHOE VORTEX FLOW IN TURBULENT FLOW

It was observed from Table 5.2, that a four vortex structure of HSV was inferred from surface oil film patterns, around circular cylinder in the range $7700 < Re < 16,000$, in accordance with Baker (1980). An independent verification of four vortices was obtained from constant total head contours at $Re \approx 8300$, $D/\delta^* \approx 11.3$. Furthermore, it was found that for $Re < 4000$, $D/\delta^* < 5.5$, two vortex structure existed around circular cylinder.

The turbulent vortex structure was found to depend on the pier leading edge shape, from consistent inference drawn both from surface oil film patterns (Table 7.3a) and constant total head contours at the mid-span of each pier model (Table 7.3b). It is concluded that four vortex turbulent structure of HSV exists for blunt and round nose pier models, and two vortex turbulent structure around the streamline nose pier models, at the present test conditions.

It appears apparent from the variation of $x_{S/D}$ with leading edge shape in laminar and turbulent flows, and the vortex oscillations around pier models that Eqs. 2.3 in Baker (1979, 1980) can be modified as

$\frac{x_S}{D}, \frac{x_{vg}}{D}, \frac{fD}{U_\infty} = \text{fn} \left(\frac{U_\infty D}{\nu}, \frac{D}{\delta^*}, \frac{D}{L}, \text{Pier Nose shape} \right)$ in laminar flow and

$\frac{x_S}{D}, \frac{x_{vg}}{D} = \text{fn} \left(\frac{U_\infty}{\nu}, \frac{D}{\delta^*}, \frac{D}{L}, \text{pier Nose shape} \right)$ in turbulent flow

Detail floor pressure measurements around the pier models were presented at the representative stations. Higher pressures and pressure gradients on the upstream plane of symmetry of rectangular pier, circular cylinder and round nose pier than those in streamline nose pier models were observed.

An attempt was made to work out a non-dimensional parameter $C_p^* = C_p \times K$, to account for the leading edge shape, where C_p is the upstream pressure and $K = \frac{A_2}{A_1}$, A_1 and A_2 being the areas of the nose region and the rectangle enclosing the nose region respectively. A tendency of the collapse of C_p^* on the pressure curve for rectangular pier is indicated in fig. 7.1. The circular cylinder and the round nose pier models appear to provide closer agreement with the rectangular pier.

7.4 THE MECHANISM OF HSV MODIFICATION

It was found in Chapter VI that the mechanism of HSV modification by the passive device explained with the round nose pier model depended on the leading edge shape of the pier model as summarized below,

- (i) The delta-wing like passive device prevented the concentration of the transverse vortex filaments at the pier nose, by the formation of an attenuated HSV (AHSV) at the apex of the passive device, which reduced the adverse pressure gradient on the floor considerably by creating a low pressure region

below the device. The large separation region around the clean pier was reduced to a localised region of separation at the apex. The weaker streamwise arms of the AHSV (apex vortex) with the same sense of rotation as the original HSV move parallel to the spinal rib and come out of the passive device by the pier side. The exit of the apex vortex from the nose region was found to depend upon the pier nose shape, as the apex vortex lifted and somersaulted at the pier like the turning of a coiled rope in case of blunt and round edge pier models, and it moved around the streamlined nose shapes.

(ii) A strong leading edge separation vortex (LESV) pair is formed at the leading edges of the delta plate, with an opposite sense of rotation to the apex vortex, and is the dominant vortex which brings the fluid towards the pier walls. Its movement along with that of the apex vortex below the device and downstream, was found to depend upon the pier leading edge shape. The apex vortex got lifted along the pier wall, after its exit from the device in case of blunt and round edge pier models. In case of blunt edge pier model, the LESV was also lifted up. Both of these vortices moved almost parallel to the pier wall and the floor in case of streamline nose pier models.

(iii) The interaction of LESV and the vertical vortices behind the pier models, modified the wake-vortex interaction, which was found to depend upon the movement of LESV and the apex

vortex along the pier wall.

368.

The above observations from $TiCl_4$ flow visualization were also indicated by the surface oil film patterns which showed the modification of the vortex flow from the flow direction towards the pier wall, but for a small patch in the region of the leading edge and the spinal rib. The surface pressures below the passive device were considerably reduced (Table 7.4a). The total head contours showed that the size and strength of LESV ^(Table 7.4b) depended on the pier nose shape, by providing a complete picture of the vortex flow at the pier side. The vortex oscillations measured on the upper surface of the passive device were suppressed in each case.

The usefulness of the passive device in restricting the extent and the depth of local scour around a pier model of round nose with passive device has been demonstrated from experiments in a water flume, with sand bed where reduction in the extent of the scour region at the pier leading edge was considerable and upto 67% reduction in the local scour depth was observed by Gupta and Gangadharaiiah (to be reported). Regions of deposits of sand along the pier side and at the rear were pronounced. The physical mechanism of this process was clarified in the present work.

7.5 FURTHER WORK

The geometry of the passive device was determined from a series of dye flow visualization studies by Gupta (1987)

for a round nose pier model. The use of this device was found quite satisfactory in modifying HSV around pier models with varying leading edge shapes. However, a parametric study of the geometrical features of this device needs to be carried out for an optimum passive device.

It is hoped that the field tests of some model bridge pier with the passive device in actual conditions of varying Reynolds number and Froude number of approach over longer durations would be interesting.

The performance of this passive device when mounted at the leading edge of yawed piers should be of practical interest to river bridge pier designers.

TABLE 7.1 a

370.

SUMMARY OF DATA ON HSV AROUND PIER MODELS FROM DYE PATTERNS AT $Re \approx 3200$, $Fr = 0.146$.

Sl. No.	Pier Model	x_s/D	w/D	x_w/D	w_{neck}/D	x_{neck}/D	Remarks
1.	Round Nose	1.25	3.25	0.5	0.5	1	Fig.4.1
2.	Circular cylinder	1.25	3.4	1	1	2.5	fig.5.2
3.	Rectangular	1.7	4.1	1	2	2	fig.6.1a
4.	Wedge nose	1	2.9	1.5	1	0.25	fig.6.1b
5.	Lenticular	0.88	2.8	2	0.5	0.65	fig.6.1c

* from L.E.

TABLE 7.2

372.

SUMMARY OF THE ONSET OF OSCILLATIONS OF HSV AROUND
PIER MODELS

Sl. Pier No. Models	Re,	D/ δ^*	Remarks
1 Round Nose	2392 ,	5.8	fig. 4.6
2 Circular cylinder	2442 ,	5.8	fig. 5.6 a
3 Rectangular	1424 ,	4.4	fig. 6.10 a
4 Wedge Nose	3258 ,	6.9	fig. 6.10 b
5 Lenticular	3313 ,	7.0	fig. 6.10 c

TABLE 7.3 a

373.

SUMMARY OF DATA ON HSV AROUND PIER MODELS
FROM SURFACE OIL FILM PATTERNS AT $Re \approx 7800, D/\delta^* \approx 11$

Sl. No.	Pier Model	No. of vortices	x_s/D *	x_{sl}/D *	w/D	x_w/D	Remarks
1	Round Nose	4	0.70	0.19	2.25	0.5	fig.4.8
2	Circular cylinder	4	0.70	0.17	3	2	fig.5.9
3	Rectangular	4	1.25	0.38	3.5	0.5	fig.6.13a
4	Wedge Nose	2	0.3	-	2.25	1	fig.6.13b
5	Lenticular	2	0.4	-	2.25	2	fig.6.13c

* from L.E.

TABLE 7.3 b

SUMMARY OF DATA OF HSV STRUCTURE FROM TOTAL HEAD SURVEY
 AT $Re \approx 8300$, $D/\delta^* \approx 11.3$

Sl. No.	Pier Model	No. of vortices	Approximate vortex location from pier wall			Remarks
			Primary 1	Secondary 1'	Primary 2	
1.	Round Nose	4	0.15D-0.5D	0.5D-0.65D	0.65D-0.9D	fig.4.11
2.	Circular cylinder	4	0.2D-0.4D	0.4D-0.5D	0.5D-0.6D	fig.5.17
3.	Rectangular	4	0.6D-1D	1D-1.2D	1.2D-1.4D	fig.6.16a
4.	Wedge Nose	2	0.1D-0.2D	-	-	fig.6.16b
5.	Lenticular	2	0.1D-0.2D	-	-	fig.6.16c

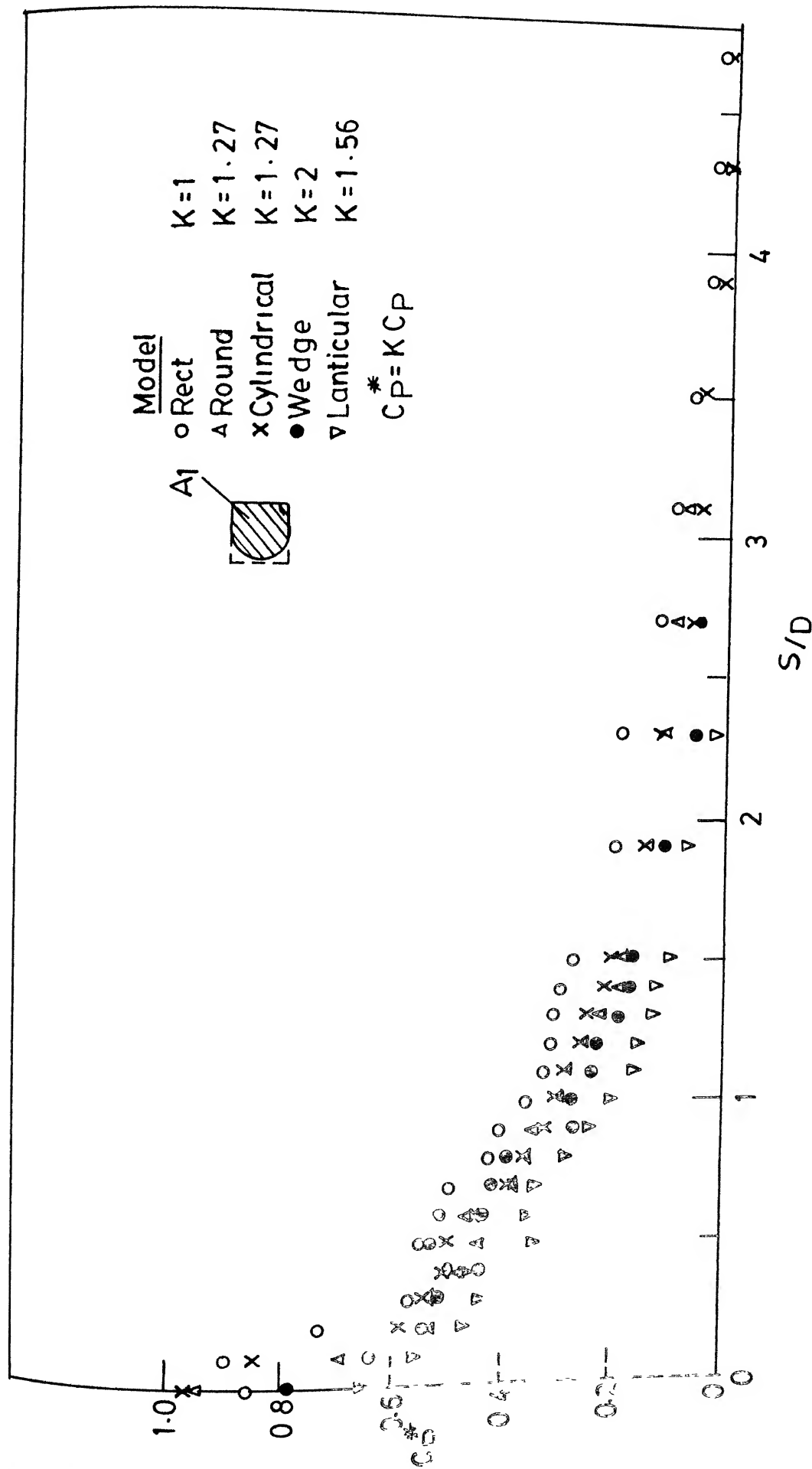


FIG 7.1 SIMILARITY OF PRESSURE DISTRIBUTION ON THE UPSTREAM PLANE OF SYMMETRY OF THE PIER MODELS

TABLE 7.4 a

REDUCTION OF PRESSURE GRADIENTS WITH PASSIVE DEVICE
 $Re \approx 8600$, $D/s^* \approx 11.5$

Sl.No.	Pier Mode	Pressure Gradient		Reductions	
		w/o Dev.	with Dev.	Pr.Grad.	C_p at LE foot
1.	Round Nose	0.35	0.054	80%	82%
2.	Circular cylinder	0.41	0.08	80%	76%
3.	Rectangular	0.42	0.055	87%	79%
4.	Wedge Nose	0.21	0.053	75%	90%
5.	Lenticular	0.21	0.067	70%	90%

TABLE 7.4 b

SUMMARY OF THE SIZE OF LESV

Sl.No.	Pier Model	Size of LESV		Remarks
		y/D^*	z/D	
1.	Round Nose	0.1-0.4	0.3-0.5	fig. 4.23
2.	Circular cylinder	0.05-0.5	0.2-0.5	fig. 5.29
3.	Rectangular	0.2-0.4	0.4-0.7	fig. 6.36 a
4.	Wedge Nose	0.2-0.4	0.3-0.5	fig. 6.36 b
5.	Lenticular	0.1-0.4	0.3-0.5	fig. 6.36 c

* from L.E.

REFERENCES

1. Anderson, J.D. (1984), 'Fundamentals of Aerodynamics', McGraw-Hill Book Company.
2. Armstrong, W.D. (1957), 'An Experimental Investigation of the Secondary Flow Occuring in a Compressor Cascade', The Aeronautical Quarterly, pp. 240-256.
3. Arunachalam, K. (1965), 'Scour around Bridge Piers', Journal of the Indian Roads Congress (No. 2), pp. 189-210.
4. Baker, C.J. (1979), 'The Laminar Horseshoe Vortex', JFM Vol. 95, pt. 2. pp. 347-367.
5. Baker, C.J. (1980), 'The Turbulent Horseshoe Vortex', Journal of Wind Engineering and Industrial Aerodynamics, Vol. 6, pp. 9-23.
6. Baker, C.J. (1980a), 'Theoretical approach to Prediction of Local Scour Around Bridge Piers', Journal of Hydraulic Research, Vol. 18, No. 1. pp. 1-12.
7. Baker, C.J. (1985), 'The Position of Points of Maximum and Minimum Shear Stress Upstream of Cylinders Mounted Normal to Flat Plates', Journal of Wind Engineering and Industrial Aerodynamics', Vol. 18, pp. 263-274.
8. Baker, C.J. (1987), 'Private Communication'.
9. Belik, L. (1973), 'The Secondary Flow about Circular Cylinders mounted Normal to a Flat Plate', The Aeronautical Quarterly, Vol. 24, pp. 47-54.
10. Bradshaw, P. (1970), 'Experimental Fluid Mechanics', Pergamon Press.
11. Bradshaw, P. (1971), 'An Introduction to Turbulence and Its Measurement', Pergamon Press.
12. Collis, D.C. and Williams, M.J. (1959), 'Two-dimensional Convection from Heated Wires at Low Reynolds Numbers', JFM, Vol. 6, 357-384.
13. Breusers, H.N.C. (1972), 'Local Scour Near Offshore Structures', Delft Hydraulics Laboratory, Publication No. 105.
14. Breusers, H.N.C., Nicollet, G., Shen, H.W. (1977), 'Local Scour Around Cylindrical Piers', Journal of Hydraulic Research', Vol. 15, No. 3, pp. 211-252.

15. Clauser, F.H. (1956), 'Advances in Applied Mechanics', Vol. IV, Academic Press, p. 1.
16. Coles, D. (1956), 'The Law of the Wake in the Turbulent Boundary Layer', Journal of Fluid Mechanics, Vol. I, pp. 191-226.
17. Elle, B.J. (1958), 'Investigation at Low Speed of the Flow Near the Apex of Thin Delta Wings with Sharp Leading Edges', A.R.C. R and M, 3176.
18. Earnshaw, P.B. (1961), 'Experimental Investigation of the Structure of a Leading Edge Vortex', A.R.C. R and M 3281.
19. Finaish, F., Freymuth, P. and Bank, W. (1986), 'Starting Flow Over Splitters, Double Steps and Cavities', Journal of Fluid Mechanics, Vol. 168, pp. 383-392.
20. Freymuth P., Bank W. and Palmer, M., (1985), 'Use of Titanium Tetrachloride For Flow Visualization of Accelerating Flow around Airfoils', Flow Visualization III, Ed. W.J. Yang, Hemisphere Publishing Corporation.
21. Freymuth, P. (1985a), 'The Vortex Patterns of Dynamic Separation : A Parametric and Comparative Study', Progress in Aerospace Sciences, Vol. 22, pp. 161-208.
22. Freymuth, P., Bank W. and Palmer, M. (1985b), 'Further Experimental Evidence of Vortex Splitting', Journal of Fluid Mechanics, Vol. 152, pp. 289-299.
23. Freymuth, P., Finaish F. and Bank, W. (1985c), 'Three-dimensional Vortex Patterns in a Starting Flow', Journal of Fluid Mechanics, Vol. 161, pp. 239-248.
24. Freymuth, P., Finaish, F. and Bank, W. (1986), 'The Physics of Fluids', Vol. 29, No. 4.
25. Freymuth, P., Finaish, F. and Bank, W. (1986a), 'Visualization of Wing Tip Vortices in Accelerating and Steady Flow', Journal of Aircraft, Vol. 23, No. 9, pp. 730-733.
26. Gangadharalah, T., Muzzamil, M. and Subramanya, K., (1985), 'Vortex Strength Approach for Bridge Pier Scour Predictions', Paper presented at the 2nd International Workshop on Alluvial River Problems, University of Roorkee, Roorkee, October, 24-26.
27. Gupta, A.K. (1987), 'Hydrodynamic Modification of the Horse-shoe Vortex at a Vertical Pier Junction with Ground', The Physics of Fluid, Vol. 30, No. 4, pp. 1213-1215.
28. Gupta, A.K., and Gangadharalah, T. (to be reported).

29. Gupta, Anil K. (1984), 'Experimental Investigation : Boundary Layer Flow Past a Circular Cylinder Mounted on a Flat Plate,' M. Tech. Thesis, Department of Civil Engineering, IIT, Kanpur.
30. Gupta, R.P. (1973), 'Experiments in Separated Flows : A New Probe and Upstream Effects of Separation', Ph.D. Thesis, Department of Mechanical Engineering, IIT, Kanpur
31. Hansen, A.G., Herzog, H.Z. and Costello (1953), 'A Visualization Study of Secondary Flows in Cascades', NACA TN 2947.
32. Harvey, J.K. (1958), 'Measurement On a Yawed Slender Delta Wing With Leading Edge Separation', ARC R and M No. 3160.
33. Harvey, J.K. and Perry, F.J. (1971), 'Flow Field Produced by Trailing Vortices in the Vicinity of the Ground', AIAA Journal, Vol. 9, No. 8,
34. Hawthorne, W.R (1954), 'The Secondary Flow About Struts and Airfoils', Journal of the Aeronautical Sciences, Vol. 21, pp. 558-609.
35. Hawthorne, W.R., (1967), 'Applicability of Secondary Flow Analyses', Fluid Mechanics of Internal Flow, Ed. G. Sovran, Elsevier Publishing Company, p. 238.
36. Head, M.R. (1971), 'A Simple Pressure Selector Switch', Journal of Physics E : Scientific Instruments, Vol. 4.
37. Hornung, H.G. and Joubert, P.N. (1973), 'The Mean Velocity Profiles in Three-dimensional Turbulent Boundary Layers', Journal of Fluid Mechanics, Vol. 15, pp. 368-384.
38. Houghton, E.L. and Carruthers, N.B. (1982), 'Aerodynamics for Engineering Students', 3rd Ed. Edward Arnold.
39. Hummel, D. (1978), 'On the Vortex Formation Over a Slender Wing at a Large Angle of Incidence', AGARD CP No. 247.
40. Hunt, J.C.R., Abell, C.J., Peterka, J.A. and Woo, H. 'Kinematical Studies of the Flows around Free or Surface-Mounted Obstacles : Applying Topology to Flow Visualization', Journal of Fluid Mechanics, Vol. 86, pt. 1, pp. 179-200.
41. Jain, B.P. and Modi, P.N. (1986), 'Comparative Study of Various Study of Various Formulae on Scour Around Bridge Piers', Journal of the Institution of Engineers (India), Civil Engineering Division, 67, pp. 149-159.
42. Jain, S.C. (1981), 'Maximum Clear Water Scour Around Circular Piers', Proc. ASCE, J. Hydraulic Div., 107, pp. 611-626.

43. Kline, S.J., Reynolds, W.C., Schraub, F.A., and Runstadler, P.W. (1967), 'The Structure of Turbulent Boundary Layer', Journal of Fluid Mechanics, Vol. 30, pp. 741-773.
44. Karman Th. von and Tsien, H.S. (1945), 'Lifting Line Theory for a Wing in Non-Uniform Flow', Quart. Applied Mathematics, Vol. III, April, 1945.
45. Kuchemann, D. (1978), 'The Aerodynamic Design of Airplane', Pergamon Press.
46. Langston, L.S. and Boyle, M.T. (1982), 'A New Surface- Stream-line Flow-Visualization Technique', Journal of Fluid Mechanics, Vol. 125, pp. 53-57.
47. Laursen, E.M. (1960), 'Scour at Bridge Crossings', Proceedings of ASCE, 86 (HY2), pp. 39-54.
48. Lawford, J.A. (1964), 'Low Speed Wind Tunnel Experiments on a Series of Sharp Edged Delta Wings Part II : Surface Flow Patterns and Boundary Layer Transition Measurements' RAE, TN Aero. 2954.
49. Mason, P.J. and Morton, B.R. (1987), 'Trailing Vortices in the wakes of Surface-Mounted Obstacles', Journal of Fluid Mechanics, Vol. 175, pp. 247-293.
50. Melville, B.W., 'Local Scour at Bridge Sites,' Univ. of Auckland, School of Engineering, Auckland, New Zealand, Rep. No. 117.
51. Melville, B.W., and Raudkivi, A.J. (1977), 'Flow Characteristics in Local Scour at Bridge Piers', Journal of Hydraulic Research, Vol. 15, pp. 373-380.
(1985)
52. Muzzamil, M., 'Experimental Investigation : Open Channel Flow Past a Circular Cylinder Mounted on a Rigid-Bed and on a Mobile Bed', M.Tech. Thesis, Department of Civil Engineer, IIT, Kanpur.
53. Muzzamil, M. and Gangadharalah, T. (1987), 'A Study of Horse-shoe Vortex' Proceedings of 15th National Conference on Fluid Mechanics and Fluid Power, R.E.C. Srinagar, July, 22-24.
54. Nghein, Tran. D. (1988), 'Laboratory Investigation of Scour Reduction near Bridge Piers by Delta-Wing-Like Passive Device', M.Tech. Thesis Dept. of Civil Engg. IIT, Kanpur.
55. Okamoto, T. and Yagita, M. (1973), 'The Experimental Investigation on the Flow Past a Circular Cylinder of Finite Length Placed Normal to the Plane Surface in a Uniform Stream', Bulletin of the JSME, Vol. 16, No. 95, pp. 805-814.

56. Ower, E. and Pankhurst, R.C. (1977), 'The Measurement of Air Flow' Pergamon Press.
57. Polhamus, E.C. (1966), 'A Concept of the Vortex Lift of Sharp-Edged Delta Wings Based on a Leading-Edge-Suction Analogy,' NASA TND 3767
58. Posey, C.J. (1974), 'Tests of Scour Protection for Bridge Piers', Proceedings of ASCE, 100, (HY12).
59. Prasad, J.K. (1975), 'Correlation Coefficient Measurement in Turbulent Near Wake of Bluff Bodies', M.Tech. Thesis, Dept. of Aero.Engg., IIT, Kanpur.
60. Preston, J.H. (1954), 'A Simple Approach to the Theory of Secondary Flows', The Aeronautical Quarterly, Vol. V.
61. Qadar, A. (1981), 'The Vortex Scour Mechanism at Bridge Piers', Proceedings of Institution of Civil Engineers, Vol. 71, pp. 739-757.
62. Rae, W.H. and Pope, A. (1984), 'Low Speed Wind Tunnel Testing', 2nd ed.
63. Raudkivi, A.J. and Ettema, R. (1985), 'Scour at Cylindrical Bridge Piers in Armored Beds', Proceedings of ASCE, Journal of Hydraulic Division, 111, pp. 713-731.
64. Schlichting, H. (1968), 'Boundary Layer Theory', 6th Ed. McGraw Hill book.
65. Shen, H.W., Schnieder, V.R., and Karaki, S. (1969), 'Local Scour Around Bridge Piers', Proceedings of ASCE, Journal of Hydraulic Division, 95, pp. 1919-1940.
66. Sinha, S.N. (1978), 'Two Dimensional Laminar and Turbulent Separating Flows Over Backward Facing Steps and Rectangular Cavities', Ph.D. Thesis, Department of Mechanical Engineering, IIT, Kanpur.
67. Sullerey, R.K. (1974), 'Investigations in the Low Speed Turbulent Near Wakes of Bluff Bodies', Ph.D. Thesis, Department of Aeronautical Engineering, IIT, Kanpur.
68. Squire, H.B. and Winter, K.G. (1951), 'The Secondary Flow in a Cascade of Airfoils in a Non-Uniform Stream', Journal of Aeronautical Sciences, Vol. 18, pp. 271-77.
69. Taylor, E.S. (1967), 'Some Problems of Recognising and Defining Separation of the Skewed Boundary Layer', Fluid Mechanics of Internal Flows, Ed. G. Sovian Elsevier Publishing Company, pp. 320-332.
70. Tison, J.L. (1961), 'Local Scour of Rivers', J. Geophysical Research, 66, pp. 4227-4232.

71. Thwaites, B. (1960), 'Incompressible Aerodynamics',
Oxford University Press.

Appendix

A schematic sketch of the flow on a surface coated with an oil-suspension mixture is given in Fig. A.1. The velocity profile at 'a' is of the free stream velocity, and the profile 1 at 'b' is a representation of the flow on the free layer of the suspension oil mixture. For simplicity a linear velocity variation may be assumed between the top layer and the surface. As the oil is drained away, this profile gets modified due to change in the layer thickness. A compatibility of the free stream and the consistency of the oil mixture, would appear to determine the nature of the surface oil patterns after certain time. It thus appears that the surface flow patterns due to oil film technique in general, may be treated as trend of the surface streamlines. Time or duration of the wind tunnel run is an important factor and there appears no alternative to making number of trial runs while using surface oil film technique.

Langston and Boyle (1982) pointed out that the results of their 'novel surface streamline technique' needed to be verified from pressure measurements. Total head survey of the stream wise arm of HSV at the mid-span of each model confirmed the inferences from surface oil film technique in the present work.

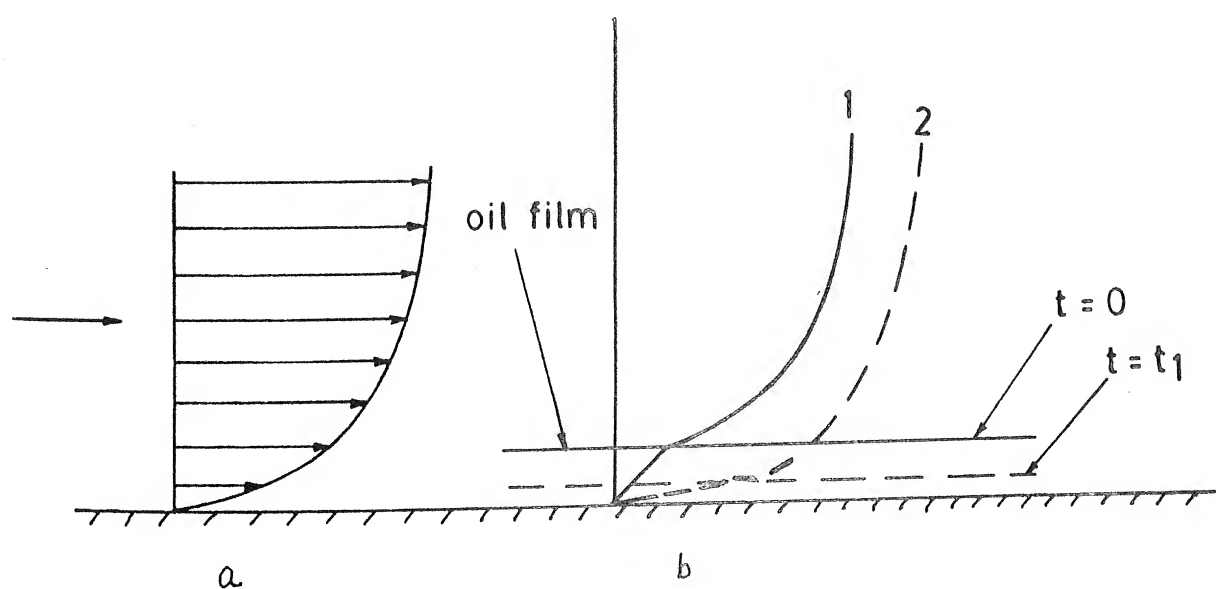
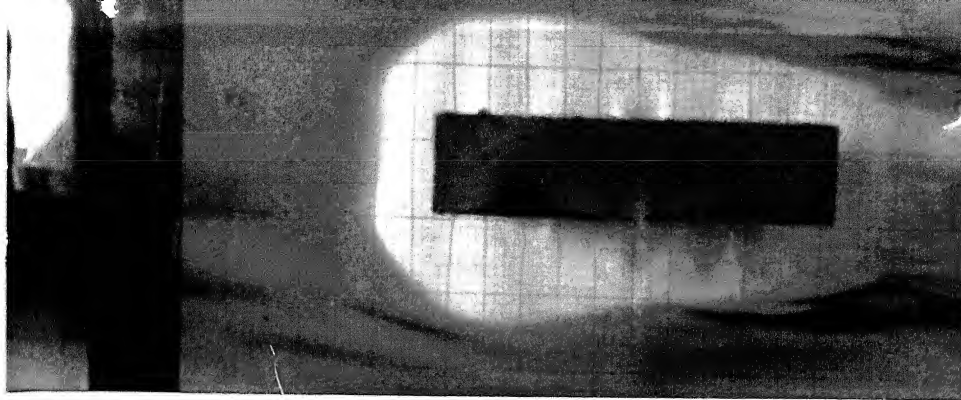
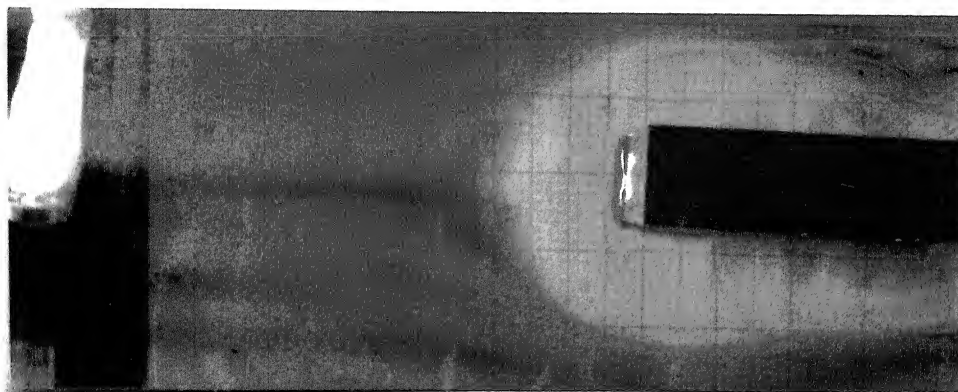


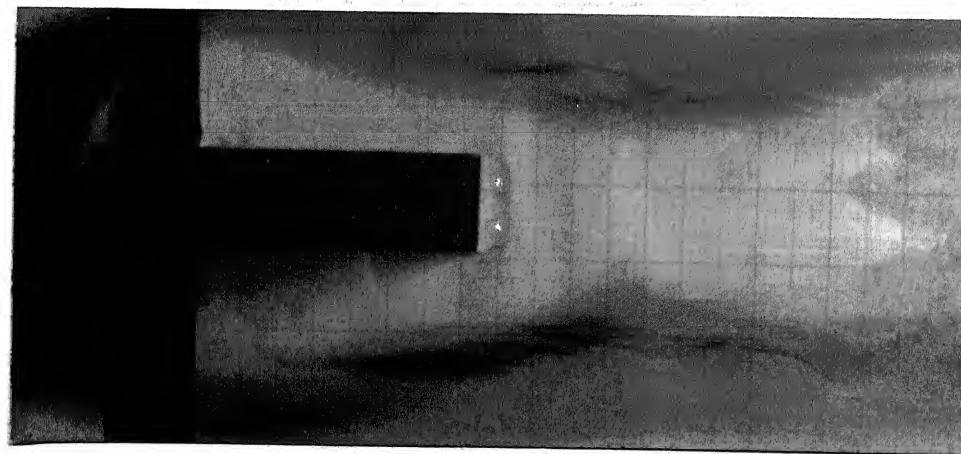
FIG. A1 SCHEMATICS OF OIL FILM FLOW OVER A FLAT WALL



a. PLAN VIEW



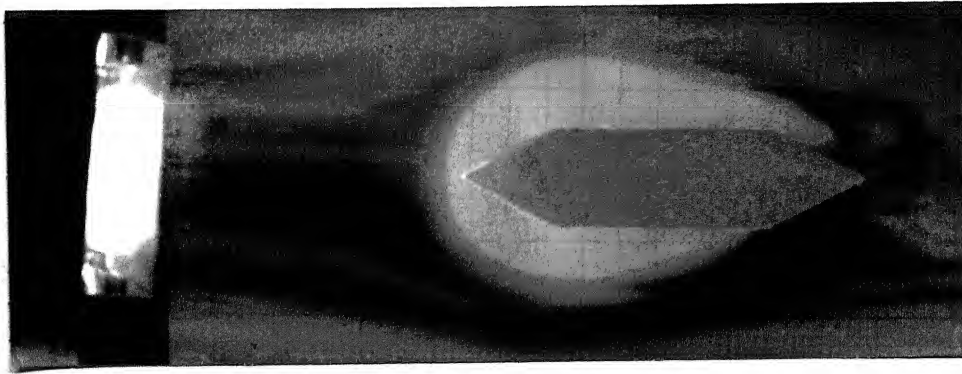
b. TOP FRONT VIEW



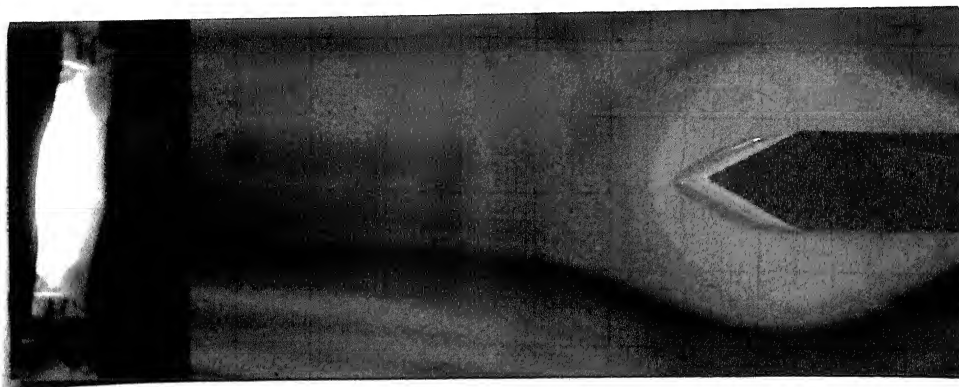
c. TOP REAR VIEW

Fig. 6.1

DYE PATTERNS AROUND RECTANGULAR PIER MODEL
 $L/D = 6$, $BR = 10\%$, $Re = 3197$, $Fr = 0.146$
 (FLOW FROM LEFT TO RIGHT)



a. PLAN VIEW



c. TOP REAR VIEW

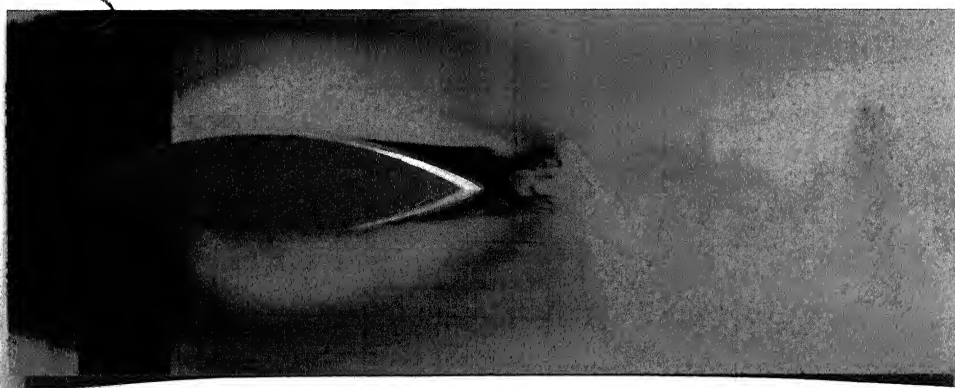
Fig. 6.2 DYE PATTERNS AROUND WEDGE NOSE PIER MODEL,
 $L/D = 6$, $BR = 10\%$, $Re = 3197$, $Fr = 0.146$
 (FLOW FROM LEFT TO RIGHT)



a. PLAN VIEW



b. TOP FRONT VIEW



c. TOP REAR VIEW

Fig. 6.3

DYE PATTERNS AROUND LENTICULAR PIER MODEL,
 $L/D = 6$, $BR = 10\%$, $Re = 3197$, $Fr = 0.146$
 (FLOW FROM LEFT TO RIGHT)

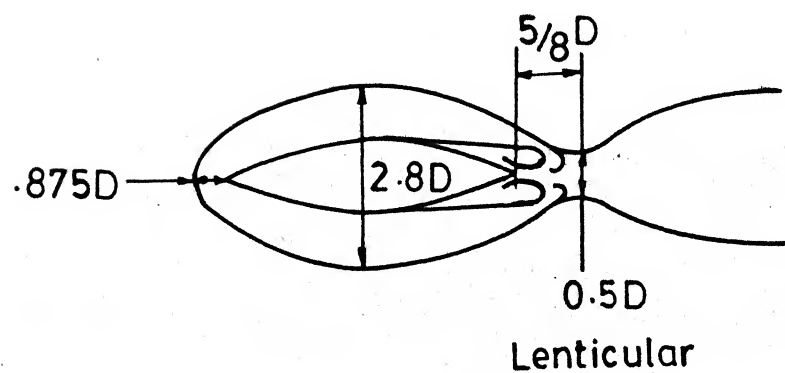
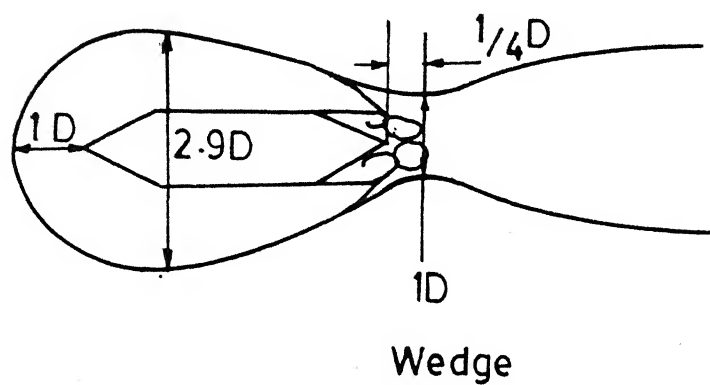
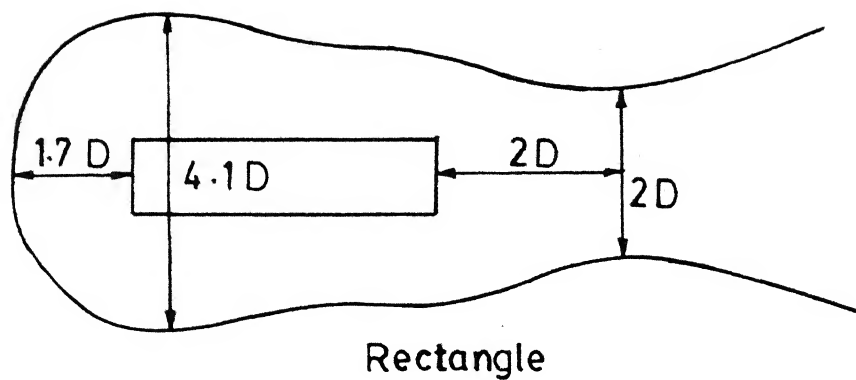
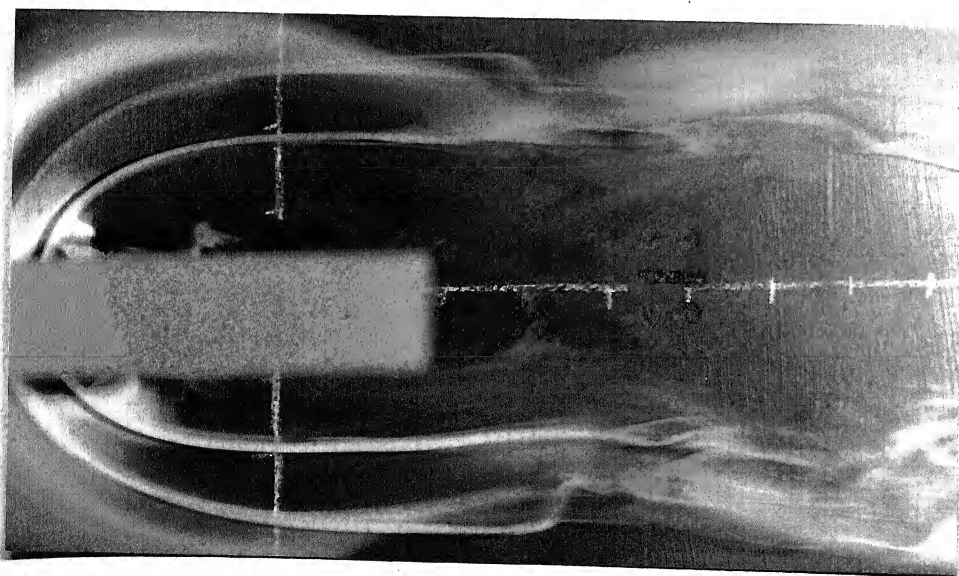


FIG.6.4 LINE SKETCHES OF DYE PATTERNS AROUND PIER MODELS



a. PERSPECTIVE VIEW

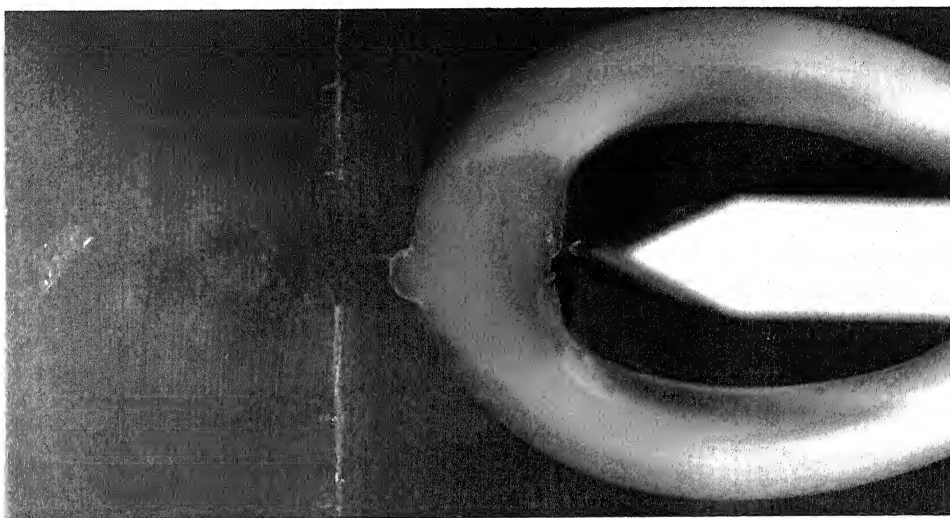


c. TOP REAR VIEW

Fig. 6.5 $TiCl_4$ FLOW AROUND RECTANGULAR PIER MODEL
 $L/D = 6$, $BR=3\%$, $Re = 1450$, $D/\delta^* = 4.5$,
 (FLOW FROM LEFT TO RIGHT)



a. PERSPECTIVE VIEW



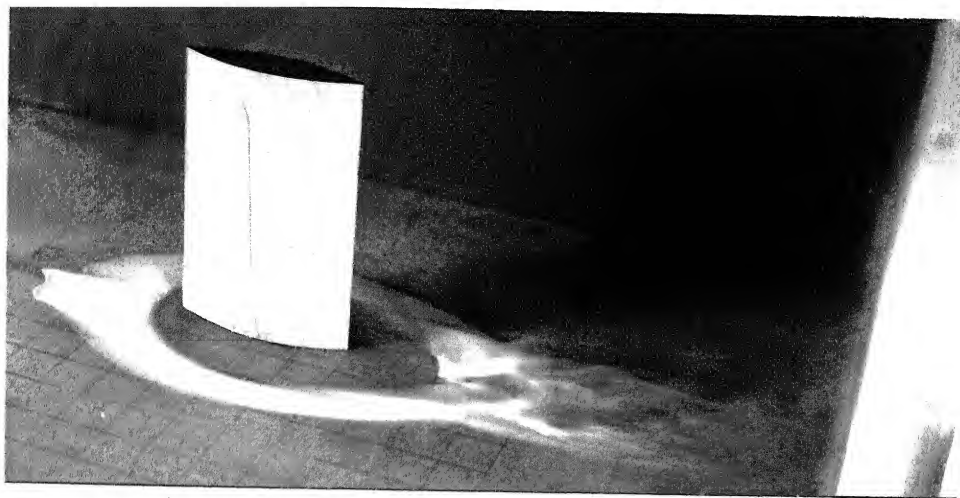
b. TOP FRONT VIEW



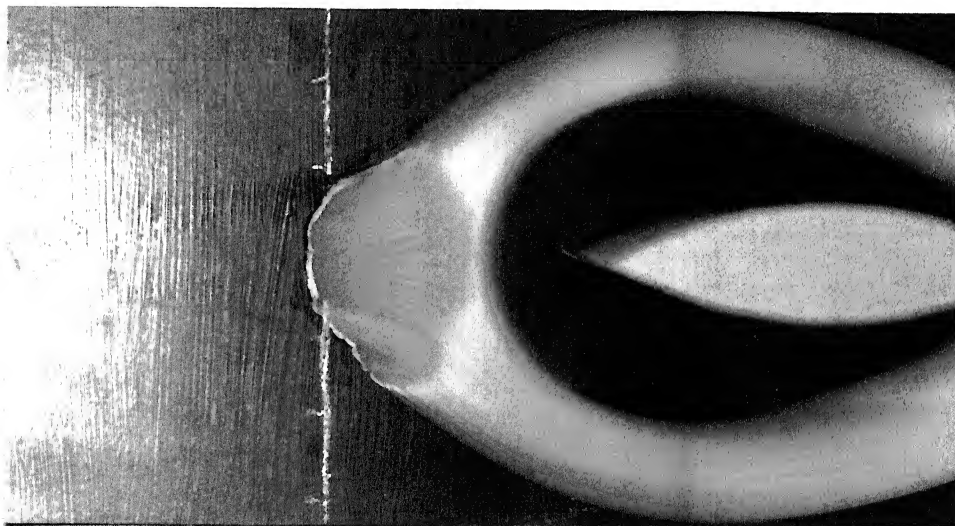
c. TOP REAR VIEW

Fig. 6.6

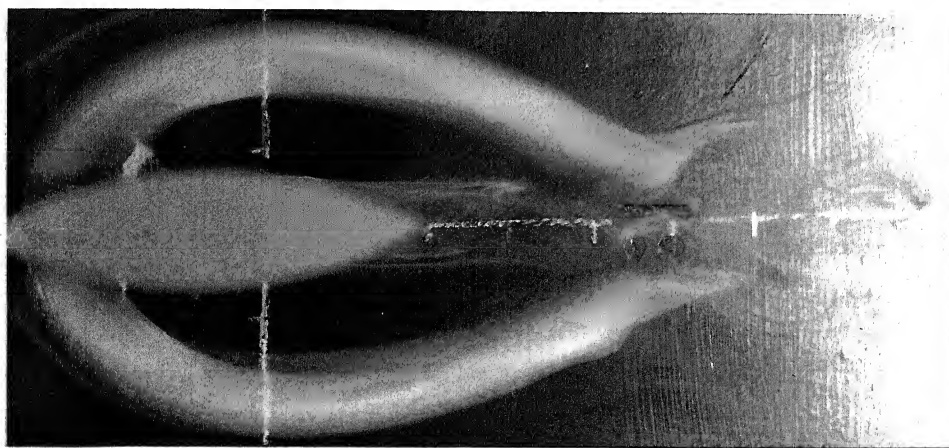
TiCl_4 FLOW AROUND WEDGE NOSE PIER MODEL,
 $L/D = 6$, $BR = 3\%$, $Re = 1450$, $D/\delta^* = 4.5$
 (FLOW FROM LEFT TO RIGHT)



a. Perspective View



b. TOP FRONT VIEW



c Top Rear View

Fig. 6.7 TiCl_4 FLOW AROUND LENTICULAR PIER MODEL,
 $L/D = 6$, $BR = 3\%$, $Re = 1450$, $D/\delta^* = 4.5$
 (FLOW FROM LEFT TO RIGHT)

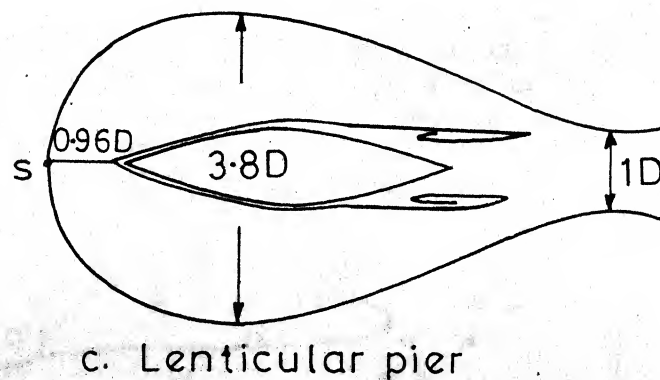
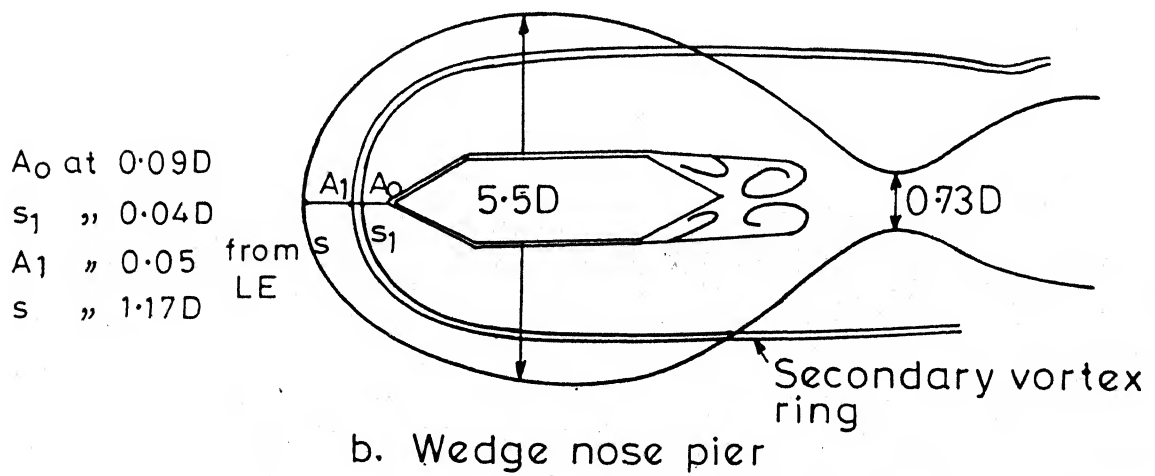
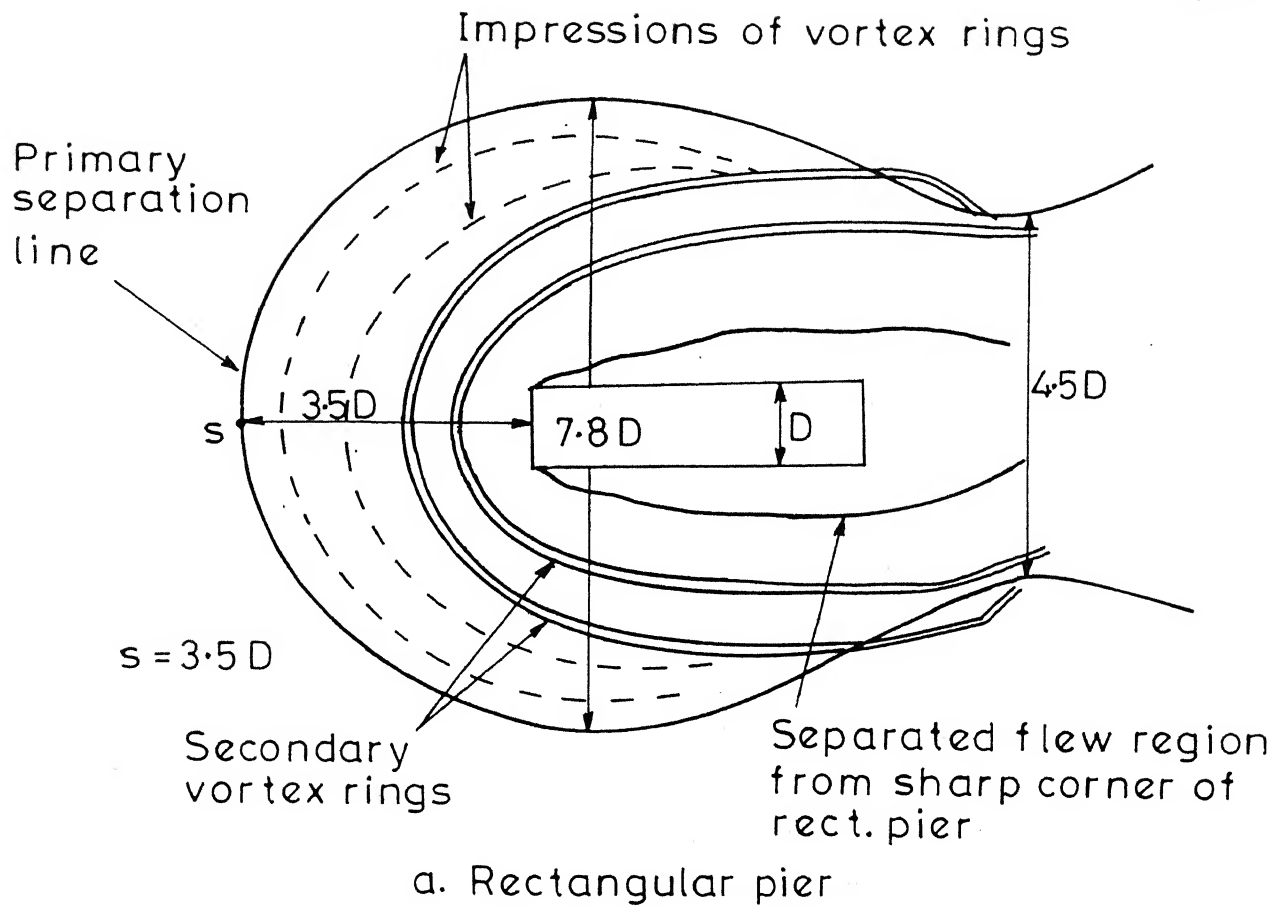


FIG. 6.8 SCHEMATIC SKETCHES OF $TiCl_4$ FLOW AROUND PIER MODELS $L/D=6$, $BR=3\%$.

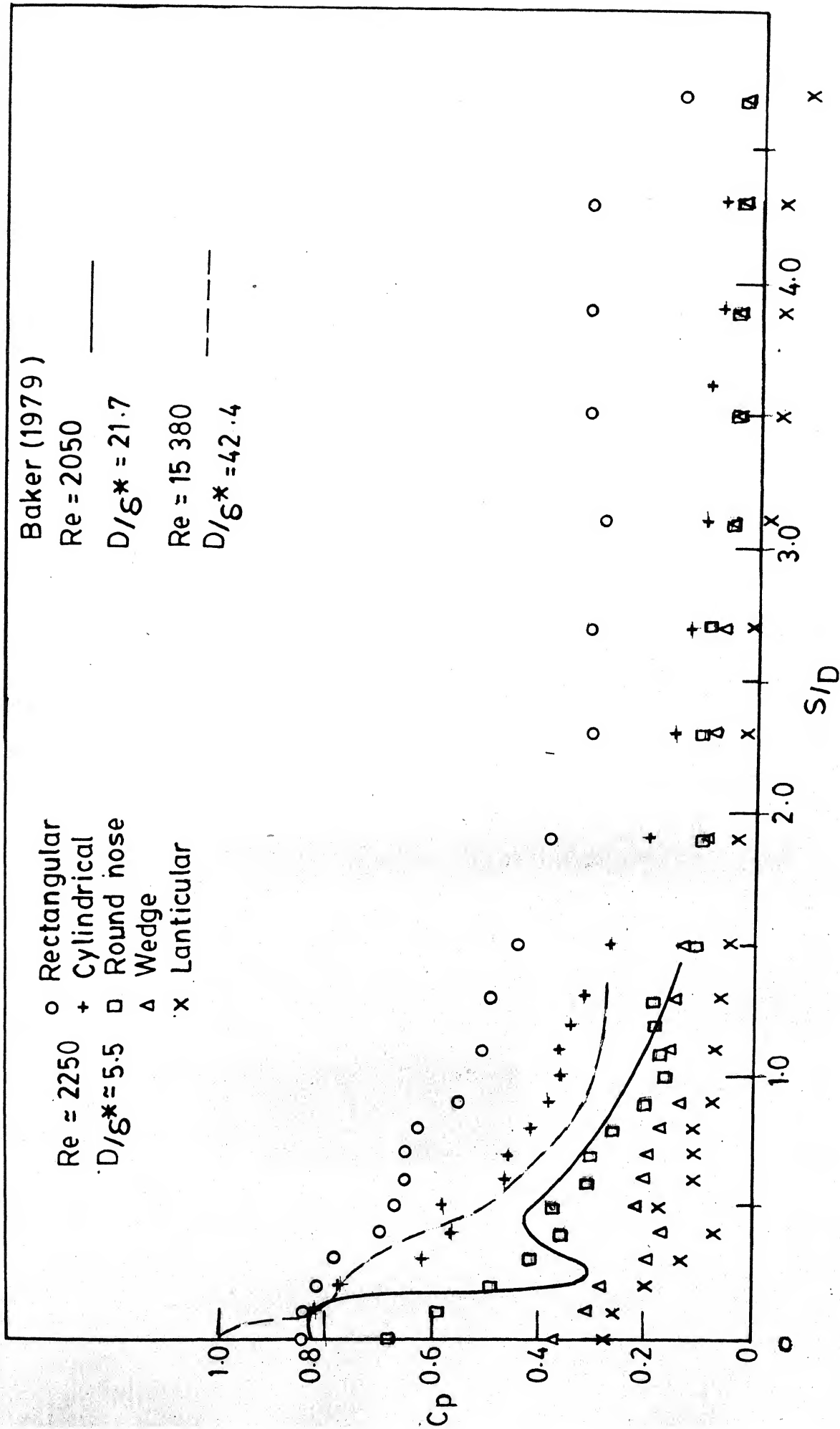


FIG. 6.9 PRESSURE DISTRIBUTION ON THE UPSTREAM PLANE OF SYMMETRY OF PIER MODELS $L/D = 6$, $BR = 3\%$

Re, D/δ*, Freq.

V/Div, t/D.
mv m s

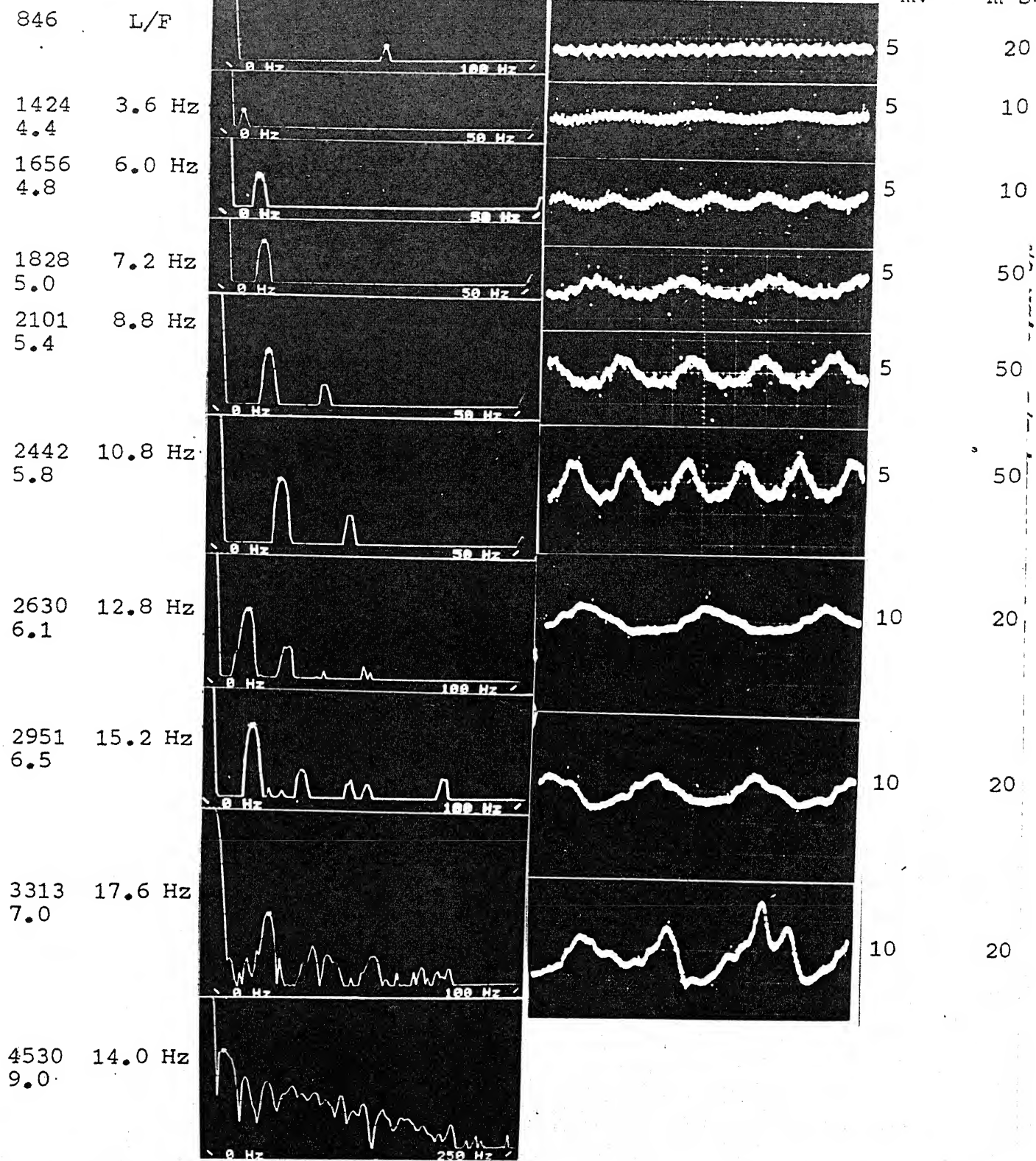


Fig. 6.10a SPECTRA AND TRACES OF VORTEX OSCILLATIONS
AROUND RECTANGULAR PIER MODEL L/D = 6, BR=3%

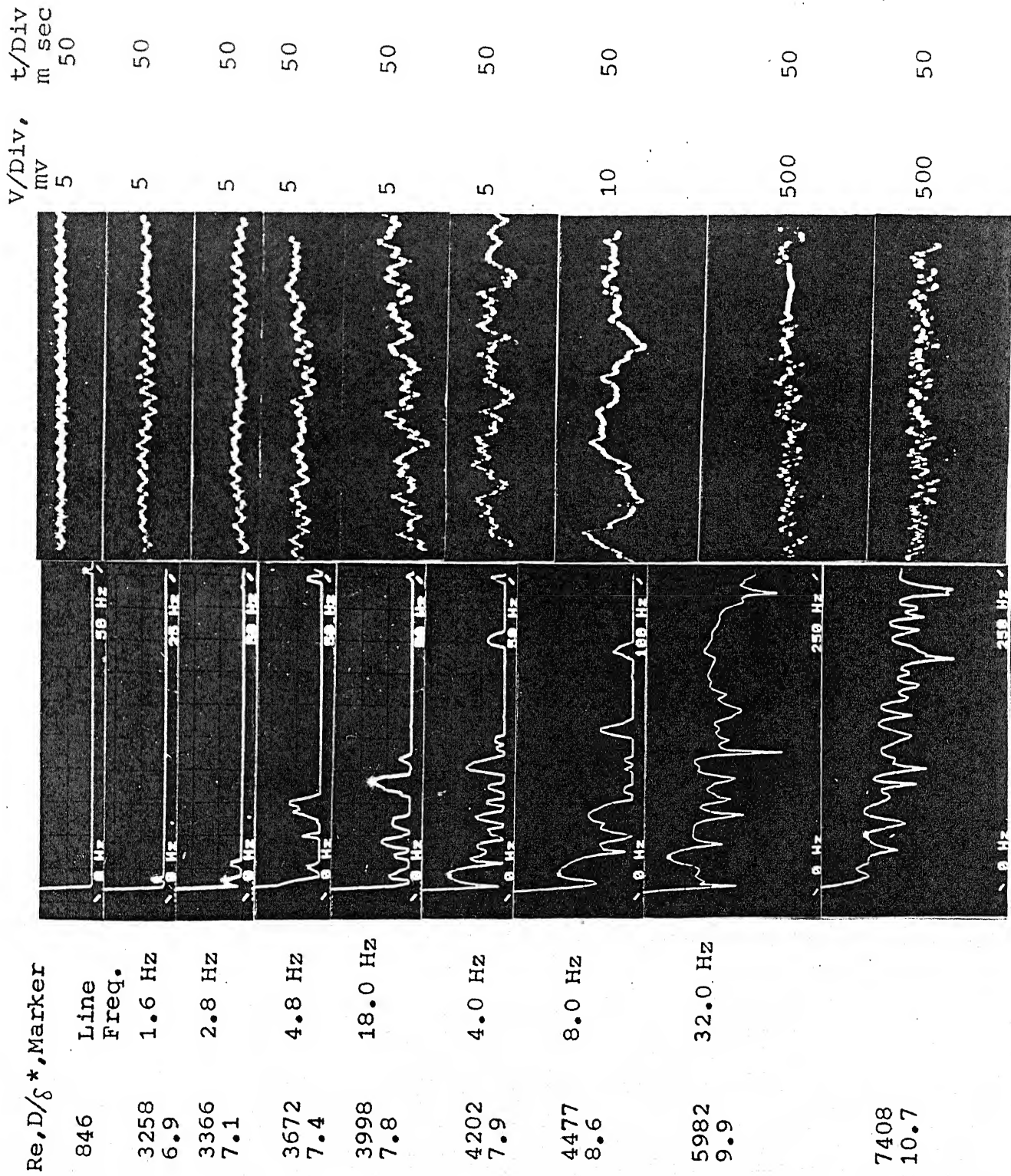


Fig. 6.10b SPECTRA AND TRACES OF VORTEX OSCILLATIONS
AROUND WEDGE NOSE PIER MODEL, $L/D = 6, BR=3\%$

Re.D/ ρ^* , Marker									
772	3184	3313	3655	3983	4188	4503	4835	6178	
Line	6.9	7.0	7.4	7.7	7.9	9.0	9.5	10.1	
Freq.	2.2 Hz	2.8 Hz	2.2 Hz	1.8 Hz	4.0 Hz	6.4 Hz	7.2 Hz		

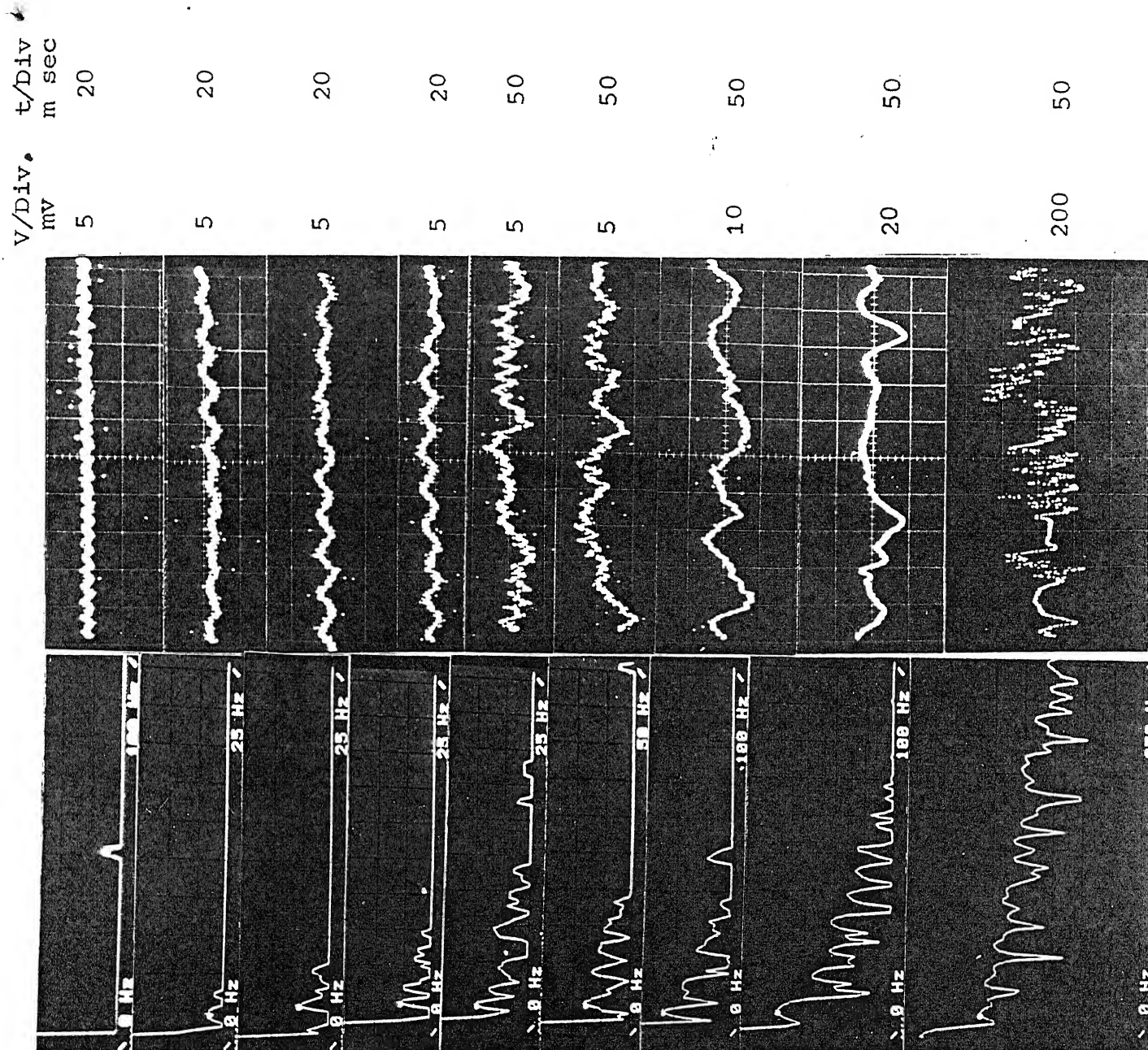
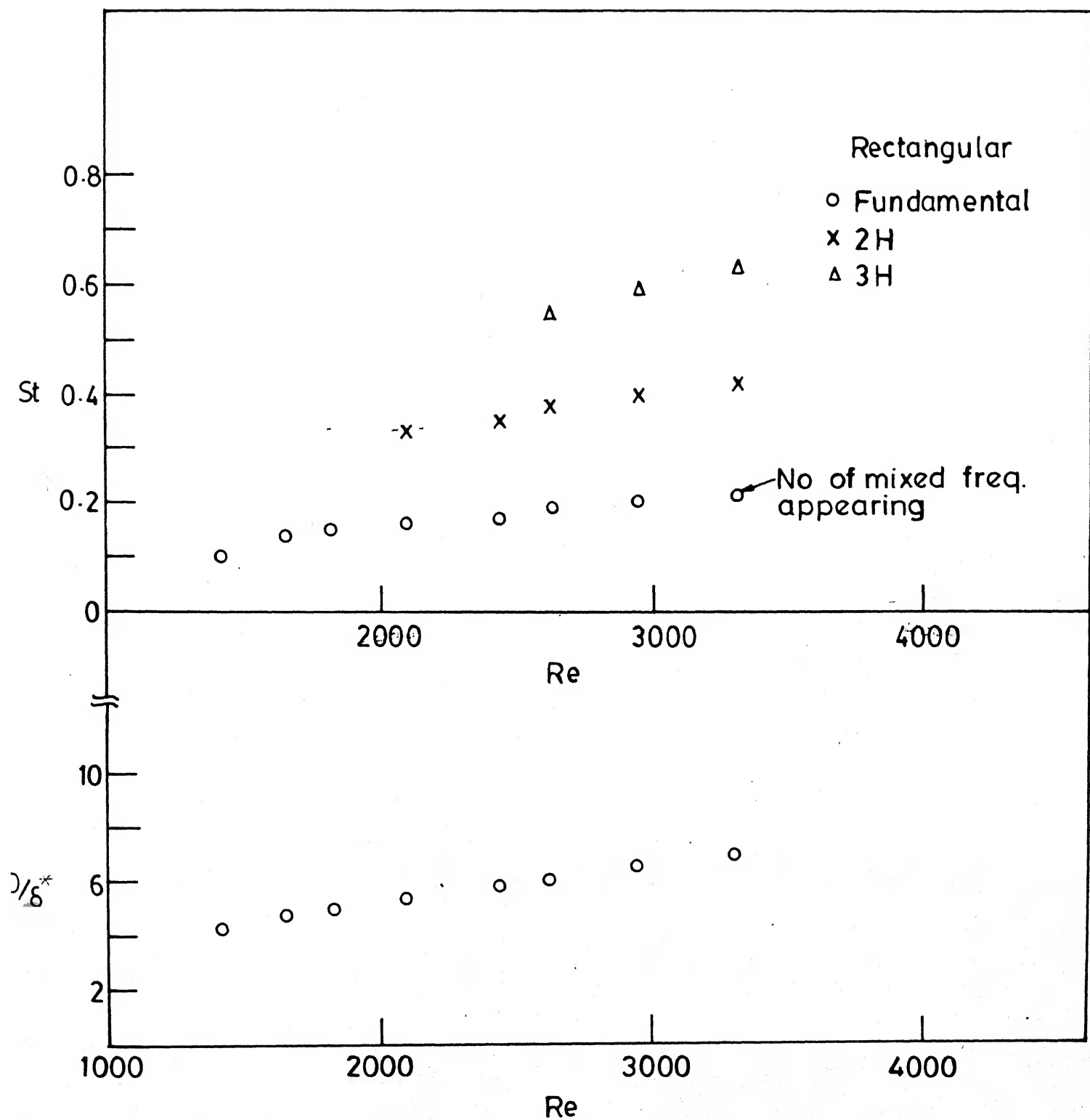
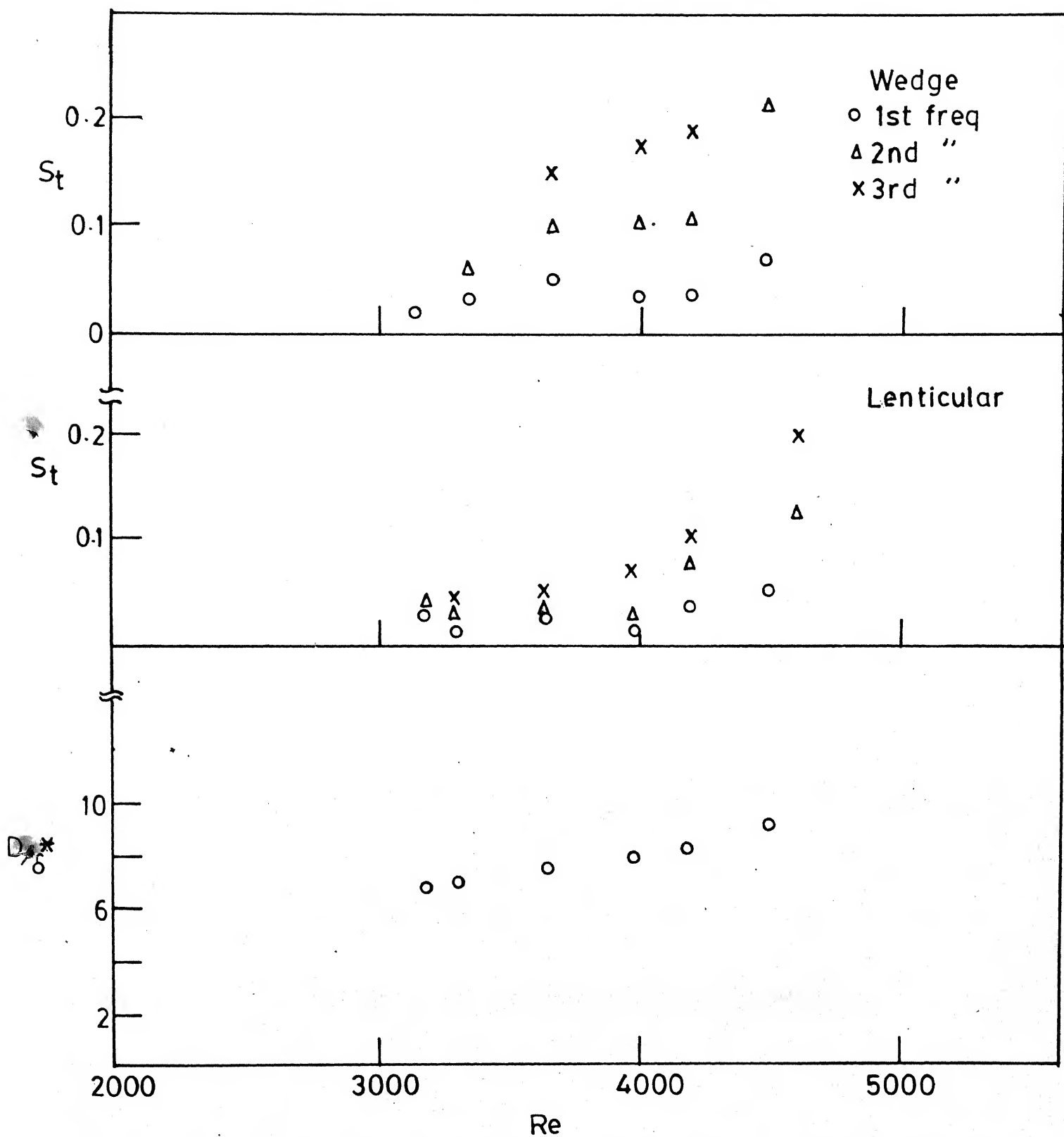


Fig. 6.10c SPECTRA AND TRACES OF VORTEX OSCILLATIONS
AROUND LENTICULAR PIER MODEL, $L/D = 6$, $BR=3\%$



(a) Rectangular pier model

FIG. 6.11 VARIATION OF VORTEX OSCILLATIONS WITH Re AND D/δ^*
 $L/D = 6$, $BR = 3\%$



(b) Streamline nose pier models $L/D=6$, $BR=3\%$

FIG. 6.11 Contd.

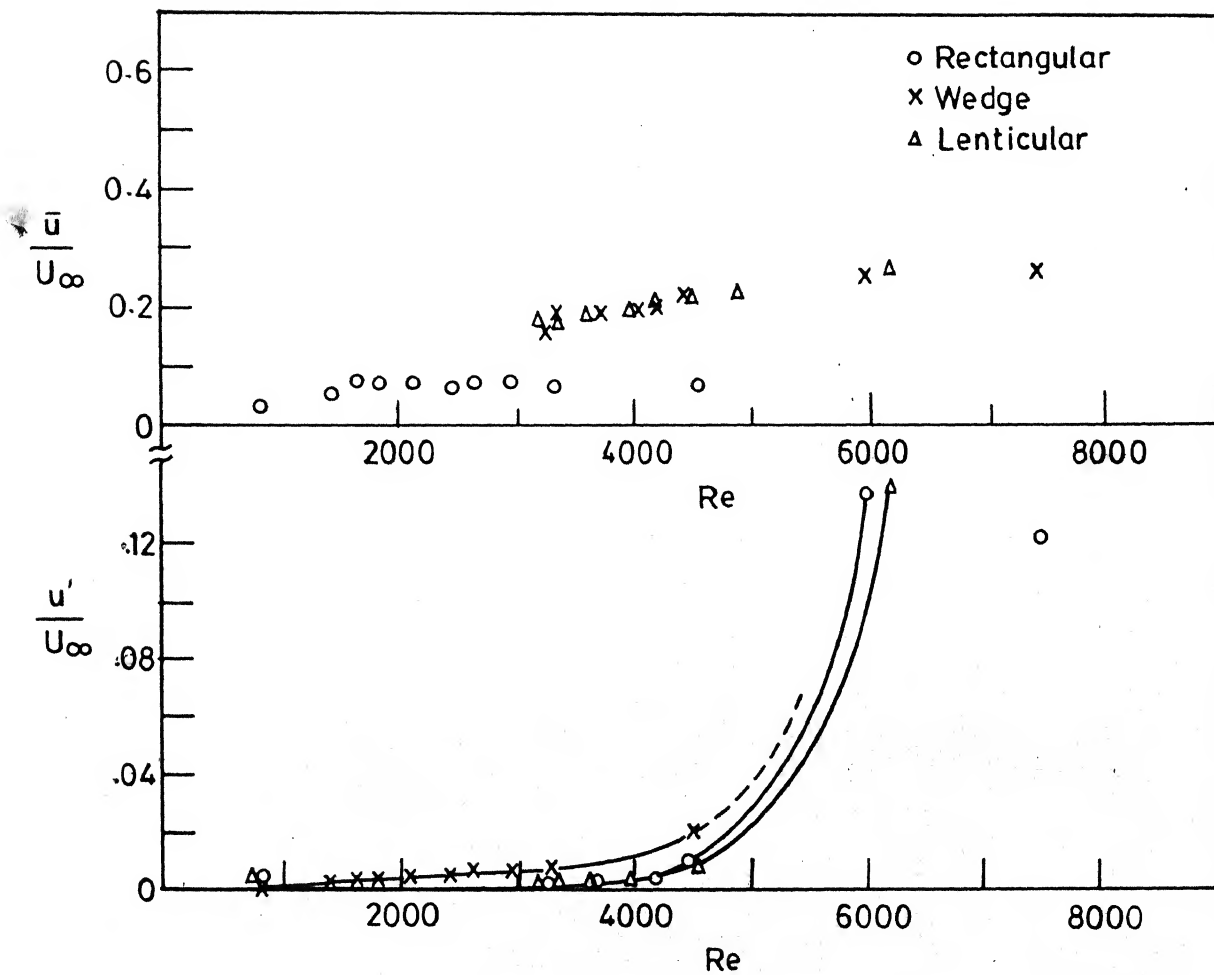
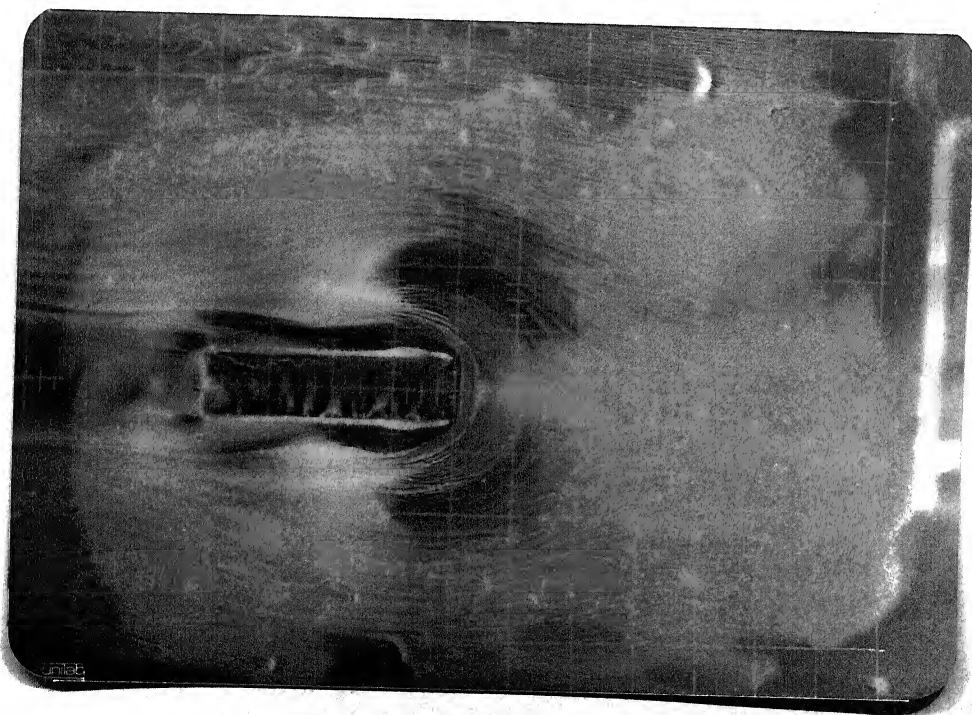
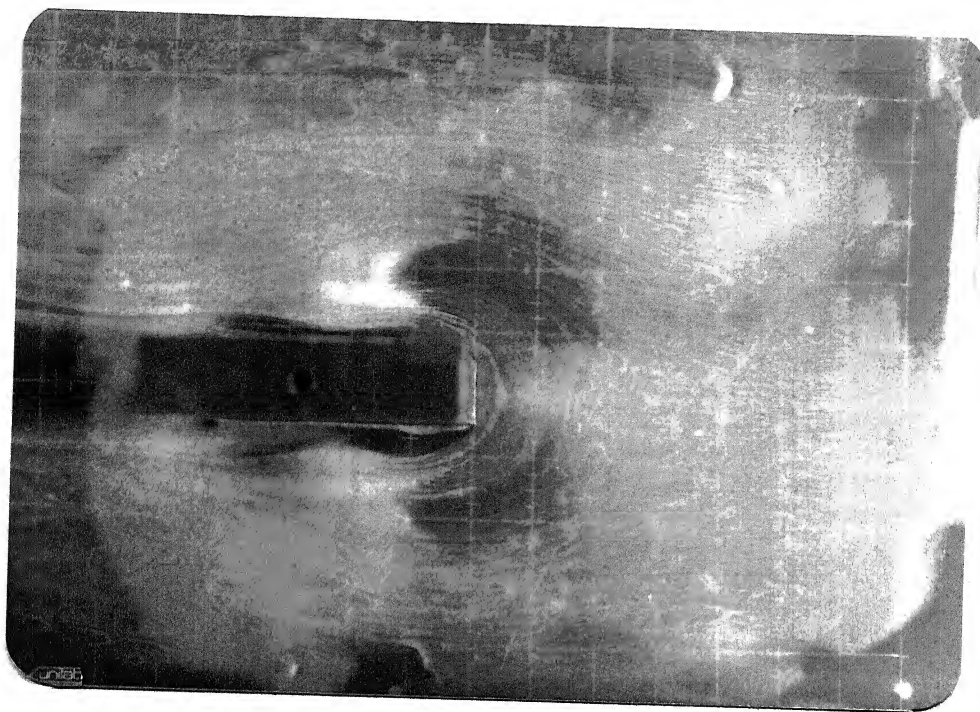
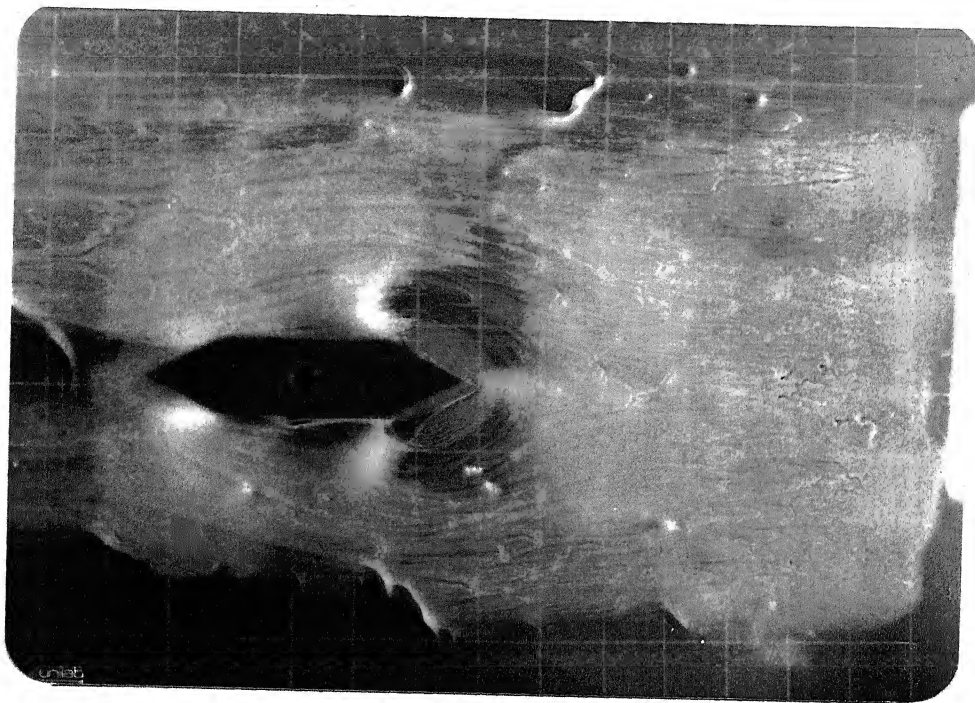


FIG. 6-12 VARIATION OF \bar{u} AND u' UPSTREAM OF PIER MODELS
 $L/D = 6$, $BR = 3\%$

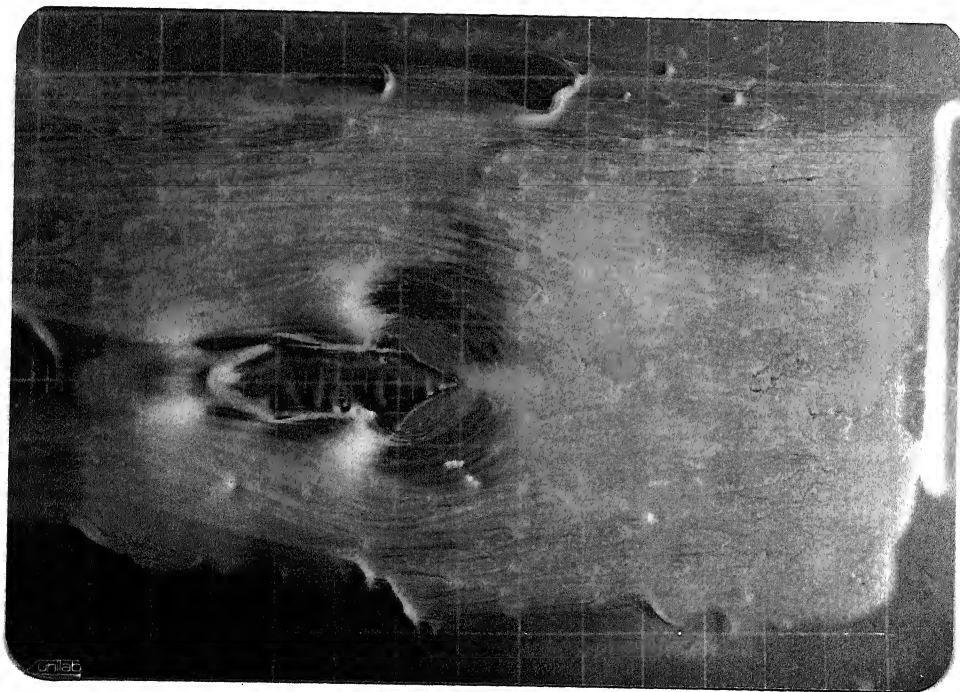


$t = 15 \text{ Min.}$

Fig. 6.13a SURFACE OIL FILM PATTERNS AROUND RECTANGULAR
PIER MODEL, $L/D = 6$, $BR = 3\%$, $Re = 7800$, $D/\delta^* = 11$

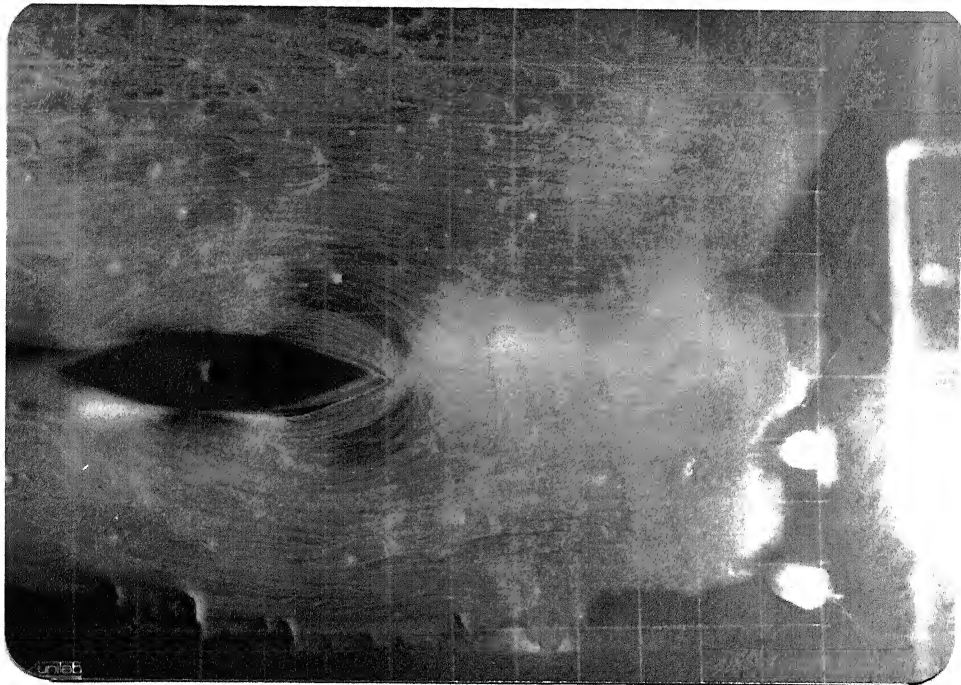


$t = 15 \text{ Min. (FLOW ON)}$



$t = 15 \text{ Min.}$

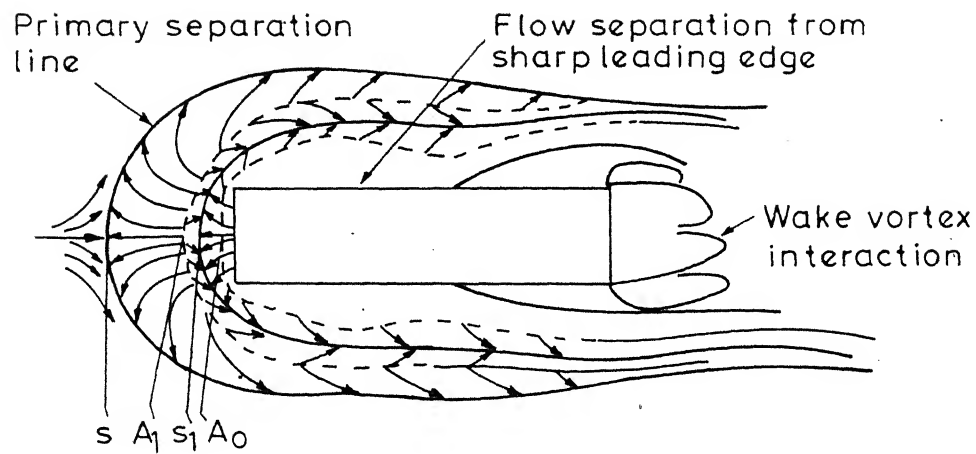
Fig. 6.13b SURFACE OIL FILM PATTERNS AROUND WEDGE NOSE
PIER MODEL, $L/D=6$, $BR=3\%$, $Re=7800$, $D/\delta^* = 11$



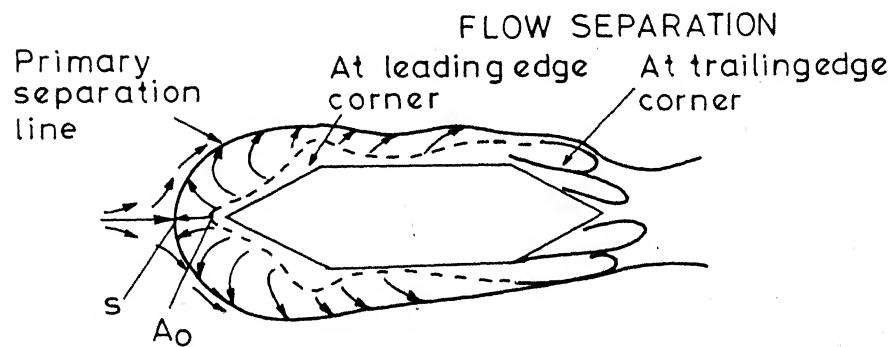
a. $t = 15$ Min. (FLOW ON)

$t = 15$ Min.

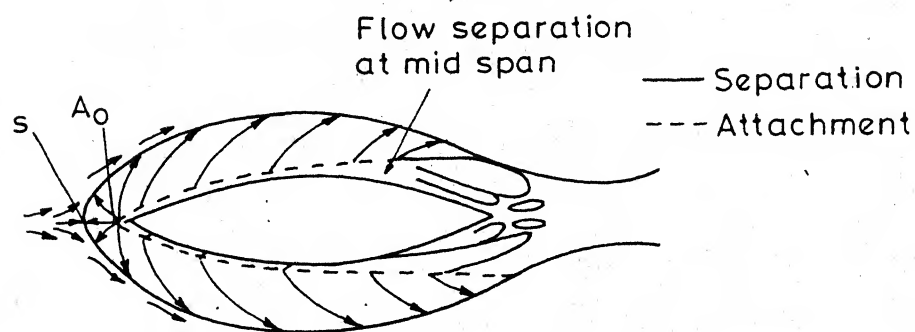
Fig. 6.13c SURFACE OIL FILM PATTERNS AROUND LENTICULAR
PIER MODEL, $L/D=6$, $BR=3\%$ $Re=7800$, $D/\delta^* = 11$



a. Rectangular pier



b. Wedge nose pier



c. Lenticular pier

FIG. 6.14 SURFACE STREAMLINES AROUND PIER
 MODELS $L/D=6$, $BR=3\%$, $Re \approx 7800$, $D/\delta^* \approx 11$

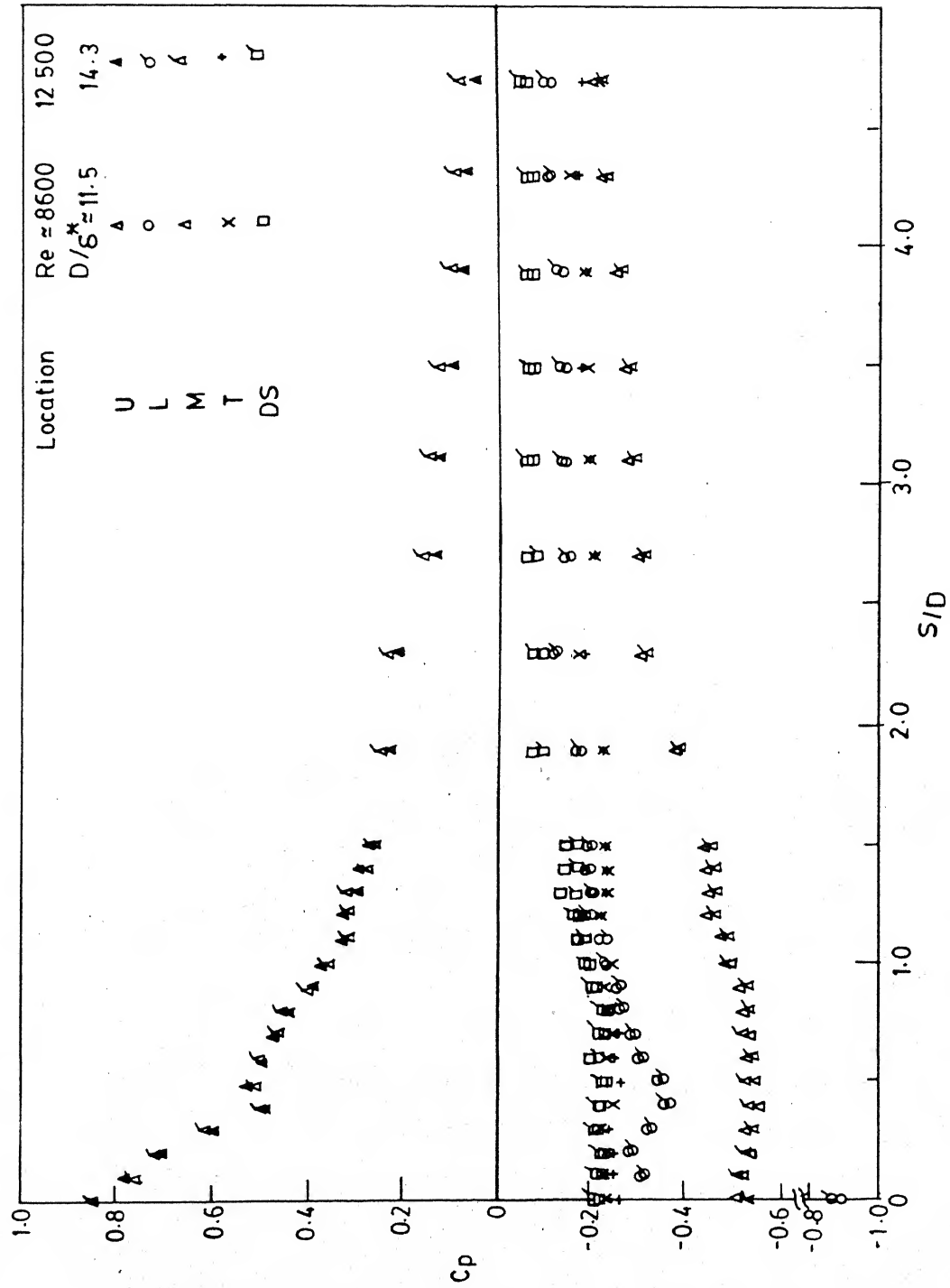
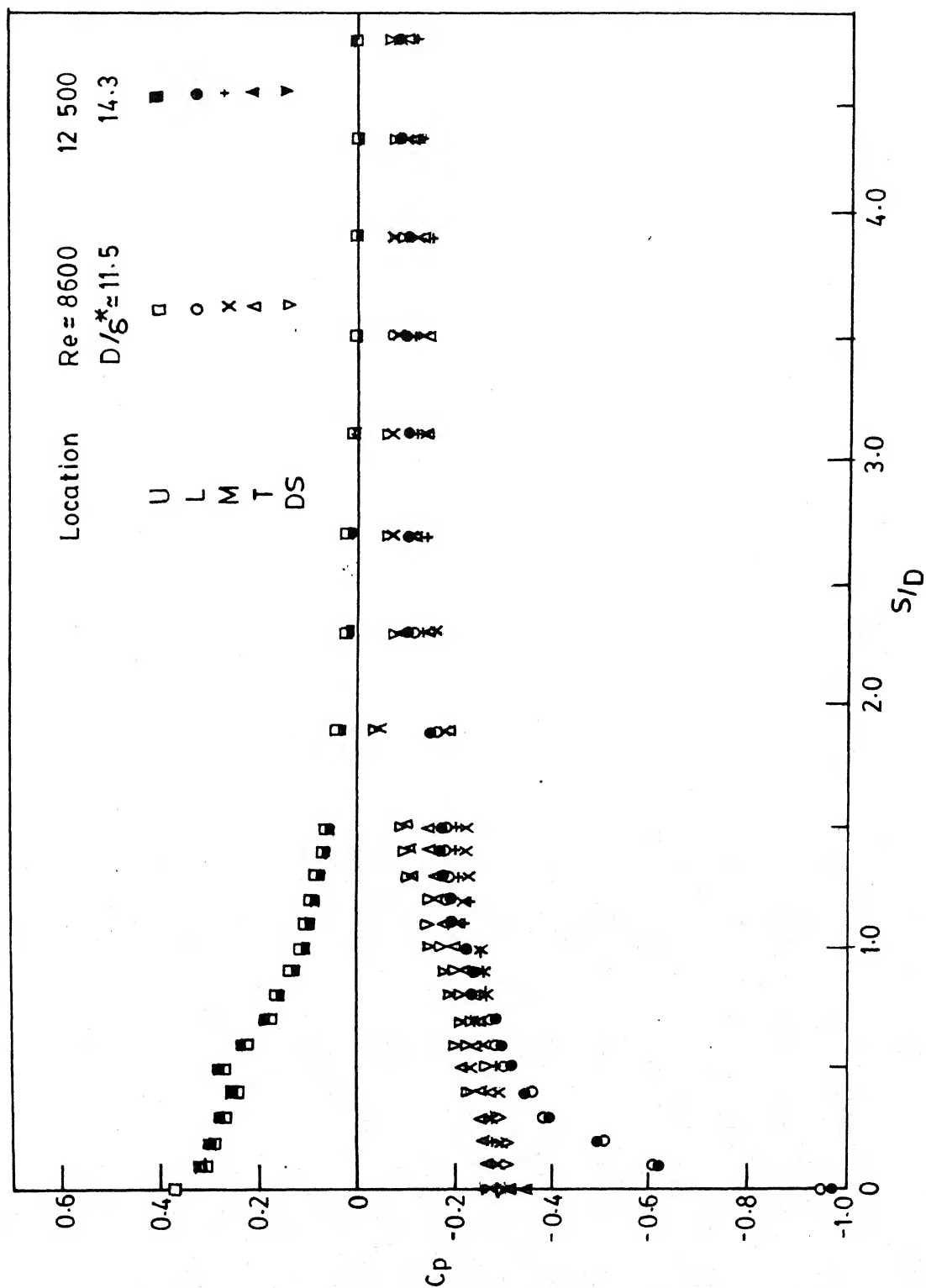


FIG. 6.15a SURFACE PRESSURES AROUND PIER MODEL



(b) Wedge nose pier

FIG. 6.15 Contd.

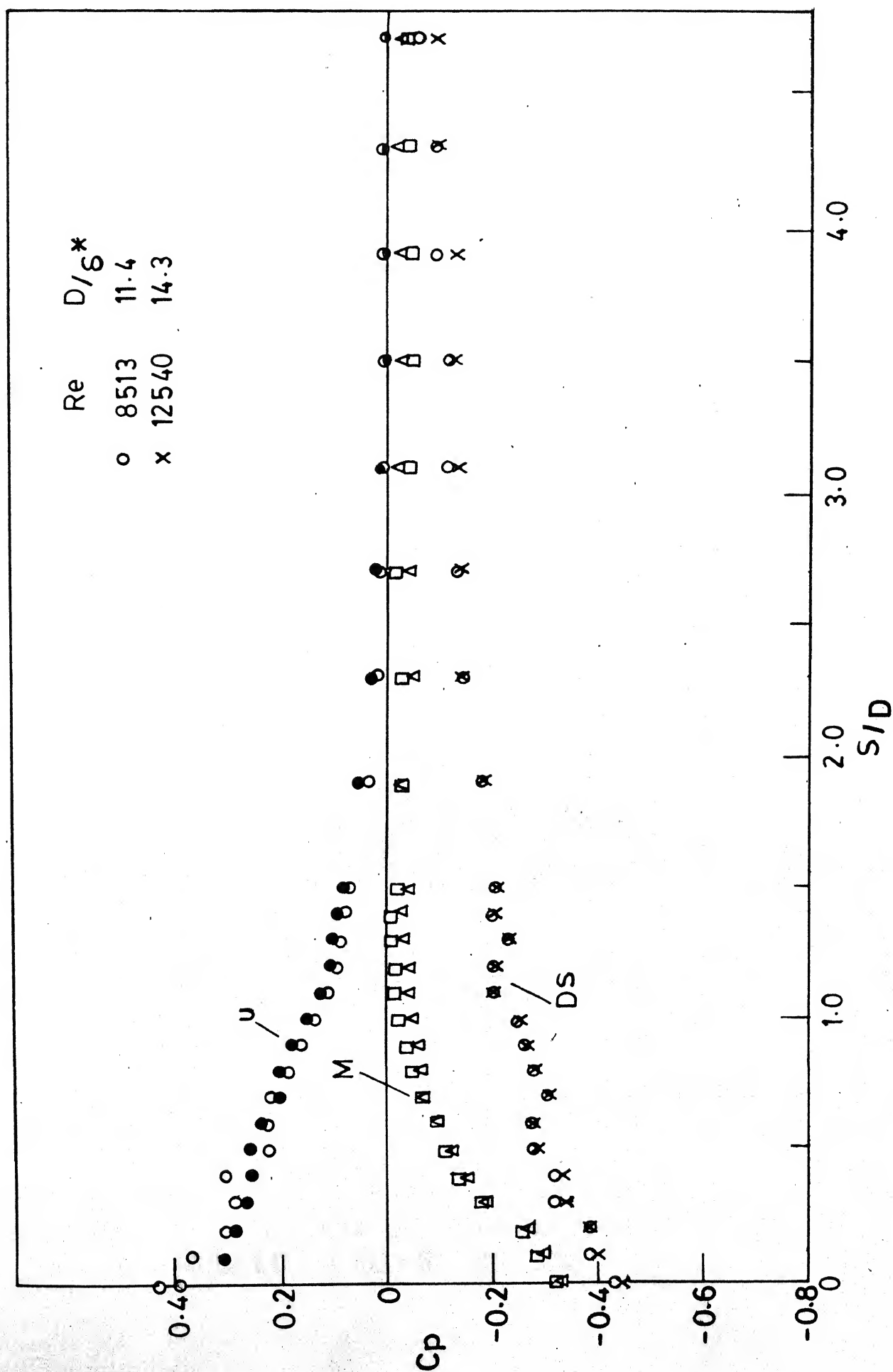


FIG.6.15c PRESSURE DISTRIBUTION ON THE WALL IN THE FLOW FIELD AROUND LENTICULAR PIER MODEL

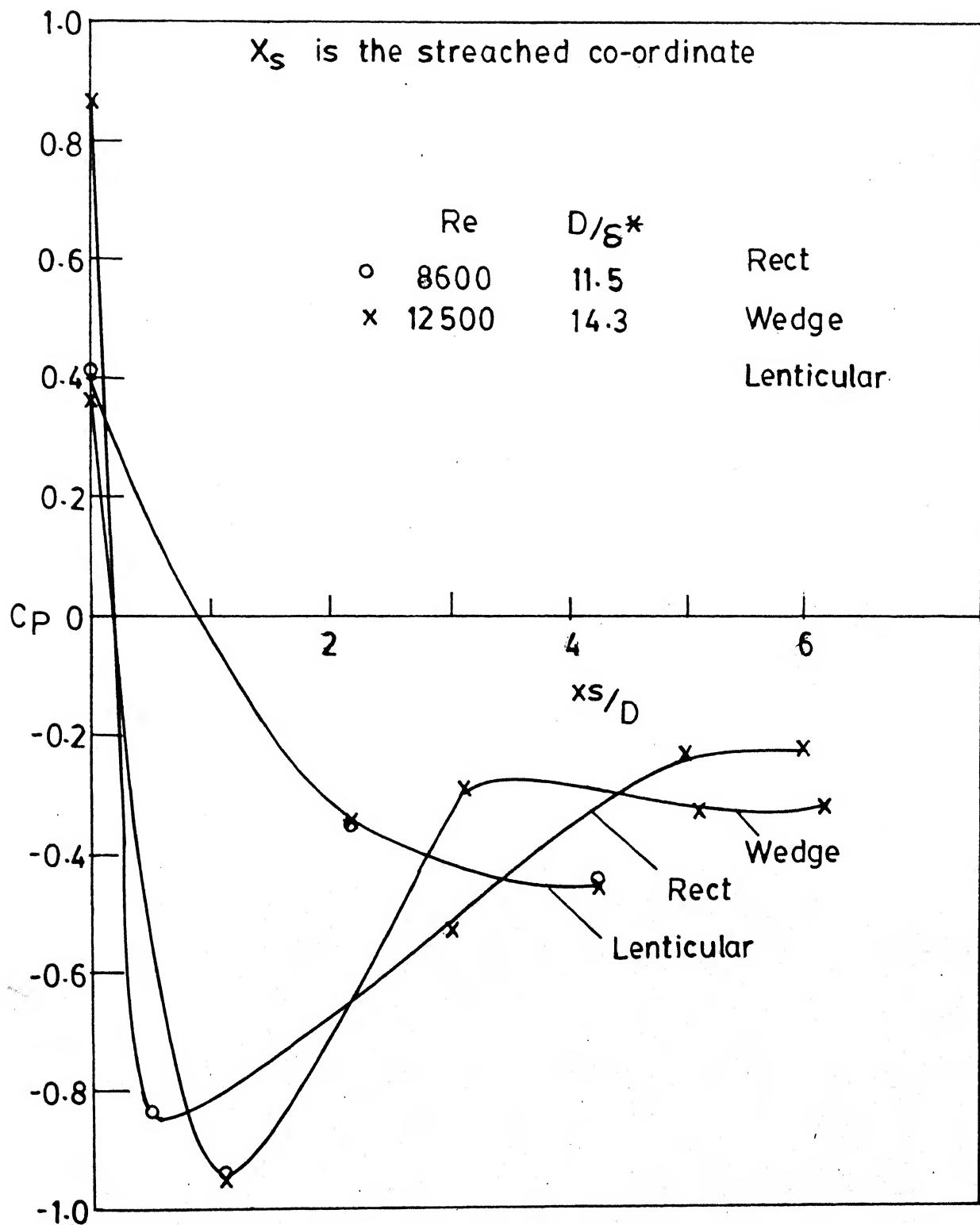


FIG. 6.15 d C_p VARIATION ALONG THE JUNCTIONS OF THE PIER MODELS $L/D = 6$, $BR = 3\%$

$$Re \approx 8300, \quad D/G^* \approx 11$$

$$H = \frac{P - p_\infty}{q_\infty}$$

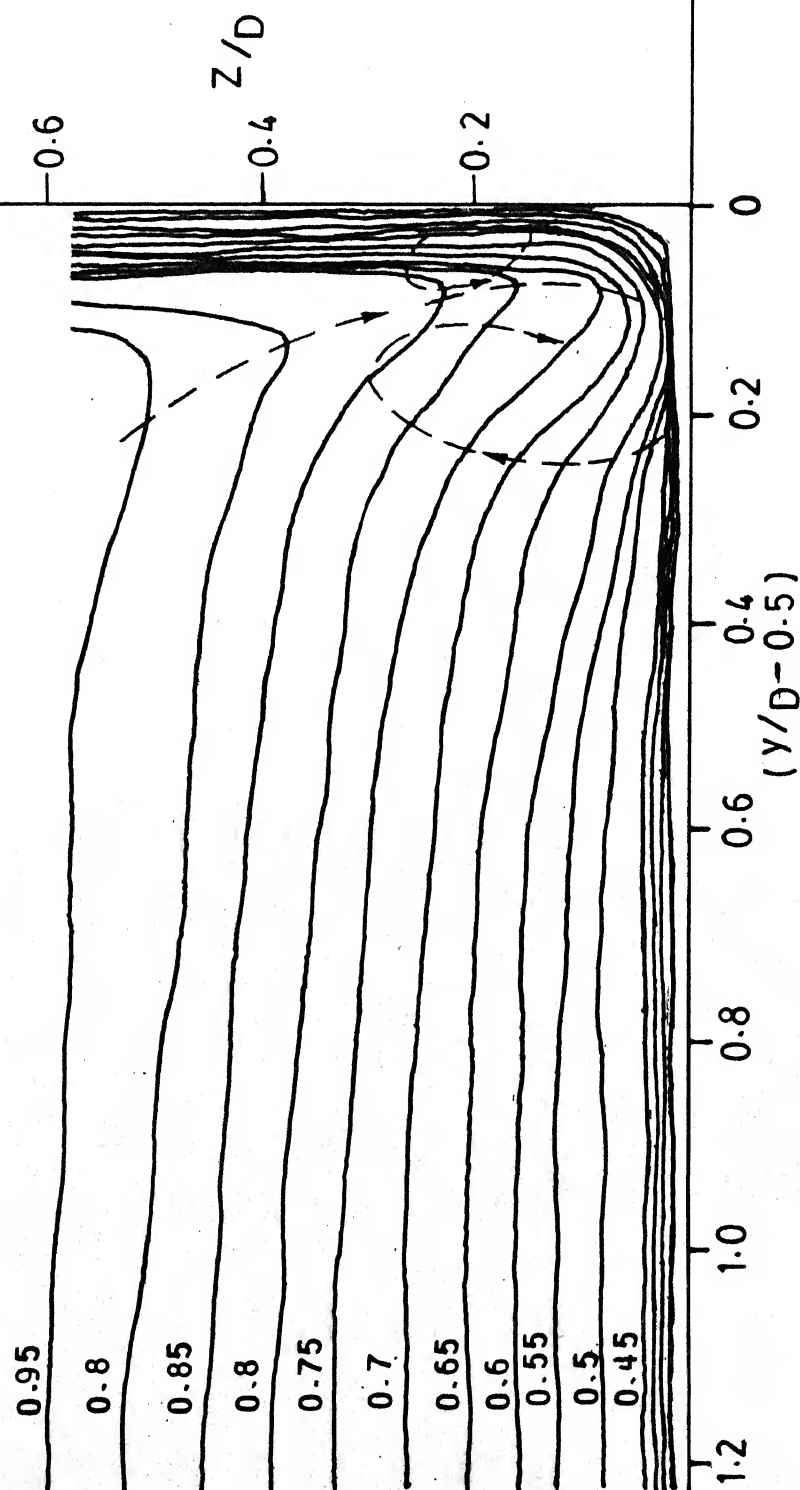
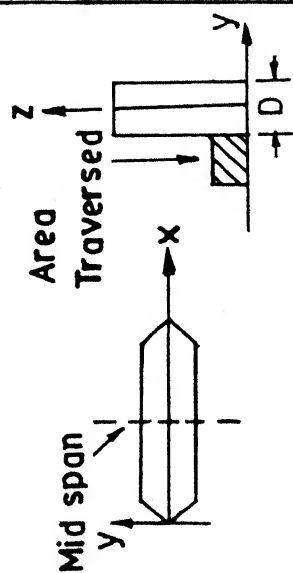


FIG 6.16 b TOTAL HEAD CONTOURS IN Y-Z PLANE AT MID SPAN OF WEDGE NOSE PIER MODEL. $L/D = 6$, $BR = 3\%$

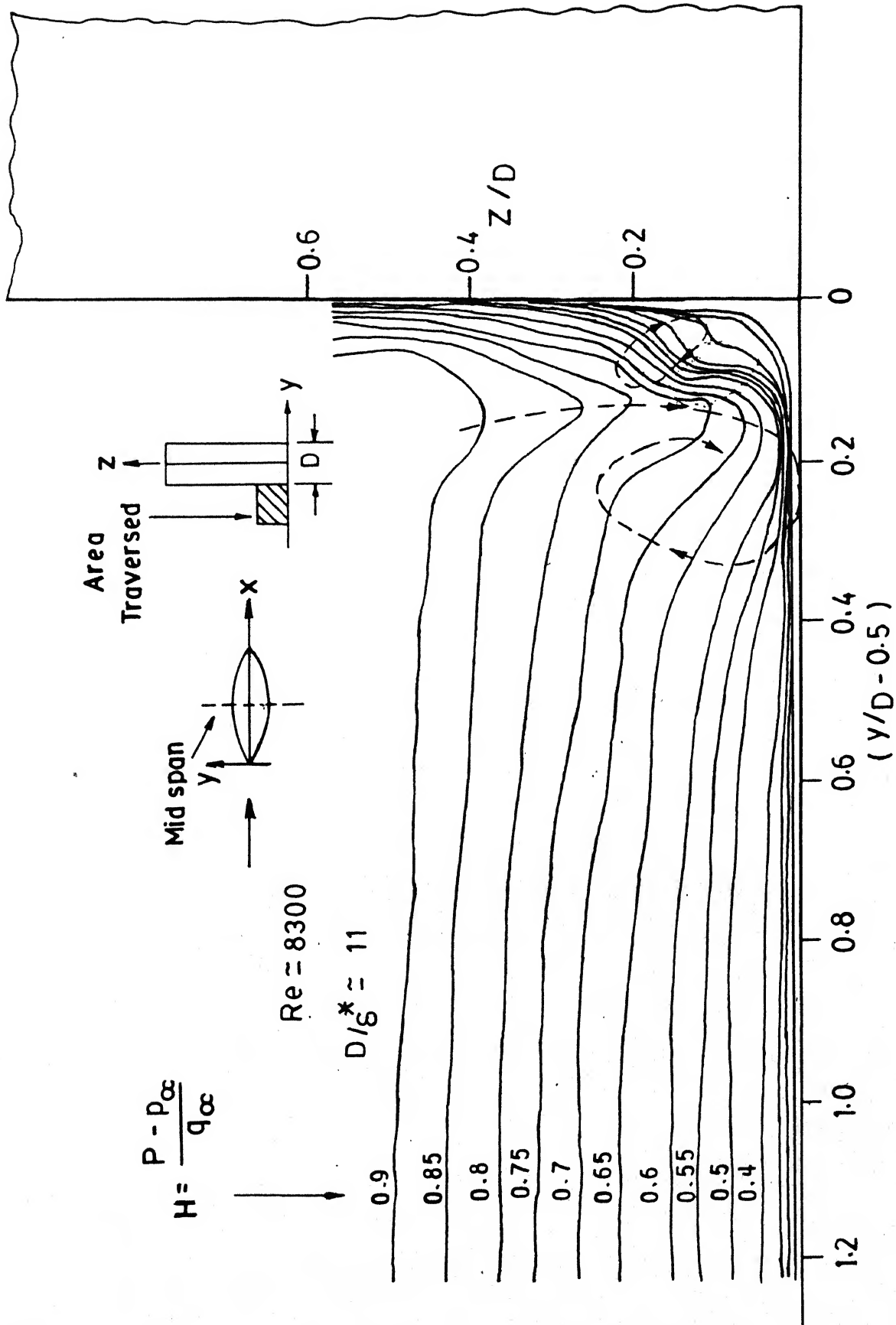


FIG 6.16c TOTAL HEAD CONTOURS IN THE y - z PLANE AT
MID SPAN OF LENTICULAR PIER MODEL. $L/D = 6$, $BR = 3\%$

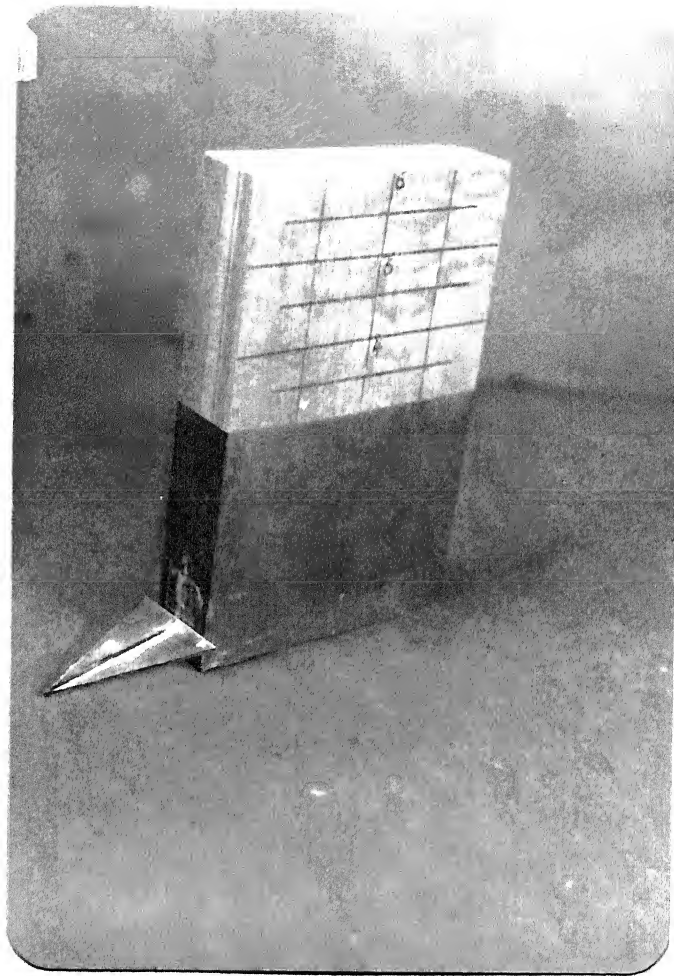


Fig. 6.17a A VIEW OF RECTANGULAR PIER MODEL WITH PASSIVE
DEVICE

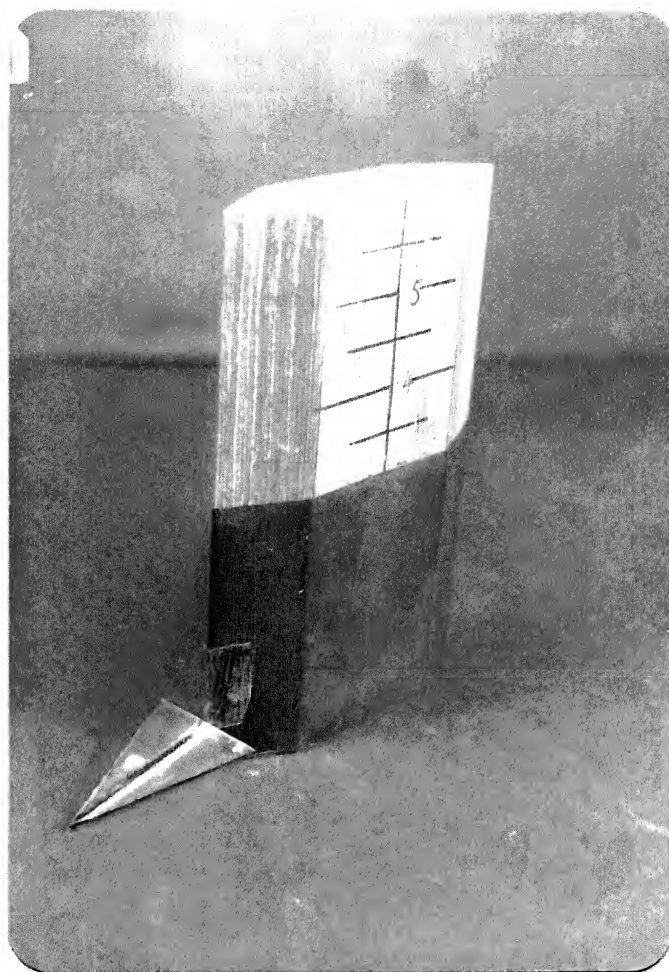


Fig. 6.17b A VIEW OF WEDGE NOSE PIER MODEL WITH PASSIVE
DEVICE

Fig. 6.17c A VIEW OF LENTICULAR PIER MODEL WITH PASSIVE
DEVICE

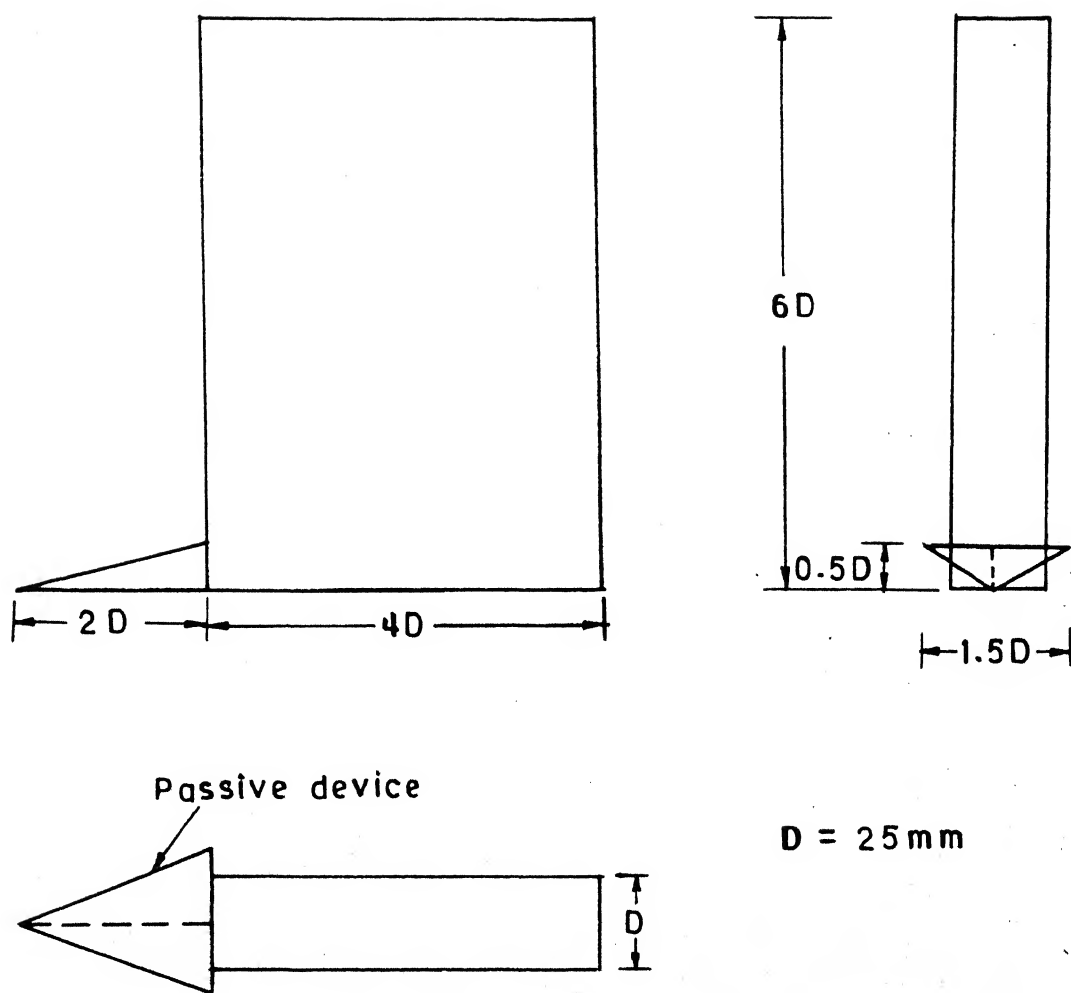


FIG.6-18a RECTANGULAR PIER MODEL WITH PASSIVE DEVICE

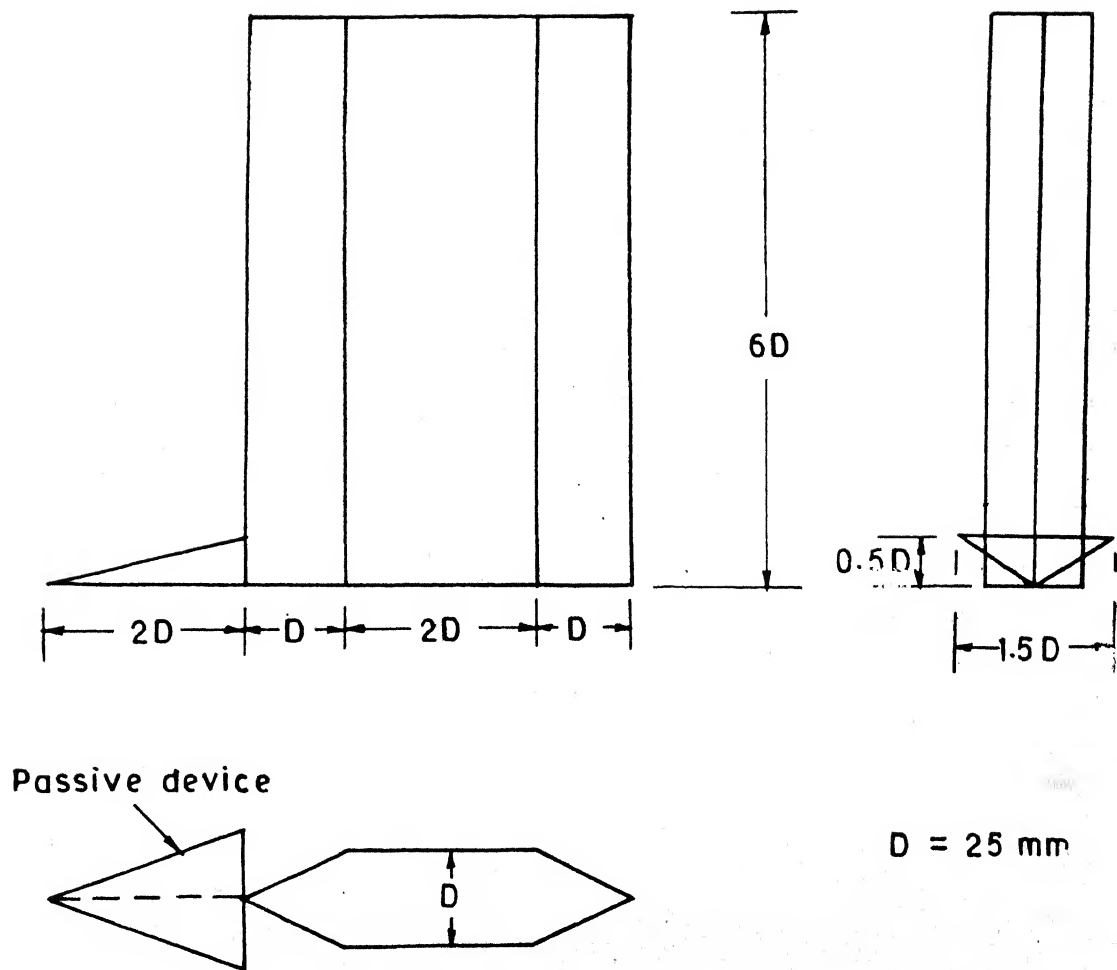


FIG.6-18b WEDGE NOSE PIER MODEL WITH PASSIVE DEVICE

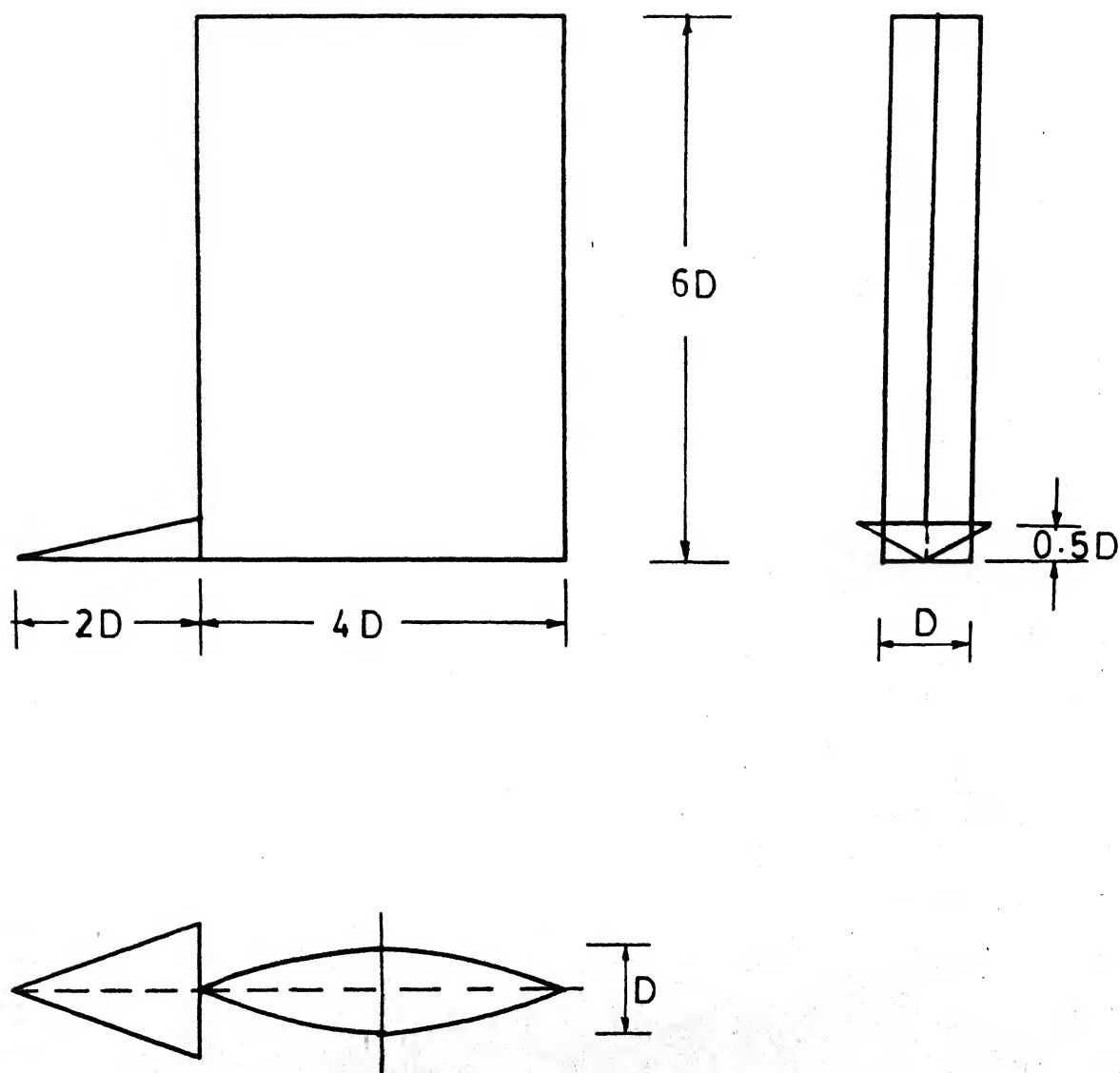
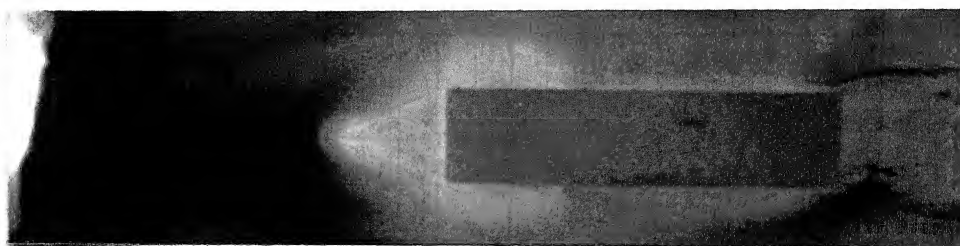
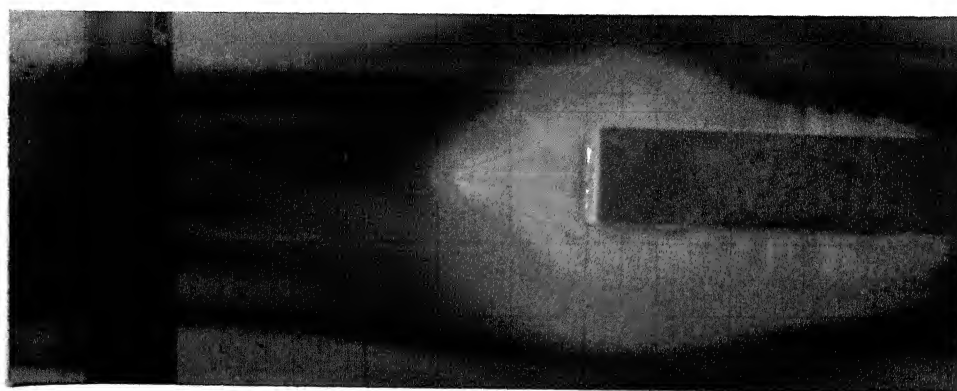


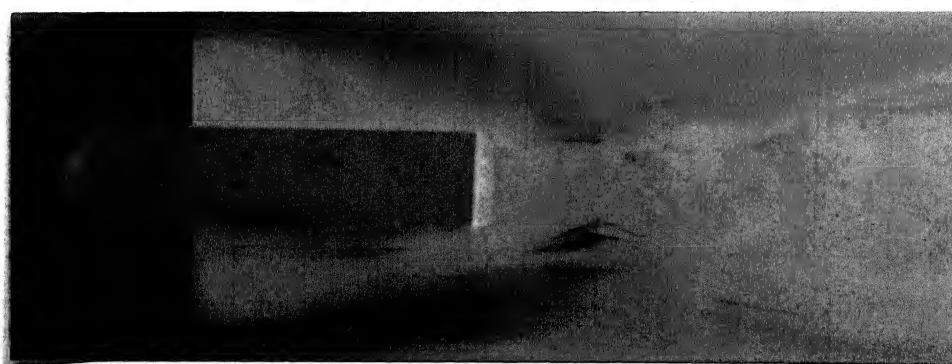
FIG. 6.18c LENTICULAR PIER MODEL WITH PASSIVE DEVICE



a. PLAN VIEW

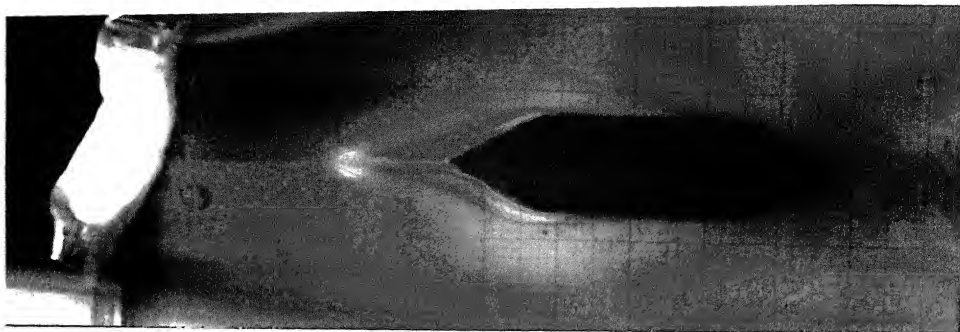


b. TOP FRONT VIEW

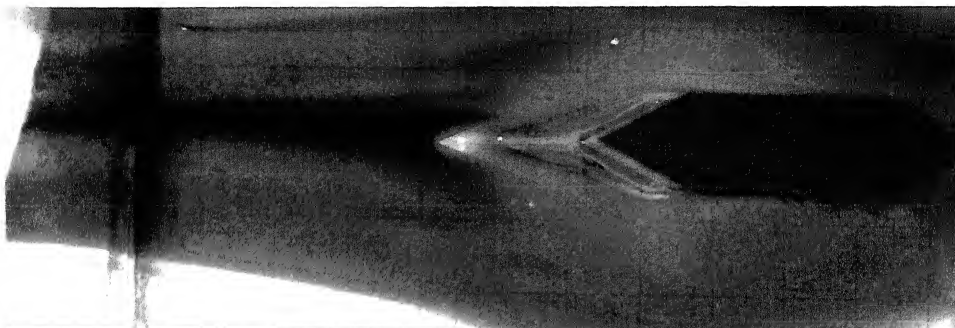


c. TOP REAR VIEW

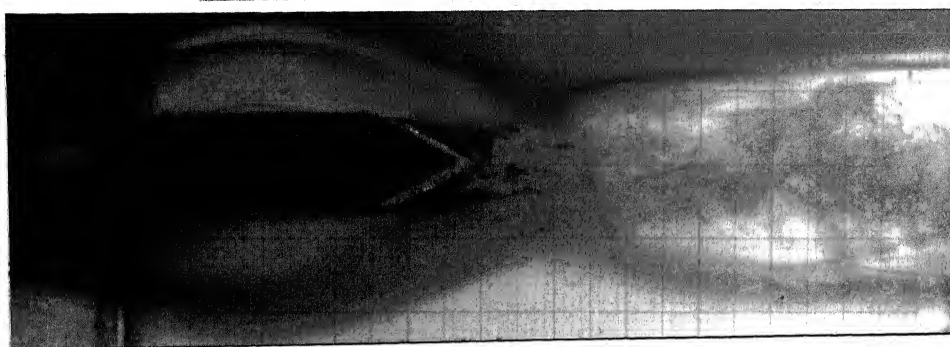
Fig. 6.19 DYE PATTERNS AROUND RECTANGULAR PIER WITH
 PASSIVE DEVICE $L/D=6$, $BR = 10\%$, $Re = 3026$,
 $Fr = 0.135$, (FLOW FROM LEFT TO RIGHT)



a. PLAN VIEW

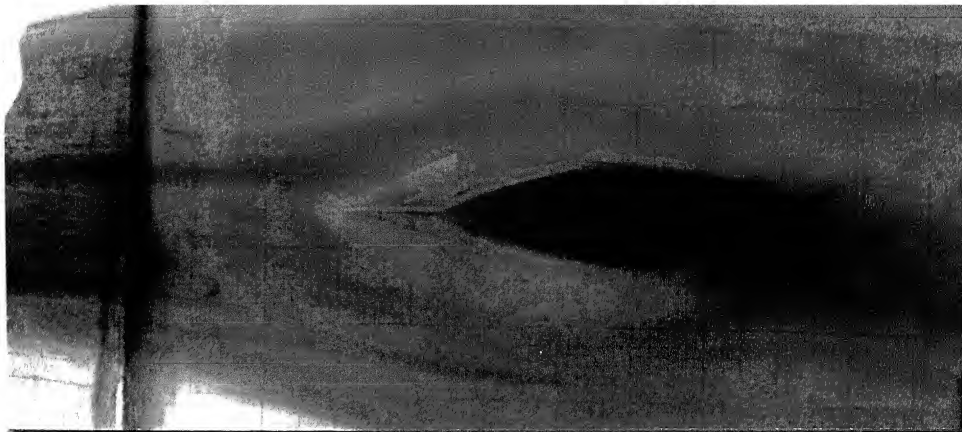


b. TOP FRONT VIEW

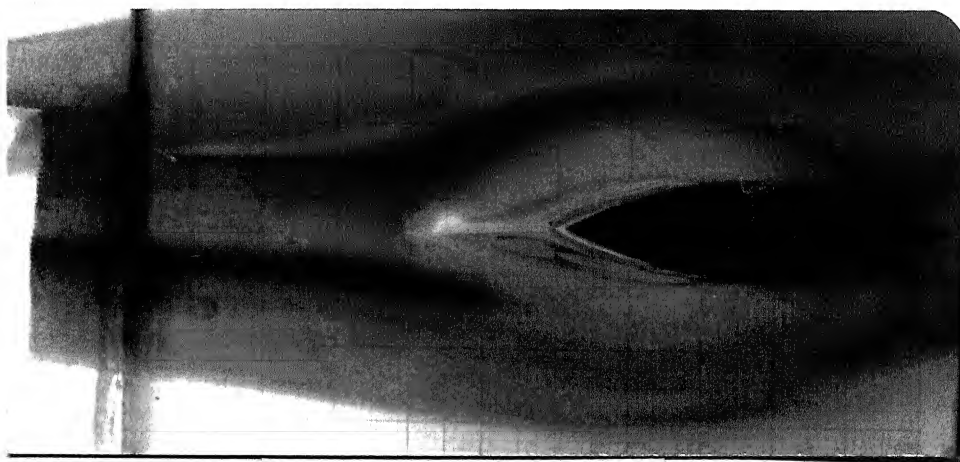


c. TOP REAR VIEW

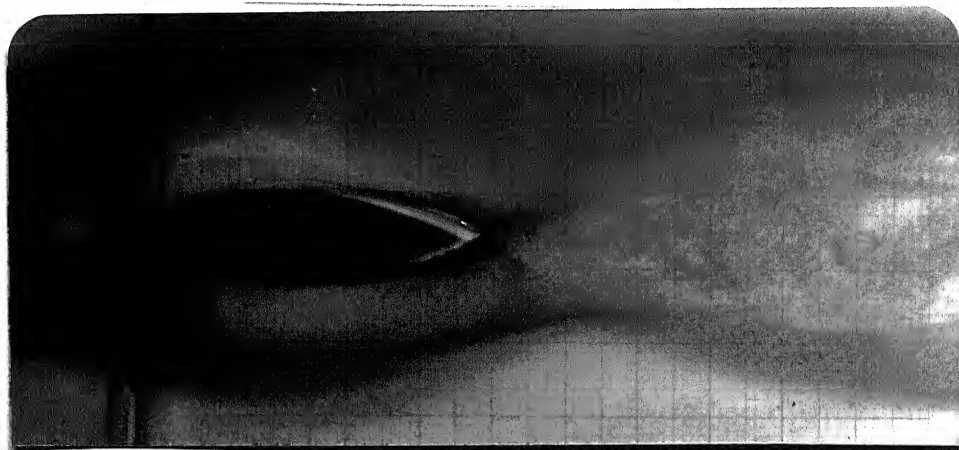
Fig. 6.20 DYE PATTERNS AROUND WEDGE NOSE PIER WITH
PASSIVE DEVICE, $L/D = 6$, $BR = 10\%$, $Re = 3026$,
 $Fr = 0.135$ (FLOW FROM LEFT TO RIGHT)



a. PLAN VIEW



b. TOP FRONT VIEW

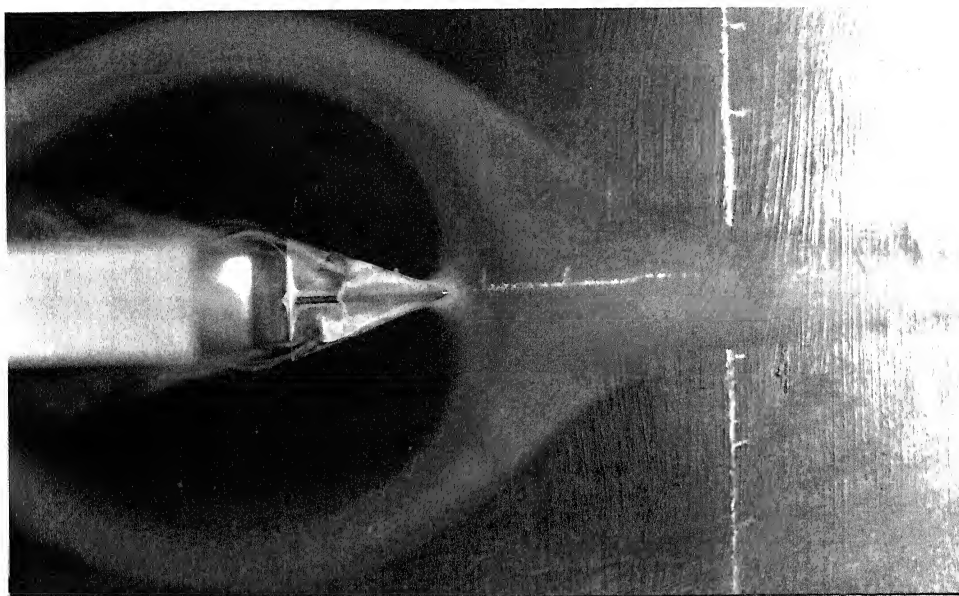


c. TOP REAR VIEW

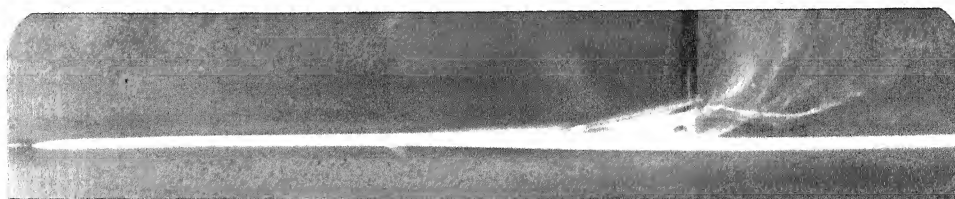
Fig. 6.21 DYE PATTERNS AROUND LENTICULAR PIER WITH PASSIVE DEVICE, $L/D = 6$, $BR = 10\%$, $Re = 3026$, $Fr = 0.135$ (FLOW FROM LEFT TO RIGHT)



a. PERSPECTIVE VIEW

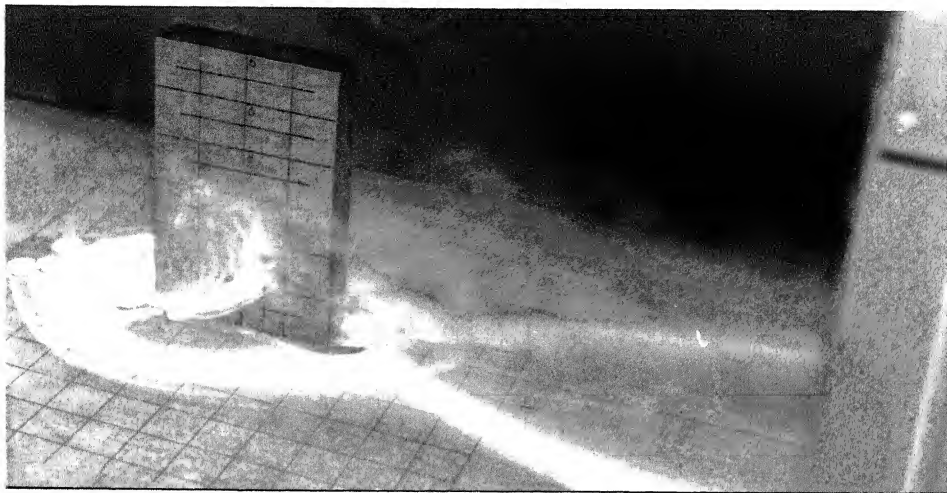


b. TOP FRONT VIEW

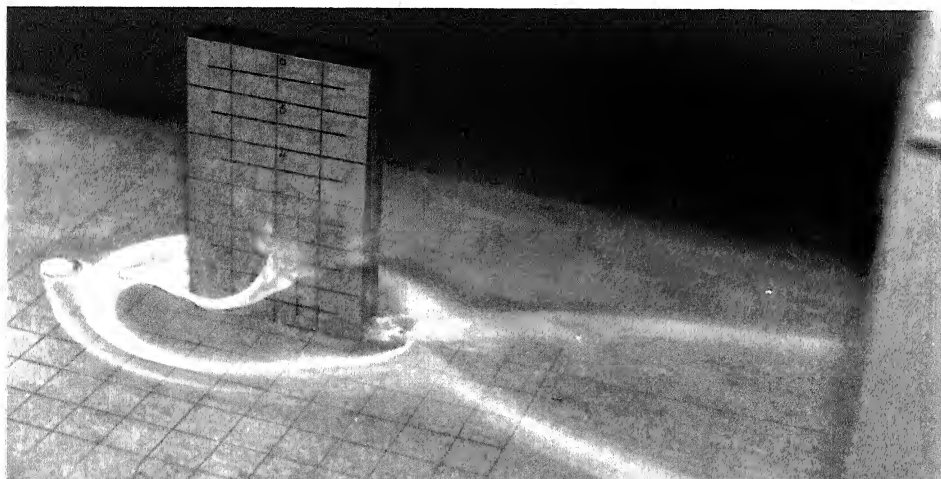


c. CLOSE UP VIEW

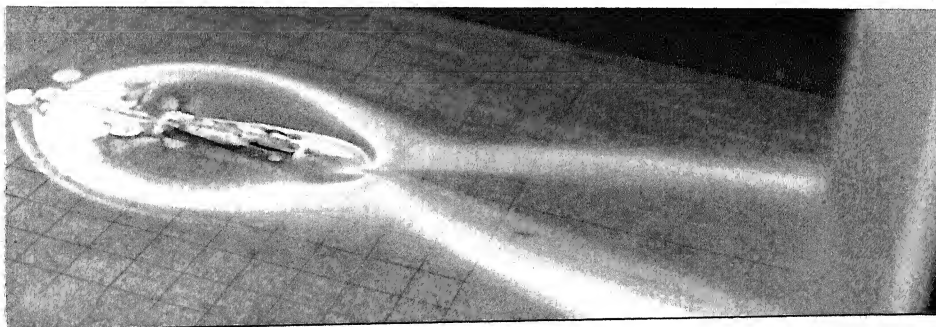
Fig. 6.22 TiCl_4 FLOW AROUND RECTANGULAR PIER WITH
PASSIVE DEVICE, $L/D = 6$, $BR = 3\%$, $Re = 1450$,
 $D/\delta^* = 4.5$



d. GROSS VIEW



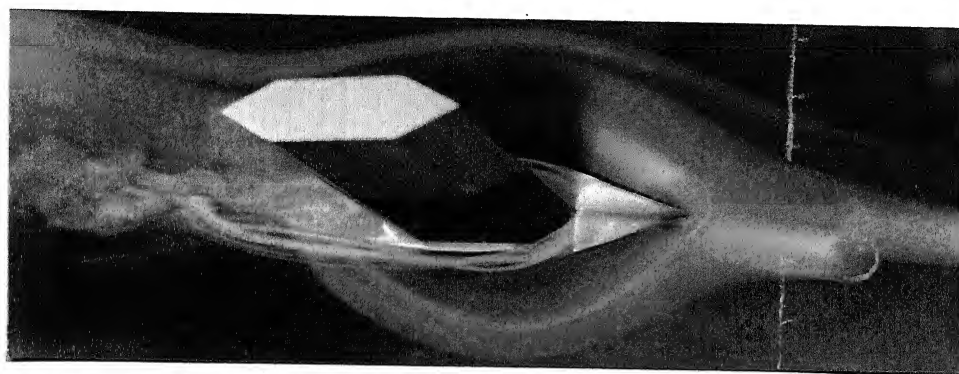
e. LESV



f. SURFACE FLOW PATTERNS

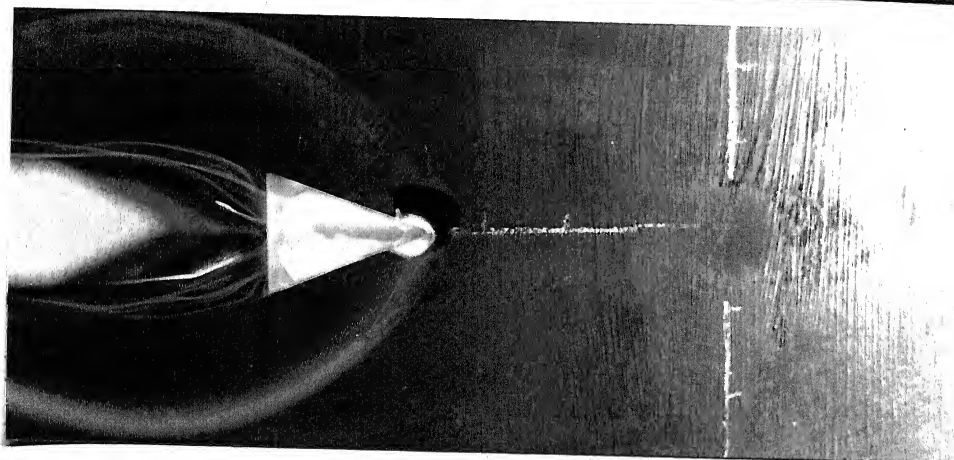
a. REAR

PERSPECTIVE VIEW

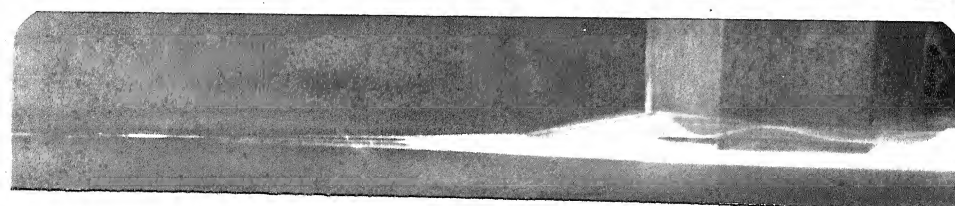


b. FRONT

PERSPECTIVE VIEW



c. TOP FRONT VIEW



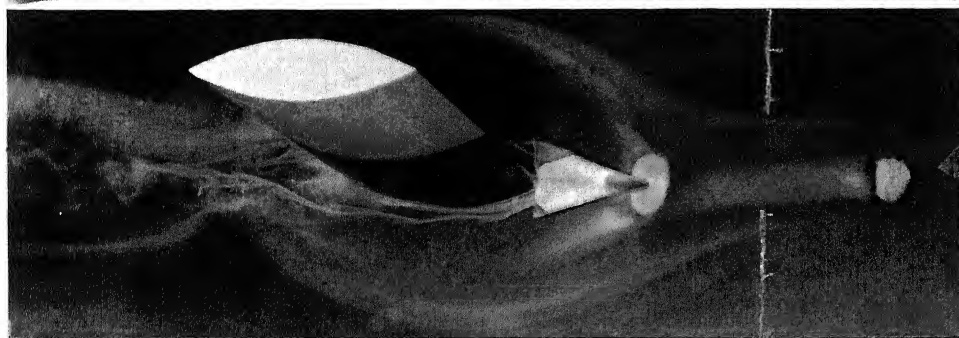
d. CLOSE UP VIEW

Fig. 6.23 $TiCl_4$ FLOW AROUND WEDGE NOSE PIER WITH
PASSIVE DEVICE $L/D = 6$, $BR = 3\%$, $Re = 1450$,
 $D/\delta^* = 4.5$



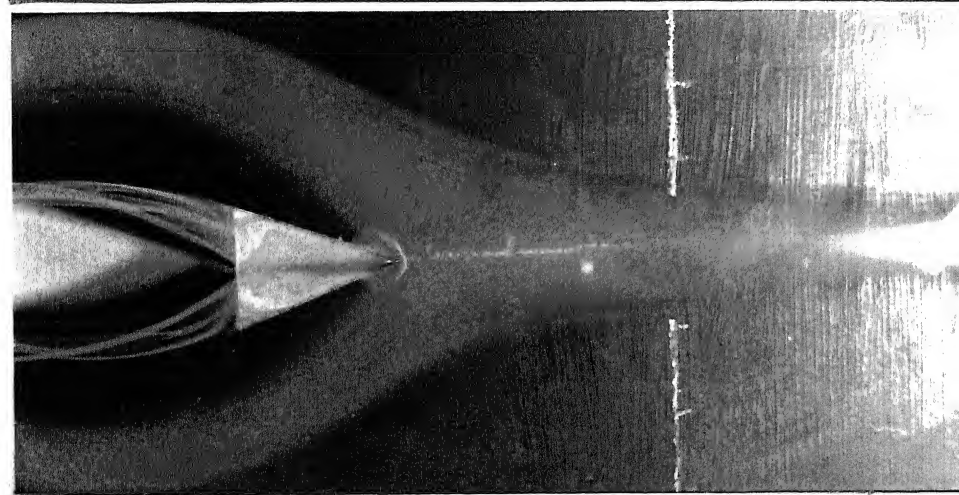
a. REAR

PERSPECTIVE VIEW



b. FRONT

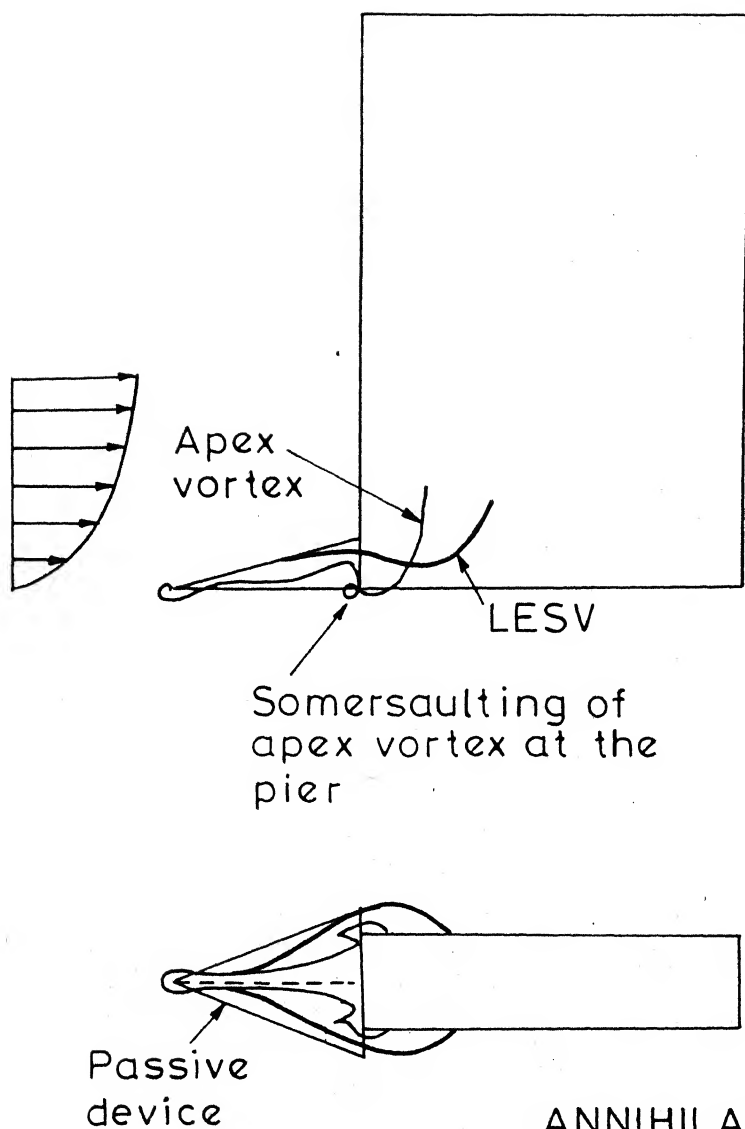
PERSPECTIVE VIEW



c. TOP FRONT VIEW

d. CLOSE UP VIEW

Fig. 6.24 TiCl_4 FLOW AROUND LENTICULAR PIER WITH DEVICE
 $L/D = 6$, $BR = 3\%$, $Re = 1450$, $D/\delta^* = 4.5$



ANNIHILATION OF APEX VORTEX
AND LESV INTO SEPARATION
BUBBLE AT PIER WALL

FIG. 6.25a SCHEMATICS OF MODIFIED VORTEX FLOW
AROUND RECTANGULAR PIER MODEL

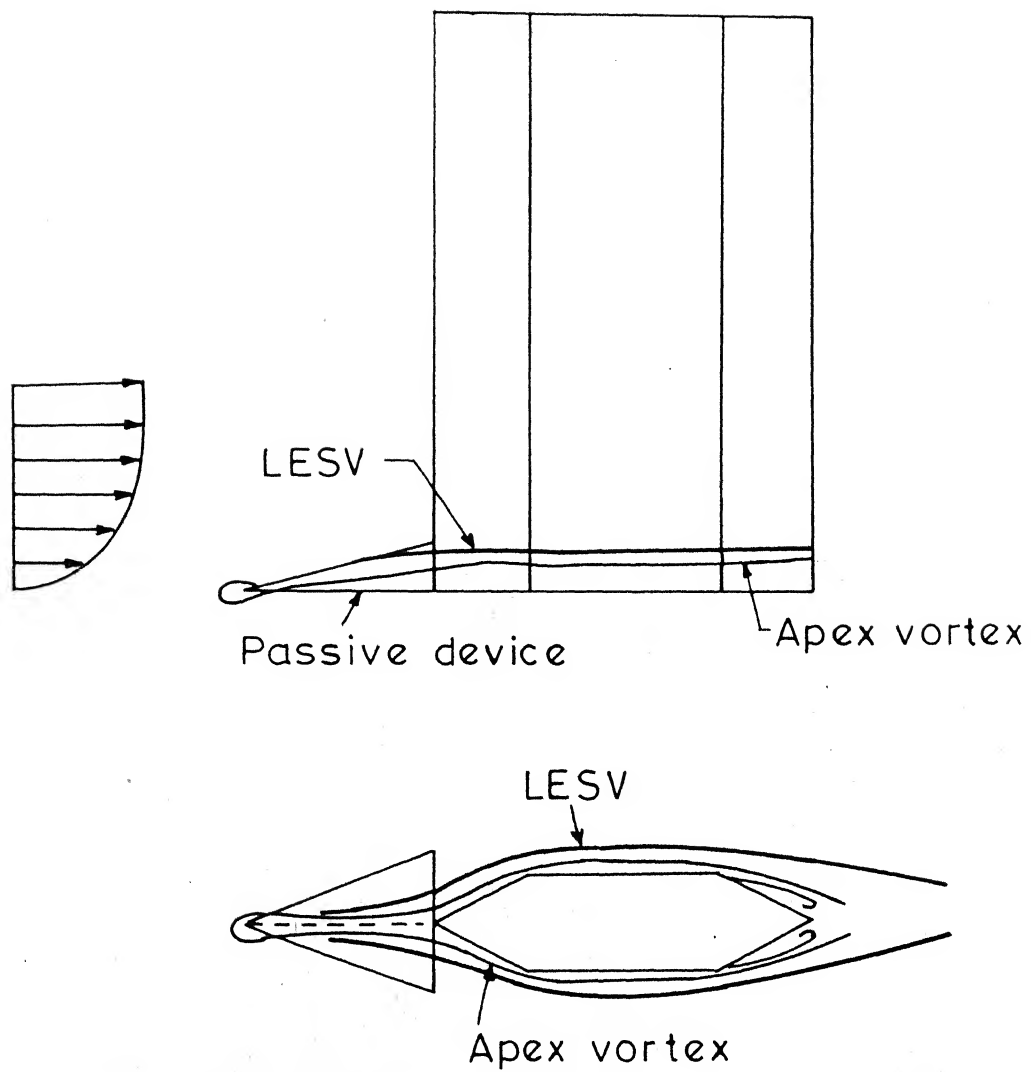


FIG. 6.25 b SCHEMATICS OF MODIFIED VORTEX FLOW
AROUND WEDGE NOSE PIER MODEL

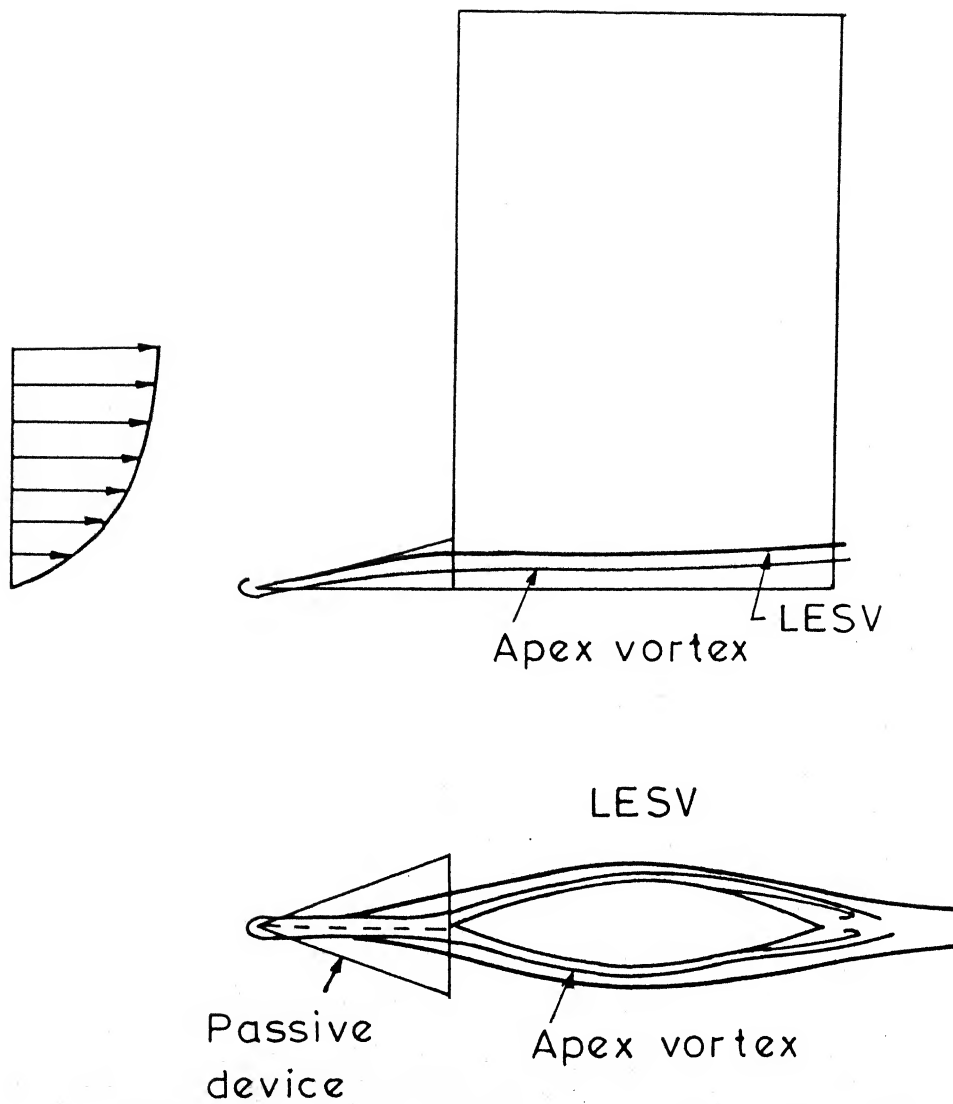


FIG. 6-25c SCHEMATICS OF MODIFIED VORTEX FLOW
AROUND WEDGE NOSE PIER MODEL

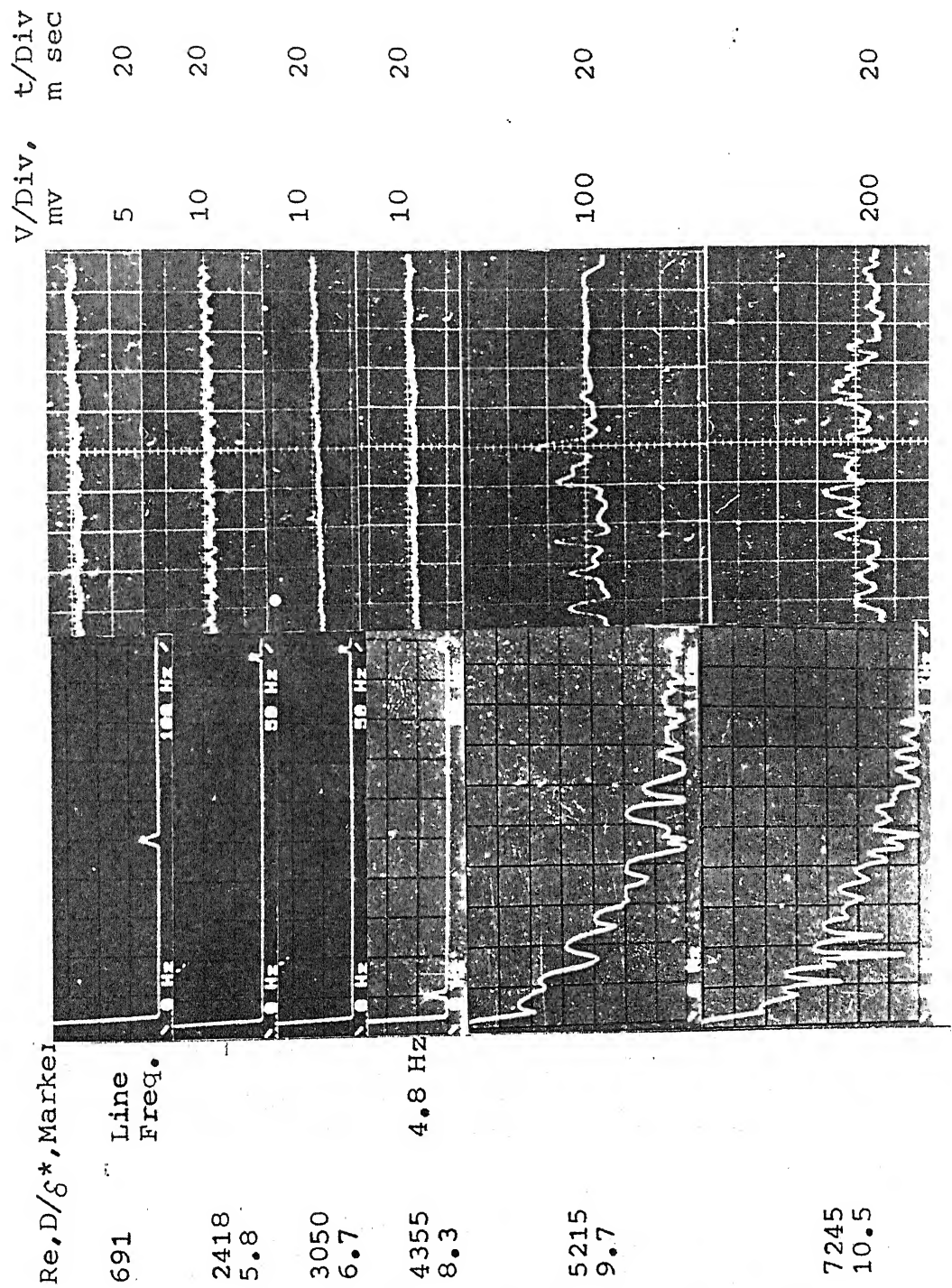


Fig. 6.26a SPECTRA AND TRACES OF MODIFIED VORTEX FLOW
AROUND RECTANGULAR PIER MODEL $L/D = 6$, $BR = 3\%$

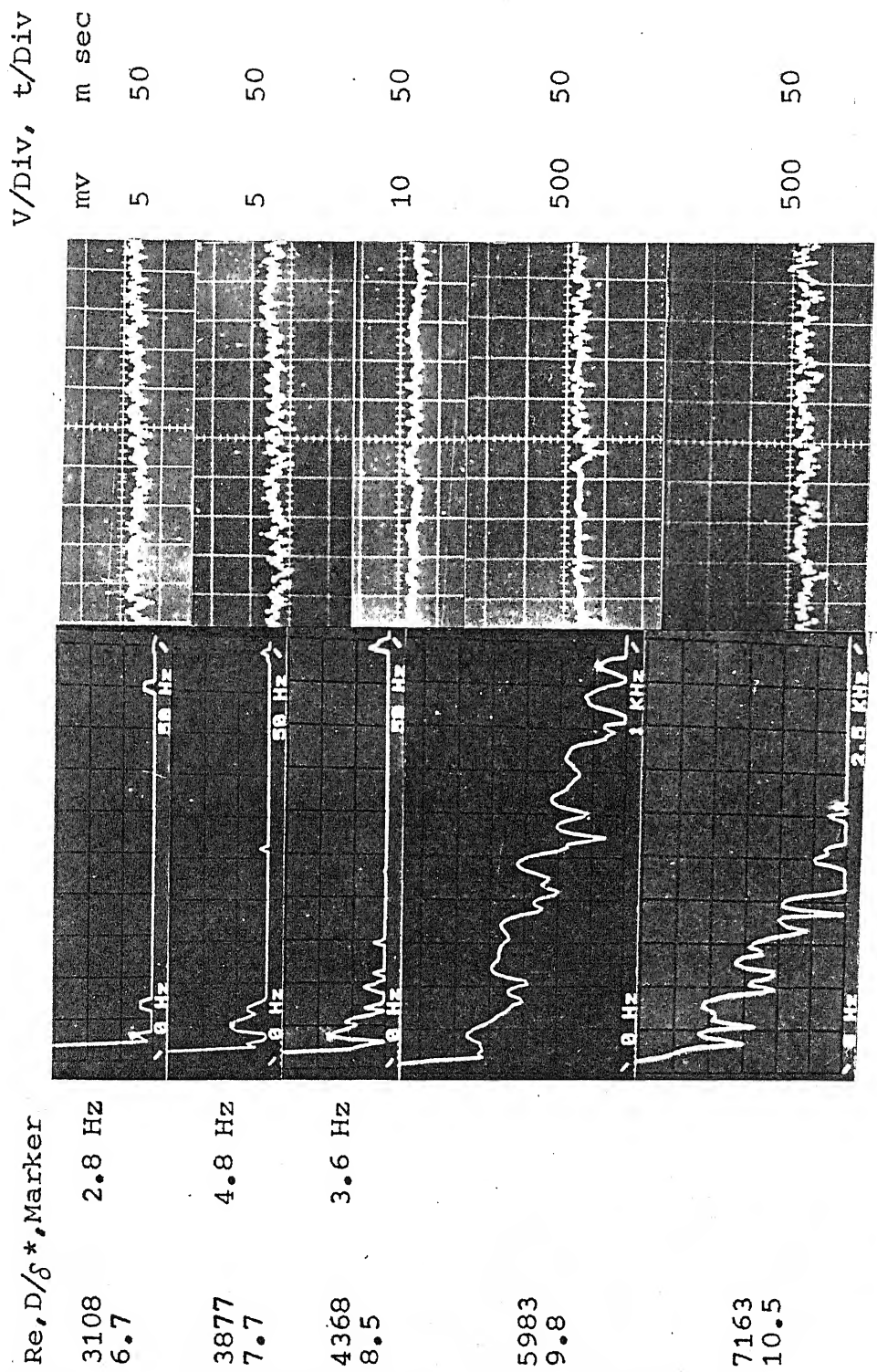


Fig. 6.26b SPECTRA AND TRACES OF MODIFIED VORTEX FLOW
AROUND WEDGE NOSE PIER MODEL $L/D = 6$, $BR = 3\%$

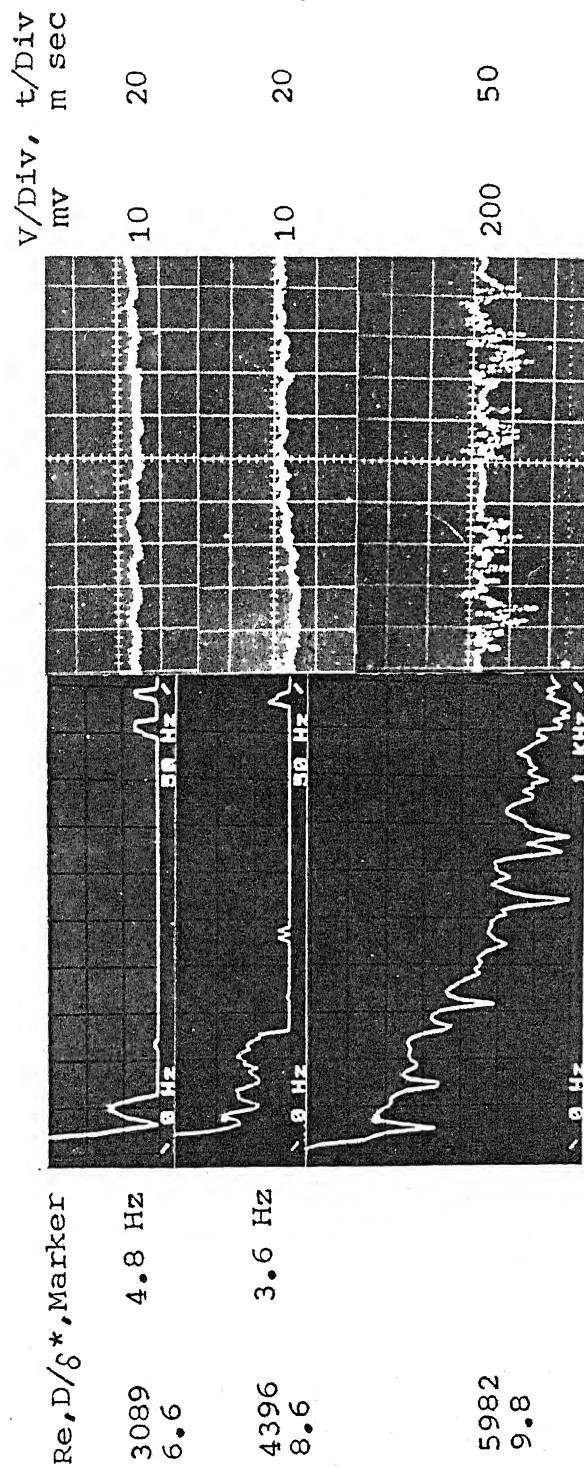
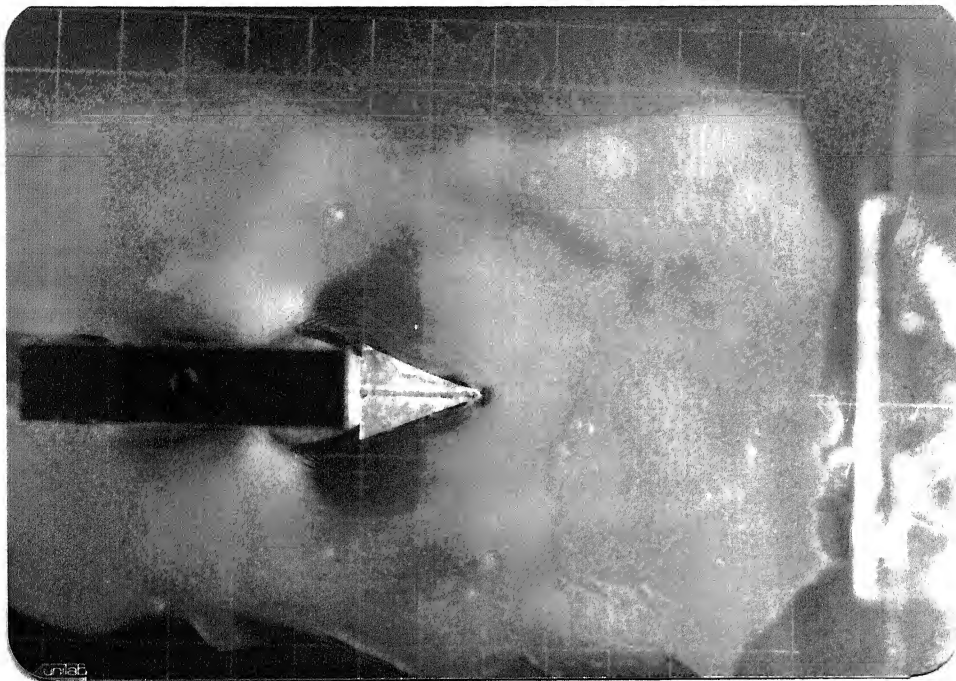
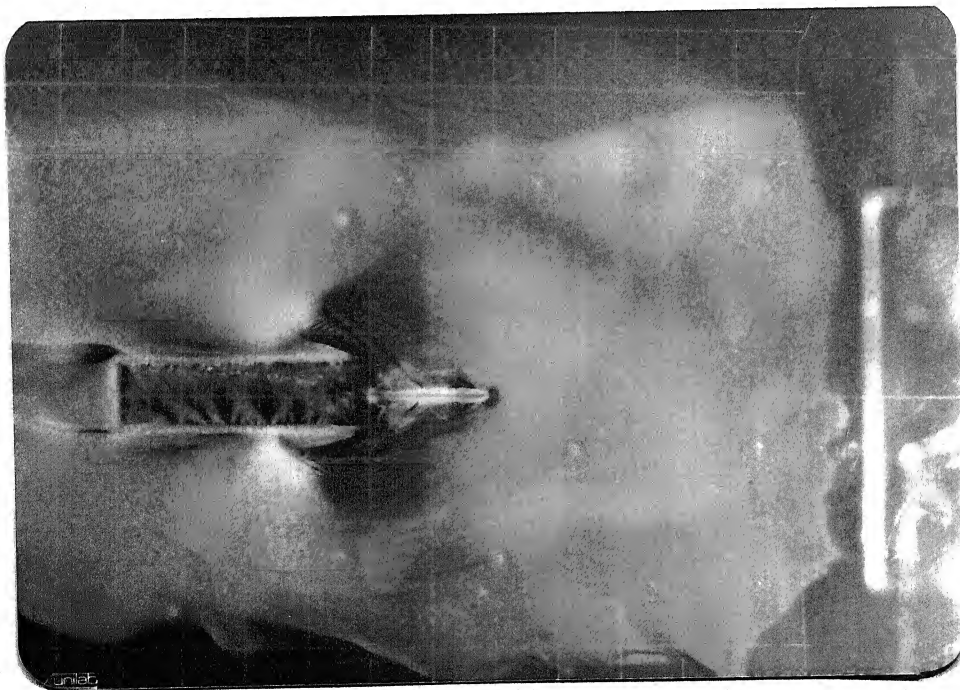


Fig. 6.26c SPECTRA AND TRACES OF MODIFIED VORTEX FLOW
AROUND LENTICULAR PIER MODEL, $L/D = 6$, $BR = 3\%$

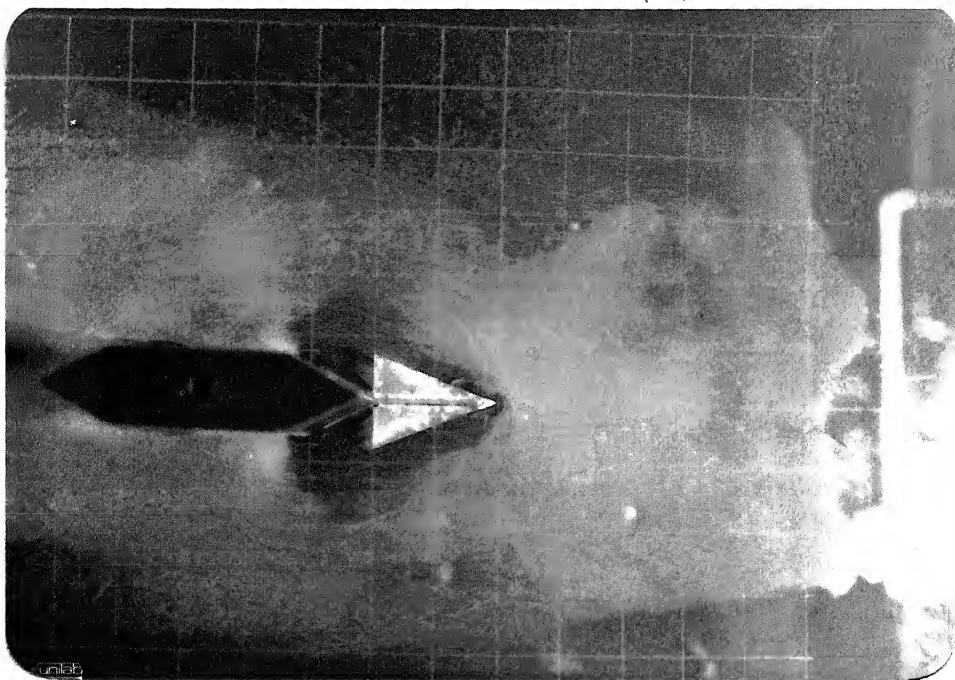


a. $t = 15$ Min. (FLOW ON)

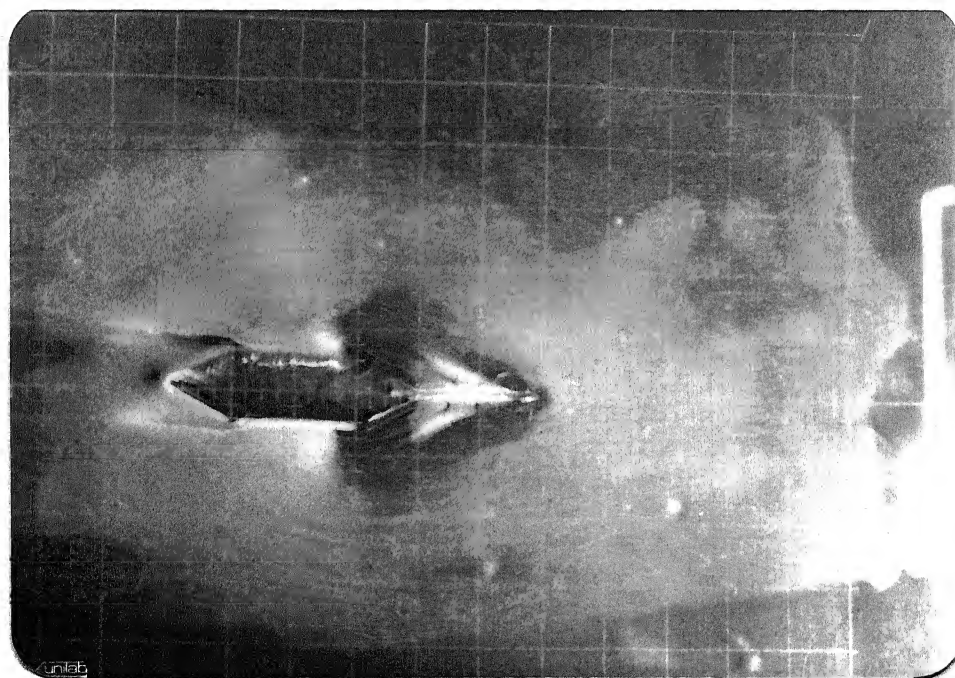


b. $t = 15$ Min.

Fig. 6.27a MODIFIED SURFACE OIL FILM PATTERNS AROUND
RECTANGULAR PIER WITH PASSIVE DEVICE, $L/D = 6$,
 $BR = 3\%$, $Re = 7800$, $D/\ast = 11$

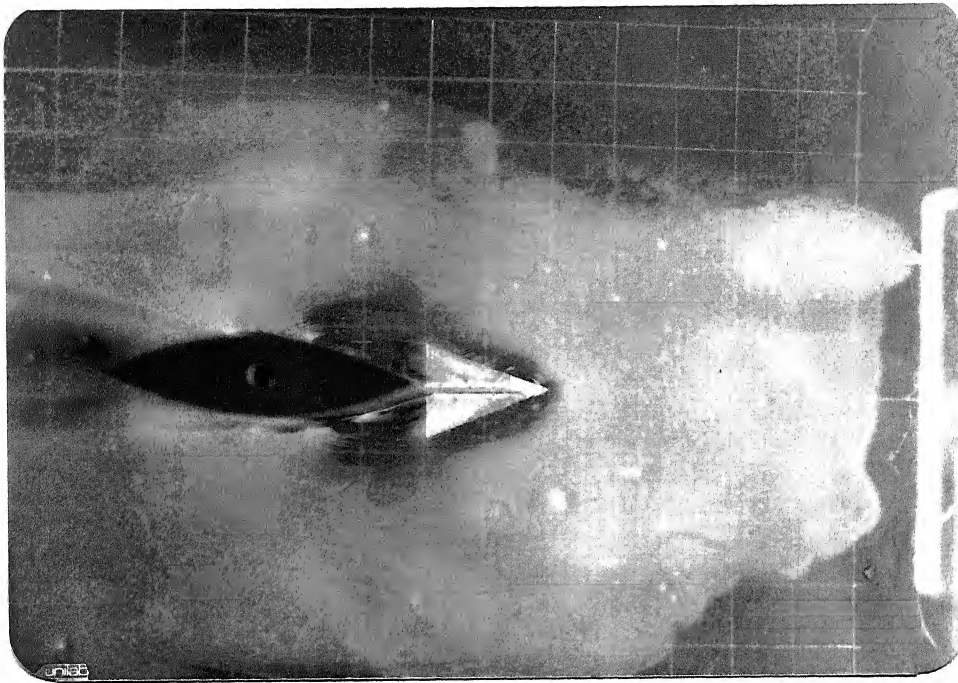


a. $t = 15 \text{ Min. (FLOW ON)}$



b. $t = 15 \text{ Min.}$

Fig. 6.27b MODIFIED SURFACE OIL FILM PATTERNS AROUND
WEDGE NOSE PIER MODEL WITH PASSIVE DEVICE
 $L/D = 6$, $BR = 3\%$, $Re = 7800$, $D/\delta^* = 11$



$t = 15 \text{ Min. (FLOW ON)}$

Fig. 6.27c MODIFIED SURFACE OIL FILM PATTERNS AROUND
LENTICULAR PIER MODEL WITH PASSIVE DEVICE,
 $L/D = 6$, $BR = 3\%$, $Re = 7800$, $D/\delta^* = 11$

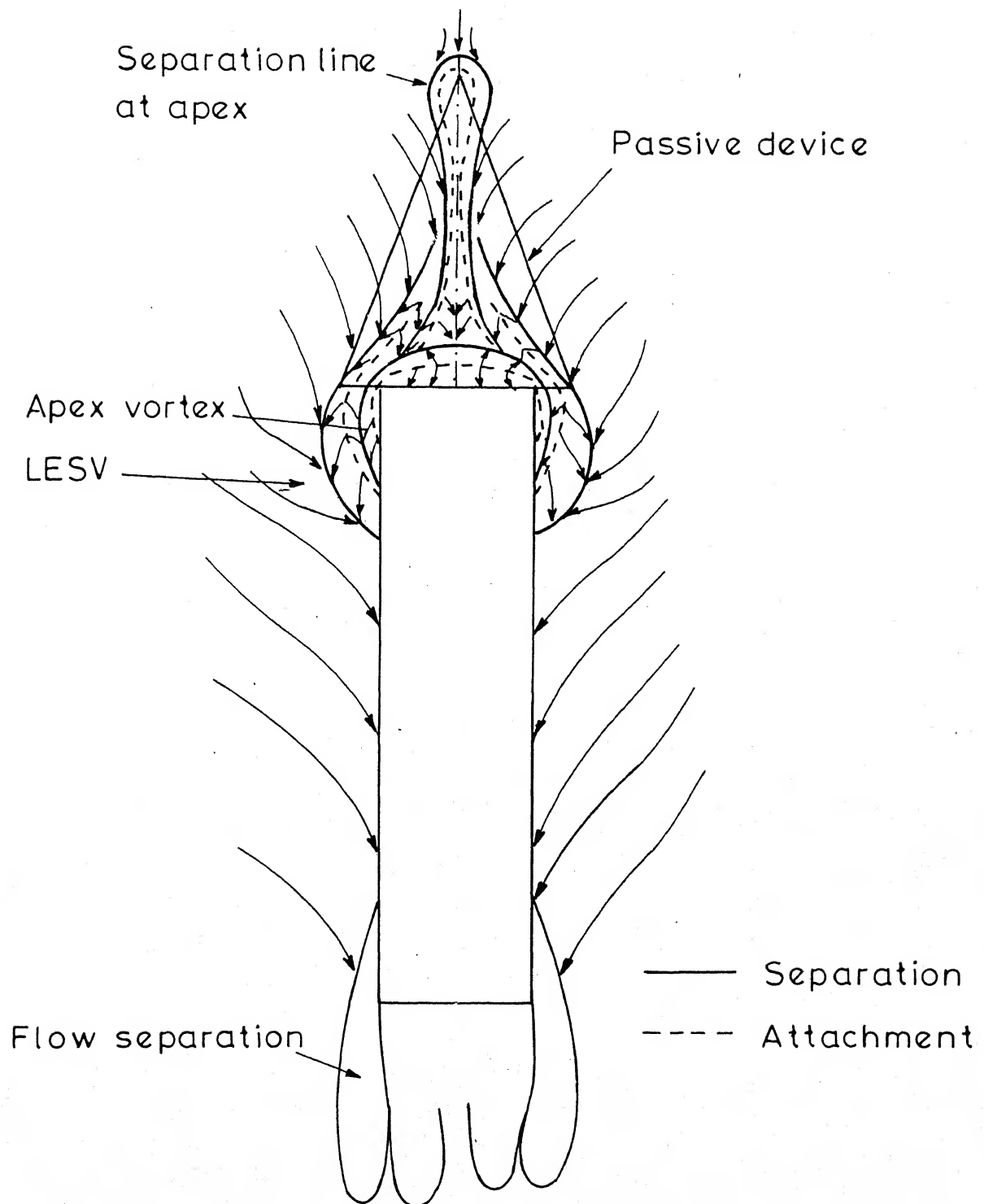


FIG.6.28a MODIFIED SURFACE STREAMLINES AROUND RECTANGULAR PIER MODEL

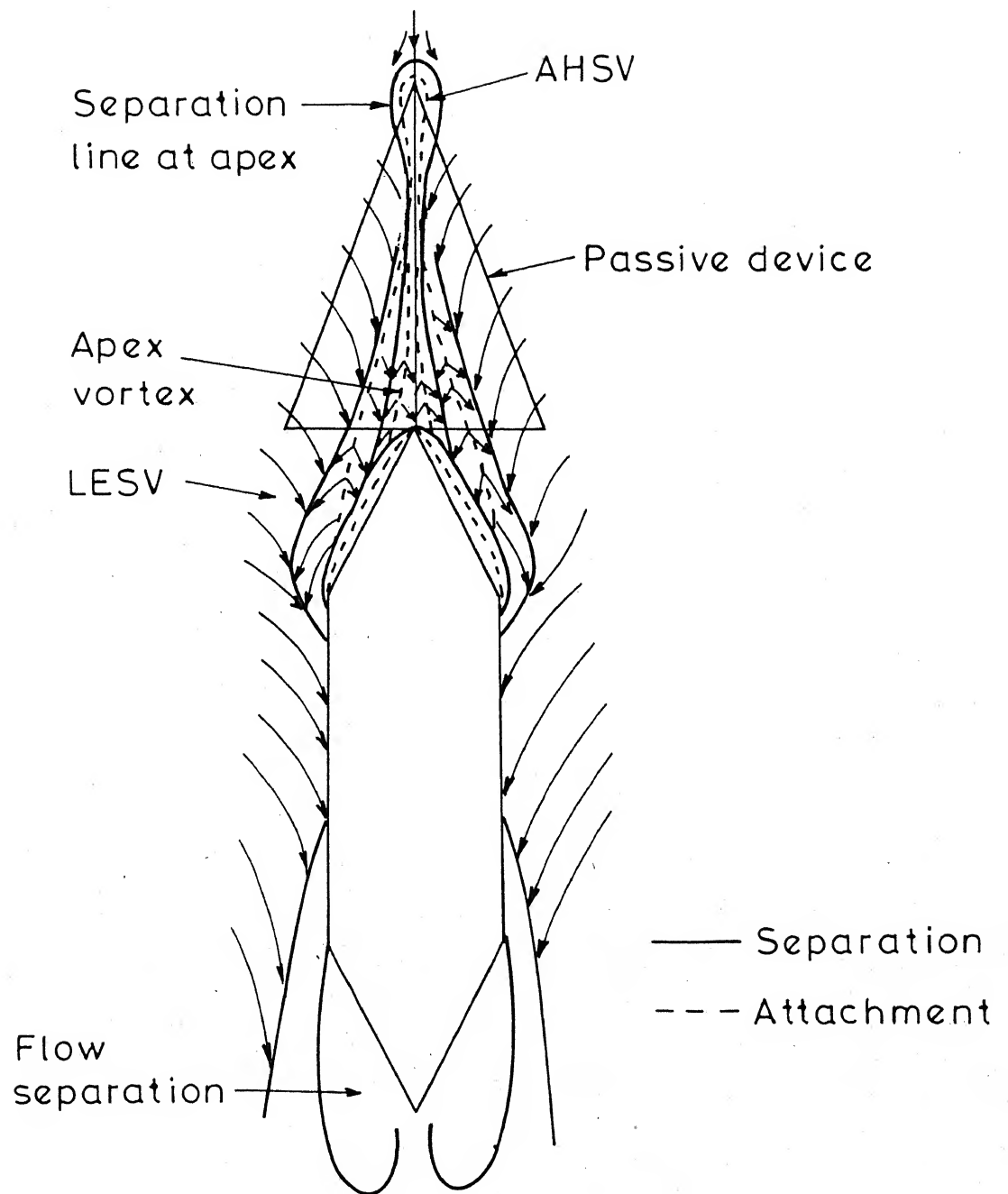


FIG. 6.28b MODIFIED SURFACE STREAMLINES AROUND WEDGE NOSE PIER MODEL

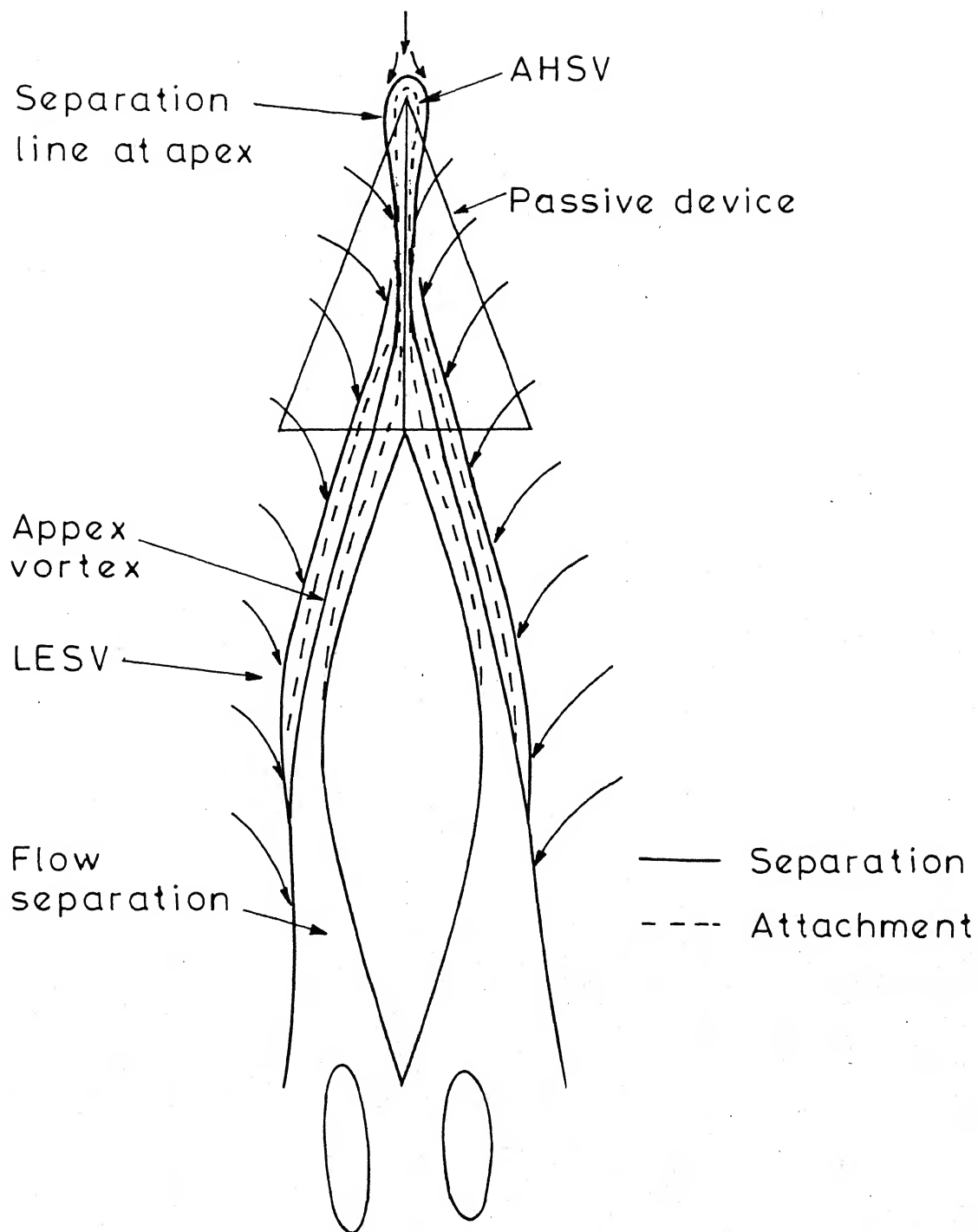
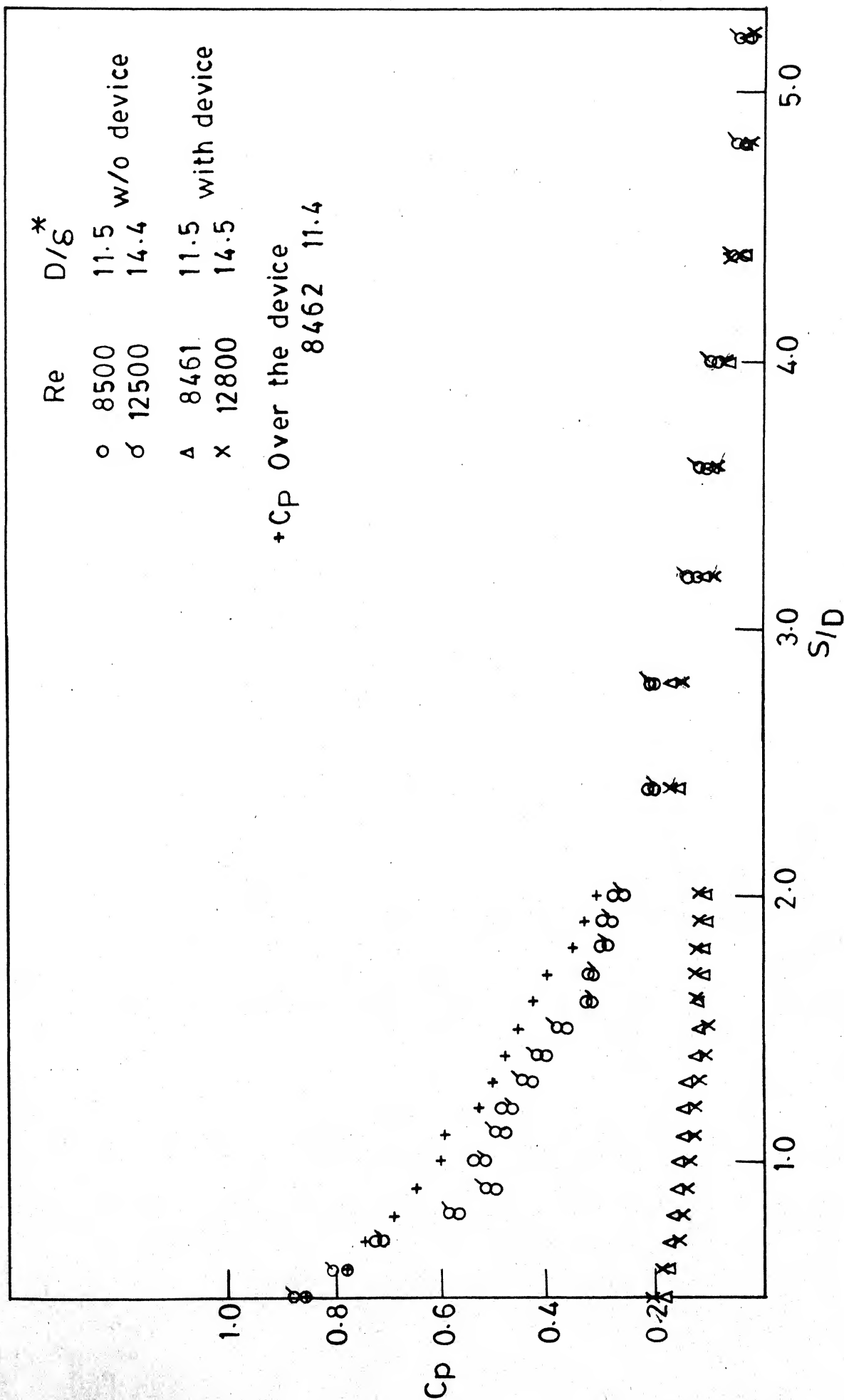


FIG.628c MODIFIED SURFACE STREAMLINES
AROUND LENTICULAR PIER MODEL



(a) Rectangular pier model

FIG. 6.29 FLOOR PRESSURE ON UPSTREAM PLANE OF SYMMETRY WITH AND WITHOUT DEVICE

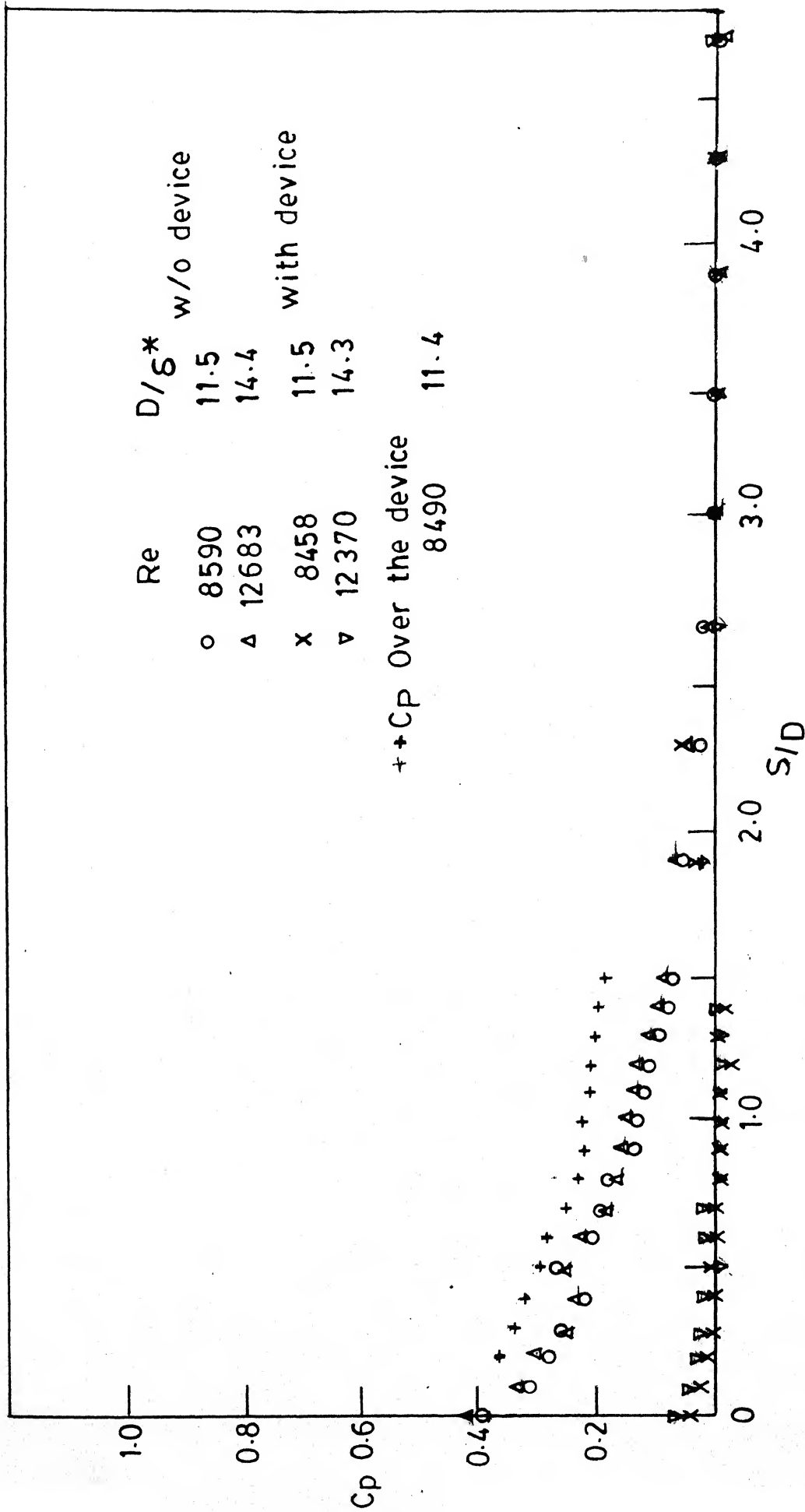
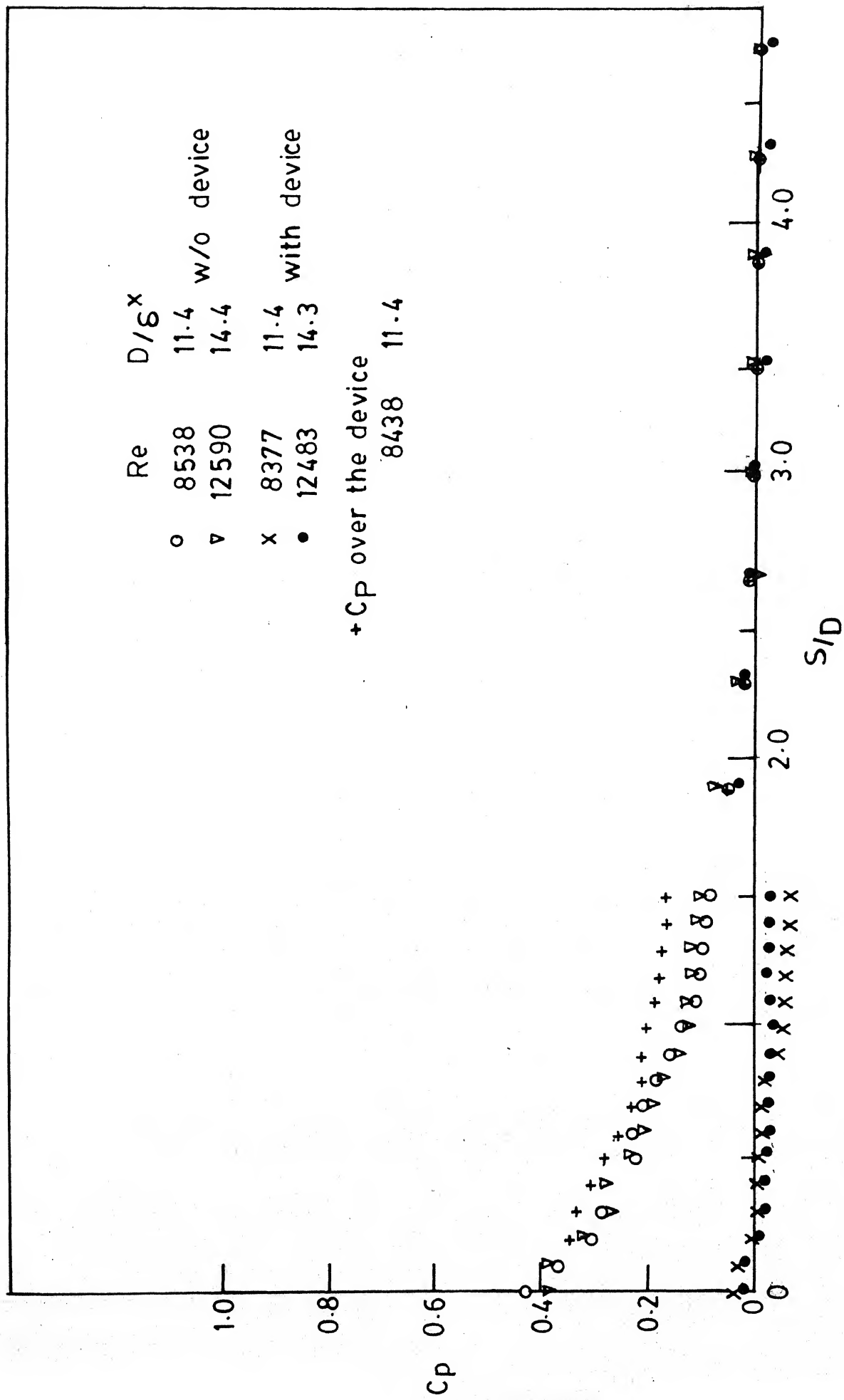


FIG. 6.29 b PRESSURE DISTRIBUTION ON THE UPSTREAM PLANE OF SYMMETRY OF WEDGE NOSE PIER MODEL $L/D = 6$, $BR = 3\%$



(c) Lenticular pier model

FIG. 6.29 Continued

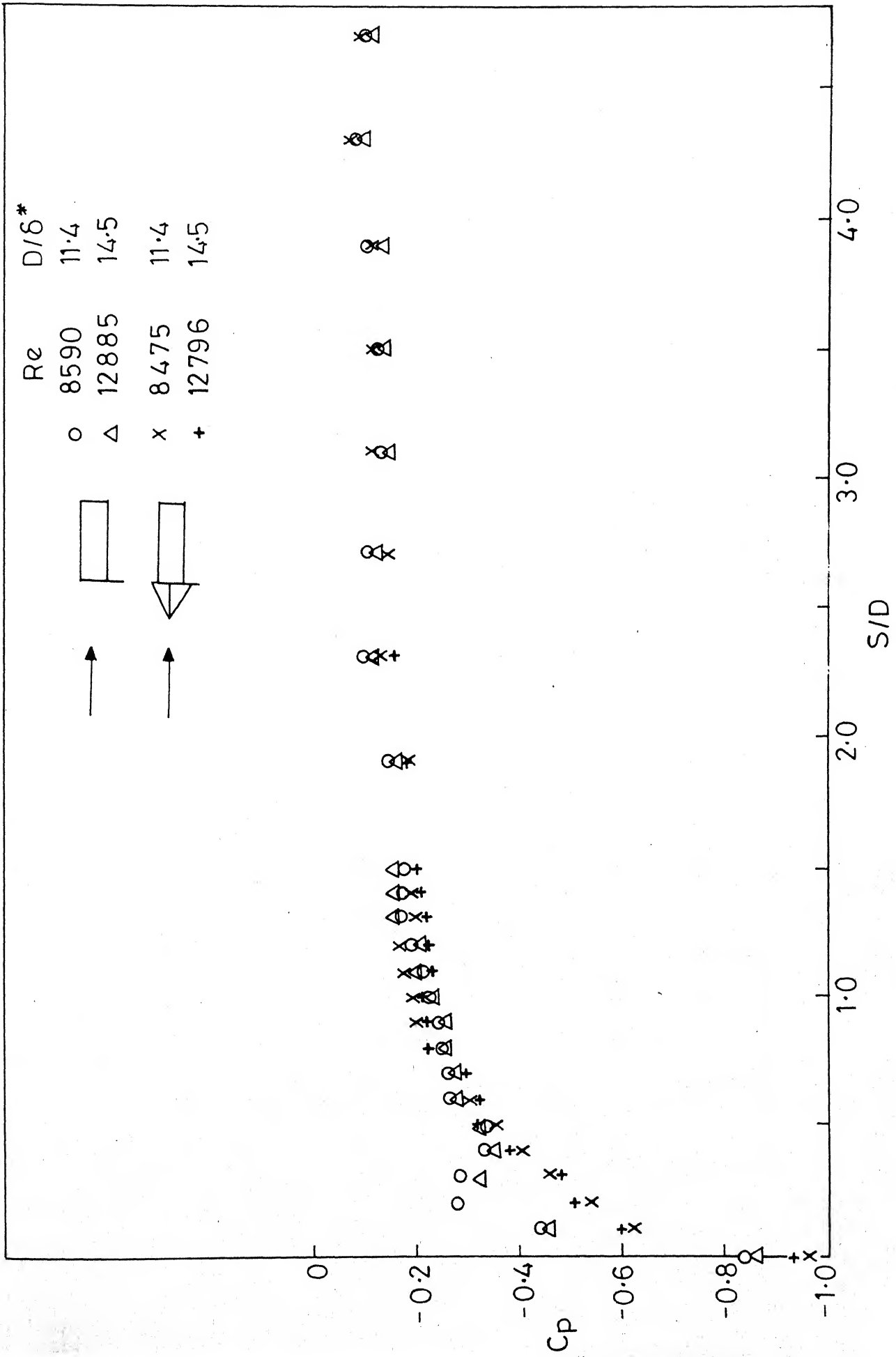


FIG. 6.30a FLOOR PRESSURE AT LEADING EDGE CORNER OF RECTANGULAR PIER
L/D=6, BR=3%. WITH AND WITHOUT PASSIVE DEVICE

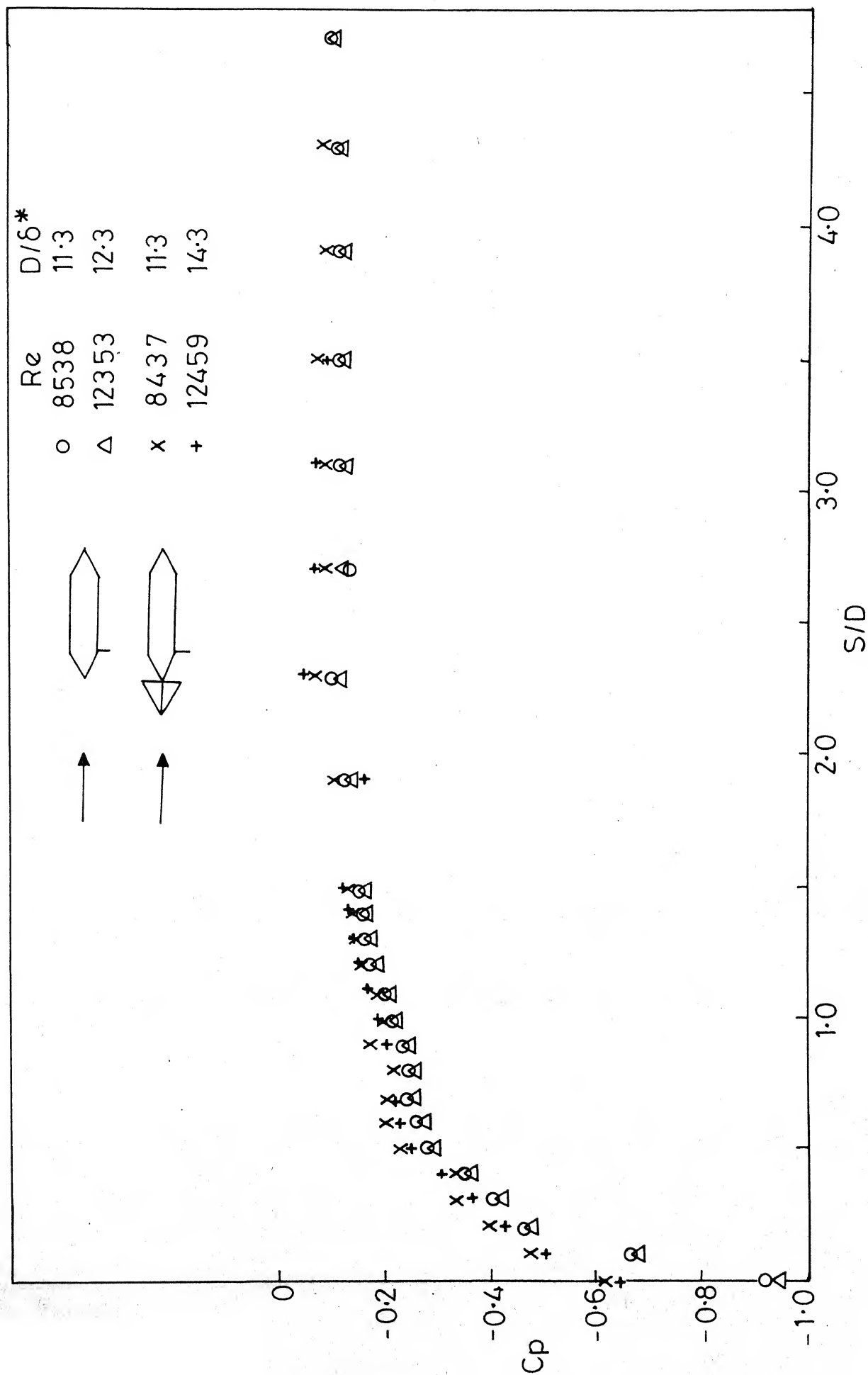


FIG. 6.30b FLOOR PRESSURE, LEADING EDGE CORNER OF WEDGE NOSE PIER
 $L/D=6$, $BR=3\%$ WITH AND WITHOUT PASSIVE DEVICE

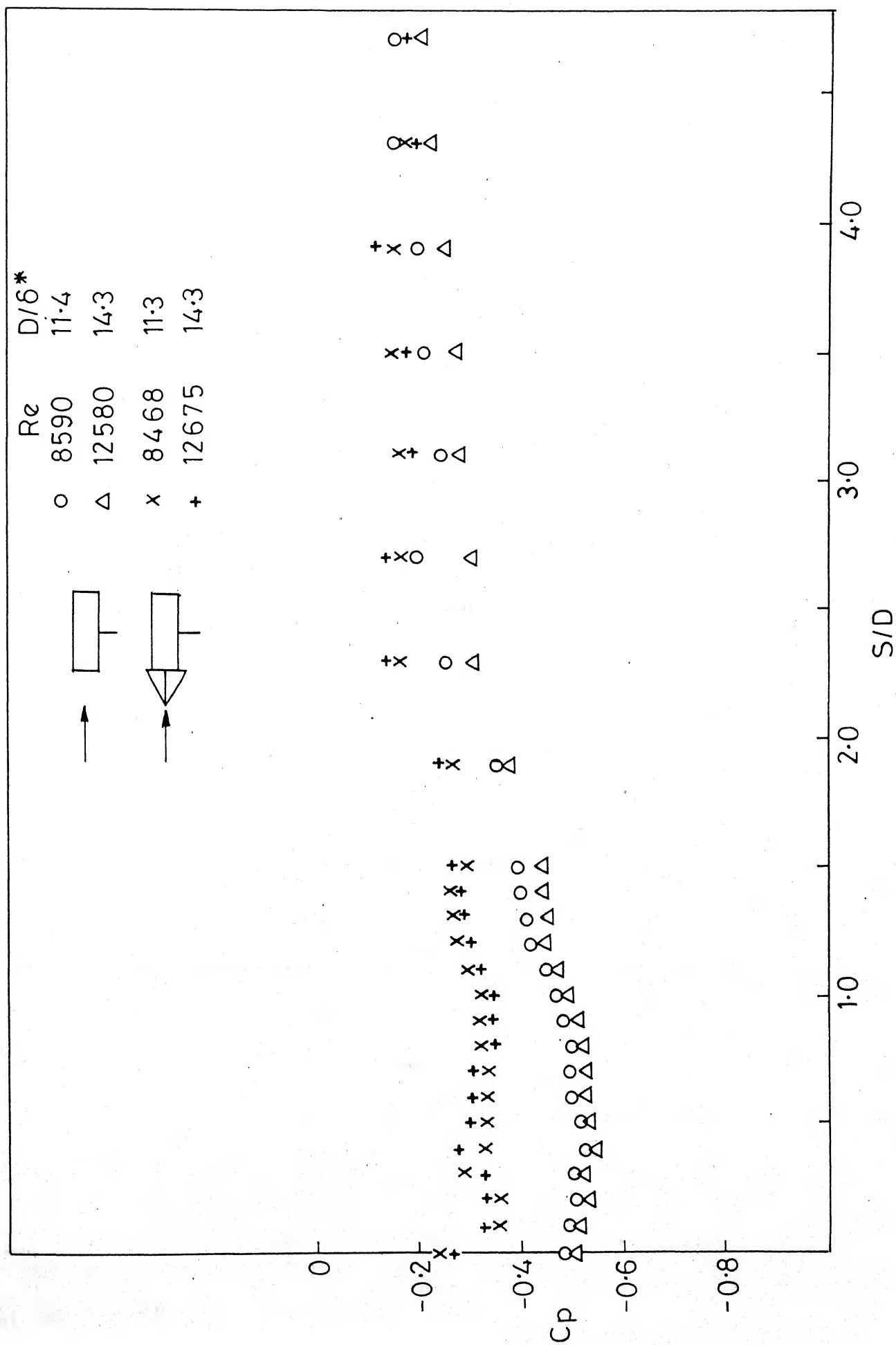


FIG.6-31a FLOOR PRESSURE AT MID SPAN OF RECTANGULAR PIER MODEL
 $L/D=6, BR=3\%$ WITH AND WITHOUT PASSIVE DEVICE

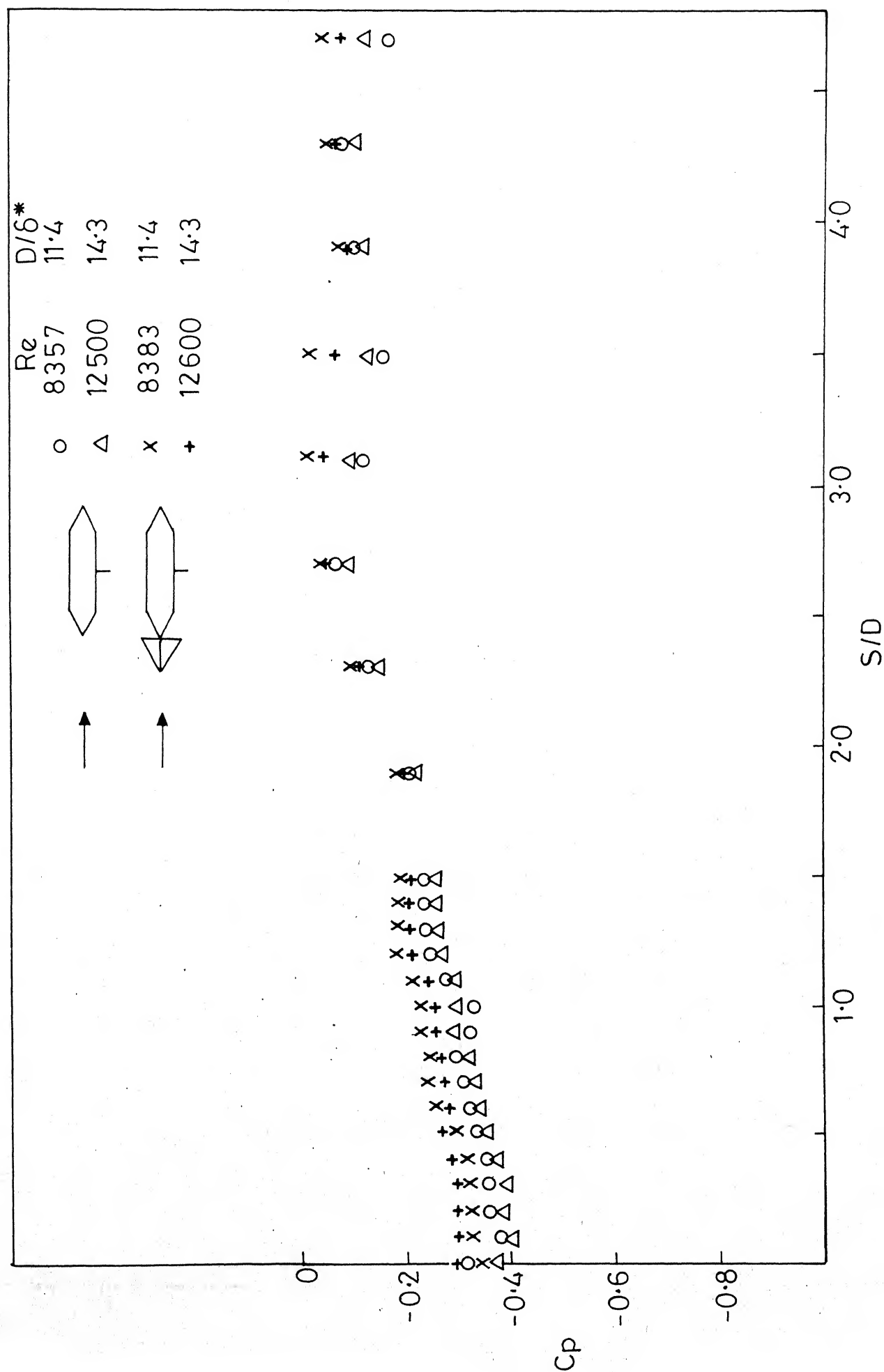


FIG-6.31b FLOOR PRESSURE AT MID SPAN OF WEDGE NOSE PIER MODEL $L/D=6, BR=3\%$
WITH AND WITHOUT DEVICE

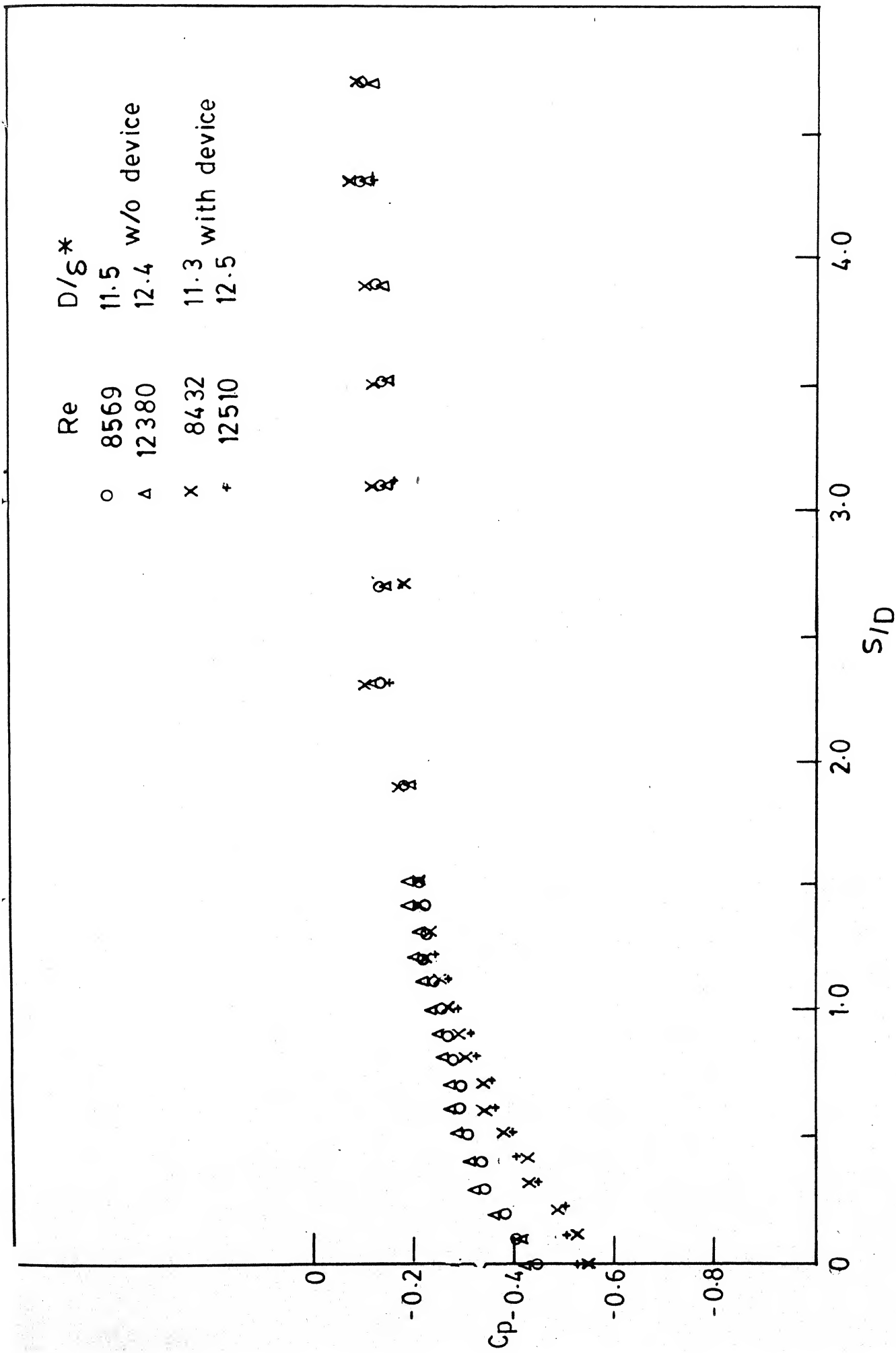


FIG.6.31c FLOOR PRESSURE AT MID SPAN OF LENTICULAR PIER MODEL $L/D=6$, $BR=3\%$
WITH AND WITHOUT PASSIVE DEVICE

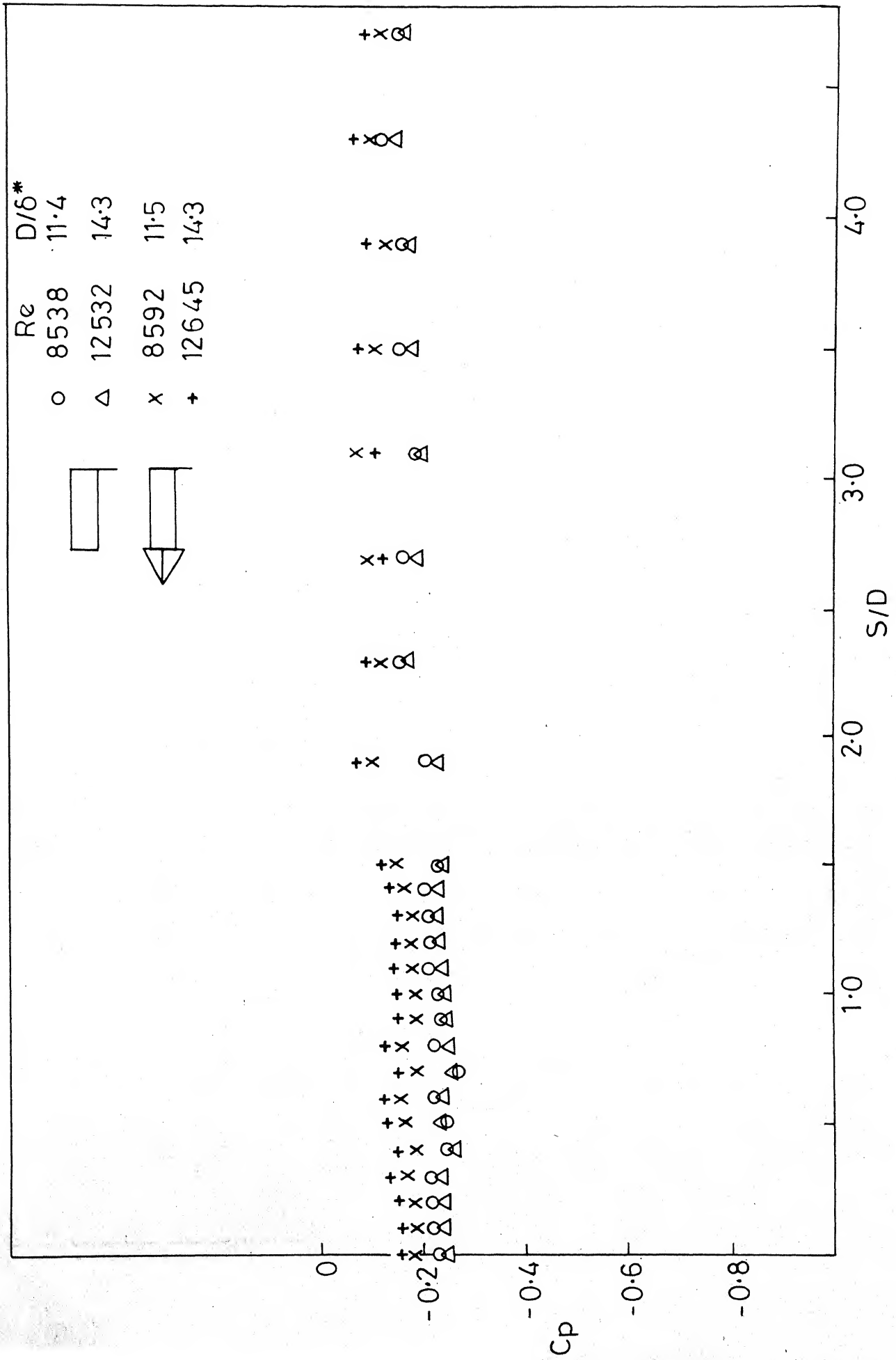


FIG.6.32a FLOOR PRESSURE TRAILING EDGE CORNER OF RECTANGULAR PIER
L/D=6, BR=3% WITH AND WITHOUT PASSIVE DEVICE

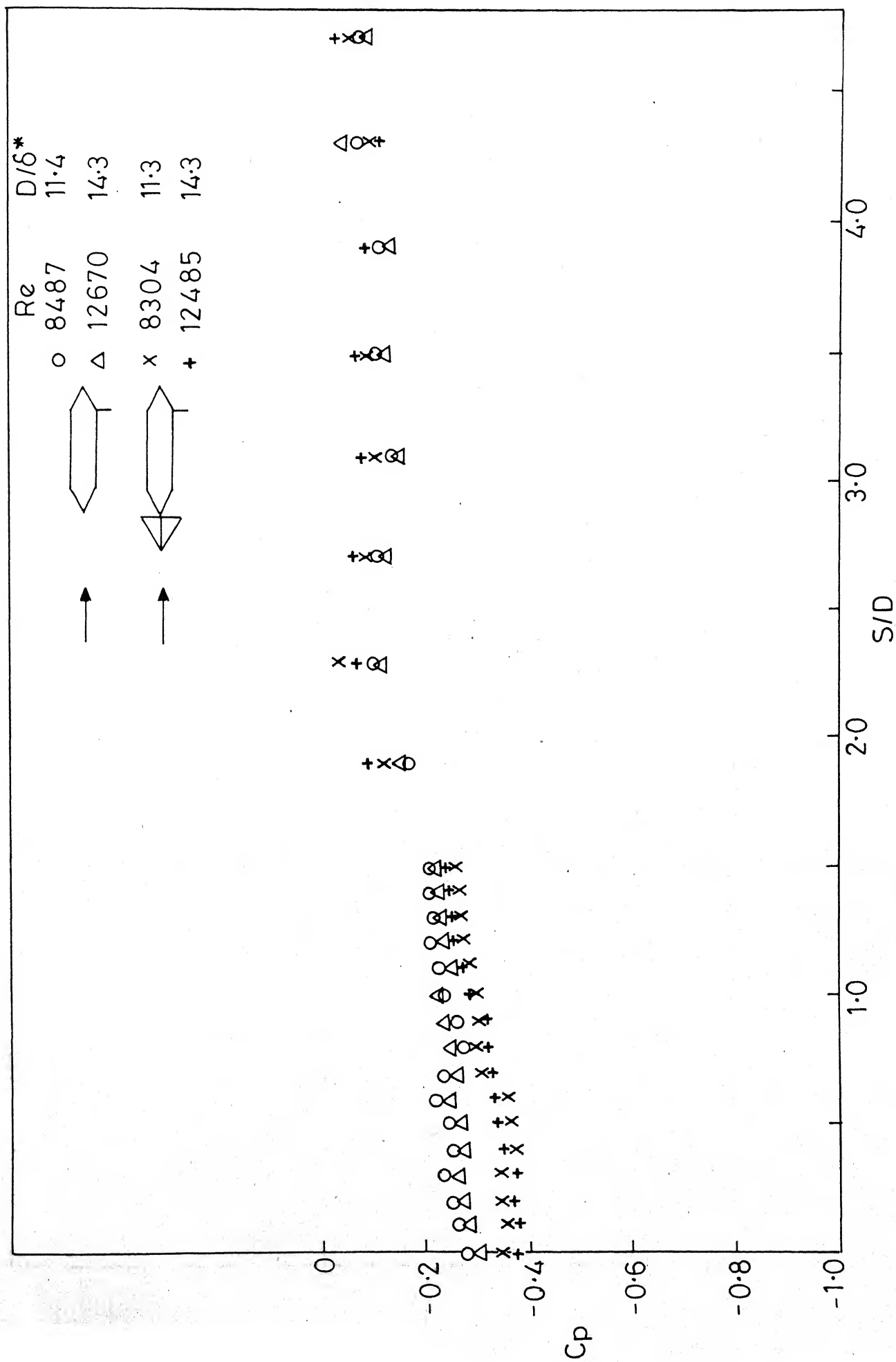


FIG.6-32b FLOOR PRESSURE AT TRAILING EDGE CORNER OF WEDGE NOSE PIER
L/D=6, BR=3%. WITH AND WITHOUT PASSIVE DEVICE

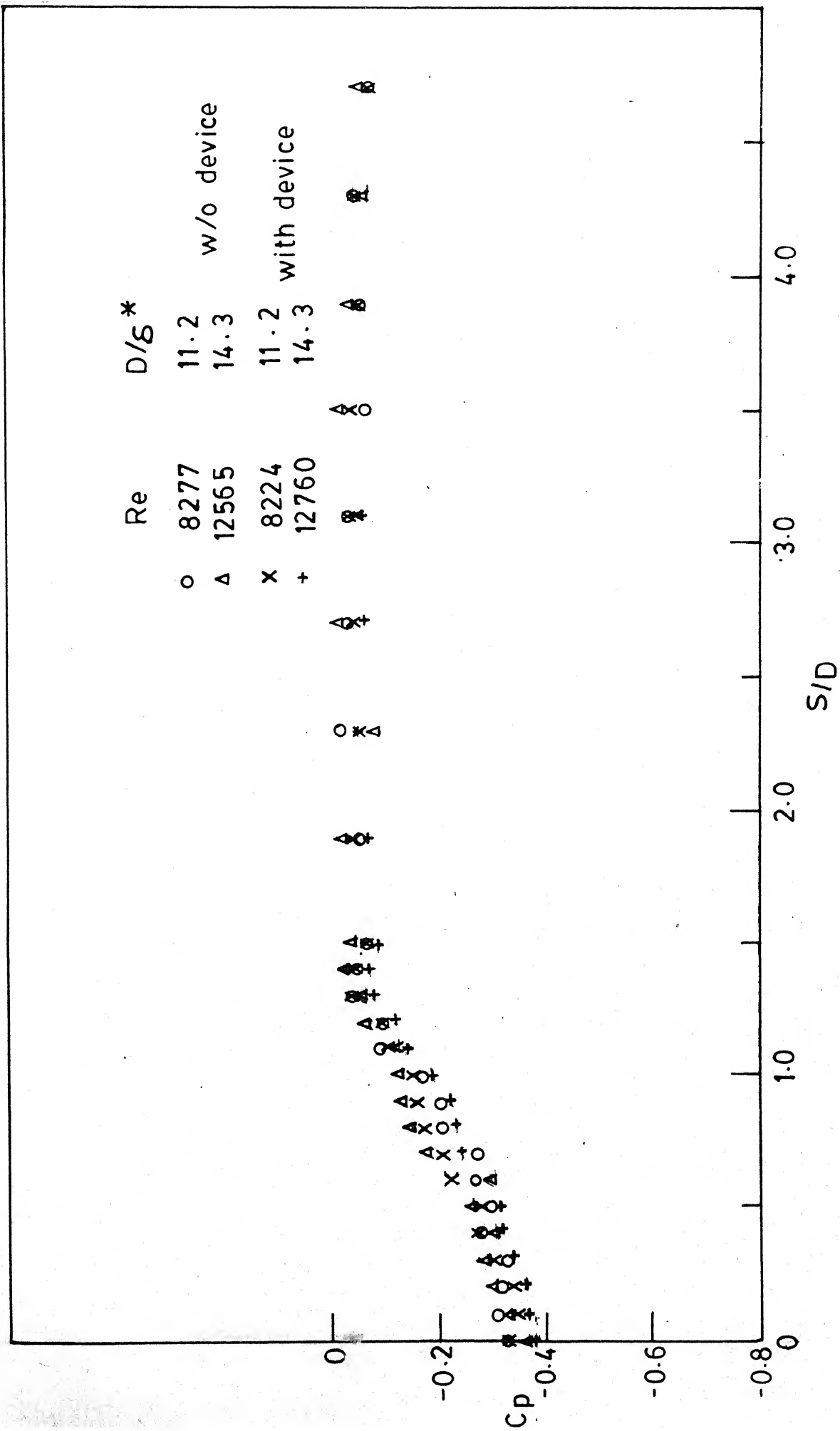


FIG. 6-33b FLOOR PRESSURE DOWN STREAM OF WEDGE NOSE PIER MODEL
 $L/D=6$, $BR=3\%$ WITH AND WITHOUT PASSIVE DEVICE

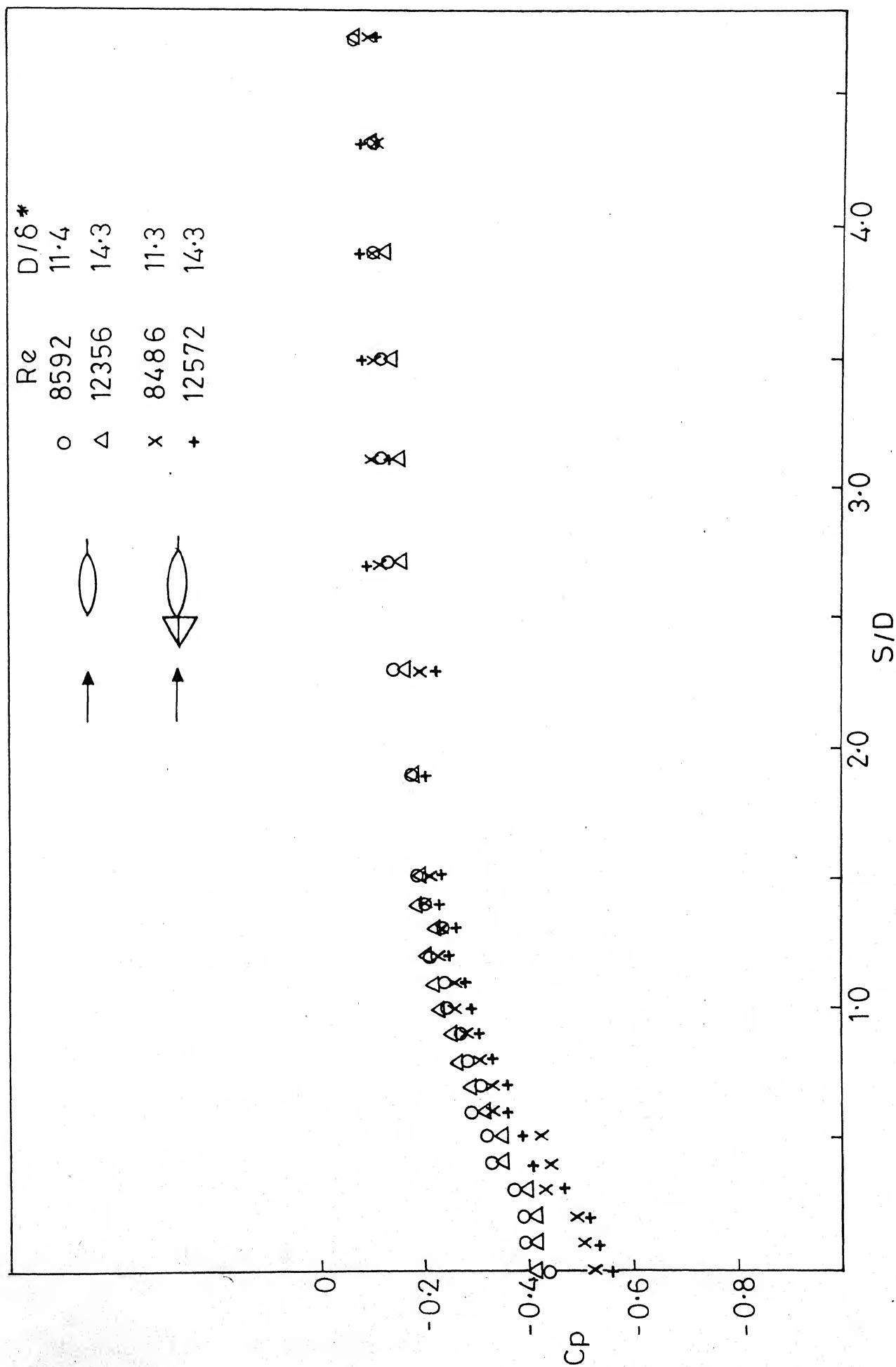
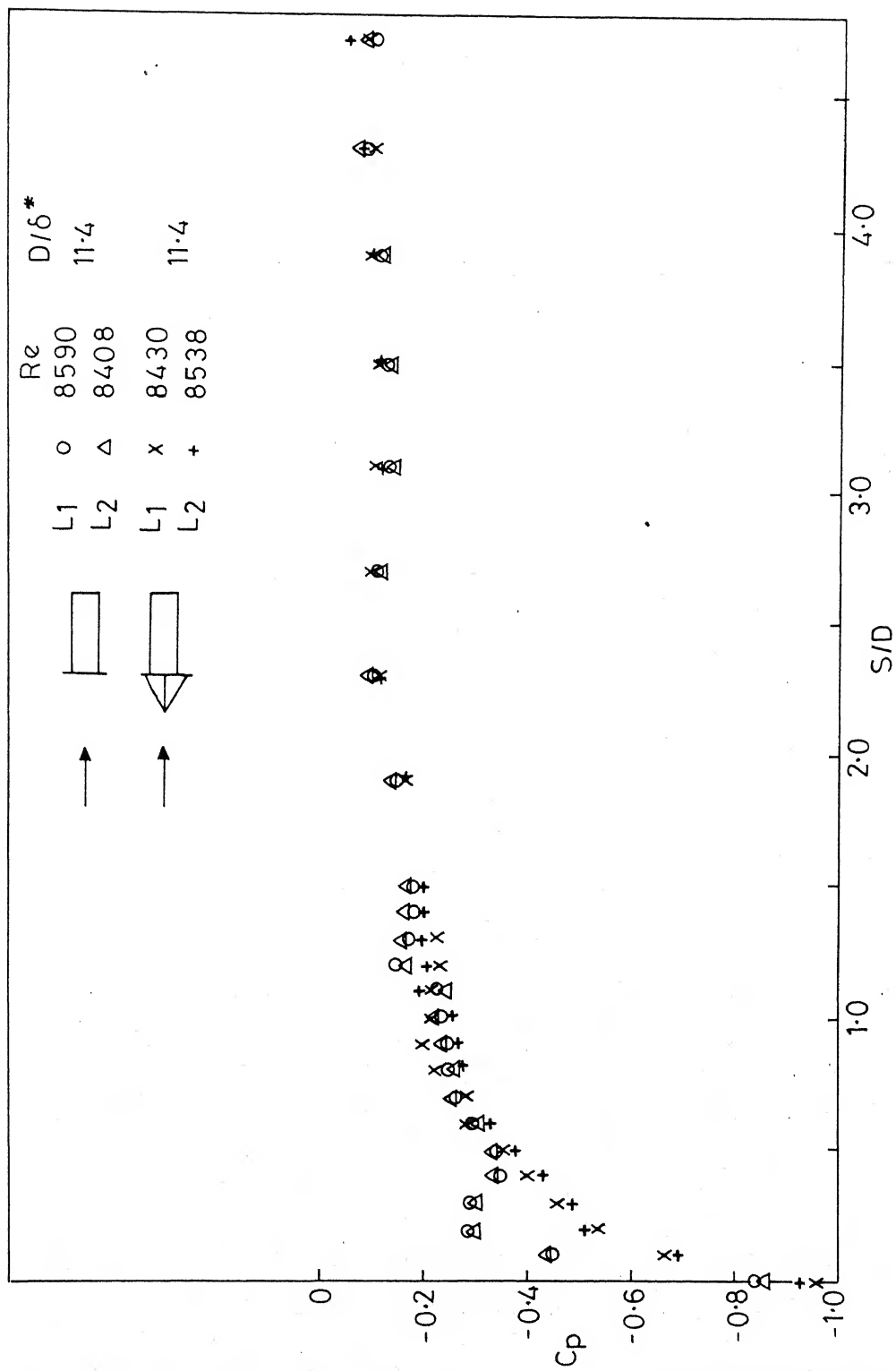
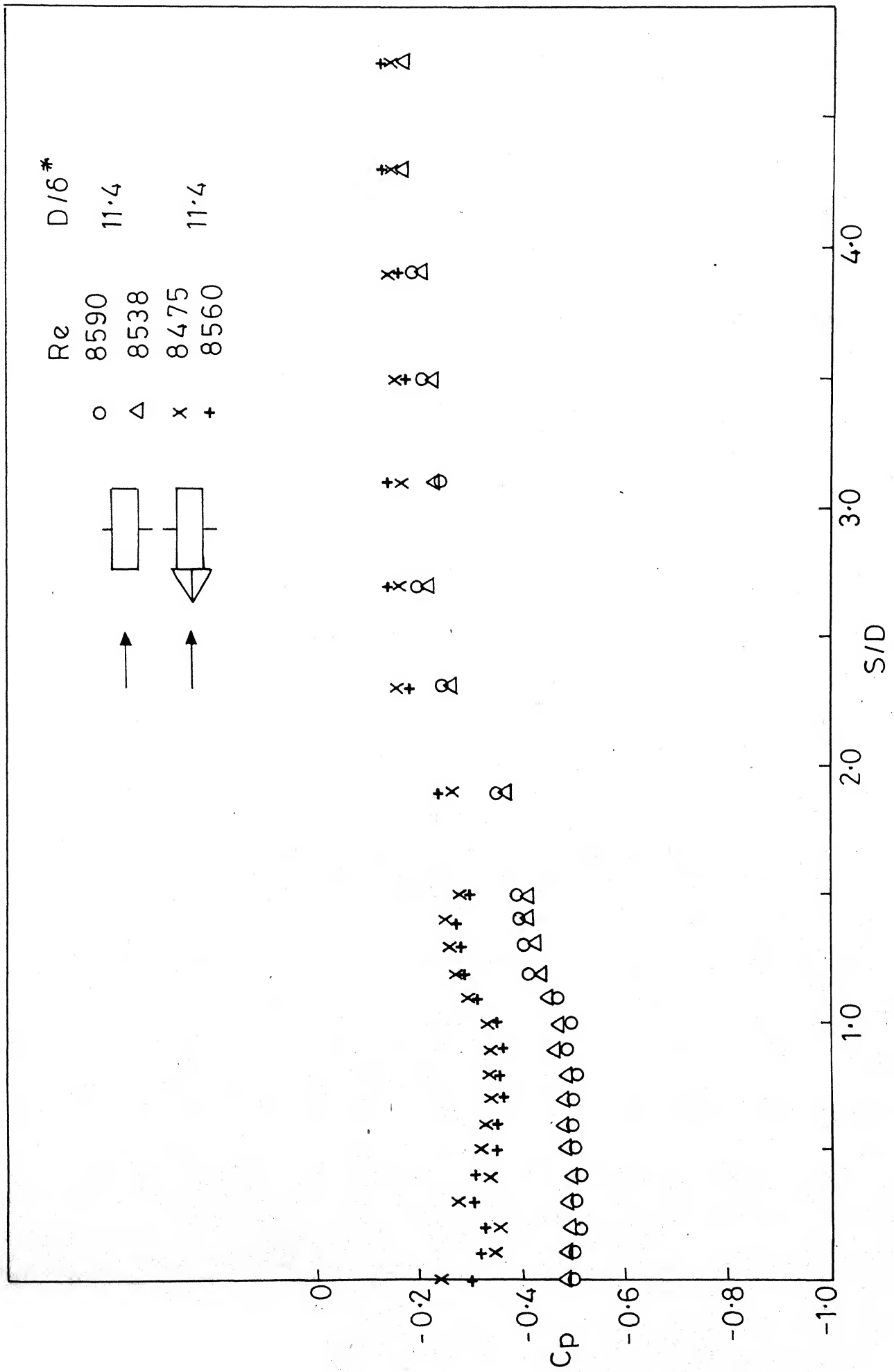


FIG.6.33c FLOOR PRESSURE DOWNSTREAM OF LENTICULAR PIER MODEL
L/D=6, BR=3% WITH AND WITHOUT PASSIVE DEVICE



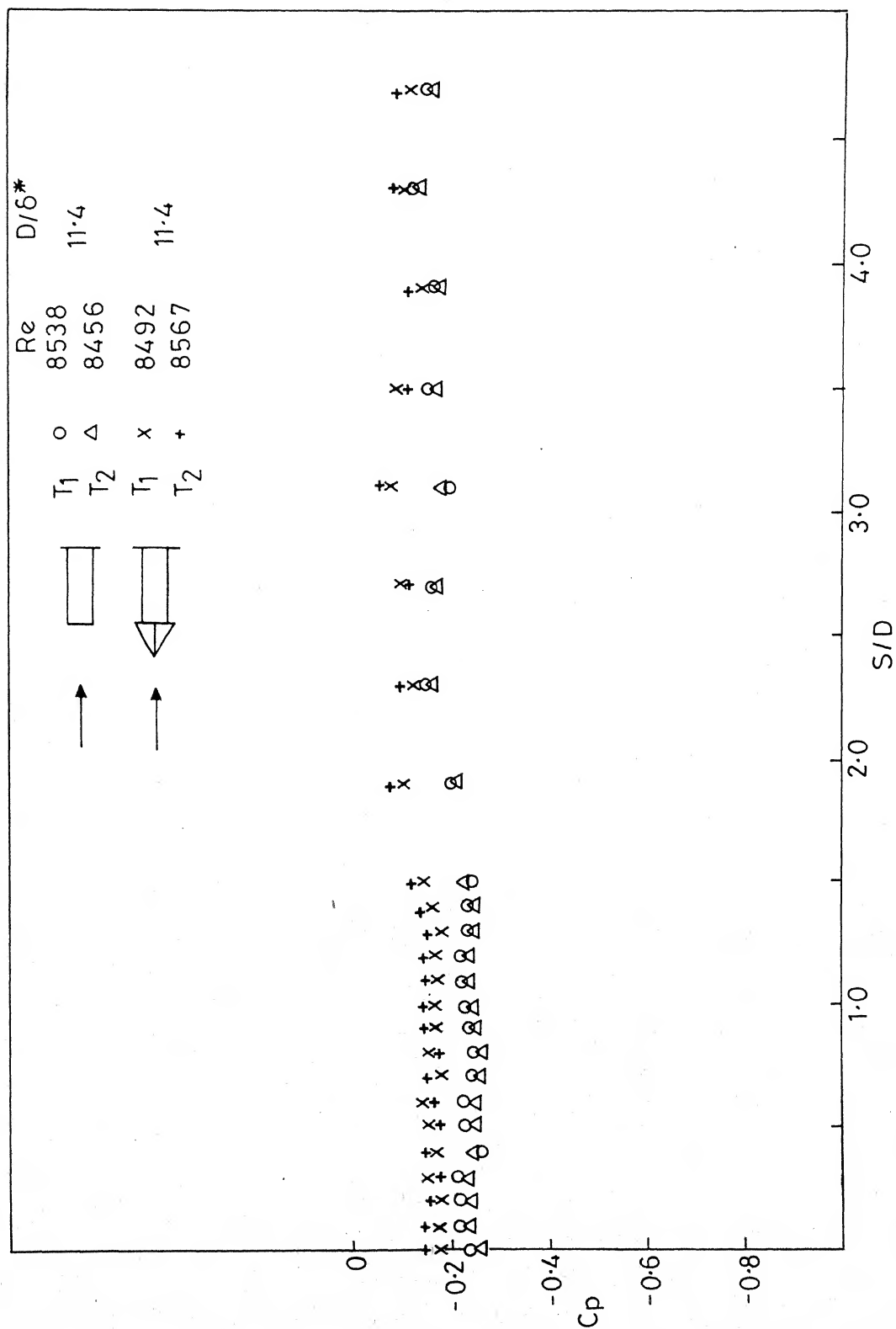
a. Leading edge corner

FIG-6-34 FLOOR PRESSURE SYMMETRY AROUND RECTANGULAR PIER $L/D=6$, $BR=3\%$
WITH AND WITHOUT PASSIVE DEVICE



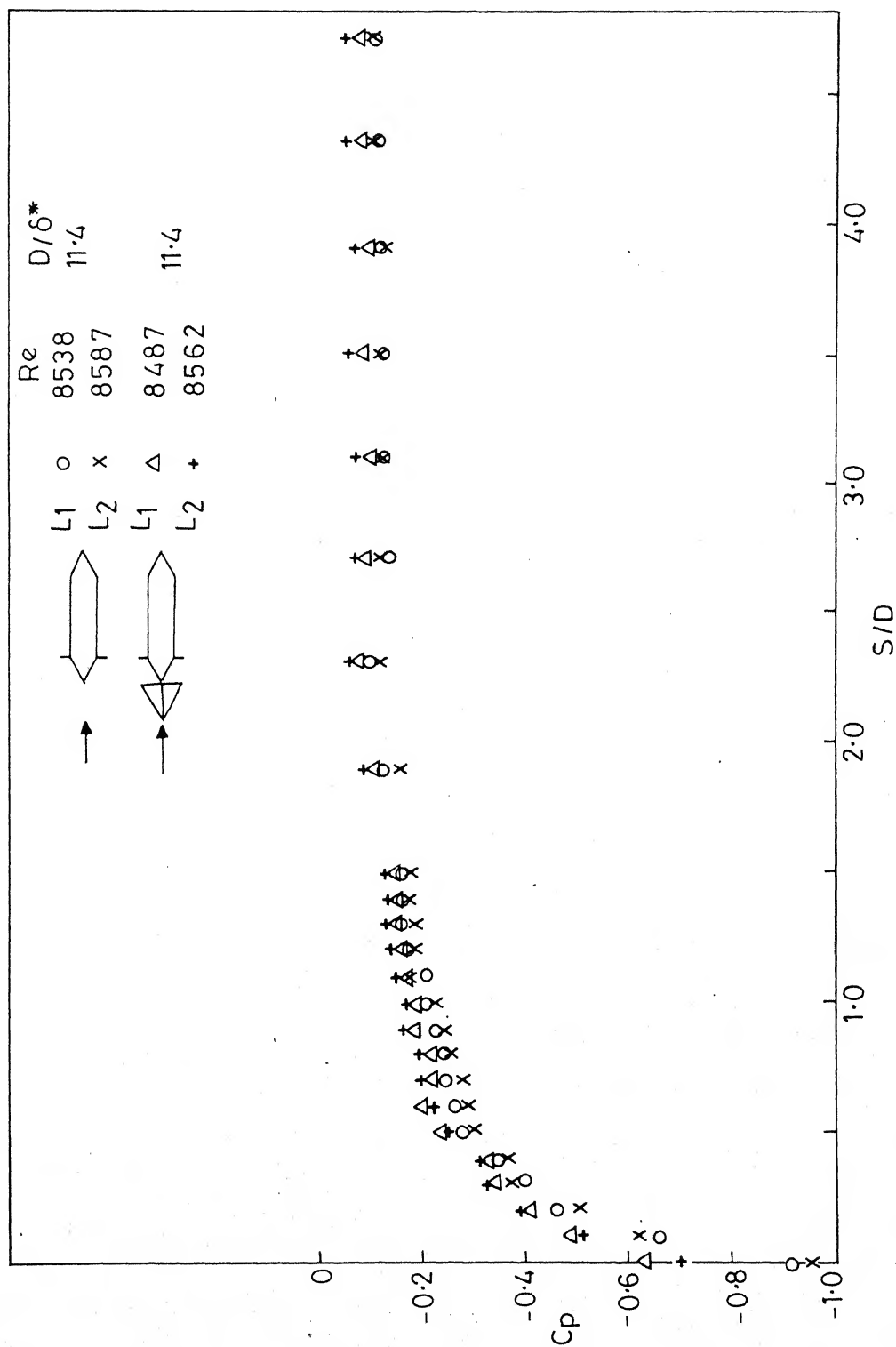
b. Mid span

FIG. 6-34 (CONTD.)



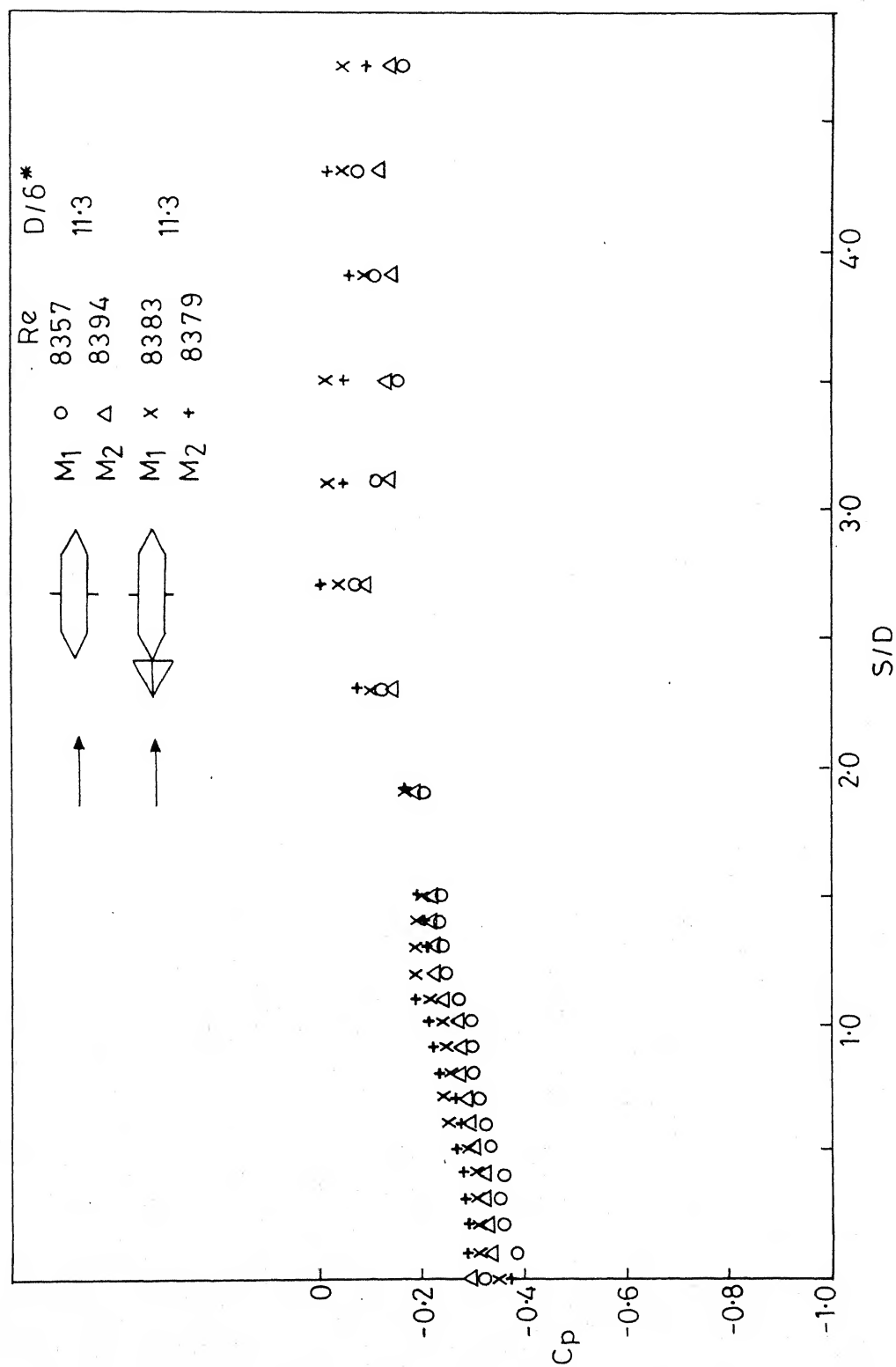
c. Trailing edge corner

FIG. 6-34 (CONTD.)



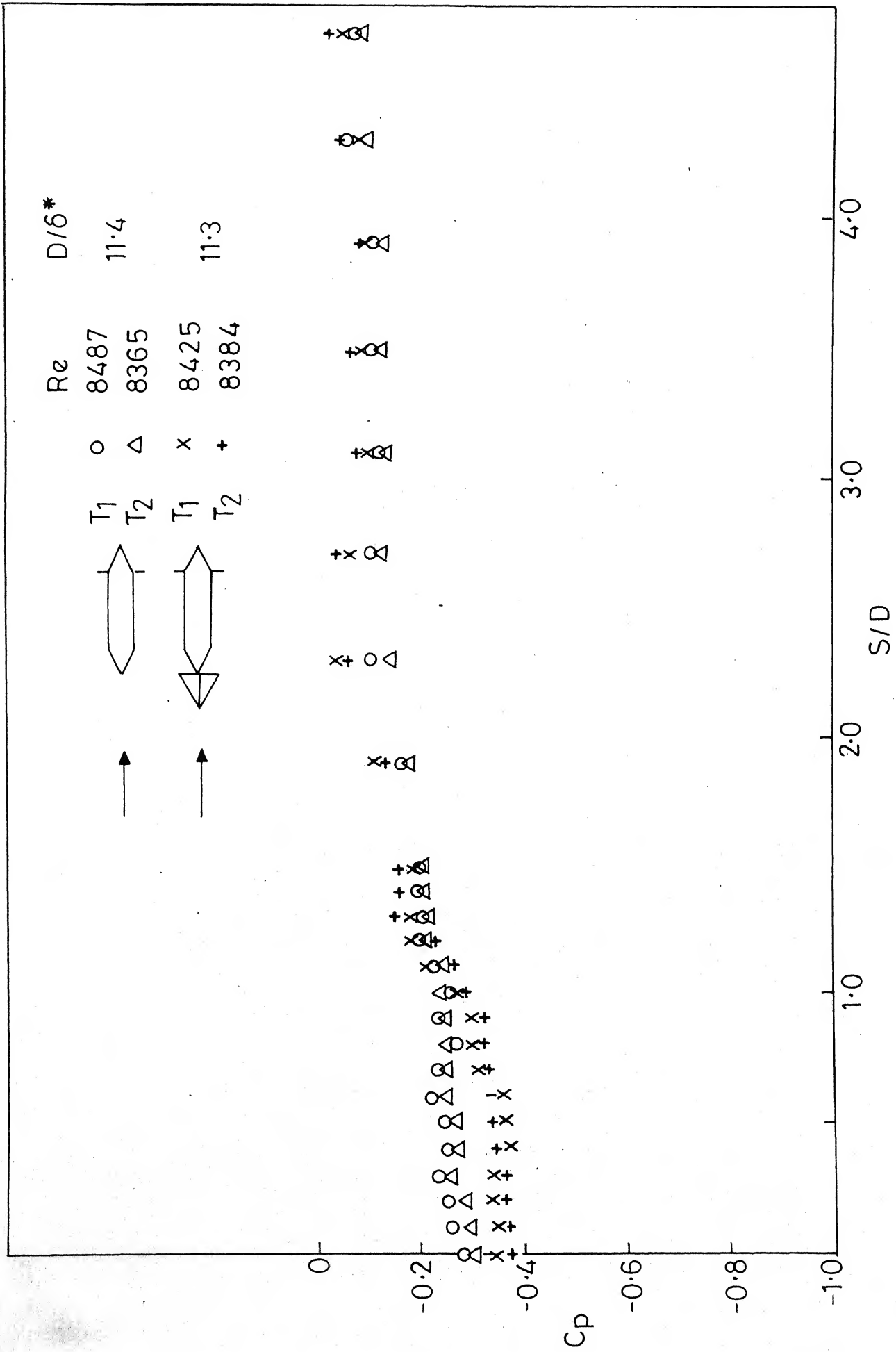
a. Leading edge corner

FIG.6.35 FLOOR PRESSURE SYMMETRY AROUND WEDGE NOSE PIER MODEL
L/D=6, BR=3% WITH AND WITHOUT DEVICE



b. Mid span

FIG. 635 (CONTD.)



c. Trailing edge corner

FIG. 6.35 (CONTD.)

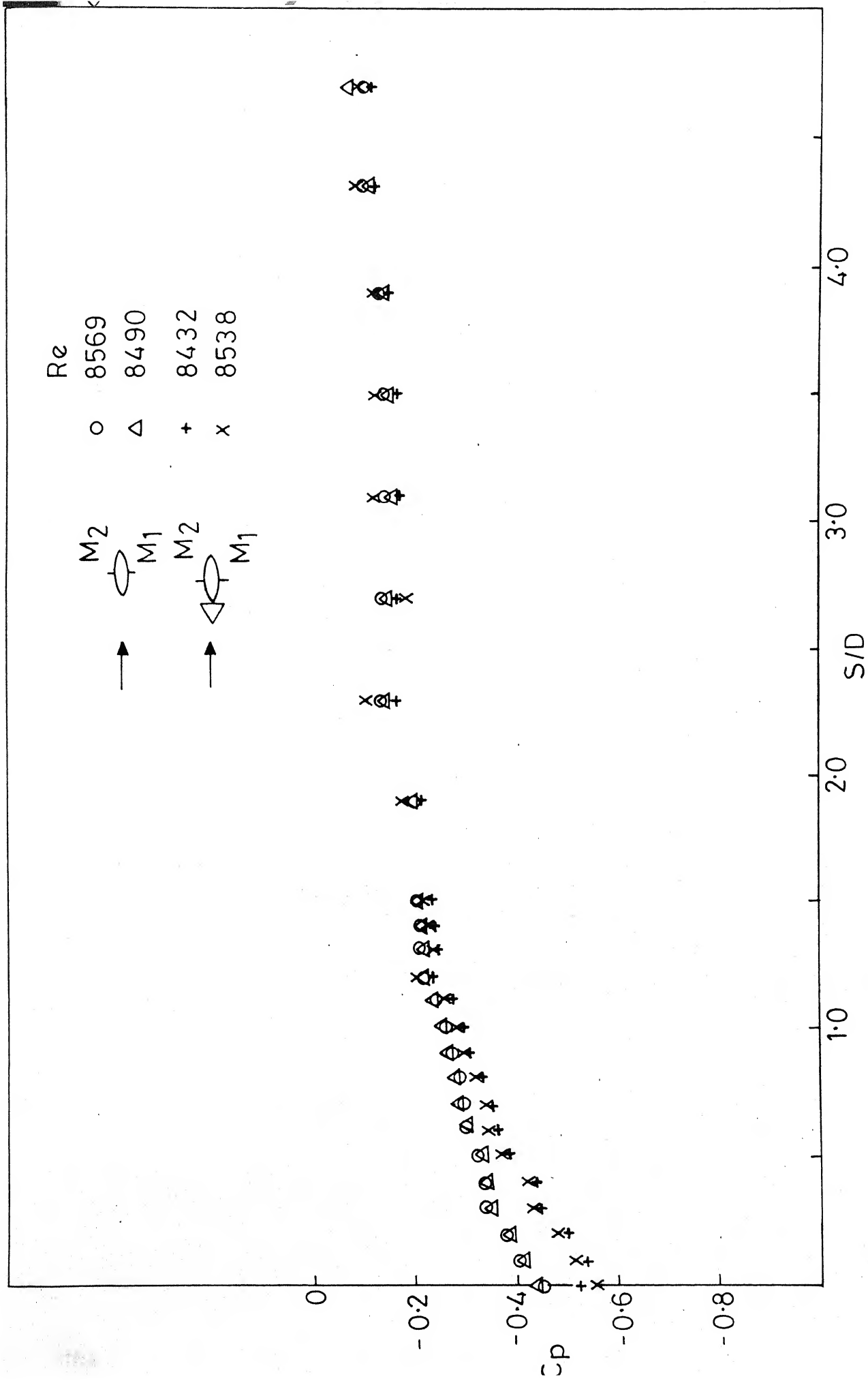


FIG. 6.35d FLOOR PRESSURE SYMMETRY AROUND LENTICULAR PIER MODEL WITH AND WITHOUT DEVICE

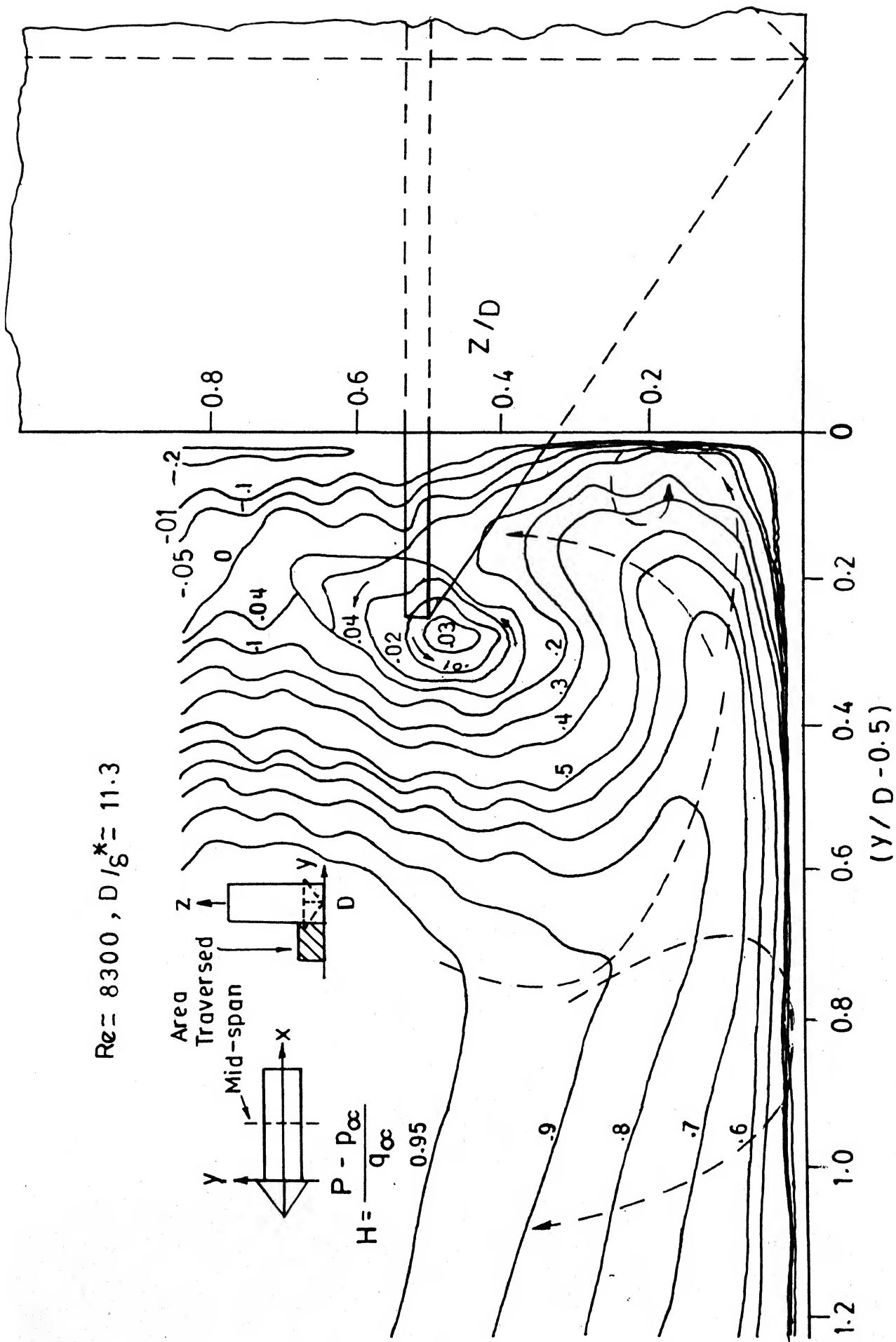


FIG6.36a TOTAL HEAD CONTOURS IN $y-z$ PLANE AT MID SPAN OF RECTANGULAR PIER MODEL WITH DEVICE

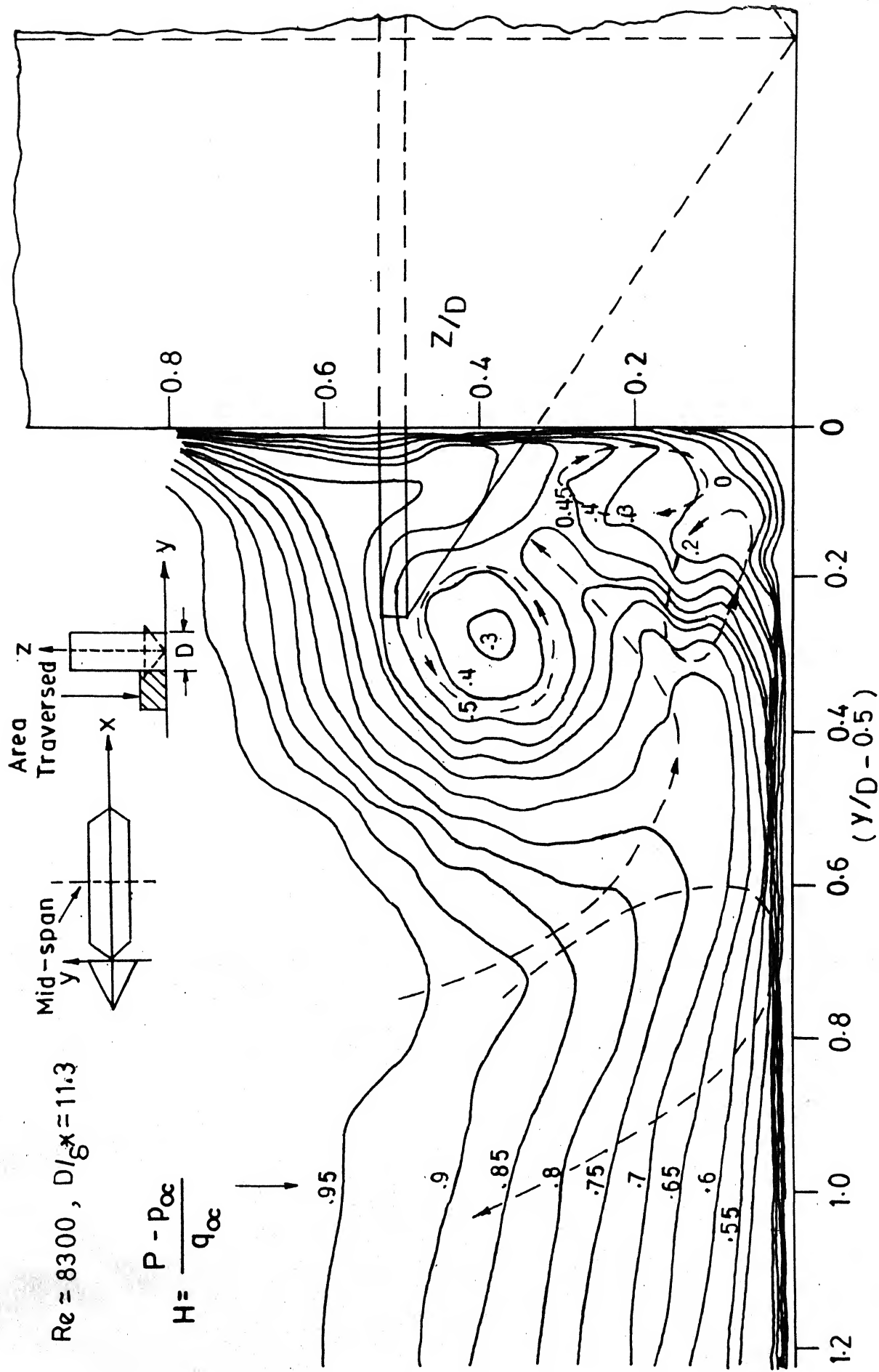


FIG 6.36b TOTAL HEAD CONTOURS IN y-z PLANE AT MID SPAN OF WEDGE NOSE
 PIER MODEL WITH DEVICE

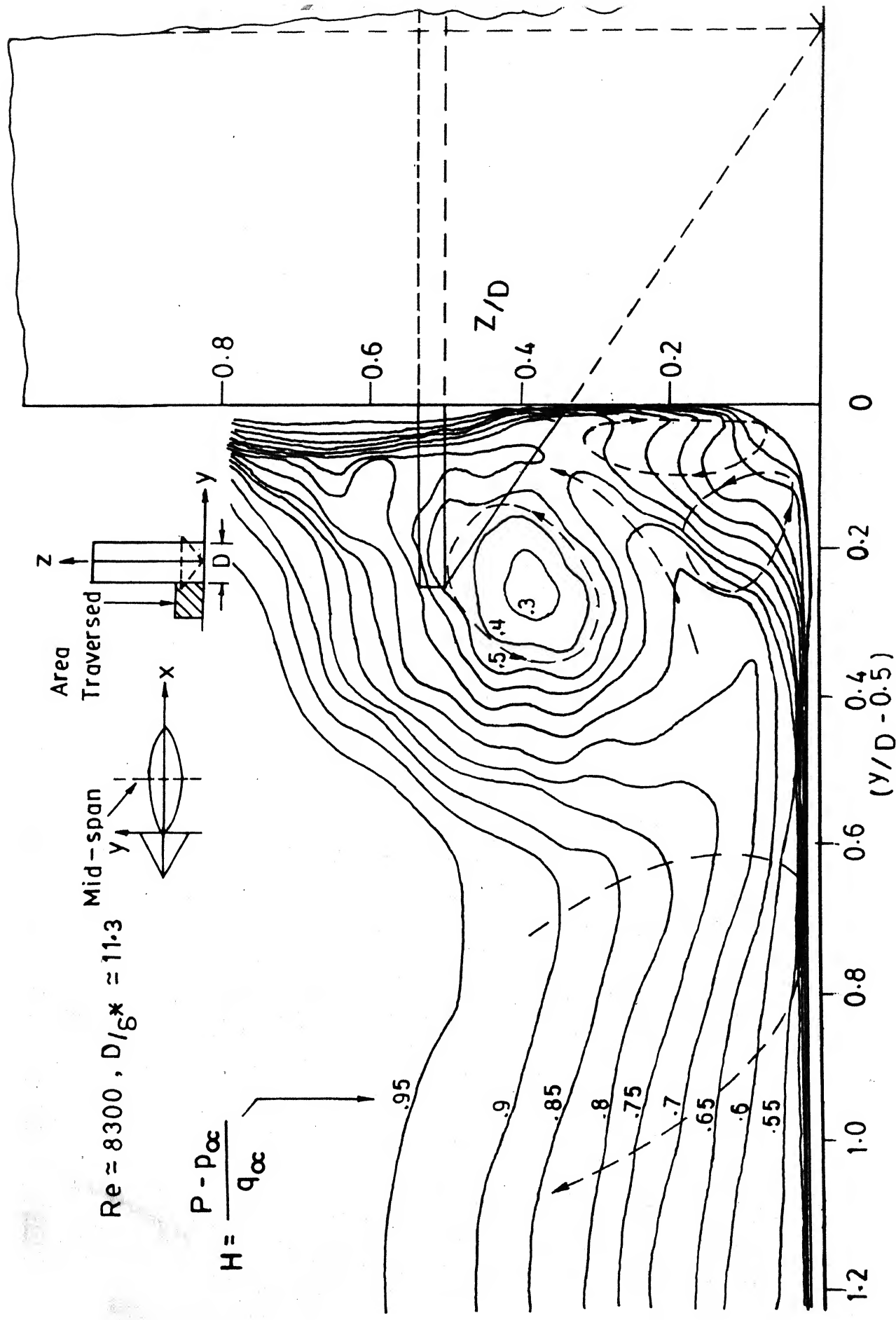


FIG.6.36c TOTAL HEAD CONTOURS IN Y-Z PLANE AT MID SPAN OF LENTICULAR PIER MODEL WITH DEVICE

Th.

629.1323

Sh 23 e

A 106218